# Anisotropic nonlinear PDE models and dynamical systems in biology

## Lisa Maria Kreusser

Murray Edwards College

Department of Applied Mathematics and Theoretical Physics
University of Cambridge

A thesis submitted for the degree of
*Doctor of Philosophy*

August 2019

# Declaration

This dissertation is the result of my own work and includes nothing which is the outcome of work done in collaboration except as declared in the Preface and specified in the text. It is not substantially the same as any that I have submitted, or, is being concurrently submitted for a degree or diploma or other qualification at the University of Cambridge or any other university or similar institution. I further state that no substantial part of my dissertation has already been submitted, or, is being concurrently submitted for any such degree, diploma or other qualification at the University of Cambridge or any other university or similar institution.

<div align="right">

Lisa Maria Kreusser

August 2019

</div>

# Summary

This thesis deals with the analysis and numerical simulation of anisotropic nonlinear partial differential equations (PDEs) and dynamical systems in biology. It is divided into two parts, motivated by the simulation of fingerprint patterns and the modelling of biological transport networks.

The first part of this thesis deals with a class of interacting particle models with anisotropic repulsive-attractive interaction forces and their continuum counterpart. These models are motivated by the simulation of fingerprint databases, which are required in forensic science and biometric applications. In existing interacting particle models, the forces are isotropic and the continuum limits of these particle models are given by nonlocal aggregation equations with radially symmetric potentials. The central novelty in the models we consider is an anisotropy induced by an underlying tensor field. This innovation does not only lead to the ability to describe real-world phenomena more accurately, but also renders their analysis significantly harder compared to their isotropic counterparts. We discuss the role of anisotropic interaction, study the steady states and present a stability analysis of line patterns. We also show numerical results for the simulation of fingerprints, based on discrete and continuum modelling approaches.

The second part of this thesis focuses on a new dynamic modeling approach on a graph for biological transportation networks which are ubiquitous in living systems such as leaf venation in plants, blood circulatory systems, and neural networks. We study the existence of solutions to this model and propose an adaptation so that a macroscopic system can be obtained as its formal continuum limit. For the spatially two-dimensional rectangular setting we prove the rigorous continuum limit of the constrained energy functional as the number of nodes of the underlying graph tends to infinity and the edge lengths shrink to zero uniformly. We also show the global existence of weak solutions of the macroscopic gradient flow. Results of numerical simulations of the discrete gradient flow illustrate the convergence to steady states, their non-uniqueness as well as their dependence on initial data and model parameters. Based on this model we propose an adapted model in the cellular context for leaf venation, investigate the model analytically and show numerically that it can produce branching vein patterns.

*To my parents.*

# Acknowledgements

First and foremost, I would like to thank my supervisors Peter A. Markowich and Carola-Bibiane Schönlieb, and my co-supervisor Bertram Düring for introducing me to interesting, challenging research problems. I am very grateful to Peter A. Markowich for his belief in me, for his support and for motivating me in my own creative thinking. I cannot thank Carola-Bibiane Schönlieb enough for all her mentorship, her support and for making numerous research visits abroad possible. I would like to thank Bertram Düring for his mentorship and his support. I am also very grateful to José A. Carrillo for sparking my interest in PDEs and supervising a research internship during my undergraduate, for his mentorship and his support.

Further, I would like to thank all my collaborators for our fruitful work and discussions: Martin Burger, José A. Carrillo, Bertram Düring, Carsten Gottschlich, Jan Haskovec, Stephan Huckemann, Henrik Jönsson, Peter A. Markowich and Carola-Bibiane Schönlieb for the research included in this thesis, and Andrea Bertozzi, Alexander Brächer, Martin Burger, Irene Fonseca, Axel Klar, Robert I. McLachlan, Christian Offen, Stanley J. Osher, Shamsul Qamar, Carola-Bibiane Schönlieb, Andreas Seidel-Morgenstern, Matthew Thorpe, Claudia Totzeck, Oliver Tse, Erik von Harbou and Bao Wang for published/ongoing research not presented in this thesis.

I am thankful for being part of a stimulating and friendly environment at the Cambridge Faculty of Mathematics, in particular through the Cambridge Centre for Analysis, the Cambridge Kinetic Group, the Cambridge Image Analysis Group and the Cambridge SIAM-IMA Student Chapter, and there are too many individuals to mention in person, both faculty, postdocs, PhD students and staff. I am grateful to Andrea Bertozzi, Irene Fonseca, Piotr Gwiazda, Robert I. McLachlan, Andrew Stuart and Agnieszka Swierczewska-Gwiazda for hosting me during my research visits at Caltech, Carnegie Mellon University, IMPAN, Massey University and UCLA. I would also like to thank Pierre Degond and Edriss Titi for examining this thesis.

I was supported by the EPSRC, the MSCA-RISE projects CHiPS and NoMADS, the Cambridge Commonwealth, European & International Trust, the German Academic Scholarship Foundation, the Cambridge Centre for Analysis, the Cambridge Philosophical Society, the CCIMI, Murray Edwards College, SIAM and IMA.

Finally, special thanks go to my family and friends for all their support.

# Preface

A detailed statement of originality and contribution is provided at the beginning of each chapter and a summary is given below:

- Chapter 1 is my own review and partly based on our recent paper [BDK$^+$18] in collaboration with Martin Burger, Bertram Düring, Peter A. Markowich and Carola-Bibiane Schönlieb, and our paper [HKM19a] in collaboration with Jan Haskovec and Peter A. Markowich.

- Chapter 2 is original research based on the journal article [BDK$^+$18] in collaboration with Martin Burger, Bertram Düring, Peter A. Markowich and Carola-Bibiane Schönlieb. This paper was published in Mathematical Models and Methods in the Applied Sciences in 2018.

- Chapter 3 is adapted from the journal article [DGH$^+$19] in collaboration with Bertram Düring, Carsten Gottschlich, Stephan Huckemann and Carola-Bibiane Schönlieb, and was published in the Journal of Mathematical Biology in 2019.

- Chapter 4 is original research, based on the paper [CDKS18] in collaboration with José A. Carrillo, Bertram Düring and Carola-Bibiane Schönlieb, and published in the SIAM Journal on Applied Dynamical Systems.

- Chapter 5 is original research, based on the paper [CDKS19] in collaboration with José A. Carrillo, Bertram Düring and Carola-Bibiane Schönlieb, and to be submitted for publication.

- Chapter 6 is original research and adapted from the paper [HKM19a] in collaboration with Jan Haskovec and Peter A. Markowich, and to appear in Communications in Mathematical Sciences.

- Chapter 7 is original research, adapted from the paper [HKM19b] in collaboration with Jan Haskovec and Peter A. Markowich, and was published in Communications in Partial Differential Equations in 2019.

- Chapter 8 is based on the paper [HJKM19] in collaboration with Jan Haskovec, Henrik Jönsson and Peter A. Markowich, and to appear in the Proceedings of the Royal Society A.

# Contents

# List of Figures

# List of Tables

# Chapter 1

# Introduction

Partial differential equations (PDEs) and dynamical systems are essential tools for the mathematical modelling of biological, socio-economic and physical processes. The use of PDE models in these applications has become an active research area in the last decades, allowing us to extend the boundaries of mathematical knowledge and advancing the understanding of real-world problems of practical importance. Through mathematical analysis and computer simulations, we can gain new insights into the qualitative properties of the underlying mathematical models which result in a better understanding of complex phenomena in nature such as biological pattern formation. Equally important, these new and challenging PDE models lead to intra-disciplinary research, involving modelling, PDE theory, dynamical systems, graph theory and numerical simulations.

In this thesis, we focus on PDEs and dynamical system for studying pattern formation in nature. Many of these mathematical models can be derived from microscopic systems. Examples of microscopic modelling approaches include models describing the interaction of a large number of individuals or graph-based models consisting of a large number of nodes and edges. For the analysis of these models, it is often very useful to consider a coarse graining procedure resulting in the corresponding macroscopic model, usually based on nonlinear PDEs. Since pattern formation in nature is often anisotropic, we consider anisotropic models for describing the formation of these complex patterns more accurately.

This thesis is divided into two parts: Part I (Chapters 2–5) is motivated by the simulation of fingerprint patterns. We consider a class of interacting particle models with anisotropic repulsive-attractive interaction forces and their continuum counterpart. In Part II (Chapters 6–8), we study mathematical models for biological

transportation networks describing living systems such as leaf venation in plants, blood circulatory systems, and neural networks. The mathematical formulation is based on a dynamic modelling approach on a graph in the discrete setting and its continuous counterpart which is rigorously proven in this thesis.

## 1.1    Anisotropic interaction equations

Nonlocal interaction models are mathematical models describing the collective behaviour of large numbers of individuals where each individual can interact not only with its close neighbours but also with individuals far away. These models serve as basis for biological aggregation and have given us many tools to understand the fundamental behaviour of collective motion and pattern formation in nature. For instance, these mathematical models are used to explain the complex phenomena observed in nature [BCC+08a, BT11, Bir07, CDF+03, CFRT10, CCG+10, DM08, DSKT01, DCBC06, EKWG98, MEK99, PEK99, PS84]. Some continuum models have been derived from individual based descriptions [BCC08b, BDP06, BCM00, BCM07, FHK11, TB04, TBL06, vBUKB12], see also the reviews [CFTV10, KCB+13], leading to an understanding of the stability of patterns at different levels [ABCvB14, BSK+15, CHM14a, CHM14b, KSUB11].

### 1.1.1    Collective behaviour in nature

There are many examples both from the living and the non-living world for the rich behaviour in systems consisting of a large number of interacting agents of similar size and body type. Examples of collective behaviour in macroscopic living systems include swarms of insects (locusts, ants, bees, . . . ), schools of fish and flocks of birds, while on the microscopic level common phenomena include the collective behaviour of cells and bacteria. Mathematical models provide a promising starting point for understanding the formation of these complex patterns in nature and the behavioural traits of the individuals.

One of the key features of many of these models is the social communication between individuals at different scales, i.e. each individual can interact not only with its neighbours but also with individuals further away. This can be described by short- and long-range interactions [BT11, EKWG98, MEK99].

An example for an anisotropic interaction model is the Kücken-Champod model [KC13] for simulating fingerprint patterns based on the interaction of certain cells.

(A) Marching locusts      (B) Colony of army ants      (C) School of fish



(D) Swarms of birds      (E) Herd of zebra      (F) Swarming of E. coli
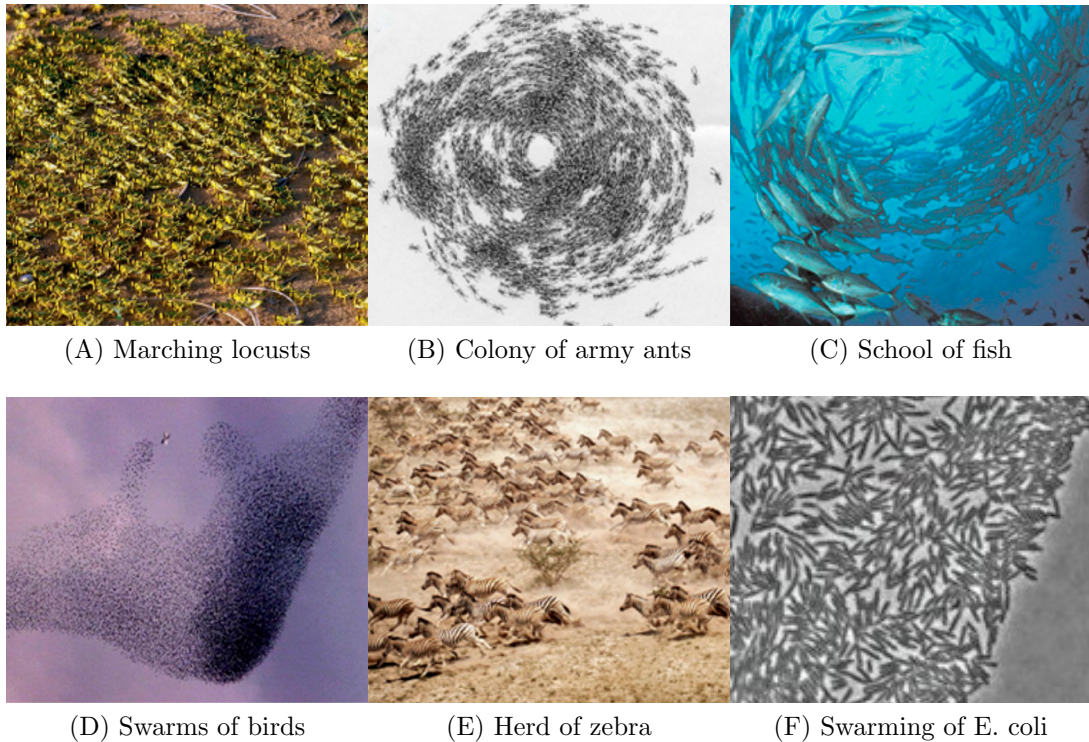
Figure 1.1: Collective behavior in nature. Figure from [LXXZ18].

The simulation of fingerprints is not only of great interest in the biological community, but also in forensic science and increasingly in biometric applications where large fingerprint databases are required for developing, validating and comparing the performance of fingerprint identification algorithms. Unfortunately, the collection of large databases of real fingerprints is usually very cost-intensive, requires time and effort, and in many countries is constrained by laws addressing data protection and privacy. Therefore it is vital to simulate large fingerprint databases on a computer.

An extensive literature [CLMS16, DM86, Irm10, KC13, MM89, MJM92, Wer11] in the biological community suggests that fingerprint patterns are formed due to the interaction of mechanical stress, trophic factors from incoming nerves and interactions between so-called Merkel cells. Merkel cells are epidermal cells that appear in the volar skin at about the 7th week of pregnancy. From that time onward they start to multiply and organise themselves in lines exactly where the primary ridges arise [KC13].

The development of fingerprints can be described by three phases [KC13]. In the first phase, growth forces in the epidermis and shrinkage of volar pad create

3

compressive mechanical stress, modelled by Kücken and Newell [KN04, KN05]. The rearrangement of Merkel cells from a random configuration into parallel ridges along the lines of smallest compressive stress forms the second phase. This phase can be regarded as the actual pattern forming process, was first modelled by Kücken and Champod [KC13], and is studied in Chapter 3. In the third phase, the primary ridges are induced by the Merkel cells.
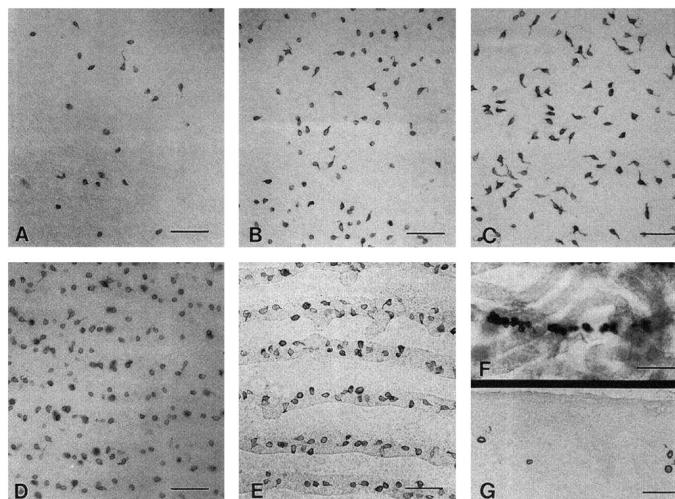


Figure 1.2: Development of Merkel cell distribution by Kim and Holbrook: Merkel cells appear at about the 7th week of pregnancy, multiply and arrange in lines at about the 10th week. Figure from [KH95].

Since the first phase of the fingerprint development has already been successfully been modelled by Kücken and Newell [KN04, KN05], while the third phase can easily be modelled based on the second phase of the fingerprint development, we focus on the second phase in the following where the stress field from the first phase is assumed as a given input. Mathematically, the formation of fingerprints can then be described as the interaction of a large number of the Merkel cells [KC13], which align themselves according to certain interaction forces and form our fingerprint lines. The central novelty in this model, leading to realistic patterns as observed in nature, is an anisotropy induced by the underlying stress field. That is, the cell interactions depend additionally on the size of the stress field at the cell locations. This additional anisotropy results in a more complicated, but also more realistic interaction model which is based on a substantial body of biological literature and experimental data. These anisotropic interaction models can be regarded as a challenging generalisation of the popular class of isotropic interaction models.

### 1.1.2 Isotropic interaction models

Isotropic interaction models have already been studied extensively studied in literature. In its simplest form, isotropic interaction models are considered with radial interaction potentials [BCLR13b]. The resulting patterns are found as stationary points of the $N$ particle interaction energy

$$E(x_1, \ldots, x_N) = \frac{1}{2N^2} \sum_{\substack{j,k=1 \\ k \neq j}}^{N} W(x_j - x_k) \tag{1.1}$$

where $W(d) = \overline{W}(|d|)$ denotes the radially symmetric interaction potential and $x_j = x_j(t) \in \mathbb{R}^n$ for $j = 1, \ldots, N$ denote the positions of the particles at time $t \geqslant 0$ [BSK$^+$15, KSUB11]. The associated gradient flow reads:

$$\frac{\mathrm{d}x_j}{\mathrm{d}t} = \frac{1}{N} \sum_{\substack{k=1 \\ k \neq j}}^{N} F(x_j - x_k) \tag{1.2}$$

where $F(x_j - x_k)$ is a conservative force, aligned along the distance vector $x_j - x_k$ with $F(d) = -\nabla W(d)$.

When the number of individuals is large as in many biological applications, it becomes essential to use continuum models for the evolution of the density of the individuals. Denoting the density of particles at location $x \in \mathbb{R}^n$ and at time $t > 0$ by $\rho = \rho(t, x)$ the interaction energy is given by

$$\mathcal{W}[\rho] = \frac{1}{2} \int_{\mathbb{R}^2} (W * \rho)(x) \rho(\mathrm{d}x)$$

and the continuum equation corresponding to (1.2), also referred to as the aggregation equation [BCL09, BSK$^+$15, KSUB11, Lau07], reads

$$\rho_t + \nabla \cdot (\rho u) = 0, \qquad u = -\nabla W * \rho \tag{1.3}$$

where $u = u(t, x)$ is the macroscopic velocity field. The aggregation equation (1.3) whose well-posedness has been proved in [BLR11] has extensively been studied recently, mainly in terms of its gradient flow structure [AGS05, CMV03, CMV06, LT04, Vil03], the blow-up dynamics for fully attractive potentials [BCL09, BLL12, CDFF$^+$11, CJLV16], and the rich variety of steady states [BCLR13a, BCLR13b, BCY14, BT11, BLL12, CCP15, CDM16, CFF$^+$12, CFP12, FR10, FR11, Rao12,

vBU12, vBUKB12].

Recently, there has been a trend to connect the microscopic and the macroscopic descriptions via kinetic modeling, see for instance [BS12, CFRT10, HT08] for different kinetic models in swarming [FHT11, HL09] for the particle to hydrodynamics passage and [KMT15] for the hydrodynamic limit of a kinetic model.

If the radially symmetric potential $W(d) = \overline{W}(|d|)$ is purely attractive, e.g. $\overline{W}$ is an increasing function with $\overline{W}(0) = 0$, the density of the particles converges to a Dirac Delta function located at the centre of mass of the density [BD08]. In this case, the Dirac Delta function is the unique stable steady state and a global attractor [CDFF$^+$11]. Under certain conditions the collapse towards the Dirac Delta function can take place in finite time [BCL09, BGL12, BL07, CDFF$^+$11].

In biological applications, however, it is not sufficient to consider purely attractive potentials since the inherently nonlocal interactions between the individual entities occur on different scales [BT11, EKWG98, MEK99]. These interactions are usually described by short-range repulsion to prevent collisions between the individuals as well as long-range attraction that keeps the swarm cohesive [MEKBS03, OL01]. The associated radially symmetric potentials $\overline{W}$, also referred to as repulsive-attractive potentials, first decrease and then increase as a function of the radius. These potentials lead to possibly more complex steady states than the purely attractive potentials and can be considered as a minimal model for pattern formation in large systems of individuals [BCLR13b].

The 1D nonlocal interaction equation with a repulsive-attractive potential has been studied in [FR10, FR11, Rao12]. The authors show that the behaviour of the solution strongly depends on the regularity of the interaction potential. More precisely, the solution converges to a sum of Dirac masses for regular interaction, while it remains uniformly bounded for singular repulsive potentials.

Pattern formation for repulsive-attractive potentials in multiple dimensions is studied in [BSK$^+$15, KSUB11, vBU12, vBUKB12]. The authors perform a linear stability analysis of ring equilibria and derive conditions on the potential to classify the different instabilities. This analysis can also be used to study the stability of flock solutions and mill rings in the associated second-order model, see [ABCvB14] and [CHM14b] for the linear and nonlinear stability of flocks, respectively. A numerical study of the $N$ particle interaction model for specific repulsion-attraction potentials [BSK$^+$15, KSUB11] outlines a wide range of radially symmetric patterns such as rings, annuli and uniform circular patches, while exceedingly complex patterns are also possible. In particular, minimisers of the interaction energy (1.1), i.e.,

stable stationary states of the microscopic model (1.2), can be radially symmetric even for radially symmetric potentials. This has been studied and discussed by instabilities of the sphere and ring solution in [BSK⁺15, vBU12, vBUKB12]. The convergence of radially symmetric solutions towards spherical shell stationary states in multiple dimensions is discussed in [BCLR13b]. Another possibility to produce concentration in lower dimensional sets is to use potentials which are not radially symmetric. This has been explored recently in the area of dislocations in the two-dimensional case in [MRS19] and its $n$-dimensional generalisation in [CMM⁺19]. Moreover, the nonlocal interaction equation in heterogeneous environments (where domain boundaries are also allowed) is investigated in [WS15]. Besides, interaction energies with boundaries have been studied in [CSW16].

Nonlocal interaction models have been studied for specific types of repulsive-attractive potentials [BCLR13a, CCH14b, CFP17, CH17, CJLV16, FHK11]. In [BCLR13a] the dimensionality of the patterns is analysed for repulsive-attractive potentials that are strongly or mildly repulsive at the origin, i.e., potentials with a singular Laplacian at the origin satisfying $\Delta W(d) \sim -|d|^{-\beta}$ as $d \to 0$ for some $0 < \beta < n$ in $n$ dimensions and potentials whose Laplacian does not blow up at the origin satisfying $W(d) \sim -|d|^{\alpha}$ as $d \to 0$ for some $\alpha > 2$, respectively. In [FHK11] a specific example of a repulsive-attractive potential is studied, given by a Newtonian potential for the repulsive and a polynomial for the attractive part, respectively.

Isotropic patterns and clustering have been studied in different contexts. In [MT14] the authors review a general class of models for self-organised dynamics and show that the tendency to bond more with those who are different rather than with those who are similar is crucial in the clustering process. Bourne, Peletier et al. study pattern formation and pattern evolution in various contexts, see [BPR14, BPT14, PV10] for instance.

### 1.1.3 Anisotropic interaction models

In most models the interactions are assumed to be *isotropic* for simplicity. However, pattern formation in nature is usually *anisotropic* [Bal09]. Motivated by the simulation of fingerprint patterns, we consider a class of interacting particle models with anisotropic interaction forces in this thesis. By considering anisotropic interaction forces, the isotropic interaction models can be generalised to anisotropic interaction models. In particular, these anisotropic interaction models capture important swarming behaviours, neglected in the simplified isotropic interaction model, such

as anisotropic steady states.

Since we are interested in pattern formation in the plane, we consider an evolutionary particle model with an anisotropic interaction force in two dimensions. More precisely, we generalise the extensively studied model (1.2) by considering an $N$ particle model of the form

$$\frac{\mathrm{d}x_j}{\mathrm{d}t} = \frac{1}{N} \sum_{\substack{k=1 \\ k \neq j}}^{N} F(x_j - x_k, T(x_j)) \tag{1.4}$$

where $F(x_j - x_k, T(x_j)) \in \mathbb{R}^2$ describes the force exerted from $x_k$ on $x_j$. Here, $T(x_j)$ denotes a tensor field at location $x_j$ which is given by

$$T(x) := \chi s(x) \otimes s(x) + l(x) \otimes l(x) \tag{1.5}$$

for orthonormal vector fields $s = s(x), l = l(x) \in \mathbb{R}^2$ and $\chi \in [0, 1]$.

As in the standard particle model (1.2) we assume that the force $F(x_j - x_k, T(x_j))$ is the sum of repulsion and attraction forces. In (1.2), attraction and repulsion forces are aligned along the distance vector $x_j - x_k$ so that the total force $F(x_j - x_k)$ is also aligned along $x_j - x_k$. In the extended model (1.4), however, the orientation of $F(x_j - x_k, T(x_j))$ depends not only on the distance vector $x_j - x_k$ but additionally on the tensor field $T(x_j)$ at location $x_j$. More precisely, the attraction force will be assumed to be aligned along the vector $T(x_j)(x_j - x_k)$. Since $T$ depends on a parameter $\chi \in [0, 1]$ the resulting force direction is regulated by $\chi$. In particular, alignment along the distance vector $x_j - x_k$ is included in (1.4) for $\chi = 1$. The additional dependence of (1.4) on the parameter $\chi$ in the definition of the tensor field $T$ introduces an anisotropy to the equation. This anisotropy leads to more complex, anisotropic patterns that do not occur in the simplified model (1.2). Due to the dependence on parameter $\chi$ the force $F$ is non-conservative in general so that it cannot be derived from a potential. However, most of the analysis of the interaction models in the literature relies on the existence of an interaction potential as outlined above. A particle interaction model of the form (1.4) with a non-conservative force term that depends on an underlying tensor field $T$ appears not to have been investigated mathematically in the literature yet. It seems that there are not many results currently available in the field of anisotropies. Evers et al. model anisotropy by adding weights to the interaction terms [EFR15]. Since the weights depend on the velocities themselves, the equation for velocities becomes implicit. This intro-

duces a fair number of new issues, such as discontinuous solutions. Hence, small inertia regularisation are introduced and studied in the follow-up paper [EFS17]. Note that the model in [EFR15, EFS17] is related to the model we consider in this work if one introduces a tensor field $T$ as the velocity direction.

Due to the generality of the formulation of the anisotropic interaction model (1.4) a better understanding of the pattern formation in (1.4) can be regarded as a first step towards understanding anisotropic pattern formation in nature. An example of an $N$ particle model of the form (1.4) is the model introduced by Kücken and Champod [KC13], describing the formation of fingerprint patterns based on the interaction of Merkel cells and mechanical stress in the epidermis [Irm10]. Even though the Kücken-Champod model [KC13] seems to be capable to produce transient patterns that resemble fingerprint patterns, the pattern formation of the Kücken-Champod model and its dependence on the model parameters have not been studied analytically or numerically before. In particular, the long-time behaviour of solutions to the Kücken-Champod model and its stationary solutions have not been understood yet. However, stationary solutions to the Kücken-Champod model are of great interest for simulating fingerprints since fingerprint patterns only change in size and not in shape after we are born so that every person has the same fingerprints from infancy to adulthood. Clearly, fingerprint patterns are of great importance in forensic science. Besides, they are increasingly used in biometric applications. Hence, understanding the model, proposed in [KC13], and in particular its pattern formation result in a better understanding of the fingerprint pattern formation process.

In Section 1.1.3, we describe a general formulation of the anisotropic microscopic model, relate it to the Kücken-Champod particle model in Section 1.1.4 and formulate the corresponding mean-field PDE.

**General formulation of the anisotropic model**

In this section, we consider $N$ particles at positions $x_j = x_j(t) \in \mathbb{R}^2$, $j = 1, \ldots, N$, at time $t$. The evolution of the particles can be described by (1.4) with initial data $x_j(0) = x_j^{in}$, $j = 1, \ldots, N$. Here, $F(x_j - x_k, T(x_j))$ denotes the total force that particle $k$ exerts on particle $j$ subject to an underlying stress tensor field $T(x_j)$ at $x_j$, describing the local stress field. The dependence on $T(x_j)$ is based on the experimental results [KH95] where an alignment of the particles along the local stress lines is observed, i.e., the evolution of particle $j$ at location $x_j$ depends on the

the local stress tensor field $T(x_j)$. Note that model (1.4) can be rewritten as

$$\frac{\mathrm{d}x_j}{\mathrm{d}t} = v_j$$
$$v_j = \frac{1}{N} \sum_{\substack{k=1 \\ k \neq j}}^{N} F(x_j - x_k, T(x_j)). \tag{1.6}$$

Starting with Newton's second law of the form

$$\frac{\mathrm{d}\overline{x}_j}{\mathrm{d}\tau} = \overline{v}_j$$
$$m\frac{\mathrm{d}\overline{v}_j}{\mathrm{d}\tau} + \lambda\overline{v}_j = \overline{F}_j$$

where we assume that the particles have identical mass $m$, $\lambda$ denotes the coefficient of friction and $\overline{F}_j$ is the total force acting on particle $j$, rescaling in time $\tau = \frac{m}{\varepsilon\lambda}t$ for small $\varepsilon > 0$ yields

$$\frac{\varepsilon\lambda}{m}\frac{\mathrm{d}\overline{x}_j}{\mathrm{d}t} = \overline{v}_j$$
$$\varepsilon\lambda\frac{\mathrm{d}\overline{v}_j}{\mathrm{d}t} + \lambda\overline{v}_j = \overline{F}_j.$$

Setting $F_j := \frac{1}{\lambda}\overline{F}_j$ where the rescaled total force $F_j$ on particle $j$ is given by the sum of all interaction forces exerted by other particles, i.e.,

$$F_j = \frac{1}{N} \sum_{\substack{k=1 \\ k \neq j}}^{N} F(x_j - x_k, T(x_j)).$$

Further we set $x_j := \frac{\varepsilon\lambda}{m}\overline{x}_j$ and $v_j := \overline{v}_j$, resulting in the rescaled second order model:

$$\frac{\mathrm{d}x_j}{\mathrm{d}t} = v_j$$
$$\varepsilon\frac{\mathrm{d}v_j}{\mathrm{d}t} = -v_j + \frac{1}{N} \sum_{\substack{k=1 \\ k \neq j}}^{N} F(x_j - x_k, T(x_j)) \tag{1.7}$$

for small $\varepsilon > 0$. Starting from (1.7) the first order model (1.6) was justified and formally derived in [BV05]. Note that (1.7) reduces to (1.6) if the inertia term is neglected, corresponding to small response times of the individuals. However, setting $\varepsilon = 0$ corresponds to instantaneous changes in velocities which need to

be justified rigorously. In [FS15] the authors proved the rigorous limit from the isotropic second order model (1.7) to the isotropic first order model (1.6) as $\varepsilon \to 0$ based on a classical Tikhonov theorem for ODEs, see e.g. [Ver05, Theorem 8.1]. A classical hypothesis is the $C^1$ regularity of $F$ with respect to $x$ and $v$ which can be relaxed to Lipschitz continuous functions $F$. However, this assumption is not sufficient and the anisotropy of the model might lead to troubles. In [EFS17], the authors consider an anisotropic aggregation model and derive its vanishing inertia limit. In this case, however, the classical result by Tikhonov is no longer valid, mainly because the anisotropy depends on the velocity variable and the roots of the limiting equation can be lost. For the anisotropic interaction model (1.6) considered in this work the anisotropies only involve positions and for $\varepsilon = 0$ we have a unique root

$$v_j = \frac{1}{N} \sum_{\substack{k=1 \\ k \neq j}}^{N} F(x_j - x_k, T(x_j)),$$

i.e., we have an isolated root. Further, the root is positively stable and its domain of influence is $\{(x_1, \ldots, x_N)\} \times \mathbb{R}^{2N}$. For further details see [FS15].

The total force $F$ in the particle model (1.4) is given by

$$F(d = d(x_j, x_k), T(x_j)) = F_A(d, T(x_j)) + F_R(d), \tag{1.8}$$

for the distance vector $d(x_j, x_k) = x_j - x_k \in \mathbb{R}^2$. Here, $F_R$ denotes the repulsion force that particle $k$ exerts on particle $j$ and $F_A$ is the attraction force exerted on particle $j$ by particle $k$. The tensor field $T(x_j)$ at $x_j$ encodes the direction of the fingerprint lines at $x_j$ and is given by $T(x_j) = \chi s(x_j) \otimes s(x_j) + l(x_j) \otimes l(x_j)$ with $\chi \in [0, 1]$. Here, $s = s(x_j) \in \mathbb{R}^2$ and $l = l(x_j) \in \mathbb{R}^2$ are orthonormal vectors, describing the directions of smallest and largest stress, respectively. Then the force is given by

$$F(d = d(x_j, x_k), T(x_j)) = f_s(|d|)(s(x_j) \cdot d)s(x_j) + f_l(|d|)(l(x_j) \cdot d)l(x_j) \tag{1.9}$$

for coefficient functions $f_s$ and $f_l$.

Defining $W_R(d) := \overline{W}_R(|d|)$ and $W_A(d) := \overline{W}_A(|d|)$ where $\overline{W}_R(r)$ and $\overline{W}_A(r)$ satisfy

$$\overline{W}'_R(r) = -f_R(r)r \quad \text{and} \quad \overline{W}'_A(r) = -f_A(r)r \tag{1.10}$$

the attractive and repulsive forces are given by

$$F_R(d = d(x_j, d_k)) = -\nabla W_R(d) = f_R(|d|)d,$$
$$F_A(d = d(x_j, x_k), T(x_j)) = -T(x_j)\nabla W_A(d) = f_A(|d|)T(x_j)d, \tag{1.11}$$

respectively. In particular, we have

$$F_R(d) = f_R(|d|)d \tag{1.12}$$

and

$$F_A(d = d(x_j, x_k), T(x_j)) = f_A(|d|)T(x_j)d \tag{1.13}$$

for the repulsive and attractive forces $F_R$ and $F_A$, respectively. The direction of the interaction forces is determined by the parameter $\chi \in [0, 1]$ in the definition of $T$. For $\chi = 1$ we have $T(x_j) = \mathbb{I}$ for the two-dimensional unit matrix $\mathbb{I}$ and the attraction force between two particles is aligned along their distance vector, while for $\chi = 0$ the attraction between two particles is oriented along $l$. Depending on the choice of the coefficient functions $f_R$ and $f_A$ in (1.10) the forces are repulsive or attractive according to the following local definition:

**Definition 1** (Strictly repulsive (attractive) forces). *Let the vector field $G = G(x, y)$ be a continuous interaction force, i.e., the vector $G(x, y)$ is the force which is exerted on $x$ by $y$. Then $G$ at $x$ in direction $x - y$ is strictly repulsive (attractive) if*

$$G(x, y) \cdot (x - y) > 0 \qquad (< 0).$$

The meaning of this definition is the following. Let $y$ be fixed and let $X = X(t)$ be the trajectory given by

$$\frac{dX}{dt} = G(X, y), \quad X(0) = x,$$

then $|X(t) - y|$ is locally at $t = 0$ strictly monotonically increasing (decreasing).

To guarantee that $F_R$ and $F_A$ are repulsion and attractive forces, we make assumptions on the coefficient functions $f_R$ and $f_A$ in (1.10).

**Assumption 1.** *We assume that $f_R \colon \mathbb{R}^2 \to \mathbb{R}$ and $f_A \colon \mathbb{R}^2 \to \mathbb{R}$ denote smooth,*

*integrable coefficient functions satisfying*

$$f_R(|d|) \geqslant 0 \quad and \quad f_A(|d|) \leqslant 0 \quad for \ all \quad d \in \mathbb{R}^2, \tag{1.14}$$

*such that the total interaction force $F$ in (1.8) exhibits short-range repulsion and long-range attraction forces along $l$, i.e., there exists a $d_a > 0$ such that*

$$(f_A + f_R)(|d|) \leqslant 0 \ for \ |d| > d_a \qquad and \qquad (f_A + f_R)(|d|) > 0 \ for \ 0 \leqslant |d| < d_a.$$

*Also, $F \in C^1$ has bounded total derivatives, i.e., there exists some $L \geqslant 0$ such that*

$$\sup_{x,x' \in \mathbb{R}^2} |D_x F(d(x, x'), T(x))| \leqslant L \quad and \quad \sup_{x,x' \in \mathbb{R}^2} |D_{x'} F(d(x, x'), T(x))| \leqslant L,$$

*where $D_x$ denotes the total derivative with respect to $x$. This implies that $F$ is Lipschitz continuous in both arguments. In particular, $F$ grows at most linearly at infinitely.*

**Remark 1.** *In the well-posedness results by Bertozzi et al. [BLR11] the authors consider mildly singular potentials $W_R$ and $W_A$ in the isotropic case $\chi = 1$ satisfying*

$$\overline{W}_R(r), \overline{W}_A(r) \simeq \begin{cases} r^\alpha, & r \ll 1 \\ \exp(-\beta r), & r \gg 1 \end{cases}$$

*where $\alpha, \beta > 0$ in two spatial dimensions. These conditions can be restated as*

$$f_R(r), f_A(r) \simeq \begin{cases} r^{\alpha-2}, & r \ll 1 \\ \exp(-\beta r), & r \gg 1. \end{cases}$$

*The range $0 < \alpha < 2$ lies outside the hypothesis in Assumption 1 and falls outside the scope of this chapter. However, this case is extremely interesting since it models singular attractive and repulsive interactions in aggregation models where the limiting Newtonian case $\alpha \searrow 0$ is the most interesting one regarding its physical consequences. There is an extensive scientific activity related to isotropic singular (first and second order) interactions, see for instance [CCH14c, HJ15, Jab14, JW16, MP18, PS17, ST17] and the references therein. Note that the restriction to Lipschitz and bounded forces in Assumption 1 is sufficient (see e.g. [JW16]) for proving the rigorous mean-field limit, but one can also show the mean-field limit for mildly singular interactions including the range $0 < \alpha < 2$ in the isotropic case $\chi = 1$, see*

*[CCH14c, HJ15] and related papers. Hence, it would be interesting to address these mildly singular interactions in the anisotropic case $\chi \in [0,1)$ and compare it with the results for isotropic mildly singular interactions.*

Note that we recover a potential attractive interaction in $F_A$ if, and only if, $T(x_j) = \mathbb{I}$ (i.e., the isotropic case $\chi = 1$), as shown in Remark 2.

**Remark 2** (Existence of an interaction potential)**.** *For the existence of interaction potentials for the attractive force $F_A$ we restrict ourselves to spatially homogeneous tensor fields first. Let $\chi \in [0,1]$, set $l = (1,0)$ and $s = (0,1)$, and let $\tilde{T} = \chi \tilde{s} \otimes \tilde{s} + \tilde{l} \otimes \tilde{l}$ denote a spatially homogeneous tensor field for orthonormal vectors $\tilde{l}, \tilde{s} \in \mathbb{R}^2$. Then,*

$$\tilde{s} = R_\theta s \quad and \quad \tilde{l} = R_\theta l, \tag{1.15}$$

*where the angle of rotation $\theta$ and the corresponding rotation matrix $R_\theta$ are given by*

$$\theta = \begin{cases} \arccos(\tilde{s}_2) & \tilde{s}_1 < 0 \\ 2\pi - \arccos(\tilde{s}_2) & \tilde{s}_1 > 0 \end{cases}, \quad and \quad R_\theta = \begin{pmatrix} \cos(\theta) & -\sin(\theta) \\ \sin(\theta) & \cos(\theta) \end{pmatrix}, \tag{1.16}$$

*respectively, and we have $\tilde{T} = R_\theta T R_\theta^T$ with $T = \chi s \otimes s + l \otimes l$. Hence,*

$$F_A(d, \tilde{T}) = f_A(|d|) \begin{pmatrix} \cos^2(\theta) + \chi \sin^2(\theta) & (1-\chi)\sin(\theta)\cos(\theta) \\ (1-\chi)\sin(\theta)\cos(\theta) & \chi \cos^2(\theta) + \sin^2(\theta) \end{pmatrix} d$$

*by (1.10) and (1.11), where $d = (d_1, d_2) \in \mathbb{R}^2$. The condition*

$$\frac{\partial(F_A)_1}{\partial d_2} = \frac{\partial(F_A)_2}{\partial d_1}$$

*for $F_A$ being a conservative force implies*

$$\cos^2(\theta) + \chi \sin^2(\theta) = \chi \cos^2(\theta) + \sin^2(\theta) \quad and \quad (1-\chi)\sin(\theta)\cos(\theta) = 0,$$

*which can only be satisfied simultaneously for $\chi = 1$ and $\theta \in [0, 2\pi)$ arbitrary. Thus, the attraction force for spatially homogeneous tensor fields is conservative for $\chi = 1$ only and the associated potential is radially symmetric. This also implies that there exists a potential for $\chi = 1$ for any tensor field, while for $\chi \in [0,1)$ there exists no potential. In particular, a potential that is not radially symmetric cannot be*

*constructed for the attraction force $F_A$ for $\chi \in [0, 1)$.*

The associated mean-field model for the distribution function $\rho = \rho(t, x)$ at position $x \in \mathbb{R}^2$ and time $t \geqslant 0$ can be derived rigorously in the 1-Wasserstein metric from the microscopic model (1.4) following the procedure described in [Gol16, CCH14c]. The Cauchy problem for the mean-field PDE reads

$$\partial_t \rho(t, x) + \nabla_x \cdot \left[ \rho(t, x) \left( F\left( \cdot, T(x) \right) * \rho(t, \cdot) \right)(x) \right] = 0 \qquad \text{in } \mathbb{R}_+ \times \mathbb{R}^2 \qquad (1.17)$$

with initial condition $\rho|_{t=0} = \rho^{in}$ in $\mathbb{R}^2$.

**Remark 3.** *Similarly as for the rigorous inertia limit $\varepsilon \to 0$ of the second order model (1.7) to the first order model (1.6) in the discrete setting one can consider the mean-field limit for $N \to \infty$ associated with the second order discrete model (1.7) and derive the hydrodynamic limit $\varepsilon \to 0$ to the mean-field PDE (1.17). The second order mean-field limit for $N \to \infty$ is given by*

$$\varepsilon \partial_t f_\varepsilon + \varepsilon v \cdot \nabla_x f_\varepsilon + \nabla_v \cdot \left[ \left( F\left( \cdot, T(x) \right) * \rho_\varepsilon \right) f_\varepsilon - v f_\varepsilon \right] = 0 \qquad in \ \mathbb{R}_+ \times \mathbb{R}^2 \times \mathbb{R}^2$$

*where $f_\varepsilon = f_\varepsilon(t, x, v)$ is the density of individuals at position $x \in \mathbb{R}^2$ with velocity $v \in \mathbb{R}^2$ and*

$$\rho_\varepsilon(t, x) = \int_{\mathbb{R}^2} f_\varepsilon(t, x, v) \, \mathrm{d}v$$

*is the macroscopic density. The hydrodynamic limit $\varepsilon \to 0$ to the first order macroscopic macroscopic PDE (1.17) can be shown as in [FS15]. Besides, one might study aggregation equations from first principles not only for regular interactions but also for mildly singular ones, see [NPS01] and in another context [BBNS07].*

### 1.1.4 Kücken-Champod particle model

Kücken and Champod introduced a particle model in [KC13] modelling the formation of fingerprint patterns by describing the interaction between so-called Merkel cells on a domain $\Omega \subseteq \mathbb{R}^2$. Merkel cells are epidermal cells that appear in the volar skin at about the 7th week of pregnancy. From that time onward they start to multiply and organise themselves in lines exactly where the primary ridges arise. The model introduced in [KC13] models this pattern formation process as the rearrangement of Merkel cells from a random initial configuration into roughly parallel ridges along the lines of smallest compressive stress. The Kücken-Champod particle

model [KC13] can be regarded as an example of (1.4). For a spatially homogeneous tensor field $T$ straight parallel ridges, e.g.

$$T = \begin{pmatrix} 1 & 0 \\ 0 & \chi \end{pmatrix},$$

can be produced and, more generally, this type of models can be considered for studying the pattern formation. For more realistic patterns the tensor field is generated from 3D finite element simulations [KN04, KN05] or from images of real fingerprints. The coefficient function $f_R$ defined by the potential $W_R$ (1.10) in the definition of the repulsion force $F_R$ (1.11) in the Kücken-Champod model (1.4) is given by

$$f_R(d) = (\alpha|d|^2 + \beta)\exp(-e_R|d|) \qquad (1.18)$$

for $d \in \mathbb{R}^2$ and nonnegative parameters $\alpha$, $\beta$ and $e_R$. The coefficient function $f_A$ in (1.10) in the definition of the attraction force (1.11) is given by

$$f_A(d) = -\gamma|d|\exp(-e_A|d|) \qquad (1.19)$$

for $d \in \mathbb{R}^2$ and nonnegative constants $\gamma$ and $e_A$. For the case that the total force (1.8) exhibits short-range repulsion and long-range attraction along $l$, we choose the parameters as follows:

$$\alpha = 270, \quad \beta = 0.1, \quad \gamma = 35, \quad e_A = 95, \quad e_R = 100, \quad \chi \in [0,1]. \qquad (1.20)$$

The coefficient functions (1.18) and (1.19) for the repulsion and attraction forces (1.11) in the Kücken-Champod model (1.4) are plotted in Figure 1.3(A) for the parameters in (1.20) and one can easily check that they satisfy Assumption 1. If not stated otherwise, we consider the parameter values in (1.20) for the force coefficient functions (1.18) and (1.19) in the following. The interaction forces between two particles with distance vectors $d = rl$ and $d = rs$ for a constant $r \in \mathbb{R}$ are given by

$$F(d) = f_R(d)d + f_A(d)Td = \begin{cases} (f_R(r) + f_A(r))rl & \text{if } d = rl \\ (f_R(r) + \chi f_A(r))rs & \text{if } d = rs. \end{cases}$$

Figure 1.3(B) shows the total interaction force along $l$ and $s$, respectively, i.e.,

$$F(rl) \cdot l = (f_R(r) + f_A(r))r \quad \text{and} \quad F(rs) \cdot s = (f_R(r) + \chi f_A(r))r, \qquad (1.21)$$

as a function of $r$ for $\chi = 0.2$, while the corresponding coefficient functions are illustrated in Figure 1.3(A). For the choice of parameters in (1.20) repulsion dominates for short distances along $l$ to prevent the collision of particles. Besides, the total force exhibits long-range attraction along $l$ whose absolute value decreases with the distance between particles. Along $s$ the particles are always repulsive for $\chi = 0.2$, independent of the distance, though the repulsion force gets weaker for longer distances.



(A) Force coefficients $f_R$ and $f_A$      (B) Total force coefficients along $l$ and $s$
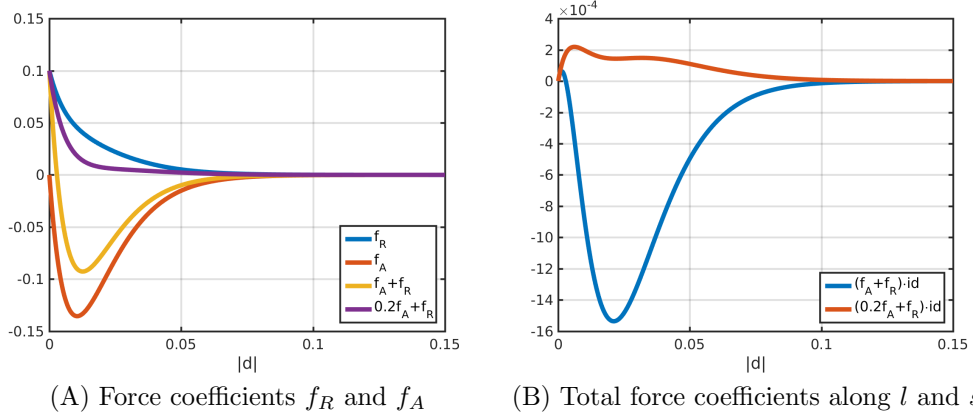
Figure 1.3: Coefficients $f_R$ in (1.18) and $f_A$ in (1.19) of repulsion and attraction forces (1.11), respectively, as well as the total interaction force along $l$ and $s$ for $\chi = 0.2$ given by (1.21) and its coefficients (i.e., $f_A + f_R$ and $0.2f_A + f_R$) for parameter values in (1.20).

## 1.2   Partial differential equations for biological networks

Network formation and transportation networks are ubiquitous in both social and biological systems. To determine the network performance, a complex trade-off involving cost, transport efficiency, and fault tolerance can be considered.

### 1.2.1 Biological transport networks

An important class of transportation networks are biological systems such as leaf venation in plants, angiogenesis of blood vessels and neural networks which transport electric charge. These biological systems continuously adapt to their environment and balance the cost of producing an efficient network with the consequences of even limited failure. Since biological transportation networks develop without centralised control [TTS+10] and have been fine-tuned by many cycles of evolutionary selection pressure, they can be regarded as optimal solutions of the underlying transportation problems where cost, efficiency, and resilience are appropriately balanced [Cor10].

Great interest has been shown for these phenomena from different scientific communities including biologists, engineers, physicists and computer scientists, particularly in terms of understanding natural networks and their optimal transport of fluids, materials and information [BHD+07, RFL+05, YDG+00, CC95]. Inspired by biological phenomena, mathematical models and methods for transportation networks can be developed which has recently become a major research area. Examples include neural networks, genetic algorithms and efficient search routines from ant colony optimisation algorithms [CDM+96] or biologically inspired models for adaptive transportation network development based on slime mould growth [TTS+10].



(A) Leaf venation          (B) Slime mold growth and rail network
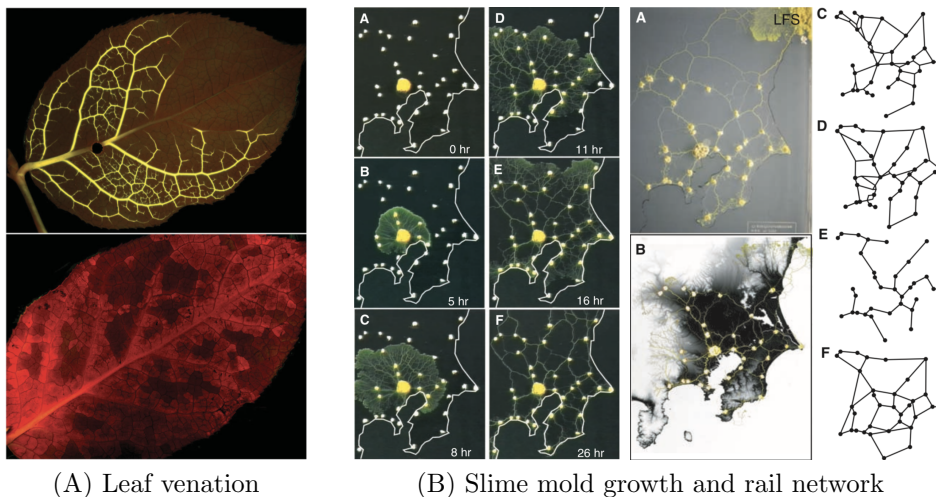
Figure 1.4: Examples of transportation networks. Subfigures from [KSmHM10, TTS+10].

Traditionally, models describing biological transportation networks have been based on discrete frameworks such as mathematical graph theory and discrete energy optimisation, where the energy consumption within the network is minimised

under the constraint of constant total material cost [BM07, BCF+00, Dur06]. These discrete mathematical models can be classified into *static* and *dynamic* modelling approaches, where the latter ones account for the adaptation of networks to fluctuations in the flow. For biological transportation networks such as blood circulation systems, it is well known that they continuously adapt their structures to meet the changing metabolic demand of the tissue. In particular, experiments have shown that blood vessels can sense the wall shear stress [PHBB86] and adapt their diameters accordingly [HCR12]. Hence, dynamic models are required for the accurate description of biological transportation networks. An example of such a dynamic model for adaptive regulation of wall shear stress has been introduced in [KBT84] where the adaptation of the vessel radius of a blood vessel network is formulated as minimizing the energy consumption of the network.

One of the main research questions are structural and topological properties of the optimal networks such as existence of loops and tree-like structures, and connectivity of the network. Connectivity of the underlying network is required for efficient transport of material, while loop structures are great benefits for animals and plants. For instance, loops are important in mitigating damages of networks [KSmHM10] and optimizing energy consumption with fluctuating flow distributions [Cor10]. Therefore, biological transportation networks for leaf venation or angiogenesis are connected structures containing many loops [Cor10, LBJ08, ND97]

A new approach to dynamic modelling of transportation networks has recently been introduced by Hu and Cai [HC13]. They propose a purely local dynamic adaptation model, based on mechanical laws. In particular, this model responds only to local information and can naturally incorporate fluctuations in the flow. The mathematical description of this model consists of a large system of ordinary differential equations on a graph coupled with a linear system of equations. Differential equations on graphs and networks are not only crucial for modelling biological or social transportation networks, but also play an important role in many data science and machine learning tasks, and can be regarded as the key area of research for solving data problems such as linking graph and the associated macroscopic models via $\Gamma$-convergence.

A different modelling approach based on macroscopic physical laws was introduced in [Hu13]. This continuum model consists of a very complex system of nonlinear partial differential equations (PDEs) and because of its unusual coupling this leads to many still open mathematical questions.

## 1.2.2 Microscopic model

In this section we describe the microscopic model introduced by Hu and Cai [HC13] and reformulated in [ABH$^+$17]. Let $\mathbb{G} = (\mathbb{V}, \mathbb{E})$ be an undirected connected graph, consisting of a finite set of vertices $\mathbb{V}$ and a finite set of edges $\mathbb{E}$ where the number of vertices is denoted by $n = |\mathbb{V}|$. We assume that any pair of vertices is connected by at most one edge and a vertex is not connected to itself by an edge. We denote the edge between vertices $i \in \mathbb{V}$ and $j \in \mathbb{V}$ by $(i, j) \in \mathbb{E}$. Since the graph is undirected we refer by $(i, j)$ and $(j, i)$ to the same edge. For each edge $(i, j) \in \mathbb{E}$ of the graph $\mathbb{G}$ we consider its length and its conductivity, denoted by $L_{ij} = L_{ji} > 0$ and $C_{ij} = C_{ji} \geqslant 0$, respectively. In the following, we assume that the lengths $L_{ij} > 0$ are given as a datum and fixed for all $(i, j) \in \mathbb{E}$. The conductivities $C_{ij}$ are subject to the energy optimisation and adaptation process. We assume that initially all edges in $\mathbb{E}$ have strictly positive conductivities. In each vertex $i \in \mathbb{V}$ we have the pressure $P_i \in \mathbb{R}$. The pressure drop between vertices $i \in \mathbb{V}$ and $j \in \mathbb{V}$ connected by an edge $(i, j) \in \mathbb{E}$ is given by

$$(\Delta P)_{ij} := P_j - P_i. \tag{1.22}$$

Note that the pressure drop is antisymmetric, i.e., by definition, $(\Delta P)_{ij} = -(\Delta P)_{ji}$. The oriented flux (flow rate) from vertex $i \in \mathbb{V}$ to $j \in \mathbb{V}$ is denoted by $Q_{ij}$; again, we have $Q_{ij} = -Q_{ji}$. For biological networks, the Reynolds number of the flow is typically small and the flow is predominantly in the laminar (Poiseuille) regime. Then the flow rate between vertices $i \in \mathbb{V}$ and $j \in \mathbb{V}$ along edge $(i, j) \in \mathbb{E}$ is proportional to the conductance $C_{ij}$ and the pressure drop $(\Delta P)_{ij} = P_j - P_i$,

$$Q_{ij} := C_{ij} \frac{P_j - P_i}{L_{ij}} \qquad \text{for all } (i, j) \in \mathbb{E}. \tag{1.23}$$

The local mass conservation in each vertex is expressed in terms of the Kirchhoff law

$$-\sum_{j \in N(i)} C_{ij} \frac{P_j - P_i}{L_{ij}} = S_i \qquad \text{for all } i \in \mathbb{V}. \tag{1.24}$$

Here $N(i)$ denotes the set of vertices connected to $i \in \mathbb{V}$ through an edge, and $S = (S_i)_{i \in \mathbb{V}}$ is the prescribed strength of the flow source ($S_i > 0$) or sink ($S_i < 0$) at vertex $i$. Clearly, a necessary condition for the solvability of (1.24) is the global

mass conservation

$$\sum_{i \in \mathbb{V}} S_i = 0, \tag{1.25}$$

which we assume in the following. Given the vector of conductivities $C = (C_{ij})_{(i,j) \in \mathbb{E}}$, the Kirchhoff law (1.24) is a linear system of equations for the vector of pressures $P = (P_i)_{i \in \mathbb{V}}$. With the global mass conservation (1.25), the linear system (1.24) is solvable if and only if the graph with edge weights $C = (C_{ij})_{(i,j) \in \mathbb{E}}$ is connected [ABH+17], where only edges with positive conductivities $C_{ij} > 0$ are taken into account (i.e., edges with zero conductivities are discarded). Note that the solution is unique up to an additive constant.

Hu and Cai [HC13] propose an energy cost functional consisting of a pumping power term and a metabolic cost term. According to the Joule's law, the power (kinetic energy) needed to pump material through an edge $(i, j) \in \mathbb{E}$ is proportional to the pressure drop $(\Delta P)_{ij} = P_j - P_i$ and the flow rate $Q_{ij}$ along the edge, i.e.,

$$(\Delta P)_{ij} Q_{ij} = \frac{Q_{ij}^2}{C_{ij}} L_{ij}.$$

The metabolic cost of maintaining the edge is assumed proportional to its length $L_{ij}$ and a power of its conductivity $C_{ij}^\gamma$, with an exponent $\gamma > 0$ of the network. For instance, in blood vessels the metabolic cost is proportional to the cross-section area of the vessel [Mur26a]. Modelling the blood flow by Hagen-Poiseuille's law, the conductivity is proportional to the square of the cross-section area, implying $\gamma = 1/2$ for blood vessel systems. For models of leaf venation the material cost is proportional to the number of small tubes, which is proportional to $C_{ij}$, and the metabolic cost is due to the effective loss of the photosynthetic power at the area of the venation cells, which is proportional to $C_{ij}^{1/2}$. Consequently, the effective value of $\gamma$ typically used in models of leaf venation lies between 1/2 and 1, [HC13]. Consequently, the energy cost functional is given by

$$E[C] := \sum_{(i,j) \in \mathbb{E}} \left( \frac{Q_{ij}[C]^2}{C_{ij}} + \frac{\nu}{\gamma} C_{ij}^\gamma \right) L_{ij}, \tag{1.26}$$

where $Q_{ij}[C]$ is given by (1.23) with pressures calculated from the Kirchhoff's law (1.24), and $\nu > 0$ is the so-called metabolic coefficient. Note that every edge of the graph $\mathbb{G}$ is counted exactly once in the above sum.

### 1.2.3 Macroscopic model

A macroscopic model for describing the fluid transport in general biological networks has recently been introduced in [Hu13] and is based on phenomenological considerations such as laws of porous medium flow. This model has been studied in [AAFM16, HMP15, HMPS16, ABH$^+$17] and is given by

$$-\nabla \cdot [(r\mathbb{I} + m \otimes m) \nabla p] = S, \tag{1.27}$$

$$\frac{\partial m}{\partial t} - D^2 \Delta m - c^2 (m \cdot \nabla p) \nabla p + |m|^{2(\gamma-1)}m = 0, \tag{1.28}$$

where $p = p(t,x) \in \mathbb{R}$ is the scalar pressure of the fluid transported within the network and $m = m(t,x) \in \mathbb{R}^d$ is the vector-valued conductance in $d \in \{1,2,3\}$ space dimensions. Here, $D^2 \geqslant 0$ denotes the diffusivity, $c^2 > 0$ is the activation parameter and $\gamma \in \mathbb{R}$. The scalar function $r = r(x) \geqslant r_0 > 0$ describes the isotropic background permeability of the medium, $\mathbb{I}$ is the identity matrix and $S = S(x)$ models sources and sinks where $S$ is assumed to be time-independent for simplicity. The PDE system (1.27)–(1.28) is posed on a bounded domain $\Omega \subset \mathbb{R}^d$, $d \in \{1,2,3\}$, with smooth boundary $\partial\Omega$ subject to homogeneous Dirichlet boundary conditions for $m$ and $p$:

$$m(t,x) = 0, \quad p(t,x) = 0 \quad \text{for } x \in \partial\Omega, \ t \geqslant 0. \tag{1.29}$$

Besides, we prescribe an initial condition for $m$:

$$m(t = 0, x) = m^0(x) \quad \text{for } x \in \Omega. \tag{1.30}$$

The macroscopic model (1.27)–(1.28) is derived in [ABH$^+$17], based on macroscopic physical laws, and we repeat the arguments here. Let the network domain $\Omega \subset \mathbb{R}^d$ be occupied by a porous medium in which a fluid moves with velocity $\nu = \nu(t,x) \in \mathbb{R}^d$. Here, $\nu$ is assumed to be a smooth function. Let $\rho = \rho(t,x)$ denote the mass density of the fluid and assume that the fluid is injected into or expelled from the medium at rate $S = S(x)$, then the density satisfies the mass-continuity equation

$$\frac{\partial \rho}{\partial t} + \nabla \cdot (\rho\nu) = \rho S.$$

Moreover, we assume that the fluid is quasi-incompressible, i.e. the fluid density is

constant along the trajectories, implying

$$\frac{D\rho}{Dt} = \frac{\partial \rho}{\partial t} + \nu \cdot \nabla \rho = 0.$$

It follows from the mass-continuity equation that

$$\nabla \cdot \nu = S. \tag{1.31}$$

Besides, the velocity $\nu$ is given by

$$\nu = -\mathbb{P}[m]\nabla p \tag{1.32}$$

by Darcy's law for slow flow in porous media. Here, $p \in \mathbb{R}$ is the scalar fluid pressure and $\mathbb{P}[m]$ denotes the permeability tensor that depends on the network conductance vector $m \in \mathbb{R}^d$. Assuming that $\mathbb{P}[m]$ is of the form

$$\mathbb{P}[m] = r\mathbb{I} + m \otimes m$$

where $\mathbb{I}$ is the identity matrix and the isotropic background permeability of the medium is denoted by the scalar function $r = r(x) \geqslant r_0 > 0$, then combining (1.31), (1.32) results in the Poisson equation (1.27), i.e.

$$-\nabla \cdot [(r\mathbb{I} + m \otimes m)\nabla p] = S.$$

Note that (1.27) with boundary conditions (1.29) has a unique weak solution $p = p[m] \in H_0^1(\Omega)$ for each $m \in L^\infty(\Omega)$. Further note that for $p = p[m]$ the formal $L^2$-gradient flow of the energy

$$\tilde{\mathcal{E}}[m] = \frac{1}{2}\int D^2|\nabla m|^2 + c^2\left(\nabla p[m] \cdot \mathbb{P}[m]\nabla p[m]\right) + \frac{|m|^{2\gamma}}{\gamma} \, dx, \tag{1.33}$$

constrained by the Poisson equation (1.27), is given by the parabolic reaction-diffusion equation (1.28), i.e.

$$\partial_t m = D^2\Delta m + c^2(m \cdot \nabla p)\nabla p - |m|^{2(\gamma-1)}m.$$

Equation (1.28) governs the evolution of the network conductance $m \in \mathbb{R}^d$. The term $D^2\Delta m$ describes random effects in the network structure. The term $c^2(m \cdot \nabla p)\nabla p$ with activation parameter $c^2$ is called the activation term and represents a driving

force in the direction of the pressure gradient $\nabla p$. The term $-|m|^{2(\gamma-1)}m$ is the algebraic relaxation term and represents the functional derivative of the metabolic cost of maintaining the network.

The main mathematical interest of the PDE system for network formation is aroused by the highly unusual coupling of the elliptic equation (1.27) for the pressure $p$ to the reaction-diffusion equation (1.28) for the conductance vector $m$. In particular, the PDE system (1.27)– (1.28) represents the formal $L^2(\Omega)$-gradient flow associated with the highly non-convex energy function $\tilde{\mathcal{E}}[m]$ in (1.33) where $p = p[m] \in H_0^1(\Omega)$ is the unique solution of the Poisson equation (1.27) for $m$ given, subject to homogeneous Dirichlet boundary conditions (1.29). The energy $\tilde{\mathcal{E}}[m]$ is nondecreasing along smooth solutions of (1.27)–(1.28) and it has been shown in [HMP15] that

$$\frac{\mathrm{d}}{\mathrm{d}t}\tilde{\mathcal{E}}[m(t)] = -\int_\Omega \left(\frac{\partial m}{\partial t}(t,x)\right)^2 \mathrm{d}x.$$

In [HMP15] the following analytical results were established for the PDE system (1.27)–(1.28) with boundary conditions (1.29) and initial data (1.30) for the case $\gamma \geqslant 1$:

- Existence of global in time weak solutions in the energy space

- Existence and uniqueness of local in time mild solutions

- Existence of nontrivial (i.e. $m \not\equiv 0$) stationary states and their stability analysis (nonlinear stability in the one dimensional setting, linearised stability in the multidimensional case)

- Limit $D \to 0$ in the one dimensional setting

The analysis of the network formation system (1.27)–(1.28) has been extended in [HMPS16] by providing the following results:

- Existence of global in time weak solutions in the energy space for $1/2 \leqslant \gamma < 1$ and of local in time mild solutions for $1/2 \leqslant \gamma < 1$

- Analysis of the system in the one dimensional setting: finite time breakdown of solutions for $\gamma < 1/2$, infinite time extinction for $1/2 \leqslant \gamma \leqslant 1$ with small sources, nonlinear stability analysis for $\gamma \geqslant 1/2$ and $D = 0$

- Construction of stationary solutions in the case $\gamma = 1$ and $D = 0$

Besides, extensive numerical examples for the PDE system (1.27)–(1.28) have been provided in [AAFM16, ABH$^+$17, HMPS16], based on a mixed finite element discretisation. In [ABH$^+$17] the phase transition behaviour of a microscopic model, given by

$$\frac{\mathrm{d}C_{ij}}{\mathrm{d}t} = \left( \frac{Q_{ij}[C]^2}{C_{ij}^2} - \nu C_{ij}^{\gamma-1} \right) L_{ij} \tag{1.34}$$

and constrained by (1.24), has been studied with respect to the parameter $\gamma$ numerically by solving a constrained energy minimisation.

Note that the macroscopic model (1.27)–(1.28) has only been derived based on the above phenomenological consideration. However, a rigorous derivation of the model, based on the microscopic modelling approach in Section 1.2.2, is still an open question. This motivates to establish the rigorous limit of the microscopic model in Section 1.2.2 which is formally derived in Chapter 6 and rigorously proven in Chapter 7.

## 1.3 Contributions

The recent, rapid advances in modern biology heavily rely on fundamental mathematical techniques and, in particular, on PDEs, an essential tool for the mathematical modelling of biological, socio-economic and physical processes. In this thesis, we focus on two important PDE models in biology, motivated by the simulation of fingerprints and the formation of biological transport networks. Through mathematical analysis and computer simulations, we have gained new insights into the qualitative properties of the underlying mathematical models which have resulted in a better understanding of complex phenomena in nature such as biological pattern formation. Equally important, these new and challenging PDE models have led to intra-disciplinary research, involving modelling, PDE theory, dynamical systems, graph theory and numerical simulations. This research has opened up a whole new range of fascinating mathematical problems, which we have studied by developing new mathematical tools.

In Part I, we focus on a class of interacting particle models with anisotropic repulsive-attractive interaction forces motivated by anisotropic pattern formation in nature. An example of this class of models is the Kücken-Champod model for describing the formation of fingerprint patterns which is not only of great interest in the biological community, but also in forensic science and increasingly in bio-

metric applications where large fingerprint databases are required for developing, validating and comparing the performance of fingerprint identification algorithms. In most existing models, the forces are isotropic and particle models lead to non-local aggregation PDEs with radially symmetric potentials. The central novelty in the models we consider is an anisotropy induced by an underlying tensor field, cf. Figure 1.5(A). This innovation does not only lead to the ability to describe real-world phenomena more accurately, but also renders their analysis significantly harder compared to their isotropic counterparts. We discuss the role of anisotropic interaction in these models by considering both the particle model and its continuum counterpart, present a stability analysis of line patterns, investigate the role of nonlinear diffusion on the widening of line patterns, and show numerical results for the simulation of fingerprints.



(A) Fingerprint model (anisotropy and stationary solution)  (B) Biological transport model
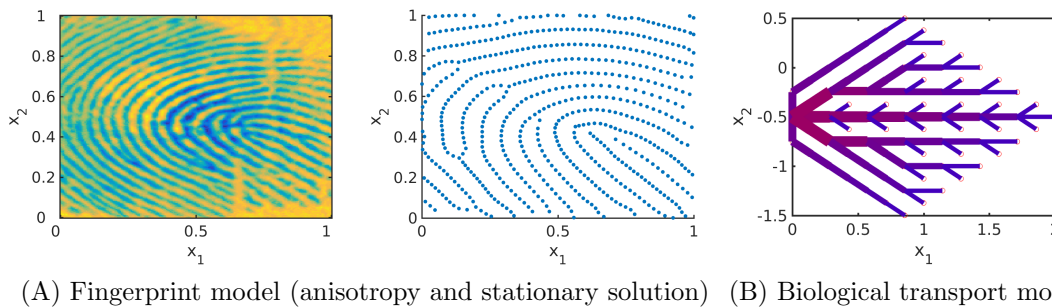
Figure 1.5: Numerical simulation results for the fingerprint (A) and the biological transport network models (B).

Part II deals with transportation networks which are ubiquitous in living systems such as leaf venation in plants, blood circulatory systems, and neural networks. Understanding the development, function, and adaptation of biologic transportation networks has been of long-standing interest in the scientific community due to the complexity of the models. A new discrete dynamic modelling approach on a graph has recently been introduced by Hu and Cai [HC13] to describe the formation of biological transport networks. The main mathematical interest of this dynamical model stems from the highly unusual coupling of a system of ODEs whose solution is defined on the edges of a graph to a linear system on the nodes of the graph. In particular, the linear system is only solvable under certain conditions and due to the coupled defining equations on both nodes and edges of the graph it is not clear under which assumptions a limit model can be derived. We study the existence of solutions to this model and propose an adaptation so that a macroscopic system

can be obtained as its formal continuum limit. For the spatially two-dimensional rectangular setting we prove the rigorous continuum limit of the constrained energy functional as the number of nodes of the underlying graph tends to infinity and the edge lengths shrink to zero uniformly. We also show the global existence of weak solutions of the macroscopic gradient flow. Results of numerical simulations of the discrete gradient flow (cf. Figure 1.5(B)) illustrate the convergence to steady states, their non-uniqueness as well as their dependence on initial data and model parameters. Based on this model we propose an adapted model in the cellular context for leaf venation, investigate the model analytically and show numerically that it can produce branching vein patterns.

The results in this thesis have been published or submitted to journals [BDK+18, CDKS18, CDKS19, DGH+19, HKM19a, HKM19b, HJKM19] and conference proceedings [Kre18, KM17] and have been presented at several national and international conferences. A detailed statement of originality and contribution is provided at the beginning of each chapter and a summary is given below:

- Chapter 2 is based on article [BDK+18] which is in collaboration with Martin Burger, Bertram Düring, Peter A. Markowich and Carola-Bibiane Schönlieb, and published in Mathematical Models and Methods in the Applied Sciences.

- Chapter 3 is based on article [DGH+19] which is in collaboration with Bertram Düring, Carsten Gottschlich, Stephan Huckemann and Carola-Bibiane Schönlieb, and published in the Journal of Mathematical Biology.

- Chapter 4 is based on article [CDKS18] which is in collaboration with José A. Carrillo, Bertram Düring and Carola-Bibiane Schönlieb, and published in the SIAM Journal on Applied Dynamical Systems.

- Chapter 5 is based on article [CDKS19] which is in collaboration with José A. Carrillo, Bertram Düring and Carola-Bibiane Schönlieb, and to be submitted for publication.

- Chapter 6 is based on article [HKM19a] which is in collaboration with Jan Haskovec and Peter A. Markowich, and to appear in Communications in Mathematical Sciences.

- Chapter 7 is based on article [HKM19b] which is in collaboration with Jan Haskovec and Peter A. Markowich, and published in Communications in Partial Differential Equations.

- Chapter 8 is based on article [HJKM19] which is in collaboration with Jan Haskovec, Henrik Jönsson and Peter A. Markowich, and to appear in the Proceedings of the Royal Society A.

## 1.4 Outline

### 1.4.1 Organisation of the thesis

This thesis deals with anisotropic nonlinear PDE models and dynamical systems in biology and is the union of seven papers [BDK+18, CDKS18, CDKS19, DGH+19, HJKM19, HKM19a, HKM19b], resulting from the collaborations of myself with Martin Burger, José A. Carrillo, Bertram Düring, Carsten Gottschlich, Jan Haskovec, Stephan Huckemann, Henrik Jönsson, Peter A. Markowich and Carola-Bibiane Schönlieb. This thesis divided into two parts:

- Part I (Chapters 2–5) is motivated by the simulation of fingerprint patterns and deals with a class of anisotropic interaction equations, based on the work in [BDK+18, CDKS18, CDKS19, DGH+19].

- Part II (Chapters 6–8) focuses on mathematical models for biological transportation networks describing living systems such as leaf venation in plants, blood circulatory systems, and neural networks, and is based on the research in [HJKM19, HKM19a, HKM19b].

Each of the Chapters 2–8 is based on one of these papers. We give an overview about the results of each chapter in this section. Finally, we conclude and give an outlook on current and possible future research in Chapter 9.

### 1.4.2 Outline of Part I

In Part I (Chapters 2–5), we consider a class of interacting particle models with anisotropic repulsive-attractive interaction forces and its continuum counterpart where the orientations of the forces depend on an underlying tensor field. An example of this class of models is the so-called Kücken–Champod model describing the formation of fingerprint patterns. This class of models can be regarded as a generalisation of a gradient flow of a nonlocal interaction potential which has a local repulsion and a long-range attraction structure. In contrast to isotropic interaction

models the anisotropic forces in our class of models cannot be derived from a potential. The underlying tensor field introduces an anisotropy leading to complex patterns which do not occur in isotropic models.

In Chapter 2, we investigate the role of the anisotropy which can be characterised by one parameter in the model. We study the variation of this parameter, describing the transition between the isotropic and the anisotropic model, analytically and numerically. We analyse the equilibria of the corresponding mean-field partial differential equation and investigate pattern formation numerically in two dimensions by studying the dependence of the parameters in the model on the resulting patterns.

In Chapter 3, we consider an anisotropic interaction model for simulating fingerprint patterns. Evidence suggests that both the interaction of so-called Merkel cells and the epidermal stress distribution play an important role in the formation of fingerprint patterns during pregnancy. To model the formation of fingerprint patterns in a biologically meaningful way these patterns have to become stationary. For the creation of synthetic fingerprints it is also very desirable that rescaling the model parameters leads to rescaled distances between the stationary fingerprint ridges. Based on these observations, as well as the model introduced by Kücken and Champod we propose a new model for the formation of fingerprint patterns during pregnancy. In this anisotropic interaction model, the interaction forces not only depend on the distance vector between the cells and the model parameters, but additionally on an underlying tensor field, representing a stress field. This dependence on the tensor field leads to complex, anisotropic patterns. We study the resulting stationary patterns both analytically and numerically. In particular, we show that fingerprint patterns can be modelled as stationary solutions by choosing the underlying tensor field appropriately.

In Chapter 4, we consider the stability of straight line patterns. Stable line patterns play a crucial role in the pattern formation of the anisotropic interaction model and are also important for the simulation of fingerprint patterns. For a given spatially homogeneous tensor field, we show that there exists a preferred direction of straight lines, i.e. straight vertical lines can be stable for sufficiently many particles, while many other rotations of the straight lines are unstable steady states, both for a sufficiently large number of particles and in the continuum limit. For straight vertical lines we consider specific force coefficients for the stability analysis of steady states, show that stability can be achieved for exponentially decaying force coefficients for a sufficiently large number of particles, and relate these results to the Kücken-Champod model for simulating fingerprint patterns. The mathematical

analysis of the steady states is completed with numerical results.

In Chapter 5, we study the equilibria of an anisotropic, nonlocal aggregation equation with nonlinear diffusion which does not possess a gradient flow structure. Here, the anisotropy is induced by an underlying tensor field. We derive equilibrium conditions for stationary line patterns which can be reformulated as the minimisers of a regularised energy functional if the underlying tensor field is spatially homogeneous. For spatially homogeneous tensor fields, we show the existence of energy minimisers, establish Γ-convergence of the regularised energy functionals as the diffusion coefficient vanishes, and prove the convergence of minimisers of the regularised energy functional to minimisers of the non-regularised energy functional. Further, we investigate properties of stationary solutions on different domains. Finally, we prove weak convergence of a numerical scheme for the numerical solution of the anisotropic, nonlocal aggregation equation with nonlinear diffusion and any underlying tensor field, and show numerical results.

### 1.4.3  Outline of Part II

In Part II (Chapters 6–8), we consider a discrete mathematical formulation for describing the formation of biological transportation networks. This model is based on a dynamic modelling approach on a graph which has recently been introduced by Hu and Cai [HC13]. The main mathematical interest of this dynamical model stems from the highly unusual coupling of a system of ODEs whose solution is defined on the edges of a graph to a linear system on the nodes of the graph. This model can also be reformulated as the minimisation of an energy consumption function constrained by a linear system on a graph.

In Chapter 6, we study the global existence of solutions of a discrete (ODE based) model on a graph. We propose an adaptation of this model so that a macroscopic (PDE based) system can be obtained as its formal continuum limit. We prove the global existence of weak solutions of the macroscopic PDE model. Finally, we present results of numerical simulations of the discrete model, illustrating the convergence to steady states, their non-uniqueness as well as their dependence on initial data and model parameters.

In Chapter 7, we study the rigorous limit of the discrete model. For the spatially two-dimensional rectangular setting we prove the rigorous continuum limit of the constrained energy functional as the number of nodes of the underlying graph tends to infinity and the edge lengths shrink to zero uniformly. The proof is based on

reformulating the discrete energy functional as a sequence of integral functionals and proving their $\Gamma$-convergence towards the respective continuum energy functional.

In Chapter 8, we propose an adapted model in the cellular context for leaf venation. The plant hormone auxin controls many aspects of the development of plants. One striking dynamical feature is the self-organisation of leaf venation patterns which is driven by high levels of auxin within vein cells. The auxin transport is mediated by specialised membrane-localised proteins. Many venation models have been based on polarly localised efflux-mediator proteins of the PIN family. Here, we investigate a modeling framework for auxin transport with a positive feedback between auxin fluxes and transport capacities that are not necessarily polar, i.e. directional across a cell wall. Our approach is derived from a discrete graph-based model for biological transportation networks, where cells are represented by graph nodes and intercellular membranes by edges. The edges are not a-priori oriented and the direction of auxin flow is determined by its concentration gradient along the edge. We prove global existence of solutions to the model and the validity of Murray's law for its steady states. Moreover, we demonstrate with numerical simulations that the model is able connect an auxin source-sink pair with a mid-vein and that it can also produce branching vein patterns. A significant innovative aspect of our approach is that it allows the passage to a formal macroscopic limit which can be extended to include network growth. We perform mathematical analysis of the macroscopic formulation, showing the global existence of weak solutions for an appropriate parameter range.

# Part I

# Anisotropic interaction equations

# Chapter 2

# Anisotropic pattern formation

## Originality and contribution

This chapter follows [BDK⁺18], written in collaboration with Martin Burger, Bertram Düring, Peter A. Markowich and Carola-Bibiane Schönlieb. While my co-authors proposed the study of the model and provided guidance and advice, [BDK⁺18] is primarily my own original work and nearly all the results, including analysis and simulations, were obtained by myself.

## Chapter summary

In this chapter, we consider a class of interacting particle models with anisotropic, repulsive–attractive interaction forces whose orientations depend on an underlying tensor field. An example of this class of models is the so-called Kücken–Champod model describing the formation of fingerprint patterns. This class of models can be regarded as a generalisation of a gradient flow of a nonlocal interaction potential which has a local repulsion and a long-range attraction structure. In contrast to isotropic interaction models the anisotropic forces in our class of models cannot be derived from a potential. The underlying tensor field introduces an anisotropy leading to complex patterns which do not occur in isotropic models. This anisotropy is characterised by one parameter in the model. We study the variation of this parameter, describing the transition between the isotropic and the anisotropic model, analytically and numerically. We analyse the equilibria of the corresponding mean-field partial differential equation and investigate pattern formation numerically in two dimensions by studying the dependence of the parameters in the model on the

resulting patterns.

## 2.1 Introduction

The goal of this chapter is to study the equilibria of the particle model (1.4), i.e.

$$\frac{\mathrm{d}x_j}{\mathrm{d}t} = \frac{1}{N} \sum_{\substack{k=1 \\ k \neq j}}^{N} F(x_j - x_k, T(x_j)), \tag{2.1}$$

and the associated mean-field PDE (1.17), i.e.

$$\partial_t \rho(t, x) + \nabla_x \cdot \left[ \rho(t, x) \left( F\left( \cdot, T(x) \right) * \rho(t, \cdot) \right)(x) \right] = 0 \qquad \text{in } \mathbb{R}_+ \times \mathbb{R}^2, \tag{2.2}$$

analytically and numerically. This can be achieved by investigating the existence of equilibria analytically. Since numerical simulations are crucial for getting a better understanding of the patterns which can be generated with the Kücken-Champod model we investigate the impact of the model parameters on the resulting transient and steady patterns numerically. In particular, we study the transition of steady states with respect to the parameter $\chi$. Based on the results in this chapter we study the solution to the particle model for non-homogeneous tensor fields, simulate the fingerprint pattern formation process and model fingerprint patterns with certain features in Chapter 3.

Note that the modelling involves multiple scales which can be seen in several different ways. Given the particle model in (2.1) we consider the associated particle density to derive the mean-field limit. Here, the interaction force exhibits short-range repulsion and long-range attraction. The direction of the attraction force depends on the parameter $\chi$ which is responsible for different transient and steady state patterns. More precisely, ring equilibria obtained for $\chi = 1$ evolve into ellipse patterns and stripe patterns as $\chi$ decreases. Besides, large-time asymptotics are considered for determining the equilibria.

This chapter is organised as follows. In Section 2.2 the solution to the mean-field PDE (2.2) is analysed. More precisely, we discuss the impact of the parameter $\chi$ on the force alignment and on the solution to the model. Besides, we study the impact of spatially homogeneous tensor fields and we show that the equilibria to the mean-field PDE (2.2) for any spatially homogeneous tensor field can be regarded as a coordinate transform of the tensor field $T = \chi s \otimes s + l \otimes l$ where $s = (0, 1)$

and $l = (1, 0)$ for any parameter $\chi \in [0, 1]$. Hence, we can restrict ourselves to this specific tensor field $T$ for the analysis. We investigate the existence of equilibria to the mean-field PDE (2.2) whose form depend on the choice of $\chi$. Under certain assumptions we show that for $\chi = 1$ there exists at most one radius $R > 0$ such that the ring state of radius $R$ is a nontrivial equilibrium mean-field PDE (2.2) for spatially homogeneous tensor fields and uniqueness can be guaranteed under an additional assumption, while for $\chi \in [0, 1)$ the ring state is no equilibrium. For $\chi \in [0, 1]$ and $R > 0$ sufficiently small there exists at most one $r > 0$ such that an ellipse with major axis $R + r$ and minor axis $R$ whose major axis is aligned along $s$ is an equilibrium. Besides, the shorter the minor axis of the ellipse, the longer the major axis of possible ellipse steady states and the smaller the value of $\chi$ the longer the major and the shorter the minor axis of the possible ellipse equilibrium. Section 2.3 contains a description of the numerical method and we discuss the simulation results for the particle model (2.1). The numerical results include an investigation of the stationary solutions and their dependence on different parameters in the model, including the impact of the parameter $\chi$ and the associated transition between the isotropic and anisotropic model. Besides, we compare the numerical with the analytical results.

## 2.2  Analysis of the model

We analyze the equilibria of the mean-field PDE (2.2) in terms of the parameter $\chi \in [0, 1]$ for the general formulation of the model, i.e., the total force is given by (1.8) where the repulsion and the attraction forces are defined in (1.11).

### 2.2.1  Interpretation of the total force

The alignment of the attraction force, defined in (1.11), and thus the pattern formation strongly depend on the choice of the parameter $\chi \in [0, 1]$. For $\chi = 1$ the total force $F$ in (1.8) can be derived from a radially symmetric potential and the mean-field PDE (2.2) reduces to the isotropic interaction equations (1.3). In particular, the solution to (2.2) is radially symmetric for $\chi = 1$ for radially symmetric initial data [BGL12].

For $\chi \in [0, 1)$ the attraction force $F_A$ of the form (1.11) is not conservative by Remark 2 and can be written as the sum of a conservative and a non-conservative

force, given by $F_A = F_{A,1} + F_{A,2}$ with

$$F_{A,1}(d) = f_A(|d|)d$$

and

$$F_{A,2}(d, T(x_j)) = f_A(|d|)(T(x_j) - \mathbb{I})d = f_A(|d|)(\chi - 1)(s(x_j) \cdot d)s(x_j),$$

where $d \equiv d(x_j, x_k) := x_j - x_k$ and $\mathbb{I}$ denotes the two-dimensional identity matrix. In particular, $F_{A,1}$ does not depend on $\chi$ and is equal to the attraction force in (1.11) with $\chi = 1$. Since the coefficient function $f_A(\chi - 1)$ of $F_{A,2}$ is nonnegative, $F_{A,2}$ is a repulsion force aligned along $s(x_j)$ and leads to an additional advection along $s(x_j)$ compared to the case $\chi = 1$. This repulsion force along $s(x_j)$ is the larger, the smaller $\chi$. In particular, for the force coefficients $f_A$ and $f_R$ in the Kücken-Champod model (2.1), given by (1.19) and (1.18) with parameters in (1.20), the total force along $s$ is purely repulsive for $\chi$ sufficiently small as illustrated in Figure 2.1.

For the spatially homogeneous tensor field $T = \chi s \otimes s + l \otimes l$ with $l = (1, 0)$ and $s = (0, 1)$ the solution is stretched along the vertical axis for $\chi < 1$. The smaller the value of $\chi$, the larger the repulsion force and the more the solution is stretched along the vertical axis. For $\chi$ sufficiently small stretching along the entire vertical axis is possible for solutions to the particle model (2.1) because of purely repulsive forces along $s$.



(A) Along $l$        (B) Along $s$
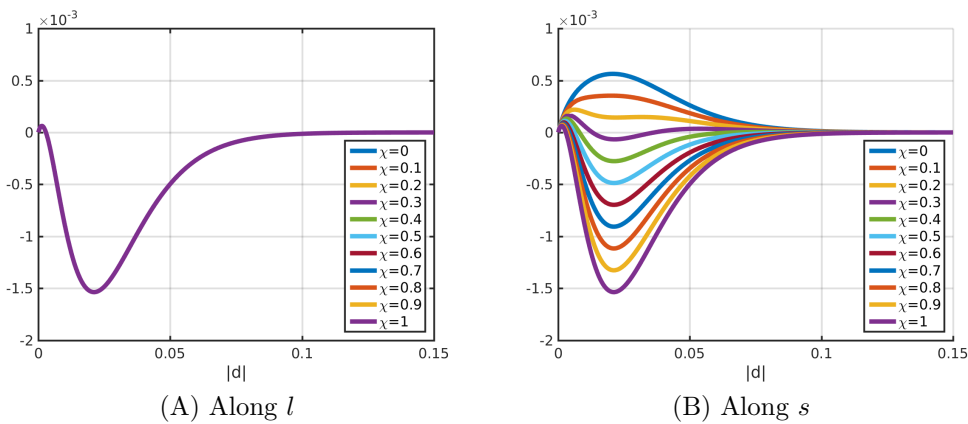
Figure 2.1: Total force along $l$ and $s$ given by (1.21) for coefficients $f_A$ in (1.19) and $f_R$ in (1.18) of the attraction and the repulsion force for parameter values in (1.20), respectively) for different values of $\chi$.

### 2.2.2  Impact of spatially homogeneous tensor fields

Let $\chi \in [0,1]$ and consider the spatially homogeneous tensor field $T = \chi s \otimes s + l \otimes l$ with $l = (1,0)$ and $s = (0,1)$. The solution of the particle model (2.1) for any spatially homogeneous tensor field $\tilde{T}$ is a coordinate transform of the solution of the particle model (2.1) for the tensor field $T$. Similarly, for the analysis of equilibria of the microscopic model (2.1) for $\tilde{T}$ it is sufficient to study the equilibria of (2.1) for $T$. For a similar statement for the mean-field PDE (2.2) we define the concept of an equilibrium state.

**Definition 2** (Equilibrium state of (2.2))**.** *A Borel probability measure $\mu \in \mathcal{P}(\mathbb{R}^2)$ is said to be an equilibrium state of the mean-field PDE (2.2) if*

$$K \in L^1_{loc}(\mathrm{d}\mu) \quad and \quad K = 0 \ on \ supp(\mu) \ \mu\text{-}a.e. \tag{2.3}$$

*where $K = F(\cdot, T) * \mu$ $\mu$-a.e.*

An equilibrium state of the mean-field equation (2.2) for any spatially homogeneous tensor field $\tilde{T}$ is the coordinate transform of an equilibrium state to the mean-field equation (2.2) for the tensor field $T$. For detailed computations see Appendix 2.A.

### 2.2.3  Existence of equilibria

Based on the discussion on the action of the total force in Section 2.2.1 possible shapes of equilibria of the mean-field PDE (2.2) depend on the choice of the parameter $\chi \in [0,1]$. To analyze the equilibria of the mean-field PDE (2.2) in two dimensions for any spatially homogeneous tensor field, it is sufficient to consider the tensor field $T = \chi s \otimes s + l \otimes l$ with $l = (1,0)$ and $s = (0,1)$ in the sequel as outlined in Section 2.2.2. Note that the forces along $l$ are assumed to be repulsive-attractive, while the forces along $s$ depend significantly on the choice of $\chi$ and may be repulsive, repulsive-attractive-repulsive or repulsive-attractive. Further note that the forces only depend on the distance vector for spatially homogeneous tensor fields. To simplify the analysis, we make the following assumption on $F$ in addition to Assumption 1 in this section:

**Assumption 2.** *We assume that $F$ is strictly decreasing along $l$ and $s$ on the interval $[0, d_e]$ for some $d_e > d_a$ where $d_a$ is defined in Assumption 1. In particular, there exits $d_e > d_a$ such that $\chi f_A + f_R$ is strictly decreasing on $[0, d_e]$ for all $\chi \in [0,1]$.*

39

Assumption 2 is clearly satisfied for the force coefficients (1.18) and (1.19) in the Kücken-Champod model (2.1) with parameter values in (1.20), cp. Figure 2.2. With this choice of parameters we have $d_a \simeq 0.0029$ and for $d_e = 0.0126$ the monotonicity property of the force holds in $[0, d_e]$ uniformly with respect to $\chi \in [0, 1]$.
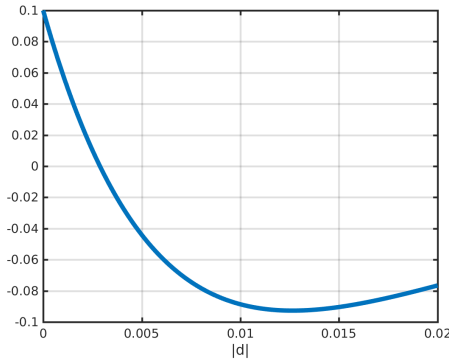


Figure 2.2: Coefficients $f_A + f_R$ for parameter values in (1.20).

**Ellipse pattern**

Solutions to the the mean-field PDE (2.2) for $T = \chi s \otimes s + l \otimes l$ with $l = (1, 0)$ and $s = (0, 1)$ are stretched along the vertical axis by the discussion in Section 2.2.1. This motivates us to consider an ellipse whose major axis is parallel to the vertical axis. Because of the spatial homogeneity of the tensor field it is sufficient to restrict ourselves to probability measures with centre of mass $(0, 0)$.

**Definition 3.** *Let $R > 0$ and let $r \geqslant 0$. The ellipse state whose minor and major axis are of lengths $R$ and $R + r$, respectively, is the probability measure which is uniformly distributed on*

$$\left\{ x = (x_1, x_2) \in \mathbb{R}^2 \colon \left(\frac{x_1}{R}\right)^2 + \left(\frac{x_2}{r + R}\right)^2 = 1 \right\}.$$

*We denote this probability measure by $\delta_{(R,r)}$.*

First, we restrict ourselves to nontrivial ring states $\delta_{(R,0)}$ of radius $R > 0$, i.e., we consider the special case of ellipse states where $r = 0$. The existence of ring equilibria for repulsive-attractive potentials that do not decay faster than $1/d^2$ as $d \to \infty$ has already been discussed in [BCLR13b]. However, the force coefficients (1.18) and (1.19) in the Kücken-Champod model [KC13] decay exponentially fast

as $d \to \infty$. Besides, a repulsive-attractive potential exists for $\chi = 1$ only by Remark 2. To analyse the ring equilibria we distinguish between the two cases $\chi = 1$ and $\chi \in [0, 1)$, starting with the case $\chi = 1$.

**Lemma 1.** *Let $\chi = 1$. The probability measure $\delta_{(R,0)}$ is a nontrivial ring equilibrium to* (2.2) *for radius $R > 0$ if and only if*

$$\int_0^\pi (f_A + f_R)\left(R\sqrt{(1 - \cos\phi)^2 + \sin^2\phi}\right)(1 - \cos\phi)\,\mathrm{d}\phi = 0. \qquad (2.4)$$

*Proof.* By symmetry of the domain one obtains that $K(x) = (F(\cdot, T(x)) * \delta_{(R,0)})(x)$ is rotation invariant for $\chi = 1$. We have

$$K(R_\theta x) = K(x), \quad x \in \mathbb{R}^2,$$

for every angle $\theta \in \mathbb{R}$, where $R_\theta$ stands for the counter-wise rotation matrix with angle $\theta$ in (1.16). In particular, for every $x$ in the circle of radius $R$ one has $K(x) = K((R, 0))$. Hence, it suffices to show for $\chi = 1$ that there exists $R > 0$ such that

$$(F(\cdot, T) * \delta_{(R,0)})((R, 0)) = \int_0^{2\pi} F(R(1 - \cos\phi, -\sin\phi), T)R\,\mathrm{d}\phi = 0$$

for nontrivial ring equilibria. By using the simplified form of

$$F(d, T) = (f_A + f_R)(|d|)d$$

for $\chi = 1$ a change of variables yields

$$\int_\pi^{2\pi} F(R(1 - \cos\phi, -\sin\phi), T)R\,\mathrm{d}\phi = \int_0^\pi F(R(1 - \cos\phi, \sin\phi), T)R\,\mathrm{d}\phi$$

due to the odd symmetry of the sine function at $\pi$. Hence, the second component of the integral $\int_0^{2\pi} F(R(1 - \cos\phi, -\sin\phi), T)R\,\mathrm{d}\phi$ is zero and we can restrict ourselves to the first component, implying that it is sufficient to show the existence of $R > 0$ such that

$$R^2 \int_0^\pi (f_A + f_R)\left(R\sqrt{(1 - \cos\phi)^2 + \sin^2\phi}\right)(1 - \cos\phi)\,\mathrm{d}\phi = 0.$$

Since we are interested in nontrivial ring equilibria with radius $R > 0$ the condition finally reduces to (2.4). $\qquad\square$

**Proposition 1.** *Let $\chi = 1$. There exists at most one radius $\bar{R} \in (0, \frac{d_e}{2}]$ such that the ring state $\delta_{(\bar{R},0)}$ of radius $\bar{R}$ is a nontrivial equilibrium to the mean-field PDE (2.2). If*

$$\int_0^\pi (f_A + f_R) \left( \frac{d_e}{2} \sqrt{(1 - \cos\phi)^2 + \sin^2\phi} \right) (1 - \cos\phi) \, \mathrm{d}\phi < 0 \qquad (2.5)$$

*there exists a unique $\bar{R} \in (\frac{d_a}{2}, \frac{d_e}{2}]$ such that the ring state $\delta_{(\bar{R},0)}$ of radius $\bar{R}$ is a nontrivial equilibrium.*

*Proof.* Consider the left-hand side of (2.4) as a function of $R$ denoted by $G(R)$. By deriving $G(R)$ with respect to $R$ and using Assumption 2 one can easily see that $G(R)$ is strictly decreasing as a function of $R$ on $[0, \frac{d_e}{2}]$. Note that $G(0) > 0$, $G(R) > 0$ for $R \leqslant \frac{d_a}{2}$ and $f_A, f_R$ are continuous by Assumption 1 on the total force. Since (2.5) is equivalent to $G(\frac{d_e}{2}) < 0$ this concludes the proof. $\qquad \square$

One can easily check that (2.5) is satisfied for the force coefficients (1.18) and (1.19) in the Kücken-Champod model (2.1) with parameter values in (1.20) if $d_e$ is the argument of the minimum of $f_A + f_R$, see Assumption 2. In particular, this implies that there exists a unique nontrivial ring equilibrium of radius $R \in (\frac{d_a}{2}, \frac{d_e}{2}]$ to the mean-field PDE (2.2) for the forces in the particle model for $\chi = 1$.

The case $\chi \in [0, 1)$ can be analysed similarly as the one for $\chi = 1$ for ring patterns except that some of the symmetry arguments do not hold.

**Proposition 2.** *Let $\chi \in [0, 1)$. There exists no $R \in (0, \frac{d_e}{2}]$ such that the ring state $\delta_{(R,0)}$ is an equilibrium to the mean-field PDE (2.2).*

*Proof.* For $\chi = 1$, $(F(\cdot, T) * \delta_{(R,0)})((R, 0)) = 0$ is equivalent to (2.4) by Lemma 1, based on the property $(F(\cdot, T) * \delta_{(R,0)})((R, 0)) \cdot s = 0$. Since

$$F(d, T) = f_A(|d|)(d_1, \chi d_2) + f_R(|d|)d$$

where $d = (d_1, d_2)$, (2.4) also has to be satisfied for $\chi \in [0, 1)$. Similarly as in the proof of Lemma 1 one can show that

$$(F(\cdot, T) * \delta_{(R,0)})((0, R)) = \int_0^{2\pi} F(R(-\cos\phi, 1 - \sin\phi), T) R \, \mathrm{d}\phi = 0$$

is equivalent to

$$\int_{\pi/2}^{3\pi/2} (\chi f_A + f_R) \left(R\sqrt{\cos^2\phi + (1-\sin\phi)^2}\right)(1-\sin\phi)\,\mathrm{d}\phi = 0 \qquad (2.6)$$

for $R > 0$. Note that (2.4) is equivalent to (2.6) for $\chi = 1$ by symmetry so that the equilibrium of radius $R \in (0, \frac{d_e}{2}]$ from Proposition 1 satisfies (2.4) and (2.6) simultaneously for $\chi = 1$. However, (2.4) and (2.6) are not satisfied simultaneously for any $R \in (0, \frac{d_e}{2}]$ and any $\chi \in [0, 1)$ which concludes the proof. $\qquad \square$

Next, we analyse the ellipse pattern.

**Corollary 1.** *Let $\chi \in [0, 1]$ be given and define*

$$w_1(\phi, R, r) = \sqrt{R^2(1-\cos\phi)^2 + (R+r)^2\sin^2\phi},$$

$$w_2(\phi, R, r) = \sqrt{R^2\sin^2\phi + (R+r)^2\cos^2\phi},$$

$$w_3(\phi, R, r) = \sqrt{R^2\cos^2\phi + (R+r)^2(1-\sin\phi)^2}.$$

*Then, necessary conditions for a stationary ellipse state $\delta_{(R,r)}$ where $R, r \geqslant 0$ are given by*

$$\int_0^\pi (f_A + f_R)(w_1(\phi, R, r))\, R\,(1-\cos\phi)\, w_2(\phi, R, r)\,\mathrm{d}\phi = 0 \qquad (2.7)$$

*and*

$$\int_{\pi/2}^{3\pi/2} (\chi f_A + f_R)(w_3(\phi, R, r))\,(R+r)\,(1-\sin\phi)\, w_2(\phi, R, r)\,\mathrm{d}\phi = 0. \qquad (2.8)$$

*Proof.* For ellipse equilibria we require $(F(\cdot, T) * \delta_{(R,r)})((R, 0)) = 0$ implying

$$\int_0^{2\pi} F((R(1-\cos\phi), -(R+r)\sin\phi), T)\sqrt{R^2\sin^2\phi + (R+r)^2\cos^2\phi}\,\mathrm{d}\phi = 0.$$

Since $e_2 \cdot (F(\cdot, T) * \delta_{(R,r)})((R, 0)) = 0$ by symmetry for any $\chi \in [0, 1)$ where $e_2 = (0, 1)$ and

$$F(d, T) = (f_A(|d|) + f_R(|d|))\begin{pmatrix} 1 & 0 \\ 0 & \chi \end{pmatrix}d$$

this implies that it is sufficient to require (2.7) where

$$w_2(\phi, R, r) = \sqrt{R^2 \sin^2 \phi + (R + r)^2 \cos^2 \phi}.$$

Similarly,

$$
\begin{aligned}
&(F(\cdot, T) * \delta_{(R,r)})((0, R + r)) \\
&= C \int_0^{2\pi} F((-R\cos\phi, (R + r)(1 - \sin\phi)), T) w_2(\phi, R, r) \, \mathrm{d}\phi \\
&= 0
\end{aligned}
$$

for a normalisation constant $C$ reduces to the necessary condition (2.8). $\qquad\square$

In the sequel, we denote the left-hand side of (2.7) by $G(R, r)$.

**Assumption 3.** *Given $r \in [0, d_e)$ we assume that there exists $R_{int} \in (0, R_e)$ such that*

$$\frac{\mathrm{d}}{\mathrm{d}R} G(R, r) > 0 \quad \text{for} \quad R \in (0, R_{int}) \quad \text{and} \quad \frac{\mathrm{d}}{\mathrm{d}R} G(R, r) < 0 \quad \text{for} \quad R \in (R_{int}, R_e).$$

**Remark 4.** *Since $G(0, r) = 0$ and Assumption 3 implies that for $r \in [0, d_e)$ given we have $G(R, r) > 0$ for all $R \in (0, R_{int})$. Besides, the uniqueness of stationary ellipse states $\delta_{(R,r)}$ for $R \in (R_{int}, R_e)$ for given $r \in [0, d_e)$ is guaranteed by Assumption 3.*

We have the following existence result for nontrivial ellipse states, including rings for $R > 0$ and $r = 0$.

**Corollary 2.** *Let $r \in [0, d_e)$ and let $R_e > 0$ such that*

$$w_1(\phi, R, r) \leqslant d_e \quad \text{for all} \quad \phi \in [0, \pi], \ R \in [0, R_e] \tag{2.9}$$

*is satisfied and assume that*

$$\int_0^\pi (f_A + f_R)(w_1(\phi, R, r))(1 - \cos\phi)(R_e^2 + R_e r \cos^2 \phi) \, \mathrm{d}\phi < 0. \tag{2.10}$$

*holds. Further define*

$$G_1(R, r) = \int_0^\pi (f_A + f_R)(w_1(\phi, R, r))(1 - \cos\phi) \, \mathrm{d}\phi$$

*and*

$$G_2(R, r) = \int_0^\pi (f_A + f_R)(w_1(\phi, R, r))(1 - \cos \phi) \cos^2 \phi \, \mathrm{d}\phi.$$

*If $r$ satisfies*

$$\min \{G_1(0, r), G_2(0, r)\} > 0 \tag{2.11}$$

*there exists an $R \in (0, R_e)$ such that the necessary condition (2.7) for a nontrivial stationary ellipse state $\delta_{(R,r)}$ to the mean-field PDE (2.2) are satisfied. For $r$ satisfying*

$$\max \{G_1(0, r), G_2(0, r)\} < 0 \tag{2.12}$$

*there exists no $R \in (0, R_e)$ such that the ellipse $\delta_{(R,r)}$ is an equilibrium to the mean-field PDE (2.2) and the trivial ellipse state $\delta_{(0,r)}$ is the only equilibrium. If, for $r \in [0, d_e)$ given, Assumption 3 is satisfied, then there exists a unique $R \in (R_{int}, R_e)$ such that the necessary condition (2.7) for a nontrivial stationary ellipse state $\delta_{(R,r)}$ is satisfied.*

**Remark 5.** *Condition (2.9) is related to the assumption that $f_A + f_R$ is strictly decreasing on $[0, d_e]$ in Assumption 2. Condition (2.10) can be interpreted as the long-range attraction forces being larger than the short-range repulsion forces. Besides, given $r \in [0, d_e)$ condition (2.12) can be interpreted as the attractive forces being too strong for the existence of a stationary ellipse patterns $\delta_{(0,r)}$ and hence for any stationary ellipse pattern $\delta_{(R,r)}$ for $R \geqslant 0$ because the forces are attractive for $R$ sufficiently large. Condition (2.11) implies that the forces are too repulsive along the vertical axis for a stationary ellipse state $\delta_{(0,r)}$, but as $R$ increases the forces become more attractive which may result in stationary ellipse state $\delta_{(R,r)}$ for $R > 0$. Assumption 3 relaxes condition (2.11), but requires additionally that $G(\cdot, r)$ first increases and then decreases to guarantee the uniqueness of a stationary ellipse pattern. In Figure 2.3(A) the function $G$ is evaluated for certain values of $r \in [0, d_e)$ for the forces in the particle model (2.1) and one can clearly see that Assumption 3 is satisfied and there exists a unique zero $R > 0$, as stated in Corollary 2.*

*Proof.* Let $r \in (0, d_e)$ be given. Note that the left-hand side of (2.9) is equal to $w_1(\phi, R, r)$ for all $\phi \in [0, \pi]$ and $w_1(\phi, R, r) \in [0, \max\{2R, R + r\}]$ for all $\phi \in [0, \pi]$. Since $f_A + f_R$ is strictly decreasing on $[0, d_e]$ by Assumption 2 we only consider $R \geqslant 0$ such that $w_1(\phi, R, r) \in [0, d_e]$ for all $\phi \in [0, \pi]$. Clearly, there exists $R_e > 0$

such that (2.9) is satisfied.

Since $w_2(\phi, R, r) \sim R + r\cos^2\phi$ we approximate (2.7) by

$$\int_0^\pi (f_A + f_R)(w_1(\phi, R, r))(1 - \cos\phi)\left(R^2 + Rr\cos^2\phi\right)\mathrm{d}\phi = 0 \qquad (2.13)$$

Note that $(f_A + f_R)(w_1(\phi, R, r))(1 - \cos\phi)$ for $\phi \in (0, \pi)$ is strictly decreasing as a function of $R$ because $f_A + f_R$ is a strictly decreasing function by Assumption 2 and $w_1(\phi, R, r)$ is strictly increasing in $R$ for $\phi \in (0, \pi)$ fixed. Hence, $G_1(R, r)$ is strictly decreasing in $R$ and has a unique zero $R_1 \in [0, R_e]$, provided $r \geqslant 0$ satisfies $G_1(0, r) > 0$ and (2.10). Similarly, one can argue that $G_2(R, r)$ is strictly decreasing in $R$ and has a unique zero $R_2 \in [0, R_e]$ if $r \geqslant 0$ such that $G_2(0, r) > 0$ and (2.10) are satisfied. The left-hand side of (2.13) is the rescaled sum of $G_1$ and $G_2$ where $\mathrm{id}^2 \cdot G_1(\cdot, r)$ as a function of $R$ is nonnegative on $[0, R_1]$ and negative on $(R_1, R_e]$, while $\mathrm{id} \cdot rG_2(\cdot, r)$ as a function of $R$ is nonnegative on $[0, R_2]$ and negative on $(R_2, R_e]$. In particular, the left-hand side of (2.13) has a zero $R \in [\min\{R_1, R_2\}, \max\{R_1, R_2\}]$ on $(0, R_e)$ if $r \geqslant 0$ satisfies (2.11) and (2.10), while there exists no zero on $(0, R_e)$ if $r \geqslant 0$ satisfies (2.12). If Assumption 3 is satisfied, then $G(\cdot, r)$ with $r \in [0, d_e)$ given has a zero at $R = 0$ and at an $R \in (0, d_e)$ because $G(\cdot, r) > 0$ on $(0, R_{int})$, $G(\cdot, r)$ strictly decreasing on $(R_{int}, R_e)$ and $G(R_e, r) < 0$ by (2.10). This concludes the proof.

$\square$

Since the equilibrium condition (2.7) for trivial ellipse states with $R = 0$ is clearly satisfied for all $r \geqslant 0$ we rewrite $G(R, r) = Rg(R, r)$ for a smooth function $g$ and require $g(0, r) = 0$. Since we are interested in nontrivial states, i.e., $r > 0$, we define

$$\bar{g}(r) = \int_0^\pi (f_A + f_R)(r|\sin\phi|)(1 - \cos\phi)|\cos\phi|\,\mathrm{d}\phi = 0$$

and and it is sufficient to require $\bar{g}(r) = 0$ for an $r > 0$. Note that $\bar{g}(r) > 0$ for all $r \in (0, d_a]$ since $f_A + f_R$ is repulsive on $[0, d_a]$. Assuming that $\bar{g}(d_e) < 0$ which is a natural condition for long-range attraction forces being stronger than short-range repulsive forces there exists a unique $\bar{r} \in (0, d_e)$ such that $\bar{g}(\bar{r}) = 0$ because $\bar{g}$ strictly decreases on $(0, d_e)$. Besides, the necessary condition (2.8) reduces to

$$\int_{\pi/2}^{3\pi/2} (\chi f_A + f_R)(\bar{r}|1 - \sin\phi|)(1 - \sin\phi)|\cos\phi|\,\mathrm{d}\phi = 0.$$

Since $f_A \leqslant 0$ and $f_R \geqslant 0$ by the definition of the attractive and repulsive force, cf. Assumption 1, there exists a unique $\bar{\chi} \in (0,1)$ such that condition (2.8) is satisfied, given by

$$\bar{\chi} = -\frac{\int_{\pi/2}^{3\pi/2} f_R \left(\bar{r}|1 - \sin\phi|\right)(1 - \sin\phi)\,|\cos\phi|\,\mathrm{d}\phi}{\int_{\pi/2}^{3\pi/2} f_A \left(\bar{r}|1 - \sin\phi|\right)(1 - \sin\phi)\,|\cos\phi|\,\mathrm{d}\phi} > 0. \qquad (2.14)$$

Note that $\bar{\chi} < 1$ by the assumption that the long-range attraction forces are stronger than the short-range repulsive forces. In summary, we have the following result.

**Lemma 2.** *There exists a unique $\bar{r} \in (0, d_e)$ such that the necessary condition (2.7) for a stationary ellipse state $\delta_{(0,\bar{r})}$ with $\bar{g}(\bar{r}) = 0$ is satisfied. In this case, the second necessary condition (2.8) is satisfied for a unique $\bar{\chi} \in [0,1]$, defined by (2.14).*

**Assumption 4.** *Assume that*

(i) *If $G(\tilde{R}, \tilde{r}) = 0$ for $\tilde{R} > 0$, $\tilde{r} \geqslant 0$, then $G(\tilde{R}, r) < 0$ for $r > \tilde{r}$.*

(ii) *There exists $R > 0$ such that $G(R, 0) < 0$.*

(iii) *For all $R > 0$ there exists $r \geqslant 0$ such that $G(R, r) < 0$.*

**Remark 6.** *Note that (1) in Assumption 4 implies that if the equilibrium condition for an ellipse state is satisfied for a specific tuple $(\tilde{R}, \tilde{r})$, then the forces are too attractive for any ellipse state $(\tilde{R}, r)$ with longer major axis $\tilde{R} + r \geqslant \tilde{R} + \tilde{r}$ for $r \geqslant \tilde{r}$. Condition (2) in Assumption 4 together with Assumption 3 implies the existence of a ring equilibrium. Besides, (3) in Assumption 4 states that for an ellipse state with a minor axis of length $R > 0$ one can choose the major axis $R + r$ sufficiently long so that the given forces are too attractive for the ellipse state $\delta_{(R,r)}$ to be stationary. Note that one can easily check that these assumptions are satisfied for the forces in the Kücken-Champod model with parameters in (1.20).*

**Proposition 3.** *Let $0 \leqslant r_1 < r_2 < d_e$ and let $R_1, R_2 \geqslant 0$ such that*

$$w_1(\phi, R, r) \leqslant d_e \quad \text{for all} \quad \phi \in [0, \pi], \quad R \in [0, \max\{R_1, R_2\}]$$

*and the necessary condition (2.7) for $\delta_{(R_1, r_1)}$ and $\delta_{(R_2, r_2)}$ being stationary ellipse states are satisfied. Suppose that Assumption 4 and Assumption 3 hold. Then, $R_1 > R_2$, i.e., the longer the major axis of the stationary ellipse state, the shorter the minor axis. Besides, there exists a continuous function $q(t) = (R(t), r(t))$ for*

$t \in [0,1]$ *where* $R(t)$ *is strictly decreasing,* $r(t)$ *is strictly increasing,* $q(0) = (0, \bar{r})$ *for the pseudo-ellipse state* $\delta_{(0,\bar{r})}$ *with* $\bar{r} > 0$ *in Lemma* 2 *and* $q(1) = (\bar{R}, 0)$ *for the unique ring state of radius* $\bar{R}$ *in Proposition* 1.

*Proof.* Note that $G(0, r) = 0$ for all $r \geqslant 0$. Further note that $(f_A + f_R)(0) > 0$ since $F$ is a short-range repulsive, long-range attractive force by Assumption 1, implying that for all $R \in (0, d_a/4]$ and all $r \in [0, d_a/4]$ we have $G(R, r) > 0$. By continuity and since $G(R, 0) < 0$ for some $R > 0$ there exists $\tilde{R} > 0$ such that $G(\tilde{R}, 0) = 0$. Besides, Assumption 4 implies that $G(\tilde{R}, r) < 0$ for all $r > 0$. In particular, $G(\tilde{R}, r_1) < 0$ and $G(\tilde{R}, r_2) < 0$ for $r_2 > r_1 > 0$ implies together with Assumption 3 that there exists a unique $\tilde{R}_1 \in [0, \tilde{R})$ such that $G(\tilde{R}_1, r_1) = 0$ which implies that $G(\tilde{R}_1, r_2) < 0$ and that there exists $\tilde{R}_2 \in [0, \tilde{R}_1)$ such that $G(\tilde{R}_2, r_2) = 0$. $\qquad \square$

In Figure 2.3(B) the tuples $(R, r)$ are plotted such that the necessary condition (2.7) for ellipse equilibria is satisfied. In particular, these tuples $(R, r)$ can be determined independently from $\chi$ from (2.7).

**Corollary 3.** *Let* $H(R, r, \chi)$ *denote the left-hand side of* (2.8) *and assume that* $H(q_1, q_2, 1)$ *is strictly increasing where the function* $q(t) = (q_1(t), q_2(t))$, $t \in [0, 1]$, *is defined in Proposition* 3. *For every tuple* $(R, r)$ *with* $R, r \geqslant 0$ *such that the condition* (2.7) *is satisfied there exists a unique* $\chi \in [0, 1]$ *so that* (2.8) *is also satisfied. If additionally* $H(q_1, q_2, \chi)$ *is strictly decreasing for all* $\chi \in [\bar{\chi}, 1]$ *then there exists a unique tuple* $(R, r)$ *such that the corresponding ellipse pattern* $\delta_{(R,r)}$ *is an equilibrium for any given* $\chi \in [\bar{\chi}, 1]$. *In particular, there exists a continuous, strictly increasing function* $p = p(t)$ *for* $t \in [0, 1]$ *with* $p(0) = \bar{\chi}$ *and* $p(1) = 1$ *such that for* $t \in [0, 1]$ *given the ellipse state* $\delta_{(q_1(t), q_2(t))}$ *is stationary for a unique value of the parameter* $\chi = p(t)$. *In other words, the smaller the value of* $\chi \in [\bar{\chi}, 1]$ *the longer the major and the shorter the minor axis for ellipse equilibria, i.e., the smaller the value of* $\chi$ *the more the ellipse is stretched along the vertical axis.*

*Proof.* Note that (2.8) can be rewritten as

$$\int_0^\pi (\chi f_A + f_R) (w_3(\phi + \pi/2, R, r)) (R + r) (1 - \cos \phi) w_2(\phi + \pi/2, R, r) \, d\phi = 0$$

(2.15)

where

$$w_3(\phi + \pi/2, R, r) = \sqrt{R^2 \sin^2 \phi + (R + r)^2 (1 - \cos \phi)^2}.$$

48

In particular, (2.15) is equal to (2.7) for $\chi = 1$ and $r = 0$, i.e., $H(q_1(1), q_2(1), 1) = 0$. However, for any tuple $(R, r)$ with $r > 0$ satisfying (2.7) we have $H(R, r, 1) < 0$ since $H(q_1, q_2, 1)$ is strictly increasing on $[0, 1]$ and $H(q_1(1), q_2(1), 1) = 0$. Besides, $H(q_1, q_2, 0) > 0$ on $[0, 1]$ since by the definition of the repulsive force coefficient in Assumption 1 we have $1 - \cos\phi \geqslant 0$ on $[0, \pi]$, $f_R \geqslant 0$ and $w_2 \geqslant 0$. Since $H(q_1(t), q_2(t), \cdot)$ is strictly decreasing as a function of $\chi$ for any $t \in [0, 1]$ fixed by the properties of the attractive force coefficient in Assumption 1 for each $t \in [0, 1]$ there exists a unique $\chi \in [0, 1]$ by continuity of $H$ such that the tuple $q(t) = (q_1(t), q_2(t))$ satisfies condition (2.8).

To show that for any $\chi \in [\bar{\chi}, 1]$ there exists a unique tuple $(R, r)$ such that $\delta_{(R,r)}$ is a stationary ellipse state note that $H(\bar{R}, 0, 1) = 0$ by the definition of $\bar{R}$ in Proposition 1 and $H(\bar{R}, 0, \chi) > 0$ for $\chi \in (0, 1]$ since $H(\bar{R}, 0, \cdot)$ strictly decreasing. Similarly, $H(0, \bar{r}, \bar{\chi}) = 0$ and $H(0, \bar{r}, \chi) < 0$ for all $\chi \in (\bar{\chi}, 1]$. Since $H(q_1, q_2, \chi)$ is strictly increasing for any $\chi \in [\bar{\chi}, 1]$ by assumption the function $H(q_1, q_2, \chi)$ for $\chi \in [\bar{\chi}, 1]$ fixed has a unique zero, i.e., there exists a unique tuple $(R, r)$ such that $\delta_{(R,r)}$ is a stationary ellipse state. Besides, if $\delta_{(R_1,r_1)}$ and $\delta_{(R_2,r_2)}$ are stationary ellipse states with $R_1 < R_2$ and $r_1 > r_2$ for $\chi_1, \chi_2 \in [\bar{\chi}, 1]$, respectively, then $\chi_1 < \chi_2$ since there exist $t_1, t_2 \in [0, 1]$ with $t_1 < t_2$ such that $q(t_1) = (R_1, r_1)$ and $q(t_2) = (R_2, r_2)$ and $H(q_1, q_2, \chi)$ strictly increasing for any $\chi \in [\bar{\chi}, 1]$. $\qquad\square$

In Figure 2.3(C) the functional $H(q_1, q_2, \chi)$ is evaluated for different values of $\chi$ and one can see that for every $\chi$ there exists a unique tuple $(R, r)$ such that the equilibrium condition (2.8) is satisfied. The eccentricity $e = \sqrt{1 - (R/(R+r))^2}$ of the ellipse is illustrated as a function of $\chi$ in Figure 2.3(D) and one can see how the eccentricity increases as $\chi$ decreases which corresponds to the evolution of the ring pattern into a stationary ellipse pattern whose minor axis becomes shorter and whose major axis becomes longer as $\chi$ decreases, proven in Corollary 3.

The existence of steady states is essential for getting an insight into the properties of the model. In order to explain the emergent behavior of the model, it is necessary to study the stability of the equilibrium and classify the convergence to equilibria in terms of initial data. This will be subject to future research.

To sum up, we have discussed the existence of stationary ellipse patterns to the mean-field PDE (2.2) with the spatially homogeneous tensor field with $s = (0, 1)$ and $l = (1, 0)$ in this subsection. Under certain assumptions on the interaction forces we showed:

- Existence and uniqueness of (non-trivial) ring steady states for at most one

(A) Evaluation of LHS of (2.7)

(B) Tuples $(R, r)$

(C) Evaluation of LHS of (2.8)

(D) $e = e(\chi)$
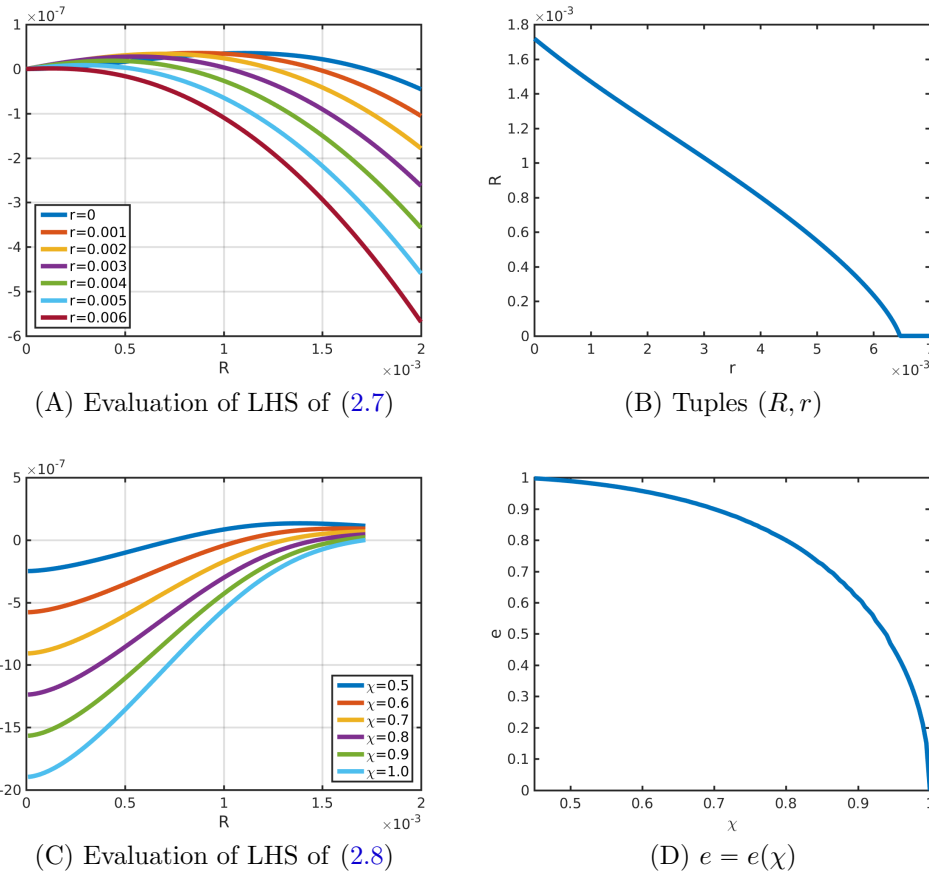
Figure 2.3: Tuples $(R, r)$ for stationary ellipse patterns to the mean-field equation (2.2) satisfying equilibrium conditions (2.7) and (2.8) for different values of $\chi$ and eccentricity $e$ as a function of $\chi$ for the forces in the particle model for parameter values in (1.20).

radius $R > 0$ for $\chi = 1$

- Non-existence of ring steady states for $\chi \in [0, 1)$

- Existence of ellipse steady states for $\chi \in [0, 1)$:

    - For any $\chi$ sufficiently close to 1, there exists a unique length for both major and minor axis of the stationary ellipse pattern.

    - Smaller values of $\chi$ lead to a longer major and a shorter minor axis of the ellipse equilibrium.

**Stripe pattern**

Based on the discussion in Section 2.2.1 for the tensor field $T = \chi s \otimes s + l \otimes l$ with $l = (1, 0)$ and $s = (0, 1)$, we consider different shapes of vertical stripe patterns in $\mathbb{R}^2$ and discuss whether they are equilibria.

**Definition 4.** *Let the centre of mass be denoted by $x_c = (x_{c,1}, x_{c,2}) \in \mathbb{R}^2$. Then we define the measure $\delta_{(x_{c,1}, \cdot)}$ by*

$$\delta_{(x_{c,1}, \cdot)}(A) = \lambda \left( A \cap (\{x_{c,1}\} \times \mathbb{R}) \right)$$

*for all measurable sets $A \subset \mathbb{R}^2$ where $\lambda$ denotes the one-dimensional Lebesgue measure.*

The measure $\delta_{(x_{c,1}, \cdot)}$ is a locally finite measure, but not a probability measures and satisfies condition (2.3) for equilibria of the mean-field PDE (2.2) for any force satisfying Assumption 1 and any $\chi \in [0, 1]$ since $F(x - x', T) = -F(-(x - x'), T)$ for all $x, x' \in \mathbb{R}^2$. Note that fully repulsive forces along the vertical axis are necessary for the occurrence of stable stripe patterns $\delta_{(x_{c,1}, \cdot)}$. Further note that as $\chi$ decreases the attraction forces disappear along the vertical direction and the mass leaks to infinity driven by purely repulsive forces along the vertical axis so that $\delta_{(x_{c,1}, \cdot)}$ cannot be the limit of an ellipse pattern. Hence, vertical lines are not stable equilibria with Definition 2 for the particle model (2.1) posed in the plane.

To obtain measures concentrating on vertical lines as solutions to the particle model (2.1) and to guarantee the conservation of mass under the variation of parameter $\chi$, we consider the associated probability measure on the two-dimensional unit torus $\mathbb{T}^2$ instead of the full space $\mathbb{R}^2$. Another possibility to obtain measures

concentrating on vertical lines as solutions is to consider confinement forces, see [MRS19, CMM$^+$19].

Solutions to the mean-field PDE (2.2) satisfying condition (2.3) include measures which are uniformly distributed on certain intervals along the vertical axis, i.e., on $\{x = (x_1, x_2) \in \mathbb{R}^2 \colon x_1 = x_{c,1}, \ x_2 \in [a, b]\}$ for some constants $a < b$, as well as measures which are uniformly distributed on unions of distinct intervals. The former occur if the total force is repulsive-attractive so that the attraction force restricts the stretching of the solution to certain subsets of the vertical axis. The latter which look like dashed lines parallel to the vertical axis can be realised by repulsive-attractive-repulsive forces, i.e., repulsive-attractive forces may lead to accumulations on subsets of the vertical axis while the additional repulsion force acting on long distances is responsible for the separation of the different subsets.

After considering these one-dimensional patterns, the question arises whether the corresponding two-dimensional vertical stripe pattern of width $\Delta$ satisfies the equilibrium condition (2.3) for any $\Delta > 0$. Let $\Delta > 0$ and consider the two-dimensional vertical stripe pattern of width $\Delta$, given by

$$
g_\Delta(x) = g_\Delta(x_1, x_2) = \begin{cases} \frac{1}{\Delta}, & x_1 \in \left[x_{c,1} - \frac{\Delta}{2}, x_{c,1} + \frac{\Delta}{2}\right], \\ 0, & \text{otherwise.} \end{cases}
$$

We assume that $g_\Delta$ satisfies the equilibrium condition (2.3) for the mean-field PDE (2.2), i.e., $g_\Delta \left( F * g_\Delta \right) = 0$, implying

$$
\int_{\left[x_{c,1} - \frac{\Delta}{2}, x_{c,1} + \frac{\Delta}{2}\right] \times \mathbb{R}} F(x - x', T) \, \mathrm{d}x' = 0 \quad \text{for all} \quad x \in \left[x_{c,1} - \frac{\Delta}{2}, x_{c,1} + \frac{\Delta}{2}\right] \times \mathbb{R}.
$$

By linear transformations this reduces to

$$
\int_{\left[-\frac{\Delta}{2}, \frac{\Delta}{2}\right] \times \mathbb{R}} F((x_1, 0) - x', T) \, \mathrm{d}x' = 0 \quad \text{for all} \quad x_1 \in \left[-\frac{\Delta}{2}, \frac{\Delta}{2}\right].
$$

Since $F(x - x', T(x)) = -F(-(x - x'), T(x))$ for all $x, x' \in \mathbb{R}^2$ we have

$$
e_1 \cdot \int_{\left[-\frac{\Delta}{2}, \frac{\Delta}{2}\right] \times \mathbb{R}} F((x_1, 0) - x', T) \, \mathrm{d}x' = 0 \quad \text{for all} \quad x_1 \in \left[-\frac{\Delta}{2}, \frac{\Delta}{2}\right]
$$

and symmetry implies

$$e_1 \cdot \int_{[x_1, \Delta - x_1] \times \mathbb{R}} F(x', T) \, \mathrm{d}x' = 0 \quad \text{for all} \quad x_1 \in \left[ 0, \frac{\Delta}{2} \right). \qquad (2.16)$$

Hence the equilibrium state can only occur for special choices of the interaction force $F$. In general, (2.16) is not satisfied and thus $g_\Delta$ is not an equilibrium state of the mean-field PDE.

## 2.3 Numerical methods and results

In this section, we investigate the long-time behavior of solutions to the particle model (2.1) and the pattern formation process numerically and we discuss the numerical results by comparing them to the analytical results of the model in Section 2.2. These numerical simulations are necessary for getting a better understanding of the long-time behavior of solutions to the particle model (2.1) and its stationary states. Since the mean-field limit shows that the particle method is convergent with a order given by $N^{-1/2} \ln(1 + N)$ (see [FG15, Gol16]) it is sufficient to use particle simulations instead of the mean-field solvers.

We consider the domain $\Omega = \mathbb{T}^2$ where $\mathbb{T}^2$ is the 2-dimensional unit torus that can be identified with the unit square $[0, 1) \times [0, 1) \subset \mathbb{R}^2$ with periodic boundary conditions. To guarantee that particles can only interact within a finite range we assume that they cannot interact with each other if they are separated by a distance of at least 0.5 in each spatial direction, i.e., for $i \in \{1, 2\}$ and all $x \in \Omega$ we require that $F(x - x', T(x)) \cdot e_i = 0$ for $|x - x'| \geqslant 0.5$ where $e_i$ denotes the standard basis for the Euclidean plane. This property of the total interaction force $F$ in (1.8) is referred to as the minimum image criterion [Erc97]. Note that the coefficient functions $f_R$ and $f_A$ in (1.18) and (1.19) in the particle model (2.1) satisfy the minimum image criterion if a spherical cutoff radius of length 0.5 is introduced for the repulsion and attraction forces.

**Remark 7** (Minimum image criterion)**.** *The minimum image criterion is a natural condition for large systems of interacting particles on a domain with periodic boundary conditions. In numerical simulations, it is sufficient to record and propagate only the particles in the original simulation box. Besides, the minimum image criterion guarantees that the size of the domain is large enough compared to the range of the total force. In particular, non-physical artefacts due to periodic boundary conditions*

*are prevented.*

## 2.3.1 Numerical methods

To solve the $N$ particle ODE system (2.1) we consider periodic boundary conditions and apply either the simple explicit Euler scheme or higher order methods such as the Runge-Kutta-Dormand-Prince method, all resulting in very similar simulation results.

## 2.3.2 Numerical results

We show numerical results for the particle model (2.1) on the domain $\Omega = T^2$ where the force coefficients are given by (1.18) and (1.19). In particular, we investigate the patterns of the corresponding stationary solutions. Unless stated otherwise we consider the parameter values in (1.20) and the spatially homogeneous tensor field $T = \chi s \otimes s + l \otimes l$ with $l = (1, 0)$ and $s = (0, 1)$. Besides, we assume that the initial condition is a Gaussian with mean $\mu = 0.5$ and standard deviation $\sigma = 0.005$ in each spatial direction.

**Dependence on the initial distribution**

The stationary solution to (2.1) for $N = 1200$ particles is shown in Figure 2.4 for $\chi = 0.2$ and $\chi = 0.7$, respectively, for different initial data. One can clearly see that the long-time behaviour of the solution depends on the chosen initial conditions and the choice of $\chi$. As discussed in Section 2.2.1 the absence of attraction forces along $s = (0, 1)$ for $\chi = 0.2$ leads to a solution stretched along the entire vertical axis and particles in a neighbourhood of these line patterns are attracted. For $\chi = 0.7$ the domain of attraction is significantly smaller and the particles remain isolated or build small clusters if they are initially too far apart from other particles. This results in many accumulations of smaller numbers of particles for $\chi = 0.7$. Note that these accumulations have the shape of ellipses for $\chi = 0.7$ which is consistent with the analysis in Section 2.2, independent of the choice of the initial data. Because of the significantly larger number of clusters for randomly uniformly distributed initial data the resulting ellipse patterns consist of fewer particles compared to Gaussian initial data with a small standard deviation. Since initial data spread over the entire simulation domain leads to multiple copies of the patterns which occur for concentrated initial data, this motivates to consider concentrated initial data for getting a

better understanding of the patterns which can be generated. In the sequel we restrict ourselves to concentrated initial data so that all particles can initially interact with each other. Besides, it is sufficient to consider smaller numbers of particles to get a better understanding of the formation of the stationary pattern to increase the speed of convergence. Further note that for $\chi = 0.2$ and randomly uniformly distributed initial data the convergence to the stationary solution, illustrated in Figure 2.5, is very slow which implies that the fingerprint formation might also be slow. However, the particle model (2.1) is able to generate very interesting patterns over time $t$, as shown in Figure 2.5. Besides, it is of interest how the resulting patterns depend on the initial data and whether the ellipse pattern is stable for $\chi = 0.7$. In Figure 2.6(A) we consider $N = 600$ particles and Gaussian initial data with mean $\mu = 0.5$ and standard deviation $\sigma = 0.005$ in each spatial direction. Given the initial position of the particles for the simulation in Figure 2.6(A) we perturb the initial position of each particle $j$ by $\delta Z_j$ where $Z_j$ is drawn from a bivariate standard normal distribution and $\delta \in \{0.0001, 0.001, 0.01, 0.1\}$. The corresponding stationary patterns are illustrated in Figures 2.6(B) to 2.6(E) and one can clearly see that the ellipse pattern is stable under small perturbations.



(A) $\chi = 0.2$     (B) $\chi = 0.7$     (C) $\chi = 0.7$, enlarged     (D) $\chi = 0.7$, enlarged

Randomly uniformly distributed

(E) $\chi = 0.2$     (F) $\chi = 0.7$     (G) $\chi = 0.7$, enlarged     (H) $\chi = 0.7$, enlarged

Gaussian with $\sigma = 0.05$
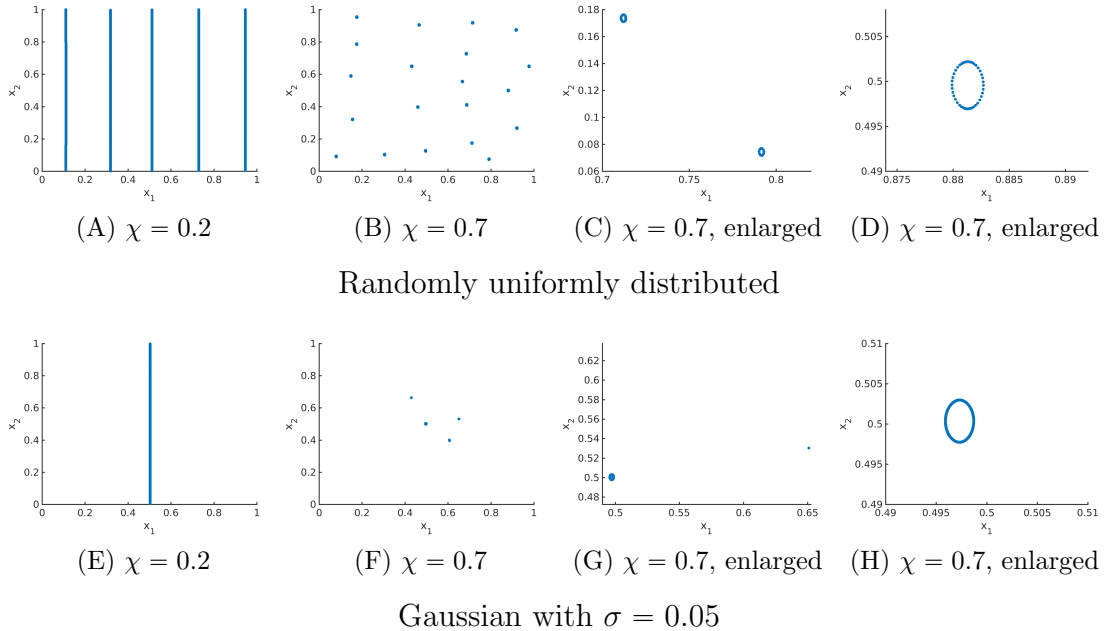
Figure 2.4: Stationary solution to the particle model (2.1) for $N = 1200$ and different initial data for $\chi = 0.2$ (left) and $\chi = 0.7$ (right).

(A) $t = 0$  (B) $t = 50000$  (C) $t = 110000$  (D) $t = 710000$
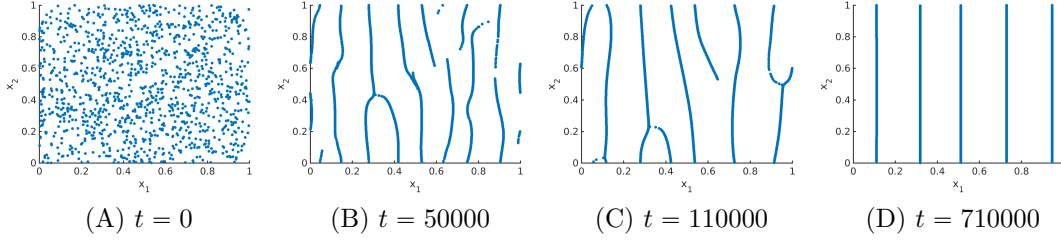
Figure 2.5: Numerical solution to the particle model (2.1) for $N = 1200$ and randomly uniformly distributed initial data for $\chi = 0.2$ and different times $t$.



(A) $\delta = 0$  (B) $\delta = 0.0001$  (C) $\delta = 0.001$  (D) $\delta = 0.01$  (E) $\delta = 0.1$
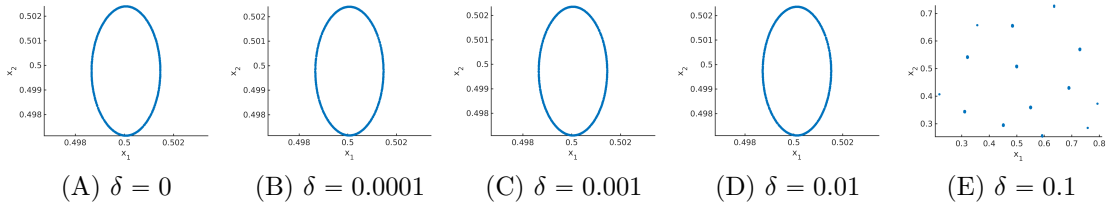
Figure 2.6: Stationary solution to the particle model (2.1) for $N = 600$ and Gaussian initial data ($\mu = 0.5$, $\sigma = 0.005$) in each spatial direction (left) and perturbation of the initial position of each particle $j$ by $\delta Z_j$ where $Z_j$ is drawn from a bivariate standard normal distribution and $\delta \in \{0.0001, 0.001, 0.01, 0.1\}$ (right).

**Evolution of the pattern**

In Figure 2.7, the numerical solution of the particle model (2.1) on $\Omega = \mathbb{T}^2$ for $N = 1200$ is shown for $\chi = 0$, $\chi = 0.2$ and $\chi = 1.0$ for different times $t$ for Gaussian initial data with mean $\mu = 0.5$ and standard deviation $\sigma = 0.005$ in each spatial direction. Compared to the initial data one can clearly see that the solution for $\chi = 0$ and $\chi = 0.2$, respectively, is stretched along the vertical axis, i.e., along $s = (0, 1)$, as time increases. This is consistent with the observations in Section 2.2.1 since the forces along the vertical axis for $\chi = 0$ and $\chi = 0.2$ are purely repulsive. In contrast, the long-range attraction forces for $\chi = 1$ prohibit stretching of the solution and the isotropic forces for $\chi = 1$ lead to ring as stationary solution whose radius is approximately 0.0017. The different sizes of the stationary patterns are also illustrated in Figure 2.7 where the solutions for $\chi = 0$ and $\chi = 0.2$ are shown on the unit square, while a smaller axis scale is considered for $\chi = 1$ because of the small radius of the ring for $\chi = 1$. Besides, the convergence to the equilibrium state is very fast for $\chi = 1$ compared to $\chi = 0$ and $\chi = 0.2$.

(A) $\chi = 0$    (B) $\chi = 0.2$    (C) $\chi = 1$
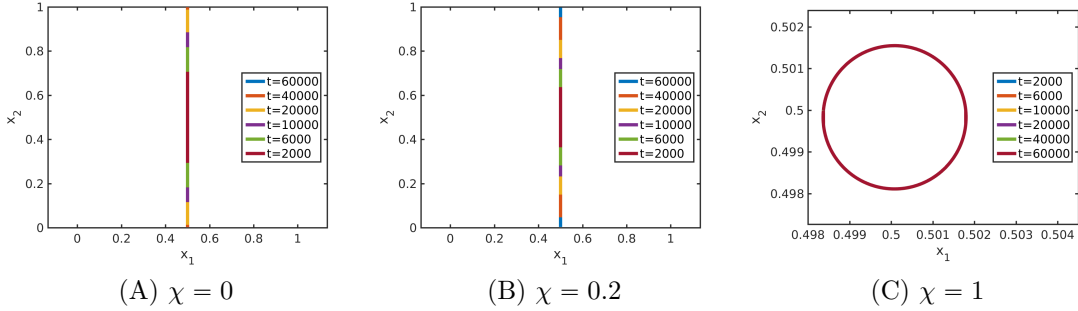
Figure 2.7: Numerical solution to the particle model (2.1) for different times $t$ and different values of $\chi$ for $N = 1200$ and Gaussian initial data ($\mu = 0.5$, $\sigma = 0.005$) in each spatial direction .

**Dependence on parameter $\chi$**

In this section we investigate the dependence of the equilibria to (2.1) on the parameter $\chi$ which strongly influences the pattern formation. Given $N = 600$ particles which are initially equiangular distributed on a circle with centre $(0.5, 0.5)$ and radius $0.005$ the stationary solution to (2.1) is displayed for different values of $\chi$ in Figures 2.8 and 2.9. Note that the same simulation results are shown in Figures 2.8 and 2.9 for different axis scales. In Figure 2.8 one can see that the size of the pattern is significantly larger for small values of $\chi$ due to stretching along the vertical axis (cf. Section 2.2). For small values of $\chi$ the stationary solution is a 1D stripe pattern of equally distributed particles along the entire vertical axis, while for larger values of $\chi$ the stationary solution can be a shorter vertical line or accumulations in the shape of lines and ellipses. The stationary patterns for different values of $\chi$



(A) $\chi = 0.08$    (B) $\chi = 0.24$    (C) $\chi = 0.40$    (D) $\chi = 0.56$    (E) $\chi = 0.72$
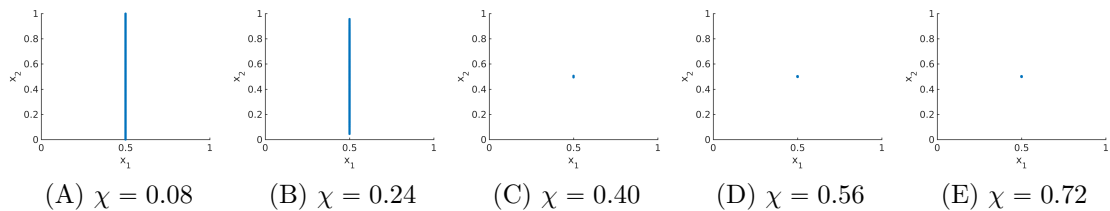
Figure 2.8: Comparison of the size of the stationary solution to the particle model (2.1) for different values of $\chi$ where $N = 600$ and the initial data is equiangular distributed on a circle with centre $(0.5, 0.5)$ and radius $0.005$.

are enlarged in Figure 2.9 by considering different axis scales. As $\chi$ increases the stationary pattern evolves from a straight line into a standing ellipse and finally into a ring for $\chi = 1.0$. Since the same particle numbers and the same initial data,

as well as the same parameters except for the parameter $\chi$ are considered in these simulations, the different stationary patterns strongly depend on the choice of $\chi$. Note that the length of the minor axis of the ellipse increases as $\chi$ increases, while the length of the major axis of the ellipse gets shorter. Further note that we have a continuous transition of the stationary patterns as $\chi$ increases due to the smoothness of the forces and the continuous dependence of the forces on parameter $\chi$ in the particle model (2.1).
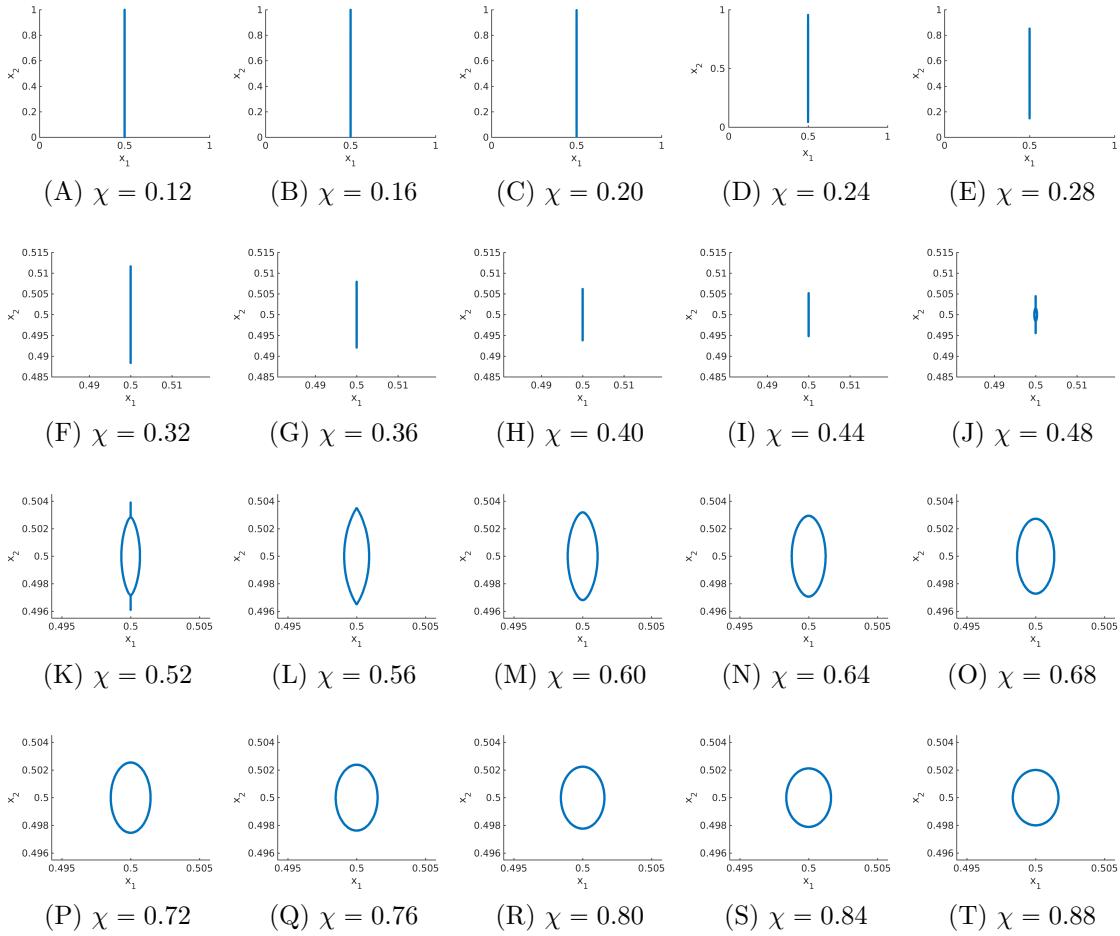


Figure 2.9: Stationary solution to the particle model (2.1) for different values of $\chi$ where $N = 600$ and the initial data is equiangular distributed on a circle with centre $(0.5, 0.5)$ and radius $0.005$.

**Dependence on parameter $e_R$**

In Figure 2.10 the stationary solution to (2.1) for $N = 1200$ and $\chi = 0.2$ is shown for different values of $e_R$ where a ring of radius $0.005$ with centre $(0.5, 0.5)$ is chosen

as initial data. One can clearly see that the size of accumulations increases for $e_R$ increasing due to strong long-range repulsion forces for smaller values of $e_R$. Besides, the stationary solution is spread over the entire domain for smaller values of $e_R$. The spreading of the solution along the entire horizontal axis can be explained by the fact that for smaller values of $e_R$ the total force along $l$, i.e., along the horizontal axis, is no longer short-range repulsive and long-range attractive, but short-range repulsive, medium-range attractive and long-range repulsive and the long-range repulsion is the stronger the smaller the value of $e_R$.



(A) $e_R = 40$    (B) $e_R = 50$    (C) $e_R = 60$    (D) $e_R = 70$    (E) $e_R = 80$
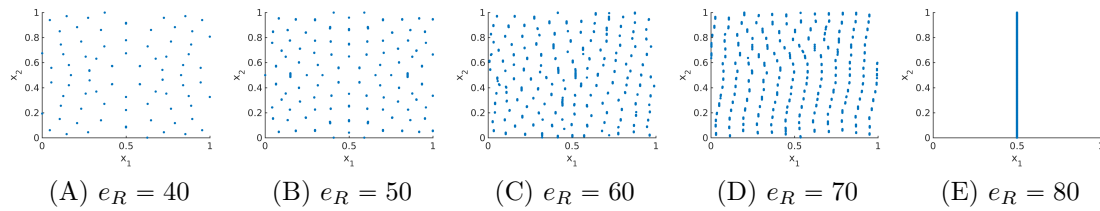
Figure 2.10: Stationary solution to the particle model (2.1) for $\chi = 0.2$ and different values for $e_R$ where $N = 1200$ and the initial data is equiangular distributed on a circle with centre $(0.5, 0.5)$ and radius $0.005$.

**Dependence on the size of the attraction force**

In this section, we assume that the total force is given by

$$F(d, T) = \delta F_A(d, T) + F_R(d)$$

for $\delta \in [0, 1]$ for the spatially homogeneous tensor field $T = \chi s \otimes s + l \otimes l$ with $l = (1, 0)$ and $s = (0, 1)$ instead of (1.8). We consider $N = 600$ particles which are initially equiangular distributed on a circle with centre $(0.5, 0.5)$ and radius $0.005$ and we investigate the influence of the size of the attraction force $F_A$ on stationary patterns by varying its coefficients. While the force is repulsive for small values of $\delta$, resulting in a stationary solution spread over the entire domain, stripe patterns and ring patterns for $\chi = 0.2$ and $\chi = 1$, respectively, arise as stationary patterns as $\delta$ increases as shown in Figures 2.11. Note that the radius of the stationary ring pattern decreases as $\delta$ increases due to an increasing attraction force.

**Dependence on the size of the repulsion force**

In this section, we consider a force of the form $F(d, T) = F_A(d, T) + \delta F_R(d)$ for $\delta \in [0, 1]$ for the spatially homogeneous tensor field $T = \chi s \otimes s + l \otimes l$ with $l = (1, 0)$

(A) $\delta = 0.1$     (B) $\delta = 0.3$     (C) $\delta = 0.5$     (D) $\delta = 0.7$     (E) $\delta = 0.9$

(F) $\delta = 0.1$     (G) $\delta = 0.3$     (H) $\delta = 0.5$     (I) $\delta = 0.7$     (J) $\delta = 0.9$
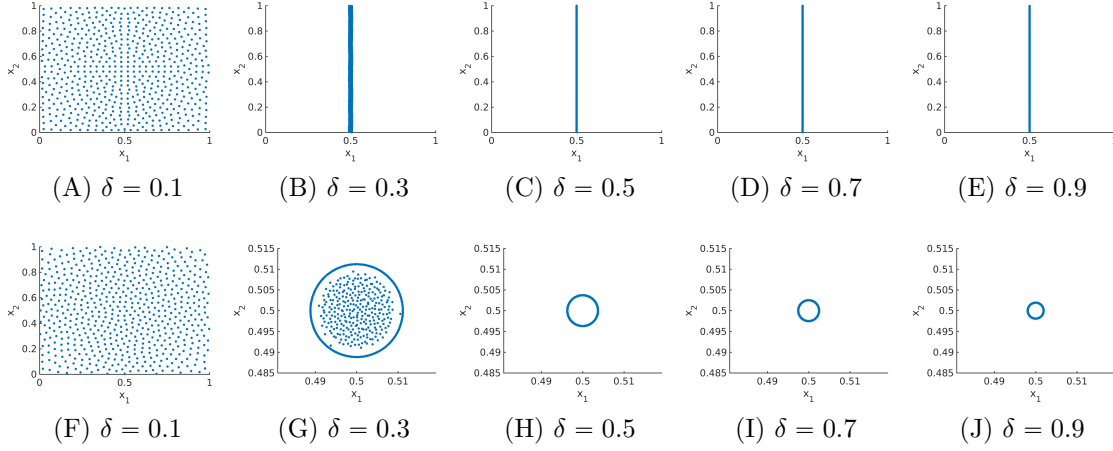
Figure 2.11: Stationary solution to the particle model (2.1) for force $F(d,T) = \delta F_A(d,T) + F_R(d)$ for different values of $\delta$ (i.e., different sizes of the attraction force $F_A$) where $\chi = 0.2$ and $\chi = 1$ (for different axis scalings) in the first and second row, respectively, where $N = 600$ and the initial data is equiangular distributed on a circle with centre $(0.5, 0.5)$ and radius $0.005$.

and $s = (0, 1)$ instead of (1.8) and we consider $N = 600$ particles which are initially equiangular distributed on a circle with centre $(0.5, 0.5)$ and radius $0.005$. The stationary solution to (2.1) for $\chi = 0.2$ stretches along the vertical axis as $\delta$ increases due to an additional repulsive force as illustrated in Figure 2.12. For $\chi = 1$, the radius of the ring pattern increases as $\delta$, see Figure 2.13.



(A) $\delta = 0.1$     (B) $\delta = 0.3$     (C) $\delta = 0.5$     (D) $\delta = 0.7$     (E) $\delta = 0.9$
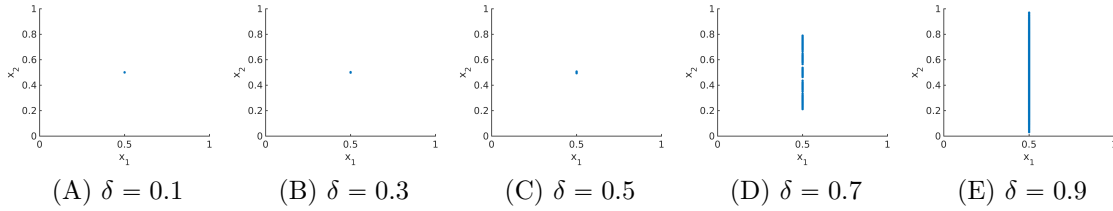
Figure 2.12: Stationary solution to the particle model (2.1) for $\chi = 0.2$ and force $F(d,T) = F_A(d,T) + \delta F_R(d)$ for different values of $\delta$ (i.e., different sizes of the repulsion force $F_R$) where $N = 600$ and the initial data is equiangular distributed on a circle with centre $(0.5, 0.5)$ and radius $0.005$.

**Dependence on the tensor field**

In Figures 2.14 and 2.15 the numerical solution to the particle model (2.1) for $N = 600$, $\chi = 0.2$ and randomly uniformly distributed data is shown for different non-homogeneous tensor fields $T = T(x)$ and different times $t$. Since $s = s(x)$ and
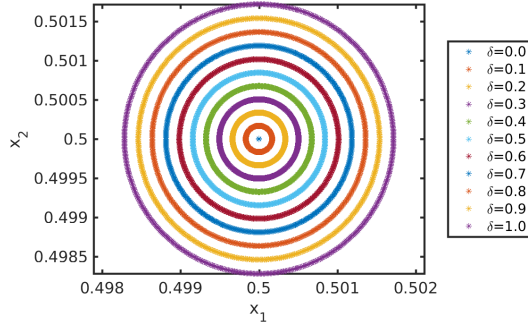
Figure 2.13: Stationary solution to the particle model (2.1) for $\chi = 1$ and force $F(d, T) = F_A(d, T) + \delta F_R(d)$ for different values of $\delta$ (i.e., different sizes of the repulsion force $F_R$) where $N = 600$ and the initial data is equiangular distributed on a circle with centre $(0.5, 0.5)$ and radius $0.005$.

$l = l(x)$ are assumed to be orthonormal vectors, the vector field $s = s(x)$ and the parameter $\chi$ determine the tensor field $T = T(x)$. One can clearly see in Figure 2.14 that the particles are aligned along the lines of smallest stress $s = s(x)$. However, these patterns are no equilibria. The evolution of the numerical solution for different tensor fields is illustrated in Figure 2.15.

### 2.3.3 Discussion of the numerical results

In this section, we study the existence of equilibria and their stability of the particle model (2.1) for the spatially homogeneous tensor field $T = \chi s \otimes s + l \otimes l$ with $l = (1, 0)$ and $s = (0, 1)$ and compare them with the numerical results.

**Ellipse**

As outlined in Section 2.2.1 the anisotropic forces for $\chi \in [0, 1)$ lead to an additional advection along the vertical axis compared to the horizontal axis for the given tensor field $T$. Hence, possible stationary ellipse patterns are stretched along the vertical axis for $\chi \in [0, 1)$. Besides, this advection leads to accumulations within the ellipse pattern, i.e., the distances of the particles are much longer along the vertical lines (e.g. at the left or right side of the ellipse) than along the horizontal lines (e.g. at the top or bottom of the ellipse). As in Section 2.2.3 we denote the length of the minor and major axis of the ellipse state by $R$ and $R + r$, respectively.

First, we consider ring patterns of radius $R > 0$. We identify $\mathbb{R}^2$ with $\mathbb{C}$ and

61

(A) Example 1          (B) Example 2



(C) Example 3          (D) Example 4
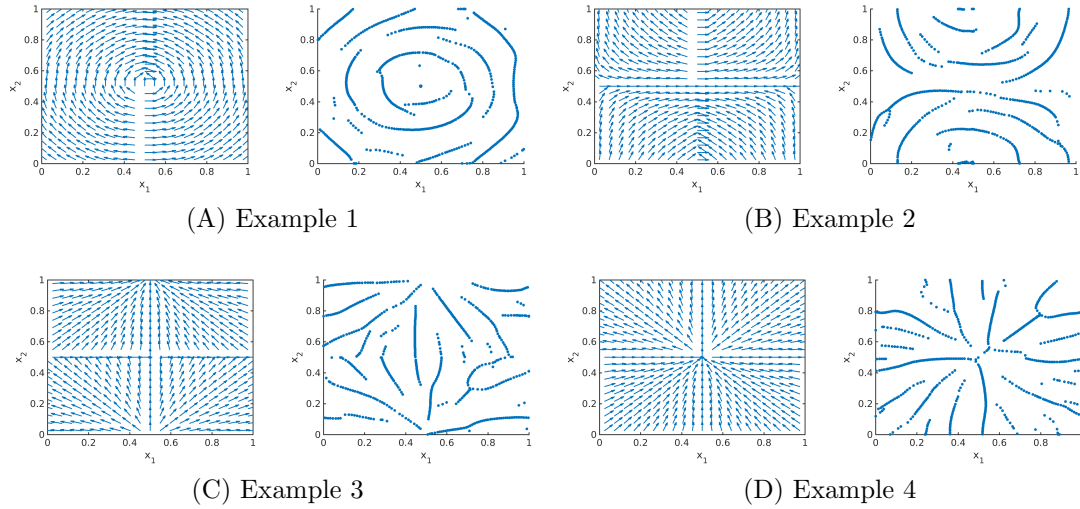
Figure 2.14: Different non-homogeneous tensor fields $T = T(x)$ given by $s = s(x)$ (left) and the numerical solution to the particle model (2.1) at time $t = 40000$ for $\chi = 0.2$, $T = T(x)$ and randomly uniformly distributed initial data (right).



(A) $s = s(x)$    (B) $t = 40000$    (C) $t = 200000$    (D) $t = 400000$

Example 5



(E) $s = s(x)$    (F) $t = 40000$    (G) $t = 200000$    (H) $t = 400000$

Example 6
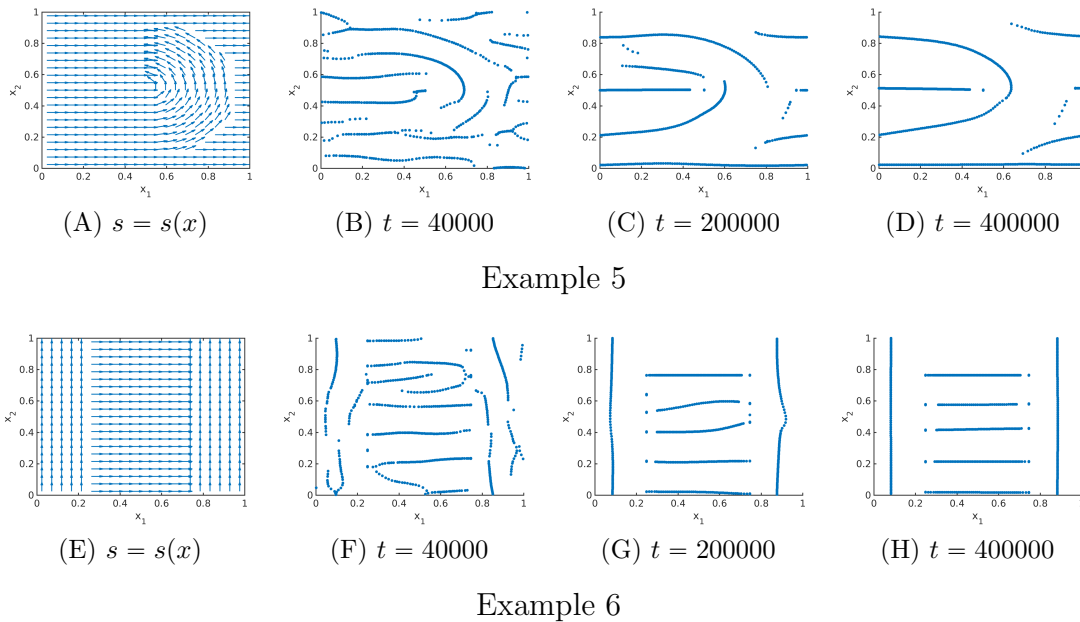
Figure 2.15: Different non-homogeneous tensor fields $T = T(x)$ given by $s = s(x)$ (left) and the numerical solution to the particle model (2.1) at different times $t$ for $\chi = 0.2$, $T = T(x)$, $N = 600$ and randomly uniformly distributed initial data (right).

consider the ansatz

$$\bar{x}_k = \bar{x}_k(R) = x_c + R \exp\left(\frac{2\pi i k}{N}\right), \quad k = 0, \ldots, N-1 \tag{2.17}$$

with centre of mass $x_c$, i.e., the particles are uniformly distributed on a ring of radius $R$ with centre $x_c$. The radius $R > 0$ has to be determined such that the ansatz functions $\bar{x}_j = \bar{x}_j(R)$ satisfy

$$\sum_{\substack{k=1 \\ k \neq j}}^{N} F(\bar{x}_k(R) - \bar{x}_j(R), T) = 0 \tag{2.18}$$

for all $j = 0, \ldots, N-1$. Denoting the left-hand side of (2.18) by $G_j(R)$, then $G_j(R)$ is highly nonlinear and zeros of $G_j$ can only be determined numerically. By symmetry and appropriate periodic extension of the force $F$ outside the unit square $[-0.5, 0.5]^2$ (see Section 4.2 for more details), it is sufficient to determine the zeros of $G_0$ for $\chi = 1$. Since $\Im G_0(R) = 0$ for all $R > 0$ by the definition of $F$ the condition simplifies to finding $R > 0$ such that $\Re G_0(R) = 0$. Using Newton's algorithm the unique nontrivial zero of $\Re G_0$ can be computed as $\bar{R} \approx 0.0017$ for the forces (1.18) and (1.19) in the particle model (2.1) with parameter values from (1.20), $N = 600$ and a fixed centre of mass $x_c$. Hence, given $x_c$ (2.17) with radius $\bar{R}$ is the unique ring equilibrium for $\chi = 1$ and $\bar{R}$ coincides with the radius of the numerically obtained ring equilibrium in Section 2.3.2. Based on a linearised stability analysis [Tur52] one can show numerically that the ring pattern is stable for $\chi = 1$ for the forces in the particle model for parameters in (1.20) and $N = 1200$. Since $\Re G_j$ is independent of $\chi$ with unique zero $\bar{R}$ and $\chi f_A \leqslant 0$, this implies that there exists no $R > 0$ such that $\Im G_j(\bar{R}) = 0$ for all $j = 0, \ldots, N$ for any $\chi \in [0, 1)$, i.e., the ring solution (2.17) is no equilibrium for $\chi \in [0, 1)$ and any $R > 0$. This is consistent with the analysis of the mean-field PDE (2.2) in Section 2.2 and with the numerical results in Section refsec:numericalresults.

For the general case of an ellipse where $r \geqslant 0$ we identify $\mathbb{R}^2$ with $\mathbb{C}$ and regard the equiangular ansatz

$$\bar{x}_k = \bar{x}_k(r, R) = x_c + R \cos\left(\frac{2\pi k}{N}\right) + i(R+r)\sin\left(\frac{2\pi k}{N}\right), \quad k = 0, \ldots, N-1,$$

$$\tag{2.19}$$

where the distances of the particles are longer along vertical than along horizontal

lines. An ellipse equilibrium has to satisfy

$$\sum_{\substack{k=1 \\ k \neq j}}^{N} F(\bar{x}_k(R,r) - \bar{x}_j(R,r), T) = 0 \tag{2.20}$$

for all $j = 0, \ldots, N - 1$. Tuples $(R,r)$ such that (2.19) is a possible equilibria to (2.1) can be determined numerically from $\Re G_0(R,r) = 0$, where $G_j((R,r))$ for $j \in \{0, \ldots, N - 1\}$ denotes the left-hand side of (2.20). For the force coefficients (1.18) and (1.19) in the particle model for parameter values (1.20) and $N = 600$, the condition in (2.20) implies that the larger $r$ the smaller $R$, i.e., as $r$ increases the ring of radius $R$ evolves into an ellipse whose major axis of length $2(R + r)$ gets longer and whose minor axis of length $2R$ gets shorter as $r$ increases. The numerically obtained tuples $(R,r)$ are shown in Figure 2.16(A). Besides, it follows from plugging the definition of the total force for spatially homogeneous tensor fields into (2.20) that each tuple $(R,r)$ can be associated to an equilibrium for at most one value of $\chi$. Further note that by Section 2.2.1 the additional advection along the vertical axis is the stronger the smaller the value of $\chi$, implying that $r$ increases as $\chi$ decreases. Hence, we can conclude that for a given value of $\chi$ there exists at most one tuple $(R,r)$ such that the ansatz (2.19) is an equilibrium to (2.1). This can also be justified by evaluating $\Im G_{N/4}(R,r)$ as a function of radius pairs $(R,r)$ for fixed values of $\chi$ for $N = 600$ particles. The eccentricity $e = \sqrt{1 - (R/(R+r))^2}$ of the stationary ellipse pattern as a function of the parameter $\chi$ is shown in Figure 2.16(B). Note that these observations are consistent with the numerical results in Section 2.3.2. Further note that the shape of the relation between $R$ and $r$ as well as the eccentricity curve in Figures 2.16(A) and 2.16(B) is similar to the ones in the continuous case, shown in Figures 2.3(B) and 2.3(D). However, there are small differences between the radius pairs for the discrete and the continuous case which is due to the additional functional determinant that has to be considered if the corresponding integrals in (2.7) and (2.8) are discretised.

**Single straight vertical line**

Because of the observations in Section 2.2.1 a natural choice for line patterns are vertical lines. Identifying $\mathbb{R}^2$ with $\mathbb{C}$ results in the ansatz

$$\bar{x}_k = x_c + i\frac{2k - 1}{2N}, \quad k = 0, \ldots, N - 1, \tag{2.21}$$

(A) Tuples $(R, r)$                  (B) $e = e(\chi)$
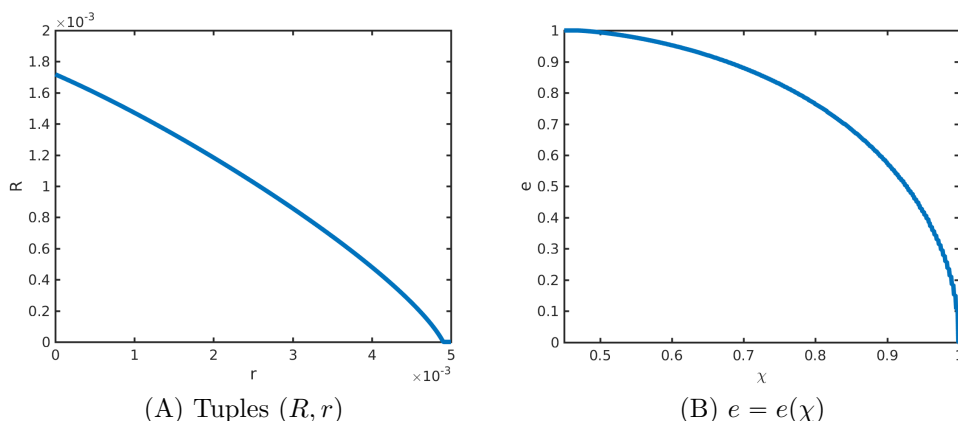
Figure 2.16: Tuples $(R, r)$ for stationary ellipse patterns to (2.1) with ansatz (2.19) and eccentricity $e$ as a function of $\chi$ for $N = 600$ and the forces in the particle model for parameter values in (1.20).

for a single straight vertical line with the centre of mass $x_c$. One can easily see that ansatz (2.21) defines an equilibrium of (2.1) for all values $\chi \in [0, 1]$ where the minimum image criterion is crucial to guarantee that (2.21) is an equilibrium for even values of $N$. Based on a linearised stability analysis [Tur52] one can show that (2.21) is a stable equilibrium of (2.1) for $N = 1200$ for $\chi \in [0, 0.27]$ which is consistent with the numerical results in Section 2.3.2.

**Clusters**

The numerical results in Section 2.3.2 crucially depend on the choice of the parameter values. As seen in Figure 2.10 the smaller the value of $e_R$ the more the particles are spread over the entire domain. Note that the coefficient of the repulsive force is given by (1.18) so that smaller values of $e_R$ correspond to a slower exponential decay and hence larger repulsion forces, resulting in a larger number of clusters. It would be very interesting to explore the dependence of the coefficients on the number of clusters in the steady state further. In future research, one might also study analytically how the number of clusters and structures depend on the cutoff radius.

## 2.A  Detailed computations of Section 2.2.2

Let $\tilde{T} = \chi \tilde{s} \otimes \tilde{s} + \tilde{l} \otimes \tilde{l}$ denote a spatially homogeneous tensor field for orthonormal vectors $\tilde{l}, \tilde{s} \in \mathbb{R}^2$. Given $l = (1, 0)$, $s = (0, 1)$ and angle of rotation $\theta$ in (1.16), then

$\tilde{T} = R_\theta T R_\theta^T$ with $T = \chi s \otimes s + l \otimes l$ and rotation matrix $R_\theta$ in (1.16).

Let $x_j = x_j(t)$, $j = 1, \ldots, N$, denote the solution to the microscopic model (2.1) on $\mathbb{R}^2$ for the tensor field $T$ and define

$$\tilde{x}_j(t) = x_c + R_\theta(x_j(t) - x_c), \quad j = 1, \ldots, N$$

where $x_c$ denotes the centre of mass. Then, $\tilde{x}_j = \tilde{x}_j(t), j = 1, \ldots, N$, is a solution to the microscopic model (2.1) on $\mathbb{R}^2$ for the tensor field $\tilde{T}$. Besides, given an equilibrium $\bar{x}_j$, $j = 1, \ldots, N$, to (2.1) on $\mathbb{R}^2$ for the tensor field $T$, then

$$\bar{\tilde{x}}_j = x_c + R_\theta(\bar{x}_j - x_c), \quad j = 1, \ldots, N,$$

is an equilibrium to (2.1) on $\mathbb{R}^2$ for the tensor field $\tilde{T}$.

We show that $\tilde{x}_j$, $j = 1, \ldots, N$, solves (2.1) for the tensor field $\tilde{T}$. Since $x_j, j = 1, \ldots, N$, solves (2.1) for the tensor field $T$, we have

$$\frac{\mathrm{d}x_j}{\mathrm{d}t} = \sum_{k \neq j} f_A(|d|) \left[ \chi \left( s \cdot d \right) s + \left( l \cdot d \right) l \right] + f_R(|d|) d$$

for all $j = 1, \ldots, N$ where $d(x_j, x_k) = x_j - x_k$. Note that $\tilde{x}_j - \tilde{x}_k = R_\theta(x_j - x_k)$ and $|\tilde{x}_j - \tilde{x}_k| = |x_j - x_k|$. Using (1.15) as well as the fact that $R_\theta$ is an orthogonal matrix we get

$$\chi \left( \tilde{s} \cdot (\tilde{x}_j - \tilde{x}_k) \right) \tilde{s} + \left( \tilde{l} \cdot (\tilde{x}_j - \tilde{x}_k) \right) \tilde{l} = R_\theta \left[ \chi \left( s \cdot (x_j - x_k) \right) s + \left( l \cdot (x_j - x_k) \right) l \right].$$

Setting $\tilde{d}(\tilde{x}_j, \tilde{x}_k) = \tilde{x}_j - \tilde{x}_k$ this implies

$$\frac{\mathrm{d}\tilde{x}_j}{\mathrm{d}t} = \sum_{k \neq j} f_A \left( |\tilde{d}| \right) \left[ \chi \left( \tilde{s} \cdot \tilde{d} \right) \tilde{s} + \left( \tilde{l} \cdot \tilde{d} \right) \tilde{l} \right] + f_R \left( |\tilde{d}| \right) \tilde{d}$$

for all $j = 1, \ldots, N$, i.e., $\tilde{x}_j$, $j = 1, \ldots, N$, solves (2.1) for the tensor field $\tilde{T}$. Similarly, one can show that $\bar{\tilde{x}}_j$ is an equilibrium to (2.1) for the tensor field $\tilde{T}$, given that $\bar{x}_j$, $j = 1, \ldots, N$, is an equilibrium to (2.1) for the tensor field $T$.

We turn to equilibria of the mean-field equation (2.2) for spatially homogeneous tensor fields now. Let $\rho = \rho(\mathrm{d}x)$ denote an equilibrium state to the mean-field PDE (2.2) on $\mathbb{R}^2$ for the tensor field $T$ and define

$$\tilde{\rho}(x) = \rho \left( x_c + R_\theta^{-1}(x - x_c) \right) \text{ a.e.} \tag{2.22}$$

where $x_c$ denotes the centre of mass. Then, $\tilde{\rho}$ is an equilibrium state to (2.2) for the tensor field $\tilde{T}$.

To show this result note that for $x \in \mathbb{R}^2$ we have

$$
(F(\cdot, T) * \tilde{\rho}) (x_c + R_\theta(x - x_c))
$$
$$
= \int_{\mathbb{R}^2} F(x_c + R_\theta(x - x_c) - (x_c + R_\theta(x - x_c')), \tilde{T})\rho(\mathrm{d}x')
$$
$$
= \int_{\mathbb{R}^2} \Big[ f_R(|x - x'|)R_\theta(x - x')
$$
$$
+ f_A(|x - x'|) \Big( \chi \left( \tilde{s} \cdot (R_\theta(x - x')) \right) \tilde{s} + \left( \tilde{l} \cdot (R_\theta(x - x')) \right) \tilde{l} \Big) \Big] \rho(\mathrm{d}x')
$$
$$
= R_\theta (F(\cdot, T) * \rho) (x)
$$

where the first equality follows from (2.22) and the substitution rule. The definitions of the repulsion and attraction forces in (1.11) are used in the second equality and (1.15) is inserted in the third equality. Since $x \in \mathrm{supp}(\tilde{\rho})$ implies $x \in \mathrm{supp}(\rho(x_c + R_\theta^{-1}(\cdot - x_c)))$ and

$$
(F(\cdot, T) * \tilde{\rho}) (x) = R_\theta (F(\cdot, T) * \rho) \left( x_c + R_\theta^{-1}(x - x_c) \right),
$$

$\tilde{\rho}$ is an equilibrium state to (2.2) for the tensor field $\tilde{T}$ provided that $\rho$ is an equilibrium state to (2.2) for the tensor field $T$.

# Chapter 3

# Simulation of fingerprint patterns

## Originality and contribution

This chapter follows [DGH$^+$19], written in collaboration with Bertram Düring, Carsten Gottschlich, Stephan Huckemann and Carola-Bibiane Schönlieb. While my co-authors proposed the study of the model and provided guidance and advice, [DGH$^+$19] is primarily my own original work and nearly all the results, including analysis and simulations, were obtained by myself.

## Chapter summary

Evidence suggests that both the interaction of so-called Merkel cells and the epidermal stress distribution play an important role in the formation of fingerprint patterns during pregnancy. To model the formation of fingerprint patterns in a biologically meaningful way these patterns have to become stationary. For the creation of synthetic fingerprints it is also very desirable that rescaling the model parameters leads to rescaled distances between the stationary fingerprint ridges. Based on these observations, as well as the model introduced by Kücken and Champod we propose a new model for the formation of fingerprint patterns during pregnancy. In this anisotropic interaction model the interaction forces not only depend on the distance vector between the cells and the model parameters, but additionally on an underlying tensor field, representing a stress field. This dependence on the tensor field leads to complex, anisotropic patterns. We study the resulting stationary patterns both analytically and numerically. In particular, we show that fingerprint patterns can be modelled as stationary solutions by choosing the underlying tensor

field appropriately.

## 3.1   Introduction

Large databases are required for developing, validating and comparing the performance of fingerprint indexing and identification algorithms. The goal of these algorithms is to search and find a fingerprint in a database (or providing the search result that the query fingerprint is not stored in that database). The database sizes for fingerprint identification can vary between several thousand fingerprints e.g. watchlists in border crossing scenarios or hundreds of millions of fingerprints in case of the national biometric ID programme of India.

Clearly, fingerprint identification is of great importance in forensic science and is increasingly used in biometric applications. Unfortunately, collecting databases of real fingerprints for research purposes is usually very cost-intensive, requires time and effort, and in many countries, it is constrained by laws addressing important aspects such as data protection and privacy. Therefore, it is very desirable to avoid all these disadvantages by simulating large fingerprint databases on a computer.

Modelling fingerprint patterns and creating synthetic fingerprint images is not only of great interest to the community of biometric and forensic researchers, as well as practitioners, but also to the biological community. The SFinGe method [CEMM00] has been proposed to this end by Cappelli et al. in 2000. This method can produce fingerprint images which look realistic enough to deceive attendees of a pattern recognition conference, however, systematic differences between real fingerprints and synthetic images by SFinGE regarding the minutiae pattern have been found which allow to distinguish between the two [GH14]. Recently, the realistic fingerprint creator (RFC) [IHG15] has been suggested to overcome the issue of unrealistic minutiae distributions. SFinGe and RFC are both based on Gabor filters [Got12] for image creation. A different approach to fingerprint creation has been introduced by Kücken and Champod in [KC13]. They strive to directly model the process of fingerprint pattern formation as it occurs in nature and their approach is inspired by existing knowledge from biology, anatomy and dermatology. Two commonalities of Gabor filters based and biology-inspired approaches are that both start with random initial conditions and both perform changes in an iterative fashion. Kücken and Champod suggest a model describing the formation of fingerprint patterns over time based on the interaction of certain cells and mechanical stress in the epidermis [Irm10].

In principle, a nature-inspired model nourishes the hope of producing more realistic fingerprints and potentially also to gain insights into the process of natural fingerprint pattern formation. Based on an extensive literature [CLMS16, DM86, Irm10, KC13, MM89, MJM92, Wer11] in the biological community we consider fingerprint patterns formed due to the interaction of mechanical stress, trophic factors from incoming nerves and interactions between so-called Merkel cells.

As described in Section 1.1.1, the fingerprint development based on the rearrangement of Merkel cells was first modelled by Kücken and Champod [KC13]. They propose that Merkel cells are the missing link between the stress distribution in the epidermis and the developing pattern due to their mechanosensing ability. For their mathematical description they use an agent-based model to describe the pattern formation process in the second phase of the fingerprint development where the underlying stress field from the first phase [KN04, KN05] is considered as an input. Due to the lack of specific information not all details of their model can be confirmed by experimental observations. Hence, they aim to propose a model as simple as possible that captures the essence of the interaction between Merkel cells and stress distribution. For instance, the sensitivity of their model to initial conditions is consistent with the long standing belief that the pattern arrangement is unique and even for identical twins the fingerprints are different. However, the resulting patterns in the model proposed by Kücken and Champod [KC13] do not seem to be stationary which is desirable for describing the formation of fingerprints accurately.

Note that a large range of models exist in literature for describing biological pattern formation, including reaction-diffusion models [KM10, Tur91, WK91] and the elastic instability mechanism, see [Bal09, KM94, Mei82] for good summaries on this topic. A generic partial differential equation, well-known for its pattern-forming behaviour, is the Swift-Hohenberg (SH) equation [SH77]. It produces patterns which are locally stripe-like, and upon inspection of simulations (e.g. [SLT$^+$15]), it seems that SH equations can, in principle, produce any patterns occurring in fingerprints, including defects such as triradii and loops in the fingerprint vernacular, and minutiae ends. To the best knowledge of the authors, however, SH equations have never been studied for actual fingerprint simulations. Besides, the well-known existence of an underlying stress field [KN04, KN05] is not included in these pattern formation models.

To describe the central phase of the fingerprint development process, i.e. the rearrangement of Merkel cells in the second of the three phases, as accurate as possible

the underlying stress field, created in the first phase of the fingerprint development process, has to be considered as an input of our class of models. Motivated by the approach by Kücken and Champod we propose a general class of evolutionary particle models with anisotropic, biology-inspired interaction forces in two space dimensions. In contrast to the Kücken-Champod model, our forces are bio-inspired and we are able to show that fingerprint patterns can be obtained as stationary solutions to our model, an important feature of a biologically meaningful fingerprint development model [Gal92, MMJP09, YJ15]. Indeed, the stability of line patterns was the focus of most studies analysing effects of growth on fingerprints. Sir Francis Galton was among the first to demonstrate scientifically the permanence of the configuration of individual ridges and furrows [Gal92]. These findings were subsequently confirmed in intensive pediatric research such as [Bab91].

In our model, we consider a tensor field, modelling the underlying (inhomogeneous) stress field, as one of the inputs of our interaction forces. Besides, the interaction force between two Merkel cells depends on the distance vector between these two cells. We model the coefficient functions of the interaction forces as damped harmonic oscillators, a well-established modelling assumption in cell biology. Besides, this choice reflects the exponential decay of the interaction over larger distances, implying that interactions over very large distances can be neglected, and reinforces an interplay between repulsive and attractive forces as the distance between two cells increases. This choice of the interaction forces is consistent with the general modelling assumption that interaction forces should be short-range repulsive to avoid collisions between cells, and attractive over larger distances to obtain cell accumulations. Note that a similar model is proposed in Chapter 2 and its stationary states are studied both analytically and numerically in the spatially homogeneous case.

Our class of models can be regarded as an biology-inspired adaptation of the Kücken-Champod model [KC13] and we describe our modelling assumptions in detail, resulting in a reproducible pattern formation for fingerprints. We show that the resulting stationary patterns depend strongly on the underlying tensor field and the given initial conditions. Perturbations in the initial configuration of the Merkel cells result in perturbed stationary patterns. This situation is analogous to the fingerprints in identical twins who have very similar fingerprints in terms of direction of the ridges and qualitative features of fingerprint lines, but the exact location of ridges and minutiae differs [JPP02, SSF06, TCYT12]. Since environmental (within the mother's womb) and genetic conditions are almost identical for twins the differences in defect location are solely due to small perturbations such as the initial

configuration of the Merkel cells and the stress field in the epidermis [KC13], implying that the fingerprint patterns of underlying identical tensor fields are different but similar. More varied fingerprints can be obtained by changing the underlying tensor field in the model.

In this chapter, we consider the particle model introduced in Chapter 1, given by $N$ interacting particles on a domain $\Omega \subset \mathbb{R}^2$ whose positions $x_j = x_j(t) \in \Omega$, $j = 1, \ldots, N$, at time $t$ satisfy (1.4), i.e.

$$\frac{\mathrm{d}x_j}{\mathrm{d}t} = \frac{1}{N} \sum_{\substack{k=1 \\ k \neq j}}^{N} F(x_j - x_k, T(x_j)), \tag{3.1}$$

equipped with initial data $x_j(0) = x_j^{in}$, $j = 1, \ldots, N$. The term $F(x_j - x_k, T(x_j))$ in (3.1) denotes the force which a particle at position $x_k$ exerts on a particle at position $x_j$. This force depends on an underlying stress tensor field $T(x_j)$ at location $x_j$. The existence of such a tensor field $T(x_j)$ is based on the experimental results in [KH95] where an alignment of the particles along the local stress lines is observed. We define the tensor field $T(x_j)$ by the directions of smallest stress at location $x_j$ by a unit vector field $s = s(x) \in \mathbb{R}^2$ and introduce a corresponding orthonormal vector field $l = l(x) \in \mathbb{R}^2$, representing the directions of largest stress. Then the force is given by (1.9) for coefficient functions $f_s$ and $f_l$.

In the previous work on the Kücken-Champod model [KC13] and its generalisation in Section 1.1.3 a dynamical system of ordinary differential equations of the form (3.1) was considered where the force that particle $k$ exerts on particle $j$ is given by (1.8) i.e. the sum of repulsion and attraction forces, $F_R$ and $F_A$, respectively. Here, the attraction force depends on the underlying tensor field $T(x_j)$ at $x_j$, modelling the local stress field. The matrix $T(x_j)$ encodes the direction of the fingerprint lines at $x_j$, defined by (1.5) for $\chi \in [0, 1]$ and orthonormal vector fields $s = s(x)$, $l = l(x) \in \mathbb{R}^2$. For studying the pattern formation with an underlying spatially homogeneous tensor field $T$ producing straight parallel ridges, e.g.

$$T = \begin{pmatrix} 1 & 0 \\ 0 & \chi \end{pmatrix},$$

is considered. The repulsion and attraction forces in the Kücken-Champod model [KC13] and its generalisation in Section 1.1.3 are of the form (1.12) and (1.13),

respectively. Note that the direction of the attraction force $F_A$ and hence also the direction of the total force $F$ are regulated by the parameter $\chi$ in the definition of the tensor field $T$. The parameter $\chi$ introduces an anisotropy to the equation leading to complex, anisotropic patterns.

For $\chi = 1$ the model (3.1) with interaction forces of the form (1.8) for repulsion and attraction force (1.12) and (1.13) reduces to a gradient flow (1.2) and $F(d) = -\nabla W(d)$ for a radially symmetric interaction potential $W$. The continuum equation associated with the isotropic particle model (1.2) is given by (1.3). This continuum model, referred to as the aggregation equation has been studied extensively recently, mainly in terms of its gradient flow structure, the blow-up dynamics for fully attractive potentials and the rich variety of steady states, see [AGS05, BCLR13a, BCLR13b, BCY14, BT11, BCL09, BLL12, vBU12, vBUKB12, CCP15, CDM16, CDFF+11, CFP12, CFF+12, CJLV16, CMV03, CMV06, FR10, FR11, LT04, Rao12, Vil03] and the references therein. There has been a trend recently to connect the microscopic and the macroscopic descriptions via kinetic modelling, see for instance [BS12, CFRT10, HT08] for different kinetic models in swarming, [FHT11, HL09] for the particle to hydrodynamics passage and [KMT15] for the hydrodynamic limit of a kinetic model. It seems that not many results are currently available in the field of anisotropies. In [EFR15, EFS17] anisotropy is modelled by adding weights to the interaction terms. One can show that the model in [EFR15, EFS17] is related to our model if a tensor field $T$ is introduced as the velocity direction.

Fingerprint simulation results are shown for certain model parameters in [KC13] where the underlying tensor field is constructed based on fingerprint images using the NBIS package from the National Institute of Standards and Technology. However, [KC13] is purely descriptive, the choice of parameters is not discussed and the model (3.1) was not studied mathematically. The model (3.1) was studied analytically and numerically for the first time in [BDK+18] (cf. Chapter 2). Here, we justify why the particles align along the vector field lines $s$ provided the parameter $\chi$ is chosen sufficiently small so that the total force is purely repulsive along $s$. Besides, the authors investigate the stationary states to the particle model (3.1) for a spatially homogeneous underlying tensor field where the chosen model parameters are consistent with the work of Kücken and Champod in [KC13]. For the simulation of fingerprints, however, non-homogeneous tensor fields have to be considered, making the analysis of the model significantly more difficult. No analytical results of the long-time behaviour of (3.1) for non-homogeneous tensor fields are currently

74

available. Besides, numerical results for the given model parameters and different non-homogeneous tensor fields are shown over time in Chapter 2 and one can clearly see that the resulting patterns are not stationary. The simulation results for realistic tensor fields for the simulation of fingerprints in [KC13] seem to be far away from being stationary too. This is illustrated in Figure 9 in [KC13] where snapshots of the solution are shown for a spatially homogeneous tensor field which should have been parallel lines for steady states. In the biological community, however, it is well-known that fingerprint patterns with their ridge lines and minutiae configuration are determined during pregnancy and remain the same during lifetime (as long as no fingerprint alterations occur). Hence, we are particularly interested in stationary solutions of the system (3.1).

The goal of this chapter is to develop an efficient algorithm for creating synthetic fingerprint patterns as stationary solutions of an evolutionary dynamical system of the form (3.1) as illustrated in Figure 3.1(D) for the underlying tensor field in Figure 3.1(C).



|     |     |     |     |
| --- | --- | --- | --- |
| (A) Original | (B) $s$ with original | (C) $s$ | (D) Stationary |
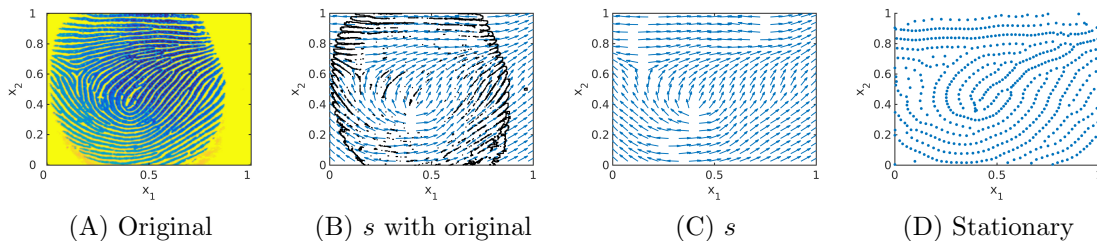
Figure 3.1: Original fingerprint image and lines of smallest stress $s = s(x)$ for the reconstructed tensor field $T = T(x)$ with an overlying mask of the original fingerprint image in black, as well as stationary solution to the interaction model (3.1) for interaction forces of the form (1.9) and randomly uniformly distributed initial data.

As a first step we study the existence of stationary solutions to (3.1) for spatially homogeneous underlying tensor fields and extend these results to certain spatially inhomogeneous tensor fields. Based on these analytical results as well as the stability analysis of line patterns in [CDKS18] we can expect stable stationary patterns along the vector field $s$. Since the solutions to the particle model (3.1) with the parameters suggested by Kücken and Champod do not seem to be stationary, we investigate the impact of the interaction forces on the resulting pattern formation numerically. In particular the size of the total attraction force plays a crucial role in the pattern formation. We adjust the model parameters accordingly and simulate fingerprints which seem to be close to being stationary, resulting in an extension of the numerical

results in Chapter 2 for inhomogeneous tensor fields. Based on real fingerprint images as in Figure 3.1(A) we determine the underlying tensor field $T$ with lines of smallest stress $s$ by extrapolating the direction field outside of the fingerprint image based on [GMM09]. In Figure 3.1(B) we overlay a mask of the original fingerprint image on the estimated tensor field with direction field $s$ and in Figure 3.1(C) only the direction field $s$ is shown. Besides, we include a novel method for the generation of the underlying tensor fields in our numerical simulations which is based on quadratic differentials as a global model for orientation fields of fingerprints [HHM08].

In the fingerprint community major features of a fingerprint, called minutiae, are of great interest. Examples include ridge bifurcation, i.e. a single ridge dividing into two ridges. We study how they evolve over time, both heuristically and numerically. Finally, we propose a new bio-inspired model for the creation of synthetic fingerprint patterns which not only allows us to simulate fingerprint patterns as stationary solution of the particle model (3.1) but also adjust the distances between the fingerprint lines by rescaling the model parameters. This is the first step towards modelling fingerprint patterns with specific features in the future.

Studying the model (3.1) and in particular its pattern formation result in a better understanding of the fingerprint pattern formation process. Due to the generality of the formulation of the anisotropic interaction model (3.1) this can be regarded as an important step towards understanding the formation of fingerprints and may be applicable to other anisotropic interactions in nature.

This chapter is organised as follows. In Section 3.2 the Kücken-Champod model [KC13] is introduced and we propose a new bio-inspired modelling approach. Section 3.3 deals with the existence of steady states to (3.1) in the form of parallel, equidistant lines for spatially homogeneous tensor fields and its extension to locally spatially homogeneous tensor fields, implying that measurable quantities, such as the almost constant distance between the stationary line patterns, can be predicted with the model. In Section 3.4 we adapt the parameters in the force coefficients (1.18) and (1.19) of the Kücken-Champod model in such a way that fingerprint patterns can be obtained as stationary solutions to the particle model (3.1). Based on these results, we propose the bio-inspired model, described in Section 3.2, to simulate fingerprints with variable distances between the fingerprint lines. For the creation of realistic fingerprints we consider a novel methods for obtaining the underlying tensor field based on quadratic differentials as well as images of real fingerprint data.

## 3.2 Description of the model

In the sequel, we consider particle models of the form (3.1) where the force $F$ is of the form (1.9) or (1.8) where the repulsion and attraction forces are given by (1.12) and (1.13), respectively.

### 3.2.1 Kücken-Champod model

In the paper [KC13] and Chapter 2, systems of evolutionary differential equations of the form (3.1) as introduced in Chapter 1 are considered where the total force, the attraction and the repulsion forces are of the forms (1.8), (1.12) and (1.13), respectively, and the underlying tensor field $T$ is defined as (1.5). The coefficient functions $f_R$ and $f_A$ of the repulsion force $F_R$ (1.12) and the attraction force (1.13) in the Kücken-Champod model are given by (1.18) and (1.19) for nonnegative constants $\alpha$, $\beta$, $\gamma$, $e_A$ and $e_R$, and, again, $d = d(x_j, x_k) = x_j - x_k \in \mathbb{R}^2$. To be consistent with the work of Kücken and Champod [KC13] we assume that the total force (1.8) exhibits short-range repulsion and long-range attraction along $l$ and we choose the parameters in an initial study as (1.20) where we set $\chi = 0.2$. These parameters are chosen in such a way that the resulting plots of the force coefficients are as close as possible to the ones shown by Kücken and Champod in [KC13]. Here, the parameter $\chi \in [0, 1]$ determines the direction of the interaction. For $\chi = 1$ the attraction force between two particles is aligned along their distance vector, while for $\chi = 0$ the attraction between two particles is oriented exactly along the lines of largest stress (cf. Chapter 2).

In Figure 3.2(A) the coefficient functions (1.18) and (1.19) for the repulsion and attraction forces (1.12) and (1.13) in the Kücken-Champod model (3.1) are plotted for the parameters in (1.20) with $\chi = 0.2$.

The sums of the coefficients of the forces $f_R + f_A$ and $f_R + \chi f_A$ for $\chi = 0.2$ are illustrated in Figure 3.2(B). Note that $f_R + f_A$ and $f_R + \chi f_A$ are the force coefficients along $l$ and $s$, respectively. For the choice of parameters in (1.20) repulsion dominates for short distances along the lines of largest stress to prevent the collision of particles and the force is long-range attractive along the lines of largest stress leading to accumulations of the particles. The absolute value of the attractive force decreases with the distance between particles. Along the lines of smallest stress the particles are always repulsive for $\chi = 0.2$, independent of the distance, though the repulsion force gets weaker for longer distances.

(A) Force coefficients $f_R$ and $f_A$



(B) Total force coefficients
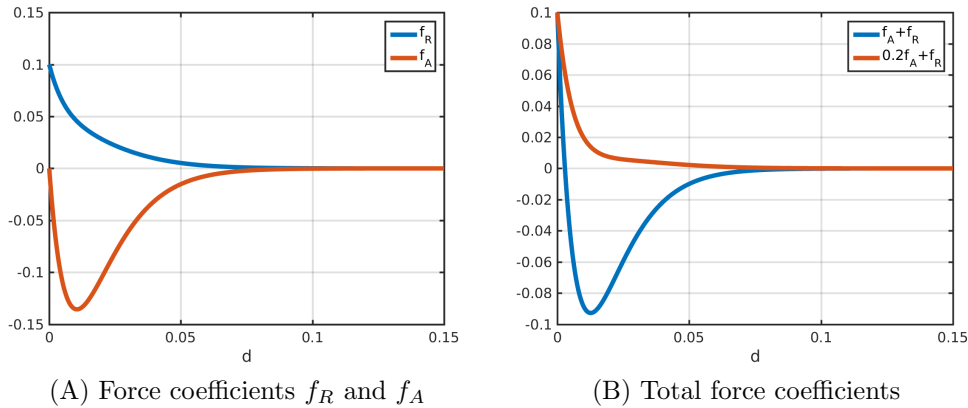
Figure 3.2: Coefficients $f_R$ in (1.18) and $f_A$ in (1.19) of repulsion force (1.12) and attraction force (1.13), respectively, as well as total force coefficients along the lines of largest and smallest stress for $\chi = 0.2$ (i.e. $f_A + f_R$ and $0.2 f_A + f_R$, respectively) for parameter values in (1.20) with $\chi = 0.2$.

### 3.2.2 Bio-inspired model

We propose a system of ordinary differential equations of the form (3.1) where the forces are of the form (1.9). Note that plugging the repulsion and attraction forces (1.12) and (1.13) as well as the definition (1.5) of the tensor field $T$ into the force term (1.8) results in forces of the form (1.9). Hence, we replace the coefficient functions $f_A$ and $f_R$ by some more general coefficient functions $f_s$ and $f_l$ which are related to the force coefficients $f_A$ and $f_R$ in the Kücken-Champod model, and are of the form

$$f_s = \chi f_A + f_R, \qquad f_l = f_A + f_R.$$

We model the force coefficients $f_s$ and $f_l$ in (1.9) as solutions to a damped harmonic oscillator. Like for the coefficient functions (1.18), (1.19) in the Kücken-Champod model we consider exponentially decaying forces describing that short-range interactions between the particles are much stronger than long-range inter-actions. Besides, the repulsion and attraction forces suggested in the Kücken-Champod model dominate on different regimes. For a more unified modelling approach one may regard this interplay of repulsion and attraction forces as oscilla-tions. This motivates to model the force coefficients $f_s$ and $f_l$ in (1.9) as solutions to a damped harmonic oscillator which is also a common modelling approach in cell biology [PKTG12, pages 21-23]. Hence, we consider the following ansatz functions

for the force coefficients $f_s$ and $f_l$:

$$f_s(d) = c \exp(e_{s_1}|d|) + c_s \sin\left(\frac{\pi|d|}{a_s}\right) \exp(e_{s_2}|d|),$$

$$f_l(d) = c \cos\left(\frac{\pi|d|}{a_l}\right) \exp(e_{l_1}|d|) + c_l \sin\left(\frac{\pi|d|}{a_l}\right) \exp(e_{l_2}|d|) \tag{3.2}$$

for real parameters $c, c_s, c_l, e_{s_1}, e_{s_2}, e_{l_1}, e_{l_2}, a_s, a_l$. The constants $e_{s_1}, e_{s_2}, e_{l_1}, e_{l_2}$ control the decay rates of the force coefficients. Since the force coefficients $f_s$ and $f_l$ both vanish over large distances, this implies that the constants $e_{s_1}, e_{s_2}, e_{l_1}, e_{l_2}$ are all negative. Note that $c, c_s, c_l$ are scaling parameters for the size of the interaction forces. Since $f_s$ has to be an exponentially decaying, repulsive force coefficient (i.e. $f_s \geqslant 0$) with (possibly) small adaptations, we require that the term $c \exp(e_{s_1}|d|)$ decays exponentially fast and dominates in the definition of $f_s$. Hence, we assume that $c$ is a nonnegative constant with $|c| > |c_s|$. The force coefficient $f_l$ is assumed to be short-range repulsive, long-range attractive. Since the cosine function can be regarded as a short-range repulsive, long-range attractive function, this implies that $c$ is nonnegative, consistent with the assumptions before, and $|c| > |c_l|$. Besides, we control the frequency of the oscillations along $s$ and $l$ by positive constants $a_s, a_l$, respectively. A possible parameter choice satisfying the above assumptions is given by

$$c = 0.1, \quad c_s = -0.05, \quad e_{s_1} = -65.0, \quad e_{s_2} = -100.0, \quad a_s = 0.03$$

$$c_l = 0.005, \quad e_{l_1} = -160.0, \quad e_{l_2} = -40.0, \quad a_l = 0.022 \tag{3.3}$$

and we will see that for this parameter choice it is possible to obtain stationary fingerprint patterns and that rescaling of the coefficient functions $f_s$ and $f_l$ leads to stationary patterns with scaled line distances. The force coefficients $f_s$ and $f_l$ for the parameters in (3.3) are shown in Figure 3.3. In comparison with the force coefficients $F_A + f_R$ and $0.2f_A + f_R$ along $l$ and $s$, respectively, the force $f_s$ along $s$ is also purely repulsive, while the force $f_l$ is less attractive which is necessary for obtaining stationary patterns as discussed in Section 3.4.2.

### 3.2.3 General setting

In this chapter, we consider the particle model (3.1) with force terms of the form $F(x_j - x_k, T(x_j))$, such as (1.9) and (1.8). As in Chapter 2 we consider the domain $\Omega = \mathbb{T}^2$ where $\mathbb{T}^2$ is the 2-dimensional unit torus that can be identified with
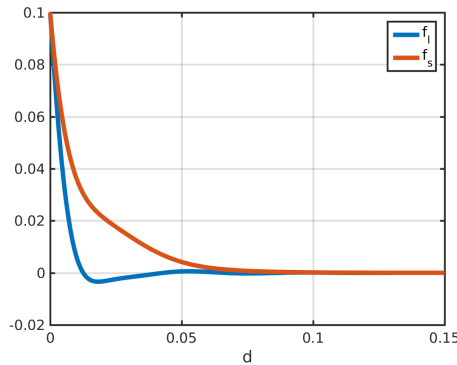
Figure 3.3: Coefficients $f_s$ and $f_l$ in (3.2) for parameter values in (3.3).

the quotient of the unit square $[0, 1) \times [0, 1) \subset \mathbb{R}^2$. This induced periodicity has proven to be very useful to simulate interactions on microscopic scales where the simulation domain is large compared to the size of the interacting particles. Besides, this periodicity is the natural choice in terms of the mathematical analysis and the derivation of the associated macroscopic model. Note that the particles on the domain $\Omega$ are separated by a distance of at most 0.5 due to the periodicity. Motivated by this we require for $j \in \{1, 2\}$ and all $x \in \Omega$

$$F(x - x', T(x)) \cdot e_j = 0 \quad \text{for} \quad |x - x'| \geqslant 0.5 \tag{3.4}$$

where $e_j$ denotes the standard basis for the Euclidean plane. The forces satisfy this assumption if a spherical cutoff radius of length 0.5 is introduced for the forces in (1.9) or (1.8), respectively. This assumptions guarantees that the size of the domain is large enough compared to the range of the total force. In particular, non-physical artefacts due to periodic boundary conditions are prevented. A cutoff radius is also very useful to make numerical simulations more efficient. Since our model describes the second phase of the fingerprint development [KC13], i.e. the rearrangement of Merkel cells from a random configuration into parallel ridges, we consider randomly uniformly distributed initial data on the torus $\mathbb{T}^2$ in the numerical simulations.

## 3.3 Mathematical analysis of steady states

To use the particle system (3.1) for the simulation of fingerprints it is of great interest to have a better understanding about the form of the steady states. The steady states are formed by a number of lines which are referred to as ridges. As

discussed in Section 3.2 we consider purely repulsive forces along $s$. In this section, we study the existence of steady states for the particle model (3.1) for spatially homogeneous and certain inhomogeneous tensor fields $T$ analytically. The stability of these line patterns is further investigated in [CDKS18]. In particular, the authors show that line patterns for purely repulsive forces along $s$ can only be stable if the patterns are aligned in direction of the vector field $s$.

### 3.3.1 Spatially homogeneous tensor field

For spatially homogeneous tensor fields $T$ it is sufficient to restrict ourselves to the tensor field given by $s = (0, 1)$ and $l = (1, 0)$ since stationary solutions to the Kücken-Champod model for any other tensor field can be obtained by coordinate transform as shown in Chapter 2. Further note that steady states are translation invariant, i.e. if $x_1, \ldots, x_N$ is a steady state, so is $x_1 + z, \ldots, x_N + z$ for any $z \in \mathbb{R}^2$. Hence it is sufficient to consider one specific constellation of particles for analysing the steady states of (3.1). Because of the stability analysis in [CDKS18] we restrict ourselves to line patterns along $s = (0, 1)$, i.e. we consider patterns of vertical lines. Note that two-dimensional vertical stripe pattern of width $\Delta$ for any $\Delta > 0$ do not satisfy the steady state condition by the analysis in Chapter 2, i.e. stable line patterns are one-dimensional structures.

**Proposition 4.** *Given $|d| \in (0, 1]$ such that $n := \frac{1}{|d|} \in \mathbb{N}$ and let $N \in \mathbb{N}$ be given such that $\frac{N}{n} \in \mathbb{N}$. Then $n$ parallel equidistant vertical lines of distance $|d|$ of $\frac{N}{n}$ uniformly distributed particles along each line are a steady state to the particle model (3.1) for forces of the form (1.9) or (1.8) where the repulsion and attraction forces are of the form (1.12) and (1.13), respectively.*

Note that the choice of the distance $|d|$ of the parallel vertical lines is consistent with the periodic boundary conditions.

*Proof.* Because of the translational invariance of steady states it is sufficient to consider any $n$ equidistant parallel vertical lines of $\frac{N}{n}$ particles distributed uniformly along each line. Without loss of generality we assume that the positions of the particles are given by

$$\bar{x}_j = \left( \frac{\left( j - j \bmod \frac{N}{n} \right) \frac{n}{N}}{n}, \frac{j \bmod \frac{N}{n}}{\frac{N}{n}} \right) = \frac{1}{N} \left( j - j \bmod \frac{N}{n}, n \left( j \bmod \frac{N}{n} \right) \right) \in \mathbb{R}^2.$$

Because of the periodic boundary conditions of the domain as well as the fact that the particles are uniformly distributed along parallel lines, it is sufficient to require that

$$\sum_{k=1}^{N-1} F(\bar{x}_N - \bar{x}_k, T(\bar{x}_N)) = 0 \tag{3.5}$$

for steady states of the particle model (3.1). Note that for forces of the form (1.9) or (1.8) where the repulsion and attraction forces are of the form (1.12) and (1.13), respectively, we have

$$F(d, T(\bar{x}_N)) = -F(-d, T(\bar{x}_N)) \quad \text{for all} \quad d \in \mathbb{R}^2. \tag{3.6}$$

As a first step we show that

$$\sum_{k=1}^{\frac{N}{n}-1} F(\bar{x}_N - \bar{x}_k, T(\bar{x}_N)) = 0. \tag{3.7}$$

Note that $\bar{x}_k \in \{0\} \times [0,1]$ for $k = 1, \ldots, \frac{N}{n}$ and $\bar{x}_N = (0,0)$ by the periodic boundary conditions, i.e. we consider all the particles of the vertical line with $x_1$-coordinate $x_1 = 0$. If $\frac{N}{n}$ is odd, then (3.7) is satisfied by the balance of forces (3.6). For even $\frac{N}{n}$ we have

$$F(\bar{x}_N - \bar{x}_k, T(\bar{x}_N)) = -F(\bar{x}_N - \bar{x}_{\frac{N}{n}-k}, T(\bar{x}_N))$$

for $k = 1, \ldots, \frac{N}{2n} - 1$. Besides,

$$F(\bar{x}_N - \bar{x}_{\frac{N}{2n}}, T(\bar{x}_N)) = 0$$

since $|\bar{x}_N - \bar{x}_{\frac{N}{2n}}| = 0.5$ and the assumption of the finite range of the forces in (3.4), implying that (3.7) is satisfied. If there is an odd number $n$ of parallel equidistant vertical lines, then the condition for steady states (3.5) is satisfied by (3.6). For $n$ even, the forces due to particles on the vertical lines at $x_1 = k|d|$ balances the interaction forces due to particles on the vertical lines at $x_1 = (n-k)|d|$ for $k = 1, \ldots, \frac{n}{2} - 1$ by (3.6), so it suffices to consider the particles on the vertical line at

$x_1 = \frac{n}{2}|d|$, i.e. the particles at positions $\bar{x}_k$ for $k = \frac{N}{2}, \ldots, \frac{N}{2} + \frac{N}{n} - 1$. Note that

$$\sum_{k=\frac{N}{2}}^{\frac{N}{2}+\frac{N}{n}-1} F(\bar{x}_N - \bar{x}_k, T(\bar{x}_N)) = 0$$

since $|\bar{x}_N - \bar{x}_k| \geqslant 0.5$ for $k = \frac{N}{2}, \ldots, \frac{N}{2} + \frac{N}{n} - 1$ and the assumption of the finite range of the forces in (3.4). This implies that the condition for steady states (3.5) is satisfied. Hence, $\bar{x}_1, \ldots, \bar{x}_N$ form a steady state of the microscopic model (3.1). $\square$

**Corollary 4.** *Given $d \in (0, 1]$ such that $n := \frac{1}{d} \in \mathbb{N}$ and let $N \in \mathbb{N}$ be given such that $\frac{N}{n} \in \mathbb{N}$. Then $n$ parallel, but not equidistant, vertical lines of $\frac{N}{n}$ uniformly distributed particles along each line are not a steady state to the particle model (3.1) for forces of the form (1.9) or (1.8) where the repulsion and attraction forces are of the form (1.12) and (1.13), respectively.*

**Remark 8.** *Even though parallel, equidistant lines form a steady state for any distance $|d|$ the line patterns in Proposition 4 are not stable for every $|d| \in (0, 1]$. The maximum distance between parallel equidistant lines is given by the cutoff radius $R_c$ of the force coefficient $f_l$ or, equivalently, by the distance $R_c$ such that $f_l(|d|)$ vanishes for all $|d| \geqslant R_c$. In particular, a steady state of parallel, equidistant lines of distance $R_c$ is also stable under perturbations. This implies that a steady state to (3.1) of parallel, equidistant vertical lines for a given choice of force coefficients $f_s$ and $f_l$ can be transformed into a steady state of parallel, equidistant vertical lines with a different line distance by rescaling the force coefficients appropriately.*

### 3.3.2   Non-constant tensor fields

Many non-constant tensor fields can locally be regarded as spatially homogeneous tensor fields. Note that by the assumptions in Section 3.2.3 we consider forces of finite range. In particular, we have local forces for the forces (1.9) with coefficients (3.2) and parameters (3.3) as well as for forces of the form (1.8) with force coefficients (1.18), (1.19) and parameters (1.20) with $\chi = 0.2$. Applying the results from Proposition 4 and Corollary 4 to a locally spatially homogeneous tensor field implies that the resulting steady states are locally parallel, equidistant line patterns where the distance of the line patterns crucially depends on the range of the interaction forces. In particular, this suggests that the steady states to (3.1) are given by roughly parallel, equidistant lines whose distance is almost constant. By rescaling

the force coefficients the (almost constant) distance between parallel lines can be adapted. This shows that the almost constant distance between (stationary) ridges can be predicted with the model.

## 3.4 Simulation of fingerprint patterns

In this section we investigate how to simulate fingerprint patterns by extending the theoretical and the numerical results in Chapter 2. In particular, we consider more realistic tensor fields for the formation of fingerprint patterns and study the dependence of the parameter values in the Kücken-Champod model on the resulting fingerprints.

### 3.4.1 Local fields in a fingerprint image

In order to use the particle model (3.1) to simulate fingerprint patterns a realistic tensor field is needed. It is well known that fingerprints are composed of two key directional features known as cores and deltas which can be regarded as local fields of a fingerprint orientation field. Hence, we consider the construction of the tensor fields for these two features first.

In [HHM08], Huckemann et al. propose to use differential equations (or more generally quadratic differentials) which naturally define analytic orientation fields on planar surfaces. The orientation field is composed of several local fields where each local field is generated by a singular point of that field: A core is the endpoint of a single line (cp. Figure 3.4(B)) and a delta occurs at the junction of three lines (cp. Figure 3.4(A)).

For the mathematical description of a local field, we identify $\mathbb{R}^2$ with the complex plane $\mathbb{C}$. For simplicity we consider the origin $\zeta = 0$ as the only singular point, but the idea can be extended to arbitrary singular points $\zeta \in \mathbb{C}$. As outlined in [HHM08] one can model the local field near the singular point $\zeta = 0$ by considering the initial value problem

$$z(r)\dot{z}(r)^2 = \phi(r), \quad z(r_0) = z_0, \tag{3.8}$$

for a smooth, positive function $\phi = \phi(r) \in \mathbb{R}$, $r \in \mathbb{R}$, and initial value $z_0 \in \mathbb{C}$. Starting from $z_0$ the solution $z = z(r) \in \mathbb{C}$ for $r \in \mathbb{R}$ can be regarded as a parametrisation of a curve in $\mathbb{C}$, and varying $z_0$ results in multiple curves. For $\phi = \frac{2}{3}$ the solution to

the differential equation (3.8) is given by

$$z(r) = \left(r + z_0^{3/2}\right)^{2/3},\tag{3.9}$$

but, in fact, the shape of the solution curves does not change for reparametrisations, provided $\phi > 0$. By considering a fixed function $\phi$ and varying $z_0 \in \mathbb{C}$, the associated solution curves form a delta at the origin ($\zeta = 0$) as illustrated in Figure 3.4(A). Hence, we require $z\dot{z}^2 > 0$ for a delta at the origin. Note that $z = |z|\exp(i\arg(z))$ where $\arg(z)$ denotes the principal argument of the complex number $z \in \mathbb{C}$. Further note that $\dot{z}/\|\dot{z}\|$ can be regarded as the unit vector in the direction of the smallest stress. As outlined in Section 3.2 the direction of smallest stress is denoted by the unit vector $s = s(z)$ for $z \in \mathbb{R}^2$ implying that $s(z) = \exp(-i\arg(z)/2)$. Thus, the lines of smallest stress on a domain $\Omega \subset \mathbb{C}$ can be obtained by evaluating $\exp(-i\arg(z)/2)$ for all $z \in \Omega$. Note that $\exp(-i\arg(z)/2)$ and $-\exp(-i\arg(z)/2)$ result in the same lines of the stress field.



(A) Delta  (B) Core
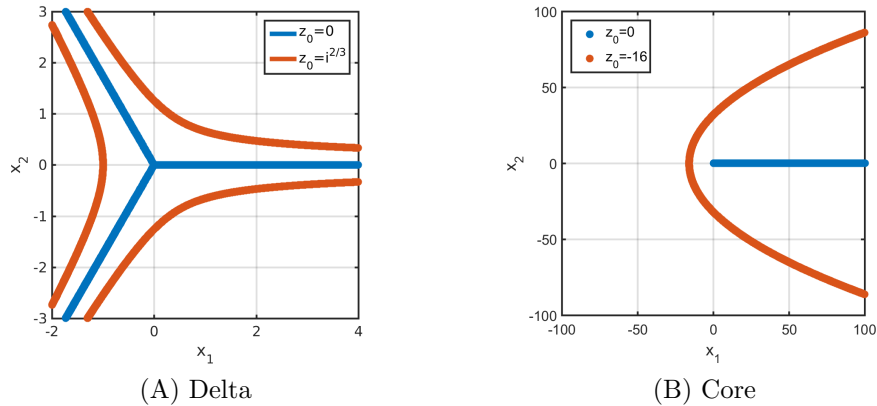
Figure 3.4: Solution curves (3.9) and (3.11) to the initial value problems (3.8) and (3.10), respectively, generating fields of quadratic differentials for a delta and a core.

Similarly, for a positive function $\phi$, the initial value problem

$$\frac{1}{z(r)}\dot{z}(r)^2 = \phi(r), \quad z(r_0) = z_0,\tag{3.10}$$

generates a field with a core at the origin. Up to reparameterisation the solution is given by

$$z(r) = \left(r + z_0^{1/2}\right)^2,\tag{3.11}$$

85

and the solution curves are illustrated for different initial conditions $z_0 \in \mathbb{C}$ in Figure 3.4(B). This leads to the condition $\dot{z}^2/z > 0$ for a core at the origin, implying $s(z) = \exp(i\arg(z)/2)$ since, as before, $\pm \exp(i\arg(z)/2)$ result in the same lines. Further note that a delta or a core at any $\zeta \in \mathbb{C}$ can be obtained by linear transformation. In Figure 3.5 the tensor field for a delta and a core at the singular point $(0.5, 0.5)$ are plotted on the unit square $[0,1]^2$.



(A) $s$ for delta          (B) $s$ for core
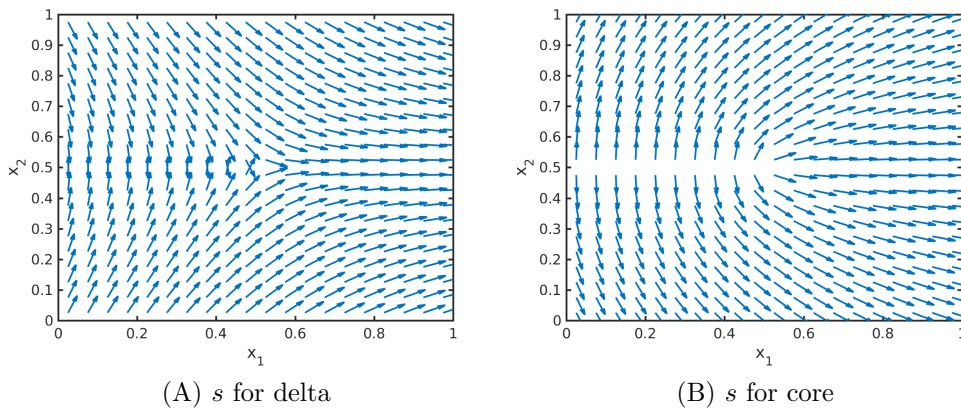
Figure 3.5: Lines of smallest stress $s = s(x)$ of tensor fields $T$ for a delta and a core.

### 3.4.2  Numerical methods

In this section, we describe the general setting for investigating the long-time behaviour of solutions to the particle model (3.1), motivated by Chapter 2.

We consider the particle model (3.1) where the forces are of the form (1.9) or (1.8) and investigate the patterns of the corresponding stationary solutions. As in Chapter 2 and outlined in Section 3.2.3 we consider the domain $\Omega = \mathbb{T}^2$, i.e. the unit square $[0,1) \times [0,1) \subset \mathbb{R}^2$ with periodic boundary conditions, and we consider a cutoff of the forces as in (3.4) to make the simulations more efficient.

To solve the $N$ particle ODE system (3.1) we apply either the simple explicit Euler scheme or higher order methods such as the Runge-Kutta-Dormand-Prince method, all resulting in very similar simulation results. For the numerical simulations we consider $\Delta t = 0.2$ for the size of the time step.

### 3.4.3  Numerical study of the Kücken-Champod model

Using the tensor fields introduced in Section 3.4.1 we consider the interaction model (3.1) with forces of the form (1.8) to simulate fingerprint patterns. Here, the repul-

sion and attraction forces are of the forms (1.12) and (1.13) with force coefficients (1.18) and (1.19), respectively, and we consider the parameters in (1.20) with $\chi = 0.2$ to make the simulations as close as possible to the model suggested by Kücken and Champod in [KC13]. It is well known that fingerprints develop during pregnancy and stay the same afterwards provided no fingerprint alterations occur. In order to simulate biologically meaningful fingerprints we aim to model fingerprint patterns as stationary solution to the particle model (3.1). Based on the analysis of steady states in Section 3.3 it is possible to obtain stationary patterns consisting of multiple roughly parallel ridges along the lines of smallest stress. However, the force coefficients need to be chosen appropriately so that the resulting patterns are also stable. For the simulations in Figure 3.6 we consider the tensor field for the delta constructed in Section 3.4.1 and depicted in Figure 3.5(A). One can clearly see in



(A) $t = 2 \cdot 10^4$  (B) $t = 4 \cdot 10^4$  (C) $t = 6 \cdot 10^4$  (D) $t = 8 \cdot 10^4$

(E) $t = 10 \cdot 10^4$  (F) $t = 20 \cdot 10^4$  (G) $t = 30 \cdot 10^4$  (H) $t = 40 \cdot 10^4$
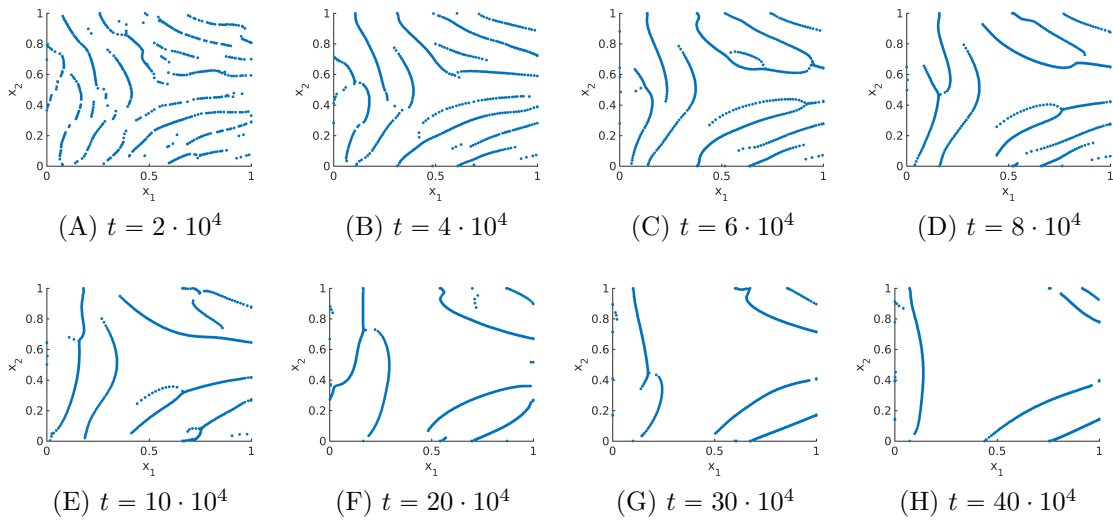
Figure 3.6: Numerical solution to the Kücken-Champod model (3.1) for $N = 600$ and $\chi = 0.2$ at different times $t$ where the stress field represents a delta and the cutoff radius is 0.5.

Figure 3.6 that the particles are aligned along the lines of smallest stress $s = s(x)$ initially, but the patterns dissolve over time and the simulation results have little similarity with fingerprint patterns over large time intervals. Besides, the patterns are clearly no stable steady states in Figure 3.6. Hence, the question arises why the patterns simplify so much over time for non-homogeneous tensor fields in contrast to the stationary patterns arising for spatially homogeneous tensor fields, cf. Chapter 2, and how this can be prohibited.

To study the long-time behaviour of the numerical solution, it is desirable to have

efficient numerical simulations and of course efficient simulations are also necessary to to simulate fingerprints based on cell interactions in practice. In Section 3.2.3 we introduced a cutoff radius for the forces, given by (3.4), in order to deal with the periodic boundary conditions. Since the forces in the Kücken-Champod model (3.1) decrease exponentially, the interaction force between two particles is very small if their distance is sufficiently large. This is also illustrated in Figure 3.2(A) for the parameters in (1.20) with $\chi = 0.2$. Hence, defining the cutoff radius as 0.1 changes the values of the forces only slightly, but it allows us to compute the numerical solution to the Kücken-Champod model (3.1) by using cell lists [AT89]. The idea of cell lists is to subdivide the simulation domain into cells with edge lengths greater than or equal to the cutoff radius of the interaction forces. All particles are sorted into these cells and only particles in the same or neighbouring cells have to be considered for interactions. This results in significantly faster simulations since we only have to consider those particle pairs with relevant sizes of the interaction forces. Note that the cutoff radius has an impact on the number of lines that occur in the solution as shown in Figure 3.7 in comparison to a cutoff radius of 0.5 in Figure 3.6. In particular the cutoff radius should not be chosen to small because this prevents the accumulation of particles.

The simulation results for the Kücken-Champod model (3.1) in Figures 3.6 and 3.7 illustrate that the particles align in roughly parallel lines along the lines of smallest stress initially, but the number of roughly parallel lines decreases as time goes on. In particular, the complex patterns that occur initially are not stationary. We can expect a similar behaviour (i.e. initial alignment along the lines of smallest stress of the stress tensor field and subsequent accumulation) of the numerical solution if the parameters in the coefficient functions of the repulsion and attraction force in (1.18) and (1.19) are slightly changed provided they are repulsive along the lines of smallest stress, as well as short-range repulsive and long-range attractive along the lines of largest stress. Denoting the directions of smallest and largest stress by $s$ and $l$, respectively, the transition of the initial pattern of multiple lines to fewer and fewer lines along $s$ suggests that the attraction forces are very strong resulting in an accumulation of the particles. Note that this transition is also observed for the long-time behaviour of the numerical solution to the Kücken-Champod model (3.1) for spatially homogeneous tensor fields in Chapter 2 where lines merge over time until finally a steady state of equidistant parallel lines is reached.

In Figure 2.15 in Chapter 2 we showed the numerical solution to (3.1) for a piecewise spatially homogeneous tensor field, randomly uniformly distributed initial

(A) $t = 20000$     (B) $t = 40000$     (C) $t = 60000$     (D) $t = 600000$

Cutoff radius 0.02

(E) $t = 20000$     (F) $t = 40000$     (G) $t = 60000$     (H) $t = 600000$

Cutoff radius 0.04

(I) $t = 20000$     (J) $t = 40000$     (K) $t = 60000$     (L) $t = 600000$

Cutoff radius 0.06
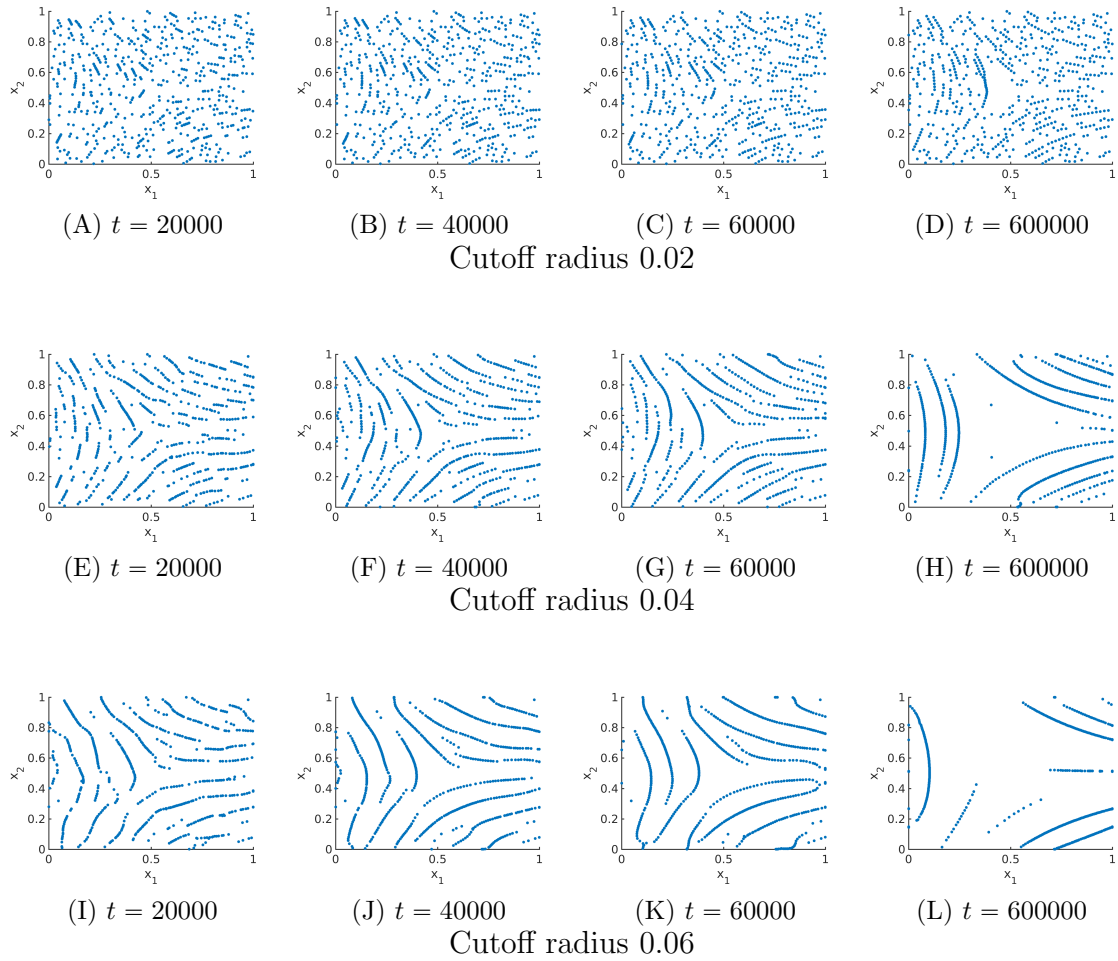
Figure 3.7: Numerical solution to the Kücken-Champod model (3.1) for different cutoff radii for $N = 600$ and $\chi = 0.2$ at different times $t$ where the stress field represents a delta.

data and $N = 600$, resulting in stationary line patterns along the lines of smallest stress $s = s(x)$. In particular, this tensor field is not smooth. This suggests that smoothness and periodicity are not necessary to obtain stationary solutions aligned along the lines of smallest stress.

The big impact of the choice of the attraction force along the lines of largest stress can be seen by considering Figure 2.11. Here, we assume that the total force is given by $F(d, T) = \delta F_A(d, T) + F_R(d)$ for $\delta \in [0, 1]$ for the spatially homogeneous tensor field $T = \chi s \otimes s + l \otimes l$ with $l = (1, 0)$, $s = (0, 1)$ and $\chi = 1$ instead of the definition of $F$ as the sum of $F_A$ and $F_R$ in (1.8), i.e. we vary the size of the attraction force and consider a radially symmetric force $F$. In Figure 2.11 the steady states to the interaction mode (3.1) are shown for different factors $\delta$ of the attraction force $F_A$, where $N = 600$ and initial data distributed equiangularly on a circle with centre $(0.5, 0.5)$ and radius $0.005$ is considered. One can see in Figure 2.11 in Chapter 2 that $\delta = 0.1$ results in a stationary solution spread over the entire domain, while ring patterns arise as $\delta$ increases. The intermediate state, occurring for $\delta = 0.3$, is of interest in the sequel, as it is an example of a more complex pattern and in particular not all the particles accumulate on one single ring as for $\delta = 0.5, \delta = 0.7$ and $\delta = 0.9$ due to too attractive forces.

The forces considered in Figure 2.11 and given by $\delta f_A + f_R$ along the lines of largest stress are plotted in Figure 3.8 for different values of $\delta$. As observed in the stationary states in Figure 3.8, the force along the lines of largest stress is purely repulsive for $\delta = 0.1$, medium- and long-range attractive for $\delta \geqslant 0.5$, as well as medium-range attractive and long-range repulsive for $\delta = 0.3$. In particular, the medium-range attractive forces for $\delta = 0.3$ are significantly smaller than for larger values of $\delta$.

## 3.5 A new model for simulating fingerprints

Based on the analysis of stationary states in Section 3.3 as well as the numerical investigation of the Kücken-Champod model in Section 3.4.3 we propose a new modelling approach for the interaction forces which can be used for simulating the formation of fingerprints based on cell interactions. In particular, fingerprints are obtained as stationary states to the model. As a next step we propose a bio-inspired model for the creation of synthetic fingerprint patterns which can not only be used to model the formation of fingerprints as stationary solutions but also allows to adjust the ridge distances of the fingerprint lines.

(A) Normal scaling

(B) Zoom
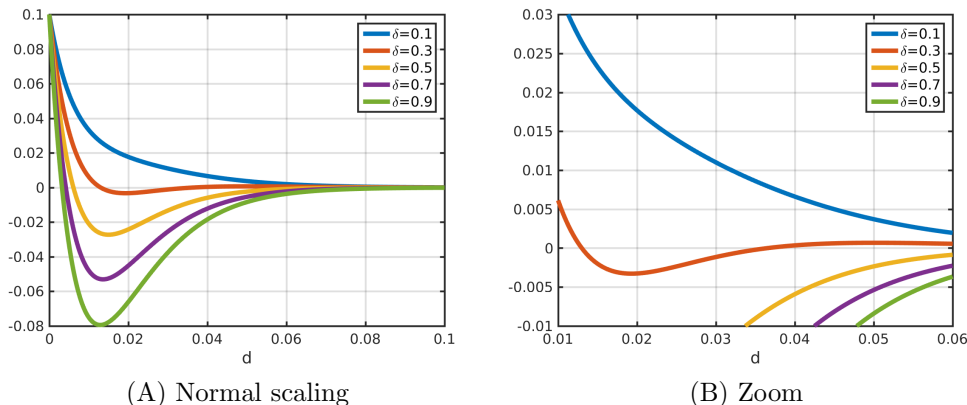
Figure 3.8: Total force coefficients $\delta f_A + f_R$ along the lines of largest stress for different values of $\delta$ and different scaling.

## 3.5.1 Stationary patterns

In this section we investigate how fingerprints can be obtained as stationary solutions to the Kücken-Champod model (3.1) where the coefficients of the repulsive and attractive forces are given by (1.18) and (1.19), respectively.

### Adaptation of the forces in the Kücken-Champod model

Repulsive forces along the lines of smallest stress are an excellent choice to guarantee that the particles form patterns along the lines of smallest stress. Hence we can consider the repulsive coefficient function $0.2f_A + f_R$ for the force along $s$ with the parameter values in (1.20) with $\chi = 0.2$ where the coefficient functions $f_A$ and $f_R$ of the attraction and repulsion force are given by (1.18) and (1.19), respectively.

Short-range repulsion forces along the lines of largest stress prevent collisions of the particles and medium-range attraction forces are necessary to make the particles form aggregates. However, the long-range forces should not be attractive for modelling complex patterns since strong long-range attraction forces prevent the occurrence of multiple roughly parallel lines as stationary solutions. Motivated by the more complex stationary pattern for $\delta = 0.3$ in Figure 2.11 and its desired structure of the forces along the lines of largest stress (short-range repulsive, medium-range attractive, long-range repulsive as depicted in Figure 3.8) we consider the coefficient function $0.3f_A + f_R$ along the lines of largest stress for the parameters in (3.13). Hence, the total force $F$ is given by (1.8) where the repulsion force $F_R$ is defined as

(1.18) and the attraction force $F_A$ with coefficient function (1.19) has the new form

$$F_A(d = d(x_j, x_k), T(x_j)) = f_A(|d|)T(x_j) = f_A(|d|)\left(0.3(l \cdot d)l + \chi(s \cdot d)s\right) \quad (3.12)$$

where we set $T(x_j) = 0.3(l \cdot d)l + \chi(s \cdot d)s$ and we consider the parameter values in (3.13) with $\chi = 0.2$.

In Figures 3.9, 3.10 and 3.11 the numerical solutions for the repulsive force (1.12), the attractive force (3.12) and different realistic tensor fields are illustrated. The tensor fields in Figure 3.9 are given by a delta and a core, respectively, introduced in Section 3.4.1, while we consider a combination of deltas and cores for the tensor fields in Figures 3.10 and 3.11. As desired the particles align in roughly parallel lines along the vector field $s = s(x)$ and because of long-range repulsion forces these nice patterns are not destroyed over time. Further note that the numerical solution in Figures 3.9, 3.10 and 3.11 is shown for very large times so that it can be regarded as stationary. In particular, this implies that the adapted forces can be used to simulate fingerprint pattern and more generally any complex patterns is in principal preserved over time.

After this adaptation of the forces it is desirable to use the original definition of the forces (1.8) with repulsion and attraction force given by (1.12) and (1.13), respectively, instead of an attraction force of the form (3.12). Along $l$ the attraction force (3.12) can be regarded as $0.3f_A$ where $f_A$ is the attraction force along $l$ in the original definition of the attraction force $F_A$ in (1.13). Note that the parameter $\gamma$ in the definition of the attractive force coefficient $f_A$ in (1.19) is a multiplicative constant. Hence, we multiply the original value of $\gamma$ in (1.20) by 0.3, resulting in

$$\alpha = 270, \quad \beta = 0.1, \quad \gamma = 10.5, \quad e_A = 95, \quad e_R = 100, \quad \chi = 0.2, \quad (3.13)$$

and consider the original definition of the forces in (1.8), (1.12) and (1.13). The forces along the lines of smallest and largest stress are plotted for the parameters in (3.13) in Figure 3.12(B). Note that they are of the same form as the adapted forces (1.8), (1.12) and (3.12) for the original parameter values (3.13), shown in Figure 3.12(A). Because of the same structure of the forces we can expect similar simulation results. In Figure 3.13 the numerical solution is shown for two examples, a delta, as well as a combination of a core and a delta. One can clearly see that the particles align along the lines of smallest stress and the resulting patterns are preserved over time. Similarly, one can obtain any complex pattern as stationary

(A) $s$    (B) $t = 40 \cdot 10^4$    (C) $t = 100 \cdot 10^4$    (D) $t = 160 \cdot 10^4$

(E) $t = 220 \cdot 10^4$    (F) $t = 280 \cdot 10^4$    (G) $t = 340 \cdot 10^4$    (H) $t = 400 \cdot 10^4$

Delta

(I) $s$    (J) $t = 40 \cdot 10^4$    (K) $t = 100 \cdot 10^4$    (L) $t = 160 \cdot 10^4$

(M) $t = 220 \cdot 10^4$    (N) $t = 280 \cdot 10^4$    (O) $t = 340 \cdot 10^4$    (P) $t = 400 \cdot 10^4$
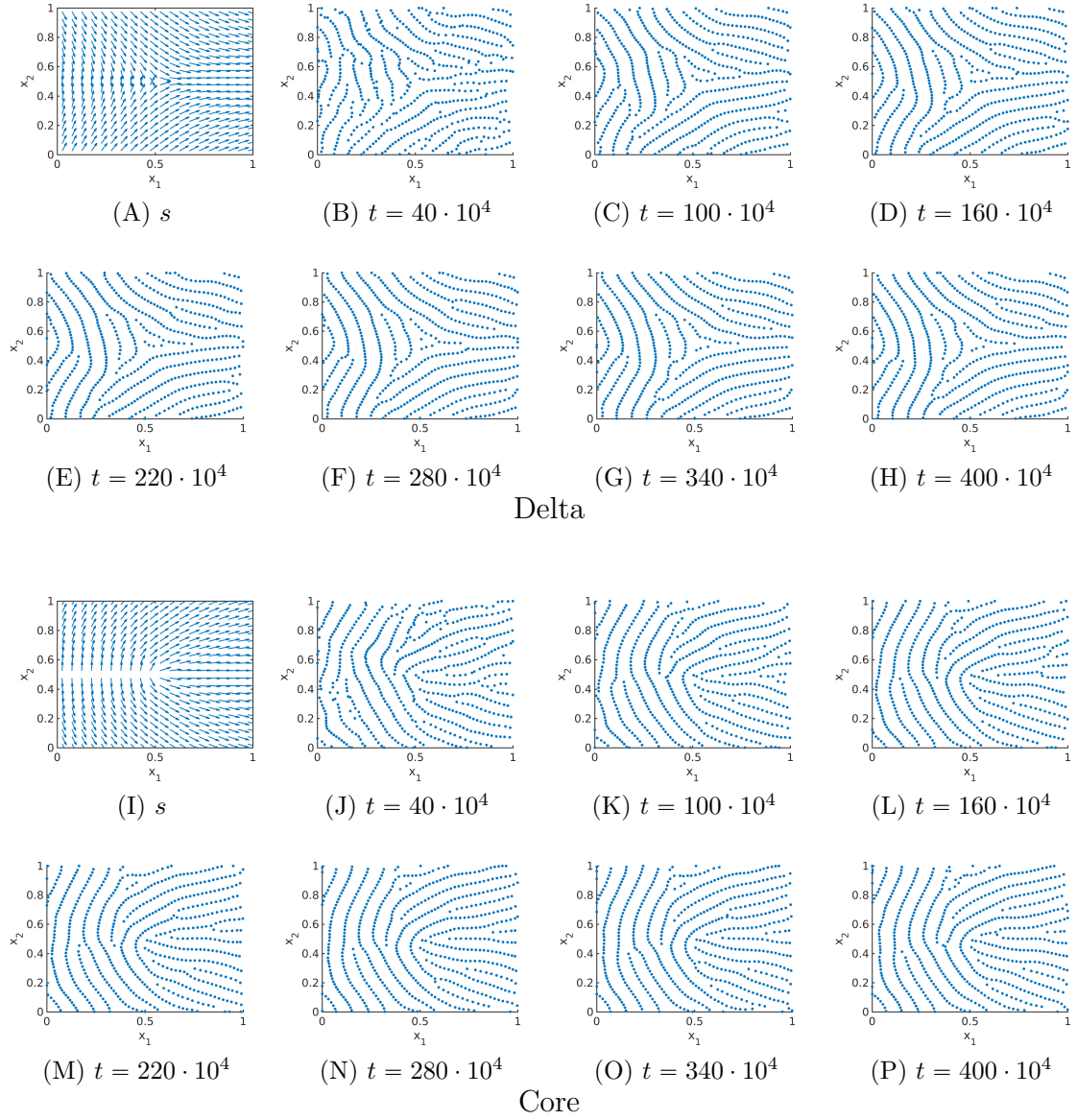
Core

Figure 3.9: Tensor fields $T = T(x)$ for delta (subfigures (A)-(H)) and core (subfigures (I)-(P)) given by $s = s(x)$ and the numerical solution to the extended Kücken-Champod model (3.1) with attraction force (3.12) at different times $t$ for $\chi = 0.2$, $N = 600$, $T = T(x)$ and randomly uniformly distributed initial data.

(A) $s$     (B) $t = 40 \cdot 10^4$     (C) $t = 100 \cdot 10^4$     (D) $t = 160 \cdot 10^4$

(E) $t = 220 \cdot 10^4$     (F) $t = 280 \cdot 10^4$     (G) $t = 340 \cdot 10^4$     (H) $t = 400 \cdot 10^4$

Example 1

(I) $s$     (J) $t = 40 \cdot 10^4$     (K) $t = 100 \cdot 10^4$     (L) $t = 160 \cdot 10^4$

(M) $t = 220 \cdot 10^4$     (N) $t = 280 \cdot 10^4$     (O) $t = 340 \cdot 10^4$     (P) $t = 400 \cdot 10^4$
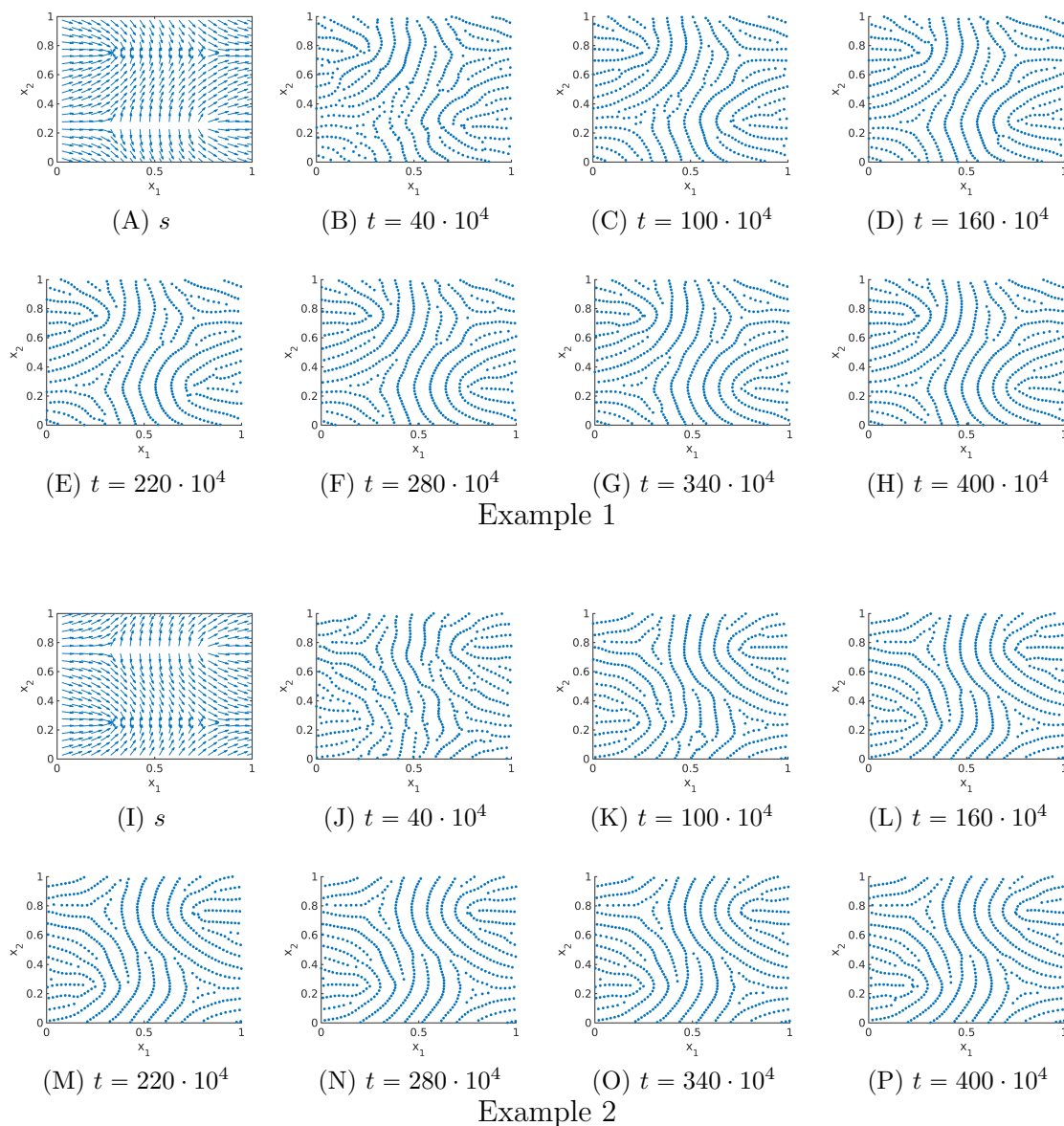
Example 2

Figure 3.10: Different non-homogeneous tensor fields $T = T(x)$ (Example 1 in subfigures (A)-(H), Example 2 in subfigures (I)-(P)) given by $s = s(x)$ and the numerical solution to the extended Kücken-Champod model (3.1) with attraction force (3.12) at different times $t$ for $\chi = 0.2$, $N = 600$, $T = T(x)$ and randomly uniformly distributed initial data.

94

(A) $s$    (B) $t = 40 \cdot 10^4$    (C) $t = 100 \cdot 10^4$    (D) $t = 160 \cdot 10^4$

(E) $t = 220 \cdot 10^4$    (F) $t = 280 \cdot 10^4$    (G) $t = 340 \cdot 10^4$    (H) $t = 400 \cdot 10^4$

Example 3
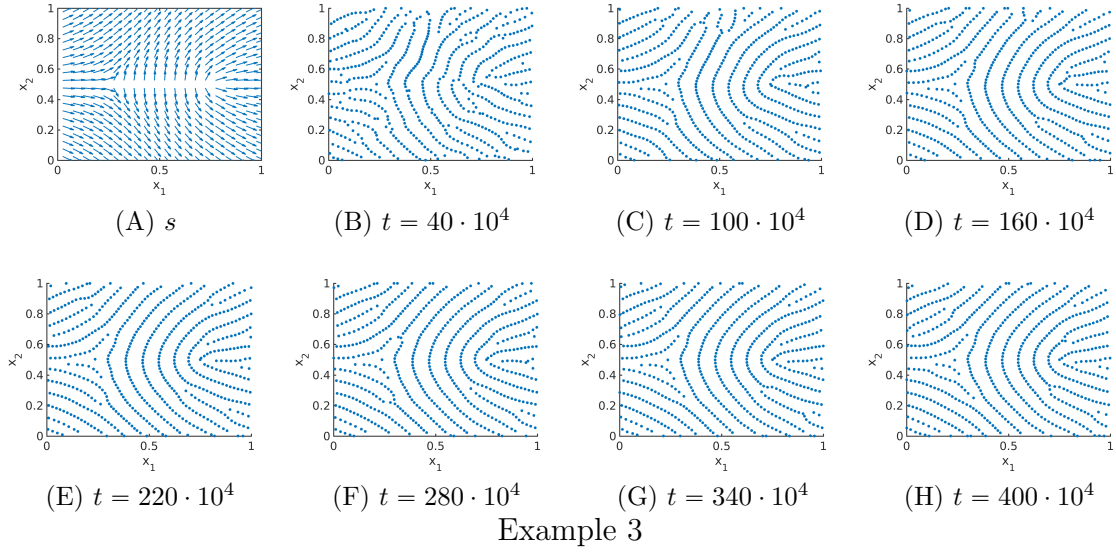
Figure 3.11: Non-homogeneous tensor field $T = T(x)$ given by $s = s(x)$ and the numerical solution to the particle model (3.1) with attraction force (3.12) at different times $t$ for $\chi = 0.2$, $N = 600$, $T = T(x)$ and randomly uniformly distributed initial data.

solution to the Kücken-Champod model (3.1) by adapting the underlying tensor field. In particular, this implies that the Kücken-Champod model (3.1) with forces defined by (1.8), (1.12) and (1.13) for the parameters in (3.13) can be used to simulate fingerprint patterns which are in principal preserved over time.

The long-time behaviour of the numerical solutions to the adapted particle model (3.1) with model parameters (3.13) is investigated in Figure 3.14 where the numerical solution at large times $t$ is illustrated for the tensor field in Example 5 in Figure 3.13. Note that the pattern changes only slightly over large time intervals, demonstrating that these patterns are close to being stationary. This slow convergence to steady states, especially for inhomogeneous underlying tensor fields, can also be seen for other pattern forming systems such as the patterns in the SH equation where the time until the steady state is reached is roughly of the order of what is called the horizontal diffusion time [Nij18].

## Pattern formation based on tensor fields from real fingerprints

In this section, we investigate how to simulate fingerprint patterns based on realistic tensor fields. As proposed in [KC13] the tensor field is constructed based on real fingerprint data. The tensor field is estimated by a combination of the line sensor

(A) $0.3f_A + f_R$ for values in (3.13)

(B) $f_A + f_R$ for values in (3.13)
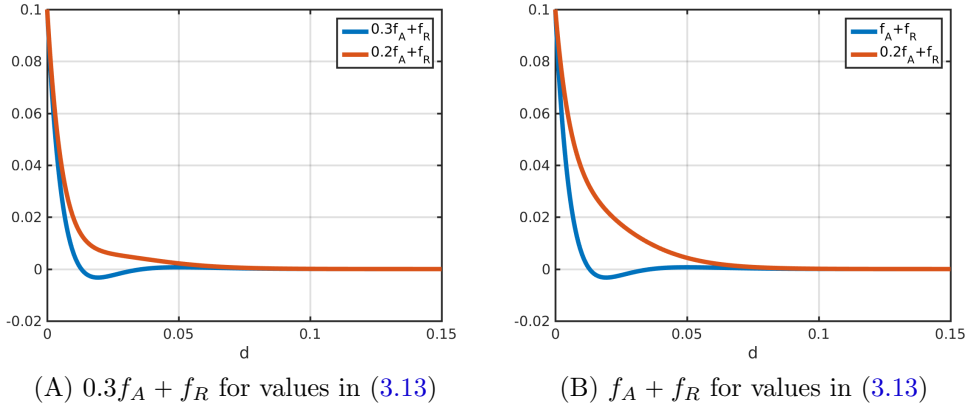
Figure 3.12: Total force coefficients $0.2f_A + f_R$ along the lines of smallest stress, as well as $0.3f_A + f_R$ for parameter values in (3.13) and $f_A + f_R$ for parameter values in (3.13) along the lines of largest stress, respectively.

method [GMM09] and a gradient based method as described in [GS12, Section 2.1].

Given some real fingerprint data the aim is to construct the vector field $s = s(x)$ for all $x \in \Omega$ as the tangents to the given fingerprint lines. This is based on the idea that the lines of smallest stress are given by $s$ and the solution to the interaction model (3.1) aligns along $s$. Let $\theta = \theta(x)$ denote the angle between the vertical axis and the direction of lines of smallest stress $s = s(x)$ at location $x$, then it is sufficient to consider the principal arguments $\theta \in [0, \pi)$ only. Note that for any $x \in \Omega$ and any given $\theta(x)$ we can reconstruct $s(x)$ as $(\cos(\theta(x)), \sin(\theta(x)))$ since $s(x)$ are defined to be unit vectors. In Figure 3.15 fingerprint data, the estimated arguments $\theta$ for constructing the tensor field and the lines of smallest stress $s = s(x)$ of the tensor field are shown. Note that the lines of smallest stress $s = s(x)$ of the tensor field and the fingerprint lines in the real fingerprint image coincide.

Considering the tensor field $T = T(x)$ shown in Figure 3.15 the associated numerical solution is plotted for two realisations of uniformly distributed initial data in Figure 3.16. One can clearly see that the particles align along the lines of smallest stress $s = s(x)$. Besides, Figure 3.16 illustrates that we obtain similar, but not exactly the same patterns for different realisations of random uniformly distributed initial data. This is consistent with the well-known fact that everyone has unique fingerprints and even the fingerprints of twins can be distinguished even if the general patterns may seem to be quite similar at first glance [CLMS16].

To quantify the distance to the steady state we consider the change of the posi-

(A) $s$     (B) $t = 40 \cdot 10^4$     (C) $t = 100 \cdot 10^4$     (D) $t = 160 \cdot 10^4$

(E) $t = 220 \cdot 10^4$     (F) $t = 280 \cdot 10^4$     (G) $t = 340 \cdot 10^4$     (H) $t = 400 \cdot 10^4$

Example 4

(I) $s$     (J) $t = 40 \cdot 10^4$     (K) $t = 100 \cdot 10^4$     (L) $t = 160 \cdot 10^4$

(M) $t = 220 \cdot 10^4$     (N) $t = 280 \cdot 10^4$     (O) $t = 340 \cdot 10^4$     (P) $t = 400 \cdot 10^4$
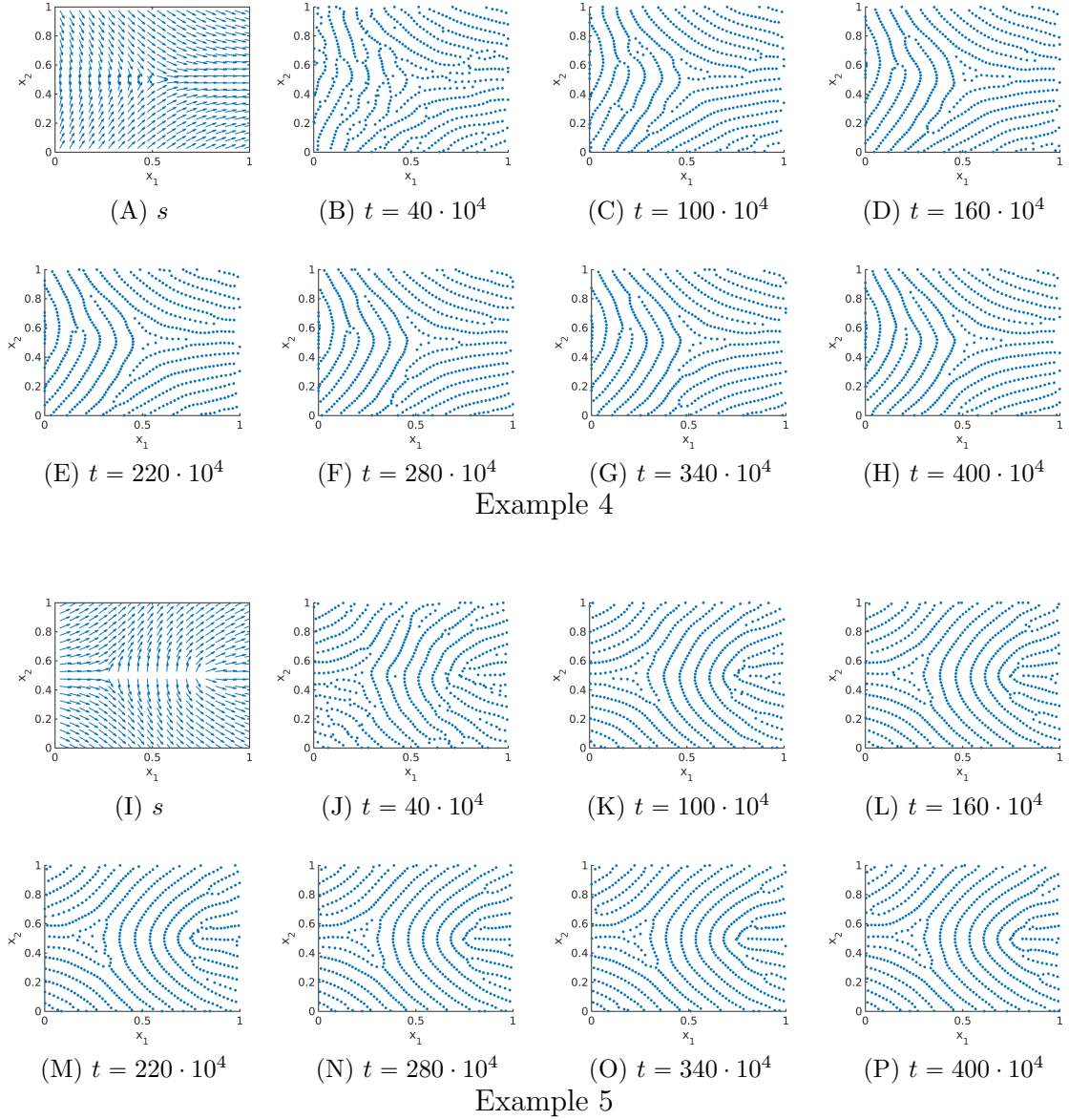
Example 5

Figure 3.13: Different non-homogeneous tensor fields $T = T(x)$ (Example 4 in subfigures (A)-(H), Example 5 in subfigures (I)-(P)) given by $s = s(x)$ and the numerical solution to the adapted particle model (3.1) for the parameters in (3.13) at different times $t$ for $\chi = 0.2$, $N = 600$, $T = T(x)$ and randomly uniformly distributed initial data.

(A) $t = 5 \cdot 10^7$  (B) $t = 10 \cdot 10^7$  (C) $t = 15 \cdot 10^7$  (D) $t = 20 \cdot 10^7$

(E) $t = 25 \cdot 10^7$  (F) $t = 30 \cdot 10^7$  (G) $t = 35 \cdot 10^7$  (H) $t = 40 \cdot 10^7$
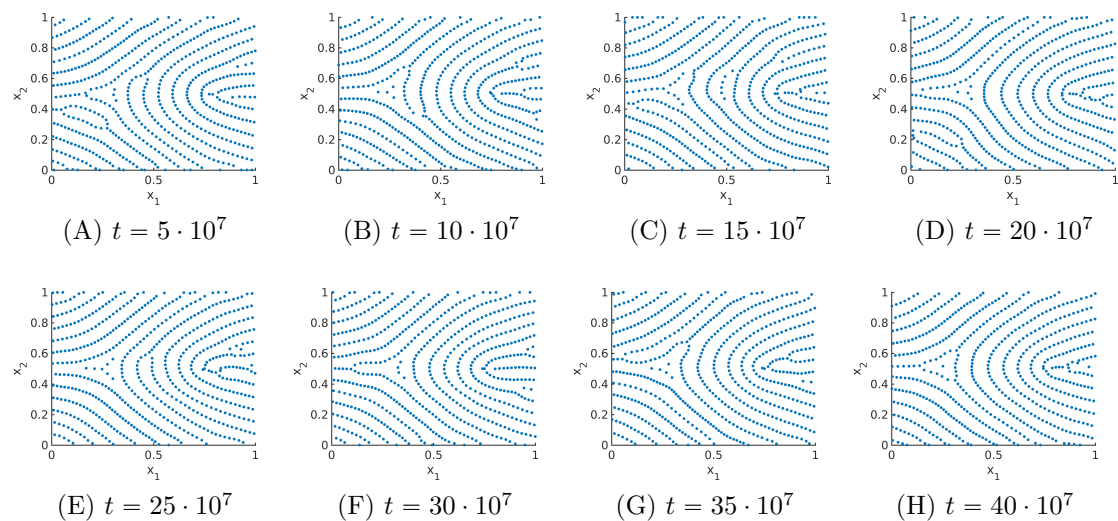
Figure 3.14: Long-time behaviour of the numerical solution to the adapted particle model (3.1) for the parameters in (3.13) at different times $t$ for $\chi = 0.2$, $N = 600$, the tensor field $T = T(x)$ in Example 5 in Figure 3.13 and randomly uniformly distributed initial data.



(A) Original  (B) $\theta$  (C) $s$
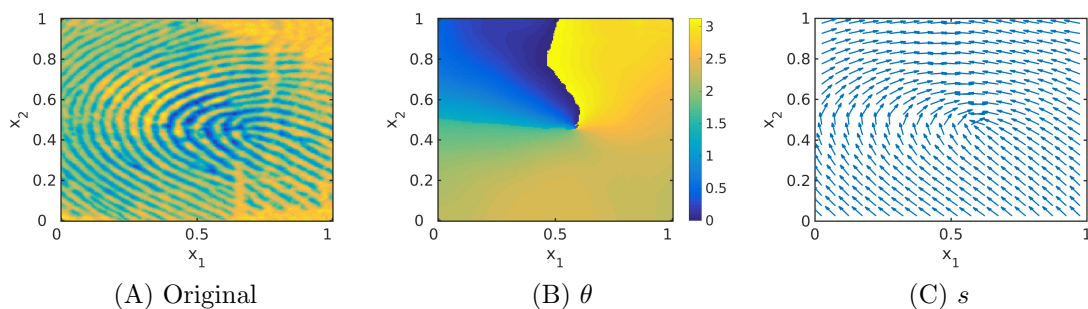
Figure 3.15: Original fingerprint image as well as arguments and lines of smallest stress $s = s(x)$ for the reconstructed tensor field $T = T(x)$.

(A) $t = 15 \cdot 10^6$  (B) $t = 30 \cdot 10^6$  (C) $t = 45 \cdot 10^6$  (D) $t = 60 \cdot 10^6$

Example 6



(E) $t = 15 \cdot 10^6$  (F) $t = 30 \cdot 10^6$  (G) $t = 45 \cdot 10^6$  (H) $t = 60 \cdot 10^6$

Example 7
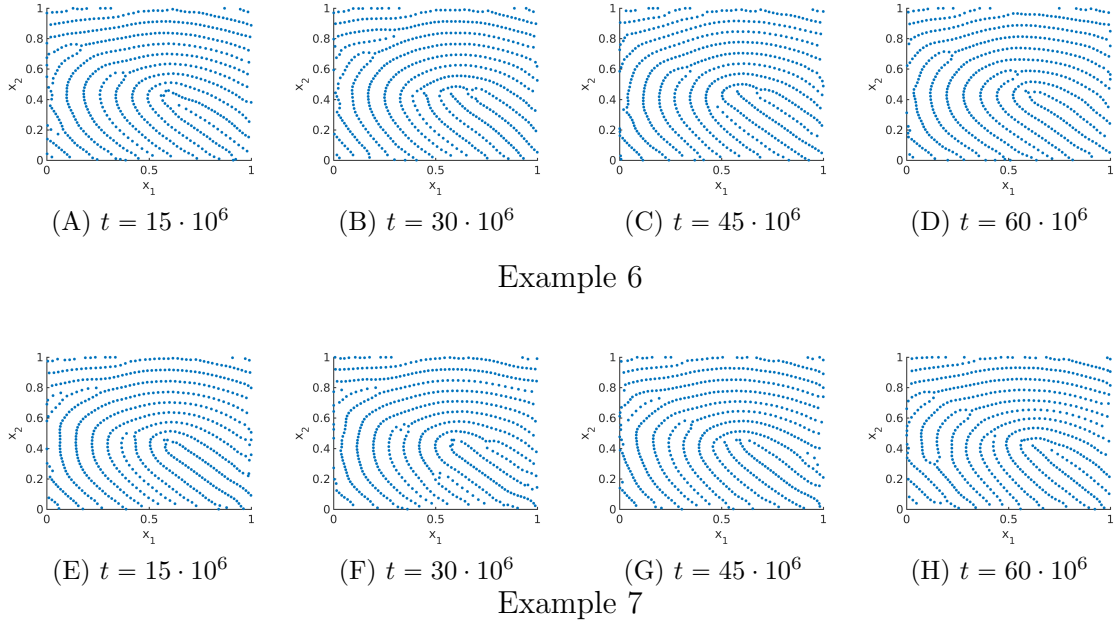
Figure 3.16: Numerical solution to the adapted particle model (3.1) for the parameters in (3.13) at different times $t$ for $\chi = 0.2$, the realistic tensor field $T = T(x)$ in Figure 3.15 and two realisations of randomly uniformly distributed initial data.

tions $x_j$ of the particles in successive time steps, given by

$$\tau(t) = \sum_{j=1}^{N} \|x_j(t + \Delta t) - x_j(t)\|_{L^1}. \tag{3.14}$$

In Figure 3.17 we show the error $\tau$ between successive time steps for the numerical solution in Example 6 in Figure 3.16 to the adapted particle model (3.1). After a sharp initial decrease the total change in positions of the particles is approximately $1.0 \cdot 10^{-5}$, i.e. the movement of the particles is roughly $1.7 \cdot 10^{-8}$ between time steps.

### Interpretation of the pattern formation

In the simulations for spatially homogeneous tensor fields in 2 as well as for realistic tensor fields in Figures 3.9, 3.10, 3.11, 3.13, 3.14, 3.16 one can see bifurcations in the solution pattern for certain time steps. More precisely, there exist points where two roughly parallel lines merge with a third roughly parallel line from the other side. These patterns are in the form of the letter 'Y'. The evolution of one of these bifurcations is shown in Figure 3.18 for the underlying tensor field in Example 6 in
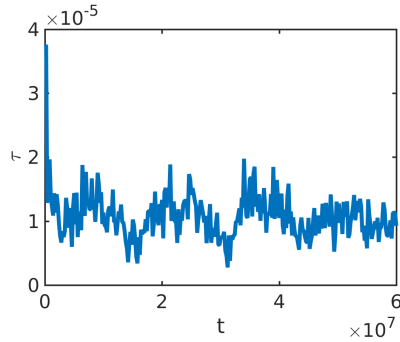
Figure 3.17: Error $\tau$ in (3.14) between successive time steps for the numerical solution in Example 6 in Figure 3.16 to the adapted particle model (3.1) for the parameters in (3.13) at different times $t$ and the realistic tensor field $T = T(x)$ in Figure 3.15.

Figure 3.16. Note that all these lines are aligned along the lines of smallest stress $s$ of the tensor field and these bifurcations move towards the two neighbouring lines over time. This behaviour can be explained by attraction forces along the lines of largest stress over medium range distances, i.e. as soon as the distance between the particles along the lines of largest stress $l$ is small enough they attract each other. In particular, the particles close to the bifurcation on the two neighbouring lines are the first ones to 'feel' the attraction force along $l$ and the two roughly parallel lines start merging close to the bifurcation. Hence, the single line on the other side of the bifurcation gets longer over time and the bifurcation moves towards the two parallel lines. While the two roughly parallel lines get shorter over time until they are finally completely merged, resulting in one single line. Since the movement of the particles is mainly along $l$ there is a different particle at the bifurcation at each time step. While the particles on the line in the middle roughly remain at the same position apart from realigning along the lines of smallest stress $s$. This realignment along $s$ is due to the additional number of particles which are aligned along one single line after the merging, as well as due to the repulsive forces along $s$ spreading the particles to make use of the space along $s$ and to avoid high particles densities after merging.

### 3.5.2 Varying the ridge distance

**Motivation for a new model**

The results in Section 3.5.1 illustrate that it is possible to simulate realistic fingerprints with the adapted particle model (3.1) for the parameters in (3.13). As seen
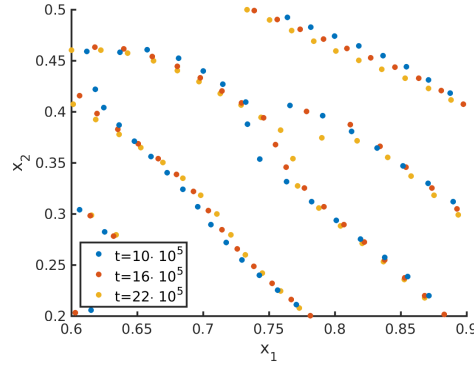
Figure 3.18: Evolution of the bifurcations in the numerical solution to the adapted particle model (3.1) for the parameters in (3.13) for the non-homogeneous tensor field $T = T(x)$ in Example 6 in Figure 3.16 at different times $t$ and randomly uniformly distributed initial data.

in the figures, there is some variability in ridge distances and in view of realistic biometric applications, it is of great interest to control them. Note that the total force $F$ in (1.8), given by the sum of repulsion and attraction force $F_R$ and $F_A$ of the form (1.12) and (1.13), respectively, can be rewritten as

$$F(d(x_j, x_k), T(x_j)) = \left[ \chi f_A(|d|) + f_R(|d|) \right] (s \cdot d)s + \left[ f_A(|d|) + f_R(|d|) \right] (l \cdot d)l \tag{3.15}$$

by using the definition of the tensor field $T$ in (1.5) and the definition of the distance vector $d(x_j, x_k) = x_j - x_k \in \mathbb{R}^2$. The coefficient functions of the repulsion and attraction forces (1.18) and (1.19), respectively, are plotted along $s$ and $l$ for the parameters in (3.13) in Figure 3.12(B). In particular, this motivates us to consider interaction forces of the form (1.9).

We are interested in rescaling the forces now to vary the distances between the fingerprint lines, i.e. we consider $F(\eta d(x_j, x_k), T(x_j))$ where $\eta > 0$ is the rescaling factor. For $\eta = 1$ we recover the same solution patterns as in Section 3.5.1, while the distances between the fingerprint lines become larger for $\eta \in (0, 1)$ and smaller for $\eta > 1$. Note that the force coefficient $f_A + f_R$ along $l$ is repulsive over long distances. For $\eta = 1$, the case that has been considered so far, this is fine for the given parameters in (3.13). For $\eta > 1$, however, the scaling results in repulsive interaction forces along $l$ for particles with shorter distances between each other. Besides, short-range forces have a stronger impact on the interactions. Hence, these short-range repulsive interaction forces prevent the accumulation of particles along

$l$, resulting in several clusters. Note that the forces along $s$ are purely repulsive so that rescaling by any $\eta$ does not change the nature of the forces.

In order to prevent this behaviour and to obtain an interaction model that can be used for different rescalings, the forces need to be changed slightly so that we have very small attractive forces along $l$ for $\eta = 1$. This does not influence the pattern formation for $\eta = 1$, but for rescaling by $\eta > 1$ we can obtain the desired line patterns with smaller distances between each other. In order to achieve this, we consider a straight-forward approach first. We consider two cutoffs $c_1$ and $c_2$ and define the adapted force $F$ piece-wise such that for $|d| < c_1$ the force $F$ is of the form (3.15) as before while for $|d| > c_2$ we consider an attraction force tending to zero as $d \to \infty$. To obtain a continuous force we consider a linear interpolation of the force on $[c_1, c_2]$. Setting

$$f(|d|, \chi) := \chi f_A(|d|) + f_R(|d|)$$

we consider the force coefficients $\bar{f}_s$ and $\bar{f}_l$ for interaction forces of the form (1.9) where the force coefficients are defined as

$$\bar{f}_l(d) = \begin{cases} f(|d|, 1) & |d| < c_1 \\ f(c_1, 1) + \frac{|d| - c_1}{c_2 - c_1}\left(-f(c_2, 1) - f(c_1, 1)\right) & |d| \in [c_1, c_2] \\ -f(|d|, 1) & |d| > c_2 \end{cases} \tag{3.16}$$

and

$$\bar{f}_s(d) = f(|d|, \chi). \tag{3.17}$$

Here, we consider the parameter values $c_1 = 0.06, c_2 = 0.07$ and the parameters in the force coefficients (1.18), (1.19) are given by (3.13). The force coefficient $f_l$ along $l$ for $|d| > c_2$ is obtained by multiplying the original force along $l$ by $-1$. This is based on the fact that the force coefficient $f(d, 1)$ is repulsive for large distances along $l$ for the parameters in (3.13). In Figure 3.19 the force coefficients $\bar{f}_l$ and $\bar{f}_s$ in (3.16) and (3.17), respectively, are shown. In particular, the piecewise definition of $\bar{f}_l$ only has a small influence of the form. In Figure 3.20, the stationary solution to the particle model (3.1) for interaction forces of the form (1.9), force coefficients (3.16), (3.17), parameter values (3.13), the underlying tensor field $T = T(x)$ in Figure 3.15 and different rescaling factors $\eta$ is shown and one can clearly see that $\eta > 1$ leads to smaller ridge distances whereas $\eta < 1$ results in larger ridge distances.

In particular, the interaction model (3.1) with interaction forces of the form (1.9) and force coefficients in (3.16) and (3.17) can be used to simulate fingerprints with variable ridge distances. Due to the smaller distances between the fingerprint lines for $\eta = 1.2$ this leads to a larger number of fingerprint lines on the given domain. Due to this increased number of lines it is desirable to run simulations with larger numbers of particles. However, particle simulations can only be applied efficiently as long as the total particle number is not too large. In order to solve this remedy one can introduce the density $\rho = \rho(t, x)$ associated with the particle positions and consider the associated macroscopic model (1.17). In Chapter 5, advanced numerical methods for solving the macroscopic model (1.17) with anisotropic interaction forces are developed for simulating fingerprint patterns.



(A) Normal scaling

(B) Zoom
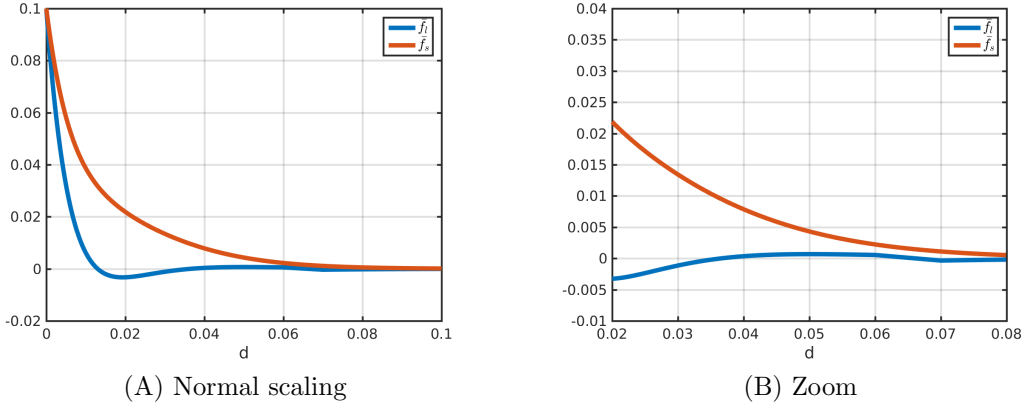
Figure 3.19: Total force coefficients $\bar{f}_l$ and $\bar{f}_s$, defined in (3.16) and (3.17) respectively, for interaction forces of the form (1.9) and parameter values (3.13).



(A) $\eta = 0.8$

(B) $\eta = 1.0$

(C) $\eta = 1.2$
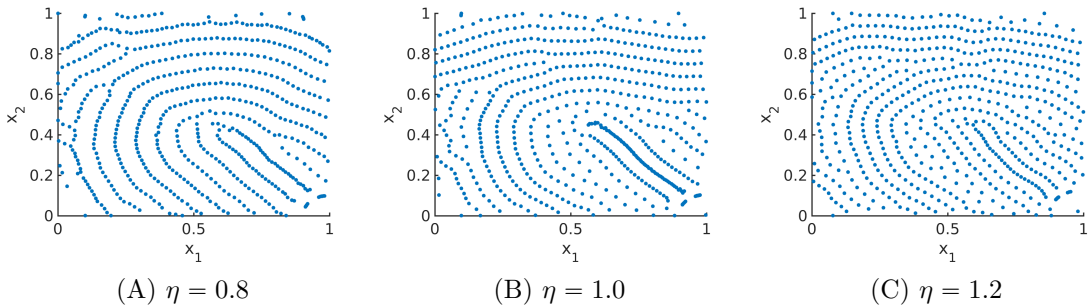
Figure 3.20: Stationary solution to the interaction model (3.1) for interaction forces of the form (1.9), force coefficients (3.16), (3.17), parameter values (3.13), the realistic tensor field $T = T(x)$ in Figure 3.15 and $N = 2400$ particles initially distributed uniformly at random.

**A bio-inspired model for simulating stationary fingerprints with variable ridge distances**

In this section, we consider interaction forces of the form (1.9) as before with the aim of simulating fingerprints with variable ridge distances based on a bio-inspired approach. The coefficient functions $f_l$ and $f_s$ in (3.16) and (3.17), respectively, are defined piecewise and it is desirable to obtain a closed form for the coefficient functions. As before we consider exponentially decaying forces describing that short-range interactions between the particles are much stronger than long-range interactions. Since the forces are repulsive and attractive on different regimes, this interplay between repulsion and attraction forces can be regarded as oscillations. Motivated by this, we model the force coefficients $f_s$ and $f_l$ in (1.9) as solutions to a damped harmonic oscillator. Note that harmonic oscillators are a common modelling approach in cell biology and the force coefficients $f_l, f_s$ are given by (3.2) and are shown in Figure 3.21 for the parameters in (3.3) in comparison with the piecewise defined force coefficients $\bar{f}_l, \bar{f}_s$ for the parameters in (3.13). Note that the parameters (3.3) are chosen in such a way that the coefficient functions $f_l, f_s$ of the harmonic oscillator approximate the piecewise defined coefficient functions $\bar{f}_l, \bar{f}_s$ in (3.16),(3.17), respectively. In Figure 3.22 the stationary patterns to (3.1) for different rescaling factors $\eta$ are shown. As expected the larger the value of $\eta$ the smaller the distances between the fingerprint lines and the more lines occur.
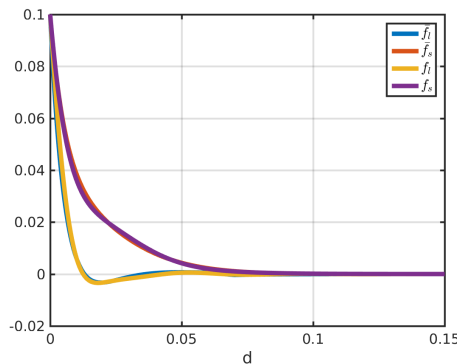


Figure 3.21: Coefficients $f_l$ and $f_s$ in (3.2) for parameter values in (3.3) as well as piecewise defined coefficients $\bar{f}_l$ and $\bar{f}_s$ in (3.16),(3.17).

**Whole fingerprint simulations**

In Figure 3.23 we construct tensor fields from real fingerprint data based on the methods discussed in Section 3.5.1. We consider a whole fingerprint image shown

(A) $\eta = 0.6$      (B) $\eta = 0.8$      (C) $\eta = 1.0$      (D) $\eta = 1.2$
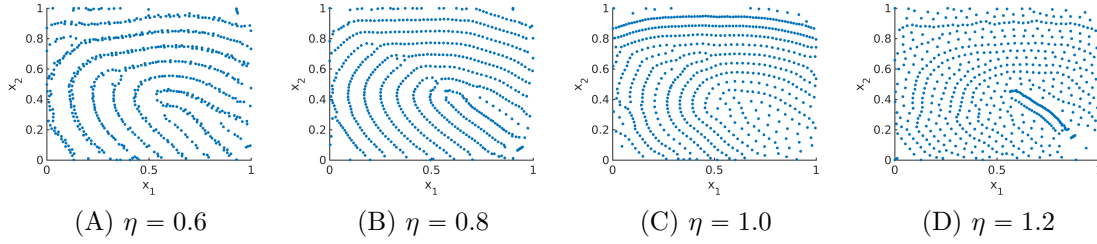
Figure 3.22: Stationary solution to the interaction model (3.1) for interaction forces of the form (1.9), force coefficients (3.2), parameter values (3.3), the realistic tensor field $T = T(x)$ in Figure 3.15, different force rescaling factor $\eta$ and $N = 2400$ particles initially distributed uniformly at random.

in Figure 3.23(A) and determine the underlying tensor field by estimating the arguments $\theta = \theta(x)$ for every $x \in \Omega$. Since we consider the domain $\Omega = \mathbb{T}^2$ we extend the tensor field via extrapolation from the original fingerprint image in Figure 3.23(A), based on [GMM09]. In Figures 3.23(B) and 3.23(C) the arguments $\theta = \theta(x)$ are shown and the arguments $\theta$ are overlayed by the mask of the original fingerprint in black in Figure 3.23(B). Since $s(x)$ is a unit vector and hence uniquely determined by its argument $\theta(x)$ we reconstruct the lines of smallest stress $s(x)$ as $(\cos(\theta(x)), \sin(\theta(x)))$ in Figures 3.23(D) and 3.23(E), and overlay the direction field $s$ by the original fingerprint image in black in Figure 3.23(D). We run simulations for these realistic tensor fields using our new bio-inspired model (3.1) with interaction forces of the form (1.9), force coefficients (3.2) inspired from harmonic oscillators and parameter values in (3.3) for randomly uniformly distributed initial data and $N = 2400$ particles. Note that the patterns are preserved over time.

In conclusion, fingerprints with variable ridge distances can obtained as stationary solutions to our bio-inspired model. We consider harmonic oscillators as force coefficients, a well-established modelling approach in biology. Due to lack of experimental data the exact form of the interaction forces, including the parameter choices, cannot be validated with experiments. For this reason, the parameters are chosen such that certain observations are satisfied and the general model formulation of the model allows to consider a large class of models. As part of future work, the numerical results can be tested for realness. The distinction between real and synthetics could be based on [GH14] where histograms of minutiae and ridge frequencies are considered. Another procedure for distinguishing real and synthetic fingerprints is based on the underlying stress field only [IGHO18].

(A) Original     (B) $\theta$ and original     (C) $\theta$     (D) $s$ and original

(E) $s$     (F) $\eta = 0.6$     (G) $\eta = 0.8$     (H) $\eta = 1.0$
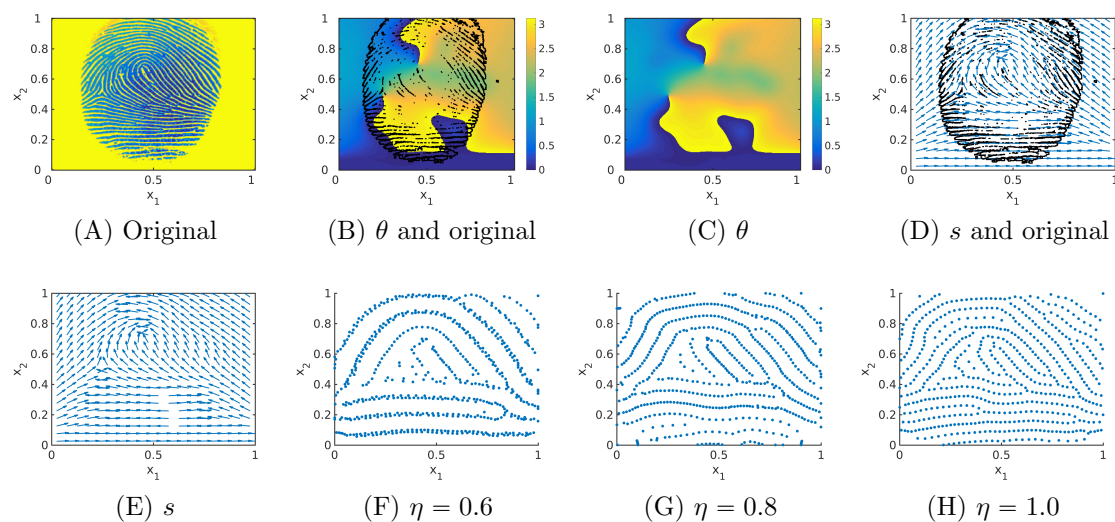
Figure 3.23: Original fingerprint image, arguments and lines of smallest stress $s = s(x)$ for the reconstructed tensor field $T = T(x)$ with an overlying mask of the original fingerprint image in black, as well as stationary solution to the interaction model (3.1) for interaction forces of the form (1.9), force coefficients (3.2), parameter values (3.3) and $N = 2400$ particles initially distributed uniformly at random.

# Chapter 4

# Stability analysis of line patterns

## Originality and contribution

This chapter is based on the paper [CDKS18] in collaboration with José A. Carrillo, Bertram Düring and Carola-Bibiane Schönlieb. While my co-authors proposed the study of the model and provided guidance and advice, [CDKS18] is primarily my own original work and nearly all the results, including analysis and simulations, were obtained by myself.

## Chapter summary

Motivated by the formation of fingerprint patterns, we consider a class of interacting particle models with anisotropic, repulsive-attractive interaction forces whose orientations depend on an underlying tensor field. This class of models can be regarded as a generalisation of a gradient flow of a nonlocal interaction potential which has a local repulsion and a long-range attraction structure. In addition, the underlying tensor field introduces an anisotropy leading to complex patterns which do not occur in isotropic models. Central to this pattern formation are straight line patterns. For a given spatially homogeneous tensor field, we show that there exists a preferred direction of straight lines, i.e. straight vertical lines can be stable for sufficiently many particles, while many other rotations of the straight lines are unstable steady states, both for a sufficiently large number of particles and in the continuum limit. For straight vertical lines we consider specific force coefficients for the stability analysis of steady states, show that stability can be achieved for exponentially decaying force coefficients for a sufficiently large number of particles, and

relate these results to the Kücken-Champod model for simulating fingerprint patterns. The mathematical analysis of the steady states is completed with numerical results.

## 4.1 Introduction

In biological applications, the interactions determined by the force $F$ or, equivalently, the interaction potential $W$, are usually described by short-range repulsion, preventing collisions between the individuals, as well as long-range attraction, keeping the swarm cohesive [MEKBS03, OL01]. In this case, the associated radially symmetric potentials $\overline{W}$ first decrease and then increase as a function of the radius. Due to the repulsive forces these potentials lead to possibly more steady states than the purely attractive potentials. In particular, these repulsive-attractive potentials can be considered as a minimal model for pattern formation in large systems of individuals [BCLR13b, KCB$^+$13] and the references therein.

Pattern formation in multiple dimensions is studied in [BSK$^+$15, KSUB11, vBU12, vBUKB12, CHM14a] for repulsive-attractive potentials. The instabilities of the sphere and ring solutions are studied in [BSK$^+$15, vBU12, vBUKB12]. The linear stability of ring equilibria is analysed and conditions on the potential are derived to classify the different instabilities. A numerical study of the $N$-particle interaction model for specific repulsion-attraction potentials is also performed in [BSK$^+$15, KSUB11] leading to a wide range of radially symmetric patterns such as rings, annuli, and uniform circular patches, as well as more complex patterns. Based on this analysis the stability of flock solutions and mill rings in the associated second order model can be studied, see [ABCvB14] and [CHM14b] for the linear and nonlinear stability of flocks, respectively.

In this chapter, we consider a generalisation of the particle model (1.2) by introducing an anisotropy given by a tensor field $T$. This leads to an extended particle model of the form (1.4), i.e.

$$\frac{\mathrm{d}x_j}{\mathrm{d}t} = \frac{1}{N} \sum_{\substack{k=1 \\ k \neq j}}^{N} F(x_j - x_k, T(x_j)), \tag{4.1}$$

where we prescribe initial data $x_j(0) = x_j^{in}$, $j = 1, \ldots, N$, for given scalars $x_j^{in}$, $j = 1, \ldots, N$. A special instance of this model has been introduced in [KC13] for simulating fingerprint patterns. The particle model in its general form (4.1) has been

studied in [BDK$^+$18, DGH$^+$19]. Here, the position of each of the $N$ particles at time $t$ is denoted by $x_j = x_j(t) \in \mathbb{R}^2$, $j = 1, \ldots, N$, and $F(x_j - x_k, T(x_j))$ denotes the total force that particle $k$ exerts on particle $j$ subject to an underlying stress tensor field $T(x_j)$ at $x_j$, given by (1.5) for orthonormal vector fields $s = s(x)$ and $l = l(x) \in \mathbb{R}^2$ and $\chi \in [0, 1]$. Here, the outer product $v \otimes w$ for two vectors $v, w \in \mathbb{R}^2$ equals the matrix multiplication $vw^T$ and results in a matrix of size $\mathbb{R}^{2,2}$. The parameter $\chi$ introduces an anisotropy in the direction $s$ in the definition of the tensor field.

For repulsive forces along $s$ and short-range repulsive, long-range attractive forces along $l$ the numerical simulations in [BDK$^+$18] suggest that straight vertical line patterns formed by the interacting particles at positions $x_j$ are stable for a certain spatially homogeneous tensor field, specified later. In this chapter, we want to rigorously study this empirical observation by providing a linear stability analysis of such patterns where particles distribute equidistantly along straight lines.

The stability analysis of steady states of the particle model (4.1) is important for understanding the robustness of the patterns that arise from applying (4.1) for numerical simulation, for instance, as for its originally intended application to fingerprint simulation in [KC13]. Indeed, in what follows, we will show that for spatially homogeneous tensor fields $T$ the solution formed by a number of vertical straight lines (referred to as ridges) is a stationary solution, whereas ridge bifurcations, i.e. a single ridge dividing into two ridges as typically appearing in fingerprint patterns, is not.

The aim of this chapter is to prove that sufficiently large numbers of particles distributed equidistantly along straight vertical lines are stable steady states to the particle model (4.1) for short-range repulsive, long-range attractive forces along $l$ and repulsive forces along $s$. All other rotations of straight lines are unstable steady states for this choice of force coefficients for a sufficiently large number of particles and for the continuum limit. We focus on this very simple class of steady states as a first step towards understanding stable formations that can be achieved by model (4.1). Note that the continuum straight line is a steady state of the associated continuum model (1.17), see [BDK$^+$18], but its asymptotic stability cannot be concluded from the linear stability analysis for finitely many particles.

This chapter is organised as follows. In Section 4.2 we describe a general formulation of an anisotropic interaction model, based on the model proposed by Kücken and Champod [KC13]. Section 4.3 is devoted to a high wave number stability analysis of line patterns for the continuum limit $N \to \infty$, including vertical, horizontal,

and rotated straight lines for spatially homogeneous tensor fields. Due to the instability of arbitrary rotations except for vertical straight lines for the considered tensor field we focus on the stability analysis of straight vertical lines for particular forces for any $N \in \mathbb{N}$ in Section 4.4. Section 4.5 illustrates the form of the steady states in the case the derived stability conditions are not satisfied.

## 4.2 Description of the model

In this section, we describe a general formulation of the anisotropic microscopic model (4.1) and relate it to the Kücken-Champod particle model [KC13]. Kücken and Champod consider the particle model (4.1) where the total force $F$ is given by (1.8) for the distance vector $d(x_j, x_k) = x_j - x_k \in \mathbb{R}^2$. Here, $F_R$ denotes the repulsion force that particle $k$ exerts on particle $j$ and $F_A$ is the attraction force particle $k$ exerts on particle $j$. The repulsion and attraction forces are of the form (1.12) and (1.13), respectively, with coefficient functions $f_R$ and $f_A$, where, again, $d = d(x_j, x_k) = x_j - x_k \in \mathbb{R}^2$. Note that the repulsion and attraction force coefficients $f_R, f_A$ are radially symmetric. The direction of the interaction forces is determined by the parameter $\chi \in [0, 1]$ in the definition of $T$ in (1.5). Motivated by plugging (1.5) into the definition of the total force (1.8), we consider a more general form of the total force, given by (1.9) where the total force is decomposed into forces along the direction $s$ and along the direction $l$. In particular, the force coefficients in the Kücken-Champod model (4.1) with repulsive and attractive forces $F_R$ and $F_A$ in (1.12) and (1.13), respectively, can be recovered for

$$f_l(|d|) = f_A(|d|) + f_R(|d|) \quad \text{and} \quad f_s(|d|) = \chi f_A(|d|) + f_R(|d|).$$

Since a steady state of the particle model (4.1) for any spatially homogeneous tensor field $\tilde{T}$ can be regarded as a coordinate transform of the steady state of the particle model (4.1) for the tensor field $T$ (see [BDK$^+$18] for details), we restrict ourselves to the study of steady states for the spatially homogeneous tensor field $T$ given by the orthonormal vectors $s = (0, 1)$ and $l = (1, 0)$, i.e.

$$T = \begin{pmatrix} 1 & 0 \\ 0 & \chi \end{pmatrix}. \tag{4.2}$$

The total force in the Kücken-Champod model (1.8) and the generalised total force

(1.9) reduce to

$$F(d) = \begin{pmatrix} (f_A(|d|) + f_R(|d|))\, d_1 \\ (\chi f_A(|d|) + f_R(|d|))\, d_2 \end{pmatrix} \tag{4.3}$$

and

$$F(d) = \begin{pmatrix} f_l(|d|)d_1 \\ f_s(|d|)d_2 \end{pmatrix} \quad \text{for } d = (d_1, d_2) \in \mathbb{R}^2, \tag{4.4}$$

respectively, for the spatially homogeneous tensor field $T$ in (4.2).

In the following, we consider the particle model (4.1) on the torus $\mathbb{T}^2$ or, equivalently, on the unit square $[0,1]^2$ with periodic boundary conditions. This can be achieved by considering the full force (4.4) on $[-0.5, 0.5]^2$, extending it periodically on $\mathbb{R}^2$, and requiring that the force coefficients are differentiable and vanish on $\partial[-0.5, 0.5]^2$ for physically realistic dynamics. That is, we use (4.4) to define its periodic extension $\bar{F} \colon \mathbb{R}^2 \to \mathbb{R}^2$ by

$$\begin{aligned} \bar{F}(d) &:= F(d) \quad \text{for } d \in [-0.5, 0.5]^2, \\ \bar{F}(d + k) &:= \bar{F}(d) \quad \text{for } d \in [-0.5, 0.5]^2, k \in \mathbb{Z}^2. \end{aligned} \tag{4.5}$$

Then, the particle model (4.1) can be rewritten as

$$\frac{\mathrm{d}x_j}{\mathrm{d}t} = \frac{1}{N} \sum_{\substack{k=1 \\ k \neq j}}^{N} \bar{F}(x_j - x_k) \tag{4.6}$$

for $x_j \in \mathbb{R}^2$, where the right-hand side can be regarded as the force acting on particle $j$. We require that the force $\bar{F}$ has to vanish for any $d \in \partial[-0.5, 0.5]^2$ to avoid interactions between periodic replicates of the particles, implying that $f_l(0.5) = f_s(0.5) = 0$ for $f_l, f_s$ in (4.4) and hence $f_l(|d|) = f_s(|d|) = 0$ for $d \in \mathbb{R}^2$ with $|d| = 0.5$. Thus, we require that $\bar{F}(d) = 0$ for all $d \in \partial[-0.5, 0.5]^2$ for physically relevant forces. To guarantee that the resulting force coefficient is differentiable which is required for the stability analysis we construct a differentiable approximation of the given force coefficient $f$ by considering $f(|d|)$ for $|d| \leqslant 0.5 - \varepsilon$ for some $\varepsilon > 0$, a cubic polynomial on $(0.5 - \varepsilon, 0.5)$ and the constant zero function for $|d| \geqslant 0.5$ such that the resulting function is continuously differentiable on $(0, \infty)$. Motivated by this,

we also consider smaller values of the cutoff radius $R_c \in (0, 0.5]$ and adapt the force coefficients as

$$
f^\varepsilon(|d|) = \begin{cases} f(|d|), & |d| \in [0, R_c - \varepsilon], \\ f'(R_c - \varepsilon) \left( \frac{(|d|-R_c)^3}{\varepsilon^2} + \frac{(|d|-R_c)^2}{\varepsilon} \right) \\ \quad + f(R_c - \varepsilon) \left( 2\frac{(|d|-R_c)^3}{\varepsilon^3} + 3\frac{(|d|-R_c)^2}{\varepsilon^2} \right), & |d| \in (R_c - \varepsilon, R_c), \\ 0, & |d| \geqslant R_c. \end{cases} \tag{4.7}
$$

Note that this definition results in a differentiable function whose absolute value and its derivative vanish for $|d| = R_c$. This is in analogy to the notion of cutoff and is only a small modification compared to the original definition provided $f(s)$ for $s \in (R_c - \varepsilon, R_c)$ is of order $\mathcal{O}(\varepsilon)$ and $f'(R_c - \varepsilon)$ is of order $\mathcal{O}(1)$. In this case, both the original force coefficients and its adaptation $f^\varepsilon$ are of order $\mathcal{O}(\varepsilon)$ on $(R_c - \varepsilon, R_c)$. Further note that the interaction forces on distances $|d| \ll R_c - \varepsilon$ are significantly larger than on $(R_c - \varepsilon, R_c)$ and, hence, the dynamics are mainly determined by interactions of range $|d| \ll R_c$. In particular, this allows us to replace $f_l$ and $f_s$ in (4.4) by differentiable approximations $f_l^\varepsilon$ and $f_s^\varepsilon$, defined as in (4.7), if necessary.

Note that the assumption to consider the unit square $[0, 1]^2$ with periodic boundary conditions is not restrictive and by rescaling in time our analysis extends to any domain $[0, \delta]^2$ with a cutoff radius $R_c \in (0, \frac{\delta}{2}]$ for $\delta \in \mathbb{R}_+$, where the cutoff of any force coefficient $f$ is defined in (4.7).

The coefficient function $f_R$ of the repulsion force $F_R$ in (1.12) in the Kücken-Champod model is originally of the form

$$
f_R(|d|) = (\alpha|d|^2 + \beta) \exp(-e_R|d|) \tag{4.8}
$$

for $d \in \mathbb{R}^2$ and nonnegative parameters $\alpha$, $\beta$, and $e_R$. The coefficient function $f_A$ of the attraction force $F_A$ in (1.13) is of the form

$$
f_A(|d|) = -\gamma|d| \exp(-e_A|d|) \tag{4.9}
$$

for $d \in \mathbb{R}^2$ and nonnegative constants $\gamma$ and $e_A$. To be as close as possible to the work by Kücken and Champod [KC13] we assume that the total force (1.8) exhibits short-range repulsion and long-range attraction along $l$ and one can choose the parameters as in (1.20) as proposed in [BDK+18]. Based on the adaptations of the force coefficients in (4.7), we consider the modified Kücken-Champod force

coefficients in the following, given by

$$
f_R^\varepsilon(|d|) = \begin{cases}
f_R(|d|), & |d| \in [0, R_c - \varepsilon], \\
f_R'(R_c - \varepsilon) \left( \frac{(|d|-R_c)^3}{\varepsilon^2} + \frac{(|d|-R_c)^2}{\varepsilon} \right) & \\
\quad + f_R(R_c - \varepsilon) \left( 2\frac{(|d|-R_c)^3}{\varepsilon^3} + 3\frac{(|d|-R_c)^2}{\varepsilon^2} \right), & |d| \in (R_c - \varepsilon, R_c), \\
0, & |d| \geqslant R_c,
\end{cases}
\tag{4.10}
$$

and

$$
f_A^\varepsilon(|d|) = \begin{cases}
f_A(|d|), & |d| \in [0, R_c - \varepsilon], \\
f_A'(R_c - \varepsilon) \left( \frac{(|d|-R_c)^3}{\varepsilon^2} + \frac{(|d|-R_c)^2}{\varepsilon} \right) & \\
\quad + f_A(R_c - \varepsilon) \left( 2\frac{(|d|-R_c)^3}{\varepsilon^3} + 3\frac{(|d|-R_c)^2}{\varepsilon^2} \right), & |d| \in (R_c - \varepsilon, R_c), \\
0, & |d| \geqslant R_c.
\end{cases}
\tag{4.11}
$$

Here, $f_R, f_A$ are very small in a neighbourhood of the cutoff $R_c = 0.5$ for the parameters in (1.20) or, more generally, for $e_R$ and $e_A$ sufficiently large. Since the derivatives $f_R'$ and $f_A'$ also contain the exponential decaying terms $\exp(-e_R|d|)$ and $\exp(-e_A|d|)$, respectively, and are scaled by a factor $\mathcal{O}(\varepsilon)$ in (1.18) and (1.19), respectively, the differences between $f_R^\varepsilon$ and $f_R$, and $f_A^\varepsilon$ and $f_A$, respectively, are very small compared to the size of the interaction forces at distances $|d| \ll R_c - \varepsilon$ and the total force exerted on particle $x_j$, given by the right-hand side of (4.6). In particular, $f_R^\varepsilon, f_A^\varepsilon$ can be regarded as differentiable approximations of $f_R, f_A$.

For the particle model (4.6) with differentiable coefficient functions $f_R^\varepsilon, f_A^\varepsilon$ and parameters (1.20), we plot the original coefficient functions $f_R, f_A$ of the total force (4.3) for a spatially homogeneous underlying tensor field $T$ with $s = (0,1)$ and $l = (1,0)$ in Figure 4.1. However, note that $f_R \approx \lim_{\varepsilon \to 0} f_R^\varepsilon$ and $f_A \approx \lim_{\varepsilon \to 0} f_A^\varepsilon$. Moreover, we show the resulting coefficient functions $\chi f_A + f_R$ with $\chi = 0.2$ and $f_A + f_R$ along $s = (0,1)$ and $l = (1,0)$, respectively, in Figure 4.1. Note that the repulsive force coefficient $f_R$ is positive and the attractive force coefficient $f_A$ is negative. Repulsion dominates for short distances along $l$ to prevent collisions of the particles. Besides, the total force exhibits long-range attraction along $l$ whose absolute value decreases with the distance between particles. Along $s$, the particles are purely repulsive for $\chi = 0.2$ and the repulsion force gets weaker for longer distances.
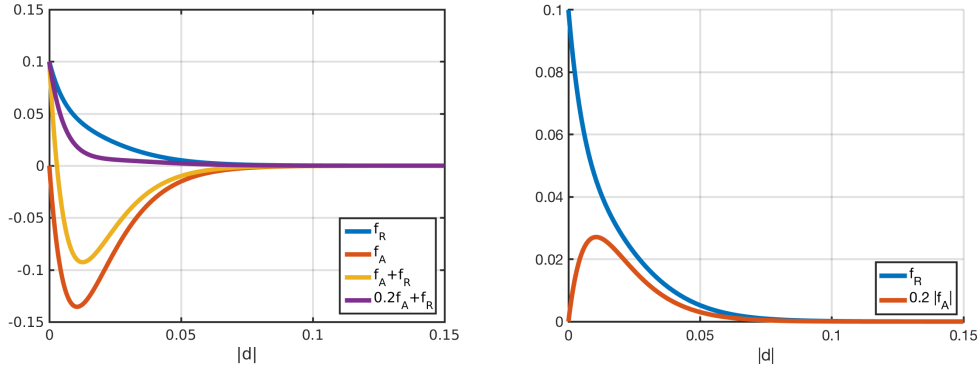
Figure 4.1: Coefficients $f_R$ in (4.8) and $f_A$ in (4.9) of repulsion force (1.12) and attraction force (1.13), respectively, as well as the force coefficients along $s = (0, 1)$ and $l = (1, 0)$ (i.e. $f_A + f_R$ and $0.2f_A + f_R$) for parameter values in (1.20).

## 4.3 Stability/instability of straight lines

In this section, we consider the total force $\bar{F}$ in (4.5), defined on $\mathbb{R}^2$ by periodic extension of $F$ on $[-0.5, 0.5]^2$ in (4.4). This total force $\bar{F}$ can be described by (periodically extending) a short-range repulsive, long-range attractive force coefficient $f_l$ along $l$ and a purely repulsive force coefficient $f_s$ along $s$. Without loss of generality we may assume that the force coefficients $f_l, f_s$ are differentiable since otherwise they may be replaced by $f_l^\varepsilon, f_s^\varepsilon$, defined as in (4.7) for given functions $f_l, f_s$. Motivated by this we require the following.

**Assumption 5.** *Let $f_l, f_s$ be continuously differentiable functions on $[0, \infty)$. Let $f_s$ be purely repulsive, i.e. $f_s \geqslant 0$ with $f_s(0) > 0$ for $s \in [0, R_c)$ and $f_s(s) = 0$ for $s \geqslant R_c$, implying $\int_0^{R_c} f_s \, \mathrm{d}s > 0$. Further let $f_l$ be short-range repulsive, long-range attractive with $f_l(R_c) = 0$.*

As shown in [BDK$^+$18] for the analysis of steady states with general spatially homogeneous tensor fields, it is sufficient to restrict ourselves to the spatially homogeneous tensor field $T$ with $s = (0, 1)$ and $l = (1, 0)$ in the following.

### 4.3.1 Straight line

In this section, we consider line patterns as steady states which were observed in the numerical simulations in [BDK$^+$18]. For $x_j \in \mathbb{R}^2, j = 1, \ldots, N$, evolving according

to the particle model (4.6), we have

$$\frac{\mathrm{d}}{\mathrm{d}t} \sum_{j=1}^{N} x_j = 0,$$

implying that the centre of mass is conserved. Hence, we can assume without loss of generality that the centre of mass is in $\mathbb{Z}^2$. By identifying $\mathbb{R}^2$ with $\mathbb{C}$, we make the ansatz

$$\bar{x}_k = \frac{k}{N} \exp(i\theta)\ell(\theta), \quad k = 1, \dots, N. \tag{4.12}$$

Here, $\theta$ denotes the angle of rotation. The length of the line pattern is denoted by $\ell = \ell(\theta) > 0$ and can be regarded as a multiplicative factor with $\ell(0) = \ell\left(\frac{\pi}{2}\right) = 1$ and $\ell\left(\frac{\pi}{4}\right) = \ell\left(\frac{3\pi}{4}\right) = \sqrt{2}$. Note that it is sufficient to restrict ourselves to $\theta \in [0, \pi)$ since ansatz (4.12) for $\theta$ and $\theta + k\pi$ with $k \in \mathbb{Z}$ leads to the same straight line after periodic extension on $\mathbb{R}^2$ and hence also on the torus $\mathbb{T}^2$. Depending on the choice of $\theta$, ansatz (4.12) might lead to multiple windings on the torus $\mathbb{T}^2$. To guarantee that ansatz (4.12) satisfies the periodic boundary conditions, we require that the winding number of the straight lines in (4.12) is a natural number and hence we can restrict ourselves to ansatz (4.12) on the torus $\mathbb{T}^2$ for $\theta \in \mathcal{A}$, where

$$\begin{aligned}
\mathcal{A} := {}& \left\{0, \frac{\pi}{4}, \frac{\pi}{2}, \frac{3\pi}{4}\right\} \cup \left\{\psi \in \left(0, \frac{\pi}{4}\right) \cup \left(\frac{3\pi}{4}, \pi\right) : \cot(\psi) \in \mathbb{Z}\right\} \\
& \cup \left\{\psi \in \left(\frac{\pi}{4}, \frac{3\pi}{4}\right) : \tan(\psi) \in \mathbb{Z}\right\}.
\end{aligned} \tag{4.13}$$

Note that considering the torus $\mathbb{T}^2$ as the domain, i.e. the unit square with periodic boundary conditions or, equivalently, $\mathbb{R}^2$ by periodic extension, is not restrictive due to the discussion in Section 4.2.

For a single vertical straight line we have $\theta = \frac{\pi}{2}$ and ansatz (4.12) reduces to

$$\bar{x}_k = \frac{k}{N}i, \quad k = 1, \dots, N, \tag{4.14}$$

and for a horizontal line with $\theta = 0$ we have

$$\bar{x}_k = \frac{k}{N}, \quad k = 1, \dots, N. \tag{4.15}$$

Note that the winding number is one for (4.12) with $\theta \in \left\{0, \frac{\pi}{4}, \frac{\pi}{2}, \frac{3\pi}{4}\right\}$, while the

winding number is larger than one for $\theta \in \mathcal{A}\backslash\{0, \frac{\pi}{4}, \frac{\pi}{2}, \frac{3\pi}{4}\}$. Translations of the ansatz (4.12) result in steady states with a shifted centre of mass. Besides, parallel equidistant straight line patterns, obtained from considering (4.12) for a fixed rotation angle (4.13) and certain translations, may also lead to steady states.

For equilibria $\bar{x}_j \in \mathbb{R}^2, j = 1, \ldots, N$, to the particle model (4.6) we require that

$$\frac{1}{N} \sum_{\substack{k=1 \\ k \neq j}}^{N} \bar{F}(\bar{x}_j - \bar{x}_k, T) = 0 \quad \text{for all } j = 1, \ldots, N.$$

Setting $\bar{x}_k$ for $k \in \mathbb{Z}$ as in (4.12), we have $\bar{F}(\bar{x}_j - \bar{x}_k) = \bar{F}(\bar{x}_j - \bar{x}_{k+nN})$ for $j, k = 1, \ldots, N$ and any $n \in \mathbb{Z}$ by the periodicity of $\bar{F}$. Since the particles are uniformly distributed along straight lines by ansatz (4.12), it is sufficient to require

$$\sum_{k=1}^{N-1} \bar{F}(\bar{x}_N - \bar{x}_k, T) = 0 \tag{4.16}$$

for steady states. Note that $\bar{F}(\bar{x}_N - \bar{x}_k, T) = -\bar{F}(\bar{x}_N - \bar{x}_{N-k}, T)$ for $k = 1, \ldots, \lceil N/2 \rceil - 1$ and for $N$ even we have $\bar{F}(\bar{x}_N - \bar{x}_{N/2}, T) = 0$ by the definition of the cutoff $R_c$. Hence, (4.16) is satisfied for the ansatz (4.12) for $\theta \in \mathcal{A}$, provided the length $\ell(\theta)$ of the lines is set such that the particles are distributed uniformly along the entire axis of angle $\theta$.

### 4.3.2 Stability conditions

In this section we derive stability conditions for equilibria of the particle model (4.6), based on a linearised stability analysis. The real parts of the eigenvalues of a stability matrix play a crucial role and we denote the real part of eigenvalue $\lambda \in \mathbb{C}$ by $\Re(\lambda)$ in the following.

**Proposition 5.** *For finite $N \in \mathbb{N}$, the steady state $\bar{x}_j$, $j = 1, \ldots, N$, of the particle model (4.6) is asymptotically stable if the eigenvalues $\lambda$ of the stability matrix*

$$M = M(j, m) = \begin{pmatrix} I_1(j, m) & I_2(j, m) \end{pmatrix} \in \mathbb{C}^{2,2}, \tag{4.17}$$

*satisfy $\Re(\lambda) < 0$ for all $j = 1, \ldots, N$ and $m = 1, \ldots, N - 1$, where*

$$
\begin{aligned}
I_1(j, m) &= \frac{1}{N} \sum_{k \neq j} \left(1 - \exp(im(\phi_k - \phi_j))\right) \frac{\partial \bar{F}}{\partial d_1}(\bar{x}_j - \bar{x}_k) \\
&= \frac{1}{N} \sum_{k \neq j} \left(1 - \exp\left(\frac{2\pi i m (k - j)}{N}\right)\right) \frac{\partial \bar{F}}{\partial d_1}(\bar{x}_j - \bar{x}_k), \\
I_2(j, m) &= \frac{1}{N} \sum_{k \neq j} \left(1 - \exp(im(\phi_k - \phi_j))\right) \frac{\partial \bar{F}}{\partial d_2}(\bar{x}_j - \bar{x}_k) \\
&= \frac{1}{N} \sum_{k \neq j} \left(1 - \exp\left(\frac{2\pi i m (k - j)}{N}\right)\right) \frac{\partial \bar{F}}{\partial d_2}(\bar{x}_j - \bar{x}_k)
\end{aligned}
\tag{4.18}
$$

*for $j = 1, \ldots, N$ and $m = 1, \ldots, N$.*

*Proof.* Let $\bar{x}_j$, $j = 1, \ldots, N$, denote a steady state of (4.6). We define the perturbation $g_j = g_j(t)$, $h_j = h_j(t) \in \mathbb{R}$ of $\bar{x}_j$ by

$$
x_j = \bar{x}_j + \begin{pmatrix} g_j \\ h_j \end{pmatrix}, \quad j = 1, \ldots, N.
$$

Linearising (4.6) around the steady state $\bar{x}_j$ gives

$$
\frac{\mathrm{d}}{\mathrm{d}t} \begin{pmatrix} g_j \\ h_j \end{pmatrix} = \frac{1}{N} \sum_{k \neq j} (g_j - g_k) \frac{\partial \bar{F}}{\partial d_1}(\bar{x}_j - \bar{x}_k) + \frac{1}{N} \sum_{k \neq j} (h_j - h_k) \frac{\partial \bar{F}}{\partial d_2}(\bar{x}_j - \bar{x}_k). \tag{4.19}
$$

We choose the ansatz functions

$$
g_j = \zeta_g \left(\exp(im\phi_j) + \exp(-im\phi_j)\right), \quad h_j = \zeta_h \left(\exp(im\phi_j) + \exp(-im\phi_j)\right),
$$
$$
j = 1, \ldots, N, \quad m = 1, \ldots, N,
$$

where $\zeta_g = \zeta_g(t), \zeta_h = \zeta_h(t)$, and $\phi_j = \frac{2\pi j}{N}$. Note that $g_j, h_j \in \mathbb{R}$ for all $j = 1, \ldots, N$ and

$$
\sum_{j=1}^{N} \exp(im\phi_j) = \sum_{j=1}^{N} \left(\exp\left(\frac{2\pi i m}{N}\right)\right)^j = \begin{cases} 0, & m = 1, \ldots, N - 1, \\ N, & m = N, \end{cases}
$$

since $\phi_j$ are the roots of $r^N = 1$ and

$$\sum_{j=0}^{N-1} r^j = \frac{1 - r^N}{1 - r}.$$

This implies

$$\sum_{j=1}^{N} g_j(t) = \sum_{j=1}^{N} h_j(t) = \begin{cases} 0, & m = 1, \ldots, N-1, \\ N, & m = N, \end{cases}$$

for all times $t \geqslant 0$, i.e. the centre of mass of the perturbations $g_j, h_j$ is preserved. We have

$$g_j - g_k = \zeta_g \left( \exp(im\phi_j) + \exp(-im\phi_j) \right) \left( 1 - \exp(im(\phi_k - \phi_j)) \right),$$
$$h_j - h_k = \zeta_h \left( \exp(im\phi_j) + \exp(-im\phi_j) \right) \left( 1 - \exp(im(\phi_k - \phi_j)) \right).$$

Plugging this into (4.19) and collecting like terms in $\exp(im\phi_j), \exp(-im\phi_j)$ results in

$$\frac{\mathrm{d}}{\mathrm{d}t} \begin{pmatrix} \zeta_g \\ \zeta_h \end{pmatrix} = \frac{\zeta_g}{N} \sum_{k \neq j} (1 - \exp(im(\phi_k - \phi_j))) \frac{\partial \bar{F}}{\partial d_1} (\bar{x}_j - \bar{x}_k)$$

$$+ \frac{\zeta_h}{N} \sum_{k \neq j} (1 - \exp(im(\phi_k - \phi_j))) \frac{\partial \bar{F}}{\partial d_2} (\bar{x}_j - \bar{x}_k),$$

i.e.

$$\frac{\mathrm{d}}{\mathrm{d}t} \begin{pmatrix} \zeta_g \\ \zeta_h \end{pmatrix} = M \begin{pmatrix} \zeta_g \\ \zeta_h \end{pmatrix}, \tag{4.20}$$

where the stability matrix $M \in \mathbb{C}^{2,2}$ is defined in (4.17). The ansatz $\zeta_g = \xi_g \exp(\lambda t)$, $\zeta_h = \xi_h \exp(\lambda t)$ solves the system (4.20) for any eigenvalue $\lambda \in \mathbb{C}$ of the stability matrix $M = M(j,m)$. Note that the stability matrix $M$ is the zero matrix for $m = N$ and any $j = 1, \ldots, N$. Hence, we have $\lambda = 0$ for $m = N$ and all $j = 1, \ldots, N$, corresponding to translations along the vertical and horizontal axes. Thus, the straight line $\bar{x}_j, j = 1, \ldots, N$, is stable if $\Re(\lambda) < 0$ for any $j = 1, \ldots, N$ and $m = 1, \ldots, N-1$. $\qquad\square$

### 4.3.3 Stability of a single vertical straight line

To study the stability of a single vertical straight line of the form (4.14) we determine the eigenvalues of the stability matrix (4.17) and derive stability conditions for steady states $\bar{x}_j, j = 1, \dots, N$, satisfying (4.16). In the continuum limit $N \to \infty$ the steady state condition (4.16) becomes

$$\int_{-0.5}^{0.5} F((0, s), T)\, \mathrm{d}s = \int_{-0.5}^{0.5} \bar{F}((0, s), T)\, \mathrm{d}s = 0.$$

Due to the cutoff radius $R_c \in (0, 0.5]$ it is sufficient to require

$$\int_{-R_c}^{R_c} F((0, s), T)\, \mathrm{d}s = 0 \tag{4.21}$$

for equilibria. This condition is clearly satisfied for forces of the form (4.4) and in particular for forces of the form (4.3).

**Theorem 1.** *For finite $N \in \mathbb{N}$, the single vertical straight line (4.14) is an asymptotically stable steady state of the particle model (4.6) with total force (4.4) if $\Re(\lambda_{i,N}(m)) < 0$ for $i = 1, 2$ and all $m = 1, \dots, N - 1$, where the eigenvalues $\lambda_{i,N} = \lambda_{i,N}(m)$ of the stability matrix (4.17) are given by*

$$
\begin{aligned}
\lambda_{1,N}(m) &= \frac{1}{N} \sum_{k=\lceil \frac{N}{2} \rceil}^{N-1+\lceil \frac{N}{2} \rceil} f_l(|d_{Nk}|)\left(1 - \exp\left(\frac{2\pi i m k}{N}\right)\right), \\
\lambda_{2,N}(m) &= \frac{1}{N} \sum_{k=\lceil \frac{N}{2} \rceil}^{N-1+\lceil \frac{N}{2} \rceil} (f_s(|d_{Nk}|) + f_s'(|d_{Nk}|)|d_{Nk}|)\left(1 - \exp\left(\frac{2\pi i m k}{N}\right)\right)
\end{aligned}
\tag{4.22}
$$

*with*

$$d_{Nk} = \begin{pmatrix} 0 \\ \frac{N-k}{N} \end{pmatrix}$$

*for $k \in \mathbb{N}$. Denoting the cutoff radius by $R_c \in (0, 0.5]$, steady states satisfying the steady state condition (4.21) in the continuum limit $N \to \infty$ are unstable if $\Re(\lambda_i(m)) > 0$ for some $m \in \mathbb{N}$ and some $i \in \{1, 2\}$, where the eigenvalues $\lambda_i =$*

$\lambda_i(m), i = 1, 2$, *of the stability matrix* (4.17) *are given by*

$$\lambda_1(m) = \int_{-R_c}^{R_c} f_l(|s|) \left(1 - \exp\left(-2\pi ims\right)\right) \mathrm{d}s,$$

$$\lambda_2(m) = \int_{-R_c}^{R_c} \left(f_s(|s|) + f_s'(|s|)|s|\right) \left(1 - \exp\left(-2\pi ims\right)\right) \mathrm{d}s. \tag{4.23}$$

*In particular,*

$$\Re(\lambda_1)(m) = 2\int_0^{R_c} f_l(s) \left(1 - \cos\left(-2\pi ms\right)\right) \mathrm{d}s,$$

$$\Re(\lambda_2)(m) = 2\int_0^{R_c} \left(f_s(s) + f_s'(s)s\right) \left(1 - \cos\left(-2\pi ms\right)\right) \mathrm{d}s. \tag{4.24}$$

*Proof.* For the spatially homogeneous tensor field $T$, defined by $s = (0,1)$ and $l = (1,0)$, the derivatives of the total force (4.4) are given by

$$\frac{\partial \bar{F}}{\partial d_1}(d) = \begin{pmatrix} f_l(|d|) + f_l'(|d|)\frac{d_1^2}{|d|} \\ f_s'(|d|)\frac{d_1 d_2}{|d|} \end{pmatrix}, \qquad \frac{\partial \bar{F}}{\partial d_2}(d) = \begin{pmatrix} f_l'(|d|)\frac{d_1 d_2}{|d|} \\ f_s(|d|) + f_s'(|d|)\frac{d_2^2}{|d|} \end{pmatrix} \tag{4.25}$$

for $d = (d_1, d_2) \in [-0.5, 0.5]^2$ and its periodic extension $\frac{\partial \bar{F}}{\partial d_i}(d + k) = \frac{\partial \bar{F}}{\partial d_i}(d)$ for $i = 1, 2$, $d \in [-0.5, 0.5]^2$, and $k \in \mathbb{Z}^2$. Note that $f_l, f_s$ are differentiable due to the smoothing assumptions at the cutoff $R_c$ in (4.7) and their derivatives vanish for $d \in [-0.5, 0.5]^2$ with $|d| \geqslant R_c$. Using ansatz (4.14) for a single vertical straight line, we obtain

$$\frac{\partial \bar{F}}{\partial d_1}(d_{jk}) = \begin{pmatrix} f_l(|d_{jk}|) \\ 0 \end{pmatrix},$$

$$\frac{\partial \bar{F}}{\partial d_2}(d_{jk}) = \begin{pmatrix} 0 \\ f_s(|d_{jk}|) + f_s'(|d_{jk}|)|d_{jk}| \end{pmatrix} \tag{4.26}$$

for $d_{jk} \in [-0.5, 0.5]^2$ and note that $\frac{\partial \bar{F}}{\partial d_i}(d_{jk}) = \frac{\partial \bar{F}}{\partial d_i}(d_{j,k+nN})$ for $i = 1, 2$, $j, k = 1, \ldots, N$, and $n \in \mathbb{N}$. This implies that the particles along the straight vertical line are indistinguishable and it suffices to consider $j = N$. The entries (4.18) of the

120

stability matrix (4.17) are given by

$$I_1(m) = \frac{1}{N} \sum_{k=1}^{N} \left(1 - \exp\left(\frac{2\pi imk}{N}\right)\right) \frac{\partial \bar{F}}{\partial d_1}(d_{Nk}),$$

$$I_2(m) = \frac{1}{N} \sum_{k=1}^{N} \left(1 - \exp\left(\frac{2\pi imk}{N}\right)\right) \frac{\partial \bar{F}}{\partial d_2}(d_{Nk}).$$

Note that for $k = \lceil\frac{N}{2}\rceil, \ldots, N$, we have $d_{Nk} \in \{0\} \times [0, 0.5] \subset [-0.5, 0.5]^2$, implying that the derivatives of $\bar{F}$ are given by (4.26), where $\bar{F}(d_{N,\lceil\frac{N}{2}\rceil}) = 0$ by the definition of the cutoff $R_c$ for $N$ even. Since $\frac{\partial \bar{F}}{\partial d_i}(d_{Nk}) = \frac{\partial \bar{F}}{\partial d_i}(d_{N,N+k})$ for $i = 1, 2$, $k = 1, \ldots, \lceil N/2 \rceil - 1$, and $d_{N,N+k} \in \{0\} \times (-0.5, 0) \subset [-0.5, 0.5]^2$, we can replace the sum over $k \in \{1, \ldots, N\}$ by the sum over $k \in \{\lceil\frac{N}{2}\rceil, \ldots, N - 1 + \lceil\frac{N}{2}\rceil\}$, resulting in

$$I_1(m) = \frac{1}{N} \sum_{k=\lceil\frac{N}{2}\rceil}^{N-1+\lceil\frac{N}{2}\rceil} \left(1 - \exp\left(\frac{2\pi imk}{N}\right)\right) \frac{\partial \bar{F}}{\partial d_1}(d_{Nk}),$$

$$I_2(m) = \frac{1}{N} \sum_{k=\lceil\frac{N}{2}\rceil}^{N-1+\lceil\frac{N}{2}\rceil} \left(1 - \exp\left(\frac{2\pi imk}{N}\right)\right) \frac{\partial \bar{F}}{\partial d_2}(d_{Nk}).$$

$$(4.27)$$

Note that the stability matrix (4.17) is a diagonal matrix whose eigenvalues are the non-trivial entries in (4.27) and are given by (4.22). Since the sums in (4.27) are Riemannian sums, we can pass to the continuum limit $N \to \infty$. Note that $\frac{k}{n} \in [0.5, 1.5]$ for $k \in \{\lceil\frac{N}{2}\rceil, \ldots, N - 1 + \lceil\frac{N}{2}\rceil\}$ appears in the entries of the stability matrix (4.27). For passing to the limit $N \to \infty$ in (4.27), we consider the domain of integration $[0.5, 1.5]$ and do a change of variables resulting in

$$I_i(m) = \int_{0.5}^{1.5} \frac{\partial \bar{F}}{\partial d_i}((0, 1 - s))\left(1 - \exp\left(2\pi ims\right)\right) \mathrm{d}s$$

$$= \int_{-0.5}^{0.5} \frac{\partial \bar{F}}{\partial d_i}((0, s))\left(1 - \exp\left(-2\pi ims\right)\right) \mathrm{d}s$$

$$= \int_{-0.5}^{0.5} \frac{\partial F}{\partial d_i}((0, s))\left(1 - \exp\left(-2\pi ims\right)\right) \mathrm{d}s$$

for $i = 1, 2$ and all $m \in \mathbb{N}$. Clearly the stability matrix (4.17) with entries $I_i, i = 1, 2$, is again a diagonal matrix and the eigenvalues $\lambda_i = \lambda_i(m), i = 1, 2$, in (4.23) are given by the diagonal entries of the stability matrix (4.17). $\qquad\square$

**Remark 9.** *In Theorem 1 we study the stability of the straight vertical line for the*

*dynamical system* (4.6) *for a finite number of particles* $N$, *where the differentiability of* $\bar{F}$ *at the cutoff* $R_c$ *is necessary for the definition of the eigenvalues in the discrete setting in* (4.22). *Note that we cannot conclude stability/instability if* $\Re(\lambda_i(m)) \leqslant 0$ *for* $i = 1, 2$ *and all* $m = 1, \ldots, N - 1$. *By the assumptions on the force coefficients* $f_s, f_l$ *in Assumption 5 we can pass to the continuum limit* $N \to \infty$ *in the definition of the eigenvalues of the stability matrix and study the stability of the steady states of the particle model* (4.6) *in the continuum limit* $N \to \infty$. *If there exists* $m \in \mathbb{N}$ *for some* $i \in \{1, 2\}$ *such that* $\Re(\lambda_i(m)) > 0$, *then the steady state is unstable in the continuum limit. However, if* $\Re(\lambda_i(m)) \leqslant 0$ *for* $i \in \{1, 2\}$ *and all* $m \in \mathbb{N}$ *stability/instability of the steady state cannot be concluded since it is difficult to give general conditions for* $\Re(\lambda_i(m)) \to \sigma$ *as* $m \to \infty$ *with* $\sigma = 0$ *or* $\sigma \in \mathbb{R}_- \backslash \{0\}$. *If* $\sigma = 0$, *we cannot say anything about the stability/instability of the steady state in the continuum setting; see also similar discussions for the stability/instability of delta-rings in the continuum setting in [Sim14] and the discussion after Theorem 2.1 in [BSK+15]. In particular, linear stability for any* $N \in \mathbb{N}$ *is not sufficient to conclude stability in the continuum setting.*

Note that the asymmetry in the definition of the eigenvalues (4.24) is due to the asymmetric steady states in (4.14). For $f = f_s = f_l$ the total force in (4.4) simplifies to $F(d) = f(|d|)d$ for $d = (d_1, d_2) \in [-0.5, 0.5]^2$. In this case, the gradient of $F = (F_1, F_2)$ is a symmetric matrix (compare (4.25)) and, hence, the eigenvalues of the stability matrix are real. Since

$$\frac{\partial F_1}{\partial d_2} = \frac{\partial F_2}{\partial d_1}$$

there exists a radially symmetric potential $W(d) = w(|d|)$ such that $F = -\nabla W$ on $[-0.5, 0.5]^2$. Hence, the stability conditions can be derived in terms of the potential $w$ and we have

$$\text{trace}(\nabla F(d)) = f'(|d|)|d| + 2f(|d|) = -\Delta w(|d|) = \lambda_1 + \lambda_2$$

for $d \in [-0.5, 0.5]^2$ and the periodic extension $\bar{F}$ of $F$ can be considered on $\mathbb{R}^2$. For $f_s = f_l$ and radially symmetric steady states, this leads to identical conditions for both eigenvalues $\lambda_k$, $k = 1, 2$. For the analysis of these symmetric steady states, however, it is helpful to consider an appropriate coordinate system such as polar coordinates for ring steady states as in [BSK+15].

Note that the stability conditions for steady states depend on the choice of the

coordinate system. Considering derivatives with respect to the coordinate axes as in (4.25) seems to be the natural choice for straight line patterns, in contrast to polar coordinates as in [BSK+15].

In the following, we investigate the high wave number stability of straight line patterns for the particle model (4.6), i.e. the stability of straight vertical lines as $m \to \infty$. This can be studied by considering the limit $m \to \infty$ of the eigenvalues (4.23) of the stability matrix (4.17) associated with the dynamical system (4.20).

**Proposition 6.** *Suppose that the coefficient functions $f_s$ and $f_l$ are continuously differentiable on $[0, +\infty)$ with $f_s(|d|) = f_l(|d|) = 0$ for $|d| \geqslant R_c$ and $f_s \geqslant 0$. The condition*

$$\int_0^{R_c} f_l(s) \, \mathrm{d}s \leqslant 0 \quad and \quad f_s(R_c) = 0 \tag{4.28}$$

*is necessary for the high wave number stability of the single straight vertical line (4.14), i.e. (4.28) is necessary for the stability of the straight vertical line for any $N \in \mathbb{N}$ and in the continuum limit $N \to \infty$.*

*Proof.* The eigenvalues (4.23) of the stability matrix (4.17) associated with the equilibrium of a single vertical straight line are of the form

$$\begin{aligned}
\lambda(m) &= \int_{-R_c}^{R_c} f(|s|)(1 - \exp(-2\pi i m s)) \, \mathrm{d}s \\
&= 2 \int_0^{R_c} f(s) \, \mathrm{d}s - \frac{1}{2\pi i m} \int_{-R_c}^{R_c} f'(|s|) \exp(-2\pi i m s) \, \mathrm{d}s \\
&\quad + \frac{1}{2\pi i m} f(R_c) \left( \exp(-2\pi i m R_c) - \exp(2\pi i m R_c) \right)
\end{aligned}$$

for a function $f \colon \mathbb{R}_+ \to \mathbb{R}$ with $f(|d|) = 0$ for $|d| \geqslant R_c$. For high wave number stability we require

$$\int_0^{R_c} f(s) \, \mathrm{d}s \leqslant 0 \qquad \text{and} \qquad |f'| \text{ is integrable on } [0, R_c].$$

Then, using the definition of the eigenvalues (4.23) this leads to the conditions

$$\int_0^{R_c} f_l(s) \, \mathrm{d}s \leqslant 0 \qquad \text{and} \qquad \int_0^{R_c} f_s(s) + f_s'(s)s \, \mathrm{d}s \leqslant 0. \tag{4.29}$$

Integration by parts of the second condition in (4.29) leads to $f_s(R_c) \leqslant 0$ and the conditions in (4.28) result from $f_s$ being repulsive, i.e. $f_s \geqslant 0$. $\qquad \square$

**Remark 10.** *The necessary condition $f_s(R_c) = 0$ in (4.28) for a stable straight vertical line is equivalent to the eigenvalue associated with $f_s$ to be equal to zero in the high wave number limit. Hence, stability/instability of straight vertical lines cannot be concluded in the continuum limit $N \to \infty$ from the linear stability analysis.*

The first condition in (4.28) implies that the total attractive force over its entire range is larger than the total repulsive force along $l$. The second condition in (4.28) implies that for high wave stability we require the total force at the cutoff radius $R_c$ should not be repulsive along $s$ which is identical to the assumptions on the cutoff in (4.7).

In comparison with the high wave number conditions in (4.29) in the proof of Proposition 6 the integrands for the stability conditions are multiplied by a factor

$$\Re(1 - \ \exp(-2\pi i m s)) = 1 - \cos(2\pi m s) \in [0, 2].$$

Even if the necessary conditions for high wave number stability (4.28) are satisfied, this does not guarantee that $\Re(\lambda_1(m)), \Re(\lambda_2(m)) \leqslant 0$ for all $m \in \mathbb{N}$ and hence necessary stability conditions for the single vertical straight line might not be satisfied for all $m \in \mathbb{N}$.

The general stability conditions for straight vertical lines can be obtained from the real parts of the eigenvalues (4.23) of the stability matrix (4.17). The conditions (4.28) suggest that stability of the straight line is possible for particular force coefficient choices. This will be investigated in Section 4.4.

**Remark 11.** *Note that differentiable approximations $f_R^\varepsilon, f_A^\varepsilon$ of the force coefficients $f_R$ and $f_A$ in the Kücken-Champod model are defined in (4.10) and (4.11), respectively. Setting $f_l^\varepsilon := f_A^\varepsilon + f_R^\varepsilon$ and $f_s^\varepsilon := \chi f_A^\varepsilon + f_R^\varepsilon$ for some $0 < \varepsilon \ll R_c$ and a parameter $\chi \in [0, 1]$ such that $f_s \geqslant 0$ on $[0, R_c)$, we consider $f_l^\varepsilon, f_s^\varepsilon$ instead of $f_l, f_s$ in the definition of the real parts of the eigenvalues (4.24). We obtain the following for the real parts of the eigenvalues of the stability matrix (4.17) in the Kücken-Champod model with total force (4.3) and the spatially homogeneous tensor field $T$ in (4.2):*

$$\Re(\lambda_1(m)) = 2 \int_0^{R_c} \left( f_A^\varepsilon(s) + f_R^\varepsilon(s) \right) \left( 1 - \cos\left(-2\pi m s\right) \right) \mathrm{d}s,$$

$$\Re(\lambda_2(m)) = 2 \int_0^{R_c} \left( \chi f_A^\varepsilon(s) + f_R^\varepsilon(s) + \chi s (f_A^\varepsilon)'(s) + s(f_R^\varepsilon)'(s) \right) \left( 1 - \cos\left(-2\pi m s\right) \right) \mathrm{d}s.$$

*The necessary stability condition (4.28) implies that $f_s^\varepsilon(R_c) = \chi f_A^\varepsilon(R_c) + f_R^\varepsilon(R_c) = 0$,*

consistent with the definition of the force coefficients (4.10) and (4.11) in the Kücken-Champod model. Hence, the necessary condition (4.28) for high wave number stability of a straight vertical line is satisfied in this case.

### 4.3.4 Instability of a single horizontal straight line

In this section we investigate the stability of a single horizontal straight line given by the ansatz (4.15) which follows from (4.12) with $\theta = 0$.

**Theorem 2.** *For $N \in \mathbb{N}$ sufficiently large and in the continuum limit $N \to \infty$, the single horizontal straight line (4.15) is an unstable steady state to the particle model (4.6) for any choice of force coefficients $f_s$ and $f_l$ of the total force (4.4), provided the total force is purely repulsive along s on $[0, R_c)$.*

*Proof.* For a single horizontal straight line, we have

$$d_{jk} = \bar{x}_j - \bar{x}_k = \begin{pmatrix} \frac{j-k}{N} \\ 0 \end{pmatrix}$$

and the derivatives of the total force are given by

$$\frac{\partial}{\partial d_1} \bar{F}(d_{jk}) = \begin{pmatrix} f_l(|d_{jk}|) + f_l'(|d_{jk}|)|d_{jk}| \\ 0 \end{pmatrix},$$

$$\frac{\partial}{\partial d_2} \bar{F}(d_{jk}) = \begin{pmatrix} 0 \\ f_s(|d_{jk}|) \end{pmatrix}$$

for $d_{jk} \in [-0.5, 0.5]^2$. Similarly as in Section 4.3.3 one can show that the eigenvalues $\lambda_1 = \lambda_1(m)$, $\lambda_2 = \lambda_2(m)$ of the stability matrix (4.17) are given by

$$\lambda_1(m) = 2 \int_0^{R_c} (f_l(s) + f_l'(s)s)(1 - \exp(-2\pi ims)) \, \mathrm{d}s,$$

$$\lambda_2(m) = 2 \int_0^{R_c} f_s(s)(1 - \exp(-2\pi ims)) \, \mathrm{d}s$$

for a cutoff radius $R_c \in (0, 0.5]$. For high wave number stability we require

$$f_l(R_c) = \frac{1}{R_c} \int_0^{R_c} f_l(s) + f_l'(s)s \, \mathrm{d}s \leqslant 0 \qquad \text{and} \qquad \int_0^{R_c} f_s(s) \, \mathrm{d}s \leqslant 0.$$

The forces are assumed to be purely repulsive along $s$ up to the cutoff $R_c$, i.e. $f_s > 0$ on $[0, R_c)$, implying

$$\int_0^{R_c} f_s(s) \, \mathrm{d}s > 0.$$

Hence, the single horizontal straight line is high wave number unstable. $\qquad \square$

## 4.3.5 Instability of rotated straight line patterns

In this section we consider the ansatz (4.12) where the angle of rotation $\theta$ satisfies (4.13), resulting in rotated straight line patterns. The entries of the stability matrix (4.17) are given by

$$I_1(m) = 2 \int_0^{R_c} \frac{\partial \bar{F}}{\partial d_1} \left( (s \cos(\theta), s \sin(\theta)) \right) (1 - \exp(-2\pi i m s)) \, \mathrm{d}s,$$

$$I_2(m) = 2 \int_0^{R_c} \frac{\partial \bar{F}}{\partial d_2} \left( (s \cos(\theta), s \sin(\theta)) \right) (1 - \exp(-2\pi i m s)) \, \mathrm{d}s,$$

where the derivatives of the total force can easily be determined by

$$\frac{\partial}{\partial d_1} \bar{F}(d) = \begin{pmatrix} f_l(|d|) + f_l'(|d|)\frac{d_1^2}{|d|} \\ f_s'(|d|)\frac{d_1 d_2}{|d|} \end{pmatrix}, \qquad \frac{\partial}{\partial d_2} \bar{F}(d) = \begin{pmatrix} f_l'(|d|)\frac{d_1 d_2}{|d|} \\ f_s(|d|) + f_s'(|d|)\frac{d_2^2}{|d|}, \end{pmatrix}$$

$d \in [-0.5, 0.5]^2$ with the cutoff radius $R_c \in (0, 0.5]$. In particular, the stability matrix (4.17) is no longer a diagonal matrix in general. To show that the rotated straight line pattern is unstable for $\theta \in (0, \pi) \backslash [\phi, \pi - \phi]$ for some $\phi \in (0, \frac{\pi}{2})$ and $N \in \mathbb{N}$ sufficiently large and in the continuum limit $N \to \infty$, it is sufficient to consider the high frequency wave limit and show high wave number instability. Denoting the entries of $I_k$ by $I_{k1}$ and $I_{k2}$ for $k = 1, 2$ with $M = (I_1, I_2)$ the high frequency limit

leads to

$$I_{11} = 2 \int_0^{R_c} f_l(s) \, \mathrm{d}s + 2 \int_0^{R_c} f_l'(s) s \cos^2(\theta) \, \mathrm{d}s,$$

$$I_{12} = 2 \int_0^{R_c} f_s'(s) s \sin(\theta) \cos(\theta) \, \mathrm{d}s,$$

$$I_{21} = 2 \int_0^{R_c} f_l'(s) s \sin(\theta) \cos(\theta) \, \mathrm{d}s,$$

$$I_{22} = 2 \int_0^{R_c} f_s(s) \, \mathrm{d}s + 2 \int_0^{R_c} f_s'(s) s \sin^2(\theta) \, \mathrm{d}s. \tag{4.30}$$

Here, $I_{12} = I_{21} = 0$ for $\theta = 0$ and $\theta = \frac{\pi}{2}$, i.e. for the straight horizontal and the straight vertical line, respectively. Hence, the eigenvalues of the stability matrix are given by $I_{11}$ and $I_{22}$ in this case whose value are given by

$$I_{11} = 2R_c f_l(R_c), \quad I_{22} = 2 \int_0^{R_c} f_s(s) \, \mathrm{d}s$$

for $\theta = 0$ and

$$I_{11} = 2 \int_0^{R_c} f_l(s) \, \mathrm{d}s, \quad I_{22} = 2R_c f_s(R_c)$$

for $\theta = \frac{\pi}{2}$. This leads to the necessary conditions for high wave number stability for $\theta = \frac{\pi}{2}$ in (4.28), while due to Assumption 5 we obtain instability of the straight horizontal line.

Note that for any $\theta \in [0, \pi)$ the eigenvalues $\lambda_k, k = 1, 2$, are either real or complex conjugated and thus the sum and the product of $\lambda_k$ are real. The condition $\Re(\lambda_k) \leqslant 0, k = 1, 2$, is equivalent to $\mathrm{trace}(M) = \lambda_1 + \lambda_2 \leqslant 0$ and $\det(M) = \lambda_1 \lambda_2 \geqslant 0$. Hence, we require, for the stability of the rotated straight line,

$$I_{11} + I_{22} \leqslant 0 \quad \text{and} \quad I_{11}I_{22} - I_{12}I_{21} \geqslant 0. \tag{4.31}$$

For showing the instability of the rotated straight line with angle of rotation $\theta \in (0, \pi) \backslash [\phi, \pi - \phi]$ for some $\phi \in (0, \frac{\pi}{2})$ we show that the two conditions in (4.31) cannot be satisfied simultaneously in this case.

**Theorem 3.** *For $N \in \mathbb{N}$ sufficiently large and in the continuum limit $N \to \infty$, the single straight line (4.12) where the angle of rotation $\theta \in (0, \pi) \backslash [\phi, \pi - \phi]$ for some $\phi \in (0, \frac{\pi}{2})$ satisfies (4.13) is an unstable steady state to the particle model (4.6) for any force coefficients $f_s$ and $f_l$ satisfying the general conditions for force coefficients in Assumption 5 and the conditions in (4.28).*

*Proof.* Note that we have

$$\int_0^{R_c} f_s'(s)s\sin^2(\theta)\,\mathrm{d}s = \sin^2(\theta)\left(f_s(R_c)R_c - \int_0^{R_c} f_s(s)\,\mathrm{d}s\right)$$

by integration by parts. For $\theta = 0$ and $f_l(R_c) = 0$ we have

$$I_{11} + I_{22} = 2R_c f_l(R_c) + 2\int_0^{R_c} f_s(s)\,\mathrm{d}s > 0,$$

while for $\theta = \frac{\pi}{2}$ we have

$$I_{11} + I_{22} = 2R_c f_s(R_c) + 2\int_0^{R_c} f_l(s)\,\mathrm{d}s \leqslant 0$$

by (4.28). Hence, there exists $\phi \in (0, \frac{\pi}{2})$ such that $I_{11} + I_{22} > 0$ on $(0, \phi)$. Since $\cos^2(\theta) = \cos^2(\pi - \theta)$ and $\sin^2(\theta) = \sin^2(\pi - \theta)$ we have $I_{11} + I_{22} > 0$ on $(\pi - \phi, \pi)$, implying that stability may only be possible on $[\phi, \pi - \phi]$. $\qquad\square$

## 4.4 Stability of vertical lines for particular force coefficients

We have investigated the high wave number stability for $m \to \infty$ in Section 4.3. Since only vertical straight lines for the considered spatially homogeneous tensor field $T$ in (4.2) can lead to stable steady states for any $N \in \mathbb{N}$ we restrict ourselves to vertical straight lines in the following. As a next step towards proving stability we now consider the stability for fixed modes $m \in \mathbb{N}$.

Due to the form of the eigenvalues in (4.23) no general stability result for the single straight vertical line for the particle system (4.6) with arbitrary force coefficients $f_s$ and $f_l$ satisfying Assumption 5 can be derived. Thus, additional assumptions on the force coefficients are necessary.

### 4.4.1 Linear force coefficients

To study the stability of the single straight vertical line for any $N \in \mathbb{N}$, we consider linear force coefficients satisfying Assumption 5. To guarantee that the force coefficient is differentiable, required for using the results from Section 4.3, we consider the differentiable adaptation (4.7) for a given linear force coefficient, leading to a linear

force coefficient on $[0, R_c - \varepsilon]$ for some $\varepsilon > 0$, a cubic polynomial on $(R_c - \varepsilon, R_c)$, and the constant zero function for $|d| \geqslant R_c$. This leads to the following conditions.

**Assumption 6.** *For any $\varepsilon > 0$ with $\varepsilon \ll R_c$, we assume that the force coefficients are linear on $[0, R_c - \varepsilon]$, i.e.*

$$f_l^\varepsilon(|d|) := \begin{cases} a_l|d| + b_l, & |d| \in [0, R_c - \varepsilon], \\ (2b_l + 2R_c a_l - a_l\varepsilon)\frac{(|d| - R_c)^3}{\varepsilon^3} \\ \quad + (3b_l + 3R_c a_l - 2a_l\varepsilon)\frac{(|d| - R_c)^2}{\varepsilon^2}, & |d| \in (R_c - \varepsilon, R_c), \\ 0, & |d| \geqslant R_c, \end{cases}$$

$$f_s^\varepsilon(|d|) := \begin{cases} a_s|d| + b_s, & |d| \in [0, R_c - \varepsilon], \\ (2b_s + 2R_c a_s - a_s\varepsilon)\frac{(|d| - R_c)^3}{\varepsilon^3} \\ \quad + (3b_s + 3R_c a_s - 2a_s\varepsilon)\frac{(|d| - R_c)^2}{\varepsilon^2}, & |d| \in (R_c - \varepsilon, R_c), \\ 0, & |d| \geqslant R_c, \end{cases}$$

$$(4.32)$$

*for constants $a_l, a_s, b_l, b_s$. Since $f_l^\varepsilon$ and $f_s^\varepsilon$ are short-range repulsive, we require*

$$b_l > 0, \quad b_s > 0.$$

*Besides, for physically realistic force coefficients the absolute values of $f_l^\varepsilon$ and $f_s^\varepsilon$ are decaying, i.e.*

$$a_l < 0, \quad a_s < 0.$$

Note that for the short-range repulsive, long-range attractive force coefficient $f_l$, we have $a_l R_c + b_l < 0$ and in particular $a_l R_c + b_l$ is of order $\mathcal{O}(1)$. Hence, the adaptation $f_l^\varepsilon$ of $f_l$ for $f_l$ linear is not negligible. However, due to the concentration of particles along a straight vertical line the adaptation $f_l^\varepsilon$ acting along the vertical axis does not influence the overall dynamics provided $0 < \varepsilon \ll R_c$. For the force coefficient $f_s$, the adaption $f_s^\varepsilon$ of $f_s$ is negligible if $a_s R_c + b_s$ is of order $\mathcal{O}(\varepsilon)$ and also results in the same stability/instability properties numerically; see Section 4.5.2. If $a_s R_c + b_s$ is of order $\mathcal{O}(1)$, then the adaptation is not negligible, but the numerical results in Section 4.5.2 illustrate that we obtain the same stability/instability results for $f_s^\varepsilon$ and $f_s$.

**Remark 12.** *Note that the modelling assumptions in Assumptions 5 and 6 can be applied to linear repulsive and attractive force coefficients $f_R^\varepsilon$ and $f_A^\varepsilon$ as in (4.32),*

*where the total force of the form (4.3) consists of repulsion and attraction forces.*
*That is, for $\varepsilon > 0$ we define*

$$
f_R^\varepsilon(|d|) := \begin{cases} a_R|d| + b_R, & |d| \in [0, R_c - \varepsilon], \\ (2b_R + 2R_c a_R - a_R\varepsilon)\frac{(|d|-R_c)^3}{\varepsilon^3} & \\ \quad + (3b_R + 3R_c a_R - 2a_R\varepsilon)\frac{(|d|-R_c)^2}{\varepsilon^2}, & |d| \in (R_c - \varepsilon, R_c), \\ 0, & |d| \geqslant R_c, \end{cases}
$$

$$
f_A^\varepsilon(|d|) := \begin{cases} a_A|d| + b_A, & |d| \in [0, R_c - \varepsilon], \\ (2b_A + 2R_c a_A - a_A\varepsilon)\frac{(|d|-R_c)^3}{\varepsilon^3} & \\ \quad + (3b_A + 3R_c a_A - 2a_A\varepsilon)\frac{(|d|-R_c)^2}{\varepsilon^2}, & |d| \in (R_c - \varepsilon, R_c), \\ 0, & |d| \geqslant R_c, \end{cases} \tag{4.33}
$$

*for constants $a_A, a_R, b_A, b_R$ and we require*

$$
f_R^\varepsilon \geqslant 0 \quad and \quad f_A^\varepsilon \leqslant 0
$$

*for all $\varepsilon > 0$ with $\varepsilon \ll R_c$, implying*

$$
a_R s + b_R \geqslant 0 \quad and \quad a_A s + b_A \leqslant 0 \quad for \quad s \in [0, R_c], \tag{4.34}
$$

*and, in particular,*

$$
b_R > 0 \quad and \quad b_A < 0. \tag{4.35}
$$

*For realistic interaction force coefficients $f_R^\varepsilon$ and $f_A^\varepsilon$ we assume that their absolute values decrease as the distance between the particles increases, implying*

$$
a_R < 0 \quad and \quad a_A > 0 \tag{4.36}
$$

*by the definition of $f_R^\varepsilon$ and $f_A^\varepsilon$ in (4.33) and by the condition for $b_R$ and $b_A$ in (4.35).*
*Combining the assumptions on $a_A, a_R$ in (4.36) and $b_A, b_R$ in (4.35), condition (4.34)*
*reduces to*

$$
a_R R_c + b_R \geqslant 0 \quad and \quad a_A R_c + b_A \leqslant 0.
$$

*Further we assume that $f_A^\varepsilon + f_R^\varepsilon$ is short-range repulsive, long-range attractive for*

*any $\varepsilon > 0$ with $\varepsilon \ll R_c$, i.e.*

$$(f_A^\varepsilon + f_R^\varepsilon)(0) = b_A + b_R > 0, \qquad (f_A^\varepsilon + f_R^\varepsilon)(R_c - \varepsilon) = (a_A + a_R)(R_c - \varepsilon) + b_A + b_R < 0$$

*for all $0 < \varepsilon \ll R_c$ implying*

$$b_A + b_R > 0 \quad and \quad a_A + a_R < 0. \tag{4.37}$$

*For any $\varepsilon > 0$, the force coefficient $\chi f_A^\varepsilon + f_R^\varepsilon$ is purely repulsive along $s$ on $[0, R_c - \varepsilon]$ if $\chi \in [0,1]$ is sufficiently small since $f_R^\varepsilon$ is repulsive. Note that (4.37) implies*

$$\chi a_A + a_R < 0, \quad \chi b_A + b_R > 0 \quad for \ all \quad \chi \in [0,1]$$

*by the positivity of $b_R$ and by the negativity of $a_R$ in (4.35) and (4.36), respectively. Since*

$$f_l^\varepsilon(|d|) = f_A^\varepsilon(|d|) + f_R^\varepsilon(|d|) = (a_A + a_R)|d| + b_A + b_R$$

*and*

$$f_s^\varepsilon(|d|) = \chi f_A^\varepsilon(|d|) + f_R^\varepsilon(|d|) = (\chi a_A + a_R)|d| + \chi b_A + b_R$$

*for $|d| \in [0, R_c - \varepsilon]$, we have*

$$a_l = a_A + a_R < 0, \quad a_s = \chi a_A + a_R < 0, \quad b_l = b_A + b_R > 0, \quad b_s = \chi b_A + b_R > 0$$

*as in Assumption 6.*

For investigating the stability of the straight line for any $N \in \mathbb{N}$, we consider the real parts of the eigenvalues in (4.24), i.e.

$$\Re(\lambda_1(m)) = 2 \int_0^{R_c} f_l^\varepsilon(s) \left(1 - \cos\left(-2\pi m s\right)\right) \mathrm{d}s,$$

$$\Re(\lambda_2(m)) = 2 \int_0^{R_c} \left(f_s^\varepsilon(s) + s(f_s^\varepsilon)'(s)\right) \left(1 - \cos\left(-2\pi m s\right)\right) \mathrm{d}s.$$

Note that the coefficient functions of the integrands in the definition of the eigenvalues are given by

$$f_l^\varepsilon(s) = a_l s + b_l, \quad f_s^\varepsilon(s) + s(f_s^\varepsilon)'(s) = 2a_s s + b_s$$

for $s \in [0, R_c - \varepsilon]$ with $a_l, a_s < 0$, $b_l, b_s > 0$, and

$$f_l^\varepsilon(s) = (2b_l + 2R_c a_l - a_l \varepsilon)\frac{(s - R_c)^3}{\varepsilon^3} + (3b_l + 3R_c a_l - 2a_l \varepsilon)\frac{(s - R_c)^2}{\varepsilon^2},$$

$$f_s^\varepsilon(s) + s(f_s^\varepsilon)'(s) = (2b_s + 2R_c a_s - a_s \varepsilon)\frac{(s - R_c)^3}{\varepsilon^3} + (3b_s + 3R_c a_s - 2a_s \varepsilon)\frac{(s - R_c)^2}{\varepsilon^2}$$

$$+ 3(2b_s + 2R_c a_s - a_s \varepsilon)\frac{s(s - R_c)^2}{\varepsilon^3}$$

$$+ 2(3b_s + 3R_c a_s - 2a_s \varepsilon)\frac{s(s - R_c)}{\varepsilon^2}$$

for $s \in [R_c - \varepsilon, R_c]$ by Assumption 6. Since $f_l^\varepsilon(s)$ and $f_s^\varepsilon(s) + s(f_s^\varepsilon)'(s)$ are bounded on $[R_c - \varepsilon, R_c]$, we obtain

$$\Re(\lambda_1(m)) = 2 \int_0^{R_c - \varepsilon} (a_l s + b_l)\left(1 - \cos(-2\pi m s)\right) \mathrm{d}s + \mathcal{O}(\varepsilon),$$

$$\Re(\lambda_2(m)) = 2 \int_0^{R_c - \varepsilon} (2a_s s + b_s)\left(1 - \cos(-2\pi m s)\right) \mathrm{d}s$$

$$+ \frac{12(b_s + R_c a_s)}{\varepsilon} \int_{R_c - \varepsilon}^{R_c} \left(\frac{s(s - R_c)^2}{\varepsilon^2} + \frac{s(s - R_c)}{\varepsilon}\right)\left(1 - \cos(-2\pi m s)\right) \mathrm{d}s + \mathcal{O}(\varepsilon).$$

$$(4.38)$$

Note that $s(f_s^\varepsilon)'$ is of order $\mathcal{O}(1/\varepsilon)$ on $[R_c - \varepsilon, R_c]$ and hence the integral over $[R_c - \varepsilon, R_c]$ also contributes to the leading order term for $\Re(\lambda_2(m))$. Here, $f_l^\varepsilon(s)$ and $f_s^\varepsilon(s) + s(f_s^\varepsilon)'(s)$ are linear functions on $[0, R_c - \varepsilon]$ of the form $f|_{[0, R_c - \varepsilon]} \to \mathbb{R}, s \mapsto as + b$ for constants $a < 0$ and $b > 0$. In particular, $\Re(\lambda_1)$ and the first term in $\Re(\lambda_2)$ are of the form

$$2 \int_0^{R_c - \varepsilon} (a_k s + b_k)\left(1 - \cos(2\pi m s)\right) \mathrm{d}s, \tag{4.39}$$

where

$$a_1 = a_l, \quad a_2 = 2a_s, \quad b_1 = b_l, \quad b_2 = b_s. \tag{4.40}$$

For ease of notation we drop the indices of $a_k$ and $b_k$ in the following. Note that

$$
\int_0^{R_c-\varepsilon} (as + b)\left(1 - \cos\left(2\pi ms\right)\right) \mathrm{d}s
$$
$$
= \frac{2\pi m\left(\pi m(R_c - \varepsilon)\left(a(R_c - \varepsilon) + 2b\right) - (a(R_c - \varepsilon) + b)\sin\left(2\pi m(R_c - \varepsilon)\right)\right)}{4\pi^2 m^2} \quad (4.41)
$$
$$
+ \frac{a - a\cos\left(2\pi m(R_c - \varepsilon)\right)}{4\pi^2 m^2}.
$$

In the limit $m \to \infty$, all terms in the second line of (4.41) vanish except for the first term. Since $R_c > 0$, we require

$$
a \leqslant -b\frac{2}{R_c - \varepsilon}
$$

for high wave number stability for any $\varepsilon > 0$ with $\varepsilon \ll R_c$. In particular, this condition is consistent with the necessary condition for high wave number stability in Proposition 6 for arbitrary force coefficients $f_s^\varepsilon$ and $f_l^\varepsilon$ satisfying Assumption 5. In the limit $\varepsilon \to 0$, it reduces to

$$
a \leqslant -b\frac{2}{R_c}. \quad (4.42)
$$

Since $R_c \in (0, 0.5]$ and $b > 0$, (4.42) implies that $a < 0$ is necessary for high wave number stability. Hence, we can assume

$$
a < 0 \quad \text{and} \quad b > 0
$$

in the following.

**Lemma 3.** *Let $b > 0$ and $R_c \in (0, 0.5]$. For $\varepsilon > 0$, set*

$$
g_\varepsilon(m) := 2\pi m\left(\pi m(R_c - \varepsilon)^2 - (R_c - \varepsilon)\sin(2\pi m(R_c - \varepsilon))\right) + 1 - \cos(2\pi m(R_c - \varepsilon)),
$$
$$
h_\varepsilon(m) := 2\pi m\left(2\pi m(R_c - \varepsilon) - \sin(2\pi m(R_c - \varepsilon))\right).
$$
$$
(4.43)
$$

*Then,*

$$
\int_0^{R_c-\varepsilon} (as + b)\left(1 - \cos\left(2\pi ms\right)\right) \mathrm{d}s \leqslant 0 \quad (4.44)
$$

*is satisfied for all $m \in \mathbb{N}$ and all $\varepsilon > 0$ with $\varepsilon \ll R_c$ if and only if $a \leqslant a_0$ with*

$$a_0 := -b \max_{m \in \mathbb{N}} \frac{h_\varepsilon(m)}{g_\varepsilon(m)} \leqslant -\frac{2b}{R_c} \leqslant 0. \tag{4.45}$$

*Proof.* Note that the numerator of (4.41) is of the form $a g_\varepsilon(m) + b h_\varepsilon(m)$ for functions $g_\varepsilon$ and $h_\varepsilon$, defined in (4.43). Condition (4.44) is equivalent to

$$a \leqslant -b \frac{h_\varepsilon(m)}{g_\varepsilon(m)} \quad \text{for all } m \in \mathbb{N}.$$

Herein, $h_\varepsilon(m) \geqslant 0$ for all $m \geqslant 0$ since $h_\varepsilon$ is an increasing function. Further note that

$$\begin{aligned}
g_\varepsilon'(m) &= 2\pi \left( \pi m (R_c - \varepsilon)^2 - (R_c - \varepsilon) \sin(2\pi m (R_c - \varepsilon)) \right) \\
&\quad + 2\pi m \left( \pi (R_c - \varepsilon)^2 - 2\pi (R_c - \varepsilon)^2 \cos(2\pi m (R_c - \varepsilon)) \right) \\
&\quad + 2\pi (R_c - \varepsilon) \sin(2\pi m (R_c - \varepsilon)) \\
&= 4\pi^2 m (R_c - \varepsilon)^2 \left( 1 - \cos(2\pi m (R_c - \varepsilon)) \right)
\end{aligned}$$

is nonnegative implying that $g_\varepsilon$ is an increasing function with $g_\varepsilon(0) = 0$. In particular, $g_\varepsilon$ and $h_\varepsilon$ are nonnegative functions for all $m \in \mathbb{N}$. Hence, (4.44) is satisfied for all $m \in \mathbb{N}$ if and only if $a < a_0$. Note that

$$\lim_{m \to \infty} \frac{h_\varepsilon(m)}{g_\varepsilon(m)} = \frac{2}{R_c - \varepsilon},$$

implying that

$$\sup_{m \in \mathbb{N}} \frac{h_\varepsilon(m)}{g_\varepsilon(m)} \in \mathbb{R}$$

by the nonnegativity and continuity of $g_\varepsilon$ and $h_\varepsilon$.

Let $R_c \in (0, 0.5]$ and $\varepsilon > 0$. We have

$$\begin{aligned}
\max_{m \in \mathbb{N}} \frac{h_\varepsilon(m)}{g_\varepsilon(m)} &\geqslant \frac{2\pi m \left( 2\pi m (R_c - \varepsilon) - \sin(2\pi m (R_c - \varepsilon)) \right)}{2\pi m \left( \pi m (R_c - \varepsilon)^2 - (R_c - \varepsilon) \sin(2\pi m (R_c - \varepsilon)) \right) + 2} \\
&= \frac{2}{R_c - \varepsilon} \left( 1 + \frac{\pi m \sin(2\pi m (R_c - \varepsilon)) - \frac{2}{R_c - \varepsilon}}{2\pi m \left( \pi m (R_c - \varepsilon) - \sin(2\pi m (R_c - \varepsilon)) \right) + \frac{2}{R_c - \varepsilon}} \right)
\end{aligned}$$

for all $m \in \mathbb{N}$. Since $R_c - \varepsilon \in (0, 0.5)$ there exists $m \in \mathbb{N}$ such that $\pi m \sin(2\pi m (R_c -$

$\varepsilon)) - \frac{2}{R_c - \varepsilon} > 0$ and hence

$$\max_{m \in \mathbb{N}} \frac{h_\varepsilon(m)}{g_\varepsilon(m)} > \frac{2}{R_c - \varepsilon} > \frac{2}{R_c}$$

for $\varepsilon > 0$ with $\varepsilon \ll R_c$. For $R_c \in (0, 0.5)$, we obtain

$$\lim_{\varepsilon \to 0} \max_{m \in \mathbb{N}} \frac{h_\varepsilon(m)}{g_\varepsilon(m)} > \frac{2}{R_c}.$$

For $R_c = 0.5$, we have

$$\lim_{\varepsilon \to 0} \frac{h_\varepsilon(m)}{g_\varepsilon(m)} = \begin{cases} \frac{2}{R_c}, & m \text{ even}, \\ \frac{4\pi^2 R_c}{2\pi^2 R_c^2 + \frac{2}{m^2}} < \frac{2}{R_c}, & m \text{ odd}, \end{cases}$$

implying that

$$\lim_{\varepsilon \to 0} \max_{m \in \mathbb{N}} \frac{h_\varepsilon(m)}{g_\varepsilon(m)} = \frac{2}{R_c}.$$

Hence, $a \leqslant a_0$ is equivalent to the necessary condition (4.42) for high wave number stability for $R_c = 0.5$. $\qquad \square$

**Remark 13.** *For the stability of line patterns with force coefficients $f_s^\varepsilon, f_l^\varepsilon$ of the form (4.32), we require $\Re(\lambda_k(m)) \leqslant 0$ for $k = 1, 2$ for the real parts of the eigenvalues $\Re(\lambda_k(m))$, $k = 1, 2$, in (4.38). Note that the nonnegativity of the leading order term of $\Re(\lambda_1)$ which is of the form (4.39) is equivalent to condition (4.44) in Lemma 3. Similarly, the nonnegativity of the first term in (4.38) which is also of the form (4.39) is equivalent to condition (4.44) in Lemma 3.*

*From the proof of Lemma 3 it follows that*

$$\frac{2}{R_c} \leqslant \max_{m \in \mathbb{N}} \frac{h_\varepsilon(m)}{g_\varepsilon(m)}. \tag{4.46}$$

*The inequality in (4.46) is strict for $R_c - \varepsilon \in (0, 0.5)$, i.e. a necessary condition for (4.44) to hold for $R_c - \varepsilon \in (0, 0.5)$ is given by*

$$a < -\frac{2b}{R_c}.$$

*For $R_c = 0.5$ and $\varepsilon \to 0$, condition (4.44) holds for any $a < 0$ satisfying the necessary condition (4.42) for high wave number stability. If the necessary condition*

(4.42) *for high wave number stability is satisfied with equality, i.e. $a = -\frac{2b}{R_c}$, the leading order term of the left-hand side of* (4.38) *vanishes for $\varepsilon \to 0$ in the high wave limit and lower order terms have to be considered.*

In Figure 4.2, we investigate the scaling factor of $a_0$, defined in (4.45), numerically. In Figure 4.2(A) the quotient $h_0/g_0$ is shown as a function of $m \in \mathbb{N}$ for different values of the cutoff radius $R_c$. Note that for smaller values of $R_c$, the maximum of $h_0/g_0$ gets larger as shown in Figure 4.2(B). In Figures 4.2(C) and 4.2(D) we consider the quotient $h_0/g_0$ scaled by $R_c$. Figure 4.2(C) shows that $R_c h_0/g_0 \to 2$ as $m \to \infty$, independently of the value of $R_c$, and that the maximum of $R_c h_0/g_0$ is obtained for smaller values of $m \in \mathbb{N}$ in general. The value of

$$R_c \max_{m\in\mathbb{N}} \frac{h_0(m)}{g_0(m)}$$

is shown in Figure 4.2(D) as a function of $R_c$. In particular, the scaled maximum is larger than 2 if and only if $R_c \in (0, 0.5)$ and is equal to 2 for $R_c = 0.5$. Hence, this numerical investigation is consistent with the results in Lemma 3.

Applying Lemma 3 to the specific form of the stability conditions for a single straight vertical line leads to the following stability results for the linear force coefficients (4.32).

**Proposition 7.** *For $R_c \in (0, 0.5)$, the single straight vertical line is an unstable steady state of* (4.6) *for any $N \in \mathbb{N}$ sufficiently large and in the continuum limit $N \to \infty$, where the forces are of the form* (4.4) *for any linear coefficient functions $f_s^\varepsilon, f_l^\varepsilon$ with $0 < \varepsilon \ll R_c$ such that Assumption 6 is satisfied. In particular, the single straight vertical line is an unstable steady state for force coefficients $f_s^\varepsilon, f_l^\varepsilon$ for $R_c \in (0, 0.5)$ in the limit $\varepsilon \to 0$.*

*Proof.* Note that the leading order term of $\Re(\lambda_1(m))$ and the first term of $\Re(\lambda_2(m))$ in (4.38) are of the form (4.39) with parameters (4.40). For stability we require $\Re(\lambda_k) \leqslant 0$ for $k = 1, 2$.

Let us consider the nonnegativity of $\Re(\lambda_2(m))$ in (4.38) first. Note that the second leading order term of $\Re(\lambda_2(m))$ in (4.38) can be rewritten as

$$12(b_s + R_c a_s) \int_{-1}^{0} \left((\varepsilon s + R_c)s^2 + (\varepsilon s + R_c)s\right)\left(1 - \cos\left(2\pi m(\varepsilon s + R_c)\right)\right) ds$$
$$= -2(b_s + R_c a_s)R_c\left(1 - \cos\left(2\pi m R_c\right)\right) + \mathcal{O}(\varepsilon). \tag{4.47}$$

(A) $\dfrac{h_0(m)}{g_0(m)}$

(B) $\max_{m\in\mathbb{N}} \dfrac{h_0(m)}{g_0(m)}$

(C) $R_c \dfrac{h_0(m)}{g_0(m)}$

(D) $R_c \max_{m\in\mathbb{N}} \dfrac{h_0(m)}{g_0(m)}$
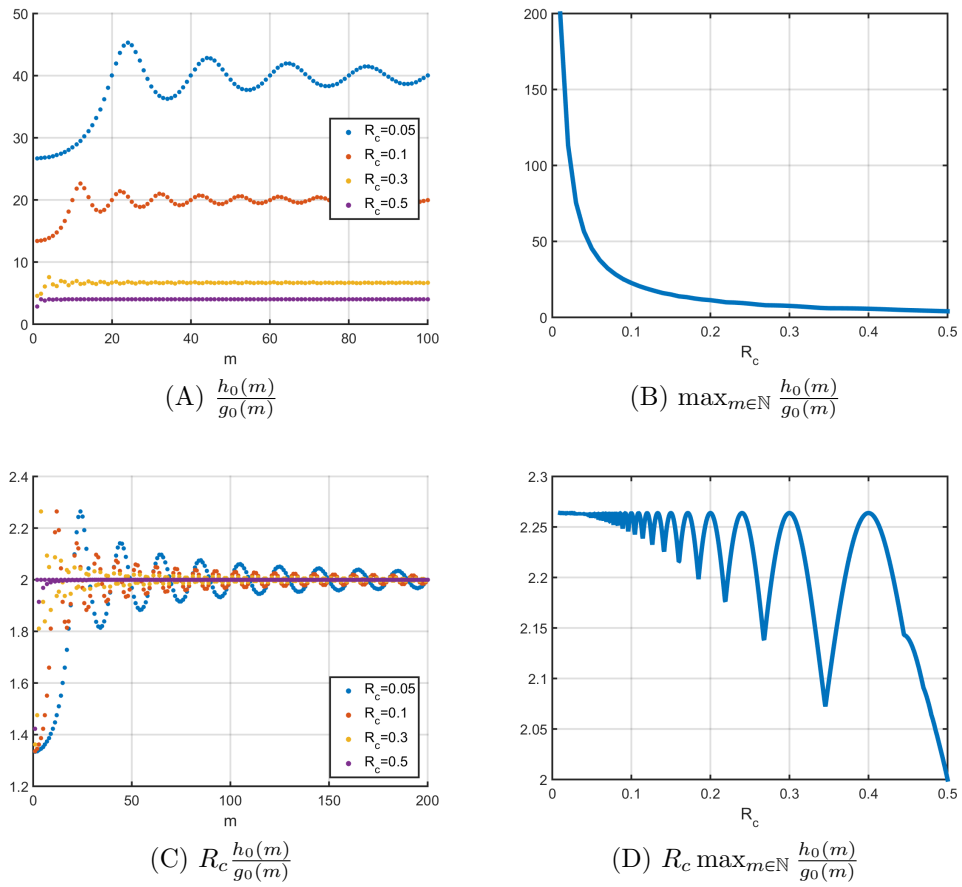
Figure 4.2: Scaling factor of $a_0$ in (4.45) as a function of $R_c$ where $g_0, h_0$ are defined in (4.43).

Hence, $\Re(\lambda_2(m))$ is of the form

$$\Re(\lambda_2(m)) = \frac{2}{4\pi^2 m^2}(2a_s g_0(m) + b_s h_0(m)) - 2(b_s + R_c a_s)R_c\left(1 - \cos\left(2\pi m R_c\right)\right) + \mathcal{O}(\varepsilon)$$

by (4.41), where $g_0, h_0$ are defined in (4.43). For the nonnegativity of the leading order term of $\Re(\lambda_2(m))$ we require

$$a_s\left(\frac{2g_0(m)}{4\pi^2 m^2} - R_c^2\left(1 - \cos\left(2\pi m R_c\right)\right)\right) + b_s\left(\frac{h_0(m)}{4\pi^2 m^2} - R_c\left(1 - \cos\left(2\pi m R_c\right)\right)\right) \leqslant 0,$$

which can be rewritten as

$$a_s\tilde{g}_0(m) + b_s\tilde{h}_0(m) \leqslant 0,$$

where

$$\tilde{g}_0(m) := 2\pi m\left(2\pi m R_c^2\cos(2\pi m R_c) - 2R_c\sin(2\pi m R_c)\right) + 2 - 2\cos(2\pi m R_c),$$
$$\tilde{h}_0(m) := 2\pi m\left(2\pi m R_c\cos(2\pi m R_c) - \sin(2\pi m R_c)\right).$$

For $m$ sufficiently large, we have

$$a_s\tilde{g}_0(m) + b_s\tilde{h}_0(m) = 4\pi^2 m^2 R_c^2\cos(2\pi m R_c)a_s + 4\pi^2 m^2 R_c\cos(2\pi m R_c)b_s + \mathcal{O}(m)$$

and by only considering the leading order term we obtain the condition

$$R_c\cos(2\pi m R_c)a_s + \cos(2\pi m R_c)b_s \leqslant 0.$$

Note that there exist infinitely many $m \in \mathbb{N}$ such that $\cos(2\pi m R_c) > 0$ and such that $\cos(2\pi m R_c) < 0$, independently of the choice of $R_c \in (0, 0.5)$. Hence, we can conclude $a_s R_c + b_s = 0$. In this case, the second leading order term of $\Re(\lambda_2(m))$ vanishes by (4.47) and thus, it is sufficient to consider $\Re(\lambda_1(m))$ and the first term of $\Re(\lambda_2(m))$ in (4.38). Applying Lemma 3 together with Remark 13 for $R_c \in (0, 0.5)$ to the linear force coefficients $f_l^\varepsilon, f_s^\varepsilon$ in (4.32) results in the stability conditions

$$a_l < -\frac{2b_l}{R_c} \quad\text{and}\quad a_s < -\frac{b_s}{R_c} \tag{4.48}$$

for any $\varepsilon > 0$ which are necessary for the nonnegativity of $\Re(\lambda_1(m))$ and the (first) leading order term of $\Re(\lambda_2(m))$. Hence, the single straight vertical line is unstable for $R_c \in (0, 0.5)$ and $0 < \varepsilon \ll R_c$, both in the continuum limit $N \to \infty$ and for any

$N \in \mathbb{N}$ sufficiently large. Similarly, we obtain instability of straight vertical line patterns for force coefficients $f_s^\varepsilon, f_l^\varepsilon$ for $R_c \in (0, 0.5)$ in the limit $\varepsilon \to 0$. $\qquad \square$

**Remark 14.** *For $R_c = 0.5$, we cannot conclude stability/instability of the straight vertical line for the linear force coefficients in (4.32) with $a_s = -\frac{b_s}{R_c}$, while we can conclude instability for $a_s \neq -\frac{b_s}{R_c}$. To see this, note that for $R_c = 0.5$ the calculations in the proof of Proposition 7 imply $a_s = -\frac{b_s}{R_c}$ as a necessary condition for stability; from Lemma 3 we obtain*

$$a_l \leqslant -\frac{2b_l}{R_c} \quad and \quad a_s \leqslant -\frac{b_s}{R_c},$$

*and together with the condition that $f_s^\varepsilon$ is purely repulsive we get the necessary conditions*

$$a_l \leqslant -\frac{2b_l}{R_c} \quad and \quad a_s = -\frac{b_s}{R_c} \tag{4.49}$$

*for the stability of the straight vertical line. Note that the conditions (4.49) are consistent with each other since $a_l, a_s < 0$ and $b_l, b_s > 0$ by Assumption 6 and it is possible to choose the parameters $a_l, a_s, b_l, b_s$ in such a way that both (4.49) and the assumptions on the force coefficients $f_s^\varepsilon, f_l^\varepsilon$ in Assumption 6 are satisfied. In this case, we have*

$$f_s^\varepsilon(s) + s(f_s^\varepsilon)'(s) = a_s(2s - 0.5)$$

*for $s \in [0, 0.5 - \varepsilon]$ with $a_s < 0$ and*

$$f_s^\varepsilon(s) + s(f_s^\varepsilon)'(s) = -a_s \frac{(s - R_c)^3}{\varepsilon^2} - 2a_s \frac{(s - R_c)^2}{\varepsilon} - 3a_s \frac{s(s - R_c)^2}{\varepsilon^2} - 4a_s \frac{s(s - R_c)}{\varepsilon}$$

*for $s \in [0.5 - \varepsilon, 0.5]$ by Assumption 6. Clearly, the leading order term of $\Re(\lambda_2(m))$ vanishes in the high wave limit $m \to \infty$ and lower order terms in $\varepsilon$ have to be considered. An easy computation reveals that*

$$\lim_{m \to \infty} \Re(\lambda_2(m)) = 2 \int_0^{0.5} f_s^\varepsilon(s) + s(f_s^\varepsilon)'(s) = 0 \tag{4.50}$$

*for any $\varepsilon > 0$ and as $\varepsilon \to 0$. Further note that using (4.50), $\Re(\lambda_2(m))$ reduces to*

$$\Re(\lambda_2(m)) = -2 \int_0^{0.5} (f_s^\varepsilon(s) + s(f_s^\varepsilon)'(s)) \cos(2\pi ms) \, \mathrm{d}s.$$

*We obtain*

$$\int_0^{0.5-\varepsilon} a_s(2s - 0.5)\cos(2\pi ms)\,\mathrm{d}s = \begin{cases} -0.5a_s\varepsilon + a_s\varepsilon^2 + \mathcal{O}(\varepsilon^3), & m \in 2\mathbb{N}, \\ -\frac{a_s}{\pi^2 m^2} + 0.5a_s\varepsilon - a_s\varepsilon^2 + \mathcal{O}(\varepsilon^3), & m \in 2\mathbb{N}+1, \end{cases}$$

$$-a_s\int_{0.5-\varepsilon}^{0.5}\left(\frac{(s - R_c)^3}{\varepsilon^2} + 2\frac{(s - R_c)^2}{\varepsilon}\right)\cos(2\pi ms)\,\mathrm{d}s = \begin{cases} -\frac{5}{12}a_s\varepsilon^2 + \mathcal{O}(\varepsilon^3), & m \in 2\mathbb{N}, \\ \frac{5}{12}a_s\varepsilon^2 + \mathcal{O}(\varepsilon^3), & m \in 2\mathbb{N}+1, \end{cases}$$

$$-3a_s\int_{0.5-\varepsilon}^{0.5}\frac{s\,(s - R_c)^2}{\varepsilon^2}\cos(2\pi ms)\,\mathrm{d}s = \begin{cases} -0.5a_s\varepsilon + \frac{3}{4}a_s\varepsilon^2 + \mathcal{O}(\varepsilon^3), & m \in 2\mathbb{N}, \\ 0.5a_s\varepsilon - \frac{3}{4}a_s\varepsilon^2 + \mathcal{O}(\varepsilon^3), & m \in 2\mathbb{N}+1, \end{cases}$$

*and*

$$-4a_s\int_{0.5-\varepsilon}^{0.5}\frac{s\,(s - R_c)}{\varepsilon}\cos(2\pi ms)\,\mathrm{d}s = \begin{cases} a_s\varepsilon - \frac{4}{3}a_s\varepsilon^2 + \mathcal{O}(\varepsilon^3), & m \in 2\mathbb{N}, \\ -a_s\varepsilon + \frac{4}{3}a_s\varepsilon^2 + \mathcal{O}(\varepsilon^3), & m \in 2\mathbb{N}+1, \end{cases}$$

*implying that*

$$\int_0^{0.5}\left(f_s^\varepsilon(s) + s(f_s^\varepsilon)'(s)\right)\cos(2\pi ms)\,\mathrm{d}s = \begin{cases} \mathcal{O}(\varepsilon^3), & m \in 2\mathbb{N}, \\ -\frac{a_s}{\pi^2 m^2} + \mathcal{O}(\varepsilon^3), & m \in 2\mathbb{N}+1. \end{cases}$$

*Since the real part of the largest eigenvalue $\Re(\lambda_2(m))$ is zero in the high wave number limit and it vanishes in the limit $\varepsilon \to 0$ for any $m \in \mathbb{N}$, we cannot conclude stability/instability of the straight vertical line for $R_c = 0.5$ and $\varepsilon > 0$ or $\varepsilon \to 0$ in the continuum limit $N \to \infty$ or any $N \in \mathbb{N}$ sufficiently large. However, the numerical results in Section 4.5.2 suggest instability for $\varepsilon > 0$ and in the limit $\varepsilon \to 0$.*

Since we have the relations $f_l^\varepsilon = f_A^\varepsilon + f_R^\varepsilon$ and $f_s^\varepsilon = \chi f_A^\varepsilon + f_R^\varepsilon$ between the force coefficients $f_l^\varepsilon, f_s^\varepsilon$ in the general force formulation (4.4) and the total force (4.3) in the Kücken-Champod model with repulsive and attractive force coefficients $f_R^\varepsilon$ and $f_A^\varepsilon$, respectively, we have

$$a_l = a_A + a_R, \quad a_s = \chi a_A + a_R, \quad b_l = b_A + b_R, \quad b_s = \chi b_A + b_R.$$

Hence, Proposition 7 leads to a similar statement for the forces in the Kücken-Champod model.

**Corollary 5.** *For $R_c \in (0, 0.5)$ the single straight vertical line is an unstable steady state of* (4.6) *for any $N \in \mathbb{N}$ sufficiently large and for the continuum limit $N \to \infty$, where the forces are of the form* (4.4) *for any choice of parameters in the definition of the linear coefficient functions $f_R^\varepsilon, f_A^\varepsilon$ in* (4.33) *with $0 < \varepsilon \ll R_c$ or $\varepsilon \to 0$. For $R_c = 0.5$, the condition*

$$a_A + a_R \leqslant -\frac{2\,(b_A + b_R)}{R_c} \quad and \quad \chi a_A + a_R = -\frac{\chi b_A + b_R}{R_c}$$

*in addition to the assumptions on $a_A, a_R, b_A, b_R$ in Remark 12 is necessary for the stability of the single straight vertical line for force coefficients $f_R^\varepsilon, f_A^\varepsilon$, where $0 < \varepsilon \ll R_c$ or $\varepsilon \to 0$. This does not guarantee the stability/instability of the straight vertical line for force coefficients $f_R^\varepsilon, f_A^\varepsilon$ with $0 < \varepsilon \ll R_c$ or $\varepsilon \to 0$ for $R_c = 0.5$ and $N \in \mathbb{N}$ sufficiently large or in the continuum limit $N \to \infty$.*

### 4.4.2 Algebraically decaying force coefficients

Since the straight vertical line is unstable for $N \in \mathbb{N}$ sufficiently large and for $N \to \infty$ for the differentiable force coefficient $f_s^\varepsilon$, defined in (4.32) along $s$, which is linear on $[0, R_c - \varepsilon]$ for $R_c \in (0, 0.5)$ and $\varepsilon > 0$, we consider faster decaying force coefficients along $s$ in the following. In this section we consider

$$f_s(|d|) = \frac{c}{(1 + a|d|)^b}$$

for $a > 0$, $b > 0$, and $c > 0$. To obtain a differentiable force coefficient $f_s^\varepsilon$ on $(0, \infty)$ we consider the modification in (4.7), i.e.

$$f_s^\varepsilon(|d|) = \begin{cases} \frac{c}{(1+a|d|)^b}, & |d| \in [0, R_c - \varepsilon], \\ -\frac{abc}{(1+a(R_c-\varepsilon))^{b+1}} \left( \frac{(|d|-R_c)^3}{\varepsilon^2} + \frac{(|d|-R_c)^2}{\varepsilon} \right) \\ \quad + \frac{c}{(1+a(R_c-\varepsilon))^b} \left( 2\frac{(|d|-R_c)^3}{\varepsilon^3} + 3\frac{(|d|-R_c)^2}{\varepsilon^2} \right), & |d| \in (R_c - \varepsilon, R_c), \\ 0, & |d| \geqslant R_c, \end{cases}$$

where $R_c \in (0, 0.5]$. Note that for this algebraically decaying force coefficient $f_s^\varepsilon$, the necessary condition $f_s^\varepsilon(R_c) = 0$ in (4.28) for high wave number stability of a straight vertical line is satisfied. To guarantee that the term $a|d|$ for $|d| \in [0, R_c]$ dominates the denominator and to avoid too large jumps we require $a \gg 1$ additionally. The assumption $a \gg 1$ also guarantees that $f_s^\varepsilon(R_c - \varepsilon) \ll 1$. In this case, differences

between the adaptation $f_s^\varepsilon$ and the algebraically decaying force coefficient $f_s$, and their derivatives $(f_s^\varepsilon)'$ and $f_s'$, are small. Without loss of generality we can assume that $c = 1$ since this positive multiplicative constant leads to a rescaled stability condition but is not relevant for change of sign of the eigenvalues. Hence, we consider the algebraically decaying force coefficient

$$
f_s^\varepsilon(|d|) = \begin{cases}
\frac{1}{(1+a|d|)^b}, & |d| \in [0, R_c - \varepsilon], \\
-\frac{ab}{(1+a(R_c-\varepsilon))^{b+1}} \left( \frac{(|d|-R_c)^3}{\varepsilon^2} + \frac{(|d|-R_c)^2}{\varepsilon} \right) & \\
\quad + \frac{1}{(1+a(R_c-\varepsilon))^b} \left( 2\frac{(|d|-R_c)^3}{\varepsilon^3} + 3\frac{(|d|-R_c)^2}{\varepsilon^2} \right), & |d| \in (R_c - \varepsilon, R_c), \\
0, & |d| \geqslant R_c
\end{cases}
\tag{4.51}
$$

in the following.

**Proposition 8.** *For the single straight vertical line to be a stable steady state of* (4.6) *with forces of the form* (1.8) *for any $n \in \mathbb{N}$ sufficiently large and for the continuum limit $N \to \infty$ with algebraically decaying force coefficients $f_s^\varepsilon$ of the form* (4.51) *it is necessary that*

$$
b > 1 \quad and \quad \frac{2}{a(b-1)} < R_c.
$$

*Proof.* Because of the definition of the eigenvalues (4.24) we consider

$$
\int_0^{R_c} \left( f_s^\varepsilon(s) + s(f_s^\varepsilon)'(s) \right) \left( 1 - \cos(-2\pi ms) \right) \mathrm{d}s
$$
$$
= \int_0^{R_c-\varepsilon} \frac{1}{(1+as)^{b+1}} \left( 1 + as(1-b) \right) \left( 1 - \cos(-2\pi ms) \right) \mathrm{d}s + \mathcal{O}(\varepsilon).
\tag{4.52}
$$

The linear function $1 + as(1-b)$ is positive for $s \in (0, s_0)$ and negative for $s \in (s_0, R_c - \varepsilon)$ for all $\varepsilon > 0$, where

$$
s_0 = \frac{1}{a(b-1)} \in (0, R_c),
$$

implying $b > 1$. Note that the integral on the right-hand side of (4.52) can be rewritten as

$$
\int_0^{R_c-\varepsilon} g(s)\,\mathrm{d}s = \int_0^{s_0} g(s)\,\mathrm{d}s + \int_{s_0}^{R_c-\varepsilon} g(s)\,\mathrm{d}s
$$

142

for any $\varepsilon > 0$, where

$$g(s) = \frac{1}{(1 + as)^{b+1}} \left(1 + as(1 - b)\right) \left(1 - \cos\left(-2\pi ms\right)\right)$$

is nonnegative on $[0, s_0]$ and not positive on $[s_0, R_c - \varepsilon]$ for any $\varepsilon > 0$ by the definition of $s_0$ and the fact that $1 - \cos(-2\pi ms) \in (0, 2)$. Setting

$$h(s) = \frac{1}{(1 + as)^{b+1}},$$

note that $h(R_c) < h(s_0) < h(0) = 1$. A lower bound of the integral can be obtained by estimating $h(s)$ on $[0, s_0]$ by $h(s_0)$ due to the nonnegativity of the integrand, and since the integrand changes sign at $s_0$ the factor $h(s)$ can be replaced by its maximum on $[s_0, R_c - \varepsilon]$ for $\varepsilon > 0$, i.e. by $h(s_0)$. Hence, a lower bound of the integral in (4.52) is given by

$$\frac{1}{(1 + as_0)^{b+1}} \int_0^{R_c - \varepsilon} \left(1 + as(1 - b)\right) \left(1 - \cos\left(-2\pi ms\right)\right) \mathrm{d}s + \mathcal{O}(\varepsilon)$$

$$= \frac{1}{(1 + as_0)^{b+1}} \left(\frac{2\pi m \left(\pi m (R_c - \varepsilon) \left(p(R_c - \varepsilon) + 2q\right)\right)}{4\pi^2 m^2}\right.$$

$$\left. + \frac{p - p\cos\left(2\pi m(R_c - \varepsilon)\right) - 2\pi m \left(p(R_c - \varepsilon) + q\right)\sin\left(2\pi m(R_c - \varepsilon)\right)}{4\pi^2 m^2}\right) + \mathcal{O}(\varepsilon)$$

with $p = a(1 - b)$ and $q = 1$, where the explicit computation is analogous to the discussion of the linear force coefficients in (4.41). For large values of $m$ the first term of the above right-hand side dominates and we require

$$pR_c + 2q = a(1 - b)R_c + 2 < 0$$

for all $\varepsilon > 0$. This concludes the proof. $\qquad\square$

In the following, we can restrict ourselves to algebraically decaying force coefficients (4.51) with $a > 0$, $b > 1$ due to Proposition 8. We show that the straight vertical line (4.14) is an unstable steady state for any $N \in \mathbb{N}$ sufficiently large and in the continuum limit $N \to \infty$ in this case. Due to the definition of the eigenvalues in (4.24) in Theorem 1 it is sufficient to show that there exists $m \in \mathbb{N}$ such that

$$0 < \int_0^{R_c - \varepsilon} \left(f_s^\varepsilon(s) + s(f_s^\varepsilon)'(s)\right) \left(1 - \cos\left(-2\pi ms\right)\right) \mathrm{d}s$$

143

for all $0 < \varepsilon \ll R_c$. This is equivalent to showing that there exists $m \in \mathbb{N}$ such that

$$0 < \lim_{\varepsilon \to 0} \int_0^{R_c - \varepsilon} \frac{1}{(1 + as)^{b+1}} \left(1 + as(1 - b)\right) \left(1 - \cos\left(-2\pi m s\right)\right) \mathrm{d}s. \qquad (4.53)$$

is satisfied.

**Lemma 4.** *For any $a > 0$, $b > 1$, and $R_c \in (0, 0.5]$ there exists $m \in \mathbb{N}$ such that* (4.53) *is satisfied.*

*Proof.* We denote the incomplete Gamma function by

$$\Gamma(y, z) = \int_z^\infty s^{y-1} \exp(-s) \, \mathrm{d}s$$

for $y \in \mathbb{R}$ and $z \in \mathbb{C}$. Then the right-hand side of (4.53) can be written as

$$
\begin{aligned}
-\frac{1}{4a\pi m \left(1 + aR_c\right)^b} \Bigg( & 2a\sin(-2\pi m R_c) \\
& + \Re\Bigg[ \sin\left(\frac{2\pi m}{a}\right) m^{b+1} \left( c_1\Gamma\left(-b, \frac{2i\pi m}{a}\right) + c_2\Gamma\left(-b, \frac{2i\pi(1 + aR_c)m}{a}\right) \right) \\
& + \sin\left(\frac{2\pi m}{a}\right) m^b \left( c_3\Gamma\left(1 - b, \frac{2i\pi m}{a}\right) + c_4\Gamma\left(1 - b, \frac{2i\pi(1 + aR_c)m}{a}\right) \right) \\
& + \cos\left(\frac{2\pi m}{a}\right) m^{b+1} \left( c_5\Gamma\left(-b, \frac{2i\pi m}{a}\right) + c_6\Gamma\left(-b, \frac{2i\pi(1 + aR_c)m}{a}\right) \right) \\
& + \cos\left(\frac{2\pi m}{a}\right) m^b \left( c_7\Gamma\left(1 - b, \frac{2i\pi m}{a}\right) + c_8\Gamma\left(1 - b, \frac{2i\pi(1 + aR_c)m}{a}\right) \right) \Bigg] \Bigg)
\end{aligned}
$$

for constants $c_i \in \mathbb{C}, i = 1, \dots, 8$, depending on $a, b$, and $R_c$, but independent of $m$ where not all constants $c_i$ are equal to zero. Note that all incomplete Gamma functions above are of the form $\Gamma(-y, iz)$ for $y, z \in \mathbb{R}$ with $y, z > 0$. Integration by parts yields

$$\Gamma(-y, iz) = (iz)^{-y-1} \exp(-iz) + (-y - 1)\Gamma(-y - 1, iz),$$

where

$$|\Gamma(-y - 1, iz)| = \left| \int_{iz}^\infty s^{-y-2} \exp(-s) \, \mathrm{d}s \right| \leqslant |(iz)^{-y-2} \exp(-iz)|.$$

In particular, we have

$$\Gamma(-y, iz) = (iz)^{-y-1} \exp(-iz) \left(1 + \mathcal{O}((iz)^{-1})\right),$$

144

implying

$$\Re(\Gamma(-y, iz)) = \tilde{c} z^{-y-1} \left(1 + \mathcal{O}(z^{-1})\right),$$

where $\tilde{c} = \Re(i^{-y-1} \exp(-iz)) \in \mathbb{R}$. This leads to the approximation

$$\Re\left[\sin\left(\frac{2\pi m}{a}\right) m^{b+1} \left(c_1 \Gamma\left(-b, \frac{2i\pi m}{a}\right) + c_2 \Gamma\left(-b, \frac{2i\pi(1 + aR_c)m}{a}\right)\right)\right.$$
$$\left. + \sin\left(\frac{2\pi m}{a}\right) m^b \left(c_3 \Gamma\left(1 - b, \frac{2i\pi m}{a}\right) + c_4 \Gamma\left(1 - b, \frac{2i\pi(1 + aR_c)m}{a}\right)\right)\right]$$
$$= \tilde{c}_1 \sin\left(\frac{2\pi m}{a}\right) \left(1 + \mathcal{O}(m^{-1})\right)$$

for some constant $\tilde{c}_1 \in \mathbb{R}$. The other terms of the right-hand side of (4.53) can be rewritten in a similar way, resulting in

$$-\frac{1}{4a\pi m (1 + aR_c)^b} \left(-2a\sin(2\pi m R_c) + \tilde{c}_1 \sin\left(\frac{2\pi m}{a}\right) + \tilde{c}_2 \cos\left(\frac{2\pi m}{a}\right) + \mathcal{O}(m^{-1})\right)$$

for constants $\tilde{c}_1, \tilde{c}_2 \in \mathbb{R}$, independent of $m$. Note that there exist infinitely many $m \in \mathbb{N}$ such that $\tilde{c}_1 \sin\left(\frac{2\pi m}{a}\right) + \tilde{c}_2 \cos\left(\frac{2\pi m}{a}\right) > 0$ and such that $\tilde{c}_1 \sin\left(\frac{2\pi m}{a}\right) + \tilde{c}_2 \cos\left(\frac{2\pi m}{a}\right) < 0$. If $R_c = \frac{1}{a}$, the second factor consists of the sum of a sine and a cosine function of the same period length and hence for $R_c \in (0, 0.5]$ given, there exists $m \in \mathbb{N}$ such that the second factor is negative and the leading order term of (4.53) is positive. If the first term in the second factor is of different period length as the second and third summand, there also exists $m \in \mathbb{N}$ such that the second factor is negative. In particular, this implies that there exists an $m \in \mathbb{N}$ such that (4.53) is satisfied. $\qquad\square$

**Corollary 6.** *For any cutoff radius $R_c \in (0, 0.5]$ the single straight vertical line is an unstable steady state of (4.6) for any $N \in \mathbb{N}$ sufficiently large and for the continuum limit $N \to \infty$ with forces of the form (1.8) with algebraically decaying force coefficients $f_s^\varepsilon$ of the form (4.51) with $b > 0$ and for any $\varepsilon > 0$ or in the limit $\varepsilon \to 0$.*

### 4.4.3 Exponential force coefficients

In this section we consider exponentially decaying force coefficients along $s$ and short-range repulsive, long-range attractive forces along $l$ such that the necessary condition (4.28) for high wave number stability is satisfied.

To express the force coefficient along $l$ in terms of exponentially decaying functions we consider

$$
f_l^\varepsilon(|d|) = \begin{cases}
c_{l_1} \exp(-e_{l_1}|d|) + c_{l_2}\exp(-e_{l_2}|d|), & |d| \in [0, R_c - \varepsilon], \\
\sum_{j=1}^2 (-\varepsilon c_{l_j} e_{l_j} + 2c_{l_j}) \exp(-e_{l_j}(R_c - \varepsilon)) \frac{(|d|-R_c)^3}{\varepsilon^3} & \\
\quad + \sum_{j=1}^2 (-\varepsilon c_{l_j} e_{l_j} + 3c_{l_j}) \exp(-e_{l_j}(R_c - \varepsilon)) \frac{(|d|-R_c)^2}{\varepsilon^2}, & |d| \in (R_c - \varepsilon, R_c), \\
0, & |d| \geqslant R_c,
\end{cases}
$$

$$(4.54)$$

for parameters $c_{l_1}, c_{l_2}, e_{l_1}$ and $e_{l_2}$ with $e_{l_1} > 0$ and $e_{l_2} > 0$. Note that exponentially decaying functions are either purely repulsive or purely attractive, depending on the sign of the multiplicative parameter. Since we require $f_l^\varepsilon$ to be short-range repulsive, long-range attractive we consider the sum of two exponentially decaying functions here. Without loss of generality we assume that the first summand in (4.54) is repulsive and the second one is attractive, i.e. $c_{l_1} > 0 > c_{l_2}$. To guarantee that $f_l^\varepsilon$ is short-range repulsive we require $c_{l_1} > |c_{l_2}|$. For long-range attractive forces we require that the second term decays slower, i.e. $e_{l_1} > e_{l_2}$. These assumptions lead to the parameter choice

$$c_{l_1} > 0 > c_{l_2}, \quad c_{l_1} > |c_{l_2}|, \quad \text{and} \quad e_{l_1} > e_{l_2} > 0. \tag{4.55}$$

Note that we have

$$
\int_0^{R_c} f_l^\varepsilon(s)\left(1 - \cos\left(-2\pi m s\right)\right) \mathrm{d}s = \int_0^{R_c - \varepsilon} f_l^\varepsilon(s)\left(1 - \cos\left(-2\pi m s\right)\right) \mathrm{d}s + \mathcal{O}(\varepsilon)
$$

due to the boundedness of $f_l^\varepsilon$ on $[R_c - \varepsilon, R_c]$ and hence it is sufficient to consider the integral on $[0, R_c - \varepsilon]$ for $\varepsilon > 0$ sufficiently small and in the limit $\varepsilon \to 0$. Further note that for constants $c, e_l \in \mathbb{R}$ we obtain

$$
\int_0^{R_c - \varepsilon} c\exp(-e_l s)\,\mathrm{d}s = (1 - \exp(-e_l(R_c - \varepsilon)))\,\frac{c}{e_l}.
$$

Hence, we require

$$
(1 - \exp(-e_{l_1}(R_c - \varepsilon)))\,\frac{c_{l_1}}{e_{l_1}} + (1 - \exp(-e_{l_2}(R_c - \varepsilon)))\,\frac{c_{l_2}}{e_{l_2}} \leqslant 0
$$

for all $\varepsilon > 0$ as in the necessary condition for high wave number stability, implying

$$\frac{c_{l_1}}{e_{l_1}} \leqslant \frac{|c_{l_2}|}{e_{l_2}}.$$

Since

$$\int_0^{R_c - \varepsilon} c_{l_1} \exp(-e_{l_1} s) \left(1 - \cos\left(-2\pi m s\right)\right) \mathrm{d}s > 0\,,$$

$$\int_0^{R_c - \varepsilon} c_{l_2} \exp(-e_{l_2} s) \left(1 - \cos\left(-2\pi m s\right)\right) \mathrm{d}s < 0$$

for all $\varepsilon > 0$ and $m \in \mathbb{N}$ the parameters $c_{l_1}, c_{l_2}, e_{l_1}, c_{l_2}$ in (4.55) can clearly be chosen in such a way that

$$\int_0^{R_c - \varepsilon} f_l^\varepsilon(s) \left(1 - \cos\left(-2\pi m s\right)\right) \mathrm{d}s \leqslant 0 \qquad (4.56)$$

is satisfied for all $m \in \mathbb{N}$ and $0 < \varepsilon \ll R_c$, where $f_l^\varepsilon$ is defined in (4.54) with a cutoff radius $R_c \in (0, 0.5]$. Note that the adaptation $f_l^\varepsilon$ of $f_l$ is not negligible. However, due to the concentration of the particles along a straight vertical axis, this adaptation does not change the overall dynamics.

For the purely repulsive force coefficient $f_s^\varepsilon$ we may consider a force coefficient of the form

$$f_s^\varepsilon \colon \mathbb{R}_+ \to \mathbb{R},$$

$$f_s^\varepsilon(|d|) = \begin{cases} c\exp(-e_s|d|), & |d| \in [0, R_c - \varepsilon], \\ -ce_s \exp(-e_s(R_c - \varepsilon)) \left(\frac{(|d| - R_c)^3}{\varepsilon^2} + \frac{(|d| - R_c)^2}{\varepsilon}\right) \\ \quad + c\exp(-e_s(R_c - \varepsilon)) \left(2\frac{(|d| - R_c)^3}{\varepsilon^3} + 3\frac{(|d| - R_c)^2}{\varepsilon^2}\right), & |d| \in (R_c - \varepsilon, R_c), \\ 0, & |d| \geqslant R_c, \end{cases}$$

by considering (4.7) for exponentially decaying force coefficients. Since

$$\Re(\lambda_2(m)) = 2\int_0^{R_c - \varepsilon} \left(f_s^\varepsilon(s) + (f_s^\varepsilon)'(s)s\right) \left(1 - \cos\left(-2\pi m s\right)\right) \mathrm{d}s + \mathcal{O}(\varepsilon),$$

we require the nonpositivity of $\Re(\lambda_2(m))$. Note that

$$\int_0^{R_c - \varepsilon} \left(f_s^\varepsilon(s) + (f_s^\varepsilon)'(s)s\right) \left(1 - \cos\left(-2\pi m s\right)\right) \mathrm{d}s$$

$$= (R_c - \varepsilon) \exp(-e_s(R_c - \varepsilon)) - \frac{8e_s\pi^2 m^2}{(4\pi^2 m^2 + e_s^2)^2}$$
$$- \frac{\exp(-e_s(R_c - \varepsilon))}{(4\pi^2 m^2 + e_s^2)^2} \Big[ e_s(4\pi^2 m^2(e_s(R_c - \varepsilon) - 2) + e_s^3(R_c - \varepsilon)) \cos(2\pi m(R_c - \varepsilon))$$
$$- 2\pi m(4\pi^2 m^2(e_s(R_c - \varepsilon) - 1) + e_s^2(e_s(R_c - \varepsilon) + 1)) \sin(2\pi m(R_c - \varepsilon))$$
$$- (R_c - \varepsilon)(4\pi^2 m^2 + e_s^2)^2 \Big],$$

implying that we have $\int_0^{R_c - \varepsilon} (f_s^\varepsilon(s) + (f_s^\varepsilon)'(s)s) \left(1 - \cos\left(-2\pi m s\right)\right) \mathrm{d}s > 0$ for any $\varepsilon > 0$ and $m \in \mathbb{N}$ sufficiently large, i.e. high wave stability cannot be achieved. However, note that $\exp(-e_s R_c)$ can be assumed to be very small for $e_s > 0$ sufficiently large. This motivates us to consider a force coefficient function of the form

$$f_s^\varepsilon \colon \mathbb{R}_+ \to \mathbb{R},$$
$$f_s^\varepsilon(|d|) = \begin{cases} c\exp(-e_s|d|) - c\exp(-e_s(R_c - \varepsilon)), & |d| \in [0, R_c - \varepsilon], \\ -ce_s \exp(-e_s(R_c - \varepsilon)) \left( \frac{(|d| - R_c)^3}{\varepsilon^2} + \frac{(|d| - R_c)^2}{\varepsilon} \right), & |d| \in (R_c - \varepsilon, R_c), \\ 0, & |d| \geqslant R_c, \end{cases}$$
(4.57)

with $c > 0$ and $e_s > 0$. Here, the first term in (4.57) represents the exponential decay of the force coefficient. To approximate the high wave number stability condition, we require $f_s(R_c - \varepsilon) = 0$ which can be guaranteed by subtracting the constant $\exp(-e_s(R_c - \varepsilon))$. Note that we can choose $e_s \gg 1$ such that $\exp(-e_s(R_c - \varepsilon))$ is a small positive number. Subtracting the constant $c\exp(-e_s(R_c - \varepsilon))$ as in (4.57) leads to $f_s^\varepsilon(R_c - \varepsilon) = 0$. This additional constant only changes the force coefficient $f_s^\varepsilon$ slightly and does not change its derivative $(f_s^\varepsilon)'$ on $[0, R_c - \varepsilon]$, i.e. $f_s' = (f_s^\varepsilon)'$ on $[0, R_c - \varepsilon]$. Note that the differences between $f_s^\varepsilon$ and $f_s$, and $(f_s^\varepsilon)'$ and $f_s'$ on $[R_c - \varepsilon, R_c]$ are negligible provided $e_s > 0$ is chosen sufficiently large such that $e_s \exp(-e_s(R_c - \varepsilon)) \ll 1$. Thus, we make the following assumption in the following.

**Assumption 7.** *We assume that the purely repulsive, exponentially decaying force coefficient $f_s$ along $s$ is given by (4.57), i.e.*

$$f_s^\varepsilon \colon \mathbb{R}_+ \to \mathbb{R},$$
$$f_s^\varepsilon(|d|) = \begin{cases} c\exp(-e_s|d|) - c\exp(-e_s(R_c - \varepsilon)), & |d| \in [0, R_c - \varepsilon], \\ -ce_s \exp(-e_s(R_c - \varepsilon)) \left( \frac{(|d| - R_c)^3}{\varepsilon^2} + \frac{(|d| - R_c)^2}{\varepsilon} \right), & |d| \in (R_c - \varepsilon, R_c), \\ 0, & |d| \geqslant R_c, \end{cases}$$

*where $c > 0$ and $e_s \gg 1$. For the forces along $l$ we either consider linear or exponentially decaying force coefficients. For a linear force coefficient we consider (4.49), i.e.*

$$
f_l^\varepsilon(|d|) := \begin{cases}
a_l|d| + b_l, & |d| \in [0, R_c - \varepsilon], \\
(2b_l + 2R_c a_l - a_l\varepsilon)\frac{(|d|-R_c)^3}{\varepsilon^3} \\
\quad + (3b_l + 3R_c a_l - 2a_l\varepsilon)\frac{(|d|-R_c)^2}{\varepsilon^2}, & |d| \in (R_c - \varepsilon, R_c), \\
0, & |d| \geqslant R_c,
\end{cases}
$$

*where we assume that the parameters $a_l, b_l$ satisfy the sign conditions $a_l < 0, \ b_l > 0$ in Assumption 6 as well as the necessary stability condition along $l$ in (4.49). For an exponentially decaying force coefficient $f_l^\varepsilon$ we assume that $f_l^\varepsilon$ is of the form (4.54), i.e.*

$$
f_l^\varepsilon(|d|) = \begin{cases}
c_{l_1}\exp(-e_{l_1}|d|) + c_{l_2}\exp(-e_{l_2}|d|), & |d| \in [0, R_c - \varepsilon], \\
\sum_{j=1}^2(-\varepsilon c_{l_j}e_{l_j} + 2c_{l_j})\exp(-e_{l_j}(R_c - \varepsilon))\frac{(|d|-R_c)^3}{\varepsilon^3} \\
\quad + \sum_{j=1}^2(-\varepsilon c_{l_j}e_{l_j} + 3c_{l_j})\exp(-e_{l_j}(R_c - \varepsilon))\frac{(|d|-R_c)^2}{\varepsilon^2}, & |d| \in (R_c - \varepsilon, R_c), \\
0, & |d| \geqslant R_c,
\end{cases}
$$

*for parameters*

$$
c_{l_1} > 0 > c_{l_2}, \quad c_{l_1} > |c_{l_2}|, \quad \text{and} \quad e_{l_1} > e_{l_2} > 0
$$

*as in (4.54)–(4.55) such that the necessary stability condition (4.56) for a straight vertical line is satisfied for all $m \in \mathbb{N}$ and $0 < \varepsilon \ll R_c$.*

**Theorem 4.** *For the cutoff radius $R_c = 0.5$, the straight vertical line is stable for the particle model (4.6) for any $N \in \mathbb{N}$ sufficiently large with the exponentially decaying force coefficient $f_s^\varepsilon$ in (4.57) along $s$ and a linear or exponentially decaying force coefficient $f_l^\varepsilon$ as in Assumption 7 along $l$ in the limit $\varepsilon \to 0$. For $R_c \in (0, 0.5)$ the straight vertical line is an unstable steady state to (4.6) for any $N \in \mathbb{N}$ sufficiently large and for the continuum limit $N \to \infty$ for any exponential decay $e_s > 0$ in the limit $\varepsilon \to 0$. For any $0 < \varepsilon \ll R_c$, the straight vertical lime is an unstable steady state for any $R_c \in (0, 0.5]$.*

*Proof.* Due to the assumptions on $f_l^\varepsilon$ in Assumption 7 the real part for the first

eigenvalue in (4.24), given by

$$\Re(\lambda_1(m)) = 2 \int_0^{R_c - \varepsilon} f_l^\varepsilon(s) \left(1 - \cos\left(-2\pi m s\right)\right) ds + \mathcal{O}(\varepsilon),$$

is not positive for any $m \in \mathbb{N}$ and any $0 < \varepsilon \ll R_c$ sufficiently small. The real part of the second eigenvalue (4.24) is given by

$$\Re(\lambda_2(m)) = 2 \int_0^{R_c - \varepsilon} \left(f_s^\varepsilon(s) + (f_s^\varepsilon)'(s)s\right) \left(1 - \cos\left(-2\pi m s\right)\right) ds + \mathcal{O}(\varepsilon).$$

For the nonpositivity of $\Re(\lambda_2(m))$ it is sufficient to require

$$\int_0^{R_c - \varepsilon} \left(f_s^\varepsilon(s) + s(f_s^\varepsilon)'(s)\right) \left(1 - \cos(2\pi m s)\right) ds \leqslant 0, \tag{4.58}$$

for any $\varepsilon > 0$ sufficiently small, where the left-hand side is given by

$$c \int_0^{R_c - \varepsilon} \left(\exp(-e_s s)(1 - e_s s) - \exp(-e_s(R_c - \varepsilon))\right) \left(1 - \cos(2\pi m s)\right) ds$$
$$= -\frac{ce_s \exp\left(-e_s(R_c - \varepsilon)\right)}{2\pi m \left(e_s^2 + 4\pi^2 m^2\right)^2} \left[2\pi m e_s^3 (R_c - \varepsilon) \cos(2\pi m(R_c - \varepsilon))\right.$$
$$- \left(e_s^3 + 4\pi^2 e_s^2 m^2 (R_c - \varepsilon) + 12\pi^2 e_s m^2 + 16\pi^4 m^4 (R_c - \varepsilon)\right) \sin(2\pi m(R_c - \varepsilon))$$
$$\left. +16\pi^3 m^3 \exp\left(e_s(R_c - \varepsilon)\right) + 8\pi^3 m^3 \left(e_s(R_c - \varepsilon) - 2\right) \cos(2\pi m(R_c - \varepsilon))\right]. \tag{4.59}$$

For $R_c = 0.5$ we have $\lim_{\varepsilon \to 0} \sin(2\pi m(R_c - \varepsilon)) = 0$ and the right-hand side of (4.59) simplifies to $g_\varepsilon(m)h_\varepsilon(m)$ where

$$g_\varepsilon(m) = -\frac{ce_s \exp\left(-e_s(R_c - \varepsilon)\right)}{\left(e_s^2 + 4\pi^2 m^2\right)^2},$$
$$h_\varepsilon(m) = \left(e_s^3(R_c - \varepsilon) + 4\pi^2 m^2 (e_s(R_c - \varepsilon) - 2)\right) \cos(2\pi m(R_c - \varepsilon))$$
$$+ 8\pi^2 m^2 \exp\left(e_s(R_c - \varepsilon)\right).$$

For determining the limit $m \to \infty$ of $g_\varepsilon(m)h_\varepsilon(m)$ note that the leading order term of $g_\varepsilon$ is $m^{-4}$ while the highest order term of $h_\varepsilon$ is $m^2$, implying that the product $g_\varepsilon(m)h_\varepsilon(m)$, i.e. the right-hand side of (4.59), goes to zero as $m \to \infty$.

Note that for $R_c = 0.5$ we have

$$\lim_{\varepsilon \to 0} \cos(2\pi m(R_c - \varepsilon)) = \begin{cases} 1, & m \text{ even}, \\ -1, & m \text{ odd}. \end{cases}$$

Let us consider $e_s > 0$ with $e_s \leqslant 4$ first, i.e. $\lim_{\varepsilon \to 0} e_s(R_c - \varepsilon) \leqslant 2$. Then,

$$\lim_{\varepsilon \to 0} h_\varepsilon(m) = \begin{cases} e_s^3 R_c + 4\pi^2 m^2 \left(e_s R_c - 2 + 2 \exp\left(e_s R_c\right)\right), & m \text{ even}, \\ -e_s^3 R_c + 4\pi^2 m^2 \left(-e_s R_c + 2 + 2 \exp\left(e_s R_c\right)\right), & m \text{ odd}. \end{cases}$$

Note that $\lim_{\varepsilon \to 0} g_\varepsilon(m) < 0$ for all $m \in \mathbb{N}$ and $\lim_{\varepsilon \to 0} h_\varepsilon(m) > 0$ for all even $m$ since $2 \exp(e_s R_c) > 2$. For $m$ odd, note that the term in brackets is positive and a lower bound of $\lim_{\varepsilon \to 0} h_\varepsilon$ is given by

$$-16 e_s R_c + 4\pi^2 \left(-e_s R_c + 2 + 2 \exp\left(e_s R_c\right)\right) \geqslant 8\pi^2 \left(-e_s R_c + 1 + \exp\left(e_s R_c\right)\right),$$

which is clearly positive. Hence, $\lim_{\varepsilon \to 0} h_\varepsilon(m)$ is positive for all $m \in \mathbb{N}$ and, thus, we obtain $\lim_{\varepsilon \to 0} g_\varepsilon(m) h_\varepsilon(m) < 0$, provided $e_s \leqslant 4$ and $R_c = 0.5$. This implies that (4.58) is satisfied for all $m \in \mathbb{N}$ in this case.

Let us now consider $\lim_{\varepsilon \to 0} e_s(R_c - \varepsilon) > 2$ with $R_c = 0.5$. Note that a lower bound of $\lim_{\varepsilon \to 0} h_\varepsilon$ is obtained from $\lim_{\varepsilon \to 0} \cos(2\pi m(R_c - \varepsilon)) \geqslant -1$, leading to the upper bound

$$\lim_{\varepsilon \to 0} g_\varepsilon(m) \left[ -\left(e_s^3 R_c + 4\pi^2 m^2 (e_s R_c - 2)\right) + 8\pi^2 m^2 \exp\left(e_s R_c\right) \right]$$

of $\lim_{\varepsilon \to 0} g_\varepsilon(m) h_\varepsilon(m)$ since $g_\varepsilon(m) < 0$ for all $\varepsilon > 0$. This upper bound can be rewritten as

$$\lim_{\varepsilon \to 0} g_\varepsilon(m) \left[ -e_s^3 R_c + 4\pi^2 m^2 \left(-e_s R_c + 2 + 2 \exp\left(e_s R_c\right)\right) \right].$$

Note that $-e_s R_c + 2 + 2 \exp\left(e_s R_c\right) > 0$. Besides,

$$\frac{e_s^3 R_c}{4\pi^2 \left(-e_s R_c + 2 + 2 \exp\left(e_s R_c\right)\right)} < 1$$

is satisfied for all $e_s > 4$, implying

$$-e_s^3 R_c + 4\pi^2 m^2 \left(-e_s R_c + 2 + 2 \exp\left(e_s R_c\right)\right) > 0$$

for all $m \in \mathbb{N}$. Hence, the right-hand side of (4.59), i.e. $g_\varepsilon(m)h_\varepsilon(m)$, is negative for all $m \in \mathbb{N}$ in the limit $\varepsilon \to 0$. In particular, this shows that condition (4.58) is satisfied for all $m \in \mathbb{N}$ for $R_c = 0.5$.

For $R_c \in (0, 0.5]$ and $\varepsilon > 0$ we have $\sin(2\pi m(R_c - \varepsilon)) > 0$ for countably many $m \in \mathbb{N}$. In particular, there exists $\delta > 0$ and a countably infinite set $\mathcal{N} \subset \mathbb{N}$ such that $\sin(2\pi m(R_c - \varepsilon)) > \delta$ for all $m \in \mathcal{N}$. Hence the second term in (4.59) is negative with upper bound

$$- \left( e_s^3 + 4\pi^2 e_s^2 m^2(R_c - \varepsilon) + 12\pi^2 e_s m^2 + 16\pi^4 m^4(R_c - \varepsilon) \right) \delta < 0$$

for all $m \in \mathcal{N}$. This implies that the right-hand side of (4.59), i.e. $g_\varepsilon(m), h_\varepsilon(m)$, can be estimated from below by

$$g_\varepsilon(m) \left[ -\frac{1}{2\pi m} \left( e_s^3 + 4\pi^2 e_s^2 m^2(R_c - \varepsilon) + 12\pi^2 e_s m^2 + 16\pi^4 m^4(R_c - \varepsilon) \right) \delta \right.$$
$$+ \max\{e_s^3(R_c - \varepsilon) + 4\pi^2 m^2(e_s(R_c - \varepsilon) - 2), -e_s^3(R_c - \varepsilon) - 4\pi^2 m^2(e_s(R_c - \varepsilon) - 2)\}$$
$$\left. + 8\pi^2 m^2 \exp\left(e_s(R_c - \varepsilon)\right) \right]$$

for all $m \in \mathcal{N}$ and $0 < \varepsilon \ll R_c$ since $g_\varepsilon(m) < 0$ for all $m \in \mathbb{N}$. Thus, there exists $m_0 \in \mathcal{N}$ such that the term in square brackets is negative for all $m \in \mathcal{N}$ with $m \geqslant m_0$ and all $\varepsilon > 0$ sufficiently small since the highest order term of power $m^4$ in the square brackets dominates for $m$ large enough. In particular, $g_\varepsilon(m_0) < 0$ for $\varepsilon > 0$ implies that we have found a positive lower bound of the right-hand side in (4.59) and one can easily show that this positive lower bound also holds in the limit $\varepsilon \to 0$. Hence, stability cannot be achieved in the case $R_c \in (0, 0.5]$ and any $\varepsilon > 0$, as well as for $R_c \in (0, 0.5)$ and $\varepsilon \to 0$, both for $N \in \mathbb{N}$ sufficiently large and in the continuum limit $N \to \infty$. $\qquad \square$

**Remark 15.** *For $R_c \in (0, 0.5)$ and $\varepsilon \to 0$, no stability can be shown analytically. However, note that an upper bound of the integral*

$$\int_0^{R_c - \varepsilon} (f_s^\varepsilon(s) + s(f_s^\varepsilon)'(s)) (1 - \cos(2\pi ms)) \, ds \tag{4.60}$$

in the necessary stability condition (4.58) is given by

$$
\begin{aligned}
-&\frac{ce_s \exp\left(-e_s(R_c - \varepsilon)\right)}{2\pi m \left(e_s^2 + 4\pi^2 m^2\right)^2} \Big[ -2\pi m \left(e_s^3(R_c - \varepsilon) + 4\pi^2 m^2(e_s(R_c - \varepsilon) - 2)\right) \\
&- \left(e_s^3 + 4\pi^2 e_s^2 m^2(R_c - \varepsilon) + 12\pi^2 e_s m^2 + 16\pi^4 m^4(R_c - \varepsilon)\right) \\
&+ 16\pi^3 m^3 \exp\left(e_s(R_c - \varepsilon)\right) \Big] \\
=-&\frac{ce_s \exp\left(-e_s(R_c - \varepsilon)\right)}{2\pi m \left(e_s^2 + 4\pi^2 m^2\right)^2} \Big[ -e_s^3 - 2\pi e_s^3(R_c - \varepsilon)m - \left(4\pi^2 e_s^2(R_c - \varepsilon) + 12\pi^2 e_s\right)m^2 \\
&+ \left(-8\pi^3(e_s(R_c - \varepsilon) - 2) + 16\pi^3 \exp\left(e_s(R_c - \varepsilon)\right)\right)m^3 - 16\pi^4(R_c - \varepsilon)m^4 \Big]
\end{aligned}
\tag{4.61}
$$

for any $0 < \varepsilon \ll R_c$ due to (4.59). For $\exp(e_s R_c) \gg 1$ there exists $m_0 \in \mathbb{N}$ of order $\exp(e_s R_c) \gg 1$ such that the term $16\pi^3 m^3 \exp\left(e_s R_c\right)$ is the dominating term in the upper bound (4.61) of the integral (4.60) for all $m \in \mathbb{N}$ with $m \leqslant m_0$. Hence negativity of the upper bound (4.61) and thus of the integral (4.60) in the necessary stability condition can be guaranteed for all $m \leqslant m_0$. For $m > m_0$, however, the highest order term of power $m^4$ dominates the sum. Since $m_0 \gg 1$, we have stability for $N \in \mathbb{N}$ sufficiently large and for the continuum limit $N \to \infty$ for almost all, but finitely many, Fourier modes for $e_s \gg 1$, $R_c \in (0, 0.5)$, and any $\varepsilon > 0$ sufficiently small or in the limit $\varepsilon \to 0$.

The integral (4.60) is explicitly evaluated in (4.59). For large values of $m \in \mathbb{N}$ the highest order term in (4.59) is associated with the summand $16\pi^4 m^4(R_c - \varepsilon)\sin(2\pi m(R_c - \varepsilon))$ and can be written in the form

$$
\frac{8\pi^3 e_s \exp(-e_s(R_c - \varepsilon))(R_c - \varepsilon)m^3 \sin(2\pi m(R_c - \varepsilon))}{\left(e_s^2 + 4\pi^2 m^2\right)^2}.
$$

Here, the numerator increases as $m^3$ for large $m$ while the denominator is of order $m^4$, multiplied by a factor $\exp(-e_s R_c) \ll 1$, leading to decaying sinusoidal oscillations around zero as $m$ increases. Since this approximation is only valid for $m > m_0 \gg 1$ the absolute value of the right-hand side in (4.59) may be so small that it is numerically zero and one may see stable vertical line patterns for exponentially decaying force coefficients $f_s^\varepsilon$ along $s$ for $R_c \in (0, 0.5)$, $\varepsilon > 0$ or in the limit $\varepsilon \to 0$, and $N \in \mathbb{N}$ sufficiently large; see the numerical experiment in Figure 4.6(E).

**Corollary 7.** *Let $c_1, c_2 \in \mathbb{R}$ with $c_1 > 0$, $c_1 > |c_2|$ be given. There exist parameters $e_2 \geqslant e_1 > 0$ such that the straight vertical line is stable for the particle model (4.6) for $N \in \mathbb{N}$ sufficiently large for the exponentially decaying force coefficient $f_s^\varepsilon$ along*

*s given by $f_s^\varepsilon \colon \mathbb{R}_+ \to \mathbb{R}$ with*

$$f_s^\varepsilon(|d|) = \begin{cases} c_1 \exp(-e_1|d|) + c_2 \exp(-e_2|d|) - c, & |d| \in [0, R_c - \varepsilon], \\ (f_s^\varepsilon)'(R_c - \varepsilon) \left( \frac{(|d| - R_c)^3}{\varepsilon^2} + \frac{(|d| - R_c)^2}{\varepsilon} \right), & |d| \in (R_c - \varepsilon, R_c), \\ 0, & |d| \geqslant R_c, \end{cases} \qquad (4.62)$$

*with*

$$c = c_1 \exp(-e_1(R_c - \varepsilon)) + c_2 \exp(-e_2(R_c - \varepsilon))$$

*and a linear or an exponential force coefficient $f_l^\varepsilon$ along $l$ as in Assumption 7 for a cutoff radius $R_c = 0.5$. For the continuum limit $N \to \infty$, stability/instability cannot be concluded.*

*Proof.* For the stability of the straight vertical line for $N \in \mathbb{N}$ sufficiently large we require that the force coefficient $f_s^\varepsilon$ in (4.62) is purely repulsive for any $\varepsilon > 0$ and hence at least one of the constants $c_1, c_2$ has to be positive. Since we can assume $c_1 > 0$ without loss of generality this implies that $c_1$ is a repulsive multiplicative factor, while the sign of $c_2$ is not given by the assumptions. Thus, we require that the first term in the definition of $f_s^\varepsilon$ in (4.62) decays slower than the second one, implying $0 < e_1 \leqslant e_2$. Hence, the conditions on the parameters are verified.

As in the proof of Theorem 4 we evaluate integrals of the form (4.59) where the term with factor $\sin(2\pi m R_c)$ vanishes for our choice of $R_c = 0.5$. If $c_2 \geqslant 0$ one can choose $e_1, e_2$ sufficiently large such that the term $16\pi^3 m^3 \exp(e_k R_c), k = 1, 2$, in the square brackets in (4.59) dominates as in the proof of Theorem 4, leading to the stability of the vertical straight line for $N \in \mathbb{N}$ sufficiently large. For $c_2 < 0$ one can choose $e_1, e_2$ sufficiently large such that the term $16\pi^3 m^3 \exp(e_k R_c), k = 1, 2$, dominates the square brackets. However, since $c_1 > 0 > c_2$ we require in addition that the term with multiplicative factor $c_1$ dominates over the term with multiplicative factor $c_2$, leading to the condition

$$-\frac{16\pi^3 m^3 c_1 e_1}{2\pi m \left(e_1^2 + 4\pi^2 m^2\right)^2} + \frac{16\pi^3 m^3 |c_2| e_2}{2\pi m \left(e_2^2 + 4\pi^2 m^2\right)^2} < 0$$

in the limit $\varepsilon \to 0$ which is equivalent to

$$-c_1 e_1 \left(e_2^2 + 4\pi^2 m^2\right)^2 + |c_2| e_2 \left(e_1^2 + 4\pi^2 m^2\right)^2 < 0.$$

Since $c_1 > |c_2|$ and $e_2 \geqslant e_1 > 0$ by assumption this condition is satisfied for $e_2 > e_1$ sufficiently large. Hence, stability of the straight vertical line can be achieved for $N \in \mathbb{N}$ sufficiently large. $\qquad\square$

The force coefficient $f_s^\varepsilon$ of the form (4.62) along $s$ is motivated by the force coefficients in the Kücken-Champod model. Here, $f_s^\varepsilon = \chi f_A^\varepsilon + f_R^\varepsilon$ for $\chi \in [0,1]$ where, motivated by this section, $f_R^\varepsilon, f_A^\varepsilon$ are defined as

$$
f_R^\varepsilon(|d|) = \begin{cases} f_R(|d|) - f_R(R_c - \varepsilon), & |d| \in [0, R_c - \varepsilon], \\ f_R'(R_c - \varepsilon)\left(\frac{(|d|-R_c)^3}{\varepsilon^2} + \frac{(|d|-R_c)^2}{\varepsilon}\right), & |d| \in (R_c - \varepsilon, R_c), \\ 0, & |d| \geqslant R_c, \end{cases} \qquad (4.63)
$$

and

$$
f_A^\varepsilon(|d|) = \begin{cases} f_A(|d|) - f_A(R_c - \varepsilon), & |d| \in [0, R_c - \varepsilon], \\ f_A'(R_c - \varepsilon)\left(\frac{(|d|-R_c)^3}{\varepsilon^2} + \frac{(|d|-R_c)^2}{\varepsilon}\right), & |d| \in (R_c - \varepsilon, R_c), \\ 0, & |d| \geqslant R_c. \end{cases} \qquad (4.64)
$$

This corresponds to the sum of an attractive and a repulsive force coefficient as in (4.62) for $c_1 > 0 > c_2$ where the repulsive term, i.e. $c_1 > |c_2|$, dominates. This motivates that we obtain stability of the straight vertical line for the force coefficients in the Kücken-Champod model for $N \in \mathbb{N}$ sufficiently large by considering force coefficients of the form (4.63), (4.64).

### 4.4.4 Kücken-Champod model

For the specific forces in the Kücken-Champod model, given by the repulsive and attractive force coefficients $f_R^\varepsilon$ and $f_A^\varepsilon$ in (4.63) and (4.64), respectively, we require the nonpositivity of the real parts of the eigenvalues $\lambda_k, k = 1, 2$, given by

$$
\Re(\lambda_1(m)) = 2 \int_0^{R_c} f_l^\varepsilon(s)\left(1 - \cos\left(-2\pi m s\right)\right) \mathrm{d}s,
$$

$$
\Re(\lambda_2(m)) = 2 \int_0^{R_c} \left(f_s^\varepsilon(s) + s(f_s^\varepsilon)'(s)\right)\left(1 - \cos\left(-2\pi m s\right)\right) \mathrm{d}s
$$

in (4.24) where $f_l^\varepsilon = f_A^\varepsilon + f_R^\varepsilon$ and $f_s^\varepsilon = \chi f_A^\varepsilon + f_R^\varepsilon$. In Figure 4.3 we evaluate $\Re(\lambda_k)$ numerically for the force coefficients (4.63) and (4.64) in the Kücken-Champod model for the parameters in (1.20) and a cutoff radius $R_c = 0.5$ in the limit $\varepsilon \to 0$.

Clearly, $\Re(\lambda_1) \leqslant 0$, while $\Re(\lambda_2)$ is negative for small modes $m$ but tends to zero for large modes $m$. Investigating the high wave number stability for the forces in the
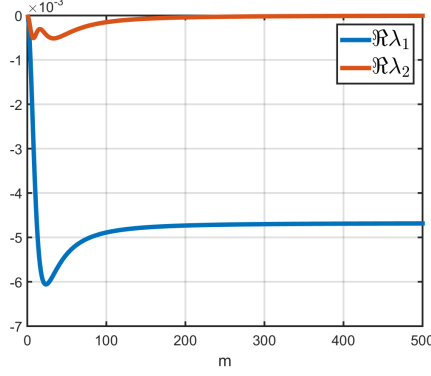


Figure 4.3: $\Re(\lambda_i)$ in (4.24) as a function of $m$ for the force coefficients $f_R^\varepsilon$ in (4.63) and $f_A^\varepsilon$ in (4.64) of repulsion force (1.12) and attraction force (1.13), respectively, for parameter values in (1.20) in the limit $\varepsilon \to 0$, where $f_l^\varepsilon = f_A^\varepsilon + f_R^\varepsilon$ and $f_s^\varepsilon = \chi f_A^\varepsilon + f_R^\varepsilon$.

Kücken-Champod model can be done analytically. For the general necessary high wave number condition (4.28) for $\lambda_1$ we require

$$\int_0^{R_c} f_l^\varepsilon \, \mathrm{d}s \leqslant 0.$$

Note that

$$\lim_{\varepsilon \to 0} \int_0^{R_c - \varepsilon} \exp(-e_R s) \left(\alpha s^2 + \beta\right) - \gamma \exp(-e_A s) s \, \mathrm{d}s$$

$$= \frac{\alpha \left(\exp(-e_R R_c)(-e_R R_c(e_R R_c + 2) - 2) + 2\right)}{(e_R)^3} + \frac{\beta - \beta \exp(-e_R R_c)}{e_R}$$

$$- \frac{\gamma \left(1 - \exp(-e_A R_c)(e_A R_c + 1)\right)}{(e_A)^2}$$

$$\approx \frac{2\alpha}{(e_R)^3} + \frac{\beta}{e_R} - \frac{\gamma}{(e_A)^2}$$

which is clearly negative for the choice of parameters in (1.20). For the high wave stability we also consider the condition associated with $\lambda_2$, leading to the condition

$$\int_0^{R_c} f_s^\varepsilon(s) + s(f_s^\varepsilon)'(s) \, \mathrm{d}s \leqslant 0.$$

We evaluate the integral

$$\int_0^{R_c - \varepsilon} \exp(-e_R s) \left( \alpha \left( 3s^2 - e_R s^3 \right) + \beta(1 - e_R s) \right) - \chi\gamma \exp(-e_A s)s(2 - e_A s) \, \mathrm{d}s$$
$$= (R_c - \varepsilon) \left[ (R_c - \varepsilon) \left[ \alpha(R_c - \varepsilon) \exp(-e_R(R_c - \varepsilon)) - \chi\gamma \exp(-e_A(R_c - \varepsilon)) \right] \right.$$
$$\left. + \beta \exp(-e_R(R_c - \varepsilon)) \right]$$
$$= (R_c - \varepsilon) \left( f_R(R_c - \varepsilon) + \chi f_A(R_c - \varepsilon) \right)$$

for $f_R$ and $f_A$ defined in (4.8) and (4.9), respectively, implying that

$$\int_0^{R_c - \varepsilon} f_s^\varepsilon(s) + s(f_s^\varepsilon)'(s) \, \mathrm{d}s = 0$$

for any $\varepsilon > 0$. In particular, the straight vertical line is high wave number stable for any $N \in \mathbb{N}$ sufficiently large and in the continuum limit $N \to \infty$ for the Kücken-Champod model with force coefficients $f_R^\varepsilon$ and $f_A^\varepsilon$ in (4.63) and (4.64), respectively, the parameters in (1.20), and $\varepsilon \to 0$. By definition of $f_s^\varepsilon = \chi f_A^\varepsilon + f_R^\varepsilon$, we have $f_s^\varepsilon(R_c) = 0$, i.e. the high wave number stability of the straight vertical line (compare Proposition 6), is satisfied. Note that

$$\lim_{\varepsilon \to 0} \chi f_A(R_c - \varepsilon) + f_R(R_c - \varepsilon) = 4.8144 \cdot 10^{-21}$$

for $R_c = 0.5$, i.e. the force coefficient $\chi f_A + f_R$ has only slightly been modified to obtain $\chi f_A^\varepsilon + f_R^\varepsilon$ with $(\chi f_A^\varepsilon + f_R^\varepsilon)' \approx (\chi f_A^\varepsilon + f_R^\varepsilon)'$, provided $e_R \exp(-e_R R_c) \ll 1$ and $e_A \exp(-e_A R_c) \ll 1$.

Note that it is not possible to analyse the stability of the straight vertical line for all modes $m \in \mathbb{N}$ for the forces $f_R^\varepsilon$ and $f_A^\varepsilon$ in (4.63) and (4.64) in the Kücken-Champod model analytically for all possible parameter values due to the large number of parameters in the model. Besides, the force coefficients strongly depend on the choice of parameters. In Corollary 7, however, we investigated the stability of the straight vertical line for $N \in \mathbb{N}$ sufficiently large where $f_s^\varepsilon$, restricted to $[0, R_c - \varepsilon]$ for some $\varepsilon > 0$, is the sum of the positive term $c_1 \exp(-e_1|d|)$, the negative term $c_2 \exp(-e_2|d|)$ and a constant to guarantee $f_s^\varepsilon(R_c - \varepsilon) = 0$ where $c_1 > |c_2| > 0$. Besides, we required $e_1 < e_2$ for the positivity of the sum $c_1 \exp(-e_1|d|) + c_2 \exp(-e_2|d|)$ for $|d| \in [0, R_c - \varepsilon]$ and showed stability of the straight vertical line for $N \in \mathbb{N}$ sufficiently large provided the parameters $e_1, e_2 > 0$ are chosen sufficiently large enough. In Figure 4.1 the absolute value of the terms $\chi f_A$ and $f_R$, defined in

(4.8)–(4.9), are plotted for the parameters in (1.20). As in Corollary 7 the positive term always dominates and the terms $\chi f_A$ and $f_R$ have fast exponential decays. This suggests that the straight vertical line is a stable steady state for the Kücken-Champod model for $N \in \mathbb{N}$ sufficiently large with the adopted force coefficient $f_s^\varepsilon = \chi f_A^\varepsilon + f_R^\varepsilon$. Besides, the numerical evaluation of the real part of the eigenvalue $\lambda_2$ for $f_s^\varepsilon$ for $\varepsilon > 0$, i.e. a differentiable force coefficient with the additional constant $-\left(\chi f_A(R_c - \varepsilon) + f_R(R_c - \varepsilon)\right)$ for $|d| \in [0, R_c - \varepsilon]$ leads to nonpositivity of the real part of the eigenvalue $\lambda_2$.

### 4.4.5  Summary

In this section, we summarise the results from the previous subsections on the stability of the straight vertical line (4.14) of the particle model (4.6) with linear, algebraically decaying, and exponentially decaying force coefficients for different values of the cutoff radius $R_c \in (0, 0.5]$. This summary is shown in Table 4.1. Note that for $R_c \in (0, 0.5)$ the straight vertical line is always unstable for large $N$ and the instability manifests itself by non-equidistant particles along vertical lines.

## 4.5  Numerical simulations

### 4.5.1  Numerical methods

As in [BDK$^+$18, DGH$^+$19] we consider the unit square with periodic boundary conditions as the domain for our numerical simulations if not stated otherwise. The particle system (4.6) is solved by either the simple explicit Euler scheme or higher order methods such as the Runge–Kutta–Dormand–Prince method, all resulting in very similar simulation results. Note that the time step has to be adjusted depending on the value of the cutoff radius $R_c$. For efficient numerical simulation we consider cell lists as outlined in [DGH$^+$19].

### 4.5.2  Numerical results

Numerical results are shown in Figures 4.4–4.9. For all numerical simulations we consider $N = 600$ particles which are initially equiangular distributed on a circle with centre $(0.5, 0.5)$ and radius $0.005$ as illustrated in Figure 4.4(A). The stationary

Table 4.1: Stability/instability of the straight vertical line (4.14) for the particle model (4.6) with force coefficients $f_s$ along $s$ and different cutoff radii $R_c \in (0, 0.5]$.

| Force coefficient $f_s$ along $s$ | $R_c \in (0, 0.5)$ | $R_c = 0.5$ |
| --- | --- | --- |
| Linear force coefficient (4.32) | Instability for any $N \in \mathbb{N}$ sufficiently large and for $N \to \infty$ (see Theorem 7) | Stability or instability since stability conditions are satisfied with equality (see Remark 14) |
| Algebraically decaying force coefficient (4.51) | Instability for any $N \in \mathbb{N}$ sufficiently large and for $N \to \infty$ (see Corollary 6) | Instability for any $N \in \mathbb{N}$ sufficiently large and for $N \to \infty$ (see Corollary 6) |
| Exponentially decaying force coefficient (4.57) | Instability for any $N \in \mathbb{N}$ sufficiently large and for $N \in \mathbb{N}$ (see Theorem 4), but stability may be seen in numerical simulations (see Remark 15) | Stability for any $N \in \mathbb{N}$ sufficiently large (see Theorem 4) |

solution for the linear force coefficient $f_s^\varepsilon$ in (4.32), i.e.

$$f_s^\varepsilon(|d|) = a_s|d| + b_s, \qquad f_l^\varepsilon(|d|) = 0.1 - 3|d|, \qquad |d| \in [0, R_c - \varepsilon],$$

for different values of $a_s, b_s$, is shown in Figure 4.4 in the limit $\varepsilon \to 0$. As proven in Section 4.4.1 equidistantly distributed particles along the vertical straight line form an unstable steady state for $N \in \mathbb{N}$ sufficiently large for $R_c \in (0, 0.5)$. Hence, the stationary solutions are no lines of uniformly distributed particles and we obtain different clusters or line patterns instead. In Figure 4.4(B), we consider $R_c = 0.3$, resulting in clusters of particles along the vertical axis. For $R_c = 0.5$ and $a_s, b_s$ chosen as $a_s = -\frac{b_s}{R_c}$, the requirement in (4.49) for the necessary stability condition to be satisfied with equality, the real part of one of the eigenvalues of the stability matrix is equal to zero. The resulting steady states are shown for different scalings of the parameters $a_s, b_s$ in Figures 4.4(C) and 4.4(D). One can see that the particles align along a vertical line along the entire interval $[0, 1]$, but are not equidistantly distributed along the vertical axis and thus the vertical straight line is an unstable steady state for any $N \in \mathbb{N}$ sufficiently large. For $a_s > -\frac{b_s}{R_c}$ and $a_s < -\frac{b_s}{R_c}$, respectively, with $R_c = 0.5$ the corresponding steady states are shown in Figures 4.4(E) and 4.4(F), resulting in clusters along the vertical axis.

In Figure 4.5, we consider the linear force coefficient $f_s^\varepsilon$ in (4.32) for different values of $a_s, b_s$, and $R_c$, where $\varepsilon = 0.01$ is fixed in contrast to $\varepsilon \to 0$ in Figure 4.4, i.e. we consider the total force (4.4) with linear force coefficients $f_l^\varepsilon(|d|) = a_l|d| + b_l$, $f_s^\varepsilon(|d|) = a_s|d| + b_s$ for $|d| \in [0, R_c - \varepsilon]$ in (4.32) with $a_l = -3, b_l = 0.1$. In Figure 4.5(A), we consider the same parameter values as in Figure 4.4(B), i.e. $a_s = -0.2, b_s = 0.1$, and $R_c = 0.3$, resulting in the same stationary solution for $\varepsilon = 0.01$ and $\varepsilon \to 0$. In particular, the straight vertical line is unstable both for $\varepsilon = 0.01$ and $\varepsilon \to 0$. For cutoff radius $R_c = 0.5$, we obtain different stationary solutions for $\varepsilon = 0.01$ and $\varepsilon \to 0$. In Figure 4.5(B), we show the stationary solutions for $a_s = -0.2, b_s = 0.1$, and $R_c = 0.5$ as in Figure 4.4(C), i.e. $a_s = -\frac{b_s}{R_c}$. Even though stability/instability could not be determined analytically the numerical results illustrate that straight vertical line is unstable both for $\varepsilon = 0.01$ and $\varepsilon \to 0$. The stationary solution for $a_s = -0.1, b_s = 0.1$, and $R_c = 0.5$ is shown in Figure 4.5(C) for $\varepsilon = 0.01$ and in Figure 4.4(E) for $\varepsilon \to 0$. Our analytical results show that the stationary solution is unstable in this case which is also consistent with the numerical results. In particular, we obtain the same instability results for $\varepsilon = 0.01$ as in Figure 4.4 where the limit $\varepsilon \to 0$ is considered.

(A) Initial data

(B) $a_s = -0.2$,
$b_s = 0.1, R_c = 0.3$

(C) $a_s = -0.2$,
$b_s = 0.1, R_c = 0.5$

(D) $a_s = -0.02$,
$b_s = 0.01, R_c = 0.5$

(E) $a_s = -0.1$,
$b_s = 0.1, R_c = 0.5$

(F) $a_s = -0.4$,
$b_s = 0.1, R_c = 0.5$
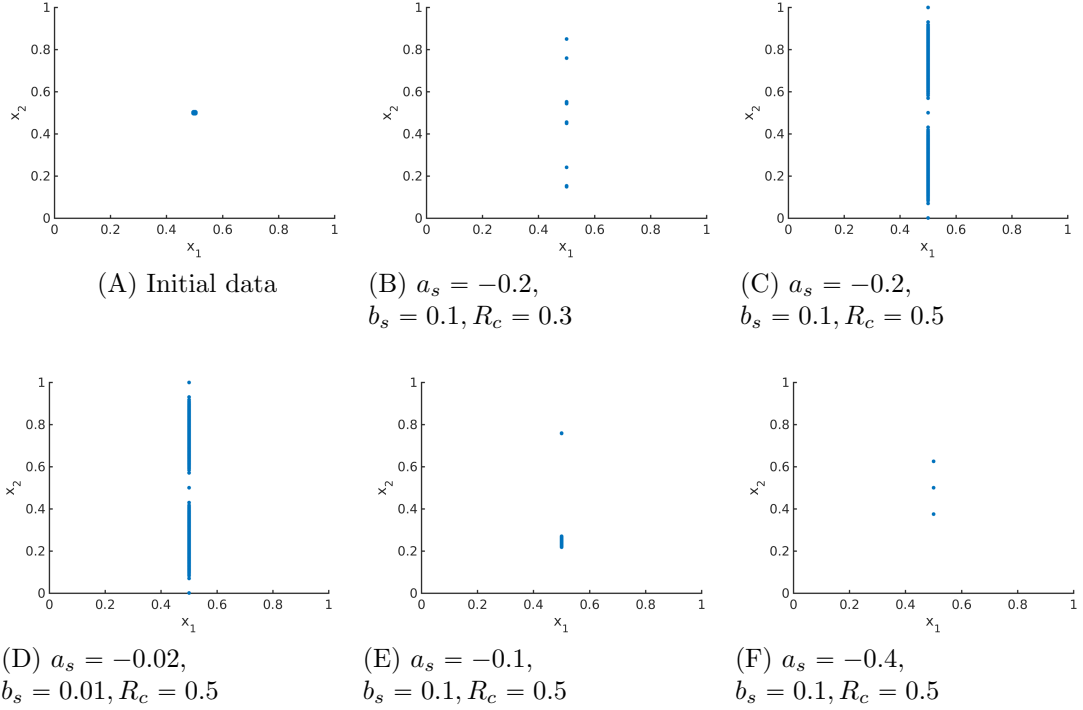
Figure 4.4: Stationary solution to the model (4.6) for total force (4.4) with linear force coefficients $f_l^\varepsilon(|d|) = a_l|d| + b_l$, $f_s^\varepsilon(|d|) = a_s|d| + b_s$ for $|d| \in [0, R_c - \varepsilon]$ in (4.32) with $a_l = -3, b_l = 0.1$, and cutoff radius $R_c$ in the limit $\varepsilon \to 0$.



(A) $\qquad\qquad a_s = -0.2$,
$b_s = 0.1, R_c = 0.3$

(B) $\qquad\qquad a_s = -0.2$,
$b_s = 0.1, R_c = 0.5$

(C) $\qquad\qquad a_s = -0.1$,
$b_s = 0.1, R_c = 0.5$
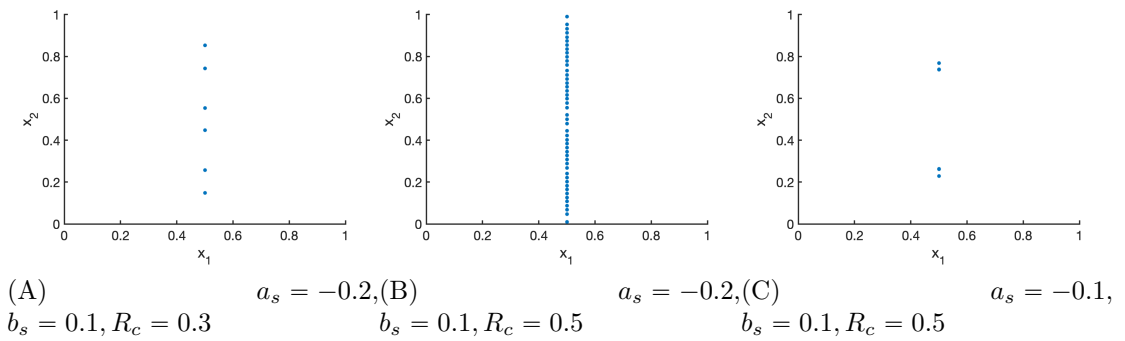
Figure 4.5: Stationary solution to the model (4.6) for total force (4.4) with linear force coefficients $f_l^\varepsilon(|d|) = a_l|d| + b_l$, $f_s^\varepsilon(|d|) = a_s|d| + b_s$ for $|d| \in [0, R_c - \varepsilon]$ in (4.32) with $a_l = -3, b_l = 0.1$, and cutoff radius $R_c$ for $\varepsilon = 0.01$.

For the exponentially decaying force coefficient $f_s^\varepsilon$ along $s$ in (4.57), given by

$$f_s^\varepsilon(|d|) = c\exp(-e_s|d|) - c\exp(-e_s(R_c - \varepsilon)), \qquad |d| \in [0, R_c - \varepsilon],$$

for $\varepsilon > 0$, we consider the parameter values $c = 0.1$ and $e_s = 100$ if not stated otherwise. The initial data is given by equiangular distributed particles on a circle with centre $(0.5, 0.5)$ and radius $0.005$ in Figure 4.6(A). In Figures 4.6(B)–4.6(F) the stationary solution for the exponentially decaying force coefficient $f_s^\varepsilon$ in the limit $\varepsilon \to 0$ is shown. As expected, for small values of $e_s$ and $R_c \in (0, 0.5)$, e.g. $e_s = 10$ as in Figure 4.6(B), the equidistantly distributed particles along the vertical axis are an unstable steady state. In this case, the steady state is given by clusters along the vertical axis and $\Re(\lambda_2(m)) \leqslant 0$ for $m < 12$ only. For $R_c = 0.5$ the straight vertical line is stable as shown in Figure 4.6(C). Note that the additional constant in the definition of $f_s^\varepsilon$ leads to $f_s^\varepsilon(R_c - \varepsilon) = f_s^\varepsilon(R_c) = 0$ and is necessary for the stability of the straight vertical line. In Figure 4.6(D) we consider $f_s^\varepsilon$ without this additional constant, i.e. $f_s^\varepsilon(|d|) = c\exp(-e_s|d|)$ for $|d| \in [0, R_c - \varepsilon]$, where the straight vertical line is clearly unstable and we have $\Re(\lambda_2(m)) \leqslant 0$ for $m < 9$ only. If $e_s$ is chosen sufficiently large, e.g. $e_s = 100$ as in Figures 4.6(E) and 4.6(F), the straight vertical line appears to be stable even for $R_c < 0.5$. An explicit calculation of the eigenvalues for $R_c = 0.1$ reveals, however, that $\Re(\lambda_2(m)) \leqslant 0$ for $m < 73723$ only. Note that we obtain stability for a much larger number of modes as in Figures 4.6(B) and 4.6(D). This is also consistent with a straight vertical line as steady state in Figure 4.6(F), while we have clusters as steady states in Figures 4.6(B) and 4.6(D). Further note that $\Re(\lambda_2(73723)) = 8.3225 \cdot 10^{-15}$ and hence it is numerically zero. As discussed in Remark 15 this explains why for $\exp(e_s R_c) \gg 1$, e.g. $e_s = 100$ and $R_c = 0.1$, the straight vertical line appears to be stable. Finally, we also obtain the straight vertical line as a steady state if we consider exponentially decaying force coefficients $f_l^\varepsilon(|d|) = 0.13\exp(-100|d|) - 0.03\exp(-10|d|)$ instead of $f_l^\varepsilon(|d|) = 0.1 - 3|d|$ for $|d| \in [0, R_c - \varepsilon]$ in the limit $\varepsilon \to 0$ as shown in Figure 4.6(F). Note that we also obtain a straight vertical line as a stationary solution in Figures 4.6(E) and 4.6(F) if $f_s^\varepsilon(|d|) = c\exp(-e_s|d|) - c\exp(-e_s(R_c - \varepsilon))$ for $|d| \in [0, R_c - \varepsilon]$ is replaced by $f_s^\varepsilon(|d|) = c\exp(-e_s|d|)$ since $\exp(-e_s R_c) \ll 1$ for $e_s \gg 1$.

In Figure 4.7 the stationary solution is shown on the domain $[0, 3]^2$ instead of the unit square. Here, we consider the same force coefficients as in Figure 4.6(F), i.e. exponentially decaying force coefficients along $l$ and $s$. We define the initial data on $[0, 3]^2$ by considering the initial data on the unit square, i.e. equiangular distributed

(A) Initial data    (B) $e_s = 10$, $R_c = 0.1$, $f_l$ lin.    (C) $e_s = 10$, $R_c = 0.5$, $f_l$ lin.

(D) $e_s = 10$, $R_c = 0.5$, $f_l$ lin., no add. constant for $f_s$    (E) $e_s = 100$, $R_c = 0.1$, $f_l$ lin.    (F) $e_s = 100$, $R_c = 0.5$, $f_l$ exp.
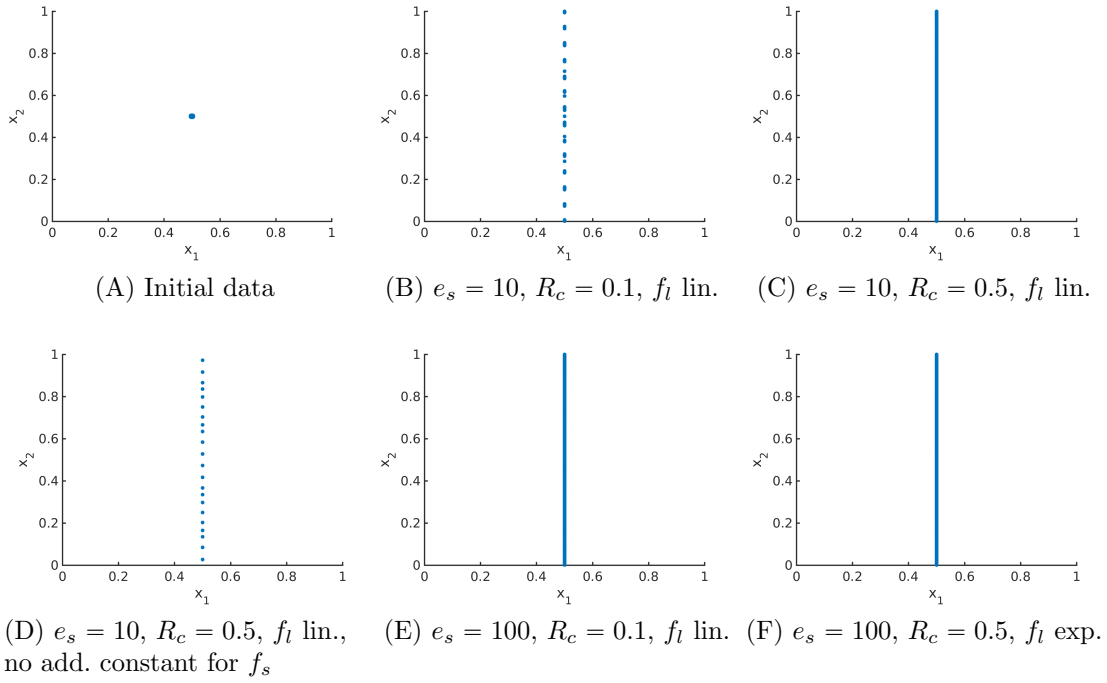
Figure 4.6: Stationary solution to the model (4.6) for total force (4.4) with exponential force coefficient $f_s^\varepsilon(|d|) = c \exp(-e_s|d|) - c \exp(-e_s(R_c - \varepsilon))$ for $|d| \in [0, R_c - \varepsilon]$ along $s$, defined in (4.57), and $f_l^\varepsilon(|d|) = 0.1 - 3|d|$ or $f_l^\varepsilon(|d|) = 0.13 \exp(-100|d|) - 0.03 \exp(-10|d|)$ for $|d| \in [0, R_c - \varepsilon]$ along $l$ with cutoff $R_c$ in the limit $\varepsilon \to 0$.

particles on a circle with centre $(0.5, 0.5)$ and radius $0.005$, and extending these initial conditions to $[0, 3]^2$ by using the periodic boundary conditions. As expected we obtain three parallel lines as the stationary solution.



(A) Initial data        (B) $R_c = 0.1$
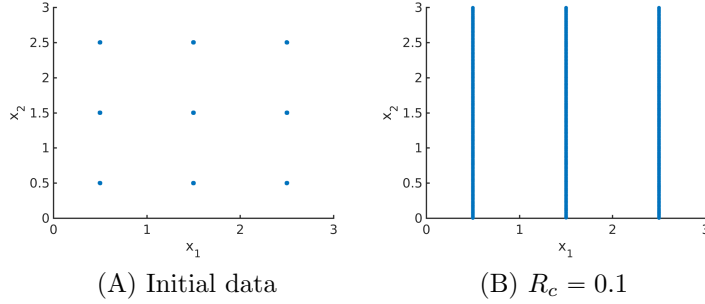
Figure 4.7: Stationary solution to the model (4.6) for total force (4.4) with exponential force coefficients $f_s^\varepsilon(|d|) = c \exp(-e_s|d|) - c \exp(-e_s(R_c - \varepsilon))$ in (4.57) and $f_l^\varepsilon(|d|) = 0.13 \exp(-100|d|) - 0.03 \exp(-10|d|)$ with cutoff $R_c$ on the domain $[0, 3]^2$.

For the underlying tensor field $T$ with $s = (0, 1)$ and $l = (1, 0)$, we have seen that vertical straight patterns are stable. More generally, stripe states along any angle can be obtained by rotating the spatially homogeneous tensor field $T$ appropriately. Examples of rotated stripe patterns are shown in Figure 4.8 where the vector fields $s = (1, 1)/\sqrt{2}, l = (-1, 1)/\sqrt{2}$ in Figure 4.8(A), $s = (1, 2)/\sqrt{5}, l = (-2, 1)/\sqrt{5}$ in Figure 4.8(B), and $s = (1, 5)/\sqrt{26}, l = (-5, 1)/\sqrt{26}$ in Figure 4.8(C) are considered. Due to the periodicity of the forces, the resulting patterns are also periodic.



(A) $s = (1, 1)/\sqrt{2}$,     (B) $s = (1, 2)/\sqrt{5}$,     (C) $s = (1, 5)/\sqrt{26}$,
$l = (-1, 1)/\sqrt{2}$       $l = (-2, 1)/\sqrt{5}$       $l = (-5, 1)/\sqrt{26}$
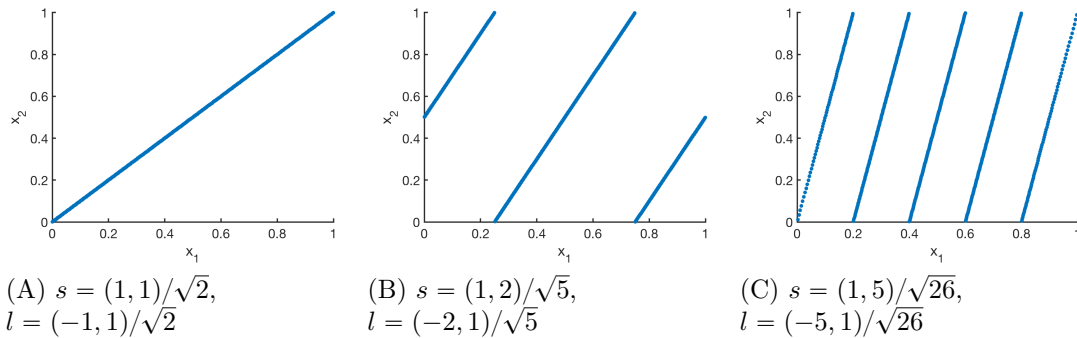
Figure 4.8: Stationary solution to the model (4.6) for different tensor fields $T$, given by $s, l$, and total force (4.4) with exponential force coefficients $f_s^\varepsilon(|d|) = c \exp(-e_s|d|) - c \exp(-e_s(R_c - \varepsilon))$ for $|d| \in [0, R_c - \varepsilon]$ in (4.57) and $f_l^\varepsilon(|d|) = 0.13 \exp(-100|d|) - 0.03 \exp(-10|d|)$ for $|d| \in [0, R_c - \varepsilon]$ with cutoff $R_c = 0.1$ in the limit $\varepsilon \to 0$.

Until now, we looked at numerical examples for a stable state aligned along a

line (or lines). However, the model (4.6) is also able to produce two-dimensional states which can result as an instability of a vertical line. To obtain two-dimensional patterns, we vary the force along $l$. In particular, the force along $l$ has to be less attractive to avoid the concentration along line patterns. In Figure 4.9, we vary parameter $e_{l_1}$ in the force coefficient $f_l^\varepsilon(|d|) = 0.13 \exp(-e_{l_1}|d|) - 0.03 \exp(-10|d|)$ for $|d| \in [0, R_c - \varepsilon]$. Here, smaller values of $e_{l_1}$ lead to stronger repulsive forces over a short distance, resulting in a horizontal spreading of the solution for the tensor field $T$ with $s = (0,1)$ and $l = (1,0)$.



| (A) $e_{l_1} = 20$ | (B) $e_{l_1} = 30$ | (C) $e_{l_1} = 50$ |
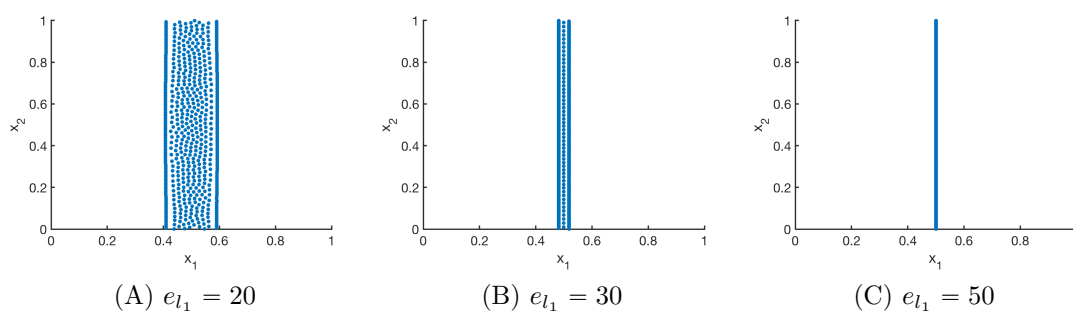
Figure 4.9: Stationary solution to the model (4.6) for tensor field $T$ with $s = (0,1), l = (1,0)$ and total force (4.4) with exponential force coefficients $f_s^\varepsilon(|d|) = c \exp(-e_s|d|) - c \exp(-e_s(R_c - \varepsilon))$ for $|d| \in [0, R_c - \varepsilon]$, defined in (4.57), and $f_l^\varepsilon(|d|) = 0.13 \exp(-e_{l_1}|d|) - 0.03 \exp(-10|d|)$ for $|d| \in [0, R_c - \varepsilon]$ with cutoff $R_c = 0.5$.

# Chapter 5

# Role of nonlinear diffusion on equilibria: Analysis and numerics

## Originality and contribution

This chapter is based on [CDKS19] in collaboration with José A. Carrillo, Bertram Düring and Carola-Bibiane Schönlieb. While my co-authors proposed the study of the model and gave advice, [CDKS19] is primarily my own original work and nearly all the results in [CDKS19], including analysis and simulations, were obtained by myself. For the numerical simulations I adapted the code in [CCH14a] which was provided by José A. Carrillo.

## Chapter summary

In this chapter, we study the equilibria of an anisotropic, nonlocal aggregation equation with nonlinear diffusion which does not possess a gradient flow structure. Here, the anisotropy is induced by an underlying tensor field. We derive equilibrium conditions for stationary line patterns which can be reformulated as the minimisers of a regularised energy functional if the underlying tensor field is spatially homogeneous. For spatially homogeneous tensor fields, we show the existence of energy minimisers, establish $\Gamma$-convergence of the regularised energy functionals as the diffusion coefficient vanishes, and prove the convergence of minimisers of the regularised energy functional to minimisers of the non-regularised energy functional. Further, we investigate properties of stationary solutions on different domains. Finally, we prove weak convergence of a numerical scheme for the numerical solution of the

anisotropic, nonlocal aggregation equation with nonlinear diffusion and any underlying tensor field, and show numerical results.

## 5.1 Introduction

The derivation, analysis and numerics of mathematical models for collective behaviour of cells, animals or humans have recently been receiving increasing attention. Based on agent-based modelling approaches, a variety of continuum models has been derived and used to describe biological aggregations such as flocks and swarms [MEK99, TBL06]. Motivated by the simulation of fingerprint patterns which can be modelled as the interaction of a large number of cells [BDK$^+$18, KC13], a continuum model can be derived, given by the anisotropic aggregation equation (1.17), i.e.

$$\partial_t \rho(t,x) + \nabla_x \cdot [\rho(t,x)(F(\cdot, T(x)) * \rho(t,\cdot))(x)] = 0 \qquad \text{in } \mathbb{R}_+ \times \mathbb{R}^2, \qquad (5.1)$$

with initial condition $\rho|_{t=0} = \rho^{in}$ in $\mathbb{R}^2$ for some given initial data $\rho^{in}$. Here,

$$u_\rho(t,x) = (F(\cdot, T(x)) * \rho(t,\cdot))(x) = \int_{\mathbb{R}^2} F(x-y, T(x))\rho(t,y)\,\mathrm{d}y \qquad (5.2)$$

is the velocity field with $|u_\rho(t,x)| \leqslant f$ for the uniform bound $f$ of $F$ where the term $F(x-y, T(x))$ denotes the force which a particle at position $y$ exerts on a particle at position $x$. The left-hand side of (5.1) represents the active transport of the density $\rho$ associated to a nonlocal velocity field $u_\rho$.

The force $F$ depends on an underlying stress tensor field $T(x)$ at location $x$. The existence of such a tensor field $T(x)$ is motivated by experimental results for simulating fingerprints [KH95, KC13], but due to the generality of the definition of the forces, model (5.1) can be regarded as a prototype for understanding complex phenomena in nature. Since an alignment of mass along the local stress lines is observed, we define the tensor field $T(x)$ by the directions of smallest stress at location $x$, i.e. we consider a unit vector field $s = s(x) \in \mathbb{R}^2$ and introduce a corresponding orthonormal vector field $l = l(x) \in \mathbb{R}^2$, representing the directions of largest stress. The tensor field $T(x)$ at $x$ is given by (1.5), i.e.

$$T(x) := \chi s(x) \otimes s(x) + l(x) \otimes l(x) \in \mathbb{R}^{2,2}. \qquad (5.3)$$

The parameter $\chi \in [0,1]$ in the definition of the tensor field introduces an anisotropy

in the direction $s$.

A typical aspect of aggregation models is the competition of social interactions (repulsion and attraction) between the particles which is also the focus of our research. Hence, we assume that the total force $F$ is given by

$$F(x - y, T(x)) = F_A(x - y, T(x)) + F_R(x - y). \tag{5.4}$$

Here, $F_R$ denotes the repulsion force that a particle at location $y$ exerts on particle at location $x$ and $F_A$ is the attraction force a particle at location $y$ exerts on particle at location $x$. The repulsion and attraction forces are of the form

$$F_R(d = d(x, y)) = f_R(|d|)d$$

and

$$F_A(d = d(x, y), T(x)) = f_A(|d|)T(x)d,$$

respectively, with radially symmetric coefficient functions $f_R$ and $f_A$, where, again, $d = d(x, y) = x - y \in \mathbb{R}^2$. An example for the force coefficients $f_R$ and $f_A$ was suggested by Kücken and Champod [KC13], given by

$$f_R(d) = (\alpha|d|^2 + \beta)\exp(-e_R|d|) \tag{5.5}$$

and

$$f_A(d) = -\gamma|d|\exp(-e_A|d|) \tag{5.6}$$

for nonnegative constants $\alpha$, $\beta$, $\gamma$, $e_A$ and $e_R$, and $d = (d_1, d_2) \in \mathbb{R}^2$. We assume that the total force (5.4) exhibits short-range repulsion and long-range attraction along $l$, and only repulsion along $s$, while the direction of the interaction forces is determined by the parameter $\chi \in [0, 1]$ in the definition of $T$ in (5.3). These assumptions on the force coefficients are satisfied for the parameters proposed in [DGH+19], given by

$$\alpha = 270, \quad \beta = 0.1, \quad \gamma = 10.5, \quad e_A = 95, \quad e_R = 100, \quad \chi = 0.2. \tag{5.7}$$

Motivated by plugging (5.3) into the definition of the total force (5.4), we consider

a more general form of the total force, given by

$$F(d = d(x, y), T(x)) = f_s(|d|)(s(x) \cdot d)s(x) + f_l(|d|)(l(x) \cdot d)l(x) \qquad (5.8)$$

for coefficient functions $f_s$ and $f_l$, where $f_s = f_R + \chi f_A$ and $f_l = f_R + f_A$ for the Kücken-Champod model.

The macroscopic model (5.1) can be regarded as the macroscopic limit of an anisotropic particle model as the number of particles $N$ goes to infinity. The $N$ interacting particles with positions $x_j = x_j(t) \in \mathbb{R}^2$, $j = 1, \ldots, N$, at time $t$ satisfy (1.4), i.e.

$$\frac{\mathrm{d}x_j}{\mathrm{d}t} = \frac{1}{N} \sum_{\substack{k=1 \\ k \neq j}}^{N} F(x_j - x_k, T(x_j)), \qquad (5.9)$$

equipped with initial data $x_j(0) = x_j^{in}$, $j = 1, \ldots, N$, for given scalars $x_j^{in}$, $j = 1, \ldots, N$. A special instance of this model has been introduced in [KC13] for simulating fingerprint patterns. The particle model in its general form (5.9) has been studied in [BDK$^+$18, CDKS18, DGH$^+$19]. In particular, the particles align in line patterns according to the underlying fields $s = s(x)$ and $l = l(x)$ [BDK$^+$18, CDKS18, DGH$^+$19]. Due to the purely repulsive forces along $s$ and the short-range repulsive, long-range attractive forces along $l$, we prove for spatially homogeneous tensor fields that the stationary solution consists of line patterns along $s$. These stationary solutions to (5.1) can be regarded as solutions with one-dimensional support and are constant along $s$. For general tensor fields, we observe from the numerical simulations that line patterns can be obtained as stationary solutions.

Since our fingerprint lines do not have a one-dimensional support and, in fact, have a certain width, we widen the support of the line structures by introducing a small nonlinear diffusion on the right-hand side of (5.1), leading to the nonlocal aggregation equation with nonlinear diffusion

$$\partial_t \rho(t, x) + \nabla_x \cdot [\rho(t, x)(F(\cdot, T(x)) * \rho(t, \cdot))(x)] = \delta \nabla_x \cdot (\rho(t, x)\nabla_x \rho(t, x)) \text{ in } \mathbb{R}_+ \times \mathbb{R}^2$$
$$(5.10)$$

where $\delta \ll 1$. In particular, for the spatially homogeneous tensor field $T$ with $s = (0, 1)$ and $l = (1, 0)$ straight vertical lines are obtained as stationary solutions [BDK$^+$18, CDKS18, DGH$^+$19] which can be regarded as constant solutions along the vertical axis. For solutions of this form, the diffusion term only acts perpendicular

to the line patterns and not parallel. Hence, a positive diffusion coefficient $\delta$ leads to nonlinear diffusion along the horizontal axis and we expect the widening of the vertical line profile.

### 5.1.1 Isotropic aggregation equations

While we consider anisotropic aggregation equations of the form (5.1) in this chapter, mainly isotropic aggregation equations [BCL09, BSK$^+$15, KSUB11, Lau07] of the form (1.3), i.e.

$$\rho_t + \nabla \cdot (\rho(-\nabla W * \rho)) = 0 \tag{5.11}$$

for a radially symmetric interaction potential $W(d) = \overline{W}(|d|)$ with $F(d) = -\nabla W(d)$, have been studied in the literature. In particular, the study of the isotropic aggregation equations in terms of its gradient flow structure [AGS05, CMV03, CMV06, LT04, Vil03], the blow-up dynamics for fully attractive potentials [BCL09, BLL12, CDFF$^+$11, CJLV16], and the rich variety of steady states [BCLR13a, BCLR13b, BCY14, BT11, BLL12, CCP15, CDM16, CFF$^+$12, CFP12, FR10, FR11, Rao12, vBU12, vBUKB12] has attracted the interest of many research groups recently. In these works, the energy

$$\mathcal{E}(\rho) = \frac{1}{2} \int_{\mathbb{R}^d} \int_{\mathbb{R}^d} W(x - y) \, \mathrm{d}\rho(x) \, \mathrm{d}\rho(y) \tag{5.12}$$

in the $d$-dimensional setting plays an important role since it governs the dynamics, and its (local) minima describe the long-time asymptotics of solutions. Sharp conditions for the existence of global minimisers for a broad class of nonlocal interaction energies on the space of probability measures have been established in [SST15].

In terms of biological applications, nonlocal interactions on different scales [BT11, EKWG98, MEK99] are considered for describing the interplay between short-range repulsion which prevents collisions between individuals, and long-range attraction which keeps the swarm cohesive [MEKBS03, OL01]. These repulsive-attractive potentials can be considered as a minimal model for pattern formation in large systems of individuals [BCLR13b]. The 1D nonlocal interaction equation with a repulsive-attractive potential has been studied in [FR10, FR11, Rao12] where the authors show that the behaviour of the solution strongly depends on the regularity of the interaction potential. More precisely, the solution converges to a sum of Dirac masses for regular interaction, while it remains uniformly bounded for singular re-

pulsive potentials. Pattern formation for repulsive-attractive potentials in multiple dimensions is studied in [BSK$^+$15, KSUB11, vBU12, vBUKB12].

It has been observed that even for quite simple repulsive-attractive potentials the energy minimizers are sensitive to the precise form of the potential and can exhibit a wide variety of patterns [KHP13, KSUB11, vBUKB12]. Nonlocal interaction models have been studied for specific types of repulsive-attractive potentials [BCLR13a, CCH14b, CFP17, CH17, CJLV16, FHK11]. In [BCLR13a], conditions for the dimensionality of the support of local minimisers of (5.12) are obtained in terms of the repulsive strength of the potential $W$ at the origin. Minimizers for the special class of repulsive-attractive potential which blow up approximately like the Newtonian potential at the origin have also been studied [CDM16, FHK11].

Very few numerical schemes apart from particle methods have been proposed to simulate solutions of isotropic aggregation equations after blow-up. The so-called sticky particle method [CDFF$^+$11] is a convergent numerical scheme, used to obtain qualitative properties of the solution such as the finite time total collapse. While numerical results have been obtained in the one-dimensional setting [JV13], this method is not practical to deal with finite time blow-up and the behavior of solutions after blow-up in dimensions larger than one. Let the solution to (5.1) with initial data $\rho^{in}$ be denoted by $\rho$ and the solution of the particle model (5.9) with initial data $\rho^{in,N}$ be denoted by $\rho^N(t) = \frac{1}{N}\sum_{j=1}^{N}\delta(x - x_j(t))$ at time $t \geqslant 0$. If $F = -\nabla W$ for some radially symmetric potential $W$ and the initial data satisfies $d_W(\rho^{in}, \rho^{in,N}) \to 0$ as $N \to \infty$ in the Wasserstein distance $d_W$, then

$$\sup_{t \in [0,T]} d_W(\rho(t), \rho^N(t)) \to 0.$$

for any given $T > 0$ [CJLV16]. From the theoretical viewpoint, this is a very nice result, but in practice a very large number of particles is required for numerical simulations of the particle model (5.9) to obtain a good control on the error after a long time. Nevertheless, particle simulations lead to a very good understanding of qualitative properties of solutions for aggregation equations where collisions do not happen [BCLR13a, BSK$^+$15, BDK$^+$18, DGH$^+$19, vBU12, vBUKB12]. For the one-dimensional setting with a nonlinear dependency of the term $\nabla W * \rho$, a finite volume scheme for simulating the behaviour after blow-up has been proposed in [JV15] and its convergence has been shown. Extremely accurate numerical schemes have been developed to study the blow-up profile for smooth solutions [HB12, HB10]. An energy decreasing finite volume method for a large class of PDEs including (5.11)

has been proposed in [CCH14a] and a convergence result for a finite volume scheme with general measures as initial data has been shown in [CJLV16]. In particular, this numerical scheme leads to numerical simulations of solutions in dimension greater than one.

The isotropic aggregation equation (5.11) may also be modified to include linear or nonlinear diffusion terms [CCY19]. While a linear diffusion term can be used to describe noise at the level of interacting particles, a nonlinear diffusion term can be used to model a system of interacting particles at the continuum level, and can be expressed by a repulsive potential. To see the latter, we consider the potential $W_\delta = W + \delta\delta_0$ for a parameter $\delta > 0$ and the Dirac delta $\delta_0$, inducing an additional strongly localised repulsion. This corresponds to a PDE with nonlinear diffusion which is given by

$$\rho_t + \nabla \cdot (\rho(-\nabla W * \rho)) = \delta\nabla \cdot (\rho\nabla\rho).$$

More generally, adding nonlinear diffusion in (5.11) results in the class of aggregation equations

$$\rho_t + \nabla \cdot (\rho(-\nabla W * \rho)) = \delta\nabla \cdot (\rho\nabla\rho^{m-1}) \tag{5.13}$$

with diffusion coefficient $\delta > 0$ and a real exponent $m > 1$. Of central importance for studies of (5.13) is its gradient flow formulation [AGS05] with respect to the energy

$$\mathcal{E}_\delta(\rho) = \frac{1}{2}\int_{\mathbb{R}^d} \rho(W * \rho + \delta\rho^{m-1})\,\mathrm{d}x. \tag{5.14}$$

In particular, stationary states of (5.13) are critical points of the energy (5.14). The existence of global minimisers of (5.14) has recently been studied in [Bed11] using techniques from the calculus of variations. While radially symmetric and non-increasing global minimisers exist for $m > 2$, the case $m = 2$ is critical and yields a global minimiser only for small enough diffusion coefficients $\delta > 0$. Burger et al. [BDFF13] have shown that the threshold for $\delta$ is $\|W\|_{L^1}$ for $m = 2$. Energy considerations have also been employed in [BD08] to study the large time behaviour of solutions to (5.13) in one dimension. The existence of finite-size, compactly supported stationary states for the general power exponent $m > 1$ is investigated in [BFH14].

### 5.1.2 Contributions

In this chapter, we consider the anisotropic counterparts of the isotropic aggregation equations (5.11) and (5.13) with $m = 2$ which are given by (5.1) and (5.10), respectively. No gradient flow formulation exists in this case. As a first aim of this chapter, we derive equilibrium conditions for stationary line patterns of (5.1) and (5.10) which can be regarded as minimisers of an energy functional, we prove the convergence of minimisers as $\delta \to 0$, and we investigate the dependence of stationary solutions on the diffusion constant $\delta$. The second aim of this chapter is to investigate the dependence of the diffusion coefficient $\delta$ on stationary solutions numerically by considering an appropriate numerical scheme for the anisotropic interaction equation (5.10) without gradient flow structure. The numerical scheme and its analysis is based on [CCH14a, CJLV16].

This chapter is organised as follows. In Section 5.2, we consider stationary solutions for general underlying tensor fields, while we restrict ourselves to spatially homogeneous tensor fields in Section 5.3 whose support is given by line patterns. For this case, we derive equilibrium conditions which can be reformulated as the minimisers of an energy functional. We show the existence of energy minimisers, and prove $\Gamma$-convergence of the regularised energies and the convergence of minimisers of the regularised energies to minimisers of the non-regularised energy functional as the diffusion coefficient goes to zero. Finally, we consider a numerical scheme for the anisotropic, nonlocal aggregation equation with nonlinear diffusion (5.10), prove its weak convergence as the diffusion coefficient goes to zero, and show numerical results in Section 5.4.

## 5.2 Stationary solutions for general tensor fields

In this section, we study the equilibria of the nonlocal aggregation equation with nonlinear diffusion (5.10). Since most applications of (5.10) require measure-valued solutions, we consider nonnegative solutions $\rho \geq 0$ only.

The stationary solutions $\rho_\infty = \rho_\infty(x, y)$ for $(x, y) \in \mathbb{R}^2$ satisfy

$$\nabla \cdot [\rho_\infty (F(\cdot, T(x, y)) * \rho_\infty - \delta \nabla \rho_\infty)] = 0 \qquad \text{a.e. in } \mathbb{R}^2,$$

implying that the argument has to be constant a.e. in $\mathbb{R}^2$. Since we are interested in stationary line patterns, the stationary solution $\rho_\infty$ should satisfy $\operatorname{supp} \rho_\infty \subsetneq \mathbb{R}^2$

for small diffusion coefficients $\delta > 0$ and hence it is sufficient to require

$$\rho_\infty(F(\cdot, T(x,y)) * \rho_\infty - \delta \nabla \rho_\infty) = 0 \qquad \text{a.e. in } \mathbb{R}^2, \tag{5.15}$$

or equivalently

$$F(\cdot, T(x,y)) * \rho_\infty = \delta \nabla \rho_\infty \qquad \text{on } \operatorname{supp}(\rho_\infty).$$

Integrating the first equality in (5.15) with respect to $x$ and the second equality with respect to $y$, we obtain

$$\frac{1}{\delta} \int_{\tilde{x}}^x (F(\cdot, T(\xi, y)) * \rho_\infty)(\xi, y) \, \mathrm{d}\xi + c_1(y) = \rho_\infty(x, y) - \rho_\infty(\tilde{x}, y),$$

$$\frac{1}{\delta} \int_{\tilde{y}}^y (F(\cdot, T(x, \eta)) * \rho_\infty)(x, \eta) \, \mathrm{d}\eta + c_2(x) = \rho_\infty(x, y) - \rho_\infty(x, \tilde{y}),$$

for $(x, y), (\tilde{x}, y), (x, \tilde{y}) \in \operatorname{supp}(\rho_\infty)$ where the functions $c_1, c_2$ can be determined uniquely. This results in the fixed point form

$$\rho_\infty(x, y) = \frac{\frac{1}{\delta} \int_{\tilde{x}}^x F(\cdot, T(\xi, y)) * \rho_\infty(\xi, y) \, \mathrm{d}\xi + c_1(y) + \rho_\infty(\tilde{x}, y)}{\iint\limits_{\operatorname{supp}(\rho_\infty)} \frac{1}{\delta} \int_{\tilde{x}}^x F(\cdot, T(\xi, y)) * \rho_\infty(\xi, y) \, \mathrm{d}\xi + c_1(y) + \rho_\infty(\tilde{x}, y) \, \mathrm{d}(x, y)}.$$

## 5.3 Stationary solutions for spatially homogeneous tensor fields

In this section, we consider stationary solutions for spatially homogeneous tensor fields. While anisotropic forces cannot be associated with a potential in general and stationary solutions of anisotropic aggregation equations generally cannot be regarded as minimizers of an energy functional, the idea of this section is to derive conditions for stationary solutions of (5.1) and (5.10) so that stationary line patterns can be obtained by minimising energy functionals which depend on a scalar potential. In particular, this dimension reduction will allow us to study the associated one-dimensional problem instead of the two-dimensional setting. Using these energy functionals, we show the existence of energy minimisers, establish $\Gamma$-convergence of a regularised energy functional with vanishing diffusion, and prove the convergence of minimisers of the regularised energy functional to minimisers of the non-regularised energy functional.

### 5.3.1 Notation and assumptions

The aim of this section is to derive a scalar force and its scalar potential in one variable that can be used to define the associated regularised and non-regularised energy functionals. For this, we study some properties of stationary solutions for spatially homogeneous tensor fields first.

As in [BDK$^+$18] one can show that a steady state of (5.10) for any spatially homogeneous tensor field $\tilde{T}$ is a coordinate transform of a steady state to the mean-field equation (5.10) for the tensor field $T$ with $l = (1,0)$ and $s = (0,1)$. Due to the choice of the tensor field $T$, we restrict ourselves to vertical line patterns as steady states in the following, i.e. we consider stationary solutions which are constant along the $y$-direction. To guarantee the existence of probability measures which are constant along the $y$-direction, we consider the domain $\Omega = \mathbb{R} \times [-0.5, 0.5]$ instead of $\mathbb{R}^2$ in this section. This assumption on the domain leads to stationary solutions on $\Omega$ of the form

$$\rho_\infty(x,y) = \rho_\infty(x,0) \quad \text{for a.e. } y \in [-0.5, 0.5]. \tag{5.16}$$

Note that this assumption on the domain $\Omega$ is not restrictive and by appropriate rescaling similar results can be obtained for any domain of the form $\mathbb{R} \times [a, b]$ for any $a, b \in \mathbb{R}$ with $a < b$.

The special form (5.16) of the stationary solutions motivates the definition of the space $\mathcal{P}_c(\Omega)$ of probability measures which are constant in $y$-direction. We define the space $\mathcal{P}_c(\Omega)$ by

$$\mathcal{P}_c(\Omega) = \left\{ \rho \in L^1_+(\Omega) \colon \int_\Omega \rho \, \mathrm{d}(x,y) = 1, \quad \rho(x,y) = \rho(x,0) \text{ for a.e. } y \in [-0.5, 0.5] \right\}.$$

Denoting the components of $F$ by $F_x, F_y$ for $d \in \Omega$, respectively, i.e. $F(d) = (F_x(d), F_y(d))$ for $d \in \Omega$, we extend $F_x, F_y$ and $\rho_\infty$, defined on $\Omega$, periodically on $\mathbb{R}^2$ with respect to the $y$-coordinate, if required, so that the convolution integrals $F_x(\cdot, T) * \rho_\infty, F_y(\cdot, T) * \rho_\infty$ can be evaluated. Since the total force $F$ in (5.8) reduces to

$$F(d, T) = \begin{pmatrix} f_l(|d|)d_1 \\ f_s(|d|)d_2 \end{pmatrix}$$

for the spatially homogeneous tensor field with $l = (1,0)$ and $s = (0,1)$, we have $F_x(d) = f_l(|d|)d_1$ and $F_y(d, T) = f_s(|d|)d_2$ for $d = (d_1, d_2)$. For $\rho_\infty$ satisfying (5.16), we have $F_y(\cdot, T) * \rho_\infty = 0$ since $F_y$ is an odd function in the $y$-coordinate and $F_y(\cdot, T) * \rho_\infty$ is periodically extended along the $y$-coordinate. In particular, the second equality in (5.15) is trivial. The convolution $F_x * \rho_\infty$ is of the form

$$
\begin{aligned}
F_x * \rho_\infty(x, y) &= \iint_\Omega F_x(w, z)\rho_\infty(x - w, y - z)\, \mathrm{d}(w, z) \\
&= \iint_\Omega F_x(x - w, y - z)\rho_\infty(w, z)\, \mathrm{d}(w, z) \\
&= \int_\mathbb{R} \rho_\infty(w, 0) \int_{[-0.5, 0.5]} F_x(x - w, y - z)\, \mathrm{d}z\, \mathrm{d}w.
\end{aligned}
$$

Since a scalar force in one variable is required for a dimension reduction, this motivates to introduce a scalar odd function $G \colon \mathbb{R} \to \mathbb{R}$ defined by

$$
G(x) = \int_{[-0.5, 0.5]} F_x(x, z)\, \mathrm{d}z = x \int_{[-0.5, 0.5]} f_l(\sqrt{x^2 + z^2})\, \mathrm{d}z \tag{5.17}
$$

where $G(0) = 0$. Due to the periodic extension of $F_x$ along the $y$-coordinate, we have $G(x) = \int_{[-0.5, 0.5]} F_x(x, y - z)\, \mathrm{d}z$ for any $y \in [-0.5, 0.5]$. Hence, there exists an interaction potential $W \colon \mathbb{R} \to \mathbb{R}$ which is even and such that

$$
G = -\frac{\mathrm{d}}{\mathrm{d}x} W. \tag{5.18}
$$

For the analysis in the following sections, we require rather relaxed conditions on the potential $W$:

**Assumption 8.** *For the interaction potential $W$ satisfying* (5.18), *we require*

**(A1).** *$W$ is even, i.e. $W(x) = W(-x)$.*

**(A2).** *$W$ is continuous.*

**(A3).** *$W$ is locally integrable on $\Omega$.*

**(A4).** *$W(x) \to 0$ as $|x| \to \infty$.*

**(A5).** *There exist $\bar\delta > 0$ and a measure $\bar\rho \in \mathcal{P}_c(\Omega)$ such that $\mathcal{E}_{\bar\delta}(\bar\rho) \leqslant 0$.*

**(A6).** *There exists some $x_W > 0$ such that*

$$
W(x) \leqslant 0 \;\text{ for }\; 0 \leqslant |x| \leqslant x_W \quad \text{and} \quad W(x) < 0 \;\text{ for some }\; x \in (0, x_W). \tag{5.19}
$$

Using the potential $W$, we define the energy functional

$$\mathcal{E}(\rho_\infty) := \frac{1}{2} \iint_\Omega \rho_\infty(W * \rho_\infty) \, \mathrm{d}(x, y) \tag{5.20}$$

where $W * \rho_\infty(x, y)$ is regarded as the convolution with respect to the first coordinate, i.e.

$$W * \rho_\infty(x, y) = \int_\mathbb{R} W(x - w)\rho_\infty(w, y) \, \mathrm{d}w, \tag{5.21}$$

which is constant with respect to the second coordinate. The regularisation of the energy $\mathcal{E}$ is defined as

$$\mathcal{E}_\delta(\rho_\infty) := \frac{1}{2} \iint_\Omega \rho_\infty(W * \rho_\infty + \delta\rho_\infty) \, \mathrm{d}(x, y) \tag{5.22}$$

on $\mathcal{P}_c(\Omega)$.

**Remark 16.** *Note that assumptions (A1), (A2), (A3), (A4) are rather relaxed conditions and allow us to consider a rather general class of interaction potentials, including the one that can be derived from $G$ based on $F_x$ in the Kücken-Champod model. In particular, the interaction potential $W(x)$ satisfies $W(0) = 0$ and is bounded. Besides, the energy $\mathcal{E} : \mathcal{P}_c(\Omega) \to \mathbb{R}$ in (5.22) is weakly lower semi-continuous with respect to weak convergence of measures.*

*Assumption (A5) is required for establishing the existence of minimisers of the energy $\mathcal{E}_\delta$ in (5.22). In particular, it follows from (A5) that there exists a measure $\bar\rho \in \mathcal{P}_c(\Omega)$ such that $\mathcal{E}_\delta(\bar\rho) \leqslant 0$ for all $0 \leqslant \delta \leqslant \bar\delta$. Assumption (A5) also implies that there exists $x \in (0, x_W)$ such that $W(x) < 0$.*

*Assumption (A6) is motivated by the form of the force $F$ in (5.4) which exhibits short-range repulsion and long-range attraction forces along $l$. Hence, there exists a constant $d_a > 0$ such that*

$$(f_A + f_R)(|d|) \leqslant 0 \ \text{for } |d| > d_a \qquad \text{and} \qquad (f_A + f_R)(|d|) > 0 \ \text{for } 0 \leqslant |d| < d_a.$$

*A slightly stronger condition is given by the existence of some $x_G > 0$ such that*

$$G(x) \geqslant 0 \ \text{for } 0 \leqslant x \leqslant x_G, \tag{5.23}$$

*where $G$ is defined in (5.17). Then, (A6) follows from (5.18). Note that condition*

(5.19) in *(A6)* is necessary for *(A5)* for $\delta > 0$ and sufficient for *(A5)* for $\delta \geqslant 0$.

**Remark 17.** *Assumption (A5) is not restrictive which is shown by the following examples for $\bar{\rho} \in \mathcal{P}_c(\Omega)$ which satisfies (A5), provided (A6) holds. We consider $\bar{\rho} = \frac{1}{|Q_W|}\chi_{Q_W}$ where $Q_W = [-x_W/2, x_W/2] \times [-0.5, 0.5]$. The non-regularised energy $\mathcal{E}$ in (5.20) is clearly negative and for $\delta > 0$ sufficiently small, assumption (A5) is satisfied, provided (A6) holds. More generally, $\bar{\rho} = \frac{1}{|Q_{W(\bar{x})}|}\chi_{Q_{W(\bar{x})}}$ satisfies (A5) for any $\bar{x} \in (0, x_{W,max})$ where*

$$x_{W,max} = \sup\left\{\bar{x} > 0\colon \int_0^{\bar{x}} W(s)\,\mathrm{d}s \leqslant 0\right\} > x_W$$

*and $Q_{W(\bar{x})} = [-\bar{x}/2, \bar{x}/2] \times [-0.5, 0.5]$, provided (A6) holds.*

*Another example for measures satisfying (A5) are mollified delta distributions. Note that $\bar{\rho}(x, y) = \delta(x) \in \mathcal{P}_c(\Omega)$ satisfies (A5) for $\mathcal{E}$ since*

$$\iint\limits_\Omega \rho_\infty(W * \rho_\infty)\,\mathrm{d}(x, y) = W(0) = 0.$$

*Further note that for the one-dimensional heat kernel*

$$\phi(x) = \frac{1}{\sqrt{4\pi}}\exp\left(-\frac{|x|^2}{4}\right)$$

*we consider the rescaled kernel*

$$\phi_\varepsilon(x, y) = \frac{1}{\sqrt{\varepsilon}}\phi\left(\frac{x}{\sqrt{\varepsilon}}\right).$$

*Due to property (5.19) of $W$ we can choose $\varepsilon > 0$ and $\delta > 0$ sufficiently small such that $\mathcal{E}_\delta(\phi_\varepsilon) \leqslant 0$.*

*The above examples show that for $\rho_\infty$ with compact, connected support (A5) is satisfied. Similarly, for any $\delta > 0$, the first term of the energy functional $\mathcal{E}_\delta$ in (5.22) is negative provided the support of $\rho_\infty$ is sufficiently small in the x-direction and (A6) holds. Hence, the parameter $\delta > 0$ can be chosen sufficiently small so that (A5) is satisfied.*

### 5.3.2 Equilibrium conditions

Using the interaction potential $W$, the condition for equilibria in (5.15) can be reformulated as

$$\rho_\infty \partial_x (W * \rho_\infty + \delta \rho_\infty) = 0 \qquad \text{a.e. in } \Omega \tag{5.24}$$

where the convolution $W * \rho_\infty$ is given by (5.21). Hence, we require

$$W * \rho_\infty + \delta \rho_\infty = C \qquad \text{on } \operatorname{supp}(\rho_\infty) \tag{5.25}$$

for some constant $C \in \mathbb{R}$. Note that we obtain by multiplying (5.25) by $\rho_\infty$ and integrating over $\operatorname{supp}(\rho_\infty)$

$$\iint\limits_{\operatorname{supp}(\rho_\infty)} \rho_\infty(x,y) W * \rho_\infty(x,y) \, \mathrm{d}(x,y) + \delta \iint\limits_{\operatorname{supp}(\rho_\infty)} \rho_\infty^2(x,y) \, \mathrm{d}(x,y) = C,$$

where the unit mass of $\rho_\infty$ was used. In particular, this shows that $C = C(\delta) \in \mathbb{R}$ is uniquely determined and the integral equation (5.25) may be expressed in the equivalent fixed point form

$$\rho_\infty(x,y) = \frac{C - W * \rho_\infty}{\iint\limits_{\operatorname{supp}(\rho_\infty)} C - W * \rho_\infty \, \mathrm{d}(x,y)}.$$

Clearly, the fixed point form is consistent with (5.16) and the dependence of $\rho_\infty$ on $\delta$ follows from $C = C(\delta)$.

It has been shown in [BDFF13] for non-trivial stationary states for purely repulsive potentials in the set $L^2(\mathbb{R}^d) \cap \mathcal{P}(\mathbb{R}^d)$ with $d \geqslant 1$ that minimisers are sufficient for solving the equilibrium conditions. A similar results can be shown in our setting of more general potentials and stationary states in the space $L^2(\Omega) \cap \mathcal{P}_c(\Omega)$ whose elements satisfy (5.16) in addition. In particular, a minimiser of the energy functional (5.22) is sufficient for solving (5.24).

**Proposition 9** (Stationary solutions via energy minimisation)**.** *Let $\rho_\infty \in L^2(\Omega)$ be a minimiser for the energy functional (5.22) on $\mathcal{P}_c(\Omega)$ which is of the form (5.16). Then, $\rho_\infty$ satisfies (5.15).*

### 5.3.3 Existence and convergence of minimisers

Motivated by Proposition 9, we consider the energy functionals $\mathcal{E}$ and $\mathcal{E}_\delta$, defined in (5.20) and (5.22). For the existence and convergence of minimisers, we have to verify that an energy minimising sequence is precompact in the sense of weak convergence of measures, and prove a $\Gamma$-convergence result. For this, we use Lions' concentration compactness lemma for probability measures [Lio84], [Str00, Section 4.3] and reformulate it to our setting.

**Lemma 5** (Concentration-compactness lemma for measures). *Let $\{\rho_n\}_{n \in \mathbb{N}} \subset \mathcal{P}_c(\Omega)$. Then, there exists a subsequence $\{\rho_{n_k}\}_{k \in \mathbb{N}}$ satisfying one of the three following possibilities:*

(i) *(tightness up to transition) There exists $z_k \in \Omega$ such that for all $\varepsilon > 0$ there exists $R > 0$ satisfying*

$$\int_{B_R(z_k) \cap \Omega} \mathrm{d}\rho_{n_k}(x, y) \geqslant 1 - \varepsilon \quad \text{for all } k;$$

(ii) *(vanishing)*

$$\lim_{k \to \infty} \sup_{z \in \Omega} \int_{B_R(z) \cap \Omega} \mathrm{d}\rho_{n_k}(x, y) = 0 \quad \text{for all } R > 0;$$

(iii) *(dichotomy) There exists $\alpha \in (0, 1)$ such that for all $\varepsilon > 0$ there exists $R > 0$ and a sequence $\{z_k\}_{k \in \mathbb{N}} \subset \Omega$ with the following property:*

*Given any $R' > R$ there are nonnegative measures $\rho_k^1$ and $\rho_k^2$ such that*

$$0 \leqslant \rho_k^1 + \rho_k^2 \leqslant \rho_{n_k},$$
$$\operatorname{supp}(\rho_k^1) \subset B_R(z_k) \cap \Omega,$$
$$\operatorname{supp}(\rho_k^2) \subset \Omega \backslash B_{R'}(z_k),$$
$$\limsup_{k \to \infty} \left( \left| \alpha - \int_\Omega \mathrm{d}\rho_k^1(x, y) \right| + \left| (1 - \alpha) - \int_\Omega \mathrm{d}\rho_k^2(x, y) \right| \right) \leqslant \varepsilon.$$

For proving the existence of minimisers of the energy functional (5.22), one can use the direct method of the calculus of variations and Lemma 5 to eliminate the cases 'vanishing' and 'dichotomy' of an energy minimising sequence. The proof of the existence of minimisers of the regularised energy $\mathcal{E}_\delta$ in (5.22) is very similar to the one for the non-regularised energy $\mathcal{E}$, provided in [SST15, Theorem 3.2]:

**Proposition 10** (Existence of minimisers). *Suppose $W$ satisfies assumptions (A1), (A2), (A3) and (A4). Then, the regularised energy $\mathcal{E}_\delta$ in (5.22) has a global minimiser in $\mathcal{P}_c(\Omega)$ if and only if it satisfies (A5). The non-regularised energy $\mathcal{E}$ in (5.20) has a global minimiser in $\mathcal{P}_c(\Omega)$ if and only if (A5) is satisfied for $\mathcal{E}$.*

**Remark 18.** *Let $\delta > 0$ be given. To see the necessity of assumption (A5) for the existence of minimisers, assume that $\mathcal{E}_\delta(\rho) > 0$ for all $\rho \in \mathcal{P}_c(\Omega)$. We consider a sequence of measures which 'vanishes' in the sense of Lemma 5(2). Let*

$$\rho(x, y) = \chi_{Q_1}(x, y),$$

*where $Q_n$ denotes the rectangle $[-0.5n, 0.5n] \times [-0.5, 0.5]$ for $n \geq 1$, and $\chi_{Q_n}$ denotes the characteristic function of $Q_n$. We consider the sequence*

$$\rho_n(x, y) = \frac{1}{n} \rho\left(\frac{x}{n}, y\right)$$

*for $n \geq 1$. Then, $\rho_n \in \mathcal{P}_c(\Omega)$ and*

$$
\begin{aligned}
0 < \mathcal{E}_\delta(\rho_n) &= \frac{1}{n^2} \iint\limits_{Q_n} \int_{[-0.5n, 0.5n]} W(x - w) \, \mathrm{d}w \, \mathrm{d}(x, y) + \frac{\delta}{n^2} \iint\limits_{Q_n} \mathrm{d}(x, y) \\
&= \frac{1}{n^2} \iint\limits_{Q_n} \iint\limits_{Q_n} W(x - w) \, \mathrm{d}(w, z) \, \mathrm{d}(x, y) + \frac{\delta}{n} \\
&\leq \frac{1}{n^2} \iint\limits_{Q_n} \iint\limits_{(x,0) + Q_n} |W(w)| \, \mathrm{d}(w, z) \, \mathrm{d}(x, y) + \frac{\delta}{n} \\
&\leq \frac{1}{n} \left( \iint\limits_{Q_R} |W(x)| \, \mathrm{d}(x, y) + \iint\limits_{Q_{2n} \setminus Q_R} |W(x)| \, \mathrm{d}(x, y) + \delta \right) \\
&\leq \frac{C(R)}{n} + 2 \sup_{|x| \geq R} |W(x)| + \frac{\delta}{n}
\end{aligned}
$$

*for any $R > 0$ where*

$$C(R) := \iint\limits_{Q_R} |W(x)| \, \mathrm{d}(x, y).$$

*Due to (A4) we have $\sup_{|x| \geq R} |W(x)| \to 0$ as $R \to 0$, implying that for any $\varepsilon > 0$ we can choose $R$ so that $2 \sup_{|x| \geq R} |W(x)| < \frac{\varepsilon}{2}$. Then, we can choose $n$ large enough*

so that $\frac{C(R)+\delta}{n} < \frac{\varepsilon}{2}$ *holds. Hence,* $\lim_{n\to\infty} \mathcal{E}_\delta(\rho_n)=0$, *implying*

$$\inf_{\rho \in \mathcal{P}_c(\Omega)} \mathcal{E}_\delta(\rho) = 0.$$

*Since* $\mathcal{E}_\delta(\rho) > 0$ *for all* $\rho \in \mathcal{P}_c(\Omega)$, $\mathcal{E}_\delta$ *does not have a minimiser in* $\mathcal{P}_c(\Omega)$.

**Theorem 5** (Γ-convergence of regularised energies)**.** *Suppose that* $W$ *satisfies* **(A1)**, **(A2)**, **(A3)** *and* **(A4)**. *The sequence of regularised energies* $\{\mathcal{E}_\delta\}_{\delta>0}$ *Γ-converges to the energy* $\mathcal{E}$ *with respect to the weak convergence of measures. That is,*

- *(Liminf) For any* $\{\rho_\delta\}_{\delta>0} \subset \mathcal{P}_c(\Omega)$ *and* $\rho \in \mathcal{P}_c(\Omega)$ *such that* $\rho_\delta$ *converges weakly to* $\rho$ *as* $\delta \to 0$, *we have*

$$\liminf_{\delta\to0} \mathcal{E}_\delta(\rho_\delta) \geqslant \mathcal{E}(\rho).$$

- *(Limsup) For any* $\rho \in \mathcal{P}_c(\Omega)$ *there exists a sequence* $\{\rho_\delta\}_{\delta>0} \in \mathcal{P}_c(\Omega)$ *such that* $\rho_\delta$ *converges weakly to* $\rho$ *as* $\delta \to 0$ *and*

$$\limsup_{\delta\to0} \mathcal{E}_\delta(\rho_\delta) \leqslant \mathcal{E}(\rho).$$

*Proof.* Step 1 (Liminf): Since $W$ is lower semi-continuous and bounded from below, the weak lower semi-continuity of the first term in the energy functional $\mathcal{E}_\delta$ in (5.22) follows from the Portmanteau Theorem [vdVW96, Theorem 1.3.4], i.e.

$$\liminf_{\delta\to0} \frac{1}{2} \iint_\Omega \rho_\delta(W * \rho_\delta) \, \mathrm{d}(x,y) \geqslant \frac{1}{2} \iint_\Omega \rho(W * \rho) \, \mathrm{d}(x,y).$$

Together with

$$\liminf_{\delta\to0} \frac{\delta}{2} \iint_\Omega \rho_\delta^2 \, \mathrm{d}(x,y) \geqslant 0,$$

the liminf inequality immediately follows.

Step 2 (Limsup): Let $\mu \in \mathcal{P}_c(\Omega)$ be given, let

$$\phi(x) = \frac{1}{\sqrt{4\pi}} \exp\left(-\frac{|x|^2}{4}\right)$$

denote the one-dimensional heat kernel and define

$$\phi_\delta(x) = \frac{1}{\sqrt{\delta}}\phi\left(\frac{x}{\sqrt{\delta}}\right).$$

Note that $\phi \in C^\infty(\Omega)$, $\phi(x,y) = \phi(-x,y)$ for all $(x,y) \in \Omega$, $\phi$ is constant in $y$, and

$$\iint_\Omega \phi\,\mathrm{d}(x,y) = 1.$$

In particular, $|\phi_\delta| \leqslant \frac{C_\phi}{\sqrt{\delta}}$ where $C_\phi$ denotes the bound of $\phi$. We define the measure $\rho_\delta := \phi_\delta * \rho$ which converges weakly to $\rho$ in $\mathcal{P}_c(\Omega)$. Note that

$$\delta \iint_\Omega \rho_\delta^2\,\mathrm{d}(x,y) \leqslant C_\phi\sqrt{\delta}\iint_\Omega \rho_\delta\,\mathrm{d}(x,y) = C_\phi\sqrt{\delta} \to 0 \qquad \text{as } \delta \to 0.$$

Due to the continuity of $W$, the term $-\iint_\Omega \rho(W*\rho)\,\mathrm{d}(x,y)$ is weakly lower semi-continuous and

$$\limsup_{\delta\to 0} \frac{1}{2}\iint_\Omega \rho_\delta(W*\rho_\delta)\,\mathrm{d}(x,y) \leqslant \frac{1}{2}\iint_\Omega \rho(W*\rho)\,\mathrm{d}(x,y),$$

resulting in the limsup inequality. $\qquad\square$

**Theorem 6** (Convergence of minimisers). *Suppose that $W$ satisfies **(A1)**, **(A2)**, **(A3)** and **(A4)**. For any $\bar\delta > 0$ sufficiently small, suppose that $\mathcal{E}_{\bar\delta}$ satisfies **(A5)** and let $\rho_\delta \in \mathcal{P}_c(\Omega)$ be a minimiser of the energy $\mathcal{E}_\delta$ in (5.22) for all $0 < \delta \leqslant \bar\delta$. Then, there exists $\rho \in \mathcal{P}_c(\Omega)$ such that, up to a subsequence and translations, $\rho_\delta$ converges weakly to $\rho$ as $\delta \to 0$, and $\rho$ minimises the energy $\mathcal{E}$ over $\mathcal{P}_c(\Omega)$.*

*Proof.* Let $\{\rho_\delta\}_{\delta>0} \subset \mathcal{P}_c(\Omega)$ be a sequence of minimisers of $\mathcal{E}_\delta$. For $\bar\delta > 0$ sufficiently small, we may assume that $\mathcal{E}_\delta(\rho_\delta) \leqslant 0$ for all $0 < \delta \leqslant \bar\delta$ since $\rho_\delta$ minimises $\mathcal{E}_\delta$. As in [SST15, Theorem 3.2] one can eliminate the cases 'vanishing' and 'dichotomy' in Lemma 5, implying that there exists a subsequence $\{\rho_{\delta_k}\}_{k\in\mathbb{N}}$ satisfying 'tightness up to translation', i.e. there exists $z_k \in \Omega$ such that for all $\varepsilon > 0$ there exists $R > 0$ satisfying

$$\int_{B_R(z_k)\cap\Omega} \mathrm{d}\rho_{\delta_k}(x,y) \geqslant 1 - \varepsilon \quad \text{for all } k.$$

We define $\tilde\rho_{\delta_k} := \rho_{\delta_k}(\cdot - z_k)$ and hence $\{\tilde\rho_{\delta_k}\}_{k\in\mathbb{N}}$ is tight. Since $\mathcal{E}_{\delta_k}(\rho_{\delta_k}) = \mathcal{E}_{\delta_k}[\tilde\rho_{\delta_k}]$,

$\{\tilde{\rho}_{\delta_k}\}_{k\in\mathbb{N}}$ is also a sequence of minimisers of $\mathcal{E}_{\delta_k}$ and by Prokhorov's Theorem (cf. [Bil71, Theorem 4.1]) there exists a further subsequence $\{\tilde{\rho}_{\delta_k}\}_{k\in\mathbb{N}}$, not relabelled, such that $\tilde{\rho}_{\delta_k}$ converges weakly to some measure $\rho \in \mathcal{P}_c(\Omega)$ as $k \to \infty$.

For showing that the measure $\rho$ minimises the energy functional $\mathcal{E}$, we consider an arbitrary measure $\mu \in \mathcal{P}_c(\Omega)$. By the limsup inequality in Theorem 5, there exists a sequence $\{\mu_{\delta_k}\}_{k\in\mathbb{N}}$ which converges weakly to $\mu$ as $k \to \infty$ such that

$$\limsup_{k\to\infty} \mathcal{E}_{\delta_k}(\mu_{\delta_k}) \leqslant \mathcal{E}(\mu).$$

Together with the liminf inequality in Theorem 5, this yields

$$\lim_{k\to\infty} \mathcal{E}_{\delta_k}(\mu_{\delta_k}) = \mathcal{E}(\mu).$$

Since the sequence of measures $\tilde{\rho}_{\delta_k}$ is a minimising sequence of $\mathcal{E}_{\delta_k}$ which converges weakly to $\rho$, we obtain, again by the liminf inequality,

$$\mathcal{E}(\rho) \leqslant \liminf_{k\to\infty} \mathcal{E}_{\delta_k}(\tilde{\rho}_{\delta_k}) \leqslant \liminf_{k\to\infty} \mathcal{E}_{\delta_k}(\mu_{\delta_k}) = \mathcal{E}(\mu).$$

$\square$

### 5.3.4  Properties of stationary solutions

Note that the odd function $G$, defined by $G(x) = \int_{[-0.5,0.5]} F_x(x,z)\,\mathrm{d}z$ in (5.17), is nonnegative for $x \geqslant 0$ for the force $F_x$ in the Kücken-Champod model, see Section 5.1 for the precise definition of the force coefficients. Since $G = -\frac{\mathrm{d}}{\mathrm{d}x}W$, we can make stronger assumptions on $G$ and $W$ than in (5.23) and (5.19), respectively, and we assume in this subsection that

$$W'(x) = G(x) \geqslant 0 \ \text{ for all } \ x \geqslant 0 \tag{5.26}$$

and

$$W(x) \leqslant 0 \ \text{ for all } \ |x| \geqslant 0. \tag{5.27}$$

In particular, the assumptions on the potential $W$ for the one-dimensional results in [BDFF13] are satisfied and the results also hold for the stationary states $\rho_\infty$ satisfying (5.16). We obtain:

**Corollary 8.** *Let $\delta > 0$ be given.*

- *If $\delta \geqslant \|W\|_{L^1}$, there exists no stationary solution $\rho_\infty$ in $L^2 \cap \mathcal{P}_c(\Omega)$ of the form (5.16) which satisfies (5.15).*

- *If $\delta < \|W\|_{L^1}$, there exists a minimiser $\rho_\infty \in L^2 \cap \mathcal{P}_c(\Omega)$ of the energy functional (5.22) which is symmetric in $x$, non-increasing on $x \geqslant 0$, and of the form (5.16).*

To relate the cases $\delta < \|W\|_{L^1}$ and $\delta \geqslant \|W\|_{L^1}$ to assumption **(A5)** note that

$$-\iint\limits_{\Omega} \rho_\infty W * \rho_\infty \, \mathrm{d}(x,y) \leqslant \|W\|_{L^1} \iint\limits_{\Omega} \rho_\infty^2 \, \mathrm{d}(x,y)$$

by Young's convolution inequality and property (5.27) of $W$, implying

$$\mathcal{E}_\delta(\rho_\infty) = \frac{1}{2} \iint\limits_{\Omega} \rho_\infty (W * \rho_\infty + \delta \rho_\infty) \, \mathrm{d}(x,y) \geqslant \frac{\delta - \|W\|_{L^1}}{2} \iint\limits_{\Omega} \rho_\infty^2 \, \mathrm{d}(x,y)$$

and hence, a necessary condition for **(A5)** is given by $\delta \leqslant \|W\|_{L^1}$.

Due to conditions (5.26) and (5.27), properties of the stationary solution of the one-dimensional case in [BDFF13] can also be extended to our setting:

**Proposition 11.** *For any given $L > 0$ there exists a unique symmetric function $\rho_\delta \in C^2([-L, L] \times [-0.5, 0.5])$ with unit mass, $\rho_\delta(x, y) = \rho_\delta(x, 0)$ for all $y \in [-0.5, 0.5]$, and $\partial_x \rho_\delta(x, y) \leqslant 0$ for $x \geqslant 0, y \in [-0.5, 0.5]$, such that $\rho_\delta$ solves (5.25) for some $\delta = \delta(L) > 0$ where $C = 2\mathcal{E}_\delta(\rho_\delta)$ in (5.25). Such a function $\rho_\delta$ also satisfies $\partial_x^2 \rho_\delta(0, y) < 0$ for all $y \in [-0.5, 0.5]$. Moreover, $\delta(L)$ is the largest eigenvalue of the compact operator*

$$\mathcal{W}_L[\rho_\delta](x) := \int_0^L \rho_\delta(w, 0) \Big( W(x - w) + W(x + w) - W(L - w) - W(L + w) \Big) \, \mathrm{d}w$$

*on the Banach space*

$$\mathcal{Y}_L := \{\rho_\delta \in C([0, L] \times [-0.5, 0.5]) : \rho_\delta(L, y) = 0 \text{ for all } y \in [-0.5, 0.5]\}.$$

*The simple eigenvalue $\delta(L)$ is uniquely determined as a function of $L$ with the following properties:*

*(i) $\delta(L)$ is continuous and strictly increasing with respect to $L$,*

*(ii) $\lim_{L \to +\delta} \delta(L) = \|W\|_{L^1}$,*

*(iii)* $\delta(0) = 0$.

**Theorem 7.** *Let $\delta < \|W\|_{L^1}$. Then, there exists a unique $\rho_\delta \in L^2 \cap \mathcal{P}_c(\Omega)$ with unit mass and zero centre of mass such that (5.24) is satisfied. Moreover,*

- *$\rho_\delta$ is symmetric in $x$ and monotonically decreasing on $x > 0$,*

- *$\rho_\delta \in C^2(\mathrm{supp}(\rho_\delta))$,*

- *$\mathrm{supp}(\rho_\delta)$ is a bounded, connected set in $\Omega$,*

- *$\rho_\delta$ has a global maximum at $x = 0$, and $\partial_x^2 \rho_\delta(0, y) < 0$ for all $y \in [-0.5, 0.5]$,*

- *$\rho_\delta$ is the global minimiser of the energy $\mathcal{E}_\delta$ in (5.22).*

### 5.3.5 Stationary solutions on the torus

To compare the analytical results to the numerical simulations, we consider the two-dimensional unit torus $\mathbb{T}^2$, or equivalently, the unit square $[-0.5, 0.5]^2$ with periodic boundary conditions as the domain in this section. For minimisers $\rho_\delta$ of the energy functional $\mathcal{E}_\delta$ in (5.22), we require $\rho_\infty(x, y) = \rho_\infty(x, 0)$ for all $y \in [-0.5, 0.5]$ with zero centre of mass. Note that the uniform distribution on $[-0.5, 0.5]^2$ also satisfies these conditions.

In contrast to steady states on $\Omega = \mathbb{R} \times [-0.5, 0.5]$ in Theorem 7, steady states on the unit torus may not have connected support and may be composed of finitely many stripes of equal width and equal distances between each other. To see this, let us consider minimisers of the non-regularised energy $\mathcal{E}$ in (5.20), and suppose that we have an odd number $n$ of stripes first. Let

$$\rho_\infty(x, y) = \frac{1}{n} \sum_{k=1}^{n} \delta_{x_k}(x) \tag{5.28}$$

for $x_1, \ldots, x_n \in (-0.5, 0.5)$ with $x_1 < \ldots < x_n$. We introduce the general velocity field $V \in C^1([-0.5, 0.5])$ such that $V(x_k) = v_k$ for some given $v_1, \ldots, v_n \in \mathbb{R}$. Let $u(x, y, s)$ be a local solution to the Cauchy problem

$$\partial_s u + \partial_x(uV) = 0,$$
$$u(x, y, 0) = \rho_\infty(x, y).$$

The evolution of the energy $\mathcal{E}$ in (5.20) along $u$ at time $s = 0$ is given by

$$\frac{\mathrm{d}}{\mathrm{d}s}\mathcal{E}(u(x,y,s))\Big|_{s=0} = \int_{[-0.5,0.5]^2} (W * u)\partial_s u \, \mathrm{d}(x,y)\Big|_{s=0}$$

$$= \int_{[-0.5,0.5]^2} \rho_\infty V(W' * \rho_\infty) \, \mathrm{d}(x,y)$$

since $\rho_\infty(-0.5, y) = \rho_\infty(0.5, y) = 0$ for all $y \in [-0.5, 0.5]$. Here, appropriate periodic extensions of $W'$ and $\rho_\infty$ are considered in the convolution integral. Note that

$$\int_{[-0.5,0.5]^2} \rho_\infty V \partial_x(W * \rho_\infty) \, \mathrm{d}(x,y) = \sum_{k=1}^{n} v_k \sum_{j=1}^{n} W'(x_k - x_j),$$

and we require $\frac{\mathrm{d}}{\mathrm{d}s}\mathcal{E}(u(x,y,s))\big|_{s=0} = 0$ for minimisers of $E$ for any velocity field $V$, implying

$$\sum_{j=1}^{n} W'(x_k - x_j) = \sum_{\substack{j=1 \\ j \neq k}}^{n} W'(x_k - x_j) = 0, \qquad (5.29)$$

since $W'(0) = G(0) = 0$. For general potentials $W$, this condition can only be satisfied for equidistant points $x_1, \ldots, x_n$ with

$$x_k = \frac{k}{n} - \frac{n+1}{2n}, \qquad k = 1, \ldots, n, \qquad (5.30)$$

since $W'(d) = -W'(-d)$ for $d \in \mathbb{R}^2$. In particular, any minimiser $\rho_\infty$ of $\mathcal{E}$ of the form (5.28) with zero centre of mass consisting of an odd number $n$ of parallel lines has to consist of $n$ equidistant lines at locations $x_k$ in (5.30). The single straight vertical line with zero centre of mass is included in the property of locations $x_k$ in (5.30).

For an even number $n$ of lines, we can proceed in a similar way as above. Condition (5.29) implies that for minimisers $\rho_\infty$ of $\mathcal{E}$ consisting of an even number of lines the property $W'(-0.5) = W'(0.5) = 0$ is required in addition to equidistant lines at locations $x_k$ in (5.30). Note that $W'(-0.5) = W'(0.5) = 0$ is equivalent to $f_l(0.5) = 0$ for the force coefficient $f_l$ in the definition of the force $F_x(d) = f_l(|d|)d$.

More generally, for minimizers of $\mathcal{E}$ we require the measure

$$\rho_\infty(x,y) = \frac{1}{n} \sum_{k=1}^{n} \delta_{x_k}(x)$$

188

for $n \in \mathbb{N}$ arbitrary to be a periodic function of period $\frac{1}{n}$. This motivates to consider measures $\rho_\infty$ which are periodic of period $\frac{1}{n}$ in $x$ for some $n \in \mathbb{N}$, constant in $y$, and whose support $\mathrm{supp}(\rho_\infty)$ is not connected, i.e. $\mathrm{supp}(\rho_\infty)$ consists of $n$ connected components $M_k, k = 1, \ldots, n$, with

$$M_k = M_j + \frac{k - j}{n}, \qquad j, k \in \{1, \ldots, n\}. \tag{5.31}$$

We further assume that $\rho_\infty$ is symmetric in $x$ on $M_k$ for $k = 1, \ldots, n$. Note that for measures with zero centre of mass, we can assume without loss of generality that $\rho_\infty(-0.5) = \rho_\infty(0.5) = 0$. For $\delta > 0$ and $\rho_\infty \in L^2([-0.5, 0.5]^2)$, we may also consider the regularised energy $\mathcal{E}_\delta$ in (5.22). For the evolution of the energy $\mathcal{E}_\delta$, we obtain

$$
\begin{aligned}
\frac{\mathrm{d}}{\mathrm{d}s} \mathcal{E}_\delta(u(x, y, s)) \Big|_{s=0} &= \int_{[-0.5, 0.5]^2} (W * u + \delta u) \partial_s u \, \mathrm{d}(x, y) \Big|_{s=0} \\
&= \int_{[-0.5, 0.5]^2} \rho_\infty V \partial_x (W * \rho_\infty + \delta \rho_\infty) \, \mathrm{d}(x, y).
\end{aligned}
$$

For any velocity field $V \in C^1([-0.5, 0.5])$ which is constant on each connected component of $\mathrm{supp}(\rho_\infty)$ with $v_k \in \mathbb{R}$ such that $V(x) = v_k$ for all $(x, y) \in M_k$ for $k = 1, \ldots, n$, we have

$$
\delta \int_{[-0.5, 0.5]^2} \rho_\infty V \partial_x \rho_\infty \, \mathrm{d}(x, y) = \frac{\delta}{2} \sum_{k=1}^n v_k \int_{M_k} \partial_x \rho_\infty^2 \, \mathrm{d}(x, y) = 0
$$

and due to the periodicity of $\rho_\infty$ we obtain

$$
\begin{aligned}
&\int_{[-0.5, 0.5]^2} \rho_\infty V \partial_x (W * \rho_\infty) \, \mathrm{d}(x, y) \\
&= \sum_{k=1}^n v_k \int_{M_k} \rho_\infty (W' * \rho_\infty) \, \mathrm{d}(x, y) \\
&= \sum_{k=1}^n v_k \int_{M_k} \rho_\infty(x, y) \sum_{j=1}^n \int_{M_j} W'(x - w) \rho_\infty(w, z) \, \mathrm{d}(w, z) \, \mathrm{d}(x, y).
\end{aligned}
$$

Since $W'$ is an odd function, we have

$$
\int_{M_k} \rho_\infty(x, y) \int_{M_k} W'(x - w) \rho_\infty(w, z) \, \mathrm{d}(w, z) \, \mathrm{d}(x, y) = 0
$$

and

$$\int_{M_k} \rho_\infty(x,y) \int_{M_{k+j}} W'(x-w)\rho_\infty(w,z)\, \mathrm{d}(w,z)\, \mathrm{d}(x,y)$$
$$= -\int_{M_k} \rho_\infty(x,y) \int_{M_{k-j}} W'(x-w)\rho_\infty(w,z)\, \mathrm{d}(w,z)\, \mathrm{d}(x,y)$$

due to the symmetry of $\rho_\infty$ in $x$ on each $M_k$ and the translation property (5.31) of two connected components of $\mathrm{supp}(\rho_\infty)$. Under the above assumptions, this implies that

$$\int_{[-0.5,0.5]^2} \rho_\infty V \partial_x(W * \rho_\infty)\, \mathrm{d}(x,y) = 0$$

for $n$ odd, while for $n$ even, we have to require in addition that $W'(-0.5) = W'(0.5) = 0$, i.e. $f_l(0.5) = 0$, as before. Note that for general potentials $W$, the conditions that $\rho_\infty$ is symmetric in $x$ on $M_k$, and all connected components $M_k$ of $\mathrm{supp}(\rho_\infty)$ are of equal size, equidistant, and given by the translation property (5.31) are necessary for minimisers $\rho_\infty$ of $\mathcal{E}_\delta$ for $\delta \geqslant 0$. In particular, this shows that the energy functionals $\mathcal{E}_\delta$ and $\mathcal{E}$ for probability measures defined on the torus $\mathbb{T}^2$ may have multiple local minimisers due to the dependence on $n$. The support of these minimisers may not be connected and may consist of a finite number of connected components of equal size, satisfying the translation property (5.31). Besides, symmetry in $x$ on each connected component $M_k$ is required for minimisers, implying the periodicity of minimisers in $x$.

## 5.4 Numerical scheme and its convergence

### 5.4.1 Numerical methods

For the numerical simulations, we consider the positivity-preserving finite-volume method for nonlinear equations with gradient structure proposed in [CCH14a] for isotropic interaction equations (5.11). We consider the domain $\mathbb{R}^2$ and extend the scheme [CCH14a] to the anisotropic interaction equations with or without diffusion in (5.10) or (5.1), respectively. This is achieved by replacing $-\nabla W$ by $F(\cdot, T)$, requiring additional care in calculating the term $(F(\cdot, T(x,y)) * \rho(t,\cdot))(x,y)$ for $(x,y) \in \mathbb{R}^2$ efficiently.

In two spatial dimensions, we consider a Cartesian grid, given by $x_i = i\Delta x$ and $y_j = j\Delta y$ for $i,j \in \mathbb{Z}$. Let $C_{ij}$ denote the cell of the spatial discretisation

$C_{ij} = [x_i, x_{i+1}) \times [y_j, y_{j+1})$, and let the time discretisation be given by $t_n = n\Delta t$ for $n \in \mathbb{Z}$. Let $\rho_{ij}^n$ denote the approximation of the solution $\rho(t_n, x_i, y_j)$ to the anisotropic nonlocal interaction equation with diffusion (5.10) with initial condition $\rho|_{t=0} = \rho^{in}$ in $\mathbb{R}^2$ for a given probability measure $\rho^{in}$. Note that (5.10) can be rewritten as

$$\partial_t \rho + \nabla \cdot (\rho u_\rho) = \delta \nabla \cdot (\rho \nabla \rho)$$

where $u_\rho$ is defined in (5.2) with

$$|u_\rho(t, x, y)| \leqslant f$$

for the uniform bound $f$ of $F$. Assuming that $\rho^{in} \in \mathcal{P}_2(\mathbb{R}^2)$ where $\mathcal{P}_2(\mathbb{R}^2)$ denotes the space of probability measures with finite second order moment, we define its discretisation

$$\rho_{ij}^0 = \frac{1}{\Delta x \Delta y} \iint\limits_{C_{ij}} \rho^{in} \, \mathrm{d}(x, y) \geqslant 0 \tag{5.32}$$

for $i, j \in \mathbb{Z}^2$. Since $\rho^{in}$ is a probability measure, the total mass of the system is $\sum_{i,j} \rho_{ij}^0 \Delta x \Delta y = 1$ initially. Given an approximating sequence $\{\rho_{ij}^n\}_{i,j}$ at time $n$, we consider the scheme

$$
\begin{aligned}
\rho_{ij}^{n+1} = \rho_{ij}^n &- \frac{\Delta t}{\Delta x} \left( (u_x)_{i+1/2,j}^n \rho_{i+1/2,j}^n - (u_x)_{i-1/2,j}^n \rho_{i-1/2,j}^n \right) \\
&- \frac{\Delta t}{\Delta y} \left( (u_y)_{i,j+1/2}^n \rho_{i,j+1/2}^n - (u_y)_{i,j-1/2}^n \rho_{i,j-1/2}^n \right) \\
&+ \frac{\Delta t}{2\Delta x} f \left( \rho_{i+1,j}^n - 2\rho_{ij}^n + \rho_{i-1,j}^n \right) + \frac{\Delta t}{2\Delta y} f \left( \rho_{i,j+1}^n - 2\rho_{ij}^n + \rho_{i,j-1}^n \right) \\
&+ \frac{\delta \Delta t}{2(\Delta x)^2} \left( (\rho_{i+1,j}^n)^2 - 2 \left( \rho_{ij}^n \right)^2 + \left( \rho_{i-1,j}^n \right)^2 \right) \\
&+ \frac{\delta \Delta t}{2(\Delta y)^2} \left( (\rho_{i,j+1}^n)^2 - 2 \left( \rho_{ij}^n \right)^2 + \left( \rho_{i,j-1}^n \right)^2 \right)
\end{aligned}
\tag{5.33}
$$

for the uniform bound $f$ of the force $F$ and parameter $\delta > 0$. Here, we use the notation

$$\rho_{i+1/2,j} = \frac{\rho_{ij} + \rho_{i+1,j}}{2}, \qquad \rho_{i,j+1/2} = \frac{\rho_{ij} + \rho_{i,j+1}}{2},$$

$$(u_x)_{i+1/2,j} = \frac{(u_x)_{ij} + (u_x)_{i+1,j}}{2}, \qquad (u_y)_{i,j+1/2} = \frac{(u_y)_{ij} + (u_y)_{i,j+1}}{2},$$

where the macroscopic velocity is defined by

$$(u_x)_{ij} = \frac{1}{\Delta x \Delta y} \sum_{k,l} \rho_{kl}(F_x)_{ij}^{kl}, \qquad (u_y)_{ij} = \frac{1}{\Delta x \Delta y} \sum_{k,l} \rho_{kl}(F_y)_{ij}^{kl} \qquad (5.34)$$

with

$$(F_x)_{ij}^{kl} = \iint\limits_{C_{kl}} \left( \iint\limits_{C_{ij}} F_x(x - x', y - y', T(x,y)) \, \mathrm{d}(x,y) \right) \mathrm{d}(x', y'),$$

$$(F_y)_{ij}^{kl} = \iint\limits_{C_{kl}} \left( \iint\limits_{C_{ij}} F_y(x - x', y - y', T(x,y)) \, \mathrm{d}(x,y) \right) \mathrm{d}(x', y')$$

for the components $F_x, F_y$ of $F$ with $F = (F_x, F_y)$. A change of variable also yields

$$(u_x)_{i+1/2,j} = \frac{1}{\Delta x \Delta y} \sum_{k,l} \rho_{k+1/2,l}(F_x)_{ij}^{kl}, \qquad (u_y)_{i,j+1/2} = \frac{1}{\Delta x \Delta y} \sum_{k,l} \rho_{k,l+1/2}(F_y)_{ij}^{kl}.$$

Note that $(F_x)_{ij}^{kl}$ and $(F_y)_{ij}^{kl}$ can be determined explicitly in the numerical simulations instead of evaluating the integrals, and can also be precomputed for making the computation of the discretised velocity fields more efficient. Further note that the last two lines of the numerical scheme (5.33) can be regarded as a discretisation of the nonlinear diffusion $\delta \nabla \cdot (\rho \nabla \rho) = \frac{\delta}{2}(\partial_x^2 \rho^2 + \partial_y^2 \rho^2)$.

## 5.4.2  Properties of the scheme: conservation of mass, positivity, convergence

In [CJLV16], the convergence of a finite volume method is shown for general measure solutions of the (isotropic) aggregation equation with mildly singular potentials. In this section, we establish a CFL condition for the numerical scheme (5.33) for the anisotropic aggregation equation (5.10) and prove its weak convergence.

**Lemma 6.** *Let $\rho^{in} \in \mathcal{P}_2(\mathbb{R}^2)$ and define $\rho_{ij}^0$ by (5.32). Then, there exists a constant $r > 0$ such that*

$$\sup_{n,i,j} \rho_{ij}^n \leqslant r, \qquad (5.35)$$

and conservation of mass is satisfied for all n, i.e.

$$\sum_{i,j\in\mathbb{Z}} \rho_{ij}^n \Delta x \Delta y = \sum_{i,j\in\mathbb{Z}} \rho_{ij}^0 \Delta x \Delta y = 1.$$

For spatially homogeneous tensor fields, conservation of the centre of mass also holds, i.e.

$$\sum_{i,j\in\mathbb{Z}} x_i \rho_{ij}^n = \sum_{i,j\in\mathbb{Z}} x_i \rho_{ij}^0, \qquad \sum_{i,j\in\mathbb{Z}} y_i \rho_{ij}^n = \sum_{i,j\in\mathbb{Z}} y_i \rho_{ij}^0.$$

*Proof.* The conservation of mass is directly obtained by summing over $i$ and $j$ in (5.33), and noting that $\sum_{i,j\in\mathbb{Z}} \rho_{ij}^0 \Delta x \Delta y = 1$. In particular, the conservation of mass implies the uniform boundedness of $\rho_{ij}^n$, i.e. there exists a constant $r > 0$ such that (5.35) is satisfied. The conservation of the centre of mass follows from a discrete integration by parts and the fact that $(F_x)_{ij}^{kl} = -(F_x)_{kl}^{ij}$ for spatially homogeneous tensor fields. $\qquad\square$

For proving the convergence of the numerical scheme, a CFL condition is required:

**Lemma 7.** *Let $\rho^{in} \in \mathcal{P}_2(\mathbb{R}^2)$ and define $\rho_{ij}^0$ by (5.32). Suppose that the force $F$ is bounded by $f$, let $r > 0$ denote the uniform bound of $\rho_{ij}^n$ in (5.33) from Lemma 6, and suppose that the condition*

$$\left( 2f \left( \frac{1}{\Delta x} + \frac{1}{\Delta y} \right) + \delta r \left( \frac{1}{(\Delta x)^2} + \frac{1}{(\Delta y)^2} \right) \right) \Delta t \leqslant 1 \tag{5.36}$$

*is satisfied. Then the sequences defined in (5.33)–(5.34) satisfy*

$$\rho_{ij}^n \geqslant 0, \qquad |(u_x)_{ij}^n| \leqslant f, \qquad |(u_y)_{ij}^n| \leqslant f,$$

*for all $i$, $j$ and $n$.*

*Proof.* By the definition of the velocity (5.34) and the uniform bound $f$ of the force $F$ we obtain

$$|(u_x)_{ij}^n| \leqslant \Delta x \Delta y f \sum_{k,l} \rho_{kl} = f, \qquad |(u_y)_{ij}^n| \leqslant f \tag{5.37}$$

for all $i, j, n$.

For proving the nonnegativity of the scheme (5.33), note that we can rewrite (5.33) as

$$
\begin{aligned}
\rho_{ij}^{n+1} = \rho_{ij}^n & \left( 1 - \frac{\Delta t}{\Delta x} \left( \frac{(u_x)_{i+1/2,j}^n - (u_x)_{i-1/2,j}^n + 2f}{2} \right) \right. \\
& \left. - \frac{\Delta t}{\Delta y} \left( \frac{(u_y)_{i,j+1/2}^n - (u_y)_{i,j-1/2}^n + 2f}{2} \right) - \frac{\delta \Delta t}{(\Delta x)^2} \rho_{ij}^n - \frac{\delta \Delta t}{(\Delta y)^2} \rho_{ij}^n \right) \\
& + \rho_{i+1,j}^n \frac{\Delta t}{2\Delta x} \left( f - (u_x)_{i+1/2,j}^n \right) + \rho_{i-1,j}^n \frac{\Delta t}{2\Delta x} \left( f + (u_x)_{i-1/2,j}^n \right) \\
& + \rho_{i,j+1}^n \frac{\Delta t}{2\Delta y} \left( f - (u_y)_{i,j+1/2}^n \right) + \rho_{i,j-1}^n \frac{\Delta t}{2\Delta y} \left( f + (u_y)_{i,j-1/2}^n \right) \\
& + \frac{\delta \Delta t}{2(\Delta x)^2} \left( (\rho_{i+1,j}^n)^2 + (\rho_{i-1,j}^n)^2 \right) + \frac{\delta \Delta t}{2(\Delta y)^2} \left( (\rho_{i,j+1}^n)^2 + (\rho_{i,j-1}^n)^2 \right).
\end{aligned}
\tag{5.38}
$$

We show the nonnegativity of $\rho_{ij}^n$ by induction on $n$. For $n \in \mathbb{N}$ given, we assume that $\rho_{ij}^n \geqslant 0$ for all $i, j \in \mathbb{Z}$. Note that due to condition (5.36), all coefficients in (5.38) of $\rho_{ij}^n$, $\rho_{i+1,j}^n$, $\rho_{i-1,j}^n$, $\rho_{i,j+1}^n$ and $\rho_{i,j-1}^n$ are nonnegative, and the terms in the last line are also nonnegative. By induction, we deduce $\rho_{ij}^{n+1} \geqslant 0$ for all $i, j \in \mathbb{Z}$.

$\square$

Next, we consider the convergence of the scheme in a weak topology. Let $\mathcal{M}_{loc}(\mathbb{R}^d)$ denote the space of local Borel measures on $\mathbb{R}^d$. For $\rho \in \mathcal{M}_{loc}(\mathbb{R}^d)$, we denote the total variation of $\rho$ by $|\rho|(\mathbb{R}^d)$ and we denote the space of measures in $\mathcal{M}_{loc}(\mathbb{R}^d)$ with finite total variation by $\mathcal{M}_b(\mathbb{R}^d)$. The space of measures $\mathcal{M}_b(\mathbb{R}^d)$ is always endowed with the weak topology $\sigma(\mathcal{M}_b, C_0)$.

Let the characteristic function on some set $[n\Delta t, (n+1)\Delta t) \times C_{ij} \subset \mathbb{R}_+ \times \mathbb{R}^2$ be denoted by $\chi_{[n\Delta t,(n+1)\Delta t) \times C_{ij}}$. For $\Delta = \max\{\Delta x, \Delta y\}$, we define the reconstruction of the discretisation by

$$
\rho_\Delta(t, x, y) = \sum_{n \in \mathbb{Z}} \sum_{i \in \mathbb{Z}} \sum_{j \in \mathbb{Z}} \rho_{ij}^n \chi_{[n\Delta t,(n+1)\Delta t) \times C_{ij}}(t, x, y),
$$

where the boundedness of $\rho_\Delta$ independent of $\Delta$ follows from Lemma 6. Using the definition $u_{ij}^n = ((u_x)_{ij}^n, (u_y)_{ij}^n)$ in (5.34), we obtain

$$
u_{ij}^n = \frac{1}{\Delta x \Delta y} \iint_{C_{ij}} F(\cdot, T(x, y)) * \rho_\Delta(t_n, \cdot)(x, y) \, \mathrm{d}(x, y)
$$

and

$$u_\Delta(t,x,y) = \sum_{n\in\mathbb{Z}}\sum_{i\in\mathbb{Z}}\sum_{j\in\mathbb{Z}} u_{ij}^n \chi_{[n\Delta t,(n+1)\Delta t)\times C_{ij}}(t,x,y).$$

**Theorem 8.** *Suppose that the continuous force $F$ is bounded by $f$ and that the tensor field $T$ is continuous. We consider $\rho^{in} \in \mathcal{P}_2(\mathbb{R}^2)$ and define $\rho_{ij}^0$ by (5.32). Let $S > 0$ be fixed, and suppose that the discretisation in time and space satisfies (5.36). Then, the discretisation $\rho_\Delta$ converges weakly in $\mathcal{M}_b([0,S]\times\mathbb{R}^2)$ towards the solution $\rho$ of (5.1) as $\Delta = \max\{\Delta x, \Delta y\}$ and $\delta$ go to 0 such that $\Delta t$ satisfies (5.36).*

*Proof.* Lemma 6 implies the nonnegativity of $\rho_{ij}^n$ provided condition (5.36) holds. Since $\{\rho_\Delta\}_{\Delta>0}$ is a bounded, nonnegative sequence of measures for all $t \in [0,S]$, conservation of mass implies that $|\rho_\Delta(t)|(\mathbb{R}^2) = 1$. Hence, there exists a subsequence, still denoted by $\{\rho_\Delta\}_{\Delta>0}$, which converges to $\rho$ in the weak topology as $\Delta t$, $\Delta x$ and $\Delta y$ go to 0 satisfying condition (5.36), i.e.

$$\int_0^S \iint_{\mathbb{R}^2} \phi(t,x,y)\rho_\Delta(t,x,y)\,\mathrm{d}(x,y)\,\mathrm{d}t \to \int_0^S \iint_{\mathbb{R}^2} \phi(t,x,y)\rho(t,x,y)\,\mathrm{d}(x,y)\,\mathrm{d}t$$

for all $\phi \in C_0([0,S]\times\mathbb{R}^2)$.

For $S > 0$ given, choose $\Delta t > 0$ and $N_S \in \mathbb{N}_{>0}$ such that $S = \Delta t N_S$ and condition (5.36) are satisfied. Let $\mathcal{D}([0,S]\times\mathbb{R}^2)$ denote the space of smooth, compactly supported test functions on $[0,S]\times\mathbb{R}^2$ and define

$$\phi_{ij}^n = \int_{t_n}^{t_{n+1}} \iint_{C_{ij}} \phi(t,x,y)\,\mathrm{d}(x,y)\,\mathrm{d}t$$

such that

$$\int_0^S \iint_{\mathbb{R}^2} \rho_\Delta(t,x,y)\phi(t,x,y)\,\mathrm{d}(x,y)\,\mathrm{d}t = \sum_{n=0}^{N_S}\sum_{i\in\mathbb{Z}}\sum_{j\in\mathbb{Z}} \rho_{ij}^n \phi_{ij}^n.$$

In particular, we have

$$\sum_{n,i,j} \frac{1}{\Delta t}\left(\rho_\Delta(t_{n+1},x_i,y_j) - \rho_\Delta(t_n,x_i,y_j)\right)\phi_{ij}^n = -\sum_{n,i,j} \rho_{ij}^n \frac{\phi_{ij}^n - \phi_{ij}^{n-1}}{\Delta t}$$

$$= -\int_0^S \iint_{\mathbb{R}^2} \rho_\Delta(t,x,y)\frac{\phi(t,x,y) - \phi(t-\Delta t,x,y)}{\Delta t}\,\mathrm{d}(x,y)\,\mathrm{d}t$$

$$\rightarrow - \int_0^S \iint_{\mathbb{R}^2} \rho(t,x,y)\partial_t\phi(t,x,y)\,\mathrm{d}(x,y)\,\mathrm{d}t$$

as $\Delta t$, $\Delta x$ and $\Delta y$ go to 0, where the limit integral follows from $\phi(t,x,y) - \phi(t - \Delta t, x, y) = \partial_t\phi(t,x,y)\Delta t + \mathcal{O}((\Delta t)^2)$, the weak convergence of $\rho_\Delta$ to $\rho$ and the boundedness of the measure $\rho_\Delta$ with a bound not depending on the mesh. Similarly,

$$\sum_{n,i,j} \frac{1}{2\Delta x} \left( \rho_\Delta(t_n, x_{i+1}, y_j) - 2\rho_\Delta(t_n, x_i, y_j) + \rho_\Delta(t_n, x_{i-1}, y_j) \right) \phi_{ij}^n$$

$$= \int_0^S \iint_{\mathbb{R}^2} \rho_\Delta(t,x,y) \frac{\phi(t, x+\Delta x, y) - 2\phi(t,x,y) + \phi(t, x-\Delta x, y)}{2\Delta x} \,\mathrm{d}(x,y)\,\mathrm{d}t \rightarrow 0$$

as $\Delta t$, $\Delta x$ and $\Delta y$ go to 0 since $|\phi(t, x+\Delta x, y) - 2\phi(t,x,y) + \phi(t, x-\Delta x, y)| \leqslant \|\partial_{xx}\phi\|_\infty(\Delta x)^2$. Due to the boundedness of the force $F(\cdot, T(x))$, we can show in a similar way as in [CJLV16] that

$$\sum_{n,i,j} \frac{1}{\Delta x} \left( (u_x)_{i+1/2,j}^n \rho_{i+1/2j}^n - (u_x)_{i-1/2,j}^n \rho_{i-1/2,j}^n \right) \phi_{i,j}^n$$

$$\rightarrow - \int_0^S \iint_{\mathbb{R}^2} \partial_x\phi(t,x,y)(F_x(\cdot, T(x,y)) * \rho(t,\cdot))(x,y)\rho(t,x,y)\,\mathrm{d}(x,y)\,\mathrm{d}t$$

as $\Delta t$, $\Delta x$ and $\Delta y$ go to 0 by the continuity of $F = (F_x, F_y)$ and $T$ where $F_x$ denotes the first component of the force $F$. Further note that we have

$$\delta \sum_{n,i,j} \frac{1}{2(\Delta x)^2} \left( (\rho_{i+1,j}^n)^2 - 2\left(\rho_{ij}^n\right)^2 + \left(\rho_{i-1,j}^n\right)^2 \right) \phi_{ij}^n$$

$$= \delta \sum_{n,i,j} \frac{1}{2(\Delta x)^2} \left(\rho_{ij}^n\right)^2 \left( \phi_{i+1,j}^n - 2\phi_{ij}^n + \phi_{i-1,j}^n \right)$$

$$\leqslant \frac{1}{2}\delta\|\partial_{xx}\phi\|_\infty \int_0^S \iint_{\mathbb{R}^2} (\rho_\Delta(t,x,y))^2 \,\mathrm{d}(x,y)\,\mathrm{d}t.$$

The boundedness of $\rho_\Delta$, independent of $\Delta$, guarantees that the right-hand side goes to 0 as $\delta$, $\Delta t$, $\Delta x$ and $\Delta y$ go to 0.

Multiplying (5.33) by $\phi_{ij}^n$, summing over $n$, $i$, $j$, and taking the limits $\delta$, $\Delta t$, $\Delta x$ and $\Delta y$ to 0, we obtain

$$\int_0^S \iint_{\mathbb{R}^2} [\partial_t\phi(t,x,y) + \nabla\phi(t,x,y) \cdot (F(\cdot, T(x,y)) * \rho(t,\cdot))(x,y)]\rho(t,x,y)\,\mathrm{d}(x,y)\,\mathrm{d}t = 0$$

in the limit, i.e. $\rho$ is a solution in the sense of distributions of the anisotropic aggregation equation (5.1). $\qquad\qquad\qquad\qquad\qquad\qquad\qquad\qquad\qquad\qquad$ $\square$

## 5.5 Numerical results

In this section, we show simulation results for solving the anisotropic aggregation equation with nonlinear diffusion (5.10) numerically using the numerical scheme (5.33). For the numerical simulations, we consider the force coefficients $f_s$ and $f_l$ in (5.8) with $f_s = f_R + \chi f_A$ and $f_l = f_R + f_A$ as suggested in [DGH$^+$19], where $f_R$ and $f_A$ are defined in (5.5) and (5.6). To be consistent with the work of Kücken and Champod [KC13], we assume that the total force (5.8) defined via the tensor field $T(x, y) := \chi s(x, y) \otimes s(x, y) + l(x, y) \otimes l(x, y)$ in (5.3) exhibits short-range repulsion and long-range attraction along $l$ and repulsion along $s$. In the following, we consider the force coefficients $f_R$ and $f_A$ with the parameter values in (5.7). The computational domain is given by $[-0.5, 0.5]^2$ with periodic boundary conditions.

### 5.5.1 Spatially homogeneous tensor fields

In this section, we show stationary solutions to the anisotropic interaction equation (5.10), obtained with the numerical scheme (5.33), for the spatially homogeneous tensor field $T$ with $s = (0, 1)$ and $l = (1, 0)$, cf. Figures 5.1–5.4. Note that the stationary solutions for the tensor field $T$ are constant in $y$-direction in all these figures.

The stationary solution to (5.10), obtained with the numerical scheme (5.33) for different values of the diffusion coefficient $\delta$, is shown in Figure 5.1. Here, we consider uniformly distributed initial data on a disc of radius $R = 0.05$ with centre $(0, 0)$ on the computational domain $[-0.5, 0.5]^2$, where the spatial discretisation is given by a grid of size 50 in each spatial direction, and the time step is chosen according to the CFL condition (5.36). Due to the choice of initial data, this leads to a single straight vertical line as stationary solution, provided $\delta$ is chosen sufficiently small. As expected, an increase in $\delta$ leads to the widening of the single straight vertical line which is stable for sufficiently small values of $\delta$. For larger values of $\delta$, e.g. $\delta = 5 \cdot 10^{-7}$, the uniform distribution is obtained as stationary solution.

In Figure 5.2, we investigate the role of the grid size on the stationary solution by considering grid sizes of 50, 100 and 200 in each spatial direction for the diffusion parameter $\delta = 10^{-10}$ and uniformly distributed initial data on a disc. Clearly, the

(A) $\delta = 10^{-10}$  (B) $\delta = 5 \cdot 10^{-8}$  (C) $\delta = 2 \cdot 10^{-7}$  (D) $\delta = 5 \cdot 10^{-7}$

Figure 5.1: Stationary solution to the anisotropic interaction equation (5.10), obtained with the numerical scheme (5.33) on a grid of size 50 in each spatial direction and different diffusion coefficients $\delta$ for the spatially homogeneous tensor field with $s = (0, 1)$ and $l = (1, 0)$ and uniformly distributed initial data on a disc on the computational domain $[-0.5, 0.5]^2$.

stationary solution is given by a step function in the $x$-coordinate. Finer grids lead to step functions with more steps and smaller step heights compared to the grid size of 50 where only one step occurs.



(A) Grid 50  (B) Grid 100  (C) Grid 200

Figure 5.2: Stationary solution to the anisotropic interaction equation (5.10), obtained with the numerical scheme (5.33) on grids of sizes 50, 100 and 200 in each spatial direction for the diffusion coefficient $\delta = 10^{-10}$ for the spatially homogeneous tensor field with $s = (0, 1)$ and $l = (1, 0)$ and uniformly distributed initial data on a disc on the computational domain $[-0.5, 0.5]^2$.

The stationary solution for grid sizes of 100 and 200 in each spatial direction and uniformly distributed initial data on the computational domain $[-0.5, 0.5]^2$ is shown in Figure 5.3, and is given by equidistant, parallel vertical line patterns. Note that we obtain the same number of parallel lines for the different grid sizes.

In Figure 5.4, we show the stationary solution for uniformly distributed initial data on the computational domain $[-0.5, 0.5]^2$ for different diffusion coefficients $\delta$. Note that as $\delta$ increases, the stable line patterns become wider and this may result in a decrease in the number of parallel lines. If $\delta$ is larger than a certain threshold, e.g.

(A) Grid 100

(B) Grid 200
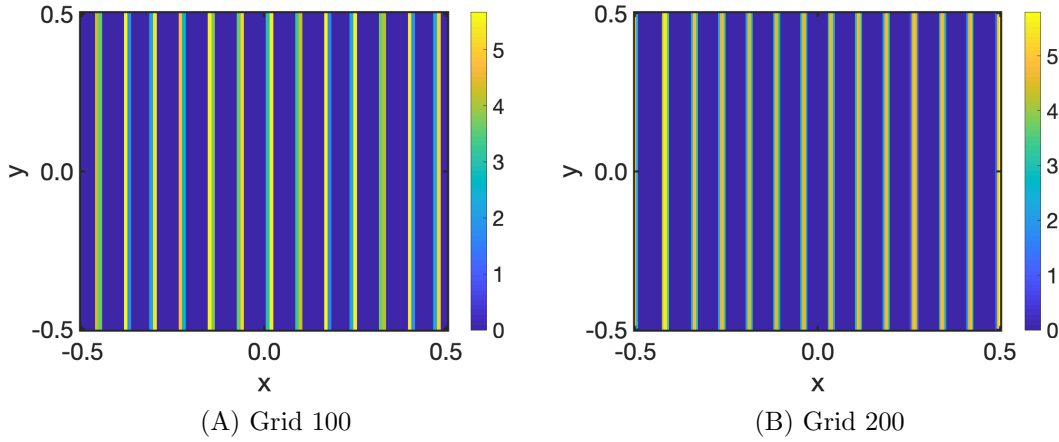
Figure 5.3: Stationary solution to the anisotropic interaction equation (5.10), obtained with the numerical scheme (5.33) on grids of sizes 100 and 200 in each spatial direction for the diffusion coefficient $\delta = 10^{-10}$ for the spatially homogeneous tensor field with $s = (0, 1)$ and $l = (1, 0)$ and uniformly distributed initial data on the computational domain $[-0.5, 0.5]^2$.

$\delta = 5 \cdot 10^{-9}$, the parallel line patterns are no longer stable and the stationary solution is given by the uniform distribution on the computational domain $[-0.5, 0.5]^2$.



(A) $\delta = 10^{-10}$

(B) $\delta = 5 \cdot 10^{-10}$

(C) $\delta = 10^{-9}$

(D) $\delta = 5 \cdot 10^{-9}$
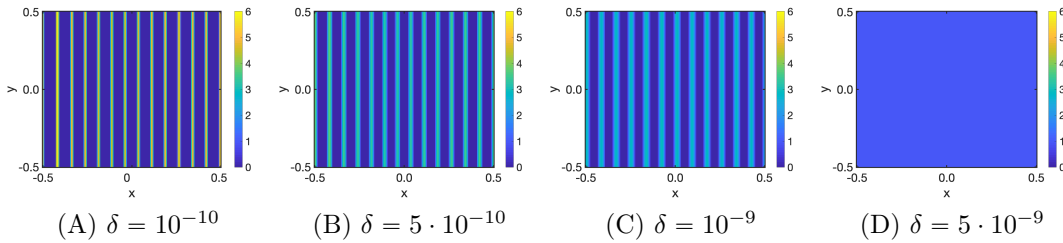
Figure 5.4: Stationary solution to the anisotropic interaction equation (5.10), obtained with the numerical scheme (5.33) on a grid of size 200 in each spatial direction and different diffusion coefficients $\delta$ for the spatially homogeneous tensor field with $s = (0, 1)$ and $l = (1, 0)$ and uniformly distributed initial data on the computational domain $[-0.5, 0.5]^2$.

## 5.5.2 Spatially inhomogeneous tensor fields

In this section, we consider stationary solutions to the anisotropic interaction equation (5.10), obtained with the numerical scheme (5.33), for different spatially inhomogeneous tensor fields.

In Figure 5.5, we consider fingerprint images in Figures 5.5(A) and 5.5(D), use

these fingerprint images to construct the vector field $s = s(x, y)$ in Figures 5.5(B) and 5.5(E), and show the resulting stationary solutions for the diffusion coefficient $\delta = 10^{-10}$ and uniformly distributed initial data on a grid of size 50 in each spatial direction in Figures 5.5(C) and 5.5(F), respectively. For the construction of the tensor field we firstly proceed as in [DGH$^+$19], and then we rescale the tensor field appropriately to the given grid size.



|  |  |  |
|---|---|---|
| (A) Original | (B) s | (C) Stationary solution |
| (D) Original | (E) s | (F) Stationary solution |
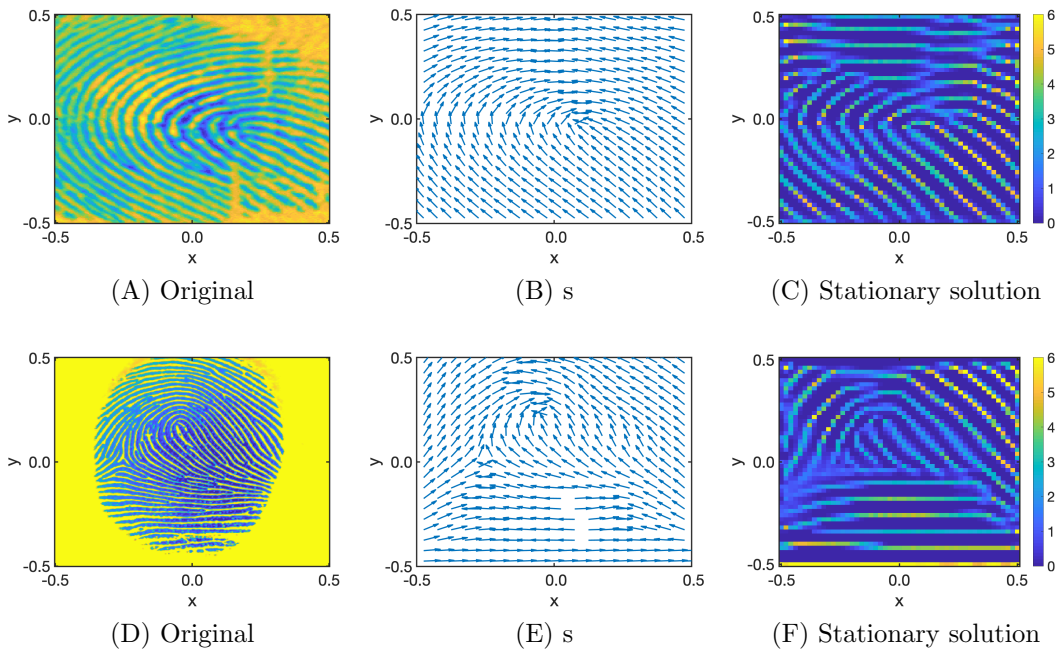
Figure 5.5: Stationary solution to the anisotropic interaction equation (5.10), obtained with the numerical scheme (5.33) on a grid of size 50 in each spatial direction and diffusion coefficient $\delta = 10^{-10}$ for different spatially inhomogeneous tensor fields from real fingerprint images and uniformly distributed initial data on the computational domain $[-0.5, 0.5]^2$.

In Figure 5.6, we consider the tensor field in Figure 5.5(B) of part of a fingerprint, and show the numerical solution at different iterations of the numerical scheme (5.33) on a grid of size 50 in each spatial direction for the diffusion coefficient $\delta = 10^{-10}$ and uniformly distributed initial data on the computational domain $[-0.5, 0.5]^2$. Note that the resulting numerical solution is close to being stationary.

Similarly as in Figure 5.4 for spatially homogeneous tensor fields, we show the stationary solution for different diffusion coefficients $\delta$ in Figure 5.7, where the spatially inhomogeneous tensor field in Figure 5.5(B) and a grid of size 50 in each spatial direction are considered. As $\delta$ increases, the line patterns become wider,

(A) $n = 100000$     (B) $n = 200000$     (C) $n = 300000$     (D) $n = 400000$
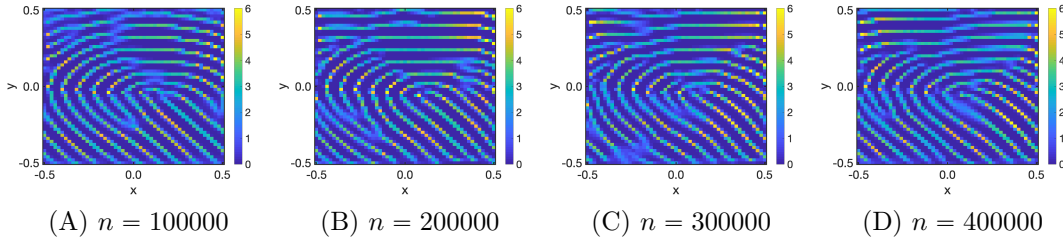
Figure 5.6: Numerical solution to the anisotropic interaction equation (5.10) after $n$ iterations, obtained with the numerical scheme (5.33) on a grid of size 50 in each spatial direction with diffusion coefficient $\delta = 10^{-10}$ for the spatially inhomogeneous tensor field of part of a fingerprint and uniformly distributed initial data on the computational domain $[-0.5, 0.5]^2$.

provided the diffusion coefficient $\delta$ is below a certain threshold. If $\delta > 0$ is above this threshold, e.g. for $\delta = 10^{-9}$, the uniform distribution is obtained as stationary solution. Note that this threshold is smaller than the one in Figure 5.4 for spatially homogeneous tensor fields.



(A) $\delta = 10^{-10}$     (B) $\delta = 5 \cdot 10^{-10}$     (C) $\delta = 10^{-9}$
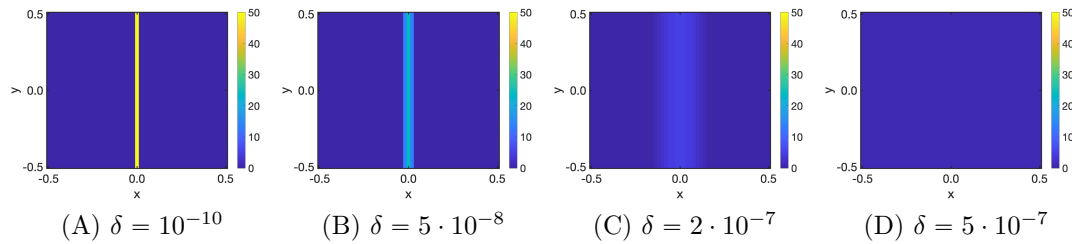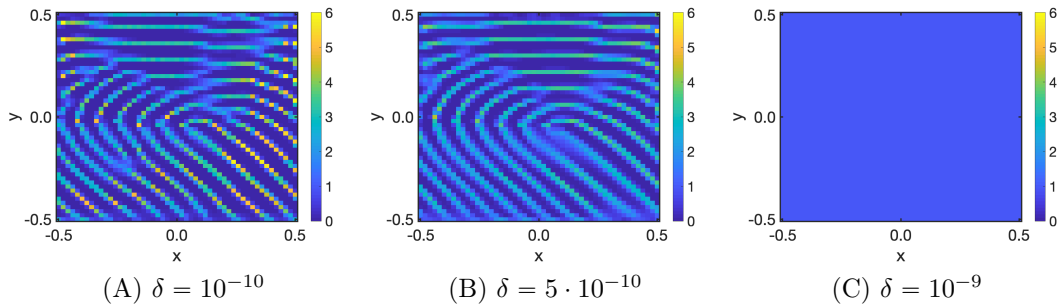
Figure 5.7: Stationary solution to the anisotropic interaction equation (5.10), obtained with the numerical scheme (5.33) on a grid of size 50 in each spatial direction for different values of the diffusion coefficient $\delta$ for a given spatially inhomogeneous tensor field and uniformly distributed initial data on the computational domain $[-0.5, 0.5]^2$.

Motivated by the simulation results in [DGH+19], we consider different rescalings of the forces in Figure 5.8 to vary the distances between the fingerprint lines, i.e. we consider $F(\eta d(x, y), T(x))$ where $\eta > 0$ is the rescaling factor. As before, we consider the diffusion coefficient $\delta = 10^{-10}$ on a grid of size 50 in each spatial direction and uniformly distributed initial data on $[-0.5, 0.5]^2$. For $\eta = 1$ we recover the same stationary solution as in Figure 5.5(C), while the distances between the fingerprint lines become larger for $\eta \in (0, 1)$ and smaller for $\eta > 1$.

(A) $\eta = 0.6$      (B) $\eta = 0.8$      (C) $\eta = 1.2$
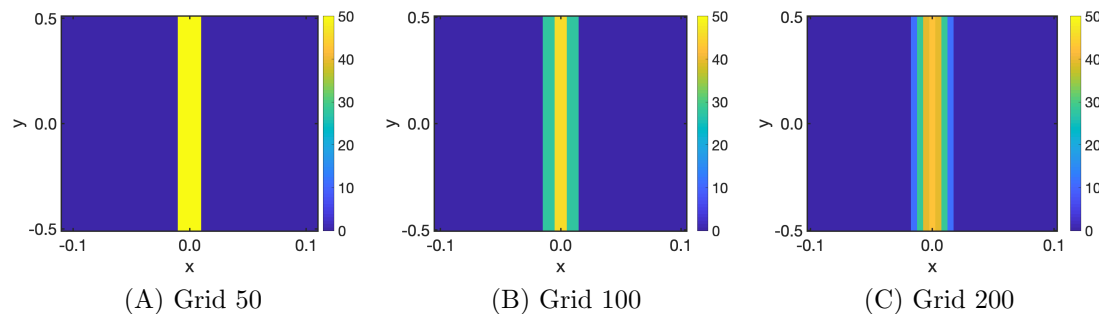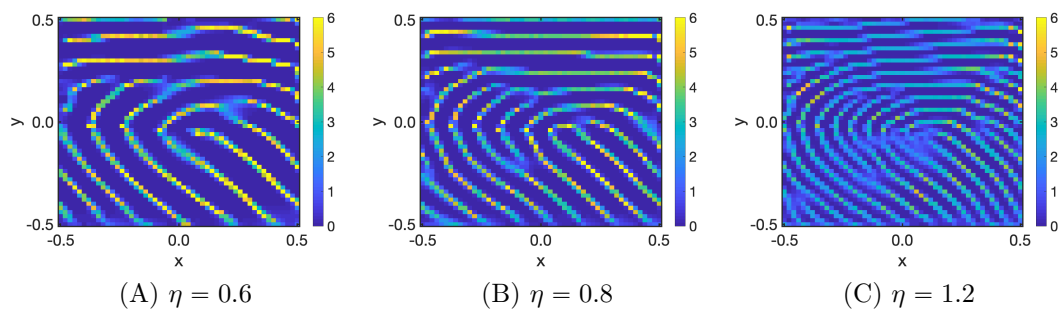
Figure 5.8: Stationary solution to the anisotropic interaction equation (5.10), obtained with the numerical scheme (5.33) on a grid of size 50 in each spatial direction, diffusion coefficient $\delta = 10^{-10}$ and different force rescalings $\eta$ for a given spatially inhomogeneous tensor field and uniformly distributed initial data on the computational domain $[-0.5, 0.5]^2$.

# Part II

# Partial differential equations for biological networks

# Chapter 6

# ODE- and PDE-based modelling

## Originality and contribution

This chapter follows in large parts the paper [HKM19a], written in collaboration with Jan Haskovec and Peter A. Markowich. While PM proposed the study of the model and provided guidance and advice, the analysis is mostly joint work by JH and myself, and all numerical simulations were carried out by myself.

## Chapter summary

In this chapter, we study the global existence of solutions of a discrete (ODE-based) model on a graph describing the formation of biological transportation networks, introduced by Hu and Cai, which is given by the gradient flow of the energy (1.26), i.e.

$$E[C] := \sum_{(i,j) \in \mathbb{E}} \left( \frac{Q_{ij}[C]^2}{C_{ij}} + \frac{\nu}{\gamma} C_{ij}^\gamma \right) L_{ij}, \tag{6.1}$$

constrained by Kirchhoff's law (1.24), i.e.

$$-\sum_{j \in N(i)} C_{ij} \frac{P_j - P_i}{L_{ij}} = S_i \qquad \text{for all } i \in \mathbb{V}. \tag{6.2}$$

We propose an adaptation of this model so that a macroscopic (PDE-based) system can be obtained as its formal continuum limit. We prove the global existence of weak solutions of the macroscopic PDE model. Finally, we present results of numerical simulations of the discrete model, illustrating the convergence to steady states, their

non-uniqueness as well as their dependence on initial data and model parameters.

## 6.1   Introduction

Transportation networks are ubiquitous in living systems such as leaf venation in plants, mammalian circulatory systems that convey nutrients to the body through blood circulation, or neural networks that transport electric charge. Understanding the development, function and adaptation of biologic transportation networks has been a long standing interest of the scientific community [BHD$^+$07, CC95, RFL$^+$05, YDG$^+$00]. Mathematical modelling of transportation networks is traditionally based on discrete frameworks, in particular mathematical graph theory and discrete energy optimisation, where the energy consumption of the network is minimised under the constraint of constant total material cost. However, networks and circulation systems in living organisms are typically subject to continuous adaptation, responding to various internal and external stimuli. For instance, for blood circulation systems it is well known that throughout the life of humans and animals, blood vessel systems are continuously adapting their structures to meet the changing metabolic demand of the tissue. In particular, it has been observed in experiments that blood vessels can sense the wall shear stress and adapt their diameters according to it [HCR12]. Consequently, for biological applications it is necessary to employ the dynamic class of models.

Motivated by this observation, Hu and Cai [HC13] introduced a new approach to dynamic modelling of transportation networks. They propose a purely local dynamic adaptation model based on mechanical laws, consisting of a system of ordinary differential equations (ODE) on a graph, coupled to a linear system of equations (Kirchhoff law). In particular, the model responds only to local information and fluctuations in flow distributions can be naturally incorporated. Global existence of solutions of the coupled ODE-algebraic system is not trivial and, to our best knowledge, has not been proved so far. The first goal of this chapter is to close this gap.

In contrast to the discrete modelling approach, models based on systems of partial differential equations (PDE) can be used to describe formation and adaptation of transportation networks based on macroscopic (continuum) physical laws. Hu and Cai proposed a PDE-based continuum model [Hu13] which was subsequently studied in a series of papers [AAFM16, ABH$^+$17, HMP15, HMPS16]. The continuum model consists of a parabolic reaction-diffusion equation for the conductivity

field, constrained by a Poisson equation for the pressure field. However, no connection between the discrete (ODE-based) and continuum (PDE-based) models for biological transportation networks has been established so far.

The second goal of this chapter is to provide a formal continuum limit of an extension of the Hu and Cai model [HC13] on regular equidistant grids; the rigorous limit passage will be studied in Chapter 7. The resulting continuum energy functional is of the form

$$\mathcal{E}[c] = \int_\Omega \nabla p \cdot c \nabla p + \frac{\nu}{\gamma} |c|^\gamma \, \mathrm{d}x, \tag{6.3}$$

with the *metabolic constant* $\nu > 0$ and *metabolic exponent* $\gamma > 0$. The energy functional is defined on the set of nonnegative diagonal tensor fields $c = c(x)$ on $\mathbb{R}^d$,

$$c = \begin{pmatrix} c^1 & & \\ & \ddots & \\ & & c^d \end{pmatrix}. \tag{6.4}$$

The symbol $|c|^\gamma$ is defined as $\sum_{k=1}^d |c^k|^\gamma$. The scalar pressure $p = p(x)$ of the fluid within the network (porous medium) is subject to the Poisson equation

$$-\nabla \cdot (c \nabla p) = S, \tag{6.5}$$

equipped with no-flux boundary condition, and the datum $S = S(x)$ represents the intensity of sources and sinks. The formal $L^2$-gradient flow (local dynamic adaptation model) of the energy (6.3) constrained by (6.5) is of the form

$$\partial_t c^k = (\partial_{x_k} p)^2 - \nu |c^k|^{\gamma-2} c^k, \qquad k = 1, \ldots, d, \tag{6.6}$$

subject to homogeneous Dirichlet boundary conditions, and coupled to (6.5). Clearly, the system suffers from two drawbacks: first, the possible strong degeneracy of the Poisson equation (6.5), and, second, the fact that (6.6) is merely a family of ODEs, parametrised by the spatial variable. Therefore, we shall consider a regularisation/extension of (6.5)–(6.6), where the Poisson equation is of the form

$$-\nabla \cdot ((r\mathbb{I} + c)\nabla p) = S, \tag{6.7}$$

where $r = r(x) \geqslant r_0 > 0$ is a prescribed function that models the isotropic background permeability of the medium, and $\mathbb{I} \in \mathbb{R}^{d \times d}$ is the unit matrix. The second drawback is addressed by equipping the transient system (6.6) with a linear diffusive term modelling random fluctuations in the medium,

$$\partial_t c^k = D^2 \Delta c^k + (\partial_{x_k} p)^2 - \nu |c^k|^{\gamma - 2} c^k, \qquad k = 1, \ldots, d, \tag{6.8}$$

subject to homogeneous Dirichlet boundary conditions, where $D^2 > 0$ is the constant diffusivity. Let us note that the model (6.7)–(6.8) is a variant of the tensor-based model proposed by D. Hu, restricted to the set of diagonal tensors [HC14]. As we will see in the derivation of the formal continuum limit, diagonal tensors can be associated with rectangular parallelotopes in the discrete setting.

The third goal of this chapter is to prove the global existence of weak solutions of the PDE system (6.7)–(6.8). The proof shall rely on the fact that it is a formal $L^2$-gradient flow of the regularised energy functional

$$\mathcal{E}[c] = \int_\Omega D^2 |\nabla c|^2 + \nabla p \cdot (r\mathbb{I} + c) \nabla p + \frac{\nu}{\gamma} |c|^\gamma \, dx, \tag{6.9}$$

where the symbol $|\nabla c|^2$ is defined as $\sum_{k=1}^d |\nabla c^k|^2$.

This chapter is organised as follows. In Section 6.2 we describe the discrete model [HC13] introduced by Hu and Cai, establish its gradient flow structure and prove the global existence of solutions of the corresponding ODE system coupled to the Kirchhoff law (linear system of equations). In Section 6.3 we motivate an adaptation of the Hu-Cai model so that a continuum model can be obtained as its formal macroscopic limit. We then derive the PDE system (6.5)–(6.6) as the formal gradient flow of the continuum energy (6.3) and prove the global existence of solutions for $\gamma > 1$. Finally, results of numerical simulations of the discrete Hu-Cai model are presented in Section 6.4, illustrating the convergence to steady states, their non-uniqueness as well as their dependence on initial data and model parameters.

## 6.2    Analysis of the microscopic model

In this section, we investigate the microscopic model for describing the formation of biological networks, introduced in Section 1.2.2.

### 6.2.1 Gradient flow

To compute the gradient flow of the energy (6.1) constrained by Kirchhoff's law (6.2), we need the following result about the derivative of the pumping term with respect to the conductivities:

**Lemma 8.** *Let $Q_{ij}[C] = C_{ij}\frac{P_j - P_i}{L_{ij}}$ for all $(i,j) \in \mathbb{E}$ as in (1.23), where $P$ is a solution of the linear system (6.2) with a given vector of conductivities $C$. Then, for any fixed $(k,l) \in \mathbb{E}$ we have*

$$\frac{\partial}{\partial C_{kl}} \sum_{(i,j)\in\mathbb{E}} \frac{Q_{ij}[C]^2}{C_{ij}} L_{ij} = -\frac{Q_{kl}[C]^2}{C_{kl}^2} L_{kl}. \tag{6.10}$$

*Proof.* Since

$$\frac{\partial}{\partial C_{kl}} \sum_{(i,j)\in\mathbb{E}} \frac{Q_{ij}[C]^2}{C_{ij}} L_{ij} = -\frac{Q_{kl}[C]^2}{C_{kl}^2} L_{kl} + 2 \sum_{(i,j)\in\mathbb{E}} \frac{Q_{ij}[C]}{C_{ij}} \frac{\partial Q_{ij}[C]}{\partial C_{kl}} L_{ij},$$

it is sufficient to show that

$$\sum_{(i,j)\in\mathbb{E}} \frac{Q_{ij}[C]}{C_{ij}} \frac{\partial Q_{ij}[C]}{\partial C_{kl}} L_{ij} = 0.$$

Let $\mathbb{A} = (\mathbb{A}_{ij})$ denote the adjacency matrix of the graph $\mathbb{G} = (\mathbb{V}, \mathbb{E})$, i.e. its coefficients are defined by

$$\mathbb{A}_{ij} = \begin{cases} 0 & \text{if } (i,j) \notin \mathbb{E}, \\ 1 & \text{if } (i,j) \in \mathbb{E}. \end{cases} \tag{6.11}$$

Note that $\mathbb{G}$ is an undirected graph, implying $\mathbb{A}_{ij} = \mathbb{A}_{ji}$. Due to the symmetry of $C_{ij}$ and $L_{ij}$ and antisymmetry of $Q_{ij}$ we have

$$2 \sum_{(i,j)\in\mathbb{E}} \frac{Q_{ij}[C]}{C_{ij}} \frac{\partial Q_{ij}[C]}{\partial C_{kl}} L_{ij} = \sum_{i=1}^n \sum_{j=1}^n \mathbb{A}_{ij} \left( \frac{P_j - P_i}{L_{ij}} \frac{\partial Q_{ij}[C]}{\partial C_{kl}} \right) L_{ij}$$

$$= \sum_{j=1}^n P_j \sum_{i=1}^n \mathbb{A}_{ij} \frac{\partial Q_{ij}[C]}{\partial C_{kl}} - \sum_{i=1}^n P_i \sum_{j=1}^n \mathbb{A}_{ij} \frac{\partial Q_{ij}[C]}{\partial C_{kl}}$$

$$= -2 \sum_{i=1}^n P_i \sum_{j=1}^n \mathbb{A}_{ij} \frac{\partial Q_{ij}[C]}{\partial C_{kl}}$$

$$= -2 \sum_{i=1}^{n} P_i \frac{\partial}{\partial C_{kl}} \sum_{j \in N(i)} Q_{ij}.$$

By the definition of the flow rate $Q_{ij}$ in (1.23) and Kirchhoff's law (6.2) we have

$$- \sum_{j \in N(i)} Q_{ij} = - \sum_{j \in N(i)} C_{ij} \frac{P_j - P_i}{L_{ij}} = S_i,$$

and since the sources/sinks $S_i$ are fixed, we conclude

$$\sum_{(i,j) \in \mathbb{E}} \frac{Q_{ij}[C]}{C_{ij}} \frac{\partial Q_{ij}[C]}{\partial C_{kl}} L_{ij} = 0$$

as required. $\qquad \square$

Using the result in (6.10) in the above lemma, it is easy to see that for $(i,j) \in \mathbb{E}$ the derivative of the energy (6.1) is given by

$$\frac{\partial}{\partial C_{ij}} E[C] = - \left( \frac{Q_{ij}[C]^2}{C_{ij}^2} - \nu C_{ij}^{\gamma-1} \right) L_{ij}.$$

Therefore, the gradient flow of (6.1) constrained by Kirchhoff's law (6.2) with respect to the Euclidean distance is given by the ODE system

$$\frac{\mathrm{d}C_{ij}}{\mathrm{d}t} = \left( \frac{Q_{ij}[C]^2}{C_{ij}^2} - \nu C_{ij}^{\gamma-1} \right) L_{ij}, \qquad (6.12)$$

coupled to Kirchhoff's law (6.2) via the definition of the flow rate (1.23).

The general formulation of a gradient flow of the functional $E$ is of the form

$$\frac{\mathrm{d}z}{\mathrm{d}t} = -\mathcal{K}[z]E'[z] \qquad \text{or, equivalently,} \qquad \mathcal{G}[z]\frac{\mathrm{d}z}{\mathrm{d}t} = -E'[z],$$

where $E'(z)$ is the Fréchet derivative of the energy functional $E: \mathcal{Z} \to \mathbb{R}$ on the subset $\mathcal{Z}$ of a linear space and $z \in \mathcal{Z}$. We denote the space of tangent vectors at a point $z \in \mathcal{Z}$ by $\mathcal{T}_z\mathcal{Z}$ and the space of cotangent vectors, i.e. the set of all linear functionals on $\mathcal{T}_z\mathcal{Z}$, by $\mathcal{T}_z^*\mathcal{Z}$. Then, the derivative $E'[z]$ is a cotangent vector and $\mathcal{G}[z], \mathcal{K}[z]$ are duality maps, mapping tangents to cotangents and vice versa, i.e. $\mathcal{G}[z]: \mathcal{T}_z\mathcal{Z} \to \mathcal{T}_z^*\mathcal{Z}$ and $\mathcal{K}[z]: \mathcal{T}_z^*\mathcal{Z} \to \mathcal{T}_z\mathcal{Z}$, with $\mathcal{K} = \mathcal{G}^{-1}$. See, e.g., [Pel] for details.

Based on this general formulation, we consider the gradient flow with respect to

a weighted Euclidean distance and introduce a duality map resulting in the ODE system of the form

$$\frac{\mathrm{d}C_{ij}}{\mathrm{d}t} = \left( \frac{Q_{ij}[C]^2}{C_{ij}} - \nu C_{ij}^{\gamma} \right) C_{ij}^{\alpha-1} L_{ij}, \tag{6.13}$$

with a fixed exponent $\alpha \in \mathbb{R}$, constrained by the Kirchhoff law (6.2). For modelling reasons (see [HC13] and the references therein) we require that the speed of metabolic decay is an increasing function of the conductivity. Therefore, we impose $\alpha > 1 - \gamma$. In particular, the choice $\alpha = 2 - \gamma$ leads to the system studied by Hu and Cai in [HC13]. Note that for $\alpha > 1 - \gamma$ the solution of (6.13) is nonnegative for nonnegative initial data. Moreover, we have the dissipation of the energy (6.1) along the solutions of (6.1), (6.2), since

$$\frac{\mathrm{d}}{\mathrm{d}t} E[C] = E'[C] \cdot \frac{\mathrm{d}C}{\mathrm{d}t} = - \sum_{(i,j)\in\mathbb{E}} \left( \frac{Q_{ij}[C]^2}{C_{ij}} - \nu C_{ij}^{\gamma} \right)^2 C_{ij}^{\alpha-2} L_{ij}^2 \leqslant 0. \tag{6.14}$$

### 6.2.2 Global existence of solutions

We shall prove the global existence of solutions for the ODE system (6.13) coupled to the Kirchhoff law (6.2) through the definition of the flow rate (1.23). We assume that the initial datum for $C = C_{ij}$ is such that the underlying graph is connected, where only edges with positive conductivity $C_{ij} > 0$ are taken into account (i.e., edges with zero initial conductivity are discarded and removed from the graph). This implies that the Kirchhoff law (6.2) is solvable for $t = 0$ (uniquely up to an additive constant) for the pressures. Depending on the values of the exponents $\alpha \in \mathbb{R}$, $\gamma > 0$, we distinguish two cases:

- If $\gamma + \alpha \geqslant 2$, then we have for all $(i,j) \in \mathbb{E}$,

$$\frac{\mathrm{d}C_{ij}}{\mathrm{d}t} \geqslant -\nu L_{ij} C_{ij}^{\gamma+\alpha-1}. \tag{6.15}$$

  Then, since the exponent $\gamma + \alpha - 1 \geqslant 1$, the solutions of (6.13) remain positive for all $t > 0$ (recall that the initial datum is strictly positive for all $(i,j) \in \mathbb{E}$). Consequently, the underlying graph remains connected and the Kirchhoff law (6.2) remains solvable for all times. Moreover, the terms $C_{ij}^{\gamma}$ and $Q_{ij}^2/C_{ij}$ remain globally bounded due to the energy dissipation (6.14). Thus, the solution of the system (6.13), (6.2) exists globally in time.

- If $0 < \gamma + \alpha - 1 < 1$, the solution may exist only locally in time and some of the conductivities $C_{ij}$ may vanish in finite time. Then the edges with $C_{ij} = 0$ are discarded and the connectivity of the graph may be lost, which would make the Kirchhoff law (6.2) unsatisfiable unless very restrictive conditions for the source/sink term $S_i$ are satisfied. Further note that conductivity is also motivated by the biological application so that fluids can be transported through the entire network. However, as we prove below, under rather mild assumptions on the source/sink term $S_i$, this does not happen, i.e., the Kirchhoff law remains solvable and the resulting subgraph remains connected even after the eventual removal of the edge(s) with vanishing conductivity. Thus, the solution $C = C(t)$ can be extended past this time simply by solving a reduced ODE system with initial datum equal to the 'terminal' state with the respective edge(s) removed.

We start by proving a result stating that if we divide the set of vertices $\mathbb{V}$ into two disjoint parts $\mathbb{V}_1$, $\mathbb{V}_2$ such that the sources/sinks $S_i$ induce a net flux $\Delta S \neq 0$ between them, then a connection (i.e., at least one edge with positive conductivity) between $\mathbb{V}_1$ and $\mathbb{V}_2$ will be maintained along the solutions of (6.13), (6.2).

**Lemma 9.** *Let $\gamma > 0$ and $0 < \gamma + \alpha - 1 < 1$. Let the set of vertices $\mathbb{V}$ be the disjoint union $\mathbb{V}_1 \cup \mathbb{V}_2$ such that*

$$\Delta S := \sum_{j \in \mathbb{V}_1} S_j = - \sum_{j \in \mathbb{V}_2} S_j \neq 0. \tag{6.16}$$

*Let $\widetilde{\mathbb{E}}$ be the set of edges connecting $\mathbb{V}_1$ to $\mathbb{V}_2$, i.e.,*

$$\widetilde{\mathbb{E}} = \{(i,j) \in \mathbb{E}; \ i \in \mathbb{V}_1 , j \in \mathbb{V}_2\},$$

*and assume that $C_{ij}(t = 0) \geqslant 0$ for all $(i,j) \in \widetilde{\mathbb{E}}$ with*

$$\sum_{(i,j) \in \widetilde{\mathbb{E}}} C_{ij}(t = 0) > 0. \tag{6.17}$$

*Then*

$$\sum_{(i,j) \in \widetilde{\mathbb{E}}} C_{ij}(t) > 0 \qquad \text{for all } t > 0 \tag{6.18}$$

*along the solutions of* (6.13), (6.2).

*Proof.* For contradiction, assume that there exists a $T > 0$ such that (6.18) holds for $t < T$ and

$$\lim_{t \to T-} \sum_{(i,j) \in \widetilde{\mathbb{E}}} C_{ij}(t) = 0. \tag{6.19}$$

For $t < T$ we have

$$\frac{\mathrm{d}}{\mathrm{d}t} \sum_{(i,j) \in \widetilde{\mathbb{E}}} C_{ij} = \sum_{(i,j) \in \widetilde{\mathbb{E}}} \left( Q_{ij}^2 C_{ij}^{\alpha-2} - \nu C_{ij}^{\gamma+\alpha-1} \right) L_{ij}. \tag{6.20}$$

Since $0 < \gamma + \alpha - 1 < 1$, we have for $t < T$ and each $(k,l) \in \widetilde{\mathbb{E}}$ the inequality

$$C_{kl}^{\gamma+\alpha-1} \leqslant \left( \sum_{(i,j) \in \widetilde{\mathbb{E}}} C_{ij} \right)^{\gamma+\alpha-1},$$

where we used that $C_{ij} \geqslant 0$ for $(i,j) \in \widetilde{\mathbb{E}}$ and $t < T$. Similarly, since $\alpha - 2 < 0$, we have

$$C_{kl}^{\alpha-2} \geqslant \left( \sum_{(i,j) \in \widetilde{\mathbb{E}}} C_{ij} \right)^{\alpha-2}.$$

Inserting this into (6.20), we obtain for $t < T$,

$$\frac{\mathrm{d}}{\mathrm{d}t} \sum_{(i,j) \in \widetilde{\mathbb{E}}} C_{ij} \geqslant \left( \sum_{(i,j) \in \widetilde{\mathbb{E}}} C_{ij} \right)^{\alpha-2} \sum_{(i,j) \in \widetilde{\mathbb{E}}} Q_{ij}^2 L_{ij} - \nu \left( \sum_{(i,j) \in \widetilde{\mathbb{E}}} C_{ij} \right)^{\gamma+\alpha-1} \sum_{(i,j) \in \widetilde{\mathbb{E}}} L_{ij}. \tag{6.21}$$

Next, we shall estimate the term $\sum_{(i,j) \in \widetilde{\mathbb{E}}} Q_{ij}^2 L_{ij}$ from below. Due to Kirchhoff's law (6.26), we have for $t < T$,

$$\sum_{(i,j) \in \widetilde{\mathbb{E}}} Q_{ij} = \Delta S \neq 0. \tag{6.22}$$

We claim that for each $t < T$ there exists an edge $(k,l) \in \widetilde{\mathbb{E}}$ such that

$$|Q_{kl}| \geqslant \frac{|\Delta S|}{|\widetilde{\mathbb{E}}|}.$$

213

If not, we would have

$$\left| \sum_{(i,j)\in\widetilde{\mathbb{E}}} Q_{ij} \right| \leqslant \sum_{(i,j)\in\widetilde{\mathbb{E}}} |Q_{ij}| < |\Delta S|,$$

a contradiction to (6.22). Consequently, for each $t < T$ we estimate

$$\sum_{(i,j)\in\widetilde{\mathbb{E}}} Q_{ij}^2 L_{ij} \geqslant \frac{|\Delta S|^2}{|\widetilde{\mathbb{E}}|^2} \min_{(i,j)\in\widetilde{\mathbb{E}}} L_{ij}.$$

Inserting this into (6.21), we obtain

$$\frac{\mathrm{d}}{\mathrm{d}t} u(t) \geqslant \kappa_1 u(t)^{\alpha-2} - \kappa_2 u(t)^{\gamma+\alpha-1}, \tag{6.23}$$

where we denoted

$$u(t) := \sum_{(i,j)\in\widetilde{\mathbb{E}}} C_{ij}(t),$$

and the constants

$$\kappa_1 := \frac{|\Delta S|^2}{|\widetilde{\mathbb{E}}|^2} \min_{(i,j)\in\widetilde{\mathbb{E}}} L_{ij} > 0, \qquad \kappa_2 := \nu \sum_{(i,j)\in\widetilde{\mathbb{E}}} L_{ij} > 0.$$

Since according to the assumption (6.17) we have $u(0) > 0$, (6.23) implies that

$$u(t) \geqslant \min\left\{ u(0), (\kappa_1/\kappa_2)^{\frac{1}{\gamma+1}} \right\} > 0$$

for $t < T$, a contradiction to (6.19). $\qquad\square$

**Theorem 9.** *Let $\gamma > 0$ and $0 < \gamma + \alpha - 1 < 1$. Assume that (6.16) holds for any disjoint sets $\mathbb{V}_1, \mathbb{V}_2 \subset \mathbb{V}$ such that $\mathbb{V} = \mathbb{V}_1 \cup \mathbb{V}_2$. Let the initial datum $C_{ij}(t = 0) \geqslant 0$ be such that the graph induced by edges $(i,j) \in \mathbb{E}$ with $C_{ij}(t = 0) > 0$ is connected. Then the graph induced by the solutions $C_{ij} = C_{ij}(t)$ of (6.13), (6.2), where edges with vanishing conductivities are discarded, remains connected for all times $t \geqslant 0$. In particular, solutions of (6.13), (6.2) with removal of edges with vanishing conductivities exist globally in time.*

*Proof.* Let us show that the graph remains connected for all times, i.e., for each $t > 0$ there exists a path of edges with positive conductivity connecting each pair

214

of vertices. For contradiction, assume that at time $t_0 > 0$ no such path exists connecting a vertex $i \in \mathbb{V}$ to vertex $j \in \mathbb{V}$. Then, collect all vertices connected by a path to $i \in \mathbb{V}$ in the set $\mathbb{V}_1$, and let $\mathbb{V}_2 := \mathbb{V} \backslash \mathbb{V}_1$ be its complement. Since $i \in \mathbb{V}$ is not connected to $j \in \mathbb{V}$ at time $t_0$, also $\mathbb{V}_1$ is not connected to $\mathbb{V}_2$, which is a contradiction to the statement of Lemma 9.

Consequently, the graph induced by the solutions $C_{ij} = C_{ij}(t)$ of (6.13), (6.2) never becomes disconnected, and thus, by the fundamental result of the graph theory [GYZ13], the Kirchhoff law (6.2) is solvable. Moreover, since the terms $C_{ij}^\gamma$ remain globally bounded due to the energy dissipation (6.14), the solution does not blow up. It can only happen that some $C_{ij}$ vanish in finite time. In this case the corresponding edge(s) are removed and the solution $C = C(t)$ is continued by solving a reduced ODE system. In this way a global solution of the system (6.13), (6.2) is constructed.

$\square$

**Remark 19.** *The assumption of Theorem 9 that* (6.16) *holds for any disjoint sets* $\mathbb{V}_1, \mathbb{V}_2 \subset \mathbb{V}$ *such that* $\mathbb{V} = \mathbb{V}_1 \cup \mathbb{V}_2$ *means that the graph cannot be partitioned into subgraphs with balanced sources/sinks (i.e.,* $\sum S_i = 0$ *over the subgraph). If the opposite is true, then the ODE system* (6.13), (6.2) *can be solved separately for each of the subgraphs (after eventual removal of edges connecting them).*

# 6.3 Derivation and properties of the macroscopic model

The goal of this section is to derive the formal macroscopic limit of the discrete model (6.2), (6.1) as the number of nodes and edges tends to infinity, and to study the existence of weak solutions of the corresponding gradient flow. The limit consists of an integral-type energy functional coupled to a Poisson equation. We shall show that the derivation requires an appropriate rescaling of the Kirchhoff law (6.2) and of the energy functional (6.1). Moreover, we have to restrict ourselves to discrete graphs represented by regular grids, i.e., tessellation of the domain $\Omega \subset \mathbb{R}^d$, $d \in \mathbb{N}$, by congruent identical parallelotopes. This restriction is dictated by the requirement that the formal gradient flow of the rescaled energy functional, constrained by the rescaled Kirchhoff law, is of the form (6.12).

### 6.3.1 Rescaling of the Kirchhoff law

Let us denote the vertices left and right of vertex $i \in \mathbb{V}$ along the $k$-th spatial dimension by $(i-1)_k$ and, resp., $(i+1)_k$. The Kirchhoff law (6.2) is then written as

$$-\sum_{k=1}^{d} \left( C_{i,(i+1)_k} \frac{P_{(i+1)_k} - P_i}{L_{i,(i+1)_k}} - C_{(i-1)_k,i} \frac{P_i - P_{(i-1)_k}}{L_{(i-1)_k,i}} \right) = S_i \qquad \text{for all } i \in \mathbb{V}. \quad (6.24)$$

Our goal is to identify the Kirchhoff law with a finite difference discretisation of the Poisson equation (6.5),

$$-\nabla \cdot (c\nabla p) = S, \tag{6.25}$$

where $S = S(x)$ is a formal limit of the sequence of discrete sources/sinks $S_i$. Clearly, for this the edge lengths in the left-hand side of (6.24) have to appear quadratically in the denominator instead of linearly. Alternatively, we can say that the sources/sinks $S_i$ in the right-hand side of (6.24) have to be rescaled appropriately, reflecting the fact that the edges of the graph are inherently one-dimensional structures. A straightforward calculation reveals that a finite difference discretisation of (6.25), where $c = c(x)$ is an appropriate limit of the sequence of discrete conductivities, is obtained if and only if

$$\frac{2}{L_{(i-1)_k,i} + L_{i,(i+1)_k}} = \frac{1}{L_{(i-1)_k,i}} = \frac{1}{L_{i,(i+1)_k}}$$

for all $i \in \mathbb{V}$ and for all directions $k = 1, \ldots, d$. Therefore, grid points must be equidistant in each spatial dimension, and we denote $h_k > 0$ the grid spacing in the $k$-th dimension. The discrete graph is thus identified with a tessellation of $\Omega$ by identical parallelotopes. For simplicity, we restrict ourselves to work with rectangular parallelotopes (bricks) in the sequel, with edges parallel to the axes. A generalisation of the result for parallelotopes instead will be given in Remark 20. The rescaled Kirchhoff law is then written as

$$-\sum_{k=1}^{d} \frac{1}{h_k} \left( C_{i,(i+1)_k} \frac{P_{(i+1)_k} - P_i}{h_k} - C_{(i-1)_k,i} \frac{P_i - P_{(i-1)_k}}{h_k} \right) = S_i \qquad \text{for all } i \in \mathbb{V}.$$

$$(6.26)$$

### 6.3.2 Rescaling of the discrete energy functional

In order to obtain an integral-type functional in the macroscopic limit of the sequence of discrete energy functionals (6.1), they need to be properly rescaled depending on the spatial dimension $d \in \mathbb{N}$. In particular, (6.1) has to be replaced by

$$E[C] = \sum_{(i,j)\in\mathbb{E}} \left( \frac{Q_{ij}[C]^2}{C_{ij}} + \frac{\nu}{\gamma} C_{ij}^\gamma \right) W_{ij}^d, \tag{6.27}$$

where $W_{ij}$ are some (abstract) weights that scale linearly with the grid spacing. Before we introduce the formal macroscopic limit of the rescaled discrete functional (6.27) constrained by the rescaled Kirchhoff law (6.26), let us make the following observation about the gradient flow (6.27)–(6.26).

**Proposition 12.** *Consider the setting introduced in Section 6.3.1 with the discrete graph realised as a rectangular tessellation of $\Omega \in \mathbb{R}^d$. Then the formal gradient flow (with respect to the Euclidean distance) of the energy functional (6.27) constrained by the rescaled Kirchhoff law (6.26) is of the type (6.12), i.e.,*

$$\frac{dC_{ij}}{dt} = \left( \frac{Q_{ij}[C]^2}{C_{ij}^2} - \nu C_{ij}^{\gamma-1} \right) W_{ij}^d, \tag{6.28}$$

*if and only if all the weights $W_{ij}$ are equal.*

*Proof.* Denoting the adjacency matrix (6.11) of the tessellation by $\mathbb{A} = (\mathbb{A}_{ij})$, we have for any edge $(l,m) \in \mathbb{E}$,

$$\frac{\partial E[C]}{\partial C_{lm}} = -\frac{Q_{lm}[C]^2}{C_{lm}^2} W_{lm} + \nu C_{lm}^{\gamma-1} W_{lm} + \frac{1}{2} \sum_{i=1}^n \sum_{j=1}^n \mathbb{A}_{ij} \left( \frac{2Q_{ij}[C]}{C_{ij}} \frac{\partial Q_{ij}[C]}{\partial C_{lm}} \right) W_{ij}^d.$$

The last term of the right-hand side is equal to

$$\begin{aligned}
&\sum_{i=1}^n \sum_{j=1}^n \mathbb{A}_{ij} \left( \frac{P_j - P_i}{L_{ij}} \frac{\partial Q_{ij}[C]}{\partial C_{lm}} \right) W_{ij}^d \\
&= -\sum_{j=1}^n P_j \sum_{i=1}^n \mathbb{A}_{ij} \frac{\partial Q_{ji}[C]}{\partial C_{lm}} \frac{W_{ij}^d}{L_{ij}} - \sum_{i=1}^n P_i \sum_{j=1}^n \mathbb{A}_{ij} \frac{\partial Q_{ij}[C]}{\partial C_{lm}} \frac{W_{ij}^d}{L_{ij}} \\
&= -2 \sum_{i=1}^n P_i \sum_{j=1}^n \mathbb{A}_{ij} \frac{\partial Q_{ij}[C]}{\partial C_{lm}} \frac{W_{ij}^d}{L_{ij}}.
\end{aligned} \tag{6.29}$$

Now note that the rescaled Kirchhoff law (6.26) is in terms of $Q_{ij}$, $L_{ij}$ written as

$$-\sum_{j \in \mathbb{V}} \mathbb{A}_{ij} \frac{Q_{ij}}{L_{ij}} = S_i \qquad \text{for all } i \in \mathbb{V}.$$

Therefore, if (and only if) all the weights $W_{ij}$ are equal to the same value $W > 0$, we have

$$\sum_{i=1}^{n} P_i \sum_{j=1}^{n} \mathbb{A}_{ij} \frac{\partial Q_{ij}[C]}{\partial C_{lm}} \frac{W_{ij}^d}{L_{ij}} = \sum_{i=1}^{n} P_i W^d \frac{\partial}{\partial C_{lm}} \left( \sum_{j=1}^{n} \mathbb{A}_{ij} \frac{Q_{ij}}{L_{ij}} \right) = 0,$$

and we obtain (6.28) as the gradient flow. $\qquad\qquad\square$

Note that for the grid consisting of a rectangular tessellation, the natural choice of the weight $W_{ij} \equiv W$ is

$$W^d = \prod_{k=1}^{d} h_k, \tag{6.30}$$

i.e., the area of the rectangles for $d = 2$ and the volume of the bricks for $d = 3$.

### 6.3.3 Formal derivation of the macroscopic model

In this section we shall show that the rescaled Kirchhoff law represents a finite difference discretisation of the Poisson equation (6.5), and that the discrete energy functional (6.27) with (6.30) is an approximation (Riemann sum) of the integral-type functional (6.3). We shall work in the setting introduced above, i.e., the discrete graph is realised as a rectangular tessellation of the rectangular domain $\Omega \in \mathbb{R}^d$.

Let us consider $p = p(x)$ a solution of the Poisson equation (6.5),

$$-\nabla \cdot (c \nabla p) = S,$$

subject to the no-flux boundary condition on $\partial\Omega$. Here $c = c(x)$ is a given diagonal permeability tensor field

$$c = \begin{pmatrix} c^1 & & \\ & \ddots & \\ & & c^d \end{pmatrix},$$

with the scalar nonnegative functions $c^k \in C(\Omega)$, $k = 1, \ldots, d$. The density of sources/sinks $S = S(x)$ is given as a datum and satisfies the global mass balance

$$\int_\Omega S(x) \, \mathrm{d}x = 0.$$

As already mentioned in Section 6.1, existence of solutions of (6.5) is not guaranteed due to the possible strong degeneracy of the permeability tensor. However, as we are interested in a formal derivation only, we assume that $p = p(x)$ exists as a strong solution of (6.5), i.e., is at least $C_b^2$ on $\Omega$. Moreover, we assume that the elements of $c = c(x)$ are at least $C_b^1$ on $\Omega$. Since $c = c(x)$ is diagonal, the left-hand side of (6.5) can be rewritten as

$$-\nabla \cdot (c \nabla p) = -\sum_{k=1}^d \partial_{x_k}(c^k \partial_{x_k} p).$$

Let $X_i \in \Omega$ be the physical location of the vertex $i \in \mathbb{V}$. Denoting the flux $q^k := c^k \partial_{x_k} p$, a finite difference approximation of the term $\partial_{x_k} q^k$ at $x = X_i$ reads

$$\partial_{x_k} q^k(X_i) \approx \frac{q^k(X_{(i+1/2)_k}) - q^k(X_{(i-1/2)_k})}{h_k} + \mathcal{O}(h_k), \tag{6.31}$$

where $X_{(i+1/2)_k}$ and, resp., $X_{(i-1/2)_k}$ denotes the midpoint of the edge connecting $X_i$ to its adjacent vertex to the right and, resp., to the left in the $k$-th spatial direction. A finite difference approximation of $q^k$ at $X_{(i+1/2)_k}$ reads

$$q^k(X_{(i+1/2)_k}) = c^k(X_{(i+1/2)_k})\frac{p(X_{(i+1)_k}) - p(X_{(i-1)_k})}{h_k} + \mathcal{O}(h_k), \tag{6.32}$$

where $X_{(i+1)_k}$, resp., $X_{(i-1)_k}$ denotes the adjacent vertex of $X_i$ to the right and, resp., to the left in the $k$-th spatial direction. We discretise $q^k(X_{(i-1/2)_k})$ analogously. Putting (6.31) and (6.32) together and denoting

$$\begin{aligned} C_{i,(i\pm1)_k} &:= c^k(X_{(i\pm1/2)_k}), & S_i &:= S(X_i), \\ P_i &:= p(X_i), & P_{(i\pm1)_k} &:= p(X_{(i\pm1)_k}), \end{aligned} \tag{6.33}$$

we conclude that the rescaled Kirchhoff law (6.26) is a first order finite difference approximation of the Poisson equation (6.5).

With the choice (6.30) for the weight $W$, we have for $k = 1, \ldots, d$ and $c^k \in C_b^1(\Omega)$,

$$\int_\Omega |c^k|^\gamma \, \mathrm{d}x = W \sum_{i \in \mathbb{V}} \left| c^k(X_{(i+1/2)_k}) \right|^\gamma + \mathcal{O}(h_k).$$

Moreover, we have

$$\int_\Omega c^k (\partial_{x_k} p)^2 \, \mathrm{d}x = W \sum_{i \in \mathbb{V}} c^k(X_{(i+1/2)_k}) \left( \frac{p(X_{(i+1)_k}) - p(X_i)}{h_k} \right)^2 + \mathcal{O}(h_k).$$

Therefore, noting that for the rectangular grid the energy functional (6.27) can be rewritten as

$$E[C] = \frac{1}{2} \sum_{k=1}^d \sum_{i \in \mathbb{V}} \sum_{j \in N(i;k)} \left( \frac{Q_{ij}[C]^2}{C_{ij}} + \frac{\nu}{\gamma} C_{ij}^\gamma \right) h_k^d,$$

we have, with the notation (6.33),

$$E[C] = \mathcal{E}[c] + \mathcal{O}(h),$$

with the continuum energy defined by (6.3), i.e.,

$$\mathcal{E}[c] = \int_\Omega \nabla p \cdot c \nabla p + \frac{\nu}{\gamma} |c|^\gamma \, \mathrm{d}x, \tag{6.34}$$

where we recall that the symbol $|c|^\gamma$ is defined as $\sum_{k=1}^d \left| c^k \right|^\gamma$.

We now calculate the formal $L^2$-gradient flow of the energy (6.3) constrained by the Poisson equation (6.5).

**Lemma 10.** *The formal $L^2$-gradient flow of the continuum energy functional (6.3) constrained by the Poisson equation (6.5) is given by (6.6), i.e.,*

$$\partial_t c^k = (\partial_{x_k} p)^2 - \nu \left| c^k \right|^{\gamma-2} c^k.$$

*Proof.* Let us calculate the first variation of $\mathcal{E}$ in the direction $\phi$ where $\phi$ denotes a diagonal matrix with entries $\phi^1, \ldots, \phi^d$. Using the expansion

$$p[c + \varepsilon \phi] = p_0 + \varepsilon p_1 + \mathcal{O}(\varepsilon^2), \tag{6.35}$$

we have

$$\frac{\mathrm{d}}{\mathrm{d}\varepsilon}\mathcal{E}[c + \varepsilon\phi]\Big|_{\varepsilon=0} = \sum_{k=1}^{d} \int_{\Omega} (\partial_{x_k}p_0)^2\, \phi^k + 2c^k(\partial_{x_k}p_0)(\partial_{x_k}p_1) + \nu|c^k|^{\gamma-2}c^k\phi^k\, \mathrm{d}x. \quad (6.36)$$

Multiplying the Poisson equation (6.5) with permeability tensor $c + \varepsilon\phi$ by $p_0$ and integration by parts gives

$$\sum_{k=1}^{d} \int_{\Omega} \left(c^k + \varepsilon\phi^k\right)(\partial_{x_k}p_0)^2 + \varepsilon c^k(\partial_{x_k}p_0)(\partial_{x_k}p_1)\, \mathrm{d}x = \int_{\Omega} Sp_0\, \mathrm{d}x + \mathcal{O}(\varepsilon^2).$$

Subtracting the identity

$$\sum_{k=1}^{d} \int_{\Omega} c^k\, (\partial_{x_k}p_0)^2\, \mathrm{d}x = \int_{\Omega} Sp_0\, \mathrm{d}x,$$

we obtain

$$\sum_{k=1}^{d} \int_{\Omega} (\partial_{x_k}p_0)^2\, \phi^k + c^k(\partial_{x_k}p_0)(\partial_{x_k}p_1)\, \mathrm{d}x = 0.$$

Plugging this into (6.36) gives

$$\frac{\mathrm{d}}{\mathrm{d}\varepsilon}\mathcal{E}[c + \varepsilon\phi]\Big|_{\varepsilon=0} = \sum_{k=1}^{d} \int_{\Omega} \left[-(\partial_{x_k}p_0)^2 + \nu|c^k|^{\gamma-2}c^k\right]\phi^k\, \mathrm{d}x.$$

$\square$

**Remark 20.** *We can easily generalise to the situation when the grid is realised by congruent identical parallelotopes with edges in linearly independent directions $\theta_1, \ldots, \theta_d \in \mathbb{R}^d$. Then the coordinate transform $e_k \mapsto \theta_k$ in (6.3)–(6.5), where $e_k$ is the k-th vector of the generic basis of $\mathbb{R}^d$, leads to the transformed continuum energy functional*

$$\mathcal{E}[c] = \int_{\Omega} \nabla p \cdot \mathbb{P}[c]\nabla p + \frac{\nu}{\gamma}|c|^{\gamma}\, dx, \quad (6.37)$$

*coupled to the Poisson equation*

$$-\nabla \cdot (\mathbb{P}[c]\nabla p) = S$$

221

with the permeability tensor

$$\mathbb{P}[c] := \sum_{k=1}^{d} c^k \theta_k \otimes \theta_k.$$

The corresponding formal $L^2$-gradient flow is of the form

$$\partial_t c^k = (\theta_k \cdot \nabla p)^2 - \nu |c^k|^{\gamma-2} c^k.$$

For general geometries of discrete networks the derivation of the macroscopic model is an open problem and one can expect that the associated macroscopic limit depends on the geometric properties of the network.

### 6.3.4 Global existence of solutions of a modified macroscopic model

As noted in Section 6.1, the model (6.5)–(6.6) suffers from two drawbacks: first, the Poisson equation (6.5) is possibly strongly degenerate since in general the eigenvalues (i.e., diagonal elements) of the permeability tensor $c = c(x)$ may vanish. To overcome this problem, we introduce a regularisation of (6.5) of the form

$$-\nabla \cdot (\mathbb{P}[c] \nabla p) = S, \tag{6.38}$$

with the permeability tensor

$$\mathbb{P}[c] := r\mathbb{I} + c, \tag{6.39}$$

where $r = r(x) \geqslant r_0 > 0$ is a prescribed function that models the isotropic background permeability of the medium, and $\mathbb{I} \in \mathbb{R}^{d \times d}$ is the unit matrix. Clearly, (6.38) is uniformly elliptic as long as the eigenvalues of $c = c(x)$ are nonnegative.

The second drawback is due to the fact that (6.6) is merely a family of ODEs, parametrised by the spatial variable $x \in \Omega$. We cure this problem by introducing a linear diffusive term modeling random fluctuations in the medium. We thus obtain

$$\partial_t c^k = D^2 \Delta c^k + (\partial_{x_k} p)^2 - \nu |c^k|^{\gamma-2} c^k, \qquad k = 1, \ldots, d, \tag{6.40}$$

subject to homogeneous Dirichlet boundary data, where $D^2 > 0$ is the constant diffusivity. By a simple modification of the proof of Lemma 10 we conclude that the

system (6.38)–(6.40) represents the formal $L^2$-gradient flow of the energy functional

$$\mathcal{E}[c] = \int_\Omega \frac{D^2}{2}|\nabla c|^2 + \nabla p \cdot \mathbb{P}[c]\nabla p + \frac{\nu}{\gamma}|c|^\gamma \, \mathrm{d}x, \tag{6.41}$$

with $\mathbb{P}[c]$ given by (6.39), the symbol $|c|^\gamma$ is defined as $\sum_{k=1}^d \left|c^k\right|^\gamma$ and the symbol $|\nabla c|^2$ is defined as $\sum_{k=1}^d \left|\nabla c^k\right|^2$. The gradient flow property is fundamental for proving the global existence of weak solutions of the PDE system (6.38)–(6.40). Note that the energy functional (6.41) is highly non-convex suggesting that the weak solutions may be non-unique. We consider the PDE system on a bounded domain $\Omega \subset \mathbb{R}^d$ with smooth boundary $\partial\Omega$, subject to homogeneous Dirichlet boundary conditions for $c$ and no-flux boundary conditions for $p$,

$$c(t, x) = 0, \quad \frac{\partial p}{\partial n}(t, x) = 0 \quad \text{for } x \in \partial\Omega, \, t \geqslant 0, \tag{6.42}$$

where $n$ denotes the exterior normal vector to the boundary $\partial\Omega$. Moreover, we prescribe the initial datum for $c$,

$$c(t = 0, x) = c^I(x) \quad \text{for } x \in \Omega, \tag{6.43}$$

where $c^I = c^I(x)$ is a diagonal tensor field in $\mathbb{R}^{d \times d}$ with nonnegative diagonal elements.

**Theorem 10.** *Let $S \in L^2(\Omega)$, $\gamma > 1$ and $c^I \in H_0^1(\Omega)^{d \times d} \cap L^\gamma(\Omega)^{d \times d}$. Then the system* (6.38)–(6.40) *subject to the data* (6.42)–(6.43) *admits a global weak solution* $(c, p)$ *such that*

$$\begin{aligned} c \in L^\infty(0, \infty; H_0^1(\Omega)) \cap L^\infty(0, \infty; L^\gamma(\Omega)), \quad \partial_t c \in L^2((0, \infty) \times \Omega), \\ \nabla p \in L^\infty(0, \infty; L^2(\Omega)), \quad c\nabla p \in L^\infty(0, \infty; L^2(\Omega)). \end{aligned} \tag{6.44}$$

*This solution satisfies the energy dissipation inequality*

$$\mathcal{E}[c(t)] + \sum_{k=1}^d \int_0^t \int_\Omega \left(\partial_t c^k(s, x)\right)^2 \mathrm{d}x \, \mathrm{d}s \leqslant \mathcal{E}[c^I] \quad \text{for all } t \geqslant 0, \tag{6.45}$$

*with $\mathcal{E}[c]$ given by* (6.41).

For the proof of the above theorem we adopt a strategy similar to [HMP15,

HMPS16]: For $\varepsilon > 0$ we introduce the regularised Poisson equation

$$-\nabla \cdot (\mathbb{P}^\varepsilon[c]\nabla p) = S \tag{6.46}$$

with the permeability tensor

$$\mathbb{P}^\varepsilon[c] := r\mathbb{I} + c * \eta_\varepsilon, \tag{6.47}$$

subject to no-flux boundary data for $p$. Here, $\eta_\varepsilon$ is a nonnegative, radially symmetric mollifier and the convolution $c * \eta_\varepsilon$ is carried out elementwise,

$$c^k * \eta_\varepsilon(x) := \int_{\mathbb{R}^d} c^k(y)\eta_\varepsilon(x-y)\,\mathrm{d}y.$$

Moreover, we regularise (6.40) as follows,

$$\frac{\partial c^k}{\partial t} = D^2 \Delta c^k + (\partial_{x_k} p)^2 * \eta_\varepsilon - \nu |c^k|^{\gamma-2} c^k, \qquad k = 1, \ldots, d. \tag{6.48}$$

By a slight adaptation of the proof of Lemma 10 it is easily shown that (6.46)–(6.48) is the formal $L^2$-gradient flow of the energy

$$\mathcal{E}^\varepsilon[c] := \int_\Omega \frac{D^2}{2}|\nabla c|^2 + \nabla p \cdot \mathbb{P}^\varepsilon[c]\nabla p + \frac{\nu}{\gamma}|c|^\gamma \,\mathrm{d}x, \tag{6.49}$$

where we used the notation

$$|\nabla c|^2 := \sum_{k=1}^d |\nabla c^k|^2, \qquad |c|^\gamma := \sum_{k=1}^d |c^k|^\gamma.$$

For proving the global existence of weak solutions of the regularised system (6.46)–(6.48) we shall need the following maximum principle for a semilinear PDE.

**Lemma 11.** *Let $\Omega$ be an open, bounded subset of $\mathbb{R}^d$. For a fixed $T > 0$ denote $\Omega_T := (0, T] \times \Omega$ and*

$$C_1^2(\Omega_T) := \{u \colon \Omega_T \to \mathbb{R} \mid u, \nabla u, \nabla^2 u, \partial_t u \in C(\Omega_T)\}.$$

*Let $\gamma > 1$ and let $u \in C_1^2(\Omega_T) \cap C(\overline{\Omega}_T)$ be the classical solution of the initial/boundary-*

*value problem*

$$\begin{cases} \partial_t u = D^2 \Delta u - \nu |u|^{\gamma-2} u & in\ \Omega_T, \\[2mm] u = 0 & on\ [0, T] \times \partial\Omega, \\[2mm] u = g & on\ \{t = 0\} \times \partial\Omega, \end{cases} \tag{6.50}$$

*with the nonnegative initial datum $g \colon \Omega \to \mathbb{R}$. Then,*

$$\min_{\overline{\Omega}_T} u \geqslant 0. \tag{6.51}$$

*Proof.* Denote $U_T := \{(t, x) \in \Omega_T \mid u(t, x) < 0\}$. Then $U_T$ is an open bounded subset of $\Omega_T$ and

$$\partial_t u - D^2 \Delta u = -\nu |u|^{\gamma-2} u > 0 \qquad in\ U_T.$$

Then using the classical weak maximum principle for the heat equation, see, e.g., [Eva10], we have

$$\min_{\overline{U}_T} u = \min_{\partial U_T} u = 0.$$

Consequently, $U_T = \varnothing$ and (6.51) holds. $\qquad\square$

**Lemma 12.** *Let $S \in L^2(\Omega)$ and $c^I \in H_0^1(\Omega)^{d \times d} \cap L^\gamma(\Omega)^{d \times d}$. Then for each $\varepsilon > 0$ the regularised system (6.46)–(6.48) subject to the data (6.42)–(6.43) admits a global weak solution $(c, p)$ satisfying (6.44). The regularised energy (6.49) satisfies*

$$\mathcal{E}^\varepsilon[c(t)] + \sum_{k=1}^d \int_0^t \int_\Omega \left(\partial_t c^k(s, x)\right)^2 \mathrm{d}x\,\mathrm{d}s = \mathcal{E}^\varepsilon[c^I] \quad for\ all\ t \geqslant 0. \tag{6.52}$$

*Proof.* We proceed along the lines of the proof of Theorem 2 of [HMP15]. We employ the Leray-Schauder fixed point theorem in the space $L^2((0, T) \times \Omega)$. For a given diagonal tensor $c \in L^2((0, T) \times \Omega)$ with nonnegative elements we construct a solution $p_\varepsilon \in H^1(\Omega)$ of the regularised Poisson equation (6.46) with no-flux boundary data using the Lax-Milgram theorem; note that for $\varepsilon > 0$ the permeability tensor (6.47) satisfies $\mathbb{P}^\varepsilon \in L^\infty(\Omega)$, and uniform ellipticity follows from the assumption $r \geqslant r_0 > 0$ in $\Omega$. Consequently, we have the uniform bound

$$\|\nabla p^\varepsilon\|_{L^2(\Omega)} \leqslant C_\Omega \|S\|_{L^2(\Omega)} \qquad for\ all\ t \geqslant 0,\ \varepsilon > 0, \tag{6.53}$$

where the constant $C_\Omega$ depends only on the domain $\Omega$; in particular, it is independent of $\varepsilon > 0$ and $c \in L^2((0,T) \times \Omega)$.

Existence of weak solutions $c_\varepsilon$ of (6.48) is obtained by a slight adaptation of Lemma 3 of [HMP15], noting that for $\nabla p \in L^2(\Omega)$ and $\varepsilon > 0$ the terms $(\partial_{x_k} p)^2 * \eta_\varepsilon$ are bounded in $L^\infty(\Omega)$. The nonnegativity of the diagonal entries of $c_\varepsilon$ follows from the fact that solutions of the semilinear PDE

$$\partial_t u = D^2 \Delta u - \nu |u|^{\gamma-2} u$$

are subsolutions to (6.48). Preservation of nonnegativity of $u$ for nonnegative initial and boundary data has been established in Lemma 11.

The proof of continuity and compactness of the Schauder fixed point mapping $c \mapsto p_\varepsilon \mapsto c_\varepsilon$ in the space $L^2((0,T) \times \Omega)$ goes again along the lines of Theorem 2 of [HMP15], using the so-called weak-strong lemma for the Poisson equation (Lemma 7 of [HMP15]) and compact Sobolev embedding $H^1(\Omega) \subset L^2(\Omega)$.

The energy identity (6.52) follows by multiplying the Poisson equation (6.46) by $p$ and integrating by parts,

$$\sum_{k=1}^{d} \int_\Omega \left( r + c^k * \eta_\varepsilon \right) \left( \partial_{x_k} p \right)^2 \mathrm{d}x = \int_\Omega S p \, \mathrm{d}x.$$

Subtracting this from (6.49) we obtain

$$\mathcal{E}^\varepsilon[c] = \sum_{k=1}^{d} \left( \int_\Omega \frac{D^2}{2} \left| \nabla c^k \right|^2 - \left( r + c^k * \eta_\varepsilon \right) \left( \partial_{x_k} p \right)^2 + \frac{\nu}{\gamma} \left| c^k \right|^\gamma \mathrm{d}x \right) + 2 \int_\Omega S p \, \mathrm{d}x.$$

Integration by parts in suitable terms and using (6.46) then yields

$$\frac{\mathrm{d}}{\mathrm{d}t} \mathcal{E}^\varepsilon[c] = \sum_{k=1}^{d} \left( \int_\Omega -D^2 \Delta c^k \partial_t c^k + 2 \partial_{x_k} \left( \left( r + c^k * \eta_\varepsilon \right) \partial_{x_k} p \right) \partial_t p - \partial_t c^k \left( \partial_{x_k} p \right)^2 \mathrm{d}x \right)$$

$$+ \nu \sum_{k=1}^{d} \left( \int_\Omega \left| c^k \right|^{\gamma-1} \partial_t c^k \, \mathrm{d}x \right) + 2 \int_\Omega S \partial_t p \, \mathrm{d}x$$

$$= -\sum_{k=1}^{d} \int_\Omega \left( D^2 \Delta c^k + \left( \partial_{x_k} p \right)^2 * \eta_\varepsilon - \nu \left| c^k \right|^{\gamma-1} \right) \partial_t c^k \, \mathrm{d}x$$

$$+ 2 \int_\Omega \left( \nabla \cdot \left( \mathbb{P}^\varepsilon[c] \nabla p \right) + S \right) \partial_t p \, \mathrm{d}x$$

$$= -\sum_{k=1}^{d} \int_{\Omega} \left( \partial_t c^k \right)^2 \mathrm{d}x.$$

and an integration in time gives (6.52). □

The passage to the limit $\varepsilon \to 0$ in (6.46)–(6.48) is based on the uniform apriori estimates

$$c \in L^\infty(0, \infty; H_0^1(\Omega)) \cap L^\infty(0, \infty; L^\gamma(\Omega)), \quad \partial_t c \in L^2((0, \infty) \times \Omega),$$

$$\nabla p \in L^\infty(0, \infty; L^2(\Omega)), \quad \sqrt{c^k * \eta_\varepsilon} \partial_{x_k} p \in L^\infty(0, \infty; L^2(\Omega)), \ k = 1, \ldots, d,$$

which follow from the energy identity (6.52) and from (6.53). Then, since a subsequence of $c^\varepsilon * \eta_\varepsilon$ converges strongly to $c$ in the norm topology of $L^2((0, T) \times \Omega)$, a slight modification of Lemma 7 in [HMP15] gives the strong convergence of $p^\varepsilon$ to $p$ in $L^2(0, T; H^1(\Omega))$ with no-flux boundary data where $p$ is the unique solution of the Poisson equation (6.38) with given $c$. Thus, $\left( \partial_{x_k} p^\varepsilon \right)^2$ converges strongly to $\left( \partial_{x_k} p \right)^2$ in $L^1((0, T) \times \Omega)$ and $\left( \partial_{x_k} p^\varepsilon \right)^2 * \eta_\varepsilon$ also converges strongly to $\left( \partial_{x_k} p \right)^2$ in $L^1((0, T) \times \Omega)$. The limit passage in the metabolic term $\left| c^k \right|^{\gamma-2} c^k$ can be shown as in Lemma 4 in [HMP15] due to the uniform boundedness of $c^\varepsilon$ in $L^\gamma((0, T) \times \Omega)$. The energy dissipation inequality (6.45) follows by passing to the limit $\varepsilon \to 0$ in (6.52) using the weak lower semicontinuity of the $L^2$-norm. This concludes the proof of Theorem 10.

## 6.4 Numerical simulations

In this section we provide results of numerical simulations for the discrete model introduced in Section 6.2. We implement a minimisation scheme for the discrete energy (6.1) constrained by the Kirchhoff law (6.2), based on the numerical methods proposed in [ABH$^+$17].

For the numerical simulations we consider a planar graph $\mathbb{G} = (\mathbb{V}, \mathbb{E})$ whose vertices and edges define a diamond shaped geometry embedded in the two-dimensional domain $\Omega = (0, 2) \times (-1.5, 0.5)$. We consider $|\mathbb{V}| = 78$ vertices and $|\mathbb{E}| = 201$ edges. For vertex $i \in \mathbb{V}$ let $(x^i, y^i)$ denote its position. The source $S$ is assumed to be positive on the subset of vertices

$$\mathbb{V}^+ := \{i \in \mathbb{V}; \ x^i \leqslant 0.1\}$$

227

and constant and negative on its complement $\mathbb{V}\backslash\mathbb{V}^+$. For $i \in \mathbb{V}$ we set

$$S_i := \begin{cases} \sigma_i^+ & i \in \mathbb{V}^+ \\ \sigma_i^- & i \in \mathbb{V}\backslash\mathbb{V}^+ \end{cases}$$

where

$$\sigma_i^+ := 10^4 \exp\left(-10\left(50x_i^2 + 10\left(y_i + 0.5\right)^4\right)\right), \quad \sigma_i^- := -\frac{1}{|\mathbb{V}\backslash\mathbb{V}^+|} \sum_{j \in \mathbb{V}^+} \sigma_j^+.$$

In the sequel we prescribe the initial condition $\overline{C} = \left(\overline{C}_{ij}\right)_{(i,j)\in\mathbb{E}}$, unless stated otherwise. We assume $\overline{C}_{ij} := 5$ for every $(i,j) \in \mathbb{E}$ on a tree, see Figure 6.1(A), and $\overline{C}_{ij} := 10^{-10}$ otherwise.

For solving the constrained energy minimisation problem we consider the following iterative procedure:

- Initialisation: For each edge $(i,j) \in \mathbb{E}$ compute its length $L_{ij}$ and define the parameters $\nu := 1$, $\tau := 0.025$ and $tol := 10^{-6}$.

- Step 1 (Pressure): For $\overline{C}$ given, compute the coefficient matrix $B = (b_{ij}) \in \mathbb{R}^{n-1,n-1}$ with entries

$$b_{ij} = \begin{cases} -\frac{C_{ij}}{L_{ij}^2} & (i,j) \in \mathbb{E} \\ 0 & (i,j) \notin \mathbb{E} \end{cases}, \quad i,j = 1,\ldots,n-1, \quad i \neq j, \tag{6.54}$$

$$b_{ii} = \sum_{j \in N(i)} \frac{C_{ij}}{L_{ij}^2}, \quad i = 1,\ldots,n-1. \tag{6.55}$$

and solve via least square minimisation:

$$\min_P \|BP - S\|_2$$

- Step 2 (Conductivity): For given pressure $P$ and conductivities $\overline{C}$ find a minimiser $C$ of the regularisation

$$E^\tau[C] := \frac{\|C - \overline{C}\|_2^2}{2\tau} + \sum_{(i,j)\in\mathbb{E}} \left(\frac{Q_{ij}(C)^2}{C_{ij}} + \nu C_{ij}^\gamma\right) L_{ij} \tag{6.56}$$

of the discrete energy functional (6.1) via interior point method for a regularisation parameter $\tau > 0$.

- Step 3 (Energy decrease): If $\left| E^\tau[C] - E^\tau[\overline{C}] \right| > tol$, set $\overline{C} := C$ and go back to step 1.

Note that for $\tau > 0$ solving (6.56) is equivalent to an implicit Euler step for (6.13). The choice of the time step $\tau > 0$ is crucial. On the one hand, the time step should not be chosen too large so that an accurate solution can be obtained. On the other hand, choosing $\tau$ too small may result in very long simulation times, especially because the convergence seems to be very slow close to the minimiser, compare Figure 6.2 where the slow decay of the energy functional is shown. Armijo's condition [NW06] suggests a good choice of the parameter $\tau$ so that sufficient decrease of the energy functional is achieved in every time step.

In the sequel we present the energy minima (stationary solutions) obtained by the above algorithm for different values of $\gamma$. For every edge $(i, j) \in \mathbb{E}$ we plot the value of the conductivity $C_{ij}$ in terms of the width of the associated edge. In Figure 6.1 we show the steady states under an $\varepsilon$-perturbation of the initial condition $\overline{C}$ for $\gamma = 0.5$, i.e., we consider $\overline{C}_{ij} + \varepsilon$ instead of $\overline{C}_{ij}$ for all edges $(i, j) \in \mathbb{E}$. As shown in Figure 6.1 the steady states are the same trees for small perturbations, e.g., $\varepsilon \leqslant 0.1$, as the tree given by the initial condition in Figure 6.1(A). In particular, the steady states are stable under small perturbations of the initial condition. For larger perturbations, e.g., $\varepsilon \in \{0.5, 1, 2\}$, we obtain steady states different from the initial condition, indicating a phase transition which can be studied further in the future. This also illustrates that the energy functional (6.1) has multiple local minima and, consequently, the system (6.13)–(6.2) has non-unique steady states. In particular, the steady states strongly depend on the choice of the initial data.

In Figure 6.2 the stationary solution of (6.13)–(6.2) and the decay of the energy functional are shown for different values of $\gamma > 0$. Note that the stationary solution is a tree for $\gamma = 0.5$ and a full network for $\gamma = 1.5$. This is in agreement with the observations of [HC13] where a phase transition at $\gamma = 1$ was suggested with steady states in the form of a tree for $\gamma < 1$ and full networks as steady states for $\gamma > 1$.

In Figure 6.3 we consider initial data in form of a tree, Figure 6.1(A), and close one of its loops, as shown in Figure 6.3(A). These initial conditions lead to the steady states in Figure 6.3(B). Note that closing one loop in the initial data leads to steady states which only differ locally (i.e., in a neighbourhood of the loop) from the original tree in Figure 6.1(A). Closing one loop in areas of smaller conductivities in the associated steady state leads to the same tree structure as in the original initial data in Figure 6.1(A) as shown for the third choice of initial data in Figure 6.3(A). In particular, closing loops at different locations leads to different steady

(A) Initial data  (B) $\varepsilon = 10^{-4}$  (C) $\varepsilon = 10^{-3}$  (D) $\varepsilon = 10^{-2}$

(E) $\varepsilon = 0.1$  (F) $\varepsilon = 0.5$  (G) $\varepsilon = 1$  (H) $\varepsilon = 2$
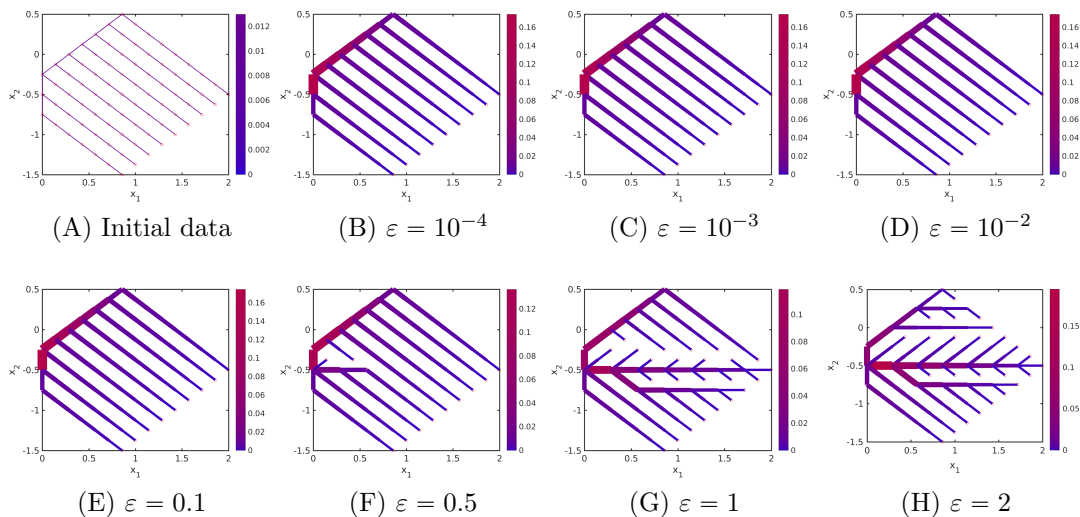
Figure 6.1: Stability of steady states under perturbations $\varepsilon$ of initial data for the discrete model.



(A) $\gamma = 0.5$  (B) $\gamma = 1.5$
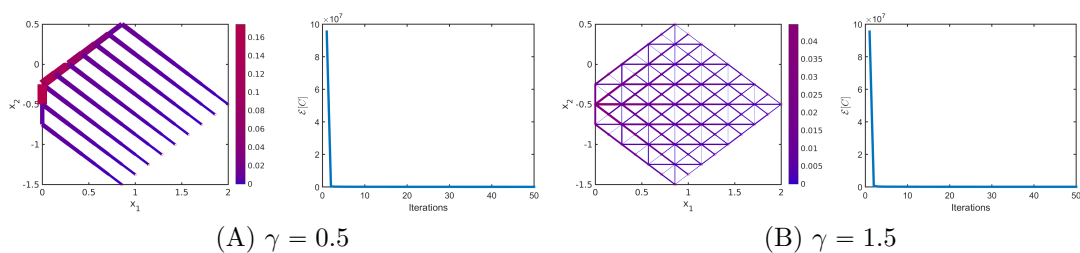
Figure 6.2: Stationary solution to the discrete model and decrease of energy for different values of $\gamma > 0$.

states in general, unless the resulting steady state is the tree in the initial condition in Figure 6.1(A). This shows again that we obtain trees as steady states for $\gamma = 0.5$, the steady states are non-unique and the form of the steady states strongly depends on the given initial data. In particular, loops in the initial data are opened over time for $\gamma = 0.5$.



(A) Initial data



(B) Associated steady states
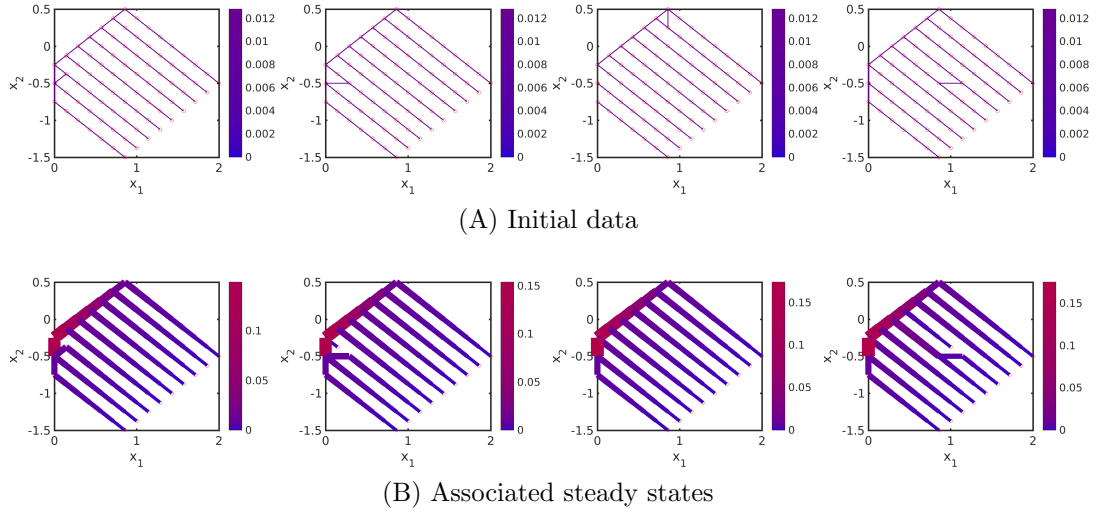
Figure 6.3: Stability of steady states when one loop in tree-structured initial data is closed.

Based on the initial condition in the first picture in Figure 6.3(A) we close more loops in the neighbourhood of this closed loop in the initial data in Figure 6.4. Closing iteratively one additional loop results in the initial conditions in Figure 6.4(A) and the associated steady states are depicted in Figure 6.4(B). Note that closing loops close to the source leads to different steady states. In particular, closing loops iteratively in the initial data leads to steady states which only differ locally. More precisely, the resulting steady states all have the same number of non-zero conductivities. Closing one loop in the initial data results in a steady state which can be obtained from steady states with the previous initial data by interchanging a non-zero with a negligible conductivity. In particular, the steady states strongly depend on the initial data.

In Figure 6.5 the steady states are shown for the same initial data as before (see Figure 6.5(A)) for different values of the parameter $\nu > 0$ in the definition of the energy functional (6.1). As $\nu$ increases the form of the steady states remain the same, i.e., positive conductivities remain positive for different values of $\nu$. However, the absolute value of the conductivities decreases as $\nu$ increases, see Figure 6.5. This is consistent with the definition of the energy functional (6.1) where the metabolic

(A) Initial data



(B) Associated steady states
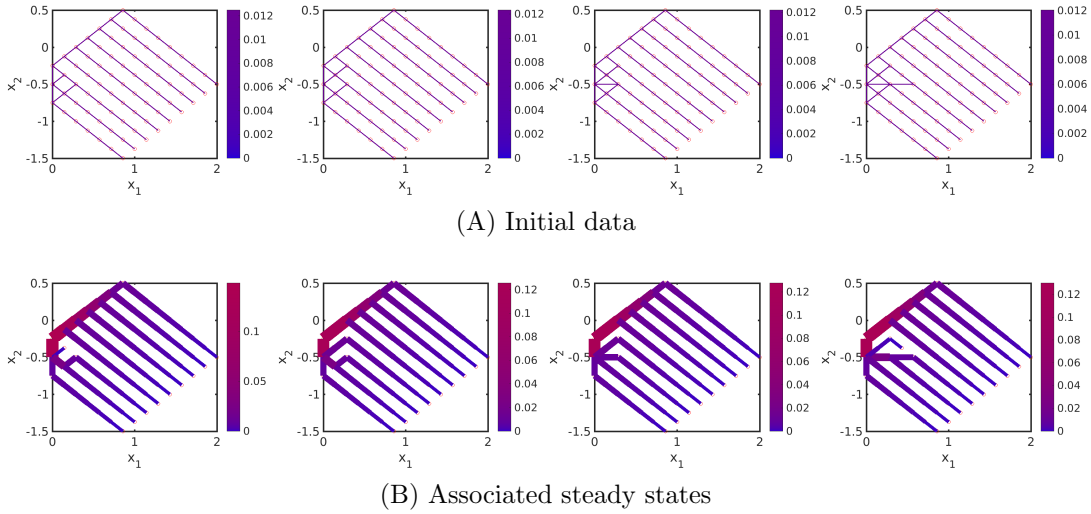
Figure 6.4: Stability of steady states when several loops in tree-structured initial data are closed in the discrete model.

term is of the form $\frac{\nu}{\gamma} C_{ij}^{\gamma}$ with $\gamma > 0$.



(A) Initial data     (B) $\nu = 1$     (C) $\nu = 100$     (D) $\nu = 10^5$
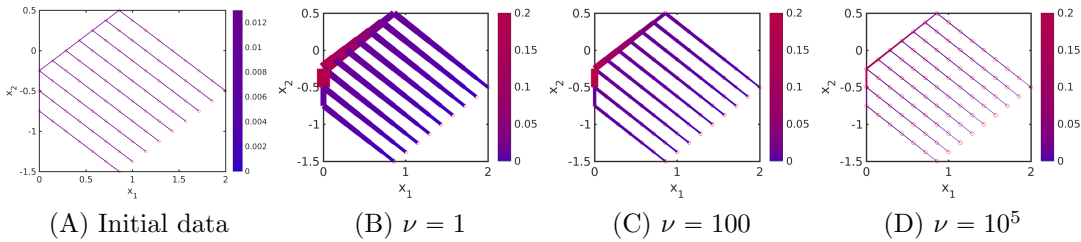
Figure 6.5: Steady states for different values of the parameter $\nu$ in the energy functional (6.1).

The absolute value of the initial conductivities is varied in Figures 6.6(A)–6.6(C) and we show the resulting steady state in Figure 6.6(D). More precisely, we consider initial data in the form of a tree as before, when only those conductivities $\bar{C} = (\bar{C}_{ij})_{(i,j)\in\mathbb{E}}$ with positive conductivities $\bar{C}_{ij}$ are considered but vary the absolute value of the initial conductivities. We consider the initial data $\bar{C}_{ij} = \delta$ for every edge $(i,j) \in \mathbb{E}$ on the tree for $\delta = 5, 50, 5000, 50000$ and $\bar{C}_{ij} = 10^{-10}$ otherwise, as shown in Figure 6.1(A) and Figures 6.6(A)–6.6(C), respectively. All these different initial data result in the same steady state shown in Figure 6.6(D).

In Figure 6.7, full graphs are considered as initial data and we show the associated steady states. We consider $\bar{C}_{ij} = 1$ for all $(i,j) \in \mathbb{E}$ and the perturbed full graph with $\bar{C}_{ij} = 1 + \mathcal{U}(0,1)$ where $\mathcal{U}(0,1)$ denotes a uniformly distributed random variable on $[0,1]$. The associated steady states are more complex transportation

(A) $\delta = 100$      (B) $\delta = 10^3$      (C) $\delta = 10^4$      (D) Steady state
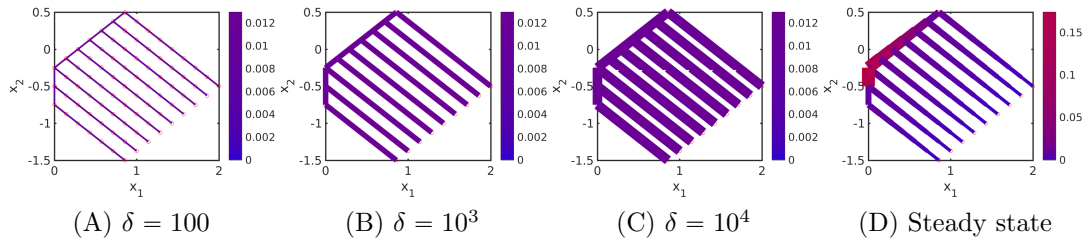
Figure 6.6: Initial data for the conductivity vector $\bar{C} = (\bar{C}_{ij})_{(i,j)\in\mathbb{E}}$ in the form of a tree where each non-zero conductivity $\bar{C}_{ij}$ is of size $\delta > 0$ (left) all leading to an identical steady state (right) for the discrete model.

networks.



(A) Full graph            (B) Steady state
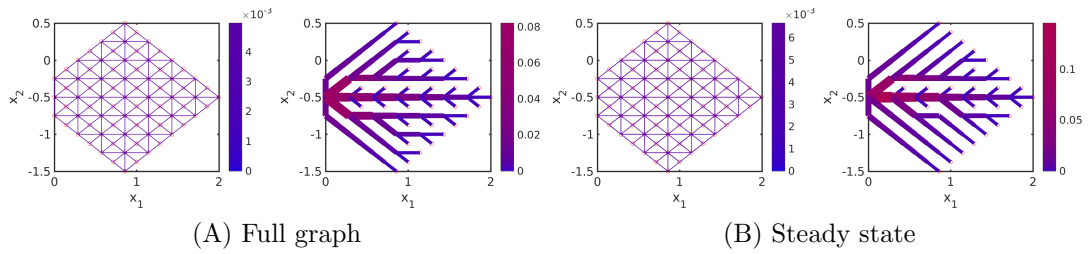
Figure 6.7: Steady states for full graph and perturbed full graph as initial data in the discrete model.

# Chapter 7

# Rigorous continuum limit

## Originality and contribution

This chapter is based on the paper [HKM19b] in collaboration with Jan Haskovec and Peter A. Markowich. While PM proposed the study of the model and provided guidance and advice, the results are mostly joint work by JH and myself.

## Chapter summary

In this chapter, we study the rigorous limit of the discrete model proposed by Hu and Cai consisting of an energy consumption function constrained by a linear system on a graph. For the spatially two-dimensional rectangular setting we prove the rigorous continuum limit of the constrained energy functional as the number of nodes of the underlying graph tends to infinity and the edge lengths shrink to zero uniformly. The proof is based on reformulating the discrete energy functional as a sequence of integral functionals and proving their $\Gamma$-convergence towards the respective continuum energy functional.

## 7.1   Introduction

In this chapter we derive the rigorous continuum limit of the discrete network formation model of Hu and Cai [HC13]. The model is posed on an a priori given graph $\mathbb{G} = (\mathbb{V}, \mathbb{E})$, consisting of the set of vertices (nodes) $\mathbb{V}$ and the set of unoriented edges (vessels) $\mathbb{E}$. Any pair of vertices $i, j \in \mathbb{V}$ is connected by at most one edge $(i, j) \in \mathbb{E}$, such that the corresponding graph $(\mathbb{V}, \mathbb{E})$ is connected. The lengths

$L_{ij} > 0$ of the vessels $(i,j) \in \mathbb{E}$ are given a priori and fixed. The adjacency matrix of the graph $(\mathbb{V}, \mathbb{E})$ is denoted by $\mathbb{A}$, i.e., $\mathbb{A}_{ij} = 1$ if $(i,j) \in \mathbb{E}$, otherwise $\mathbb{A}_{ij} = 0$.

Let us emphasise that by fixing $(\mathbb{V}, \mathbb{E})$, the set of possible flow directions in the network is also fixed. For each node $j \in \mathbb{V}$ we prescribe the strength of source/sink $S_j \in \mathbb{R}$ and we adopt the convention that $S_j > 0$ denotes sources, while $S_j < 0$ sinks. We also allow for $S_j = 0$, i.e., no external in- or outgoing flux in this node. We impose the global mass conservation

$$\sum_{j \in \mathbb{V}} S_j = 0. \tag{7.1}$$

We denote $C_{ij}$ and, resp., $Q_{ij}$ the conductivity and, resp., the flow through the vessel $(i,j) \in \mathbb{E}$. Note that the flow is oriented and we adopt the convention that $Q_{ij} > 0$ means net flow from node $j \in \mathbb{V}$ to node $i \in \mathbb{V}$. An overview of the notation is provided in Table 7.1. We assume low Reynolds number of the flow through the network, so that the flow rate through a vessel $(i,j) \in \mathbb{E}$ is proportional to its conductivity and the pressure drop between its two ends, i.e.,

$$Q_{ij} = C_{ij} \frac{P_j - P_i}{L_{ij}}. \tag{7.2}$$

Local conservation of mass is expressed in terms of the Kirchhoff law,

$$\sum_{i \in \mathbb{V}} \mathbb{A}_{ij} C_{ij} \frac{P_j - P_i}{L_{ij}} = S_j \qquad \text{for all } j \in \mathbb{V}. \tag{7.3}$$

Note that for any given vector of conductivities $C := (C_{ij})_{(i,j) \in \mathbb{E}}$, (7.3) represents a linear system of equations for the vector of pressures $(P_j)_{j \in \mathbb{V}}$. The system has a solution, unique up to an additive constant, if and only if the graph with edge weights given by $C$ is connected [GYZ13], where only edges with positive conductivities are taken into account (i.e., edges with zero conductivity are discarded).

Assuming that the material cost for an edge $(i,j) \in \mathbb{E}$ of the network is proportional to a power $C_{ij}^{\gamma}$ of its conductivity, Hu and Cai [HC13] consider the energy consumption function of the form

$$E[C] := \frac{1}{2} \sum_{i \in \mathbb{V}} \sum_{j \in \mathbb{V}} \left( \frac{Q_{ij}^2}{C_{ij}} + \frac{\nu}{\gamma} C_{ij}^{\gamma} \right) \mathbb{A}_{ij} L_{ij}, \tag{7.4}$$

where $\nu > 0$ is the metabolic coefficient and $Q_{ij}$ is given by (7.2), where the pressure

Table 7.1: Notation. (*) denotes variables that are given as data.

| Variable | Meaning | Related to |
|---|---|---|
| $S_j$ (∗) | intensity of source/sink | vertex $j \in \mathbb{V}$ |
| $P_j$ | pressure | vertex $j \in \mathbb{V}$ |
| $L_{ij}$ (∗) | length of an edge | edge $(i, j) \in \mathbb{E}$ |
| $Q_{ij}$ | flow from $j \in \mathbb{V}$ to $i \in \mathbb{V}$ | edge $(i, j) \in \mathbb{E}$ |
| $C_{ij}$ | conductivity | edge $(i, j) \in \mathbb{E}$ |

drop $\frac{P_j - P_i}{L_{ij}}$ is determined by (7.3). The first part of the energy consumption (7.4) represents the kinetic energy (pumping power) of the material flow through the vessels, and we shall call it *pumping term* in the sequel. The second part represents the metabolic cost of maintaining the network and shall be called *metabolic term*. For instance, the metabolic cost for a blood vessel is proportional to its cross-section area [Mur26a]. Modelling blood flow by Hagen-Poiseuille's law, the conductivity of the vessel is proportional to the square of its cross-section area. This implies $\gamma = 1/2$ for blood vessel systems. For leaf venations, the material cost is proportional to the number of small tubes, which is proportional to $C_{ij}$, and the metabolic cost is due to the effective loss of the photosynthetic power at the area of the venation cells, which is proportional to $C_{ij}^{1/2}$. Consequently, the effective value of $\gamma$ typically used in models of leaf venation lies between $1/2$ and $1$, [HC13]. Hu and Cai showed that the optimal networks corresponding to minimisers of (7.3)-(7.4) exhibit a phase transition at $\gamma = 1$, with a "uniform sheet" (the network is tiled with loops) for $\gamma > 1$ and a "loopless tree" for $\gamma < 1$, see also [HMR18]. Moreover, they consider the gradient flow of the energy (7.4) constrained by the Kirchhoff law (7.3), which leads to the ODE system for the conductivities $C_{ij}$,

$$\frac{\mathrm{d}C_{ij}}{\mathrm{d}t} = \left( \frac{Q_{ij}^2}{C_{ij}^2} - \nu C_{ij}^{\gamma-1} \right) L_{ij} \qquad \text{for } (i, j) \in \mathbb{E}, \tag{7.5}$$

coupled to the Kirchhoff law (7.3) through (7.2). This system represents an adaptation model which dynamically responds to local information and can naturally incorporate fluctuations in the flow.

This chapter focuses on deriving the rigorous continuum limit of the energy functional (7.3)-(7.4) as the number of nodes of the underlying graph tends to

infinity and the edge lengths $L_{ij}$ tend uniformly to zero. In a general setting with a sequence of unstructured graphs this is a mathematically very challenging task. In particular, one has to expect that the object obtained in the limit will depend on the structural and statistical properties of the graph sequence (connectivity, edge directions and density etc.). Therefore, we consider the particular setting where the graphs correspond to regular equidistant meshes in 1D and 2D. As we explain in Section 7.3, the energy minimization problem for (7.3)-(7.4) in the one-dimensional case is in fact trivial, and the form of the limiting functional is obvious. However, we use this setting as a toy example and carry out the rigorous limit passage anyway. The reason is that in the 1D setting we avoid most of the technical peculiarities of the two-dimensional case and we can focus on the essential idea of the method. Equipped with this insight, we shall turn to the two-dimensional case (Section 7.4), where the graph is an equidistant rectangular mesh on a square-shaped domain $\Omega$.

In both the 1D and 2D cases, it is necessary to adopt the additional assumption that the conductivities are a priori bounded away from zero. In particular, we introduce a modification of the system (7.3)-(7.4) where the conductivities are of the form $r + C_{ij}$, where $r > 0$ is a fixed global constant. The reason is that we need to guarantee the solvability of the Poisson equation (7.10) below, which will be obtained in the continuum limit. Moreover, in the 2D case, the additive terms in the energy functional have to be scaled by the square of the edge length $L_{ij}$. This is due to the fact that we are embedding the inherently one-dimensional edges of the graph into two spatial dimensions; see [HKM19a, Section 3.2] for details. Thus, we shall work with the energy functional

$$E[C] := \frac{1}{2} \sum_{i \in \mathbb{V}} \sum_{j \in \mathbb{V}} \left( \frac{Q_{ij}^2}{r + C_{ij}} + \frac{\nu}{\gamma}(r + C_{ij})^{\gamma} \right) \mathbb{A}_{ij} L_{ij}^d, \qquad (7.6)$$

where $d = 1, 2$ is the space dimension, coupled to the (properly rescaled) Kirchhoff law

$$\sum_{i \in \mathbb{V}} \mathbb{A}_{ij}(r + C_{ij}) \frac{P_j - P_i}{L_{ij}} = L_j S_j \qquad \text{for all } j \in \mathbb{V} \qquad (7.7)$$

through

$$Q_{ij} = (r + C_{ij}) \frac{P_j - P_i}{L_{ij}}, \qquad (7.8)$$

where $L_j$ are (abstract) weights that scale linearly with the mean edge length; see [HKM19a, Section 3.1] for details about the scaling in (7.7). The main benefit of this chapter is the rigorous derivation of the limiting energy functional, which for the two-dimensional case is of the form

$$\mathcal{E}[c] = \int_\Omega \nabla p[c] \cdot (r\mathbb{I} + c)\nabla p[c] + \frac{\nu}{\gamma} \left( |r + c_1|^\gamma + |r + c_2|^\gamma \right) \, \mathrm{d}\mathbf{x}, \qquad (7.9)$$

with $\mathbf{x} = (x, y) \in \mathbb{R}^2$ and where $p[c] \in H^1(\Omega)$ is a weak solution of the Poisson equation

$$-\nabla \cdot ((r\mathbb{I} + c)\nabla p) = S \qquad (7.10)$$

subject to no-flux boundary conditions on $\partial\Omega$, where $\mathbb{I}$ is the unit matrix and $c$ is the diagonal $2 \times 2$-tensor

$$c = \begin{pmatrix} c_1 & 0 \\ 0 & c_2 \end{pmatrix}. \qquad (7.11)$$

Here, $S \in L^2(\Omega)$ denotes the source/sink term and in analogy to (7.1) we require $\int_\Omega S \, \mathrm{d}\mathbf{x} = 0$. The derivation is based on three steps:

(i) Establish a connection between the discrete solutions of the Kirchhoff law (7.7) and weak solutions of the Poisson equation (7.10); see Section 7.3.1 in 1D and Sections 7.4.1, 7.4.2 in 2D.

(ii) Reformulate the discrete energy functional (7.6) as an integral functional defined on the set of bounded functions; see Section 7.3.1 in 1D and Section 7.4.2 in 2D.

(iii) Show that the sequence of integral functionals $\Gamma$-converges to the energy functional (7.9); see Section 7.3.2 in 1D and Section 7.4.3 in 2D. See, e.g., [DM93, Bra02] for details about $\Gamma$-convergence.

The $\Gamma$-convergence opens the door for constructing global minimisers of (7.9)–(7.10) as limits of sequences of minimisers of the discrete problem (7.6)–(7.7). However, for this we need strong convergence of the minimisers in an appropriate topology. In agreement with [HMP15, HMPS16, ABH$^+$17] we introduce diffusive terms into

239

the discrete energy functionals, modeling random fluctuations in the medium (Section 7.3.3 for 1D and Section 7.4.4 in 2D). The diffusive terms provide compactness of the minimizing sequences in a suitable topology and facilitate the construction of global minimisers of (7.9)–(7.10).

Let us note that the steepest descent minimization procedure for (7.9)–(7.10) is represented by the formal $L^2$-gradient flow. This leads to the system of partial differential equations for $c_1 = c_1(t, x, y)$, $c_2 = c_2(t, x, y)$,

$$
\begin{aligned}
\partial_t c_1 &= (\partial_x p)^2 - \nu(r + c_1)^{\gamma-1}, \\
\partial_t c_2 &= (\partial_y p)^2 - \nu(r + c_2)^{\gamma-1},
\end{aligned}
\tag{7.12}
$$

subject to homogeneous Dirichlet boundary data and coupled to (7.10) through (7.11). The existence of weak solutions and their properties are studied in [HKM19a]. Finally, let us remark that [Hu13] proposed a different PDE system, derived from the discrete model [HC13] by certain phenomenological considerations (laws of porous medium flow, see [ABH+17] for details). The system consists of a parabolic reaction-diffusion equation for the vector-valued conductivity field, constrained by a Poisson equation for the pressure, and was studied in the series of papers [HMP15, HMPS16, AAFM16, ABH+17]. However, a rigorous derivation of the model is still lacking; moreover, no explicit connection to the system (7.12) has been established so far.

## 7.2   An auxiliary Lemma

**Lemma 13.** *Fix $r > 0$, a bounded domain $\Omega \subset \mathbb{R}^d$ with $d \geqslant 1$, and $S \in L^2(\Omega)$. Let $(c^N)_{N \in \mathbb{N}} \subset L^\infty(\Omega)$ be a sequence of nonnegative, essentially bounded functions on $\Omega$, such that $c^N \to c \in L^2(\Omega)$ in the norm topology of $L^2(\Omega)$. Let $(p^N)_{N \in \mathbb{N}} \subset H^1(\Omega)$ be a sequence of zero-average weak solutions of the Poisson equation*

$$
-\nabla \cdot ((r + c^N)\nabla p^N) = S
\tag{7.13}
$$

*subject to homogeneous Neumann boundary conditions on $\partial\Omega$. Then $\nabla p^N$ converges to $\nabla p$ and $\sqrt{c^N}\nabla p^N$ converges to $\sqrt{c}\nabla p$ strongly in $L^2(\Omega)$, where $p$ is the zero-average weak solution of*

$$
-\nabla \cdot ((r + c)\nabla p) = S
\tag{7.14}
$$

*subject to homogeneous Neumann boundary conditions on $\partial\Omega$. In particular, we have*

$$\lim_{N\to\infty}\int_\Omega (r+c^N)|\nabla p^N|^2\,d\mathbf{x} = \int_\Omega (r+c)|\nabla p|^2\,d\mathbf{x}. \tag{7.15}$$

**Remark 21.** *Note that we do* not *assume that $(c^N)_{N\in\mathbb{N}}$ is uniformly bounded in $L^\infty(\Omega)$, nor that $c\in L^\infty(\Omega)$.*

*Proof.* Using $p^N$ as a test function in (7.13), due to the nonnegativity of $c^N$, we have

$$r\left\|\nabla p^N\right\|^2_{L^2(\Omega)} \leqslant \int_\Omega (r+c^N)|\nabla p^N|^2\,\mathrm{d}\mathbf{x} = \int_\Omega Sp^N\,\mathrm{d}\mathbf{x} \tag{7.16}$$
$$\leqslant \frac{1}{2\varepsilon}\left\|S\right\|^2_{L^2(\Omega)} + \frac{\varepsilon C_P}{2}\left\|\nabla p^N\right\|^2_{L^2(\Omega)},$$

where $C_P$ is the Poincaré constant. With a suitable choice of $\varepsilon > 0$ we obtain a uniform estimate on $p^N$ in $H^1(\Omega)$. Consequently, there exists a subsequence of $p^N$ that converges weakly in $H^1(\Omega)$ to some $p\in H^1(\Omega)$. Since $c^N \to c$ strongly in $L^2(\Omega)$, we can pass to the limit in the distributional formulation of (7.13) to obtain

$$\int_\Omega (r+c)\nabla p\cdot\nabla\phi\,\mathrm{d}\mathbf{x} = \int_\Omega S\phi\,\mathrm{d}\mathbf{x} \qquad \text{for all } \phi\in C_0^\infty(\Omega). \tag{7.17}$$

Noting that (7.16) also implies a uniform bound on $\int_\Omega c^N|\nabla p^N|^2\,\mathrm{d}\mathbf{x}$, we have due to the weak lower semicontinuity of the $L^2$-norm,

$$\int_\Omega (r+c)|\nabla p|^2\,\mathrm{d}\mathbf{x} \leqslant \liminf_{N\to\infty}\int_\Omega (r+c^N)|\nabla p^N|^2\,\mathrm{d}\mathbf{x} < +\infty. \tag{7.18}$$

Consequently, we can use $p$ as a test function in (7.17) to obtain

$$\int_\Omega (r+c)|\nabla p|^2\,\mathrm{d}\mathbf{x} = \int_\Omega Sp\,\mathrm{d}\mathbf{x}.$$

Therefore, using $p^N$ as a test function in (7.13),

$$\lim_{N\to\infty}\int_\Omega (r+c^N)|\nabla p^N|^2\,\mathrm{d}\mathbf{x} = \lim_{N\to\infty}\int_\Omega Sp^N\,\mathrm{d}\mathbf{x} = \int_\Omega Sp\,\mathrm{d}\mathbf{x} = \int_\Omega (r+c)|\nabla p|^2\,\mathrm{d}\mathbf{x},$$

which gives (7.15) and, further,

$$\limsup_{N\to\infty} \int_\Omega |\nabla p^N|^2 \, d\mathbf{x} \leqslant \limsup_{N\to\infty} \int_\Omega (r + c^N)|\nabla p^N|^2 \, d\mathbf{x} + \limsup_{N\to\infty} \left( -\int_\Omega c^N |\nabla p^N|^2 \, d\mathbf{x} \right)$$
$$= \int_\Omega (r + c)|\nabla p|^2 \, d\mathbf{x} - \liminf_{N\to\infty} \int_\Omega c^N |\nabla p^N|^2 \, d\mathbf{x}.$$

Now, using (7.18), we have

$$-\liminf_{N\to\infty} \int_\Omega c^N |\nabla p^N|^2 \, d\mathbf{x} = -\liminf_{N\to\infty} \int_\Omega |\sqrt{c^N}\nabla p^N|^2 \, d\mathbf{x} \leqslant -\int_\Omega |\sqrt{c}\nabla p|^2 \, d\mathbf{x}.$$

Therefore,

$$\limsup_{N\to\infty} \int_\Omega |\nabla p^N|^2 \, d\mathbf{x} \leqslant \int_\Omega |\nabla p|^2 \, d\mathbf{x},$$

so that $\lim_{N\to\infty} \|\nabla p^N\|_{L^2(\Omega)} = \|\nabla p\|_{L^2(\Omega)}$, which directly implies that (a subsequence of) $p^N$ converges towards $p$ strongly in $H^1(\Omega)$. $\square$

## 7.3 The 1D equidistant setting

In this section we consider the spatially one-dimensional setting of the discrete network formation problem, where the graph $(\mathbb{V}, \mathbb{E})$ is given as a mesh on the interval $[0, 1]$. Moreover, for simplicity we consider the equidistant case, where for a fixed $N \in \mathbb{N}$ construct the sequence of meshpoints $x_i$,

$$x_i = ih \qquad \text{for } i = 0, \dots, N, \text{ with } h := 1/N.$$

We identify the meshpoints $x_i$ with the vertices of the graph, i.e., we set $\mathbb{V} := \{x_i; \ i = 0, \dots, N\}$. The segments $(x_{i-1}, x_i)$ connecting any two neighbouring nodes are identified with the edges of the graph, i.e., $\mathbb{E} := \{(x_{i-1}, x_i); \ i = 1, \dots, N\}$. By a slight abuse of notation, we shall write $i \in \mathbb{V}$ instead of $x_i \in \mathbb{V}$ in the sequel, and similarly $i \in \mathbb{E}$ instead of $(x_{i-1}, x_i) \in \mathbb{E}$. Moreover, we shall use the notation $C := (C_i)_{i=1}^N$ with $C_i \geqslant 0$ the conductivity of the edge $i \in \mathbb{E}$, $P_i \in \mathbb{R}$ for the pressure in node $i \in \mathbb{V}$ and $S_i^N \in \mathbb{R}$ for the source/sink in node $i \in \mathbb{V}$ with $\sum_{i=1}^N S_i^N = 0$ by (7.1). With this notation we rewrite the energy functional (7.6) as $E^N[C] : \mathbb{R}_+^N \mapsto \mathbb{R}$,

$$E^N[C] := h \sum_{i=1}^N \frac{Q_i^2}{r + C_i} + \frac{\nu}{\gamma}(r + C_i)^\gamma, \tag{7.19}$$

with the fluxes

$$Q_i := (r + C_i)\frac{P_{i-1} - P_i}{h}, \qquad \text{for } i = 1, \ldots, N. \tag{7.20}$$

Note that we orient the fluxes $Q_i$ such that $Q_i > 0$ if the material flows from $x_{i-1}$ to $x_i$. The Kirchhoff law (7.7) is then written in the form

$$(r + C_i)\frac{P_i - P_{i-1}}{h} + (r + C_{i+1})\frac{P_i - P_{i+1}}{h} = hS_i^N \qquad \text{for } i = 1, \ldots, N-1, \tag{7.21}$$

while for the terminal nodes we have

$$(r + C_1)\frac{P_0 - P_1}{h} = hS_0^N, \qquad (r + C_N)\frac{P_N - P_{N-1}}{h} = hS_N^N.$$

Obviously, in the 1D setting the fluxes $Q_i$ are explicitly calculable from the given set of sources/sinks $(S_i)_{i=0}^N$ since the Kirchhoff law (7.21) is the chain of equations

$$Q_1 = hS_0^N,$$
$$-Q_i + Q_{i+1} = hS_i^N \quad \text{for } i = 1, \ldots, N-1,$$
$$-Q_N = hS_N^N,$$

which has the explicit solution

$$Q_i = h\sum_{j=0}^{i-1} S_j^N \qquad \text{for } i = 1, \ldots, N-1. \tag{7.22}$$

Note that due to the assumption of the global mass balance (7.1) the "terminal condition" for $i = N$ is implicitly satisfied,

$$-Q_N = -h\sum_{j=0}^{N-1} S_j = hS_N^N. \tag{7.23}$$

With the fluxes given by (7.22)–(7.23), it is trivial to find the global energy minimiser of (7.19), namely, $(r + C_i)^{\gamma+1} = Q_i^2/\nu$. It is also easy to prove that the sequence of the functionals (7.19) converges as $h = 1/N \to 0$ to the continuous functional

$$\mathcal{E}[c] := \int_0^1 \frac{q(x)^2}{r + c(x)} + \frac{\nu}{\gamma}(r + c(x))^\gamma \, dx, \tag{7.24}$$

with $q(x) := \int_0^x S(\sigma) \, d\sigma$, in the sense of Riemannian sums if $c$ is a continuous,

nonnegative function. Therefore, the limit passage to continuum description in the one-dimensional case is trivial. However, we shall use it as a "training example" which avoids most of the technical difficulties of the two-dimensional setting to gain a clear understanding of the main ideas of the method.

Therefore, we shall ignore the explicit formula (7.22) for the fluxes $Q_i$ and study the limit as $h = 1/N \to 0$ of the sequence of energy functionals (7.19)–(7.20), i.e.,

$$E^N[C] = h \sum_{i=1}^{N} (r + C_i) \left( \frac{P_i - P_{i-1}}{h} \right)^2 + \frac{\nu}{\gamma} (r + C_i)^{\gamma}, \qquad (7.25)$$

where the pressures $P_i$ are calculated as a solution of the Kirchhoff law (7.21). Note that since $r + C_i > 0$ for all $i \in \mathbb{V}$, (7.21) is solvable, uniquely up to an additive constant. In the following we shall show that the sequence (7.25) converges, as $h = \frac{1}{N} \to 0$, to the functional (7.24) with $q := (r + c)\partial_x p[c]$, i.e.,

$$\mathcal{E}[c] = \int_0^1 (r + c)(\partial_x p[c])^2 + \frac{\nu}{\gamma} (r + c)^{\gamma} \, dx, \qquad (7.26)$$

where $p[c] \in H^1(0, 1)$ is a weak solution of the Poisson equation

$$-\partial_x((r + c)\partial_x p) = S \qquad (7.27)$$

on $(0, 1)$, subject to no-flux boundary conditions. Here and in the sequel we fix the source/sink term $S \in L^2(0, 1)$ and, in agreement with (7.1), we assume the global mass balance $\int_0^1 S(x) \, dx = 0$. Since for $c(x) \geqslant 0$ the weak solution $p = p(x)$ of (7.27) is unique up to an additive constant, we shall, without loss of generality, always choose the zero-average solution, i.e., $\int_0^1 p(x) \, dx = 0$.

We shall proceed in several steps: First, we put the discrete energy functionals (7.25) into an integral form, and find an equivalence between solutions of the Kirchhoff law (7.21) and the above Poisson equation with appropriate conductivity. Then we show the convergence of the sequence of reformulated discrete energy functionals towards a continuum one as $h = 1/N \to 0$. Finally, we introduce a diffusive term into the energy functional, which will allow us to construct global minimisers of the continuum energy functional.

### 7.3.1 Reformulation of the discrete energy functional

In the first step we reformulate the energy functionals (7.25) such that they are defined on the space $L^\infty_+(0,1)$ of essentially bounded nonnegative functions on $(0,1)$. For this purpose, we define the sequence of operators $\mathbb{Q}^N_0 : \mathbb{R}^N \to L^\infty(0,1)$ by

$$\mathbb{Q}^N_0 : (C_i)^N_{i=1} \mapsto c, \qquad \text{with } c(x) \equiv C_i \text{ for } x \in (x_{i-1}, x_i), \ i = 1, \ldots, N.$$

I.e., $\mathbb{Q}^N_0$ maps the sequence $(C_i)^N_{i=1}$ onto the bounded function $c = c(x)$, constant on each interval $(x_{i-1}, x_i)$, $i = 1, \ldots, N$. Then, we define the functionals $\mathcal{E}^N : L^\infty_+(0,1) \mapsto \mathbb{R}$,

$$\mathcal{E}^N[c] := \int_0^1 (r+c) \left(\mathbb{Q}^N_0[\Delta^h P]\right)^2 + \frac{\nu}{\gamma}(r+c)^\gamma \, dx, \tag{7.28}$$

with

$$(\Delta^h P)_i := \frac{P_i - P_{i-1}}{h}, \quad i = 1, \ldots, N, \tag{7.29}$$

and $P = (P_i)^N_{i=0}$ a solution of the Kirchhoff law (7.21) with the conductivities $C = (C_i)^N_{i=1}$,

$$C_i := \frac{1}{h} \int_{x_{i-1}}^{x_i} c(x) \, dx, \quad i = 1, \ldots, N.$$

Then, noting that for each $C = (C_i)^N_{i=1} \in \mathbb{R}^N_+$,

$$\frac{1}{h} \int_{x_{i-1}}^{x_i} \mathbb{Q}^N_0[C](x) \, dx = C_i \qquad \text{for all } i = 1, \ldots, N,$$

the discrete energy functional (7.25) can be written in the integral form as $E^N[C] = \mathcal{E}^N[\mathbb{Q}^N_0[C]]$.

Moreover, we establish a connection between the solutions of the Kirchhoff law (7.21) and weak solutions of the Poisson equation (7.27) with $c = \mathbb{Q}^N_0[C]$:

**Lemma 14.** *For any $C = (C_i)^N_{i=1} \in \mathbb{R}^N_+$ and $S \in L^2(0,1)$ with $\int_0^1 S(x) \, dx = 0$, let $p = p(x) \in H^1(0,1)$ be a weak solution of the Poisson equation (7.27) with $c = \mathbb{Q}^N_0[C]$, i.e.,*

$$-\partial_x \left((r + \mathbb{Q}^N_0[C])\partial_x p\right) = S, \tag{7.30}$$

subject to no-flux boundary conditions on $(0,1)$. Then,

$$P_i := p(x_i), \qquad i = 0, \dots, N, \qquad (7.31)$$

is a solution of the Kirchhoff law (7.21) with the conductivities $C = (C_i)_{i=1}^N$ and the source/sink terms

$$S_i^N := \frac{1}{h} \int_0^1 S(x) \phi_i^N(x) \, dx, \qquad i = 0, \dots, N, \qquad (7.32)$$

with the hat functions $\phi_i^N = \phi_i^N(x)$ defined in (7.33) below.

*Proof.* Note that for any $C \in \mathbb{R}_+^N$ there exists a weak solution $p = p(x) \in H^1(0,1)$ of (7.30), unique up to an additive constant. For $i = 1, \dots, N$ we construct the family of piecewise linear test functions $\phi_i^N$, supported on $(x_{i-1}, x_{i+1})$, with

$$\phi_i^N(x) = \begin{cases} 1 + \frac{x - x_i}{h} & \text{for } x \in (x_{i-1}, x_i), \\ 1 - \frac{x - x_i}{h} & \text{for } x \in (x_i, x_{i+1}). \end{cases} \qquad (7.33)$$

Using the hat function $\phi_i^N$ as a test function in (7.30), we obtain

$$(r + C_i)\frac{p(x_i) - p(x_{i-1})}{h} + (r + C_{i+1})\frac{p(x_i) - p(x_{i+1})}{h} = hS_i^N,$$

where we used the fact that, by construction, $\mathbb{Q}_0^N[C] \equiv C_i$ on the interval $(x_{i-1}, x_i)$. Note that due to the embedding $H^1(0,1) \hookrightarrow C(0,1)$ any weak solution $p = p(x)$ of (7.30) is a continuous function on $[0,1]$, so the pointwise values $p(x_i)$ are well defined for all $i = 0, \dots, N$. Thus, defining $P_i$ as in (7.31) we obtain a solution of the Kirchhoff law (7.21) with the conductivities $C = (C_i)_{i=1}^N$ and source/sink terms (7.32). $\square$

Note that since $\frac{1}{h} \int_0^1 \phi_i^N(x) \, dx = 1$ and $S \in L^2(0,1)$, the Lebesgue differentiation theorem gives

$$S_i^N = \frac{1}{h} \int_0^1 S(x) \phi_i^N(x) \, dx \to S(\bar{x}) \qquad \text{for a.e. } \bar{x} = x_i \text{ as } h = 1/N \to 0.$$

Consequently, for a fixed $S \in L^2(0,1)$ and any $N \in \mathbb{N}$, we have the following reformulation of the discrete problem:

**Proposition 13.** *For any vector $C = (C_i)_{i=1}^N \in \mathbb{R}_+^N$, we have*

$$E^N[C] = \mathcal{E}^N[\mathbb{Q}_0^N[C]],$$

*where $E^N[C]$ is the discrete energy functional (7.25) coupled to the Kirchhoff law (7.21) with sources/sinks $S_i^N$ given by (7.32), and $\mathcal{E}^N$ is the integral form (7.28)– (7.29) with the pressures given by $P_i = p(x_i)$, $i = 0, \ldots, N$, where $p \in H^1(0,1)$ solves the Poisson equation (7.30).*

### 7.3.2 Convergence of the energy functionals

Due to Proposition 13, we are motivated to prove the convergence of the sequence of functionals $\mathcal{E}^N$ given by (7.28)–(7.29) towards $\mathcal{E}[c]$ given by (7.26) with $p[c] \in H^1(0,1)$ a weak solution of (7.27) with conductivity $c = c(x)$, equipped with no-flux boundary conditions. We choose to work in the space of essentially bounded functions on $(0,1)$ equipped with the topology of $L^2(0,1)$. The choice of topology is motivated by the need for strong convergence of piecewise constant approximations of bounded functions. Of course, this is true in $L^q(0,1)$ with any $q < +\infty$; our particular choice of $L^2(0,1)$ is further dictated by the fact that we shall apply Lemma 13 in the sequel.

**Lemma 15.** *Let $\gamma \geqslant 0$. For any sequence of nonnegative functions $(c^N)_{N \in \mathbb{N}}$, uniformly bounded in $L^\infty(0,1)$ and such that $c^N \to c$ in the norm topology of $L^2(0,1)$ as $N \to \infty$, we have*

$$\mathcal{E}^N[c^N] \to \mathcal{E}[c] \qquad as \ h = 1/N \to 0.$$

*Proof.* By assumption, $c^N \to c$ in the norm topology of $L^2(0,1)$. Consequently, there is a subsequence converging almost everywhere on $(0,1)$ to $c$, and thus $\left(r + c^N(x)\right)^\gamma$ converges almost everywhere to $(r + c(x))^\gamma$. Since, by assumption, the sequence $\left(r + c^N(x)\right)^\gamma$ is uniformly bounded in $L^\infty(0,1)$, we have by the dominated convergence theorem

$$\int_0^1 \left(r + c^N(x)\right)^\gamma \mathrm{d}x \to \int_0^1 (r + c(x))^\gamma \mathrm{d}x \qquad as \ h = 1/N \to 0.$$

We recall that the pumping part of the discrete energy $\mathcal{E}^N[c^N]$ (7.28) is of the form

$$\int_0^1 (r + c^N) \left( \mathbb{Q}_0^N[\Delta^h p^N] \right)^2 \, \mathrm{d}x, \tag{7.34}$$

with

$$(\Delta^h p^N)_i := \frac{p^N(x_i) - p^N(x_{i-1})}{h}, \quad i = 1, \dots, N,$$

where $p^N \in H^1(0,1)$ is a solution of the Poisson equation (7.27) with conductivity $c^N$, subject to the no-flux boundary condition. Let us show that (a subsequence of) $\mathbb{Q}_0^N[\Delta^h p^N]$ converges to $\partial_x p[c]$ strongly in $L^2(0,1)$. We proceed in three steps:

- **Weak convergence.** By Jensen inequality we have

$$\|\mathbb{Q}_0^N[\Delta^h p^N]\|_{L^2(0,1)}^2 = h \sum_{i=1}^N \left( \frac{p^N(x_i) - p^N(x_{i-1})}{h} \right)^2 \tag{7.35}$$

$$= h \sum_{i=1}^N \left( \frac{1}{h} \int_{x_{i-1}}^{x_i} \partial_x p^N(x) \, \mathrm{d}x \right)^2 \leqslant \int_0^1 (\partial_x p^N)^2 \, \mathrm{d}x.$$

  Due to the nonnegativity of the functions $c^N$, the right-hand side is uniformly bounded. Consequently, there exists a weakly converging subsequence of $\mathbb{Q}_0^N[\Delta p^N]$ in $L^2(0,1)$.

- **Identification of the limit.** For a smooth, compactly supported test function $\psi \in C_0^\infty(0,1)$ we write

$$\int_0^1 \mathbb{Q}_0^N[\Delta^h p^N](x)\psi(x) \, \mathrm{d}x$$

$$= \sum_{i=1}^N \frac{p^N(x_i) - p^N(x_{i-1})}{h} \int_{x_{i-1}}^{x_i} \psi(x) \, \mathrm{d}x$$

$$= \frac{1}{h} \sum_{i=1}^{N-1} p^N(x_i) \left( \int_{x_{i-1}}^{x_i} \psi(x) \, \mathrm{d}x - \int_{x_i}^{x_{i+1}} \psi(x) \, \mathrm{d}x \right) + \text{"boundary terms"},$$

  where "boundary terms" are the two terms with $i = 0$ and $i = N$, which we however can neglect for large enough $N$ since $\psi$ has a compact support. Then, Taylor expansion for $\psi$ gives

$$\int_{x_{i-1}}^{x_i} \psi(x) \, \mathrm{d}x - \int_{x_i}^{x_{i+1}} \psi(x) \, \mathrm{d}x = -h \int_{x_{i-1}}^{x_i} \partial_x \psi(x) \, \mathrm{d}x + \frac{h^2}{2} \int_{x_{i-1}}^{x_i} \partial_{xx}^2 \psi(\xi(x)) \, \mathrm{d}x,$$

with $\xi(x) \in (x_{i-1}, x_i)$. Due to the estimate

$$\left| \frac{h^2}{2} \int_{x_{i-1}}^{x_i} \partial_{xx}^2 \psi(\xi(x)) \, \mathrm{d}x \right| \leqslant \frac{h^3}{2} \left\| \partial_{xx}^2 \psi \right\|_{L^\infty(0,1)}$$

we have

$$\int_{x_{i-1}}^{x_i} \psi(x) \, \mathrm{d}x - \int_{x_i}^{x_{i+1}} \psi(x) \, \mathrm{d}x = -h \int_{x_{i-1}}^{x_i} \partial_x \psi(x) \, \mathrm{d}x + \mathcal{O}(h^3),$$

so that

$$\int_0^1 \mathbb{Q}_0^N [\Delta^h p^N](x) \psi(x) \, \mathrm{d}x = - \int_0^1 \overline{p^N} \partial_x \psi(x) \, \mathrm{d}x + \mathcal{O}(h),$$

where $\overline{p^N}$ is the piecewise constant function

$$\overline{p^N}(x) \equiv p^N(x_i) \quad \text{for } x \in (x_{i-1}, x_i], \, i = 1, \dots, N.$$

It is easy to check that, due to the strong convergence of $c^N$ towards $c$ in $L^2(0,1)$, $p^N$ converges to $p[c]$ weakly in $H^1(0,1)$. Due to the compact embedding $H^1(0,1) \hookrightarrow C(0,1)$, (a subsequence of) $p^N$ converges uniformly to $p[c]$ on $(0,1)$, and, therefore $\overline{p^N}$ converges strongly to $p[c]$. Therefore,

$$\int_0^1 \mathbb{Q}_0^N [\Delta^h p^N](x) \psi(x) \, \mathrm{d}x \to - \int_0^1 p(x) \partial_x \psi(x) \, \mathrm{d}x \qquad \text{as } h = 1/N \to 0,$$

$$= \int_0^1 \psi(x) \partial_x p(x) \, \mathrm{d}x.$$

We conclude that weak limit of (the subsequence of) $\mathbb{Q}_0^N[\Delta^h p^N]$ is $\partial_x p[c]$.

- **Strong convergence.** Finally, due to (7.35), we have

$$\left\| \mathbb{Q}_0^N [\Delta^h p^N] - \partial_x p[c] \right\|_{L^2(0,1)}^2$$

$$= \left\| \mathbb{Q}_0^N [\Delta^h p^N] \right\|_{L^2(0,1)}^2 - 2 \langle \mathbb{Q}_0^N [\Delta^h p^N], \partial_x p[c] \rangle_{L^2(0,1)} + \left\| \partial_x p[c] \right\|_{L^2(0,1)}^2$$

$$\leqslant \left\| \partial_x p^N \right\|_{L^2(0,1)}^2 - 2 \langle \mathbb{Q}_0^N [\Delta^h p^N], \partial_x p[c] \rangle_{L^2(0,1)} + \left\| \partial_x p[c] \right\|_{L^2(0,1)}^2,$$

which vanishes in the limit $h = 1/N \to 0$ due to the weak convergence of $\mathbb{Q}_0^N[\Delta p^N]$ and strong convergence of $\partial_x p^N$ in $L^2(0,1)$ due to Lemma 13. Thus, $\mathbb{Q}_0^N[\Delta p^N]$ converges strongly to $\partial_x p[c]$ in $L^2(0,1)$.

We conclude that due to the weak-$*$ convergence of $(r + c^N)$ towards $(r + c)$ in $L^\infty(0, 1)$, and strong convergence of $\left(\mathbb{Q}_0^N[\Delta^h p^N]\right)^2$ towards $(\partial_x p[c])^2$ in $L^1(0, 1)$, we can pass to the limit as $h = 1/N \to 0$ in (7.34) to obtain

$$\int_0^1 (r + c) \left(\partial_x p[c]\right)^2 \, \mathrm{d}x.$$

$\square$

### 7.3.3 Diffusion and construction of continuum energy minimisers

In Lemma 15 we proved the convergence of the sequence of energy functionals $\mathcal{E}^N$ towards $\mathcal{E}$, i.e., for any $c^N \to c$ in the norm topology of $L^2(0, 1)$, we have $\mathcal{E}^N[c^N] \to \mathcal{E}[c]$ as $N \to \infty$. In order to construct energy minimisers of $\mathcal{E}$ as limits of sequences of minimisers of the functionals $\mathcal{E}^N$, we need to introduce a term into $\mathcal{E}^N$ that shall guarantee compactness of the sequence of discrete minimisers. This is done, in agreement with [HMP15, HMPS16, ABH$^+$17], by introducing a diffusive term into the discrete energy functional (7.25), modelling random fluctuations in the medium. Thus, we construct the sequence $E_{\mathrm{diff}}^N : \mathbb{R}_+^N \to \mathbb{R}$,

$$E_{\mathrm{diff}}^N[C] := D^2 h \sum_{i=1}^{N-1} \left(\frac{C_{i+1} - C_i}{h}\right)^2 + E^N[C], \tag{7.36}$$

with $E^N[C]$ defined in (7.25), coupled to the Kirchhoff law (7.21) with sources/sinks $S_i^N$ given by (7.32), and $D^2 > 0$ the diffusion constant. Note that the new term is a discrete Laplacian acting on the conductivities $C$.

We now need to reformulate the discrete energy functionals (7.36) in terms of integrals. For this sake, we construct the sequence of operators $\mathbb{Q}_1^N : \mathbb{R}^N \to C(0, 1)$, where $\mathbb{Q}_1^N[C]$ is a continuous function on $[0, 1]$, linear on each interval $(x_i - h/2, x_i + h/2)$, with

$$\mathbb{Q}_1^N[C](x_i - h/2) = C_i \quad \text{for } i = 1, \dots, N,$$

and

$$\mathbb{Q}_1^N[C](x) \equiv C_1 \quad \text{for } x \in [0, h/2), \qquad \mathbb{Q}_1^N[C](x) \equiv C_N \quad \text{for } x \in (1 - h/2, 1].$$

Then we write the finite difference term in (7.36) as

$$D^2 h \sum_{i=1}^{N-1} \left( \frac{C_{i+1} - C_i}{h} \right)^2 = D^2 \int_0^1 \left( \partial_x \mathbb{Q}_1^N[C] \right)^2 \, dx,$$

and we have

**Proposition 14.** *For any vector* $C = (C_i)_{i=1}^N \in \mathbb{R}_+^N$,

$$E_{\mathrm{diff}}^N[C] = D^2 \int_0^1 \left( \partial_x \mathbb{Q}_1^N[C] \right)^2 \, dx + \mathcal{E}^N[\mathbb{Q}_0^N[C]],$$

*where* $E_{\mathrm{diff}}^N$ *defined in* (7.36) *and* $\mathcal{E}^N$ *is given by* (7.28)–(7.29) *with the pressures given by* $P_i = p(x_i)$, $i = 0, \dots, N$, *where* $p \in H^1(0,1)$ *solves the Poisson equation* (7.30).

We are now ready to prove the main result of this section:

**Theorem 11.** *Let* $\gamma \geqslant 0$, $S \in L^2(0,1)$ *with* $\int_0^1 S(x) \, dx$ *and* $S_i^N$ *given by* (7.32). *Let* $(C^N)_{N \in \mathbb{N}}$ *be a sequence of global minimisers of the discrete energy functionals* $E_{\mathrm{diff}}^N$ *given by* (7.36). *Then the sequence* $\mathbb{Q}_1^N[C^N]$ *converges weakly in* $H^1(0,1)$ *to* $c \in H^1(0,1)$, *a global minimiser of the functional* $\mathcal{E}_{\mathrm{diff}} : H_+^1(0,1) \to \mathbb{R}$,

$$\mathcal{E}_{\mathrm{diff}}[c] := D^2 \int_0^1 (\partial_x c)^2 \, dx + \mathcal{E}[c],$$

*where* $\mathcal{E}[c]$ *is given by* (7.26).

*Proof.* Let us observe that

$$E_{\mathrm{diff}}^N[C^N] \leqslant E_{\mathrm{diff}}^N[0] = rh \sum_{i=1}^N \left( \frac{\widetilde{P}_i - \widetilde{P}_{i-1}}{h} \right)^2 + \frac{\nu}{\gamma} r^\gamma,$$

where $(\widetilde{P}_i)_{i=1}^N$ is a solution of the Kirchhoff law (7.21) with zero conductivities and sources/sinks given by (7.32). Thus, $\widetilde{P}_i = \widetilde{p}(x_i)$ for $i = 1, \dots, N$, where $\widetilde{p} = \widetilde{p}(x)$ is a weak solution of $-r\Delta p = S$ subject to no-flux boundary conditions. Then we have by the Jensen inequality

$$D^2 h \sum_{i=1}^N \left( \frac{\widetilde{P}_i - \widetilde{P}_{i-1}}{h} \right)^2 = D^2 h \sum_{i=1}^N \left( \frac{1}{h} \int_{x_{i-1}}^{x_i} \partial_x \widetilde{p} \, dx \right)^2$$

$$\leqslant D^2 \int_0^1 (\partial_x \widetilde{p})^2 \, dx.$$

251

Consequently, the sequence $\mathcal{E}_{\mathrm{diff}}^N[C^N]$ is uniformly bounded.

Since the sequence

$$D^2 \int_0^1 \left(\partial_x \mathbb{Q}_1^N[C^N]\right)^2 \,\mathrm{d}x = D^2 h \sum_{i=1}^{N-1} \left(\frac{C_{i+1} - C_i}{h}\right)^2 \leqslant E_{\mathrm{diff}}^N[C^N]$$

is uniformly bounded, there exists a subsequence of $\mathbb{Q}_1^N[C^N]$ converging to some $c \in H^1(0,1)$ weakly in $H^1(0,1)$, and strongly in $L^2(0,1)$; moreover, the sequence is uniformly bounded in $L^\infty(0,1)$. It is easy to check that also $\mathbb{Q}_0^N[C^N]$ converges to $c$ strongly in $L^2(0,1)$, and is uniformly bounded in $L^\infty(0,1)$. Therefore, by Lemma 15, we have $E^N[C^N] = \mathcal{E}^N[\mathbb{Q}_0^N[C^N]] \to \mathcal{E}[c]$ as $h = 1/N \to 0$. Moreover, due to the weak lower semicontinuity of the $L^2$-norm, we have

$$\int_0^1 (\partial_x c)^2 \,\mathrm{d}x \leqslant \liminf_{N\to\infty} \int_0^1 \left(\partial_x \mathbb{Q}_1^N[C^N]\right)^2 \,\mathrm{d}x \,.$$

Consequently,

$$\mathcal{E}_{\mathrm{diff}}[c] \leqslant \liminf_{N\to\infty} E_{\mathrm{diff}}^N[C^N]. \tag{7.37}$$

We claim that $c$ is a global minimiser of $\mathcal{E}_{\mathrm{diff}}$ in $H_+^1(0,1)$. For contradiction, assume that there exists $\bar{c} \in H_+^1(0,1)$ such that

$$\mathcal{E}_{\mathrm{diff}}[\bar{c}] < \mathcal{E}_{\mathrm{diff}}[c].$$

We define the sequence $(\bar{C}^N)_{N\in\mathbb{N}}$ by

$$\bar{C}_i^N := \frac{1}{h} \int_{x_{i-1}}^{x_i} \bar{c}(x) \,\mathrm{d}x, \quad i = 1, \dots, N.$$

Then, by assumption, we have for all $N \in \mathbb{N}$,

$$E_{\mathrm{diff}}^N[\bar{C}^N] \geqslant E_{\mathrm{diff}}^N[C^N]. \tag{7.38}$$

It is easy to check that the sequence $\mathbb{Q}_1^N[\bar{C}^N]$ converges strongly in $H^1(0,1)$ towards $\bar{c}$, therefore

$$\int_0^1 \left(\partial_x \mathbb{Q}_1^N[\bar{C}^N]\right)^2 \,\mathrm{d}x \to \int_0^1 (\partial_x \bar{c})^2 \,\mathrm{d}x \qquad \text{as } h = 1/N \to 0.$$

Moreover, the sequence $\mathbb{Q}_0^N[\bar{C}^N]$ converges to $\bar{c}$ strongly in $L^2(0,1)$, therefore, by Lemma 15, $\mathcal{E}^N[\mathbb{Q}_0^N[\bar{C}^N]] \to \mathcal{E}[\bar{c}]$ as $h = 1/N \to 0$. Consequently,

$$\lim_{h=1/N \to 0} E_{\text{diff}}^N[\bar{C}^N] = \mathcal{E}_{\text{diff}}[\bar{c}] < \mathcal{E}_{\text{diff}}[c],$$

a contradiction to (7.37)–(7.38). $\qquad\qquad\qquad\qquad\qquad\qquad\qquad\qquad\square$

## 7.4 The 2D rectangular equidistant setting

In this section we consider the spatially two-dimensional setting of the discrete network formation problem, where the graph $(\mathbb{V}, \mathbb{E})$ is embedded in the rectangle $\Omega := [0,1]^2$. We introduce the notation $\mathbf{x} := (x,y) \in \Omega$. For $N \in \mathbb{N}$ we construct the sequence of equidistant rectangular meshes in $\Omega$ with mesh size $h := 1/N$ and mesh nodes $\mathbf{X}_i = (X_i, Y_i)$,

$$X_i = (i \bmod N + 1)h, \quad Y_i = (i \operatorname{div} N + 1)h, \qquad \text{for } i = 0, \dots, (N+1)^2 - 1,$$

where $(i \operatorname{div} N + 1)$ denotes the integer part of $i/(N+1)$ and $(i \bmod N + 1)$ the remainder. We identify the mesh nodes $\mathbf{X}_i = (X_i, Y_i)$ with the vertices of the graph, i.e., we set $\mathbb{V} := \{\mathbf{X}_i; \ i = 0, \dots, (N+1)^2 - 1\}$. By a slight abuse of notation, we shall write $i \in \mathbb{V}$ instead of $X_i \in \mathbb{V}$ in the sequel. For each node $\mathbf{X}_i$, we denote by $\mathbf{X}_{i,E}$, $\mathbf{X}_{i,W}$, $\mathbf{X}_{i,N}$, $\mathbf{X}_{i,S}$ its direct neighbours to the East, West, North and South, respectively (if they exist); see Fig. 7.1. Then, the set $\mathbb{E}$ of edges of the graph is composed of the horizontal and vertical segments connecting the neighbouring nodes, i.e., $(\mathbf{X}_i, \mathbf{X}_{i,\star})$ for $\star \in \{E, W, N, S\}$ and $i \in \mathbb{V}$. We shall denote $C_i^\star$ the conductivity of the edge $(\mathbf{X}_i, \mathbf{X}_{i,\star})$, and $P_i$, resp., $P_{i,\star}$, denote the pressure in the vertex $\mathbf{X}_i$, resp., $\mathbf{X}_{i,\star}$. Similarly, $S_i^h$ denotes the source/sink in vertex $i \in \mathbb{V}$.

With this notation, the discrete energy functional (7.6) takes the particular form

$$E^h[C] = \frac{h^2}{2} \sum_{i \in \mathbb{V}} \sum_{\star \in \{E,W,N,S\}} (r + C_i^\star) \left( \frac{P_i - P_{i,\star}}{h} \right)^2 + \frac{\nu}{\gamma}(r + C_i^\star)^\gamma, \qquad (7.39)$$

and the Kirchhoff law (7.7) is written as

$$\sum_{\star \in \{E,W,N,S\}} (r + C_i^\star) \frac{P_i - P_{i,\star}}{h} = h S_i^h. \qquad \text{for } i \in \mathbb{V}, \qquad (7.40)$$
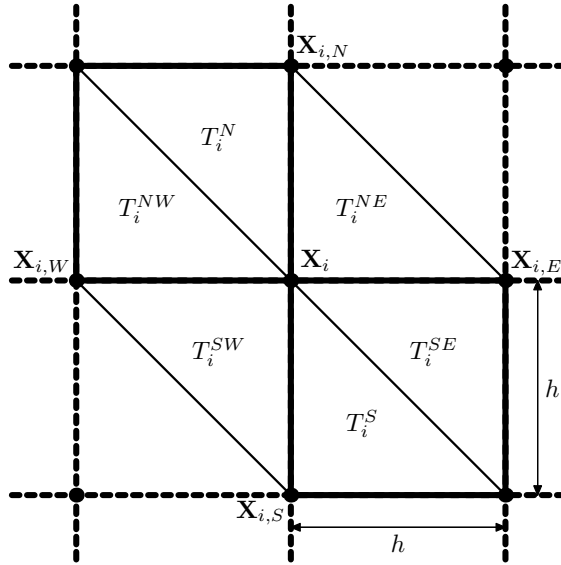
Figure 7.1: Interior node $\mathbf{X}_i$ with its four neighbouring nodes $\mathbf{X}_{i,E}$, $\mathbf{X}_{i,W}$, $\mathbf{X}_{i,N}$, $\mathbf{X}_{i,S}$ and its six adjacent triangles, $T_i^{NE}$, $T_i^N$, $T_i^{NW}$, $T_i^{SW}$, $T_i^S$, $T_i^{SE}$.

For reasons explained later, we shall restrict to the case $\gamma > 1$ in the sequel.

Our strategy is to perform a program analogous to the 1D case of Section 7.3: first, to put the discrete energy functionals (7.39) into an integral form and find an equivalence between solutions of the Kirchhoff law (7.40) and the above Poisson equation with appropriate conductivity. However, in the 2D case the situation is more complicated and we need to introduce a finite element discretisation of the Poisson equation which allows us to use convergence results from the theory of finite elements. We then establish a connection between the FE-discretisation and the Kirchhoff law (7.40). In the next step we show the convergence of the sequence of reformulated discrete energy functionals towards a continuum one as $h = 1/N \to 0$, using standard results of the theory of finite elements. Finally, we introduce a diffusive term into the energy functional, which will allow us to construct global minimisers of the continuum energy functional.

### 7.4.1 Finite element discretization of the Poisson equation

We construct a regular triangulation on the domain $\Omega$ such that each interior node $\mathbf{X}_i$ has six adjacent triangles, $T_i^{NE}$, $T_i^N$, $T_i^{NW}$, $T_i^{SW}$, $T_i^S$, $T_i^{SE}$, see Fig. 7.1. Boundary nodes have three, two or only one adjacent triangles, depending on their location. The union of the triangles adjacent to each $\mathbf{X}_i$ is denoted by $U_i$. The collection of all triangles constructed in $\Omega$ is denoted by $\mathcal{T}^h$.

We fix $S \in L^2(\Omega)$ with $\int_\Omega S \, \mathrm{d}\mathbf{x} = 0$ and consider a discretisation of the Poisson equation

$$-\nabla \cdot ((r\mathbb{I} + c)\nabla p) = S \tag{7.41}$$

on $\Omega$ subject to the no-flux boundary conditions, using the first-order (piecewise linear) $H^1$ finite element method on the triangulation $\mathcal{T}^h$. Therefore, on each $NE$-triangle $T_i^{NE}$ we construct the linear basis functions $\phi_{i;1}^{NE}$, $\phi_{i;2}^{NE}$, $\phi_{i;3}^{NE}$ with

$$\begin{aligned}
\phi_{i;1}^{NE}(\mathbf{X}_i) = 1, \quad & \phi_{i;1}^{NE}(\mathbf{X}_{i,E}) = 0, \quad & \phi_{i;1}^{NE}(\mathbf{X}_{i,N}) = 0, \\
\phi_{i;2}^{NE}(\mathbf{X}_i) = 0, \quad & \phi_{i;2}^{NE}(\mathbf{X}_{i,E}) = 1, \quad & \phi_{i;2}^{NE}(\mathbf{X}_{i,N}) = 0, \\
\phi_{i;3}^{NE}(\mathbf{X}_i) = 0, \quad & \phi_{i;3}^{NE}(\mathbf{X}_{i,E}) = 0, \quad & \phi_{i;3}^{NE}(\mathbf{X}_{i,N}) = 1,
\end{aligned}$$

and analogously for the other triangles in $U_i$, see Section 7.A.1 of the Appendix for explicit formulae. Denoting $W^h \subset H^1(\Omega)$ the space of continuous, piecewise linear functions on the triangulation $\mathcal{T}^h$, the finite element discretisation of (7.41) reads

$$\int_\Omega \nabla p^h \cdot (r\mathbb{I} + c)\nabla \psi^h \, \mathrm{d}\mathbf{x} = \int_\Omega S\psi^h \, \mathrm{d}\mathbf{x} \qquad \text{for all } \psi^h \in W^h. \tag{7.42}$$

Using standard arguments (coercivity and continuity of the corresponding bilinear form) we construct a solution $p^h \in W^h$ of (7.42), unique up to an additive constant; without loss of generality we fix $\int_\Omega p^h(\mathbf{x}) \, \mathrm{d}\mathbf{x} = 0$. The solution is represented by its vertex values $P_i^h := p^h(\mathbf{X}_i)$, $i \in \mathbb{V}$. In particular, on each $NE$-triangle $T_i^{NE}$ we have

$$p^h(\mathbf{x}) = P_i^h \phi_{i;1}^{NE}(\mathbf{x}) + P_{i,E}^h \phi_{i;2}^{NE}(\mathbf{x}) + P_{i,N}^h \phi_{i;3}^{NE}(\mathbf{x}), \qquad \mathbf{x} \in T_i^{NE},$$

and the gradient of $p^h$ on $T_i^{NE}$ is the constant vector

$$\nabla p^h(\mathbf{x}) = \frac{1}{h}(P_{i,E}^h - P_i^h, P_{i,N}^h - P_i^h), \qquad \mathbf{x} \in T_i^{NE}. \tag{7.43}$$

Analogous formulae hold for all other triangles in $U_i$, as explicitly listed in Section 7.A.2 of the Appendix.

We now establish a connection between the discretised Poisson equation (7.42) and the Kirchhoff law (7.40). For this purpose, we define the sequence of operators $\mathbb{Q}_0^h$ mapping the vector of conductivities $(C_i)_{i \in \mathbb{E}}$ onto piecewise constant $2 \times 2$

diagonal tensors,

$$\mathbb{Q}_0^h : (C_i)_{i\in\mathbb{E}} \mapsto \begin{pmatrix} c_1 & 0 \\ 0 & c_2 \end{pmatrix}. \tag{7.44}$$

The functions $c_1 = c_1(\mathbf{x})$, $c_2 = c_2(\mathbf{x})$, defined on $\Omega$, are constant on each triangle $T \in \mathcal{T}^h$ and $c_1$ takes the value of the conductivity of the horizontal edge of $T$ and $c_2$ takes the value of the conductivity of the vertical edge of $T$. In particular, we have

$$c_1 := \begin{cases} C_i^E & \text{on } T_i^{NE}, \\ C_i^E & \text{on } T_i^{SE}, \\ C_i^W & \text{on } T_i^{SW}, \\ C_i^W & \text{on } T_i^{NW}, \end{cases} \qquad c_2 := \begin{cases} C_i^N & \text{on } T_i^{NE}, \\ C_i^S & \text{on } T_i^{S}, \\ C_i^S & \text{on } T_i^{SW}, \\ C_i^N & \text{on } T_i^{N}. \end{cases} \tag{7.45}$$

Then, for a given vector of conductivities $C = (C_i)_{i\in\mathbb{E}}$ we consider the discretised Poisson equation (7.42) with the conductivity tensor $c := \mathbb{Q}_0^h[C]$. For each $i \in \mathbb{V}$ we construct the test function $\psi_i^h$ as

$$\psi_i^h := \phi_{i;1}^{NE} + \phi_{i;1}^{SE} + \phi_{i;1}^{S} + \phi_{i;1}^{SW} + \phi_{i;1}^{NW} + \phi_{i;1}^{N},$$

with the basis functions on the right-hand side defined in Section 7.A.1 of the Appendix. Consequently, each $\psi_i^h$ is supported on $U_i$, linear on each triangle belonging to $U_i$, and continuous on $\Omega$. Then, obviously, $\psi_i^h \in W^h$ and using it as a test function in (7.42), we calculate, for the triangle $T_i^{NE}$,

$$\int_{T_i^{NE}} \nabla p^h \cdot \left(r\mathbb{I} + \mathbb{Q}_0^h[C]\right) \nabla \psi_i^h \, d\mathbf{x} = \frac{r + C_i^E}{2}\left(P_i^h - P_{i,E}^h\right) + \frac{r + C_i^N}{2}\left(P_i^h - P_{i,N}^h\right),$$

where we used (7.43), the identity $\nabla \psi_i^h \equiv -\frac{1}{h}(1,1)$ on $T_i^{NE}$, and orthogonality relations between gradients of the basis functions (for instance, $\nabla \phi_{i;2}^{NE} \cdot \nabla \phi_{i;3}^{NE} = 0$). Performing analogous calculations for the remaining triangles constituting $U_i$, namely, $T_i^{SE}, T_i^{S}, T_i^{SW}, T_i^{NW}$ and $T_i^{N}$, see Section 7.A.3 of the Appendix for explicit details, we obtain

$$\int_{\Omega} \nabla p^h \cdot \left(r\mathbb{I} + \mathbb{Q}_0^h[C]\right) \nabla \psi_i^h \, d\mathbf{x} = \sum_{\star \in \{E,W,N,S\}} (r + C_i^\star)(P_i^h - P_{i,\star}^h). \tag{7.46}$$

Consequently, (7.42) gives the identity

$$\sum_{\star \in \{E,W,N,S\}} (r + C_i^\star) \frac{P_i^h - P_{i,\star}^h}{h} = \frac{1}{h} \int_\Omega S \psi_i^h \, \mathrm{d}\mathbf{x}$$

for all $i \in \mathbb{V}$. Thus, defining

$$S_i^h := \frac{1}{h^2} \int_\Omega S \psi_i^h \, \mathrm{d}\mathbf{x}, \tag{7.47}$$

we have the following result:

**Lemma 16.** *For any vector of nonnegative conductivities $C = (C_i)_{i \in \mathbb{E}}$ and $S \in L^2(\Omega)$ with $\int_\Omega S \, d\mathbf{x} = 0$, let $p^h \in W^h$ be a solution of the finite element discretisation (7.42) with $c := \mathbb{Q}_0^h[C]$. Then, $P_i^h := p^h(\mathbf{X}_i)$, $i \in \mathbb{V}$, is a solution of the rescaled Kirchhoff law (7.40) with the source/sink terms $S_i^h$ given by (7.47).*

Note that since $\frac{1}{h^2} \int_\Omega \psi_i^h(\mathbf{x}) \, \mathrm{d}\mathbf{x} = 1$, and, by assumption, $S \in L^2(\Omega)$, the Lebesgue differentiation theorem gives

$$S_i^h = \frac{1}{h^2} \int_\Omega S \psi_i^h \, \mathrm{d}\mathbf{x} \to S(\bar{\mathbf{x}}) \qquad \text{for a.e. } \bar{\mathbf{x}} = \mathbf{X}_i \text{ as } h = 1/N \to 0.$$

Consequently, $(S_i^h)_{h>0}$ is an approximating sequence for the datum $S = S(\mathbf{x})$.

### 7.4.2 Reformulation of the discrete energy functional

We reformulate the energy functionals (7.39)–(7.40) such that they are defined on the space $L_+^\infty(\Omega)_{\mathrm{diag}}^{2\times 2}$ of essentially bounded diagonal nonnegative tensors on $\Omega$. We define the functional $\mathcal{E}^h : L_+^\infty(\Omega)_{\mathrm{diag}}^{2\times 2} \to \mathbb{R}$,

$$\mathcal{E}^h[c] := \int_\Omega \nabla p^h[c] \cdot (r\mathbb{I} + c) \nabla p^h[c] + \frac{\nu}{\gamma} \left( |r + c_1|^\gamma + |r + c_2|^\gamma \right) \mathrm{d}\mathbf{x}, \tag{7.48}$$

where $p^h[c] \in W^h$ is a solution of the finite element problem (7.42).

**Proposition 15.** *Let $S \in L^2(\Omega)$ with $\int_\Omega S \, d\mathbf{x} = 0$ and $S_i^h$ be given by (7.47). Then for any vector of nonnegative conductivities $C = (C_i)_{i \in E^N}$, we have*

$$E^h[C] = \mathcal{E}^h[\mathbb{Q}_0^h[C]],$$

*with $E^h$ defined in (7.39) and $\mathcal{E}^h$ given by (7.48).*

*Proof.* We have shown in Section 7.4.1 that if $p^h = p^h(\mathbf{x})$ denotes a solution of the finite element problem (7.42) with $c = \mathbb{Q}_0^h[C]$, then the vertex values $P_i^h := p^h(\mathbf{X}_i)$ satisfy the Kirchhoff law (7.40). Moreover, using (7.43) and the definition (7.44)–(7.45) of $\mathbb{Q}_0^h[C]$, we calculate

$$\int_{T_i^{NE}} \nabla p^h \cdot (r\mathbb{I} + \mathbb{Q}_0^h[C]) \nabla p^h \, d\mathbf{x}$$

$$= |T_i^{NE}| \left( (r + C_i^E) \left( \frac{P_{i,E}^h - P_i^h}{h} \right)^2 + (r + C_i^N) \left( \frac{P_{i,N}^h - P_i^h}{h} \right)^2 \right)$$

for each $i \in \mathbb{V}$, and analogously for all other triangles. Noting that $|T_i^{NE}| = h^2/2$ and summing over all triangles, we obtain the formula (7.39) for the discrete energy $E^h[C]$. $\qquad\square$

### 7.4.3 Convergence of the energy functional

With Proposition 15, our task is now to prove the convergence of the sequence of functionals $\mathcal{E}^h$ given by (7.48) towards

$$\mathcal{E}[c] := \int_\Omega \nabla p[c] \cdot (r\mathbb{I} + c) \nabla p[c] + \frac{\nu}{\gamma} \left( |r + c_1|^\gamma + |r + c_2|^\gamma \right) d\mathbf{x}, \qquad (7.49)$$

where $p[c] \in H^1(\Omega)$ is a weak solution of the Poisson equation (7.41) subject to no-flux boundary conditions, and $c_1$, $c_2$ are the diagonal entries of

$$c = \begin{pmatrix} c_1 & 0 \\ 0 & c_2 \end{pmatrix}.$$

Similarly as in Section 7.3.2 we choose to work in the space $L_+^\infty(\Omega)_{\text{diag}}^{2\times2}$ of diagonal nonnegative tensors on $\Omega$ with essentially bounded entries, equipped with the norm topology of $L^2(\Omega)$. Note that for $c \in L_+^\infty(\Omega)_{\text{diag}}^{2\times2}$ the Poisson equation (7.41) has a solution $p[c] \in H^1(\Omega)$, unique up to an additive constant, and $\mathcal{E}[c] < +\infty$.

**Lemma 17.** *For any sequence of nonnegative diagonal tensors $(c^N)_{N\in\mathbb{N}} \subset L_+^\infty(\Omega)_{\text{diag}}^{2\times2}$ with entries uniformly bounded in $L^\gamma(\Omega)$ and converging entrywise to $c \in L_+^\gamma(\Omega)_{\text{diag}}^{2\times2}$*

*in the norm topology of $L^2(\Omega)$ as $h = 1/N \to 0$, we have,*

$$\mathcal{E}[c] \leqslant \liminf_{h=1/N\to0} \mathcal{E}^h[c^N], \tag{7.50}$$

*with $\mathcal{E}^h$ given by (7.48) and $\mathcal{E}$ defined in (7.49).*

*Proof.* Due to the strong convergence of the entries of $c^N$ in $L^2(\Omega)$ there exist a subsequence converging almost everywhere in $\Omega$ to $c$. Then, we have by the Fatou Lemma,

$$\int_\Omega |r + c_1|^\gamma \, d\mathbf{x} \leqslant \liminf_{h=1/N\to0} \int_\Omega |r + c_1^N|^\gamma \, d\mathbf{x}, \tag{7.51}$$

which is finite due to the uniform boundedness of $c_1^N$ in $L^\gamma(\Omega)$. Similarly for $c_2^N$.

For the sequel let us denote $p := p[c] \in H^1(\Omega)$ is a solution of the Poisson equation (7.41) with conductivity $c$, $p^N := p[c^N]$ a solution of the Poisson equation (7.41) with conductivity $c^N$ and $p^h := p^h[c^N] \in W^h$ a solution of the finite element discretisation (7.42) with $h = 1/N$ and conductivity $c^N$. Then, by an obvious modification of the auxiliary Lemma 13 for diagonal tensor-valued conductivities we have by (7.15),

$$\int_\Omega \nabla p \cdot (r\mathbb{I} + c)\nabla p \, d\mathbf{x} = \lim_{N\to\infty} \int_\Omega \nabla p^N \cdot (r\mathbb{I} + c^N)\nabla p^N \, d\mathbf{x}. \tag{7.52}$$

Let us define the bilinear forms $B^N : H^1(\Omega) \times H^1(\Omega) \to \mathbb{R}$,

$$B^N(u, v) = \int_\Omega \nabla u \cdot (r\mathbb{I} + c^N)\nabla v \, dx.$$

Note that $B^N(u, v) < +\infty$ for $u, v \in H^1(\Omega)$ since $c^N \in L^\infty_+(\Omega)^{2\times2}_{\mathrm{diag}}$. Moreover, since $r\mathbb{I} + c^N$ is symmetric and positive definite, $B^N$ induces a seminorm on $H^1(\Omega)$,

$$|u|_{B^N} := \sqrt{B^N(u, u)} \qquad \text{for } u \in H^1(\Omega).$$

With this notation we have

$$\int_\Omega \nabla p^N \cdot (r\mathbb{I} + c^N)\nabla p^N \, d\mathbf{x} = \left|p^N\right|^2_{B^N}.$$

We now proceed along the lines of standard theory of the finite element method (proof of Céaś Lemma in the energy norm, see, e.g., [Cia78]). Due to the Galerkin

orthogonality

$$B^N(p^N - p^h, \psi) = 0 \qquad \text{for all } \psi \in W^h, \tag{7.53}$$

we have, noting that $p^h \in W^h$,

$$\left|p^N\right|^2_{B^N} = \left|p^N - p^h\right|^2_{B^N} + \left|p^h\right|^2_{B^N}.$$

Then, again by (7.53) and by the Cauchy-Schwartz inequality, we have for all $\psi \in W^h$,

$$\left|p^N - p^h\right|^2_{B^N} = B^N(p^N - p^h, p^N - \psi) \leqslant \left|p^N - p^h\right|_{B^N} \left|p^N - \psi\right|_{B^N}.$$

Therefore, with the triangle inequality,

$$\left|p^N - p^h\right|_{B^N} \leqslant \inf_{\psi \in W^h} \left|p^N - \psi\right|_{B^N} \leqslant \left|p^N - p\right|_{B^N} + \inf_{\psi \in W^h} \left|p - \psi\right|_{B^N}.$$

Due to the strong convergence of $c^N \to c$ in $L^2(\Omega)$ and the standard result of approximation theory, see, e.g., [Cia78], we have

$$\lim_{h=1/N \to 0} \inf_{\psi \in W^h} |p - \psi|^2_{B^N} \leqslant \lim_{h \to 0} \inf_{\psi \in W^h} \int_\Omega \nabla(p - \psi) \cdot (r\mathbb{I} + c)\nabla(p - \psi)\,\mathrm{d}\mathbf{x}$$

$$+ \lim_{N \to \infty} \int_\Omega \nabla p \cdot (c^N - c)\nabla p\,\mathrm{d}\mathbf{x}$$

$$= 0.$$

Due to (7.52) and the weak convergence of $p^N \rightharpoonup p$ in $H^1(\Omega)$,

$$\lim_{N \to \infty} \left|p^N - p\right|_{B^N} = 0. \tag{7.54}$$

Thus, collecting the above results from (7.52) up to (7.54), we conclude that

$$\int_\Omega \nabla p \cdot (r\mathbb{I} + c)\nabla p\,\mathrm{d}\mathbf{x} = \lim_{N \to \infty} \left|p^N\right|^2_{B^N} = \lim_{h=1/N \to 0} \left|p^h\right|^2_{B^N}$$

$$= \lim_{h=1/N \to 0} \int_\Omega \nabla p^h \cdot (r\mathbb{I} + c^N)\nabla p^h\,\mathrm{d}\mathbf{x},$$

which together with (7.51) gives (7.50). $\qquad\square$

**Remark 22.** *Note that if $\gamma > 1$ and with the assumption that the sequence $(c^N)_{N \in \mathbb{N}}$*

converges (entrywise) in the norm topology of $L^\gamma(\Omega)$, the statement of Lemma 17 can be strengthened to

$$\mathcal{E}[c] = \lim_{h=1/N\to 0} \mathcal{E}^h[c^N].$$

This follows directly from the fact that in this case we have for the metabolic term

$$\int_\Omega |r+c_1|^\gamma + |r+c_2|^\gamma \, d\mathbf{x} = \lim_{h=1/N\to 0} \int_\Omega |r+c_1^N|^\gamma + |r+c_2^N|^\gamma \, d\mathbf{x}.$$

Lemma 17 and Remark 22 trivially imply the $\Gamma$-convergence of the sequence of energy functionals $\mathcal{E}^h$ in the norm topology of $L^\gamma(\Omega)$ for $\gamma > 1$:

**Theorem 12.** *Let $\gamma > 1$, $S \in L^2(\Omega)$ with $\int_\Omega S \, d\mathbf{x} = 0$ and $S_i^h$ be given by (7.47). Then the sequence $\mathcal{E}^h$ given by (7.48) $\Gamma$-converges to $\mathcal{E}$ defined in (7.49) with respect to the norm topology of $L^\gamma(\Omega)$ on the set $L^\infty_+(\Omega)^{2\times 2}_{\mathrm{diag}}$. In particular:*

- *For any sequence $(c^N)_{N\in\mathbb{N}} \subset L^\infty_+(\Omega)^{2\times 2}_{\mathrm{diag}}$ converging entrywise to $c \in L^\gamma_+(\Omega)^{2\times 2}_{\mathrm{diag}}$ in the norm topology of $L^\gamma(\Omega)$ as $h = 1/N \to 0$, we have*

$$\mathcal{E}[c] \leqslant \liminf_{h=1/N\to 0} \mathcal{E}^h[c^N].$$

- *For any $c \in L^\infty_+(\Omega)^{2\times 2}_{\mathrm{diag}}$ there exists a sequence $(c^N)_{N\in\mathbb{N}} \subset L^\infty_+(\Omega)^{2\times 2}_{\mathrm{diag}}$ converging entrywise to $c \in L^\gamma_+(\Omega)^{2\times 2}_{\mathrm{diag}}$ in the norm topology of $L^\gamma(\Omega)$ as $h = 1/N \to 0$, such that*

$$\mathcal{E}[c] \geqslant \limsup_{h=1/N\to 0} \mathcal{E}^h[c^N].$$

*Proof.* The $\liminf$-statement follows directly from Lemma 17. For the $\limsup$-statement it is sufficient to set $c^N := c$ for all $N \in \mathbb{N}$ and use Remark 22, which in fact leads to the stronger statement

$$\mathcal{E}[c] = \lim_{h=1/N\to 0} \mathcal{E}^h[c^N].$$

$\square$

### 7.4.4 Introduction of diffusion and construction of continuum energy minimisers

As in the one-dimensional case, we introduce a diffusive term into the discrete energy functionals, which shall provide compactness of the sequence of energy minimisers. We again construct a piecewise linear approximation of the discrete conductivities $C$, which, however, turns out to be technically quite involved in the two-dimensional situation.

We shall describe the process for the conductivities of the horizontal edges, and by a slight abuse of notation, we denote $C_{i+1/2,j}$ the conductivity of the horizontal edge connecting the node $(ih, jh)$ to $((i + 1)h, jh)$ for $i = 0, \ldots, N - 1, j = 0, \ldots, N$ where $h = 1/N$. Moreover, we denote $\mathbf{M}_{i+1/2,j}$ the midpoint of this edge, i.e., $\mathbf{M}_{i+1/2,j} = ((i + 1/2)h, jh)$. For a given vector of conductivities $C$, we construct the continuous function $\mathbb{Q}_1^h[C]$ on $\Omega$, such that

$$\mathbb{Q}_1^h[C](\mathbf{M}_{i+1/2,,j}) = C_{i+1/2,j}, \qquad \text{for } i = 0, \ldots, N - 1, \ j = 0, \ldots, N,$$

and $\mathbb{Q}_1^h[C]$ is linear on each triangle spanned by the nodes $\mathbf{M}_{i-1/2,j}$, $\mathbf{M}_{i+1/2,j}$, $\mathbf{M}_{i-1/2,j+1}$ and on each triangle spanned by the nodes $\mathbf{M}_{i+1/2,j}$, $\mathbf{M}_{i+1/2,j+1}$, $\mathbf{M}_{i-1/2,j+1}$, for $i = 1, \ldots, N - 1, \ j = 0, \ldots, N - 1$. Let us denote the union of such two triangles, i.e., the square spanned by the nodes $\mathbf{M}_{i-1/2,j}$, $\mathbf{M}_{i+1/2,j}$, $\mathbf{M}_{i-1/2,j+1}$ and $\mathbf{M}_{i+1/2,j+1}$, by $W_{ij}$. Then, a simple calculation reveals that

$$\int_{W_{ij}} |\nabla \mathbb{Q}_1^h[C]|^2 \, \mathrm{d}\mathbf{x} = \frac{1}{2} \left[ (C_{i-1/2,j} - C_{i+1/2,j})^2 + (C_{i+1/2,j} - C_{i+1/2,j+1})^2 \right. \tag{7.55}$$

$$\left. + (C_{i+1/2,j+1} - C_{i-1/2,j+1})^2 + (C_{i-1/2,j+1} - C_{i-1/2,j})^2 \right].$$

On the "boundary stripe" $(0, h/2) \times (0, 1)$ and $(1 - h/2, 1) \times (0, 1)$ the function is defined to be constant in the $x$-direction, such that it is globally continuous on $\Omega$, i.e., for $j = 0, \ldots, N - 1$ we have

$$\mathbb{Q}_1^h[C](\mathbf{x}) := \frac{C_{1/2,j+1} - C_{1/2,j}}{h}(x_2 - jh) + C_{1/2,j}$$

for $\mathbf{x} = (x_1, x_2) \in (0, h/2) \times (jh, (j + 1)h)$ and

$$\mathbb{Q}_1^h[C](\mathbf{x}) := \frac{C_{N-1/2,j+1} - C_{N-1/2,j}}{h}(x_2 - jh) + C_{N-1/2,j}$$

for $\mathbf{x} = (x_1, x_2) \in (1 - h/2, 1) \times (jh, (j+1)h)$. Summing up (7.55) over all squares $W_{ij}$ and the boundary stripe, we arrive at

$$\int_\Omega |\nabla \mathbb{Q}_1^h[C]|^2 \, d\mathbf{x} = \mathbb{D}_x[C], \tag{7.56}$$

with

$$\mathbb{D}_x[C] := \sum_{i=0}^{N-1} \sum_{j=0}^{N-1} (C_{i+1/2,j} - C_{i+1/2,j+1})^2 + \sum_{i=1}^{N-1} \sum_{j=1}^{N-1} (C_{i-1/2,j} - C_{i+1/2,j})^2$$
$$+ \frac{1}{2} \sum_{i=1}^{N-1} \left[ (C_{i-1/2,0} - C_{i+1/2,0})^2 + (C_{i-1/2,N} - C_{i+1/2,N})^2 \right].$$

Performing the same procedure for the vertical edges, we obtain

$$\int_\Omega |\nabla \mathbb{Q}_2^h[C]|^2 \, d\mathbf{x} = \mathbb{D}_y[C], \tag{7.57}$$

with obvious definitions of $\mathbb{Q}_2^h[C]$ and $\mathbb{D}_y[C]$.

Consequently, we define the sequence of discrete energy functionals $E_{\text{diff}}^h$,

$$E_{\text{diff}}^h[C] := D^2 \left( \mathbb{D}_x[C] + \mathbb{D}_y[C] \right) + E^h[C], \tag{7.58}$$

with $D^2 > 0$ diffusion constant and $E^h[C]$ defined in (7.39), coupled to the Kirchhoff law (7.40) with sources/sinks $S_i^h$ given by (7.47). We then have:

**Proposition 16.** *For any vector $C = (C_i)_{i \in \mathbb{E}}$ of nonnegative entries, we have*

$$E_{\text{diff}}^h[C] = D^2 \int_\Omega |\nabla \mathbb{Q}_1^h[C]|^2 + |\nabla \mathbb{Q}_2^h[C]|^2 \, d\mathbf{x} + \mathcal{E}^h[\mathbb{Q}_0^h[C]],$$

*with $E_{\text{diff}}^h$ defined in (7.58) and $\mathcal{E}^h$ given by (7.48) with the pressures $p^h$ being a solution of the FEM-discretised Poisson equation (7.42) with $c = \mathbb{Q}_0^N[C]$.*

We are now in shape to prove the main result of this section:

**Theorem 13.** *Let $\gamma > 1$, $S \in L^2(\Omega)$ with $\int_\Omega S \, d\mathbf{x} = 0$ and $S_i^h$ be given by (7.47). Let $(C^N)_{N \in \mathbb{N}} \subset \mathbb{R}^N$ be a sequence of global minimisers of the discrete energy functionals*

$E_{\text{diff}}^h$ *given by* (7.58) *with* $h = 1/N$. *Then the sequence of diagonal* $2 \times 2$ *matrices*

$$
c^N := \begin{pmatrix} \mathbb{Q}_1^h[C^N] & 0 \\ 0 & \mathbb{Q}_2^h[C^N] \end{pmatrix}
$$

*converges weakly in* $H^1(\Omega)^{2\times 2}$ *to* $c \in H^1(\Omega)_+^{2\times 2}$ *as* $h = 1/N \to 0$, *with* $c$ *a global minimiser of the functional* $\mathcal{E}_{\text{diff}} : H_+^1(\Omega)_{\text{diag}}^{2\times 2} \to \mathbb{R}$,

$$
\mathcal{E}_{\text{diff}}[c] := D^2 \int_\Omega |\nabla c_1|^2 + |\nabla c_2|^2 \, d\mathbf{x} + \mathcal{E}[c],
$$

*where* $\mathcal{E}[c]$ *is given by* (7.49).

*Proof.* Let us observe that

$$
E_{\text{diff}}^h[C^N] \leqslant E_{\text{diff}}^h[0] = \frac{h^2}{2} \sum_{i\in\mathbb{V}} \sum_{\star\in\{E,W,N,S\}} r\left(\frac{\widetilde{P}_i - \widetilde{P}_{i,\star}}{h}\right)^2 + \frac{\nu}{\gamma} r^\gamma,
$$

where $(\widetilde{P}_i)_{i\in\mathbb{V}}$ is a solution of the Kirchhoff law (7.40) with conductivities $C = 0$ and sources/sinks given by (7.47). As shown in Section 7.4.1, the pressures $\widetilde{P}_i$ correspond to pointwise values $\widetilde{P}_i^h := \tilde{p}^h(\mathbf{X}_i)$, $i \in \mathbb{V}$, of the solution $\tilde{p}^h$ of the discretised Poisson equation (7.42) with conductivity tensor $c = 0$. Moreover, due to formula (7.43) we have

$$
\frac{h^2}{2} \sum_{i\in\mathbb{V}} \sum_{\star\in\{E,W,N,S\}} r\left(\frac{\widetilde{P}_i - \widetilde{P}_{i,\star}}{h}\right)^2 = r \int_\Omega |\nabla\tilde{p}^h|^2 \, d\mathbf{x},
$$

and the uniform boundedness of $\nabla\tilde{p}^h$ in $L^2(\Omega)$ implies a uniform bound on $E_{\text{diff}}^h[C^N]$.

Since the sequence

$$
D^2 \int_\Omega |\nabla\mathbb{Q}_1^h[C^N]|^2 + |\nabla\mathbb{Q}_2^h[C^N]|^2 \, d\mathbf{x} = D^2 \left(\mathbb{D}_x[C^N] + \mathbb{D}_y[C^N]\right) \leqslant E_{\text{diff}}^h[C^N]
$$

is uniformly bounded, there exist subsequences of $\mathbb{Q}_1^h[C^N]$ and $\mathbb{Q}_2^h[C^N]$ converging to some $c_1$, $c_2 \in H^1(\Omega)$ weakly in $H^1(\Omega)$, and strongly in $L^2(\Omega)$. It is easy to check that then also $\mathbb{Q}_0^h[C^N]$ converges to $c := \begin{pmatrix} c_1 & 0 \\ 0 & c_2 \end{pmatrix}$ strongly in $L^2(0,1)^{2\times 2}$.

Clearly, we also have $\mathbb{Q}_0^h[C^N] \in L_+^\infty(\Omega)_{\text{diag}}^{2\times 2}$ with entries uniformly bounded in $L^\gamma(\Omega)$.

Consequently, by Lemma 17, we have

$$\mathcal{E}[c] \leqslant \liminf_{h=1/N \to 0} \mathcal{E}^h[c^N].$$

Moreover, due to the weak lower semicontinuity of the $L^2$-norm, we have

$$\int_\Omega |\nabla c_1|^2 + |\nabla c_2|^2 \, d\mathbf{x} \leqslant \liminf_{h=1/N \to 0} \int_\Omega |\nabla \mathbb{Q}_1^h[C^N]|^2 + |\nabla \mathbb{Q}_2^h[C^N]|^2 \, d\mathbf{x}.$$

Consequently,

$$\mathcal{E}_{\mathrm{diff}}[c] \leqslant \liminf_{h=1/N \to 0} E_{\mathrm{diff}}^h[C^N]. \tag{7.59}$$

We claim that $c$ is a global minimiser of $\mathcal{E}_{\mathrm{diff}}$ in $H_+^1(\Omega)_{\mathrm{diag}}^{2 \times 2}$. For contradiction, assume that there exists $\bar{c} \in H_+^1(\Omega)_{\mathrm{diag}}^{2 \times 2}$ such that

$$\mathcal{E}_{\mathrm{diff}}[\bar{c}] < \mathcal{E}_{\mathrm{diff}}[c].$$

We define the sequence $(\bar{C}^N)_{N \in \mathbb{N}}$ by setting the conductivity $\bar{C}_i^N$ of each horizontal edge $i \in \mathbb{E}$ to the average of $\bar{c}_1$ over the two triangles $T_{i;1}, T_{i;2} \in \mathcal{T}^h$ that contain the edge $i$, i.e.,

$$\bar{C}_i^N := \frac{1}{h^2} \int_{T_{i;1} \cup T_{i;2}} \bar{c}_1(x) \, d\mathbf{x}.$$

Similarly, we use the averages of $\bar{c}_2$ to define the conductivities of the vertical edges. Then, by assumption, we have for all $h = 1/N$, $N \in \mathbb{N}$,

$$E_{\mathrm{diff}}^h[\bar{C}^N] \geqslant E_{\mathrm{diff}}^h[C^N]. \tag{7.60}$$

It is easy to check that the sequence $\mathbb{Q}_1^h[\bar{C}^N]$ converges strongly in $H^1(\Omega)$ towards $\bar{c}_1$, therefore

$$\int_\Omega |\nabla \mathbb{Q}_1^h[\bar{C}^N]|^2 \, d\mathbf{x} \to \int_\Omega |\nabla \bar{c}_1|^2 \, d\mathbf{x} \qquad \text{as } h = 1/N \to 0,$$

and analogously for $\mathbb{Q}_2^h[\bar{C}^N]$ and $\bar{c}_2$. Moreover, the sequence $\mathbb{Q}_0^h[\bar{C}^N]$ converges to $\bar{c}$ strongly in $L^\gamma(\Omega)_{\mathrm{diag}}^{2 \times 2}$, therefore, by Remark 22, $\mathcal{E}^h[\mathbb{Q}_0^N[\bar{C}^N]] \to \mathcal{E}[\bar{c}]$ as $h = 1/N \to$

0. Consequently,

$$\lim_{h=1/N \to 0} E^h_{\text{diff}}[\bar{C}^N] = \mathcal{E}_{\text{diff}}[\bar{c}] < \mathcal{E}_{\text{diff}}[c],$$

a contradiction to (7.59)–(7.60). □

**Remark 23.** *We can easily generalise to the situation when the two-dimensional grid is not rectangular, but consists of parallelograms with sides of equal length in linearly independent directions $\theta_1$, $\theta_2 \in \mathbb{S}^1$, where $\mathbb{S}^1$ is the unit circle in $\mathbb{R}^2$. Then the coordinate transform*

$$(1,0) \mapsto \theta_1, \qquad (0,1) \mapsto \theta_2$$

*in (7.49) leads to the transformed continuum energy functional*

$$\mathcal{E}[c] = \int_\Omega \nabla p[c] \cdot \mathbb{P}[c] \nabla p[c] + \frac{\nu}{\gamma} \left( |r + c_1|^\gamma + |r + c_2|^\gamma \right) \, d\mathbf{x}$$

*coupled to the Poisson equation*

$$-\nabla \cdot (\mathbb{P}[c] \nabla p) = S$$

*with the permeability tensor*

$$\mathbb{P}[c] = r \mathbb{I} + c_1 \theta_1 \otimes \theta_1 + c_2 \theta_2 \otimes \theta_2.$$

*The eigenvalues of $\mathbb{P}[c]$ (principal permeabilities) are*

$$\lambda_{1,2} = \frac{1}{2} \left( c_1 + c_2 \pm \sqrt{(c_1 - c_2)^2 - 4c_1 c_2 (\theta_1 \cdot \theta_2)^2} \right)$$

*and the corresponding eigenvectors (principal directions)*

$$u_{1,2} = \theta_1 + \frac{c_2 - c_1 \pm \sqrt{(c_1 - c_2)^2 - 4c_1 c_2 (\theta_1 \cdot \theta_2)^2}}{2 c_1 \theta_1 \cdot \theta_2} \theta_2.$$

## 7.A   Detailed computations of Section 7.4.1

Here we provide more technical details for the constructions and calculations performed in Section 7.4.1.

## 7.A.1   Linear basis functions

We list the explicit definitions for the piecewise linear basis functions on the triangulation $\mathcal{T}^h$, constructed in Section 7.4.1. Any interior node $i \in \mathbb{V}$ has six adjacent triangles, denoted clockwise by $T_i^{NE}$, $T_i^{SE}$, $T_i^{S}$, $T_i^{SW}$, $T_i^{NW}$, $T_i^{N}$, see Fig. 7.1. For each triangle we construct three basis functions, supported on the respective triangle and linear on their support. Obviously, the basis functions are uniquely determined by their values on the triangle vertices. For later reference we list their gradients, which are constant vectors on the respective triangles.

- On the $NE$-triangle $T_i^{NE}$ we construct the linear basis functions $\phi_{i;1}^{NE}$, $\phi_{i;2}^{NE}$, $\phi_{i;3}^{NE}$ defined by

$$\phi_{i;1}^{NE}(\mathbf{X}_i) = 1, \quad \phi_{i;1}^{NE}(\mathbf{X}_{i,E}) = 0, \quad \phi_{i;1}^{NE}(\mathbf{X}_{i,N}) = 0,$$
$$\phi_{i;2}^{NE}(\mathbf{X}_i) = 0, \quad \phi_{i;2}^{NE}(\mathbf{X}_{i,E}) = 1, \quad \phi_{i;2}^{NE}(\mathbf{X}_{i,N}) = 0,$$
$$\phi_{i;3}^{NE}(\mathbf{X}_i) = 0, \quad \phi_{i;3}^{NE}(\mathbf{X}_{i,E}) = 0, \quad \phi_{i;3}^{NE}(\mathbf{X}_{i,N}) = 1,$$

so that

$$\nabla \phi_{i;1}^{NE} \equiv -\frac{1}{h}(1,1), \qquad \nabla \phi_{i;2}^{NE} \equiv \frac{1}{h}(1,0), \qquad \nabla \phi_{i;3}^{NE} \equiv \frac{1}{h}(0,1), \qquad \text{on } T_i^{NE}.$$

- On the $SE$-triangle $T_i^{SE}$ we construct the linear basis functions $\phi_{i;1}^{SE}$, $\phi_{i;2}^{SE}$, $\phi_{i;3}^{SE}$ defined by

$$\phi_{i;1}^{SE}(\mathbf{X}_i) = 1, \quad \phi_{i;1}^{SE}(\mathbf{X}_{i,E}) = 0, \quad \phi_{i;1}^{SE}(\mathbf{X}_{i,SE}) = 0,$$
$$\phi_{i;2}^{SE}(\mathbf{X}_i) = 0, \quad \phi_{i;2}^{SE}(\mathbf{X}_{i,E}) = 1, \quad \phi_{i;2}^{SE}(\mathbf{X}_{i,SE}) = 0,$$
$$\phi_{i;3}^{SE}(\mathbf{X}_i) = 0, \quad \phi_{i;3}^{SE}(\mathbf{X}_{i,E}) = 0, \quad \phi_{i;3}^{SE}(\mathbf{X}_{i,SE}) = 1,$$

so that

$$\nabla \phi_{i;1}^{SE} \equiv -\frac{1}{h}(1,0), \qquad \nabla \phi_{i;2}^{SE} \equiv \frac{1}{h}(1,1), \qquad \nabla \phi_{i;3}^{SE} \equiv -\frac{1}{h}(0,1), \qquad \text{on } T_i^{SE}.$$

- On the $S$-triangle $T_i^{S}$ we construct the linear basis functions $\phi_{i;1}^{S}$, $\phi_{i;2}^{S}$, $\phi_{i;3}^{S}$ defined by

$$\phi_{i;1}^{S}(\mathbf{X}_i) = 1, \quad \phi_{i;1}^{S}(\mathbf{X}_{i,SE}) = 0, \quad \phi_{i;1}^{S}(\mathbf{X}_{i,S}) = 0,$$
$$\phi_{i;2}^{S}(\mathbf{X}_i) = 0, \quad \phi_{i;2}^{S}(\mathbf{X}_{i,SE}) = 1, \quad \phi_{i;2}^{S}(\mathbf{X}_{i,S}) = 0,$$

$$\phi_{i;3}^{S}(\mathbf{X}_i) = 0, \quad \phi_{i;3}^{S}(\mathbf{X}_{i,SE}) = 0, \quad \phi_{i;3}^{S}(\mathbf{X}_{i,S}) = 1,$$

so that

$$\nabla\phi_{i;1}^{S} \equiv \frac{1}{h}(0,1), \qquad \nabla\phi_{i;2}^{S} \equiv \frac{1}{h}(1,0), \qquad \nabla\phi_{i;3}^{S} \equiv -\frac{1}{h}(1,1), \qquad \text{on } T_i^{S}.$$

- On the $SW$-triangle $T_i^{SW}$ we construct the linear basis functions $\phi_{i;1}^{SW}$, $\phi_{i;2}^{SW}$, $\phi_{i;3}^{SW}$ defined by

$$\phi_{i;1}^{SW}(\mathbf{X}_i) = 1, \quad \phi_{i;1}^{SW}(\mathbf{X}_{i,S}) = 0, \quad \phi_{i;1}^{SW}(\mathbf{X}_{i,W}) = 0,$$
$$\phi_{i;2}^{SW}(\mathbf{X}_i) = 0, \quad \phi_{i;2}^{SW}(\mathbf{X}_{i,S}) = 1, \quad \phi_{i;2}^{SW}(\mathbf{X}_{i,W}) = 0,$$
$$\phi_{i;3}^{SW}(\mathbf{X}_i) = 0, \quad \phi_{i;3}^{SW}(\mathbf{X}_{i,S}) = 0, \quad \phi_{i;3}^{SW}(\mathbf{X}_{i,W}) = 1,$$

so that

$$\nabla\phi_{i;1}^{SW} \equiv \frac{1}{h}(1,1), \qquad \nabla\phi_{i;2}^{SW} \equiv -\frac{1}{h}(0,1), \qquad \nabla\phi_{i;3}^{SW} \equiv -\frac{1}{h}(1,0), \qquad \text{on } T_i^{SW}.$$

- On the $NW$-triangle $T_i^{NW}$ we construct the linear basis functions $\phi_{i;1}^{NW}$, $\phi_{i;2}^{NW}$, $\phi_{i;3}^{NW}$ defined by

$$\phi_{i;1}^{NW}(\mathbf{X}_i) = 1, \quad \phi_{i;1}^{NW}(\mathbf{X}_{i,W}) = 0, \quad \phi_{i;1}^{NW}(\mathbf{X}_{i,NW}) = 0,$$
$$\phi_{i;2}^{NW}(\mathbf{X}_i) = 0, \quad \phi_{i;2}^{NW}(\mathbf{X}_{i,W}) = 1, \quad \phi_{i;2}^{NW}(\mathbf{X}_{i,NW}) = 0,$$
$$\phi_{i;3}^{NW}(\mathbf{X}_i) = 0, \quad \phi_{i;3}^{NW}(\mathbf{X}_{i,W}) = 0, \quad \phi_{i;3}^{NW}(\mathbf{X}_{i,NW}) = 1,$$

so that

$$\nabla\phi_{i;1}^{NW} \equiv \frac{1}{h}(1,0), \qquad \nabla\phi_{i;2}^{NW} \equiv -\frac{1}{h}(1,1), \qquad \nabla\phi_{i;3}^{NW} \equiv \frac{1}{h}(0,1), \qquad \text{on } T_i^{NW}.$$

- On the $N$-triangle $T_i^{N}$ we construct the linear basis functions $\phi_{i;1}^{N}$, $\phi_{i;2}^{N}$, $\phi_{i;3}^{N}$ defined by

$$\phi_{i;1}^{N}(\mathbf{X}_i) = 1, \quad \phi_{i;1}^{N}(\mathbf{X}_{i,NW}) = 0, \quad \phi_{i;1}^{N}(\mathbf{X}_{i,N}) = 0,$$
$$\phi_{i;2}^{N}(\mathbf{X}_i) = 0, \quad \phi_{i;2}^{N}(\mathbf{X}_{i,NW}) = 1, \quad \phi_{i;2}^{N}(\mathbf{X}_{i,N}) = 0,$$
$$\phi_{i;3}^{N}(\mathbf{X}_i) = 0, \quad \phi_{i;3}^{N}(\mathbf{X}_{i,NW}) = 0, \quad \phi_{i;3}^{N}(\mathbf{X}_{i,N}) = 1,$$

so that

$$\nabla\phi_{i;1}^N \equiv -\frac{1}{h}(0,1), \qquad \nabla\phi_{i;2}^N \equiv -\frac{1}{h}(1,0), \qquad \nabla\phi_{i;3}^N \equiv \frac{1}{h}(1,1), \qquad \text{on } T_i^N.$$

## 7.A.2   Gradients of $p^h$

Here we provide the gradient of the solution $p^h \in W^h$ of (7.42), constructed in Section 7.4.1. Since $p^h$ is continuous on $\Omega$ and linear on each triangle in $\mathcal{T}^h$, it is represented by its vertex values $P_i^h := p^h(\mathbf{X}_i)$, $i \in \mathbb{V}$. Then, for any interior node $i \in \mathbb{V}$ we readily have

$$\nabla p^h = \frac{1}{h}\begin{cases} (P_{i,E}^h - P_i^h, P_{i,N}^h - P_i^h) & \text{on } T_i^{NE}, \\ (P_{i,E}^h - P_i^h, P_i^h - P_{i,SE}^h) & \text{on } T_i^{SE}, \\ (P_{i,SE}^h - P_i^h, P_i^h - P_{i,S}^h) & \text{on } T_i^S, \\ (P_i^h - P_{i,W}^h, P_i^h - P_{i,S}^h) & \text{on } T_i^{SW}, \\ (P_i^h - P_{i,W}^h, P_{i,NW}^h - P_i^h) & \text{on } T_i^{NW}, \\ (P_i^h - P_{i,NW}^h, P_{i,N}^h - P_i^h) & \text{on } T_i^N. \end{cases}$$

## 7.A.3   Explicit calculation for (7.46)

Finally, we provide the detailed calculation for the identity (7.46). Noting that $\psi_i^h$ is supported on $U_i = T_i^{NE} \cup T_i^{SE} \cup T_i^S \cup T_i^{SW} \cup T_i^{NW} \cup T_i^N$, and taking into account the results listed in Sections 7.A.1 and 7.A.2, we have

$$\int_{T_i^{NE}} \nabla p^h \cdot \left(r\mathbb{I} + \mathbb{Q}_0^h[C]\right)\nabla\psi_i^h\,\mathrm{d}\mathbf{x} = \frac{r+C_i^E}{2}\left(P_i^h - P_{i,E}^h\right) + \frac{r+C_i^N}{2}\left(P_i^h - P_{i,N}^h\right),$$

$$\int_{T_i^{SE}} \nabla p^h \cdot \left(r\mathbb{I} + \mathbb{Q}_0^h[C]\right)\nabla\psi_i^h\,\mathrm{d}\mathbf{x} = \frac{r+C_i^E}{2}\left(P_i^h - P_{i,E}^h\right),$$

$$\int_{T_i^S} \nabla p^h \cdot \left(r\mathbb{I} + \mathbb{Q}_0^h[C]\right)\nabla\psi_i^h\,\mathrm{d}\mathbf{x} = \frac{r+C_i^S}{2}\left(P_i^h - P_{i,S}^h\right),$$

$$\int_{T_i^{SW}} \nabla p^h \cdot \left(r\mathbb{I} + \mathbb{Q}_0^h[C]\right)\nabla\psi_i^h\,\mathrm{d}\mathbf{x} = \frac{r+C_i^W}{2}\left(P_i^h - P_{i,W}^h\right) + \frac{r+C_i^S}{2}\left(P_i^h - P_{i,S}^h\right),$$

$$\int_{T_i^{NW}} \nabla p^h \cdot \left(r\mathbb{I} + \mathbb{Q}_0^h[C]\right)\nabla\psi_i^h\,\mathrm{d}\mathbf{x} = \frac{r+C_i^W}{2}\left(P_i^h - P_{i,W}^h\right),$$

$$\int_{T_i^N} \nabla p^h \cdot \left(r\mathbb{I} + \mathbb{Q}_0^h[C]\right)\nabla\psi_i^h\,\mathrm{d}\mathbf{x} = \frac{r+C_i^N}{2}\left(P_i^h - P_{i,N}^h\right).$$

Summing up, we arrive at

$$\int_\Omega \nabla p^h \cdot (r\mathbb{I} + \mathbb{Q}_0^h[C])\nabla \psi_i^h \, \mathrm{d}\mathbf{x}$$
$$= (r + C_i^E)\left(P_i^h - P_{i,E}^h\right) + (r + C_i^N)\left(P_i^h - P_{i,N}^h\right)$$
$$+ (r + C_i^W)\left(P_i^h - P_{i,W}^h\right) + (r + C_i^S)\left(P_i^h - P_{i,S}^h\right),$$

which is (7.46).

# Chapter 8

# Application to auxin transport in leaf venation

## Originality and contribution

This chapter mainly follows the paper [HJKM19], written in collaboration with Jan Haskovec, Henrik Jönsson and Peter A. Markowich. My main (mathematical) contributions to [HJKM19] are the analysis and numerical simulations of the discrete model. In addition, I wrote the description of the model and the conclusion, and contributed to the introduction.

## Chapter summary

The plant hormone auxin controls many aspects of the development of plants. One striking dynamical feature is the self-organisation of leaf venation patterns which is driven by high levels of auxin within vein cells. The auxin transport is mediated by specialised membrane-localised proteins. Many venation models have been based on polarly localised efflux-mediator proteins of the PIN family. Here, we investigate a modeling framework for auxin transport with a positive feedback between auxin fluxes and transport capacities that are not necessarily polar, i.e. directional across a cell wall. Our approach is derived from a discrete graph-based model for biological transportation networks, where cells are represented by graph nodes and intercellular membranes by edges. The edges are not a-priori oriented and the direction of auxin flow is determined by its concentration gradient along the edge. We prove global existence of solutions to the model and the validity of Murray's law for

its steady states. Moreover, we demonstrate with numerical simulations that the model is able connect an auxin source-sink pair with a mid-vein and that it can also produce branching vein patterns. A significant innovative aspect of our approach is that it allows the passage to a formal macroscopic limit which can be extended to include network growth. We perform mathematical analysis of the macroscopic formulation, showing the global existence of weak solutions for an appropriate parameter range.

## 8.1 Introduction

The hormone auxin plays a central role in many developmental processes in plants [HHK$^+$10, SMFB06, SS13, SES13]. During the development of a leaf, a connected network of veins is formed in a highly predictable order, generating a well defined pattern in the final leaf [Hic73]. High levels of auxin are present in the forming vein cells compared to the neighboring tissues. It has been shown that the membrane localized PIN-FORMED (PIN) family of auxin transport mediators is essential for the correct patterning of the vein network [Sac69, SMFB06]. The patterns could result from a canalisation mechanism where the auxin flux feeds back itself to a polarised transport connecting sources and sinks of auxin [Sac81, Mit80, MHS81]. This idea has been revisited recently and has led to models with polarised PIN transporters [RP05, FMI05, FFM15]. No flux-sensing mechanism has been identified but models have been used to suggest alternatives [Kra09, CRP15]. While newer models have solved the issue of unrealistically low levels of auxin within veins in flux-based models [FMI05], it is still an open question how looped veins can form [RP05, DZ06] and if specified auxin production can provide an answer.

PIN proteins are involved in several patterning processes in plants. Alternative models, not based on auxin flux, have been proposed, for instance for producing Turing-like dynamics in the context of phyllotaxis [JHS$^+$06, SGM$^+$06, BBL$^+$16], and for single cell polarity resulting in planar polarity [ASGMC16].

Since the discovery of PINs, many venation models have been based on polarised transport via PINs, while recent data suggests that polar auxin transport mediated by PINs is not crucial for forming veins [SS13, SES13]. Although characteristic vein patterns and leaf shapes can be obtained with these PIN-based models, veins can also form in chemical perturbations when PIN-mediated auxin transport is blocked, or when multiple membrane-localised PIN proteins are mutated. This raises the question if alternative mechanisms work in parallel or together with the PIN-based

272

polar transporters during the initiation of veins. This motivates to consider a more general modelling approach where alternative feedbacks between auxin, auxin fluxes and auxin transport can be included.

The ultimate goal for modelling vein networks is to accurately predict vein network geometries seen in different plants. Our novel dynamical description could complement the PIN-based models which have focused on more basic dynamic patterns of veins, such as connecting sources and sinks, and breaking the symmetry of graded diffusion into veins. Examples of these PIN-based models include the traditional PIN-based flux models that have been studied since approximately 40 years, see [Sac81, Mit80, MHS81]. The impact of auxin concentration on the pattern formation has been studied in [MEB+17]. It would be very interesting to investigate the emergence of patterns in the setting where PINs are removed. As noted above, the traditional PIN-based flux models are yet to provide a full description of the diverse patterns seen in plants.

Given the strong directional distribution of PINs and the ability of veins to form without PINs, it is important to introduce and analyse alternative mechanisms. Whether these mechanisms are identical/redundant to PIN mechanisms in terms of their dynamical behaviour or whether other mechanisms need to be considered is still unknown. Hence, it would be interesting to show that polar/directional transport activity and directional flux measurements are not required, and that vein-like patterns can also result from mere measurement of magnitudes. This may also inspire scientists to reconsider their current data or design new experiments.

In this chapter, we study a modeling framework for leaf venation which does not assume polarity of auxin transport mediators across cell walls. The model is introduced in Section 8.2, and is based on a positive feedback loop between auxin fluxes and transport capacities that are not necessarily polar. Our approach is derived from a recent discrete graph-based model for biological transportation networks introduced by Hu and Cai [HC13]. We represent cells by graph nodes and intercellular membranes (connections) by edges. The edges are not a-priori oriented and the direction of auxin flow is determined by its concentration gradient along the edge. The transport capacity of each edge is represented by the local concentration of the auxin mediator. Our approach can be understood as a modeling framework, which can be equipped or extended with various biologically relevant features that will produce experimentally testable hypotheses. We admit that in its present setting it does not capture all relevant biological features, however, its main advantage is a rather simple form that facilitates rigorous mathematical analysis.

273

In particular, the first aim of this chapter is the proof of global existence and nonnegativity of solutions of the discrete model (Section 8.3). Moreover, in Section 8.4 we show that the stationary solutions satisfy a generalized Murray's law. The second aim of the chapter is to gain a better understanding of the pattern formation capacity of the model by means of numerical simulations (Section 8.5). In particular, we show that it is capable of generating patterns connecting an auxin source-sink pair with a mid-vein and that it can produce branching vein patterns. The main novelty of our modelling approach is that it facilitates a (formal) passage to a continuum limit, which is the subject of Section 8.6. The resulting system of partial differential equations captures network growth and is expected to exhibit a rich patterning capacity (see [ABH+17] for results of numerical simulations of a related continuum model). Here we prove the existence of weak solutions of the transient problem and of its steady states.

## 8.2 Description of the model

Hu and Cai considered a discrete model for describing the formation of biological transport networks in [HC13]. This model was studied in terms of the existence of solutions, its formal continuum limit, as well as its qualitative behaviour in Chapter 6. Based on this model, we propose an adapted model in the cellular context for describing the auxin transport in plant leafs via transporter proteins, where the orientation of the flow is determined by auxin concentration gradient. Our approach shares many similarities with the one introduced by Mitchison in [Mit80] where the transport capacity is updated as a function of the flux (gradient) between cells. However, while Mitchison suggested an asymmetric update of the transport capacities across a cell wall, our model assumes a symmetric transport capacity across a cell wall. In this section we shall first introduce the Hu and Cai model, then shortly discuss the Mitchison model, and finally describe the adaptation to the cellular context.

### 8.2.1 Model of Hu and Cai

The discrete model introduced by Hu and Cai [HC13] and reformulated in [ABH+17] is posed on a given, fixed undirected connected graph $\mathbb{G} = (\mathbb{V}, \mathbb{E})$, consisting of a finite set of vertices $\mathbb{V}$ of size $N = |\mathbb{V}|$ and a finite set of edges $\mathbb{E}$. Any pair of vertices is connected by at most one edge and no vertex is connected to itself. We

denote the edge between vertices $i \in \mathbb{V}$ and $j \in \mathbb{V}$ by $(i,j) \in \mathbb{E}$. Since the graph is undirected, $(i,j)$ and $(j,i)$ refer to the same edge. For each edge $(i,j) \in \mathbb{E}$ of the graph $\mathbb{G}$ we consider its length and its conductivity, denoted by $L_{ij} = L_{ji} > 0$ and $C_{ij} = C_{ji} \geqslant 0$, respectively. The edge lengths $L_{ij} > 0$ are given as a datum and fixed for all $(i,j) \in \mathbb{E}$. With each vertex $i \in \mathbb{V}$ the fluid pressure $P_i \in \mathbb{R}$ is associated. The pressure drop between vertices $i \in \mathbb{V}$ and $j \in \mathbb{V}$ connected by an edge $(i,j) \in \mathbb{E}$ is given by (1.22). Note that the pressure drop is antisymmetric, i.e., by definition, $(\Delta P)_{ij} = -(\Delta P)_{ji}$. The oriented flux (flow rate) from vertex $i \in \mathbb{V}$ to $j \in \mathbb{V}$ is denoted by $Q_{ij}$; again, we have $Q_{ij} = -Q_{ji}$. Since the Reynolds number of the flow is typically small for biological networks and the flow is predominantly laminar, the flow rate between vertices $i \in \mathbb{V}$ and $j \in \mathbb{V}$ along edge $(i,j) \in \mathbb{E}$ is proportional to the conductance $C_{ij}$ and the pressure drop $(\Delta P)_{ij} = P_j - P_i$ and is given by (1.23). The local mass conservation in each vertex is expressed in terms of the Kirchhoff law (1.24), i.e.

$$- \sum_{j \in N(i)} C_{ij} \frac{P_j - P_i}{L_{ij}} = S_i \qquad \text{for all } i \in \mathbb{V}. \tag{8.1}$$

Clearly, a necessary condition for the solvability of (8.1) is the global mass conservation (1.25) which we assume in the following. Given the vector of conductivities $C = (C_{ij})_{(i,j) \in \mathbb{E}}$, the Kirchhoff law (8.1) is a linear system of equations for the vector of pressures $P = (P_i)_{i \in \mathbb{V}}$. With the global mass conservation (1.25), the linear system (8.1) is solvable if and only if the graph with edge weights $C = (C_{ij})_{(i,j) \in \mathbb{E}}$ is connected [ABH+17], where only edges with positive conductivities $C_{ij} > 0$ are taken into account (i.e., edges with zero conductivities are discarded). Note that the solution is unique up to an additive constant.

The conductivities $C_{ij}$ are subject to an energy optimisation and adaptation process. Hu and Cai [HC13] propose an energy cost functional consisting of a pumping power term and a metabolic cost term. According to Joule's law, the power (kinetic energy) needed to pump material through an edge $(i,j) \in \mathbb{E}$ is proportional to the pressure drop $(\Delta P)_{ij} = P_j - P_i$ and the flow rate $Q_{ij}$ along the edge, i.e., $(\Delta P)_{ij} Q_{ij} = \frac{Q_{ij}^2}{C_{ij}} L_{ij}$. The metabolic cost of maintaining the edge is assumed to be proportional to its length $L_{ij}$ and a power of its conductivity $C_{ij}^\gamma$, where the exponent $\gamma > 0$ depends on the network. For models of leaf venation the material cost is proportional to the number of small tubes, which is proportional to $C_{ij}$, and the metabolic cost is due to the effective loss of the photosynthetic power at the

area of the venation cells, which is proportional to $C_{ij}^{1/2}$. Consequently, the effective value of $\gamma$ typically used in models of leaf venation lies between $1/2$ and $1$; see [HC13]. The energy cost functional is thus given by (1.26), i.e.

$$E[C] := \sum_{(i,j)\in\mathbb{E}} \left( \frac{Q_{ij}[C]^2}{C_{ij}} + \frac{\nu}{\gamma}C_{ij}^{\gamma} \right) L_{ij}, \tag{8.2}$$

where $Q_{ij}[C]$ is given by (1.23) with pressures calculated from the Kirchhoff's law (8.1), and $\nu > 0$ is the so-called metabolic coefficient. Note that every edge of the graph $\mathbb{G}$ is counted exactly once in the above sum. Hu and Cai [HC13] propose an energy optimisation and adaptation process for the conductivities $C_{ij}$ based on the gradient flow of the energy (8.2),

$$\frac{\mathrm{d}C_{ij}}{\mathrm{d}t} = \sigma \left( \frac{Q_{ij}[C]^2}{C_{ij}^{\gamma+1}} - \tau^2 \right) C_{ij}L_{ij} \tag{8.3}$$

with parameters $\sigma, \tau > 0$, constrained by the Kirchhoff law (8.1), see Chapter 6 for details.

### 8.2.2 Mitchison model

As described in the introduction, auxins are a class of plant hormones (or plant growth regulators) that play a cardinal role in coordination of many growth and behavioural processes in the plant's life cycle and are essential for plant body development including for developing its own transport network. This has been captured in a model proposed by Mitchison [Mit80], where auxin dynamics within an array of cells with indices $i \in \mathbb{V}$ is considered. For two cells $i, j \in \mathbb{V}$ with signal concentrations $s_i, s_j$, respectively, the diffusion constant at the interface between the cells is denoted by $D_{ij} = D_{ji} \geqslant 0$ and can be specified independently for each cell-cell interface. The oriented flux from vertex $i \in \mathbb{V}$ to $j \in \mathbb{V}$ is given by Fick's law [Cra56],

$$\phi_{ij} = D_{ij}\frac{s_i - s_j}{L_{ij}}, \tag{8.4}$$

where $L_{ij} = L_{ji} > 0$ denotes the (average) length of cells $i$ and $j$. In particular, we have $\phi_{ij} = -\phi_{ji}$. The dependence of the diffusion constant $D_{ij}$ on the flux $\phi_{ij}$ is of the form

$$\frac{\mathrm{d}D_{ij}}{\mathrm{d}t} = f(|\phi_{ij}|, D_{ij})$$

276

for a suitable function $f$ such that $|\phi_{ij}|/D_{ij}$ decreases as $|\phi_{ij}|$ increases. For instance, $f$ can be chosen such that $D_{ij} \approx \phi_{ij}^2$ at least in a neighbourhood of $f^{-1}(0)$. Assuming that cell $i \in \mathbb{V}$ receives fluxes $\phi_{ji}$ for $j \in \mathcal{N}(i)$, the evolution of the signal $s_i$ is of the form

$$\frac{\mathrm{d}s_i}{\mathrm{d}t} = \sigma_i + \frac{1}{v} \sum_{j \in \mathcal{N}(i)} A_{ij}\phi_{ji}. \tag{8.5}$$

Here, $\mathcal{N}(i)$ denotes the index set of neighbouring cells of cell $i \in \mathbb{V}$. The parameter $\sigma_i$ is the source activity for signal production in cell $i \in \mathbb{V}$. All cells have volume $v > 0$ and $A_{ij} = A_{ji} > 0$ is the area of the interface between cell $i$ and its neighbour $j \in \mathcal{N}(i)$. Note that the term $\sum_{j \in \mathcal{N}(i)} A_{ij}\phi_{ji}$ can be regarded as the difference between influx and outflux since $\phi_{ij} = -\phi_{ji}$ for $j \in \mathcal{N}(i)$. For the conservation of the signal we require that the source activity $\sigma_i$ for signal production and degradation is chosen such that $\frac{\mathrm{d}}{\mathrm{d}t} \sum_{i \in \mathbb{V}} s_i = 0$.

It is worth noting that while it was well established that auxin was important for generating the vascular or vein patterns (e.g. [Sac81]), auxin 'transporters' were not identified at the time when these models were introduced. The models received great attention later, when auxin transport mediator proteins with similar polar localisation as predicted by the models were identified [SMFB06]. In particular, PIN proteins are integral membrane proteins that transport the anionic form of auxin across membranes. Most of the PIN proteins localise at the plasma membrane where they serve as secondary active transporters involved in the efflux of auxin. They show asymmetrical localisations on the membrane and are therefore responsible for polar auxin transport. Still, while PIN loss of function mutants generate phenotypes in venation patterns, they do not completely abolish the formation of veins [SS13], and as such alternative mechanisms can contribute to the dynamics of vein formation. While individual mutants do not show strong phenotypes, this is also implied by the existence of other auxin transport proteins, such as AUX1/LAX influx mediators [Kra04, PSF⁺12, SS13], regulating intracellular and intercellular transport. In the following discussion we will often use PIN as a descriptor of the auxin transporter protein for simplicity, but it should be seen as a more general description of auxin transport mediated by polar and/or nonpolar membrane proteins, where polar relates to the difference of transport capacity (PIN localisation) on the two sides of a wall.

### 8.2.3  Adapted Hu-Cai model in cellular context

Given the known auxin flows generated from sources to sinks in a plant tissue, the sometimes clear expression but unclear polarisation of PIN auxin transporter proteins in these veins, and the ability to generate veins without any PIN transport, it is of interest to investigate alternative mechanisms for the vein dynamics in an auxin context. Such an alternative can be given by the Hu and Cai model for transport networks [HC13]. The mechanism where pressure differences feeds back on conductance between elements has similarity with the auxin transport case, as described in the flux-based models [Mit80, MHS81], where auxin sources and concentration differences (pressure in the Hu-Cai model) generates diffusive fluxes between cells (spatial elements), which positively feeds back on transport rates between the cells (conductance). However, in contrast to the polarised transport connecting sources and sinks of auxin in [Mit80, MHS81], we investigate a modelling framework for auxin transport with a positive feedback between auxin fluxes and transport capacities that are not necessarily polar, i.e. directional across a cell wall. To modify the Hu-Cai model to a cellular context of plant venation dynamics we consider $n = |\mathbb{V}|$ cells with indices $i \in \mathbb{V}$ and replace the pressure $P_i$ at vertex $i \in \mathbb{V}$ in the Hu-Cai model with the auxin concentration $a_i \geqslant 0$.

   The conductance $C_{ij}$ of edge $(i, j) \in \mathbb{E}$ in the Hu and Cai model is replaced by the transport activity $X_{ij} = X_{ji} \geqslant 0$ in the membrane connecting cells $i \in \mathbb{V}$ and $j \in \mathbb{V}$ which is the main difference from PIN-based flux models (and experiments) with PINs $\mathcal{P}_{ij}$ where $\mathcal{P}_{ij} \neq \mathcal{P}_{ji}$. Due to this modelling approach auxin transporters are not directional, i.e. polar, and as we shall see, measuring the magnitudes $X_{ij}$ is sufficient for producing vein-like dynamics. However, cells, in general, do not transport auxin equally well in all directions (i.e. $X_{ij}$ is typically not equal to $X_{ik}$ for two cell neighbours $i$ and $k$). Based on the definition of $X_{ij}$, we define the auxin flow rate $\mathcal{Q}_{ij} = -\mathcal{Q}_{ji} \in \mathbb{R}$ from cell $i \in \mathbb{V}$ to cell $j \in \mathbb{V}$ by $\mathcal{Q}_{ij} = X_{ij} \frac{a_j - a_i}{L_{ij}}$, where $L_{ij} = L_{ji} > 0$ denotes the (average) length of cells $i$ and $j$. Based on the framework of Mitchison (8.5) and Hu and Cai (8.3) we propose to describe the auxin transport in the cellular context by the ODE system

$$\frac{\mathrm{d}a_i}{\mathrm{d}t} = S_i - I_i a_i + \delta \sum_{j \in \mathcal{N}(i)} X_{ij} \frac{a_j - a_i}{L_{ij}} \qquad \text{for all } i \in \mathbb{V}, \qquad (8.6)$$

where $\mathcal{N}(i)$ denotes the index set of neighbouring cells of cell $i \in \mathbb{V}$ and the parameter $\delta > 0$ denotes the (scaled) diffusion rate. To account for the auxin production

and destruction in the cells, we introduced the source terms $S_i \geqslant 0$ and decay rates $I_i \geqslant 0$ for $i \in \mathbb{V}$. For simplicity, we assume $S_i$ and $I_i$ to be independent of time. For the transport activity $X_{ij}$ in the membrane we consider

$$\frac{\mathrm{d}X_{ij}}{\mathrm{d}t} = \sigma \left( \frac{|\mathcal{Q}_{ij}|^{\kappa}}{X_{ij}^{\gamma+1}} - \tau \right) X_{ij} L_{ij}, \tag{8.7}$$

where $\gamma > 0$ is a control parameter and $\sigma$, $\kappa$, $\tau$ are nonnegative parameters denoting, respectively, the conductance update rate, the flux feedback and the conductance degradation rate. In particular, the flux feedback $\kappa$ is an important parameter of the model and is also a relevant parameter in the Mitchison model [Mit80, MHS81]. The system (8.6)–(8.7) is equipped with the initial datum

$$X_{ij}(0) = X_{ij}^0 = X_{ji}^0 \geqslant 0 \qquad \text{for all } i, j \in \mathbb{V}, \tag{8.8}$$

$$a_i(0) = a_i^0 > 0 \qquad \text{for all } i \in \mathbb{V}. \tag{8.9}$$

Clearly, (8.7) satisfies the symmetry requirement $X_{ij} = X_{ji}$. The conductance equation (8.3) and the transport activity equation (8.7) are of similar form. However, the term $\mathcal{Q}_{ij}^2$ in the conductance equation (8.3) is replaced by the more general term $|\mathcal{Q}_{ij}|^{\kappa}$ in the transport activity equation (8.7) so that (8.7) reduces to (8.3) for $\kappa = 2$. Besides, the linear algebraic system (8.1) is relaxed by the introduction of the time derivative of the auxin concentration in (8.15), leading to a system of linear ordinary differential equations. While the system (8.3), (8.1) is a constrained gradient flow for the energy (8.2), the system (8.7), (8.6) does not seem to have a gradient flow structure.

## 8.3 Global existence and nonnegativity of solutions

**Theorem 14.** *Let $0 < \kappa - \gamma \leqslant 1$ and fix $T > 0$. The system (8.7), (8.6) subject to the initial datum (8.8)–(8.9) has a solution $X_{ij} \in C^1(0, T)$, $a_i \in C^1(0, T)$, satisfying $X_{ij}(t) \geqslant 0, a_i(t) > 0$ for all $t \in [0, T)$ and $i, j \in \mathbb{V}$. Moreover, if $S_i = 0$ for all $i \in \mathbb{V}$ in (8.6), then $a_i$ is uniformly globally bounded, i.e., there exists a constant $\alpha > 0$ such that*

$$a_i(t) \leqslant \alpha \qquad \text{for all } t \in [0, \infty) \text{ and } i \in \mathbb{V}. \tag{8.10}$$

279

*Proof.* **Nonnegativity for $X_{ij}$.** With (8.7) we have $\frac{\mathrm{d}X_{ij}}{\mathrm{d}t} \geqslant -\sigma\tau X_{ij}$, as long as the solution exists. Consequently, $X_{ij}(0) \geqslant 0$ implies $X_{ij}(t) \geqslant 0$ on the interval of existence.

**Boundedness for $|a_i|$.** Let us denote the adjacency matrix of the graph $\mathbb{G} = (\mathbb{V}, \mathbb{E})$ by $\mathbb{A} \in \mathbb{R}^{n \times n}$, i.e. its entries are given by

$$\mathbb{A}_{ij} = \begin{cases} 0 & \text{if } (i,j) \notin \mathbb{E}, \\ 1 & \text{if } (i,j) \in \mathbb{E}. \end{cases}$$

For the solutions $a_i$ of the auxin equation (8.6) on their joint interval of existence we have

$$\frac{1}{2}\frac{\mathrm{d}}{\mathrm{d}t}\sum_{i=1}^{N} a_i^2 = \sum_{i=1}^{N} S_i a_i - \sum_{i=1}^{N} I_i a_i^2 + \delta \sum_{i=1}^{N}\sum_{j=1}^{N} \mathbb{A}_{ij} X_{ij} a_i (a_j - a_i)$$

$$\leqslant \sum_{i=1}^{N} S_i a_i - \frac{\delta}{2}\sum_{i=1}^{N}\sum_{j=1}^{N} \mathbb{A}_{ij} X_{ij} (a_i - a_j)^2 ,$$

where we used the nonnegativity of $I_i$ in the estimate and the usual symmetrisation trick (recall that both $\mathbb{A}_{ij}$ and $X_{ij}$ are symmetric). Now, due to the nonnegativity of $X_{ij}$, we have

$$\frac{1}{2}\frac{\mathrm{d}}{\mathrm{d}t}\sum_{i=1}^{N} a_i^2 \leqslant \sum_{i=1}^{N} S_i a_i \leqslant \left(\sum_{i=1}^{N} S_i^2\right)^{1/2}\left(\sum_{i=1}^{N} a_i^2\right)^{1/2},$$

implying at most quadratic growth of $a_i^2$ in time, i.e., at most linear growth of $|a_i| = |a_i|(t)$. Clearly, if $S_i = 0$ for all $i \in \mathbb{V}$, then we have the uniform bound (8.10) with

$$\alpha := \sqrt{\sum_{i=1}^{N} a_i(0)^2}.$$

**Boundedness for $X_{ij}$.**

$$\frac{\mathrm{d}X_{ij}}{\mathrm{d}t} \leqslant \sigma \frac{|\mathcal{Q}_{ij}|^{\kappa}}{X_{ij}^{\gamma}} L_{ij},$$

and the boundedness of $|a_i|$ on bounded time intervals implies

$$|\mathcal{Q}_{ij}|^{\kappa} = \left|X_{ij}\frac{a_j - a_i}{L_{ij}}\right|^{\kappa} \leqslant C|X_{ij}|^{\kappa}$$

280

for a suitable constant $C > 0$. Hence,

$$\frac{\mathrm{d}X_{ij}}{\mathrm{d}t} \leqslant C X_{ij}^{\kappa - \gamma},$$

and, therefore, for $0 < \kappa - \gamma < 1$, $X_{ij} = X_{ij}(t)$ grows at most algebraically in time, while for $\kappa - \gamma = 1$ the growth is at most exponential.

**Positivity for $a_i$.** According to the assumption, there exists $\underline{a} > 0$ such that $a_i(0) \geqslant \underline{a}$ for all $i \in \mathbb{V}$. Let us assume that $t_0 < +\infty$ is the first instant when any of the curves $a_i = a_i(t)$ hits zero. Due to continuity, we have $t_0 > 0$, and, clearly, $a_i(t) > 0$ for $t \in [0, t_0)$ for all $i \in \mathbb{V}$. With the nonnegativity of the sources $S_i \geqslant 0$, (8.6) implies

$$\frac{\mathrm{d}a_i}{\mathrm{d}t} \geqslant -I_i a_i + \delta \sum_{j \in \mathcal{N}(i)} X_{ij} \frac{a_j - a_i}{L_{ij}} \qquad \text{for } i \in \mathbb{V}, \, t > 0,$$

and with the nonnegativity of $X_{ij}$ we have

$$\frac{\mathrm{d}a_i}{\mathrm{d}t} \geqslant -I_i a_i - \delta \left( \sum_{j \in \mathcal{N}(i)} \frac{X_{ij}}{L_{ij}} \right) a_i \qquad \text{for } i \in \mathbb{V}, \, t \in (0, t_0).$$

Finally, since $X_{ij} = X_{ij}(t)$ grow at most exponentially in time, there exist constants $C, \lambda > 0$ independent of $t_0$ such that

$$\frac{\mathrm{d}a_i}{\mathrm{d}t} \geqslant -C e^{\lambda t} a_i \qquad \text{for } i \in \mathbb{V}, \, t \in (0, t_0),$$

implying

$$a_i(t) \geqslant a_i(0) \exp \left( \frac{\lambda}{C} (1 - \exp(\lambda t)) \right).$$

Therefore, $a_i(t_0) > 0$ for all $i \in \mathbb{V}$, a contradiction to the assumption $t_0 < +\infty$. $\square$

Note that under the relaxed initial condition

$$a_i(0) = a_i^0 \geqslant 0 \qquad \text{for all } i \in \mathbb{V} \tag{8.11}$$

with an initial auxin concentration $\sum_{i \in \mathbb{V}} a_i(0) > 0$ some cells may get no auxin over time. If $a_i(0) = 0$ for some $i \in \mathbb{V}$, it follows from (8.6) that cell $i$ gets no auxin as long as its neighbouring cells have zero auxin. However, if $a_i(0) = 0$ for some $i \in \mathbb{V}$

and $a_j(0) > 0$ for some $j \in \mathcal{N}(i)$, then (8.6) implies that

$$
\frac{\mathrm{d}a_i(t)}{\mathrm{d}t}\bigg|_{t=0}
\begin{cases}
> 0 & X_{ij}(0) > 0, a_j(0) > 0, \\
= 0 & \text{otherwise.}
\end{cases}
$$

In particular, the relaxed initial condition (8.11) guarantees the nonnegativity for $a_i$.

## 8.4 Murray's law

In this section we demonstrate the validity of the Murray's law [Mur26a, Mur26b] for the steady states of the auxin transport activity model (8.7), (8.6). Murray's law is a basic physical principle for transportation networks which predicts the thickness or conductivity of branches, such that the cost for transport and maintenance of the transport medium is minimised. This law is observed in the vascular and respiratory systems of animals, xylem in plants, and the respiratory system of insects [She81].

The stationary version of the auxin transport activity model (8.7), (8.6) consists of the algebraic system

$$
\delta \sum_{j \in N(i)} \mathcal{Q}_{ji} = S_i - I_i a_i \qquad \text{for all } i \in \mathbb{V}, \tag{8.12}
$$

$$
\left( \frac{|\mathcal{Q}_{ij}|^{\kappa}}{X_{ij}^{\gamma+1}} - \tau \right) X_{ij} = 0 \qquad \text{for all } (i, j) \in \mathbb{E}. \tag{8.13}
$$

Noting that $\mathcal{Q}_{ij} = 0$ if $X_{ij} = 0$, (8.13) implies

$$
|\mathcal{Q}_{ij}|^{\kappa} = \tau X_{ij}^{\gamma+1} \qquad \text{for all } (i, j) \in \mathbb{E}. \tag{8.14}
$$

Then, we rewrite (8.12) in the form

$$
\delta \sum_{j \in N^+(i)} |\mathcal{Q}_{ij}| + S_i - I_i a_i = \delta \sum_{j \in N^-(i)} |\mathcal{Q}_{ij}| \qquad \text{for all } i \in \mathbb{V}
$$

with

$$
N^+(i) := \{j \in N(i); \ \mathcal{Q}_{ij} > 0\}, \qquad N^-(i) := \{j \in N(i); \ \mathcal{Q}_{ij} < 0\}.
$$

Using (8.14), we have

$$\delta \sum_{j \in N^+(i)} (\tau X_{ij}^{\gamma+1})^{1/\kappa} + S_i - I_i a_i = \delta \sum_{j \in N^-(i)} (\tau X_{ij}^{\gamma+1})^{1/\kappa} \qquad \text{for all } i \in \mathbb{V}.$$

In particular, when all $I_i = 0$, we obtain the generalised Murray's law

$$\delta \sum_{j \in N^+(i)} (\tau X_{ij}^{\gamma+1})^{1/\kappa} + S_i = \delta \sum_{j \in N^-(i)} (\tau X_{ij}^{\gamma+1})^{1/\kappa} \qquad \text{for all } i \in \mathbb{V}.$$

## 8.5 Numerical simulation

In this section, we provide numerical results for the discrete model (8.6)–(8.7). Since the problem is stiff, implicit formulas are necessary and we consider a multi-step solver based on the numerical differentiation formulas of orders 1 to 5 [SR97].

We consider a planar graph $\mathbb{G} = (\mathbb{V}, \mathbb{E})$, whose vertices and edges define a diamond shaped geometry embedded in the two-dimensional domain $\Omega = (-0.5, 2) \times (-1.5, 0.5)$ with $|\mathbb{V}| = 81$ vertices and $|\mathbb{E}| = 208$ edges. Let $(x^i, y^i)$ denote the position of vertex $i \in \mathbb{V}$. We assume that the source terms $S_i \geqslant 0$ are positive on the subset of vertices

$$\mathbb{V}^+ := \{i \in \mathbb{V}; \ x^i \leqslant -0.4\},$$

and vanish on its complement $\mathbb{V}\backslash\mathbb{V}^+$,

$$S_i := \begin{cases} \xi_S, & i \in \mathbb{V}^+, \\ 0, & i \in \mathbb{V}\backslash\mathbb{V}^+, \end{cases}$$

where $\xi_S := 100$, implying that we have a single source in the top corner of the diamond. The decay terms $I_i$, $i \in \mathbb{V}$, are assumed to positive on the complement $\mathbb{V}\backslash\mathbb{V}^+$,

$$I_i := \begin{cases} 0, & i \in \mathbb{V}^+, \\ \xi_I, & i \in \mathbb{V}\backslash\mathbb{V}^+, \end{cases}$$

where $\xi_I := 1$. Note that in terms of the distribution of source and sink terms, we consider the same situation as in Chapter 6. We prescribe the initial condition $\bar{X}_{ij} := 1$ for every $(i, j) \in \mathbb{E}$ and $a_i := 1$ for all $i \in \mathbb{V}$, unless stated otherwise.

283

Besides, we consider $\delta := 1$, $\sigma := 1$, $\kappa := 2$, $\gamma := 0.5$ and $\tau := 1$ in the numerical simulations, if not stated otherwise.

In the sequel, we present the stationary solutions obtained by solving the system (8.6)–(8.7). We plot the value of the transport activity $X_{ij}$ for every edge $(i, j) \in \mathbb{E}$ in terms of its width and colour. The auxin concentration in each cell $i \in \mathbb{V}$ is indicated by the colour of that cell.

In Figure 8.1, we show the stationary transport activity for perturbed initial data $\bar{X}_{ij}$, i.e., we consider $\bar{X}_{ij} + \varepsilon \mathcal{U}(0, 1)$ instead of $\bar{X}_{ij}$ as initial data, where $\mathcal{U}(0, 1)$ denotes a uniformly distributed random variable on $[0, 1]$. In particular, the resulting network is stable under small perturbation. This can be seen by comparing the results with Figure 8.2(G) where the same parameters without perturbation are considered. The perturbations of the initial data result in more complex steady states compared to the steady states obtained from unperturbed initial data.



(A) $\varepsilon = 0.5$     (B) $\varepsilon = 1$     (C) $\varepsilon = 5$     (D) $\varepsilon = 10$
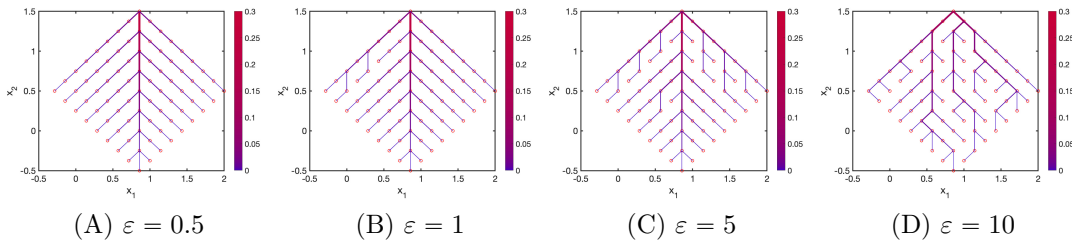
Figure 8.1: Steady states for transport activity for perturbation $\varepsilon \mathcal{U}(0, 1)$ of the initial transport activity $\bar{X}_{ij}$ with initial data $\bar{X}_{ij}, \bar{a}_i$.

In Figure 8.2 we vary the strength $\xi_S$ of the source in the top corner of the diamond. As $\xi_S$ increases, auxin is transported over a larger area, resulting in lower auxin levels and transport activity close to the source in the top corner of the diamond. Note that the area of large auxin levels and transport activities coincide in the steady states. Further note that not the entire graph is covered with auxin for $\xi_S \in \{10, 50\}$ and the resulting pattern is symmetric due to symmetric initial data for the auxin levels and the transport activity.

In Figure 8.3 we consider different grids (round, oval). As in Figure 8.2 we vary the strength $\xi_S$ of the source in the top middle corner of these grids. The resulting pattern formation for round and oval grids is very similar to the patterns obtained with the same source strengths in Figure 8.2 for the diamond grid. In particular, this demonstrates the robustness of the model to variations of the underlying grid. Note that due to the larger size of the oval grid compared to the other considered grids, a stronger source is required for obtaining stationary patterns covering the

Figure 8.2: Steady states for auxin concentration and transport activity for different background source strengths $\xi_S$ with initial data $\bar{X}_{ij}, \bar{a}_i$.

entire simulation domain.

In Figure 8.4, we vary the strength of the sink in the bottom corner, denoted by $\xi_I^C$, while keeping the values of $I_i$ for all other vertices $i \in \mathbb{V}$ as before. Similarly as for the variation of $\xi_I$, the area of the network decreases as $\xi_I^C$ increases for both auxin levels and transport activity. In this case, however, it decreases outside a neighbourhood of the line connecting the source in the top corner and the increasing sink of size $\xi_I^C$ in the bottom corner. In particular, the network structure for large $\xi_S^C$ is given by a high auxin levels and transport activity along the line of cells, connecting the source in the top corner with the strong sink in the bottom corner. Moreover, this variation of the size of the source $\xi_S$ in Figures 8.2 and 8.3, as well as, of the sinks $\xi_I$ and $\xi_I^C$ in Figure 8.4 illustrate how crucial the choice of sources and sinks for the resulting pattern formation is.

In Figures 8.5 and 8.6, we investigate the dependence of the stationary states on the model parameters $\delta$ and $\tau$ in (8.6)–(8.7). For small values of $\delta$, more complex stationary patterns for the transport activity can be seen in Figure 8.5 and auxin is transported over the entire graph. As $\delta$ increases, the auxin levels and the transport activity increase close to the source, but they are no longer transported over the entire graph. As before, the area covered by auxin transport activity and auxin levels are of a similar size, i.e., auxin transport activity and auxin levels are co-existent. The increase of $\tau$ shows a similar change of the steady states of both the auxin transport activity and auxin levels as the increase of $\delta$.
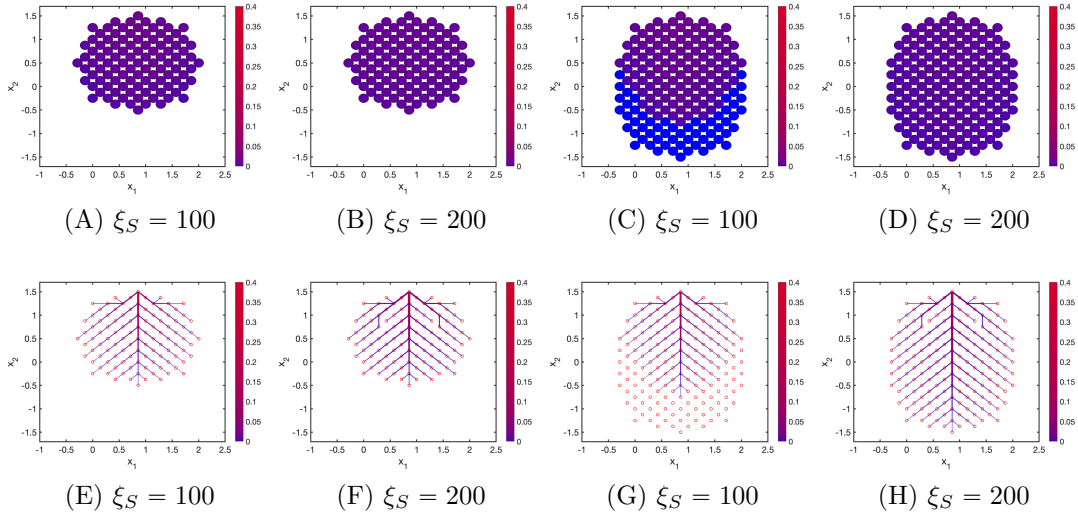
Figure 8.3: Steady states for auxin concentration and transport activity for different background source strengths $\xi_S$ and different grid shapes (round, oval) with initial data $\bar{X}_{ij}, \bar{a}_i$.
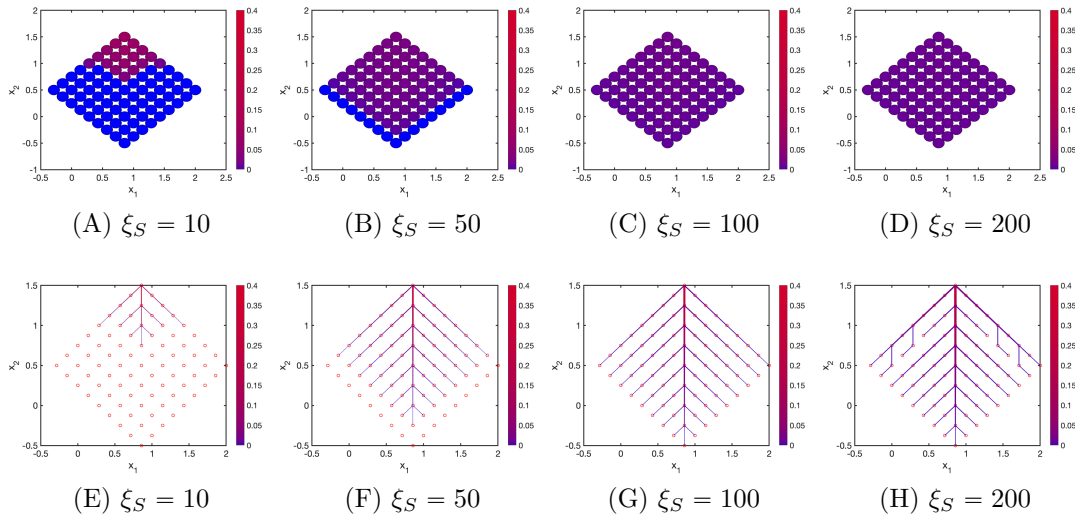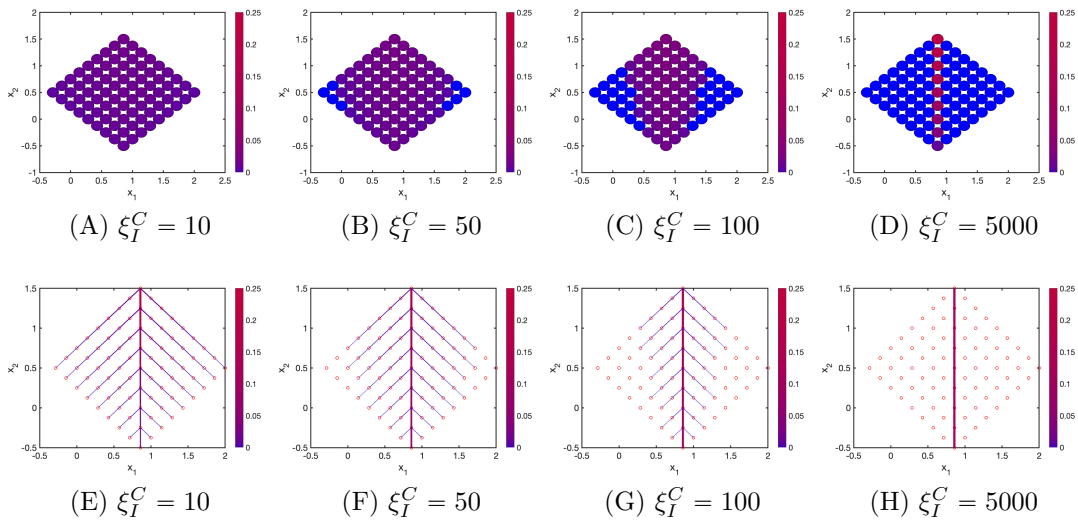


Figure 8.4: Steady states for auxin concentration and transport activity for different sink strengths $\xi_I^C$ with initial data $\bar{X}_{ij}, \bar{a}_i$.

(A) $\delta = 0.1$   (B) $\delta = 0.5$   (C) $\delta = 2$   (D) $\delta = 10$

(E) $\delta = 0.1$   (F) $\delta = 0.5$   (G) $\delta = 2$   (H) $\delta = 10$

Figure 8.5: Steady states for auxin transport activity and auxin levels for different parameter values $\delta$ with initial data $\bar{X}_{ij}, \bar{a}_i$.



(A) $\tau = 0.5$   (B) $\tau = 2$   (C) $\tau = 5$   (D) $\tau = 10$

(E) $\tau = 0.5$   (F) $\tau = 2$   (G) $\tau = 5$   (H) $\tau = 10$
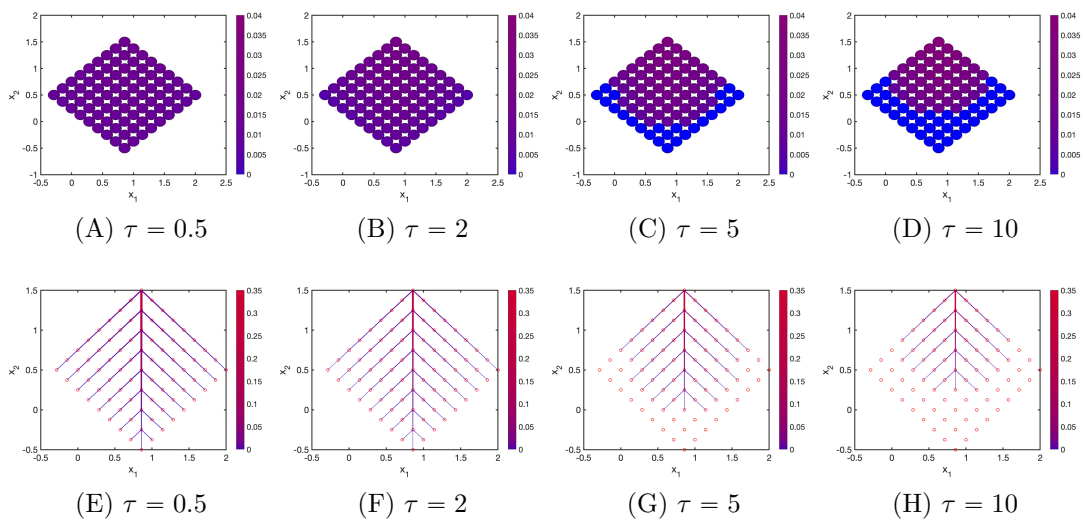
Figure 8.6: Steady states for auxin transport activity and auxin levels for different parameter values $\tau$ with initial data $\bar{X}_{ij}, \bar{a}_i$.

In Figures 8.7–8.9, we vary the initial auxin transport activity and no longer consider the initial data $\bar{X}_{ij}$. In Figure 8.7, the steady states for the transport activity are shown where the initial transport activity is chosen as $\theta + 0.00001\varepsilon$ for parameter $\varepsilon \in \{0.5, 5, 50, 100\}$ and a random variable $\theta$ with $\theta = 1$ with probability 0.2 and $\theta = 0$ with probability 0.8. In particular, the resulting patterns of the transport activity have no symmetries and the location of the mid-veins strongly depend on the choice of parameters, illustrating that model (8.6)–(8.7) can produce complex vein patterns. Note that the size of the stationary pattern increases as $\varepsilon$ and, thus, as the absolute value of the initial transport activity increases.



(A) $\varepsilon = 0.5$    (B) $\varepsilon = 5$    (C) $\varepsilon = 50$    (D) $\varepsilon = 100$
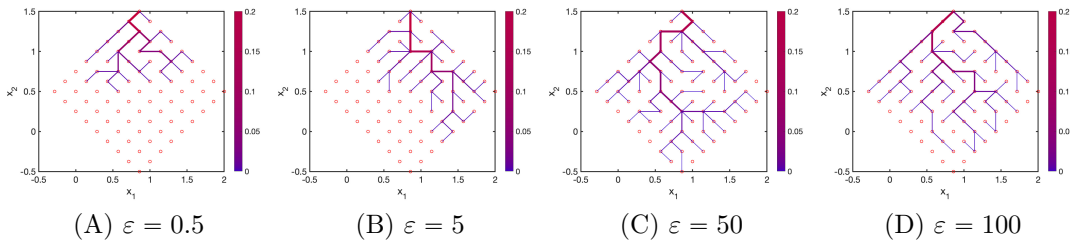
Figure 8.7: Steady states for the transport activity for initial transport activity $\theta + 0.00001\varepsilon$ where $\theta$ is a random variable with $\theta = 1$ with probability 0.2 and $\theta = 0$ with probability 0.8.

In Figure 8.8, we consider the initial transport activity $\varepsilon \mathcal{U}(0, 1)$ where $\varepsilon \in \{0.5, 1, 5, 100\}$. These numerical results demonstrate that model 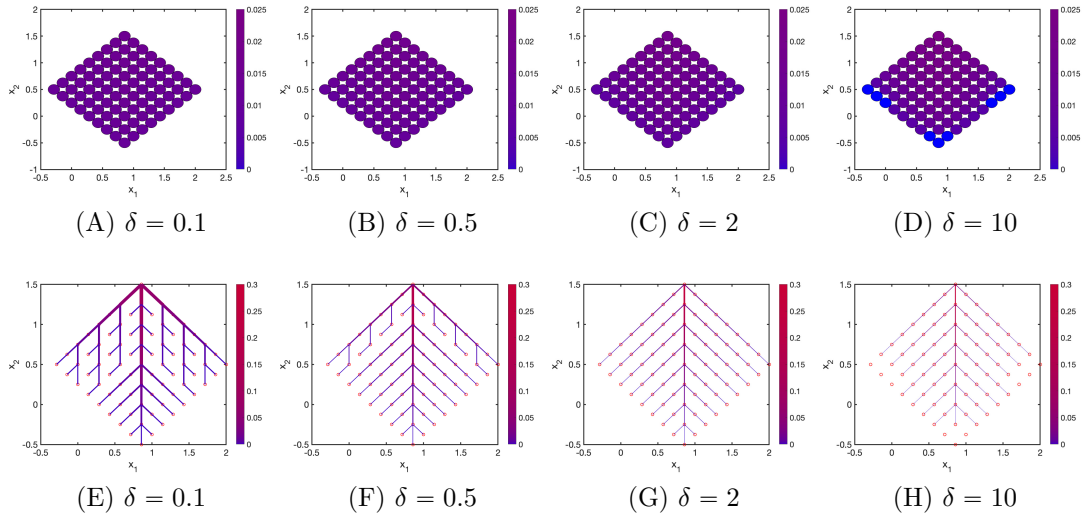(8.6)–(8.7) is capable to produce different complex stationary state, not only on subdomains as in Figure 8.7, but on the entire underlying network. In particular, the stationary transport activity connects auxin sources and sinks.



(A) $\varepsilon = 0.5$    (B) $\varepsilon = 1$    (C) $\varepsilon = 5$    (D) $\varepsilon = 100$
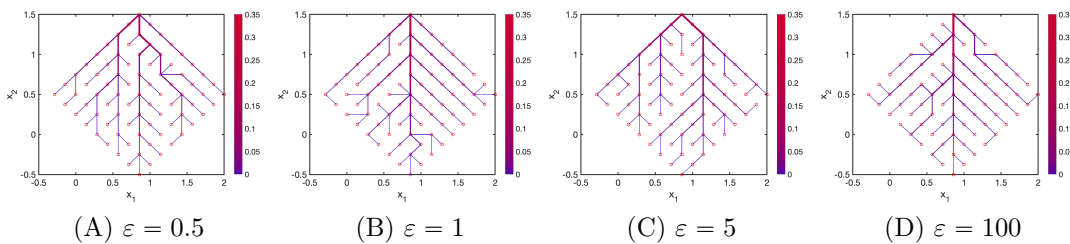
Figure 8.8: Steady states for transport activity for initial transport activity $\varepsilon \mathcal{U}(0, 1)$.

In Figure 8.9, we consider the same initial condition for the transport activity as in Figure 8.8(D), i.e. $100 \mathcal{U}(0, 1)$, but we vary the strengths $10\varepsilon$ and $\varepsilon$ of the auxin background source strengths $\xi_S$ and sink strengths $\xi_I$, respectively, where $\varepsilon \in \{1, 5, 50, 100\}$. One can clearly see in Figure 8.9 that the auxin sources and

sinks are not strong enough for $\varepsilon = 1$ for transport activity to connect the top and bottom corners of the underlying network, while for larger values of $\varepsilon$ mid-veins become visible and get stronger as auxin sources and sinks increase. This shows that complex stationary transport activity patterns with no symmetries and major mid-veins can be obtained.



(A) $\varepsilon = 1$     (B) $\varepsilon = 5$     (C) $\varepsilon = 50$     (D) $\varepsilon = 100$
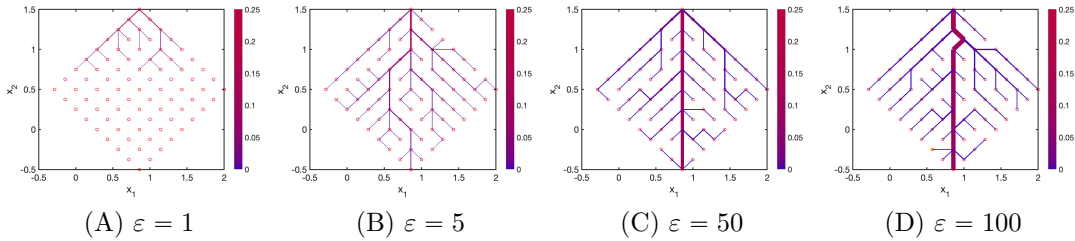
Figure 8.9: Steady states for transport activity for initial transport activity $100\,\mathcal{U}(0,1)$ with source $10\varepsilon$ and sink $\varepsilon$.

In Figures 8.10 and 8.11 we consider multiple sources and sinks for obtaining more realistic vein networks. Starting from a certain configuration of sources and sinks in Figures 8.10(A) and 8.11(A) we subsequently add sources and sinks in the subfigures further to the right. In Figure 8.10 we consider a diamond grid as in most figures, but apart from a source at the top corner and a sink at the bottom corner of the grid, we add sources which are located symmetrically with respect to the longest vertical axis of the grid. Denoting the distance between the left and the top corner of grid by $l$, these sources are located on the boundary of the grid at a distance of $l/4$ from the top corner (Figures 8.10(A), 8.10(B), 8.10(C), 8.10(D)), the left corner (Figures 8.10(B), 8.10(C), 8.10(D)) and at distances of $3l/4$ and $5l/8$ from the top corner in Figures 8.10(C), 8.10(D) and Figure 8.10(D), respectively. Similarly, the sources are located on the right side of the grid by symmetry of the source locations in each figure. One can clearly see that multiple sources result in a more complex transportation network between the sources and the sink in comparison to the simulation results in the previous figures with merely one point source.

In Figure 8.11 we consider a rectangular underlying grid with sources at the top and the bottom of the boundary of the grid. We denote the length between the left top and right top corner of the grid by $l$. We consider a sink in the middle of the bottom boundary and sources in the middle of the top boundary and at a distance of $l/4$ left and right of the middle on the top boundary in all subfigures of Figure 8.11. Additional sources are located at the left top and the right top corner

289

(A) 3 sources      (B) 5 soures      (C) 7 sources      (D) 9 sources
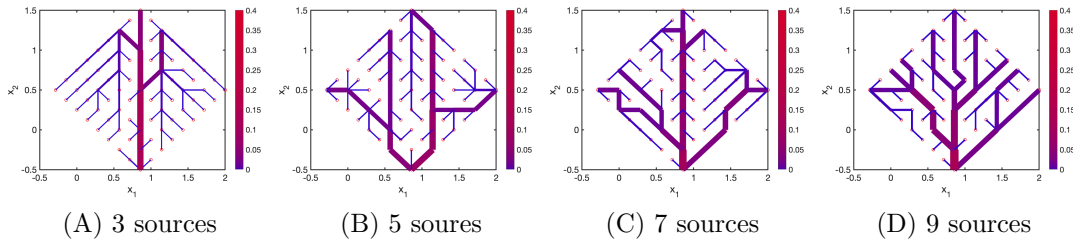
Figure 8.10: Steady states for transport activity for initial transport activity $100\,\mathcal{U}(0,1)$ with different number of sources of strength 1000 and sinks of strength 100.

in Figures 8.11(B), 8.11(C), 8.11(D). In Figures 8.11(C), 8.11(D) additional sinks are added at the bottom boundary in a distance of $l/4$ left and right of the middle of the bottom boundary, while in Figure 8.11(D) additional sinks are considered in the left bottom and right bottom corner of the grid. In particular, the resulting patterns look very similar to those in leaves.



(A) 3 sources, 1 sink    (B) 5 soures, 1 sink    (C) 5 sources, 3 sinks    (D) 5 sources, 5 sinks
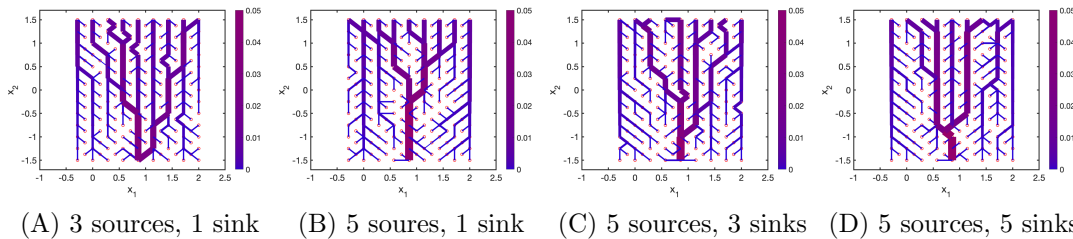
Figure 8.11: Steady states for transport activity for initial transport activity $100\,\mathcal{U}(0,1)$ with different number of sources of strength 1000 and different number of sinks of strength 100.

Model (8.6)–(8.7) describes the auxin transport with a positive feedback between auxin fluxes and auxin transporters where the auxin transporters are not necessarily polar. The above numerical results illustrate that the model (8.6)–(8.7) is able to connect an auxin source-sink pair with a mid-vein and that branching vein patterns can also be produced. A nice feature of the model is that the veins end up with high auxin levels. This was not achieved with the original Mitchinson models and this has been discussed in some detail. A solution to this has been to adapt the conservative approach $X_{tot} = \sum_{j\in\mathcal{N}(i)} X_{ij} = \text{const}$ for the auxin transporters which (together with feedback on the localisation of auxin transporters from auxin flux) can lead to high auxin in veins.

We want to stress here that our model (8.6)–(8.7) is able to generate a venation/transport network without a polar input, as seen in the case when auxin

290

transporters are knocked out in the various numerical examples.

## 8.6 The formal continuum limit

The main reason for focusing on discrete models is that the patterns form when the leaves have very few cells, e.g. the (first) mid-vein forms when the leaf is about five cells wide. Cells split over time, resulting in a larger number of cells and network growth. Besides, there is an auxin peak at the tip before the high auxin/transport activity vein forms downwards from this. Still, this does not discard alternative mechanisms setting up an intitial pattern that connects the leaf tip with the vasculature in the stem (thought to be auxin sink). These phenomena can be modelled much better in a diffusion driven setting instead of the discrete setting and motivates us to consider the associated macroscopic model.

The goal of this section is to derive the formal macroscopic limit of the discrete model (8.7), (8.6) as the number of nodes and edges tends to infinity, and to study the existence of weak solutions of the resulting PDE system. The derivation requires an appropriate rescaling of the auxin production equation (8.6). Moreover, since the derivation of macroscopic limits of systems posed on general (unstructured) graphs is a highly nontrivial topic, see, e.g., [Lov12], we restrict ourselves to discrete graphs represented by regular equidistant grids, i.e., tessellations of a rectangular domain $\Omega \subset \mathbb{R}^d$, $d \in \mathbb{N}$, by congruent identical rectangles (in 2D) or cubes (in 3D) with edges parallel to the axis. The results can be generalised to parallelotopes, see Section 6.3 of Chapter 6 for details of the formal procedure applied to the Hu-Cai model (8.3)–(8.1), and Chapter 7 for the rigorous procedure in the spatially one- and two-dimensional setting.

### 8.6.1 Formal derivation of the continuum limit

Given the graph $\mathbb{G} = (\mathbb{V}, \mathbb{E})$ as a rectangular tesselation of the rectangular domain $\Omega$, let us denote the vertices left and right of vertex $i \in \mathbb{V}$ along the $k$-th spatial dimension by $(i-1)_k$ and, resp., $(i+1)_k$. Moreover, let us denote $h_k > 0$ the equidistant grid spacing in the $k$-th dimension. The rescaled auxin production

equation (8.6) is then written as

$$\frac{\mathrm{d}a_i}{\mathrm{d}t} = S_i - I_i a_i + \delta \sum_{k=1}^{d} \frac{1}{h_k} \left( X_{i,(i+1)_k} \frac{a_{(i+1)_k} - a_i}{h_k} - X_{i,(i-1)_k} \frac{a_i - a_{(i-1)_k}}{h_k} \right) \quad \text{for } i \in \mathbb{V}.$$

(8.15)

The rescaling of the sum on the right hand side by $h_k$ is reflecting the fact that the edges of the graph are inherently one-dimensional structures, embedded into the $d$-dimensional space, cf. Section 6.3. A straightforward calculation reveals that (8.15) is a finite difference discretisation of the parabolic equation

$$\frac{\partial a}{\partial t} = \delta \nabla \cdot (X \nabla a) + S - Ia,$$

(8.16)

on the regular grid $G = (\mathbb{V}, \mathbb{E})$, where $a = a(t, x)$ is a formal limit of the sequence of discrete auxin concentrations $(a_i)_{i \in \mathbb{V}}$ as $|\mathbb{V}| \to \infty$, and $I = I(x)$ is a formal limit of the sequence $(I_i)_{i \in \mathbb{V}}$. Here, $X = X(t, x)$ is the diagonal tensor $X = \mathrm{diag}(X_1, \dots, X_d)$ where $X_k$ is the formal limit of the sequence $(X_{ij})_{i,j \in \mathbb{V}}$ on edges $(i, j) \in \mathbb{E}$ oriented along the $k$-th spatial direction. A formal continuum limit of (8.7) yields the family of ODEs for $X = X(t, x)$,

$$\frac{\partial X_k}{\partial t} = \left( \frac{|q_k|^\kappa}{X_k^{\gamma+1}} - \tau \right) X_k,$$

(8.17)

with $q_k = X_k \partial_{x_k} a$. Note that the product $X \nabla a$ is the vector

$$X \nabla a = (X_1 \partial_{x_1} a, \dots, X_d \partial_{x_d} a).$$

Observe that (8.17) is in fact a family of ODEs for $X_k = X_k(t, x)$, parametrised by $x \in \Omega$. Consequently, in analogy to Chapter 6, we introduce the diffusive terms $D^2 \Delta X_k$ that model random fluctuations in the medium. Thus, the updated version of (8.17) reads

$$\frac{\partial X_k}{\partial t} = D^2 \Delta X_k + \left( \frac{|q_k|^\kappa}{X_k^{\gamma+1}} - \tau \right) X_k,$$

(8.18)

with the diffusion coefficient $D^2 > 0$.

Biological observations suggest that the auxin dynamics takes place on a faster time scale than the dynamics of the transporter proteins in the order of minutes for auxin movement [DMIG96], and in the order of hours for e.g. PIN1 reorientation

[HHK$^+$10]. This motivates to consider a formal fast time scale limit of (8.16), leading to the elliptic equation

$$-\delta \nabla \cdot (X \nabla a) = S - Ia. \tag{8.19}$$

Note that the system (8.18)–(8.19) is very similar to the original Hu–Cai model (8.1), (8.3), except that there is an additional linearly decaying term in (8.19) in comparison to Kirchhoff's law (8.1).

The system (8.16), (8.18) is equipped with the no-flux boundary condition

$$\nu \cdot X \nabla a = 0, \qquad \nu \cdot \nabla X_k = 0 \qquad \text{on } \partial \Omega, \ k = 1, \ldots, d, \tag{8.20}$$

where $\nu = \nu(x)$ is the outer unit normal vector on $\partial \Omega$. The no-flux boundary condition reflects the modelling assumption that there is no flow of auxin or the auxin transporters through the boundary of the domain. More general boundary conditions can be considered, leading to only slight modifications in the forthcoming analysis. Moreover, we prescribe the initial datum for the auxin transporters

$$X_k(0, x) = X_k^0(x) \geqslant 0 \qquad \text{for } x \in \Omega, \ k = 1, \ldots, d. \tag{8.21}$$

**Remark 24.** *The choice to work with the elliptic-parabolic system (8.18), (8.19) instead of the parabolic-parabolic system (8.16), (8.18) simplifies the mathematical analysis, since one can apply the so-called weak-strong lemma for the elliptic equation (8.19), see Lemma 19 below. The analysis of the full parabolic-parabolic PDE system (8.16), (8.18) will be the subject of a further work.*

### 8.6.2 Existence of weak solutions

The weak formulation of (8.19), subject to the no-flux boundary condition (8.20), with a test function $\phi \in C^\infty(\Omega)$ reads

$$\delta \int_\Omega (X \nabla a) \cdot \nabla \phi \, \mathrm{d}x = \int_\Omega (S - Ia) \phi \, \mathrm{d}x, \tag{8.22}$$

for almost all $t > 0$, and the weak formulation of (8.18), (8.20) with a test function $\psi \in C^\infty(\Omega)$ is

$$\frac{\mathrm{d}}{\mathrm{d}t} \int_\Omega X_k \psi \, \mathrm{d}x = -D^2 \int_\Omega \nabla X_k \cdot \nabla \psi \, \mathrm{d}x + \int_\Omega \left( |\partial_{x_k} a|^\kappa X_k^{\kappa - \gamma} - \tau X_k \right) \psi \, \mathrm{d}x, \tag{8.23}$$

for almost all $t > 0$. The system is subject to the initial datum (8.21) with

$$X_k^0 \in L^\infty(\Omega), \quad k = 1, \ldots, d. \tag{8.24}$$

We assume the uniform positivity $X_k^0 \geqslant \bar{X}^0 > 0$ almost everywhere on $\Omega$, which prevents degeneracy of the elliptic term $\nabla \cdot (X\nabla a)$ in (8.16). Moreover, we assume that

$$S \in L^2(\Omega), \qquad I \in L^\infty(\Omega) \text{ with } I(x) \geqslant \bar{I} > 0 \text{ almost everywhere on } \Omega. \tag{8.25}$$

To prove the existence of solutions of the system (8.22), (8.23) subject to the initial condition (8.24) we shall use the Schauder fixed point iteration in an appropriate function space. We start by proving suitable a-priori estimates.

**Lemma 18.** *Let $S \in L^2(\Omega)$ and $I \in L^\infty(\Omega)$ verify (8.25). Let the diagonal tensor $X \in L^2(\Omega)$ be uniformly positive on $\Omega$, i.e., let there be $\bar{X} > 0$ such that $X_k \geqslant \bar{X}$ almost everywhere on $\Omega$, for $k = 1, \ldots, d$. Then there exists a unique solution $a \in H^1(\Omega)$ of (8.22) and a constant $C > 0$ depending only $\delta$, $\bar{X}$, $S$ and $\bar{I}$, such that*

$$\|a\|_{H^1(\Omega)} \leqslant C. \tag{8.26}$$

*Proof.* Let us consider a sequence of uniformly positive diagonal tensors $X^n \in L^\infty((0, T) \times \Omega)$, $X_k^n \geqslant \bar{X}$ almost everywhere on $\Omega$ for all $n \in \mathbb{N}$, such that $X^n \to X$ in the norm topology of $L^2((0, T) \times \Omega)$ as $n \to \infty$. For each $n \in \mathbb{N}$ a unique solution $a^n \in H^1(\Omega)$ of (8.22) is constructed using the Lax-Milgram Theorem, see, e.g., [Eva10]. The continuity of the bilinear form $B : H^1(\Omega) \times H^1(\Omega) \to \mathbb{R}$ associated with (8.22),

$$B(a, \phi) := \delta \int_\Omega (X\nabla a) \cdot \nabla \phi \, dx - \int_\Omega (S - Ia)\phi \, dx,$$

follows from a straightforward application of the Cauchy-Schwarz inequality. The coercivity of $B$ follows from

$$-\int_\Omega Sa \, dx \geqslant -\frac{1}{4\bar{I}} \int_\Omega S^2 \, dx - \bar{I} \int_\Omega a^2 \, dx$$

and the uniform boundedness $I(x) \geqslant \bar{I}$. Using $\phi := a^n$ as a test function in (8.22)

gives

$$\delta \int_\Omega \nabla a^n \cdot X^n \nabla a^n \, \mathrm{d}x = \int_\Omega S a^n \, \mathrm{d}x - \int_\Omega I(a^n)^2 \, \mathrm{d}x,$$

By (8.25), the Cauchy-Schwartz inequality and the uniform boundedness $X_k^n \geqslant \bar{X} > 0$ we have

$$\delta \bar{X} \int_\Omega |\nabla a^n|^2 \, \mathrm{d}x + \frac{\bar{I}}{2} \int_\Omega (a^n)^2 \, \mathrm{d}x \leqslant \frac{1}{2\bar{I}} \int_\Omega S^2 \, \mathrm{d}x \tag{8.27}$$

and thus a uniform bound on $a^n$ in $H^1(\Omega)$.

Consequently, we can extract a subsequence converging to some $a$ weakly in $H^1(\Omega)$ and strongly in $L^2(\Omega)$. Then, it is trivial to pass to the limit in (8.22), where the term $X^n \nabla a^n$ converges to $X \nabla a$ due to the strong convergence of $X^n$ in $L^2(\Omega)$. Consequently, the limiting object $a$ verifies the weak formulation (8.22). Moreover, it satisfies the a-priori estimates (8.27) due to the weak lower semicontinuity of the respective norms. Uniqueness of the solution follows from (8.27) and the linearity of the equation. $\qquad\square$

**Remark 25.** *With a straightforward modification of its proof, we shall apply Lemma 18 for time-dependent permeability tensors $X \in L^\infty(0, T; L^2(\Omega))$ in the sequel. We then obtain the unique solution $a \in L^2(0, T; H^1(\Omega))$ satisfying the uniform estimate*

$$\|a\|_{L^2(0,T;H^1(\Omega))} \leqslant C \tag{8.28}$$

*with $C = C(\delta, \bar{X}, S, \bar{I}) > 0$.*

The following Lemma is an instance of the so-called weak-strong lemma for elliptic problems, see, e.g. Lemma 13. Here we formulate it in the time-dependent setting with $a = a(t, x)$.

**Lemma 19.** *Fix $T > 0$ and let $(X^n)_{n\in\mathbb{N}} \subset L^\infty(0, T; L^2(\Omega))$ be a sequence of diagonal tensors in $\mathbb{R}^{d\times d}$ such that for some $\bar{X} > 0$, $X_k^n \geqslant \bar{X} > 0$ almost everywhere on $(0, T) \times \Omega$, $k = 1, \ldots, d$, $n \in \mathbb{N}$. Moreover, assume that $X^n \to X$ in the norm topology of $L^2((0, T) \times \Omega)$. Let $(a^n)_{n\in\mathbb{N}}$ be a sequence of weak solutions of (8.22) with the permeability tensors $X^n$. Then $\nabla a^n$ converges to $\nabla a$ strongly in $L^q((0, T) \times \Omega)$ for any $q < 2$, where $a$ is the solution of (8.22) with permeability tensor $X$.*

*Proof.* Due to the uniform estimate on $a^n$ in $L^2(0, T; H^1(\Omega))$ of Lemma 18, $a^n$ that converges weakly in $L^2(0, T; H^1(\Omega))$ to some $a$. Since $a^n \to a$ strongly in

$L^2((0,T) \times \Omega)$, we can pass to the limit $n \to \infty$ in (8.22). With the uniform estimate on $\sqrt{X^n} \nabla a^n$ in $L^2((0,T) \times \Omega)$ provided by (8.28), the weak lower semicontinuity of the $L^2$-norm implies

$$\int_0^T \int_\Omega X \nabla a \cdot \nabla a \, \mathrm{d}x \, \mathrm{d}t = \int_0^T \int_\Omega |\sqrt{X} \nabla a|^2 \, \mathrm{d}x \, \mathrm{d}t$$
$$\leqslant \liminf_{n \to \infty} \int_0^T \int_\Omega |\sqrt{X^n} \nabla a^n|^2 \, \mathrm{d}x \, \mathrm{d}t < +\infty$$

for almost all $t > 0$. Consequently, we can use $a$ as a test function in the time-integrated version of (8.22) to obtain

$$\delta \int_0^T \int_\Omega X \nabla a \cdot \nabla a \, \mathrm{d}x \, \mathrm{d}t = \int_0^T \int_\Omega (S - Ia) a \, \mathrm{d}x \, \mathrm{d}t.$$

Then, using $a^N$ as a test function in (8.22) with $X^n$, we have

$$\lim_{N \to \infty} \delta \int_0^T \int_\Omega X^n \nabla a^n \cdot \nabla a^n \, \mathrm{d}x = \int_0^T \int_\Omega (S - Ia) a \, \mathrm{d}x \, \mathrm{d}t = \delta \int_0^T \int_\Omega X \nabla a \cdot \nabla a \, \mathrm{d}x \, \mathrm{d}t.$$

Consequently,

$$\int_0^T \int_\Omega |\sqrt{X} \nabla a|^2 \, \mathrm{d}x \, \mathrm{d}t = \lim_{n \to \infty} \int_0^T \int_\Omega |\sqrt{X^n} \nabla a^n|^2 \, \mathrm{d}x \, \mathrm{d}t,$$

so that we have the strong convergence of $\sqrt{X^n} \nabla a^n$ to $\sqrt{X} \nabla a$ in $L^2((0,T) \times \Omega)$. Now we write,

$$\int_0^T \int_\Omega |\partial_{x_k} a^n - \partial_{x_k} a| \, \mathrm{d}x \, \mathrm{d}t \leqslant \bar{X}^{-1/2} \int_0^T \int_\Omega |\sqrt{X_k} \partial_{x_k} a^n - \sqrt{X_k} \partial_{x_k} a| \, \mathrm{d}x \, \mathrm{d}t$$
$$\leqslant \bar{X}^{-1/2} \|\nabla a^n\|_{L^2((0,T) \times \Omega)} \left\| \sqrt{X_k^n} - \sqrt{X_k} \right\|_{L^2((0,T) \times \Omega)}$$
$$+ \bar{X}^{-1/2} \int_0^T \int_\Omega |\sqrt{X_k^n} \partial_{x_k} a^n - \sqrt{X_k} \partial_{x_k} a| \, \mathrm{d}x \, \mathrm{d}t,$$

for $k = 1, \dots, d$, and the first term of the right-hand side converges to zero due to the assumed strong convergence of $X^n$ in $L^2((0,T) \times \Omega)$, while the second term does so due to the strong convergence of $\sqrt{X^n} \nabla a^n$. Thus, we have the strong convergence of $\nabla a^n$ to $\nabla a$ in $L^1((0,T) \times \Omega)$. Since $\nabla a^n$ is also uniformly bounded in $L^2((0,T) \times \Omega)$, a simple consequence of the interpolation inequality [Rou13, Chapter 1] implies strong convergence in $L^q((0,T) \times \Omega)$ for $q < 2$. $\qquad \square$

**Lemma 20.** *Fix $T > 0$ and let $\nabla a \in L^2((0,T) \times \Omega)$. Let $\kappa > \gamma$ and,*

$$\kappa < 2 \quad \text{for } d \in \{1,2\}, \qquad \kappa \leqslant \frac{\gamma + 5}{4} \quad \text{for } d = 3, \tag{8.29}$$

*depending on the space dimension d. Then there exists a unique solution*

$$X_k \in L^2(0,T; H^1(\Omega)) \cap L^\infty(0,T; L^2(\Omega)) \cap C([0,T); H^{-1}(\Omega)), \qquad k = 1, \ldots, d,$$

*of* (8.23) *subject to the initial datum* (8.24) *with $X_k^0 \geqslant \bar{X}^0 > 0$ almost everywhere on $\Omega$. Moreover, the solution stays uniformly bounded away from zero on $(0,T) \times \Omega$, i.e., there exists $\bar{X} > 0$ depending on $\bar{X}^0$, $T$, $D^2$ and $\tau$, but independent of a, such that*

$$X_k \geqslant \bar{X} > 0 \qquad \text{almost everywhere on } (0,T) \times \Omega. \tag{8.30}$$

*Moreover, there exists a constant $K_0 > 0$ independent of $X$ and a such that*

$$\|X_k\|^2_{L^\infty(0,T;L^2(\Omega))} \leqslant \|X_k^0\|^2_{L^2(\Omega)} + K_0 \|\partial_{x_k} a\|^2_{L^2((0,T)\times\Omega)} \tag{8.31}$$

*and, for $k = 1, \ldots, d$,*

$$\|\nabla X_k\|^2_{L^2(0,T;L^2(\Omega))} \leqslant \|X_k^0\|^2_{L^2(\Omega)} + K_0 \|\partial_{x_k} a\|^2_{L^2((0,T)\times\Omega)}. \tag{8.32}$$

**Remark 26.** *Observe that the necessary condition for the mutual validity of the assumptions $\kappa > \gamma$ and* (8.29) *is $\gamma, \kappa < 2$ for $d \in \{1,2\}$ and $\gamma, \kappa \leqslant 5/3$ for $d = 3$.*

*Proof.* Let us fix $k \in \{1, \ldots, d\}$ and use $\psi := X_k$ as a test function in (8.23),

$$\frac{1}{2}\frac{\mathrm{d}}{\mathrm{d}t} \int_\Omega X_k^2 \,\mathrm{d}x = -D^2 \int_\Omega |\nabla X_k|^2 \,\mathrm{d}x + \int_\Omega |\partial_{x_k} a|^\kappa X_k^{\kappa-\gamma+1} \,\mathrm{d}x - \tau \int_\Omega X_k^2 \,\mathrm{d}x, \quad (8.33)$$

where we used the identity $q_k = X_k \partial_{x_k} a$. Using the Hölder inequality with exponents $p$ and $p'$, $\frac{1}{p} + \frac{1}{p'} = 1$, we have

$$\int_\Omega |\partial_{x_k} a|^\kappa X_k^{\kappa-\gamma+1} \,\mathrm{d}x \leqslant C_\varepsilon \int_\Omega |\partial_{x_k} a|^{\kappa p} \,\mathrm{d}x + \varepsilon \int_\Omega |X_k|^{(\kappa-\gamma+1)p'} \,\mathrm{d}x \tag{8.34}$$

for $\varepsilon > 0$ and a suitable constant $C_\varepsilon$. Due to the assumed $L^2$-integrability of $\partial_{x_k} a$, we choose $\kappa p = 2$, so that $p' = \frac{2}{2-\kappa}$. Denote $\alpha := (\kappa - \gamma + 1)p'$ and observe that $\alpha > 0$ due to the assumption $\kappa > \gamma$. Let us distinguish the following two cases: If

$\alpha \leqslant 2$, then by the Hölder inequality we have

$$\int_\Omega |X_k|^\alpha \, \mathrm{d}x \leqslant C_\Omega \int_\Omega |X_k|^2 \, \mathrm{d}x,$$

so that (8.33) and (8.34) imply

$$\frac{1}{2}\frac{\mathrm{d}}{\mathrm{d}t}\int_\Omega X_k^2 \, \mathrm{d}x \leqslant -D^2 \int_\Omega |\nabla X_k|^2 \, \mathrm{d}x + C_\varepsilon \int_\Omega |\partial_{x_k} a|^2 \, \mathrm{d}x - (\tau - \varepsilon C_\Omega)\int_\Omega X_k^2 \, \mathrm{d}x,$$

and choosing $\varepsilon > 0$ such that $\tau - \varepsilon C_\Omega > 0$ directly implies the a-priori estimates (8.31) and (8.32). On the other hand, if $\alpha > 2$, we apply the Sobolev inequality [Eva10]

$$\int_\Omega |X_k|^\alpha \, \mathrm{d}x \leqslant C_S \left( \int_\Omega |\nabla X_k|^2 \, \mathrm{d}x + \int_\Omega |X_k|^2 \, \mathrm{d}x \right)$$

with $C_S = C_S(\Omega)$ the Sobolev constant. Depending on the space dimension, we have:

- For $d \in \{1, 2\}$,

$$\|X_k\|_{L^\alpha(\Omega)} \leqslant C_S \left( \int_\Omega |\nabla X_k|^2 \, \mathrm{d}x + \int_\Omega |X_k|^2 \, \mathrm{d}x \right) \tag{8.35}$$

  for any $\alpha < \infty$, i.e., we admit any $p > 1$ and, consequently, $\kappa < 2$.

- For $d = 3$ we have (8.35) for $\alpha \leqslant 6$, i.e., we need $(\kappa - \gamma + 1)p' = \frac{2(\kappa - \gamma + 1)}{2 - \kappa} \leqslant 6$, which gives the condition $\kappa \leqslant \frac{\gamma + 5}{4}$.

Consequently, we have

$$\frac{1}{2}\frac{\mathrm{d}}{\mathrm{d}t}\int_\Omega X_k^2 \, \mathrm{d}x \leqslant -(D^2 - \varepsilon C_S)\int_\Omega |\nabla X_k|^2 \, \mathrm{d}x + C_\varepsilon \int_\Omega |\partial_{x_k} a|^2 \, \mathrm{d}x - (\tau - \varepsilon C_S)\int_\Omega X_k^2 \, \mathrm{d}x,$$

and choosing $\varepsilon > 0$ such that $\varepsilon C_S < \min\{D^2, \tau\}$ directly implies the a-priori estimates (8.31) and (8.32). The uniform positivity (8.30) follows from the fact that solutions $u = u(t, x)$ of the linear parabolic equation $\frac{\partial u}{\partial t} = D^2 \Delta u - \tau u$ are subsolutions to (8.17), and they remain uniformly positive on bounded time intervals for uniformly positive initial data, see, e.g., [Eva10].

Finally, note that we have the identity (in distributional sense)

$$\frac{\partial X_k}{\partial t} = D^2 \Delta X_k + |\partial_{x_k} a|^\kappa X_k^{\kappa - \gamma} - \tau X_k.$$

An easy calculation reveals that, for the aforementioned range of $\kappa$ and $\gamma$,

$$|\partial_{x_k} a|^\kappa X_k^{\kappa - \gamma} \in L^1(0, T; L^{6/5}(\Omega)) \subset L^1(0, T; H^{-1}(\Omega)),$$

implying $\frac{\partial X_k}{\partial t} \in L^1(0, T; H^{-1}(\Omega))$, so that $X_k \in C([0, T); H^{-1}(\Omega))$, see, e.g., [Rou13, Chapter 7]. □

**Theorem 15.** *Fix $T > 0$ and let $\kappa > \gamma$, and, in dependence of the space dimension $d$,*

$$\kappa < \frac{\gamma + 4}{3} \quad \text{for } d \in \{1, 2\}, \qquad \kappa \quad < \frac{\gamma + 5}{4} \quad \text{for } d = 3. \tag{8.36}$$

*Then the system* (8.22)–(8.23) *subject to the initial datum* (8.24) *with $X_k^0 \geqslant \bar{X}^0 > 0$ almost everywhere on $\Omega$ admits a weak solution $(X, a)$ on $(0, T)$ such that*

$$
\begin{aligned}
X_k &\in L^\infty(0, T; L^2(\Omega)) \cap L^2(0, T; H^1(\Omega)) \cap C([0, T); H^{-1}(\Omega)), \\
a &\in L^\infty(0, T; L^2(\Omega)) \cap L^2(0, T; H^1(\Omega)) \cap C([0, T); W^{-1,4/3}(\Omega)).
\end{aligned}
\tag{8.37}
$$

*Proof.* We construct a solution using the Schauder fix-point theorem on the set

$$
\begin{aligned}
\mathcal{B}_T := \Big\{ &X \in (L^\infty(0, T; L^2(\Omega)))_{\text{diag}}^{d \times d}; \; \|X_k\|_{L^\infty(0,T;L^2(\Omega))}^2 \leqslant \|X_k^0\|_{L^2(\Omega)}^2 + K_0 B_T^2, \\
&X_k \geqslant \bar{X} \text{ almost everywhere on } (0, T) \times \Omega, \; k = 1, \ldots, d \Big\}.
\end{aligned}
$$

Here $(L^\infty(0, T; L^2(\Omega)))_{\text{diag}}^{d \times d}$ denotes the space of diagonal $d \times d$-tensors with entries in $L^\infty(0, T; L^2(\Omega))$, and $K_0$ and $\bar{X}$ are the constant defined in Lemma 20; note that they depend only on $\bar{X}^0$, $T$, and the parameters $\kappa$, $\gamma$, $D^2$ and $\tau$. Moreover, we denoted

$$B_T^2 := \frac{1}{2\delta\bar{X}} \left( (Te^T + 1) \|a^0\|_{L^2(\Omega)}^2 + Te^T \|S\|_{L^2(\Omega)}^2 \right).$$

The set $\mathcal{B}_T$ shall be equipped with the norm topology of $L^2((0, T) \times \Omega)$. Obviously, $\mathcal{B}_T$ is nonempty, convex and closed. We define the mapping $\Phi : \mathcal{B}_T \to L^\infty(0, T; L^2(\Omega))$,

$$\Phi : X \in \mathcal{B}_T \mapsto \tilde{X},$$

where given $X \in \mathcal{B}_T$ we construct $a$ the unique weak solution of (8.22) by Lemma 18, and, subsequently, construct $\tilde{X}$ as the unique weak solution of (8.23) by Lemma 20.

Clearly, due to the a-priori estimates (8.26) and (8.31), $\tilde{X} \in \mathcal{B}_T$.

To prove the continuity of the mapping $\Phi$, let us consider a sequence $(X_n)_{n \in \mathbb{N}} \subset \mathcal{B}_T$, converging to $X \in \mathcal{B}_T$ in the norm topology of $L^2((0,T) \times \Omega)$. Denote $(a_n)_{n \in \mathbb{N}}$ and, resp., $a$, the solutions of (8.22) corresponding to $X_n$ and, resp., $X$. Then, due to Lemma 19, $\nabla a_n$ converges to $\nabla a$ in the norm topology of $L^q((0,T) \times \Omega)$ for any $q < 2$. Let $\tilde{X}_n := \Phi(X_n)$ and $\tilde{X} := \Phi(X)$. Due to Lemma 20 and the Aubin-Lions theorem, a subsequence of $\tilde{X}_n$ converges strongly to some $\tilde{X}^*$ in $L^2(0,T;L^q(\Omega))$ with $q < \infty$ if $d \in \{1,2\}$ and $q = 6$ if $d = 3$. The limit passage $n \to \infty$ in (8.23) is trivial for the linear terms. For the term $|\partial_{x_k} a_n|^\kappa \tilde{X}_n^{\kappa-\gamma}$ we observe that, due to Lemma 19, the term $|\partial_{x_k} a_n|^\kappa$ converges to $|\partial_{x_k} a|^\kappa$ in the norm topology of $L^q((0,T) \times \Omega)$ for $q < 2/\kappa$. Moreover:

- For $d \in \{1,2\}$, the interpolation inequality between the spaces $L^\infty(0,T;L^2(\Omega))$ and $L^2(0,T;L^q(\Omega))$ with $q < \infty$ implies that $\tilde{X}^n$ is uniformly bounded, and thus converges, in the norm topology of $L^q((0,T) \times \Omega)$ for $q < 4$. Consequently, since $\kappa < 2$, the product $|\partial_{x_k} a_n|^\kappa \tilde{X}_n^{\kappa-\gamma}$ converges strongly in (at least) $L^1((0,T) \times \Omega)$ to $|\partial_{x_k} a|^\kappa (\tilde{X}_n^*)^{\kappa-\gamma}$ if $\frac{\kappa}{2} + \frac{\kappa-\gamma}{4} < 1$, which is equivalent to $\kappa < \frac{\gamma+4}{3}$.

- For $d = 3$ the interpolation inequality between the spaces $L^\infty(0,T;L^2(\Omega)$ and $L^2(0,T;L^6(\Omega))$ implies that $\tilde{X}^n$ is uniformly bounded in the norm topology of $L^{10/3}((0,T) \times \Omega)$. Then the sufficient condition for $L^1$-convergence of the product $|\partial_{x_k} a_n|^\kappa \tilde{X}_n^{\kappa-\gamma}$ reads $\frac{\kappa}{2} + \frac{3(\kappa-\gamma)}{10} < 1$, which is equivalent to $\kappa < \frac{10+3\gamma}{8}$. This condition is weaker than (8.36).

By the uniqueness of solutions of (8.22), we conclude that $\tilde{X}^* = \tilde{X}$, i.e., the mapping $\Phi$ is continuous on $\mathcal{B}_T$ with respect to the norm topology of $L^2((0,T) \times \Omega)$.

To prove the compactness of the mapping $\Phi$, we employ the Aubin-Lions lemma [Aub63]. Let us again consider a sequence $(X_n)_{n \in \mathbb{N}} \subset \mathcal{B}_T$ and denote $\tilde{X}_n := \Phi(X_n)$. Due to the a-priori estimates (8.26) and (8.31), (8.32), the sequence $\tilde{X}_n$ is bounded in $L^\infty(0,T;L^2(\Omega))$ and in $L^2(0,T;H^1(\Omega))$. Moreover, $\partial_t \tilde{X}_n$ is bounded in $L^1(0,T;H^{-1}(\Omega))$. Then, since $H^1(\Omega)$ is compactly embedded into $L^2(\Omega)$ and $L^2(\Omega) \subset H^{-1}(\Omega)$, the Aubin-Lions theorem provides the relative compactness of the sequence $\tilde{X}_n$ with respect to the norm topology of $L^2((0,T) \times \Omega))$. Consequently, the Schauder fix-point theorem provides a solution $(X,a)$ of the system (8.22)–(8.24), satisfying (8.37). $\qquad\square$

**Remark 27.** *For the case $\kappa = \gamma = 2$ the system (8.18) simplifies to*

$$\frac{\partial X_k}{\partial t} = D^2 \Delta X_k + (\partial_{x_k} a)^2 - \tau X_k. \tag{8.38}$$

*Then, (8.19), (8.38) is similar to the system studied in Chapter 6 and Chapter 7, the main difference being that the permeability tensor in the elliptic equation is of the form $rI + X$ in Chapter 6 and Chapter 7, where $r > 0$ is a constant. The significant property of (8.19), (8.38) is its energy-dissipation structure. Indeed, defining*

$$\mathcal{E}[X] := \frac{D^2}{2} \sum_{k=1}^{d} \int_{\Omega} |\nabla X_k|^2 \, dx + \int_{\Omega} \nabla a \cdot X \nabla a \, dx + \tau \sum_{k=1}^{d} \int_{\Omega} X_k^2 \, dx,$$

*where $a = a[X]$ is the unique weak solution of (8.19), a simple calculation (see Lemma 10) reveals that,*

$$\frac{d}{dt} \mathcal{E}[X] = -\sum_{k=1}^{d} \int_{\Omega} \left( \frac{\partial X_k}{\partial t} \right)^2 \, dx$$

*along the solutions of (8.19), (8.38). The energy dissipation naturally provides uniform a-priori estimates on $X$ and $a$ in the energy space. However, these still do not allow us to extend the validity of Theorem 15 to $\kappa = \gamma = 2$. The problem is that in the proof of continuity of the fix-point mapping $\Phi$, it is not clear how to pass to the (weak) limit in the sequence $(\partial_{x_k} a)^2$. Note that Lemma 19 only provides (strong) convergence of $\partial_{x_k} a$ in $L^q((0, T) \times \Omega)$ with $q < 2$.*

**Remark 28** (Steady states of the system (8.18), (8.19) with $D^2 = 0$). *The steady states of the system (8.18), (8.19) with $D^2 = 0$ satisfy, in the weak sense,*

$$\delta \nabla \cdot (X \nabla a) + S - Ia = 0, \tag{8.39}$$

$$|\partial_{x_k} a|^\kappa X_k^{\kappa - \gamma} - \tau X_k = 0, \tag{8.40}$$

*for $k = 1, \dots, d$, with $q_k = X_k \partial_{x_k} a$. For $\kappa > \gamma > 0$, (8.40) implies that there exist measurable sets $\mathcal{A}_k \subset \Omega$, $k = 1, \dots, d$, such that*

$$X_k = \left( \frac{|\partial_{x_k} a|^\kappa}{\tau} \right)^{\frac{1}{\gamma - \kappa + 1}} \chi_k,$$

*where $\chi_k = \chi_k(x)$ is the characteristic function of $\mathcal{A}_k$. Inserting this into (8.39),*

*we obtain*

$$-\delta\tau^{\frac{1}{\kappa-\gamma-1}} \sum_{k=1}^{d} \partial_{x_k} \left( \chi_k |\partial_{x_k} a|^{\frac{\kappa}{\gamma-\kappa+1}} \partial_{x_k} a \right) = S - Ia. \qquad (8.41)$$

*Due to the presence of the characteristic functions $\chi_k$, this is a strongly degenerate elliptic equation, rendering its analysis a very challenging task, which we leave for a future work. Let us only note that the degeneracy in (8.41) induces strong nonuniqueness of its solutions. Consequently, it is necessary to equip (8.41) with suitable selection criteria in order to obtain unique solutions. This is to be done through further modelling inputs. For $\kappa = \gamma > 0$, contrarily, (8.40) gives $X_k = \tau^{-1} |\partial_{x_k} a|^{\kappa}$, and (8.39) reads*

$$-\delta\tau^{-1} \sum_{k=1}^{d} \partial_{x_k} \left( |\partial_{x_k} a|^{\kappa} \partial_{x_k} a \right) = S - Ia. \qquad (8.42)$$

*Equipped with the no-flux boundary condition (8.20), its weak formulation reads*

$$\delta\tau^{-1} \sum_{k=1}^{d} \int_{\Omega} |\partial_{x_k} a|^{\kappa} (\partial_{x_k} a)(\partial_{x_k} \psi) \, dx + \int_{\Omega} (a - S)\psi \, dx = 0 \qquad (8.43)$$

*for all test functions $\psi \in C^{\infty}(\Omega)$. Weak solutions $a \in W^{1,\kappa+2}(\Omega)$ of (8.43) are constructed as the global minima of the functional $\mathcal{F} : W^{1,\kappa+2} \to \mathbb{R}$,*

$$\mathcal{F}[a] := \frac{\delta\tau^{-1}}{\kappa+2} \sum_{k=1}^{d} \int_{\Omega} |\partial_{x_k} a|^{\kappa+2} \, dx + \frac{1}{2} \int_{\Omega} a^2 \, dx - \int_{\Omega} Sa \, dx.$$

*Obviously, for $\kappa > 0$ the functional is uniformly convex. Moreover, a straightforward application of the Cauchy-Schwartz inequality implies boundedness below and coercivity of $\mathcal{F}$ with respect to the norm of $W^{1,\kappa+2}(\Omega)$. Then the classical theory (see, e.g., [Eva10]) provides the existence of a unique minimiser $a \in W^{1,\kappa+2}(\Omega)$ of $\mathcal{F}$, which is the unique solution of the corresponding Euler-Lagrange equation (8.43).*

## 8.7 Conclusion

In this chapter, we proposed a new dynamic modelling framework for leaf venation, which is not dependent on polar localisation of auxin transporters. Given that it is still an open question how you get leaf veins, also in the absence of transport

activity, we argue that the current work is of interest since it the first model, to our knowledge, trying to address this question. Due to its new description of possible mechanisms in leaf venation, our model is of interest to the modelling community. Our work can be regarded as a general modelling framework for auxin transport, which can be equipped or extended with various biologically relevant features that would then produce experimentally testable hypotheses. The main advantage is the rather simple form of the model, allowing a rigorous mathematical analysis, which is one of the main aims of this chapter. Moreover, it facilitates the derivation of a continuum limit, which can capture network growth and is expected to exhibit a much richer patterning capacity, bearing again potential for delivering testable hypotheses. The analytical and numerical study of the continuum model is currently a work in progress.

# Chapter 9

# Conclusion and outlook

In this thesis, we studied two different PDE models, motivated by the simulation of fingerprint patterns and biological transport networks.

## 9.1 Part I: Anisotropic interaction equations

In Part I, we focused on modelling fingerprint patterns which is not only of great interest in the biological community, but also in forensic science and increasingly in biometric applications where large fingerprint databases are required for developing, validating and comparing the performance of fingerprint identification algorithms. Besides, similar models have proven to be very useful for modelling swarming in nature, including flocks of birds or colonies of bacteria/cells, and has got significant attention in the scientific community recently due to its great practical relevance.

The formation of fingerprints can mathematically be described as the interaction of a large number of so-called Merkel cells, which align themselves due to anisotropic repulsive-attractive interaction forces and form our fingerprint lines. The central novelty in this model, leading to realistic patterns as observed in nature, is an anisotropy induced by an underlying tensor field. This additional anisotropy is crucial for the accurate description of real-world phenomena, but also makes the analysis significantly harder. Due to the non-existence of an interaction potential and a gradient flow formulation, much of the existing analytic theory does not apply to these anisotropic interaction models and new methods are required for studying these models rigorously.

We studied the role of anisotropic interaction in Chapter 2 and proposed a bio-inspired model to simulate realistic fingerprint patterns in Chapter 3, featuring

important properties of a biologically meaningful fingerprint development model. We gave a rigorous proof of the stability of line patterns in Chapter 4. Moreover, we investigated the role of nonlinear diffusion on the widening of line patterns both analytically and numerically, and simulated realistic fingerprint patterns efficiently in Chapter 5.

Part I (Chapters 2–5) is mainly based on four papers [BDK$^+$18, CDKS18, CDKS19, DGH$^+$19] which are among the first works on the analysis of anisotropic interaction models. Using innovations on the modelling, analysis, and computational methods, this research on anisotropic interaction is a crucial step towards the accurate description of real-world phenomena.

Possible future research projects can be subdivided into two categories: anisotropic pattern formation in more realistic (and mathematically more challenging) settings, and the application of the obtained results to real-world phenomena.

In Part I, we investigated anisotropic pattern formation and the role of anisotropic interaction on stationary solutions, mainly on $\mathbb{R}^2$ and on the two-dimensional torus $\mathbb{T}^2$. An interesting future aspect of this research would be the study of anisotropic pattern formation in more general settings which are of practical relevance. While studying anisotropic pattern formation in the plane, has given us a better understanding about the possible patterns which might arise, the form of the underlying surface may also influence the resulting stationary patterns. Motivated by the fact that many complex patterns in nature occur on curved or evolving surfaces, anisotropic pattern formation on these more general surfaces can be studied in the future. In terms of the application to fingerprint simulations, note that our fingerprints are not on flat surface and hence it is of interest to understand anisotropic interaction on curved surfaces in higher dimensions. To mimic the growth of fingerprints, anisotropic interaction on evolving surfaces may also be investigated.

While we studied the impact of the underlying tensor field on stationary solutions in this thesis, an interesting question which arises is whether for a given pattern, a tensor field can be estimated such that the stationary solution obtained with this tensor field as an input is close to the original pattern with respect to the Wasserstein distance. This approach results in an optimal control problem whose solution would allow us to produce any desired pattern as stationary solution to the anisotropic interaction model.

The collection of large databases of real fingerprints is usually very cost-intensive, requires time and effort, and in many countries, it is constrained by laws addressing data protection and privacy. Therefore it is vital to simulate large fingerprint

databases on a computer. Our bio-inspired model for the creation of synthetic fingerprint patterns does not only allow us to simulate fingerprint patterns as stationary solutions, but also to adjust the distances between the fingerprint lines by rescaling the model parameters. This is crucial for modelling fingerprint patterns with specific features in the future. As part of this work, the numerical results can be tested for realness. The distinction between real and synthetics could be based on [GH14] where histograms of minutiae and ridge frequencies are considered. Another procedure for distinguishing real and synthetic fingerprints is based on the underlying stress field only [IGHO18].

## 9.2 Part II: Partial differential equations for biological networks

Part II focused on biological transportation networks which are ubiquitous in living systems such as leaf venation in plants, blood circulatory systems, and neural networks. Understanding the development, function, and adaptation of biological transportation networks has been of long-standing interest in the scientific community, including mathematics due to the complexity of the models. Using methods from various fields within mathematics, we investigated the global existence of solutions of the microscopic and the associated macroscopic models in Chapter 6, which can be written as the unusual coupling of a linear system and a system of ordinary differential equations on a graph and its continuum counterpart. Moreover, we proved the rigorous limit between the microscopic and macroscopic model in Chapter 7 for the two-dimensional regular setting which required the formal derivation of an appropriate macroscopic model. These analytical results were complemented by numerical simulations of the discrete model. Based on this model, we proposed an adapted model in the cellular context for leaf venation, investigated the model analytically and showed numerically that it can produce branching vein patterns in Chapter 8.

Part II (Chapters 6–8) is based on the papers [HJKM19, HKM19a, HKM19b]. In particular, this research resulted in a better understanding of the model suggested by Hu and Cai and its continuum counterpart.

In terms of the application to leaf venation, we showed similarities in crude vein formation in Chapter 8, but more elaborate investigations are essential, such as combining the current description with PIN-based mechanisms and testing with

more complex configurations of auxin sources and sinks. Besides, it is important to understand the impact of the levels of auxin to the pattern formation. These numerical results will contribute to a better understanding of the pattern formation in this model for leaf venation.

In reality, the venation patterns appear while the leaf is growing. Our simulations (and many previous PIN-based flux models simulated on static geometries) do not consider any growth processes. Changing the extension of connecting sources and sinks in the model would be expected to lead to differences in patterns in the final leaf. These changes of patterns when PINs are removed would be very interesting to investigate.

The main advantage of our discrete modelling approach for leaf venation is the rather simple form of the model, allowing a rigorous mathematical analysis and in particular the formal derivation of a continuum limit, which can capture network growth. It is expected to exhibit a much richer patterning capacity, bearing again potential for delivering testable hypotheses. The analytical and numerical study of the continuum model is currently a work in progress.

Differential equations on graphs and networks are not only crucial for modelling biological or social transportation networks, but also play an important role in many data science and machine learning tasks, and can be regarded as the key area of research for solving data problems such as linking graph and the associated macroscopic models via $\Gamma$-convergence. As part of future research, more general systems of differential equations on graphs can be investigated analytically and numerically.

# Bibliography

[AAFM16]  G. Albi, M. Artina, M. Foransier, and P. A. Markowich. Biological trans-
portation networks: Modeling and simulation. *Anal. Appl.*, 14(01):185–206,
2016. (Cited on pages 22, 25, 206, and 240).

[ABCvB14]  G. Albi, D. Balagué, J. A. Carrillo, and J. von Brecht. Stability analysis of
flock and mill rings for second order models in swarming. *SIAM J. Appl.
Math.*, 74(3):794–818, 2014. (Cited on pages 2, 6, and 108).

[ABH+17]  G. Albi, M. Burger, J. Haskovec, P. Markowich, and M. Schlottbom. Contin-
uum modelling of biological network formation. In N. Bellomo, P. Degond,
and E. Tadmor, editors, *Active Particles, Volume 1: Advances in Theory,
Models, and Applications*, Modeling and Simulation in Science, Engineering
and Technology. Birkhäuser, 2017. (Cited on pages 20, 21, 22, 25, 206, 227,
239, 240, 250, 274, and 275).

[AGS05]  L. A. Ambrosio, N. Gigli, and G. Savaré. *Gradient flows in metric spaces and
in the space of probability measures*. Lectures in Mathematics. Birkhäuser,
2005. (Cited on pages 5, 74, 171, and 173).

[ASGMC16]  K. Abley, S. Sauret-Güeto, A. Marée, and E. Coen. Formation of polarity
convergences underlying shoot outgrowths. *eLife*, page e18165, 2016. (Cited
on page 272).

[AT89]  M. Allen and D. Tildesley. *Computer Simulation of Liquids*. Oxford Univ.
Press, 1989. (Cited on page 88).

[Aub63]  J.-P. Aubin. Un théoréme de compacité. *C. R. Acad. Sci. Paris.*, 256:5042–
5044, 1963. (Cited on page 300).

[Bab91]  W. J. Babler. Embryologic development of epidermal ridges and their con-
figurations. *Birth defects original article series*, 27 2:95–112, 1991. (Cited
on page 72).

[Bal09]      P. Ball. *Nature's patterns: A tapestry in three parts.* Oxford Univ. Press, 2009. (Cited on pages 7 and 71).

[BBL+16]    N. Bhatia, B. Bozorg, A. Larsson, C. K. Ohno, H. Jönsson, and M. G. Heisler. Auxin acts through monopteros to regulate plant cell polarity and pattern phyllotaxis. *Current Biology*, 26(23):3202–3208, 2016. (Cited on page 272).

[BBNS07]    N. Bellomo, A. Bellouquid, J. Nieto, and J. Soler. Multicellular biological growing systems: Hyperbolic limits towards macroscopic description. *Math. Models Methods Appl. Sci.*, 17:1675–1692, 2007. (Cited on page 15).

[BCC+08a]   M. Ballerini, N. Cabibbo, R. Candelier, A. Cavagna, E. Cisbani, I. Giardina, V. Lecomte, A. Orlandi, G. Parisi, A. Procaccini, M. Viale, and V. Zdravkovic. Interaction ruling animal collective behaviour depends on topological rather than metric distance: evidence from a field study. *Proc. Natl. Acad. Sci. USA*, 105:1232–1237, 2008. (Cited on page 2).

[BCC08b]    A. Blanchet, V. Calvez, and J. A. Carrillo. Convergence of the Mass-Transport Steepest Descent Scheme for the Subcritical Patlak–Keller–Segel Model. *SIAM J. Numer. Anal.*, 46(2):691–721, 2008. (Cited on page 2).

[BCF+00]    J. R. Banavar, F. Colaiori, A. Flammini, A. Maritan, and A. Rinaldo. Topology of the fittest transportation network. *Phys. Rev. Lett.*, 84(20):4745–4748, 2000. (Cited on page 19).

[BCL09]     A. L. Bertozzi, J. A. Carrillo, and T. Laurent. Blow-up in multidimensional aggregation equations with mildly singular interaction kernels. *Nonlinearity*, 22(3):683, 2009. (Cited on pages 5, 6, 74, and 171).

[BCLR13a]   D. Balagué, J. A. Carrillo, T. Laurent, and G. Raoul. Dimensionality of local minimizers of the interaction energy. *Arch. Ration. Mech. Anal.*, 209(3):1055–1088, 2013. (Cited on pages 6, 7, 74, 171, and 172).

[BCLR13b]   D. Balagué, J. A. Carrillo, T. Laurent, and G. Raoul. Nonlocal interactions by repulsive-attractive potentials: radial ins/stability. *Phys. D*, 260:5–25, 2013. (Cited on pages 5, 6, 7, 40, 74, 108, and 171).

[BCM00]     S. Boi, V. Capasso, and D. Morale. Modeling the aggregative behavior of ants of the species polyergus rufescens. *Nonlinear Anal. Real World Appl.*, 1(1):163–176, 2000. (Cited on page 2).

[BCM07]    M. Burger, V. Capasso, and D. Morale. On an aggregation model with long
           and short range interactions. *Nonlinear Anal. Real World Appl.*, 8(3):939–
           958, 2007. (Cited on page 2).

[BCY14]    D. Balagué, J. A. Carrillo, and Y. Yao. Confinement for repulsive-attractive
           kernels. *Discrete Cont. Dyn. Syst. Ser. B*, 19:1227–1248, 2014. (Cited on
           pages 6, 74, and 171).

[BD08]     M. Burger and M. DiFrancesco. Large time behavior of nonlocal aggregation
           models with nonlinear diffusion. *Netw. Heterog. Media*, 3(4):749–785, 2008.
           (Cited on pages 6 and 173).

[BDFF13]   M. Burger, M. Di Francesco, and M. Franek. Stationary states of quadratic
           diffusion equations with long-range attraction. *Commun. Math. Sci.*,
           11(3):709–738, 2013. (Cited on pages 173, 180, 185, and 186).

[BDK+18]   M. Burger, B. Düring, L. M. Kreusser, P. A. Markowich, and C.-B.
           Schönlieb. Pattern formation of a nonlocal, anisotropic interaction model.
           *Math. Models Methods Appl. Sci.*, 28(03):409–451, 2018. (Cited on pages xi,
           27, 28, 35, 74, 109, 110, 112, 114, 158, 168, 170, 172, 176, and 306).

[BDP06]    A. Blanchet, J. Dolbeault, and B. Perthame. Two-dimensional keller-segel
           model: Optimal critical mass and qualitative properties of the solutions.
           *Electron. J. Differential Equations*, 44:1–33, 2006. (Cited on page 2).

[Bed11]    J. Bedrossian. Global minimizers for free energies of subcritical aggregation
           equations with degenerate diffusion. *Appl. Math. Lett.*, 24(11):1927–1932,
           2011. (Cited on page 173).

[BFH14]    M. Burger, R. Fetecau, and Y. Huang. Stationary states and asymptotic
           behavior of aggregation models with nonlinear local repulsion. *SIAM J.
           Appl. Dyn. Syst.*, 13(1):397–424, 2014. (Cited on page 173).

[BGL12]    A. L. Bertozzi, J. B. Garnett, and T. Laurent. Characterization of radially
           symmetric finite time blowup in multidimensional aggregation equations.
           *SIAM J. Math. Anal.*, 44(2):651–681, 2012. (Cited on pages 6 and 37).

[BHD+07]   D. P. Bebber, J. Hynes, P. R. Darrah, L. Boddy, and M. D. Fricker. Biolog-
           ical solutions to transport network design. *Proc. R. Soc. B*, 274:2307–2315,
           2007. (Cited on pages 18 and 206).

[Bil71]    P. Billingsley. *Weak convergence of measures: Applications in probability.*
           Society for Industrial and Applied Mathematics, Philadelphia, 1971. (Cited
           on page 185).

# BIBLIOGRAPHY

[Bir07]     B. Birnir. An ode model of the motion of pelagic fish. *J. Stat. Phys.*, 128(1):535–568, 2007. (Cited on page 2).

[BL07]      A. L. Bertozzi and T. Laurent. Finite-time blow-up of solutions of an aggregation equation in $\mathbb{R}^n$. *Comm. Math. Phys.*, 274(3):717–735, 2007. (Cited on page 6).

[BLL12]     A. L. Bertozzi, T. Laurent, and F. Léger. Aggregation and spreading via the newtonian potential: The dynamics of patch solutions. *Math. Models Methods Appl. Sci.*, 22(supp01):1140005, 2012. (Cited on pages 5, 6, 74, and 171).

[BLR11]     A. L. Bertozzi, T. Laurent, and J. Rosado. $L^p$ theory for the multidimensional aggregation equation. *Comm. Pure Appl. Math.*, 64(1):45–83, 2011. (Cited on pages 5 and 13).

[BM07]      S. Bohn and M. O. Magnasco. Structure, scaling, and phase transition in the optimal transport network. *Phys. Rev. Lett.*, 98:088702, 2007. (Cited on page 19).

[BPR14]     D. Bourne, M. A. Peletier, and S. Roper. Hexagonal patterns in a simplified model for block copolymers. *SIAM Journal of Applied Maths*, 74:1315–1337, 2014. (Cited on page 7).

[BPT14]     D. Bourne, M. A. Peletier, and F. Theil. Optimality of the triangular lattice for a particle system with Wasserstein interaction. *Comm. Math. Phys.*, 329(1):117–140, 2014. (Cited on page 7).

[Bra02]     A. Braides. *Gamma-convergence for Beginners.* Oxford Lecture Series in Mathematics and Its Applications. Oxford Univ. Press, 2002. (Cited on page 239).

[BS12]      N. Bellomo and J. Soler. On the mathematical theory of the dynamics of swarms viewed as complex systems. *Math. Models Methods Appl. Sci.*, 22(1), 2012. (Cited on pages 6 and 74).

[BSK+15]    A. L. Bertozzi, H. Sun, T. Kolokolnikov, D. Uminsky, and J. H. von Brecht. Ring patterns and their bifurcations in a nonlocal model of biological swarms. *Commun. Math. Sci.*, 13(4):955–985, 2015. (Cited on pages 2, 5, 6, 7, 108, 122, 123, 171, and 172).

[BT11]      A. J. Bernoff and C. M. Topaz. A primer of swarm equilibria. *SIAM J. Appl. Dyn. Syst.*, 10:212–250, 2011. (Cited on pages 2, 6, 74, and 171).

[BV05]     M. Bodnar and J. J. L. Velazquez. Derivation of macroscopic equations for individual cell-based models: a formal approach. *Math. Methods Appl. Sci.*, 28(15):1757–1779, 2005. (Cited on page 10).

[CC95]     G. E. Cantarella and E. Cascetta. Dynamic processes and equilibrium in transportation networks: towards a unifying theory. *Transp. Sci.*, 29:305–329, 1995. (Cited on pages 18 and 206).

[CCG⁺10]   A. Cavagna, A. Cimarelli, I. Giardina, G. Parisi, R. Santagati, F. Stefanini, and R. Tavarone. From empirical data to inter-individual interactions: unveiling the rules of collective animal behavior. *Math. Models Methods Appl. Sci.*, 20, 2010. (Cited on page 2).

[CCH14a]   J. A. Carrillo, A. Chertock, and Y. Huang. A finite-volume method for nonlinear nonlocal equations with a gradient flow structure. *Commun. Comput. Phys.*, 17(1):233–258, 2014. (Cited on pages 167, 173, 174, and 190).

[CCH14b]   J. A. Carrillo, M. Chipot, and Y. Huang. On global minimizers of repulsive–attractive power-law interaction energies. *Philos. Trans. Roy. Soc. A*, 372(2028), 2014. (Cited on pages 7 and 172).

[CCH14c]   J. A. Carrillo, Y.-P. Choi, and M. Hauray. The derivation of swarming models: Mean-field limit and Wasserstein distances. In *Collective Dynamics from Bacteria to Crowds: An Excursion Through Modeling, Analysis and Simulation*, pages 1–46. Springer Vienna, Vienna, 2014. (Cited on pages 13, 14, and 15).

[CCP15]    J. A. Cañizo, J. A. Carrillo, and F. S. Patacchini. Existence of compactly supported global minimisers for the interaction energy. *Arch. Ration. Mech. Anal.*, 217(3):1197–1217, 2015. (Cited on pages 6, 74, and 171).

[CCY19]    J. Carrillo, K. Craig, and Y. Yao. Aggregation-diffusion equations: dynamics, asymptotics, and singular limits. In N. Bellomo, P. Degond, and E. Tadmor, editors, *Active Particles, Volume 2: Advances in Theory, Models, and Applications*, Modeling and Simulation in Science, Engineering and Technology, pages 65–108. Birkhäuser, 2019. (Cited on page 173).

[CDF⁺03]   S. Camazine, J.-L. Deneubourg, N. R. Franks, J. Sneyd, G. Theraulaz, and E. Bonabeau. Self-organization in biological systems. *Princeton Univ. Press, Princeton*, 2003. (Cited on page 2).

[CDFF⁺11]  J. A. Carrillo, M. Di Francesco, A. Figalli, T. Laurent, and D. Slepčev. Global-in-time weak measure solutions and finite-time aggregation for non-

local interaction equations. *Duke Math. J.*, 156(2):229–271, 2011. (Cited on pages 5, 6, 74, 171, and 172).

[CDKS18]    J. A. Carrillo, B. Düring, L. M. Kreusser, and C.-B. Schönlieb. Stability analysis of line patterns of an anisotropic interaction model. *SIAM J. Appl. Dyn. Syst.*, 18(4):1798–1845, 2018. (Cited on pages xi, 27, 28, 75, 81, 107, 170, and 306).

[CDKS19]    J. A. Carrillo, B. Düring, L. M. Kreusser, and C.-B. Schönlieb. Equilibria of an anisotropic nonlocal interaction equation: Analysis and numerics. To be submitted, 2019. (Cited on pages xi, 27, 28, 167, and 306).

[CDM⁺96]    A. Colorni, M. Dorigo, F. Maffioli, V. Maniezzo, G. Righini, and M. Trubian. Heuristics from nature for hard combinatorial optimization problems. *Int. T. Oper. Res.*, 3(1):1–21, 1996. (Cited on page 18).

[CDM16]    J. A. Carrillo, M. G. Delgadino, and A. Mellet. Regularity of local minimizers of the interaction energy via obstacle problems. *Comm. Math. Phys.*, 343(3):747–781, 2016. (Cited on pages 6, 74, 171, and 172).

[CEMM00]    R. Cappelli, A. Erol, D. Maio, and D. Maltoni. Synthetic fingerprint-image generation. In *Proc. 15th Int. Conf. Pattern Recogn. (ICPR)*, pages 3–7, Barcelona, Spain, 2000. (Cited on page 70).

[CFF⁺12]    J. A. Carrillo, M. Di Francesco, A. Figalli, T. Laurent, and D. Slepčev. Confinement in nonlocal interaction equations. *Nonlinear Anal.*, 75(2):550–558, 2012. (Cited on pages 6, 74, and 171).

[CFP12]    J. A. Carrillo, L. C. F. Ferreira, and J. C. Precioso. A mass-transportation approach to a one dimensional fluid mechanics model with nonlocal velocity. *Adv. Math.*, 231(1):306–327, 2012. (Cited on pages 6, 74, and 171).

[CFP17]    J. A. Carrillo, A. Figalli, and F. S. Patacchini. Geometry of minimizers for the interaction energy with mildly repulsive potentials. *Ann. Inst. H. Poincaré Anal. Non Linéaire*, 34(5):1299–1308, 2017. (Cited on pages 7 and 172).

[CFRT10]    J. A. Carrillo, M. Fornasier, J. Rosado, and G. Toscani. Asymptotic Flocking Dynamics for the Kinetic Cucker–Smale Model. *SIAM J. Math. Anal.*, 42(1):218–236, 2010. (Cited on pages 2, 6, and 74).

[CFTV10]    J. A. Carrillo, M. Fornasier, G. Toscani, and F. Vecil. Particle, kinetic, and hydrodynamic models of swarming. In *Mathematical modeling of collective*

314

*behavior in socio-economic and life sciences*, Model. Simul. Sci. Eng. Technol., pages 297–336. Birkhäuser Boston, Inc., Boston, MA, 2010. (Cited on page 2).

[CH17]      J. A. Carrillo and Y. Huang. Explicit equilibrium solutions for the aggregation equation with power-law potentials. *Kinet. Relat. Models*, 10(1):171, 2017. (Cited on pages 7 and 172).

[CHM14a]    J. A. Carrillo, Y. Huang, and S. Martin. Explicit flock solutions for Quasi-Morse potentials. *European J. Appl. Math.*, 25(5):553–578, 2014. (Cited on pages 2 and 108).

[CHM14b]    J. A. Carrillo, Y. Huang, and S. Martin. Nonlinear stability of flock solutions in second-order swarming models. *Nonlinear Anal. Real World Appl.*, 17:332–343, 2014. (Cited on pages 2, 6, and 108).

[Cia78]     P.G. Ciarlet. *The Finite Element Method for Elliptic Problems*. Studies in Mathematics and its Applications. Elsevier Science, 1978. (Cited on pages 259 and 260).

[CJLV16]    J. A. Carrillo, F. James, F. Lagoutière, and N. Vauchelet. The filippov characteristic flow for the aggregation equation with mildly singular potentials. *J. Differential Equations*, 260(1):304–338, 2016. (Cited on pages 5, 7, 74, 171, 172, 173, 174, 192, and 196).

[CLMS16]    C. Champod, C. J. Lennard, P. Margot, and M. Stoilovic. *Fingerprints and Other Ridge Skin Impressions, Second Edition*. International Forensic Science and Investigation. CRC Press, 2016. (Cited on pages 3, 71, and 96).

[CMM⁺19]    J. A. Carrillo, J. Mateu, M. G. Mora, L. Rondi, L. Scardia, and J. Verdera. The equilibrium measure for an anisotropic nonlocal energy. Preprint, arXiv:1907.00417, 2019. (Cited on pages 7 and 52).

[CMV03]     J. A. Carrillo, R. J. McCann, and C. Villani. Kinetic equilibration rates for granular media and related equations: entropy dissipation and mass transportation estimates. *Rev. Math. Iberoam.*, 19:971–1018, 2003. (Cited on pages 5, 74, and 171).

[CMV06]     J. A. Carrillo, R. J. McCann, and C. Villani. Contractions in the 2-Wasserstein length space and thermalization of granular media. *Arch. Ration. Mech. Anal.*, 179(2):217–263, 2006. (Cited on pages 5, 74, and 171).

[Cor10]     F. Corson. Fluctuations and redundancy in optimal transport networks. *Phys. Rev. Lett.*, 104:048703, 2010. (Cited on pages 18 and 19).

[Cra56]     J. Crank. *The mathematics of diffusion*. Oxford Univ. Press, 1956. (Cited on page 276).

[CRP15]     M. Cieslak, A. Runions, and P. Prusinkiewicz. Auxin-driven patterning with unidirectional fluxes. *Journal of Experimental Botany*, 66(16):5083–5102, 2015. (Cited on page 272).

[CSW16]     J. A. Carrillo, D. Slepčev, and L. Wu. Nonlocal-interaction equations on uniformly prox-regular sets. *Discrete Contin. Dyn. Syst.*, 36(3):1209–1247, 2016. (Cited on page 7).

[DCBC06]     M. R. D'Orsogna, Y. L. Chuang, A. L. Bertozzi, and L. S. Chayes. Self-propelled particles with soft-core interactions: Patterns, stability, and collapse. *Phys. Rev. Lett.*, 96, 2006. (Cited on page 2).

[DGH+19]     B. Düring, C. Gottschlich, S. Huckemann, L. M. Kreusser, and C.-B. Schönlieb. An anisotropic interaction model for simulating fingerprints. *J. Math. Biol.*, 78(7):2171–2206, 2019. (Cited on pages xi, 27, 28, 69, 109, 158, 169, 170, 172, 197, 200, 201, and 306).

[DM86]     D. Dell and B. Munger. The early embryogenesis of papillary sweat duct ridges in primate glabrous skin: the dermatotopic map of cutaneous mechanoreceptors and dermatoglyphics. *J. Comp. Neurol.*, 244:511–532, 1986. (Cited on pages 3 and 71).

[DM93]     G. Dal Maso. *An Introduction to Γ-convergence*. Progress in nonlinear differential equations and their applications. Birkhäuser, 1993. (Cited on page 239).

[DM08]     P. Degond and S. Motsch. Large scale dynamics of the persistent turning walker model of fish behavior. *J. Stat. Phys.*, 131:989–1021, 2008. (Cited on page 2).

[DMIG96]     A. Delbarre, P. Muller, Viviane Imhoff, and Jean Guern. Comparison of mechanisms controlling uptake and accumulation of 2,4-dichlorophenoxy acetic acid, naphthalene-1-acetic acid, and indole-3-acetic acid in suspension-cultured tobacco cells. *Planta*, 198(4):532–541, 1996. (Cited on page 292).

[DSKT01]     A M. Delprato, A. Samadani, A. Kudrolli, and L. S. Tsimring. Swarming ring patterns in bacterial colonies exposed to ultraviolet radiation. *Phys. Rev. Lett.*, 87, 2001. (Cited on page 2).

[Dur06]     M. Durand. Architecture of optimal transport networks. *Phys. Rev. E*, 73:016116, 2006. (Cited on page 19).

[DZ06]     P. Dimitrov and S. W. Zucker. A constant production hypothesis guides leaf venation patterning. *Proc. Natl. Acad. Sci. USA*, 103(24):9363–9368, 2006. (Cited on page 272).

[EFR15]    J. H. M. Evers, R. C. Fetecau, and L. Ryzhik. Anisotropic interactions in a first-order aggregation model. *Nonlinearity*, 28(8):2847–2871, 2015. (Cited on pages 8, 9, and 74).

[EFS17]    J. H. M. Evers, R. C. Fetecau, and W. Sun. Small inertia regularization of an anisotropic aggregation model. *Math. Models Methods Appl. Sci.*, 27(10):1795–1842, 2017. (Cited on pages 9, 11, and 74).

[EKWG98]   L. Edelstein-Keshet, J. Watmough, and D. Grunbaum. Do travelling band solutions describe cohesive swarms? An investigation for migratory locusts. *J. Math. Biol.*, 36:515–549, 1998. (Cited on pages 2, 6, and 171).

[Erc97]    F. Ercolessi. A molecular dynamics primer. Spring College in Computational Physics, ICTP, 1997. (Cited on page 53).

[Eva10]    L. C. Evans. *Partial Differential Equations*. Grad. Stud. Math. Amer. Math. Soc., Providence, R.I., 2010. (Cited on pages 225, 294, 298, and 302).

[FFM15]    C. Feller, E. Farcot, and C. Mazza. Self-organization of plant vascular systems: Claims and counter-claims about the flux-based auxin transport model. *PLOS ONE*, 10(3):1–18, 2015. (Cited on page 272).

[FG15]     N. Fournier and A. Guillin. On the rate of convergence in Wasserstein distance of the empirical measure. *Probab. Theory Related Fields*, 162(3-4):707–738, 2015. (Cited on page 53).

[FHK11]    R.C. Fetecau, Y. Huang, and T. Kolokolnikov. Swarm dynamics and equilibria for a nonlocal aggregation model. *Nonlinearity*, 24:2681–2716, 2011. (Cited on pages 2, 7, and 172).

[FHT11]    M. Fornasier, J. Haskovec, and G. Toscani. Fluid dynamic description of flocking via the Povzner–Boltzmann equation. *Phys. D*, 240(1):21–31, 2011. (Cited on pages 6 and 74).

[FMI05]    F. G. Feugier, A. Mochizuki, and Y. Iwasa. Self-organization of the vascular system in plant leaves: Inter-dependent dynamics of auxin flux and carrier proteins. *J. Theoret. Biol.*, 236(4):366–375, 2005. (Cited on page 272).

[FR10]      K. Fellner and G. Raoul. Stable stationary states of non-local interaction equations. *Math. Models Methods Appl. Sci.*, 20(12):2267–2291, 2010. (Cited on pages 6, 74, and 171).

[FR11]      K. Fellner and G. Raoul. Stability of stationary states of non-local equations with singular interaction potentials. *Math. Comput. Modelling*, 53(7–8):1436–1450, 2011. Mathematical Methods and Modelling of Biophysical Phenomena. (Cited on pages 6, 74, and 171).

[FS15]      R. C. Fetecau and W. Sun. First-order aggregation models and zero inertia limits. *J. Differential Equations*, 259(11):6774–6802, 2015. (Cited on pages 11 and 15).

[Gal92]     F. Galton. *Finger Prints*. MacMillan, London, U.K., 1892. (Cited on page 72).

[GH14]      C. Gottschlich and S. Huckemann. Separating the real from the synthetic: Minutiae histograms as fingerprints of fingerprints. *IET Biometrics*, 3(4):291–301, 2014. (Cited on pages 70, 105, and 307).

[GMM09]     C. Gottschlich, P. Mihăilescu, and A. Munk. Robust orientation field estimation and extrapolation using semilocal line sensors. *IEEE Trans. Inf. Forensics Security*, 4(4):802–811, 2009. (Cited on pages 76, 96, and 105).

[Gol16]     F. Golse. *Macroscopic and Large Scale Phenomena: Coarse Graining, Mean Field Limits and Ergodicity*, chapter On the Dynamics of Large Particle Systems in the Mean Field Limit, pages 1–144. Springer International Publishing, Cham, 2016. (Cited on pages 15 and 53).

[Got12]     C. Gottschlich. Curved-region-based ridge frequency estimation and curved Gabor filters for fingerprint image enhancement. *IEEE Trans. Image Process.*, 21(4):2220–2227, 2012. (Cited on page 70).

[GS12]      C. Gottschlich and C.-B. Schönlieb. Oriented diffusion filtering for enhancing low-quality fingerprint images. *IET Biometrics*, 1(2):105–113, 2012. (Cited on page 96).

[GYZ13]     J. Gross, J. Yellen, and P. Zhang. *Handbook of Graph Theory*. CRC Press, 2nd edition, 2013. (Cited on pages 215 and 236).

[HB10]      Y. Huang and A. L. Bertozzi. Self-similar blowup solutions to an aggregation equation in $\mathbb{R}^n$. *SIAM J. Appl. Math.*, 70(7/8):2582–2603, 2010. (Cited on page 172).

[HB12]      Y. Huang and A. Bertozzi. Asymptotics of blowup solutions for the aggrega-
            tion equation. *Discrete Contin. Dyn. Syst. Ser. B*, 17(4):1309, 2012. (Cited
            on page 172).

[HC13]      D. Hu and D. Cai. Adaptation and Optimization of Biological Transport
            Networks. *Phys. Rev. Lett.*, 111:138701, 2013. (Cited on pages 19, 20, 21, 26,
            30, 206, 207, 208, 211, 229, 235, 236, 237, 240, 273, 274, 275, 276, and 278).

[HC14]      D. Hu and D. Cai. Private communication, 2014. (Cited on page 208).

[HCR12]     D. Hu, D. Cai, and W. Rangan. Blood vessel adaptation with fluctuations in
            capillary flow distribution. *PLoS ONE*, 7(9):1–13, 2012. (Cited on pages 19
            and 206).

[HHK+10]    M. G. Heisler, O. Hamant, P. Krupinski, M. Uyttewaal, C. Ohno,
            H. Jönsson, and et al. Alignment between pin1 polarity and microtubule
            orientation in the shoot apical meristem reveals a tight coupling between
            morphogenesis and auxin transport. *PLOS Biology*, 8(10):1–12, 2010. (Cited
            on pages 272 and 293).

[HHM08]     S. Huckemann, T. Hotz, and A. Munk. Global models for the orientation
            field of fingerprints: An approach based on quadratic differentials. *IEEE
            Trans. Pattern Anal. Mach. Intell.*, 30:1507–1519, 2008. (Cited on pages 76
            and 84).

[Hic73]     L. J. Hickey. Classification of the architecture of dicotyledonous leaves. *Am
            J Bot*, 60(1):17–33, 1973. (Cited on page 272).

[HJ15]      M. Hauray and P.E. Jabin. Particles approximations of Vlasov equations
            with singular forces: Propagation of chaos. *Ann. Sci. Ec. Norm. Super.*,
            48(4):891–940, 2015. (Cited on pages 13 and 14).

[HJKM19]    J. Haskovec, H. Jönsson, L. M. Kreusser, and P. A. Markowich. Auxin-PIN
            transport model for leaf venation. Preprint, arXiv:1901.03244, to appear in
            *Proc. R. Soc. A*, 2019. (Cited on pages xii, 27, 28, 271, and 307).

[HKM19a]    J. Haskovec, L. M. Kreusser, and P. A. Markowich. ODE- and PDE-based
            modeling of biological transportation networks. Preprint, arXiv:1805.08526,
            to appear in *Commun. Math. Sci.*, 2019. (Cited on pages xi, 27, 28, 205,
            238, 239, 240, and 307).

[HKM19b]    J. Haskovec, L. M. Kreusser, and P. A. Markowich. Rigorous Continuum
            Limit for the Discrete Network Formation Problem. *Comm. Partial Differ-
            ential Equations*, pages 1–27, 2019. (Cited on pages xi, 27, 28, 235, and 307).

[HL09]       S.-Y. Ha and J.-G. Liu. A simple proof of the cucker-smale flocking dynamics and mean-field limit. *Commun. Math. Sci.*, 7:297–325, 2009. (Cited on pages 6 and 74).

[HMP15]      J. Haskovec, P. Markowich, and B. Perthame. Mathematical analysis of a PDE system for biological network formation. *Comm. Partial Differential Equations*, 40(5):918–956, 2015. (Cited on pages 22, 24, 206, 224, 225, 226, 227, 239, 240, and 250).

[HMPS16]     J. Haskovec, P. Markowich, B. Perthame, and M. Schlottbom. Notes on a PDE system for biological network formation. *Nonlinear Anal.*, 138:127–155, 2016. (Cited on pages 22, 24, 25, 206, 224, 239, 240, and 250).

[HMR18]      J. Haskovec, P. Markowich, and H. Ranetbauer. A mesoscopic model of biological transportation networks. Preprint, arXiv:1806.00120, 2018. (Cited on page 237).

[HT08]       S.-Y. Ha and E. Tadmor. From particle to kinetic and hydrodynamic descriptions of flocking. *Kinet. Relat. Models*, 1:415–435, 2008. (Cited on pages 6 and 74).

[Hu13]       D. Hu. Optimization, Adaptation, and Initialization of Biological Transport Networks. Notes from lecture, 2013. (Cited on pages 19, 22, 206, and 240).

[IGHO18]     C. Imdahl, C. Gottschlich, S. Huckemann, and K. Ohshika. Möbius moduli for fingerprint orientation fields. *J. Math. Imaging Vision*, 60:651–660, 2018. (Cited on pages 105 and 307).

[IHG15]      C. Imdahl, S. Huckemann, and C. Gottschlich. Towards generating realistic synthetic fingerprint images. In *Proc. ISPA*, pages 78–82, Zagreb, Croatia, 2015. (Cited on page 70).

[Irm10]      M. K. Irmak. Multifunctional merkel cells: their roles in electromagnetic reception, fingerprint formation, reiki, epigenetic inheritance and hair form. *Med. Hypotheses*, 75:162–168, 2010. (Cited on pages 3, 9, 70, and 71).

[Jab14]      P.-E. Jabin. A review of the mean field limits for vlasov equations. *Kinet. Relat. Models*, 7(4):661–711, 2014. (Cited on page 13).

[JHS+06]     H. Jönsson, M. G. Heisler, B. E. Shapiro, E. M. Meyerowitz, and E. Mjolsness. An auxin-driven polarized transport model for phyllotaxis. *Proc. Natl. Acad. Sci. USA*, 103(5):1633–1638, 2006. (Cited on page 272).

[JPP02]   A. K. Jain, S. Prabhakar, and S. Pankanti. On the similarity of identical twin fingerprints. *Pattern Recognition*, 35(11):2653–2663, 2002. (Cited on page 72).

[JV13]    F. James and N. Vauchelet. Chemotaxis: from kinetic equations to aggregate dynamics. *NoDEA Nonlinear Differential Equations Appl.*, 20(1):101–127, 2013. (Cited on page 172).

[JV15]    F. James and N. Vauchelet. Numerical methods for one-dimensional aggregation equations. *SIAM J. Numer. Anal.*, 53:895–916, 2015. (Cited on page 172).

[JW16]    P. E. Jabin and Z. Wang. Mean Field Limit and Propagation of Chaos for Vlasov Systems with Bounded Forces. *J. Funct. Anal.*, 271(12):3588–3627, 2016. (Cited on page 13).

[KBT84]   A. Kamiya, R. Bukhari, and T. Togawa. Adaptive regulation of wall shear stress optimizing vascular tree function. *Bull. Math. Biol.*, 46(1):127–137, 1984. (Cited on page 19).

[KC13]    M. Kücken and C. Champod. Merkel cells and the individuality of friction ridge skin. *J. Theoret. Biol.*, 317:229–237, 2013. (Cited on pages 2, 3, 4, 9, 15, 16, 40, 70, 71, 72, 73, 74, 75, 76, 77, 80, 87, 95, 108, 109, 110, 112, 168, 169, 170, and 197).

[KCB+13]  T. Kolokolnikov, J. A. Carrillo, A. Bertozzi, R. Fetecau, and M. Lewis. Emergent behaviour in multi-particle systems with non-local interactions [Editorial]. *Phys. D*, 260:1–4, 2013. (Cited on pages 2 and 108).

[KH95]    D.-K. Kim and K. A. Holbrook. The appearance, density, and distribution of merkel cells in human embryonic and fetal skin: Their relation to sweat gland and hair follicle development. *Journal of Investigative Dermatology*, 104(3):411–416, 1995. (Cited on pages 4, 9, 73, and 168).

[KHP13]   T. Kolokolnikov, Y. Huang, and M. Pavlovski. Singular patterns for an aggregation model with a confining potential. *Phys. D*, 260:65–76, 2013. (Cited on page 172).

[KM94]    A. J. Koch and H. Meinhardt. Biological pattern-formation—from basic mechanisms to complex structures. *Rev. Mod. Phys.*, 66:1481, 1994. (Cited on page 71).

[KM10]     S. Kondo and T. Miura. Reaction-diffusion model as a framework for understanding biological pattern formation. *Science*, 329 5999:1616–20, 2010. (Cited on page 71).

[KM17]     L. M. Kreusser and P. A. Markowich. Discrete and continuum modeling of biological network formation. In *SIAM Workshop on Network Science (NS17)*, 2017. (Cited on page 27).

[KMT15]    T. K. Karper, A. Mellet, and K. Trivisa. Hydrodynamic limit of the kinetic cucker–smale flocking model. *Math. Models Methods Appl. Sci.*, 25(01):131–163, 2015. (Cited on pages 6 and 74).

[KN04]     M. Kücken and A. Newell. A model for fingerprint formation. *Europhysics Letters*, 68:141–146, 2004. (Cited on pages 4, 16, and 71).

[KN05]     M. Kücken and A. Newell. Fingerprint formation. *J. Theoret. Biol.*, 235:71–83, 2005. (Cited on pages 4, 16, and 71).

[Kra04]    E. M. Kramer. Pin and aux/lax proteins: their role in auxin accumulation. *Trends Plant Sci*, 9(12):578–582, 2004. (Cited on page 277).

[Kra09]    E. M. Kramer. Auxin-regulated cell polarity: an inside job? *Trends Plant. Sci.*, 14(5):242–247, 2009. (Cited on page 272).

[Kre18]    L. M. Kreusser. Analysis of Anisotropic Interaction Equations for Fingerprint Simulations. In *PAMM. Proc. Appl. Math. Mech.*, 2018. (Cited on page 27).

[KSmHM10]  E. Katifori, G. J. Szöllősi, and M. O. Magnasco. Damage and fluctuations induce loops in optimal transport networks. *Phys. Rev. Lett.*, 104:048704, 2010. (Cited on pages 18 and 19).

[KSUB11]   T. Kolokolnikov, H. Sun, D. Uminsky, and A. L. Bertozzi. Stability of ring patterns arising from two-dimensional particle interactions. *Phys. Rev. E*, 84(1):015203, 2011. (Cited on pages 2, 5, 6, 108, 171, and 172).

[Lau07]    T. Laurent. Local and global existence for an aggregation equation. *Comm. Partial Differential Equations*, 32:1941–1964, 2007. (Cited on pages 5 and 171).

[LBJ08]    M. Laguna, S. Bohn, and E. Jagla. The role of elastic stresses on leaf venation morphogenesis. *PLOS Comput. Biol.*, 4:e1000055, 2008. (Cited on page 19).

[Lio84]     P.-L. Lions. The concentration-compactness principle in the calculus of variations. the locally compact case, part 1. *Ann. Inst. H. Poincaré Anal. Non Linéaire*, 1(2):109–145, 1984. (Cited on page 181).

[Lov12]     L. Lovász. *Large Networks and Graph Limits*, volume 60. Amer. Math. Soc., Providence, R.I., 2012. (Cited on page 291).

[LT04]      H. Li and G. Toscani. Long-time asymptotics of kinetic models of granular flows. *Arch. Ration. Mech. Anal.*, 172(3):407–428, 2004. (Cited on pages 5, 74, and 171).

[LXXZ18]    C. Liu, T. Xu, L.-P. Xu, and X. Zhang. Controllable swarming and assembly of micro/nanomachines. *Micromachines*, 9(1), 2018. (Cited on page 3).

[MEB⁺17]    S. A.M. McAdam, M. P. Eléouët, M. Best, T. J. Brodribb, M. C. Murphy, S. D. Cook, M. Dalmais, T. Dimitriou, A. Gélinas-Marion, W. M. Gill, M. Hegarty, J. M. I. Hofer, M. Maconochie, E. L. McAdam, P. McGuiness, D. S. Nichols, J. J. Ross, F. C. Sussmilch, and S. Urquhart. Linking auxin with photosynthetic rate via leaf venation. *Plant Physiology*, 175(1):351–360, 2017. (Cited on page 273).

[Mei82]     H. Meinhardt. *Models of Biological Pattern Formation*. Academic Press, 1982. (Cited on page 71).

[MEK99]     A. Mogilner and L. Edelstein-Keshet. A non-local model for a swarm. *J. Math. Biol.*, 38:534–570, 1999. (Cited on pages 2, 6, 168, and 171).

[MEKBS03]   A. Mogilner, L. Edelstein-Keshet, L. Bent, and A. Spiros. Mutual interactions, potentials, and individual distance in a social aggregation. *J. Math. Biol.*, 47(4):353–389, 2003. (Cited on pages 6, 108, and 171).

[MHS81]     G. J. Mitchison, D. E. Hanke, and A. R. Sheldrake. The polar transport of auxin and vein patterns in plants [and discussion]. *Philos. Trans. Roy. Soc. B*, 295(1078):461–471, 1981. (Cited on pages 272, 273, 278, and 279).

[Mit80]     G. J. Mitchison. A model for vein formation in higher plants. *Proc. R. Soc. B*, 207(1166):79–109, 1980. (Cited on pages 272, 273, 274, 276, 278, and 279).

[MJM92]     K. Morohunfola, T. Jones, and B. Munger. The differentiation of the skin and its appendages - normal development of the papillary ridges. *Anat. Rec.*, 232:587–598, 1992. (Cited on pages 3 and 71).

[MM89]     S. Moore and B. Munger. The early ontogeny of the afferent nerves and papillary ridges in human digital glabrous skin. *Dev. Brain. Res.*, 48:119–141, 1989. (Cited on pages 3 and 71).

[MMJP09]   D. Maltoni, D. Maio, A. K. Jain, and S. Prabhakar. *Handbook of Fingerprint Recognition*. Springer Publishing Company, Incorporated, 2nd edition, 2009. (Cited on page 72).

[MP18]     P. B. Mucha and J. Peszek. The Cucker–Smale equation: Singular communication weight, measure solutions and weak-atomic uniqueness. *Arch. Ration. Mech. Anal.*, 227(1):273–308, 2018. (Cited on page 13).

[MRS19]    M. G. Mora, L. Rondi, and L. Scardia. The Equilibrium Measure for a Nonlocal Dislocation Energy. *Comm. Pure Appl. Math.*, 72(1):136–158, 2019. (Cited on pages 7 and 52).

[MT14]     S. Motsch and E. Tadmor. Heterophilious dynamics enhances consensus. *SIAM Rev.*, 56(4):577–621, 2014. (Cited on page 7).

[Mur26a]   C. D. Murray. The Physiological Principle of Minimum Work: I. The Vascular System and the Cost of Blood Volume. *Proc. Natl. Acad. Sci. USA*, 12(3):207–214, 1926. (Cited on pages 21, 237, and 282).

[Mur26b]   C. D. Murray. The Physiological Principle of Minimum Work: II. Oxygen Exchange in Capillaries. *Proc. Natl. Acad. Sci. USA*, 12(5):299–304, 1926. (Cited on page 282).

[ND97]     T. Nelson and N. Dengler. Leaf vascular pattern formation. *The Plant Cell*, 9:1121–1135, 1997. (Cited on page 19).

[Nij18]    H. F. Nijhout. *Pattern Formation In The Physical And Biological Sciences*. CRC Press, 2018. (Cited on page 95).

[NPS01]    J. Nieto, F. Poupaud, and J. Soler. High-field limit for the Vlasov-Poisson-Fokker-Planck system. *Arch. Ration. Mech. Anal.*, 158:29–59, 2001. (Cited on page 15).

[NW06]     J. Nocedal and S. J. Wright. *Numerical Optimization*. Springer, New York, NY, USA, 2nd edition, 2006. (Cited on page 229).

[OL01]     A. Okubo and S.A. Levin. *Interdisciplinary Applied Mathematics: Mathematical Biology*, chapter Diffusion and Ecological Problems, pages 197–237. Springer, New York, 2001. (Cited on pages 6, 108, and 171).

[PEK99]     J. K. Parrish and L. Edelstein-Keshet. Complexity, Pattern, and Evolution-
            ary Trade-Offs in Animal Aggregation. *Science*, 284:99–101, 1999. (Cited
            on page 2).

[Pel]       M. A. Peletier. Variational modelling: Energies, gradient flows, and large
            deviations. Lecture Notes, Würzburg. Available at `http://www.win.tue.`
            `nl/~mpeletie/`. (Cited on page 210).

[PHBB86]    U. Pohl, J. Holtz, R. Busse, and E. Bassenge. Crucial role of endothelium
            in the vasodilator response to increased flow in vivo. *Hypertension*, 8:37–44,
            1986. (Cited on page 19).

[PKTG12]    R. Phillips, J. Kondev, J. Theriot, and H. Garcia. *Physical Biology of the
            Cell*. CRC Press, 2012. (Cited on page 78).

[PS84]      I. Prigogine and I. Stenger. *Order out of Chaos*. Bantam Books, New York,
            1984. (Cited on page 2).

[PS17]      D. Poyato and J. Soler. Euler-type equations and commutators in singular
            and hyperbolic limits of kinetic Cucker-Smale models. *Math. Models Methods
            Appl. Sci.*, 27(06):1089–1152, 2017. (Cited on page 13).

[PSF⁺12]    B. Péret, K. Swarup, A. Ferguson, M. Seth, Y. Yang, S. Dhondt, N. James,
            I. Casimiro, and et al. Aux/lax genes encode a family of auxin influx trans-
            porters that perform distinct functions during arabidopsis development. *The
            Plant Cell*, 24(7):2874–2885, 2012. (Cited on page 277).

[PV10]      M. A. Peletier and M. Veneroni. Stripe patterns in a model for block copoly-
            mers. *Math. Models Methods Appl. Sci.*, 20:843–907, 2010. (Cited on page 7).

[Rao12]     G. Raoul. Non-local interaction equations: Stationary states and stabil-
            ity analysis. *Differential Integral Equations*, 25:417–440, 2012. (Cited on
            pages 6, 74, and 171).

[RFL⁺05]    A. Runions, M. Fuhrer, B. Lane, P. Federl, A.-G. Rolland-Lagan, and
            P. Prusinkiewicz. Modeling and visualization of leaf venation patterns. *ACM
            Trans. Graph.*, 24:702–711, 2005. (Cited on pages 18 and 206).

[Rou13]     T. Roubíček. *Nonlinear Partial Differential Equations with Applications*.
            International Series of Numerical Mathematics 153. Springer Basel, 2013.
            (Cited on pages 296 and 299).

[RP05]    A.-G. Rolland-Lagan and P. Prusinkiewicz. Reviewing models of auxin canalization in the context of leaf vein pattern formation in arabidopsis. *The Plant Journal*, 44(5):854–865, 2005. (Cited on page 272).

[Sac69]   T. Sachs. Polarity and the induction of organized vascular tissues. *Ann Bot*, 33(2):263–275, 1969. (Cited on page 272).

[Sac81]   T. Sachs. The control of the patterned differentiation of vascular tissues. volume 9 of *Advances in Botanical Research*, pages 151–262. Academic Press, 1981. (Cited on pages 272, 273, and 277).

[SES13]   M. G. Sawchuk, A. Edgar, and E. Scarpella. Patterning of leaf vein networks by convergent auxin transport pathways. *PLOS Genetics*, 9(2):1–13, 2013. (Cited on page 272).

[SGM$^+$06]   R. S. Smith, S. Guyomarc'h, T. Mandel, D. Reinhardt, C. Kuhlemeier, and P. Prusinkiewicz. A plausible model of phyllotaxis. *Proc. Natl. Acad. Sci. USA*, 103(5):1301–1306, 2006. (Cited on page 272).

[SH77]    J. Swift and P. C. Hohenberg. Hydrodynamic fluctuations at the convective instability. *Phys. Rev. A*, 15:319–328, 1977. (Cited on page 71).

[She81]   T. F. Sherman. On connecting large vessels to small: The meaning of murray's law. *The Journal of General Physiology*, 78(4):431–453, 1981. (Cited on page 282).

[Sim14]   R. Simione. *Properties of Minimizers of Nonlocal Interaction Energy*. ProQuest LLC, Ann Arbor, MI, 2014. Thesis (Ph.D.)–Carnegie Mellon University. (Cited on page 122).

[SLT$^+$15]   N. Stoop, R. Lagrange, D. Terwagne, P. M. Reis, and J. Dunkel. Curvature-induced symmetry breaking determines elastic surface patterns. *Nature Materials*, 14:337–342, 2015. (Cited on page 71).

[SMFB06]   E. Scarpella, D. Marcos, J. Friml, and T. Berleth. Control of leaf vascular patterning by polar auxin transport. *Genes & development*, 20(8):1015–1027, 2006. (Cited on pages 272 and 277).

[SR97]    L. F. Shampine and M. W. Reichelt. The matlab ode suite. *SIAM J. Sci. Comput.*, 18:1–22, 1997. (Cited on page 283).

[SS13]    M. G. Sawchuk and E. Scarpella. Control of vein patterning by intracellular auxin transport. *Plant Signaling & Behavior*, 8(11):e27205, 2013. PMID: 24304505. (Cited on pages 272 and 277).

[SSF06]     S. N. Srihari, H. Srinivasan, and G. Fang. Discriminability of fingerprints of twins. 2006. (Cited on page 72).

[SST15]     R. Simione, D. Slepčev, and I. Topaloglu. Existence of ground states of nonlocal-interaction energies. *J. Stat. Phys.*, 159(4):972–986, 2015. (Cited on pages 171, 181, and 184).

[ST17]      R. Shvydkoy and E. Tadmor. Eulerian dynamics with a commutator forcing. *Trans. Mathematics and Applications*, 1(1):1–26, 2017. (Cited on page 13).

[Str00]     M. Struwe. *Variational Methods: Applications to Nonlinear Partial Differential Equations and Hamiltonian Systems*, volume 34 of *A Series of Modern Surveys in Mathematics*. Springer-Verlag Berlin Heidelberg, 2000. (Cited on page 181).

[TB04]      C. M. Topaz and A. L. Bertozzi. Swarming patterns in a two-dimensional kinematic model for biological groups. *SIAM J. Appl. Dyn. Syst.*, 65:152–174, 2004. (Cited on page 2).

[TBL06]     C. M. Topaz, A. L. Bertozzi, and M. A. Lewis. A nonlocal continuum model for biological aggregation. *Bull. Math. Biol.*, 68(7):1601–1623, 2006. (Cited on pages 2 and 168).

[TCYT12]    X. Tao, X. Chen, X. Yang, and J. Tian. Fingerprint recognition with identical twin fingerprints. *PLOS ONE*, 7(4):1–7, 2012. (Cited on page 72).

[TTS+10]    A. Tero, S. Takagi, T. Saigusa, K. Ito, D. P. Bebber, M. D. Fricker, K. Yumiki, R. Kobayashi, and T. Nakagaki. Rules for biologically inspired adaptive network design. *Science*, 327(5964):439–442, 2010. (Cited on page 18).

[Tur52]     A. M. Turing. The Chemical Basis of Morphogenesis. *Philos. Trans. Roy. Soc. B*, 237:37–72, 1952. (Cited on pages 63 and 65).

[Tur91]     G. Turk. Generating textures on arbitrary surfaces using reaction-diffusion. In *Proceedings of the 18th Annual Conference on Computer Graphics and Interactive Techniques*, SIGGRAPH '91, pages 289–298, New York, NY, USA, 1991. ACM. (Cited on page 71).

[vBU12]     J. H. von Brecht and D. Uminsky. On soccer balls and linearized inverse statistical mechanics. *J. Nonlinear Sci.*, 22(6):935–959, 2012. (Cited on pages 6, 7, 74, 108, 171, and 172).

[vBUKB12]   J. H. von Brecht, D. Uminsky, T. Kolokolnikov, and A. L. Bertozzi. Predicting pattern formation in particle interactions. *Math. Models Methods*

*Appl. Sci.*, 22(supp01):1140002, 2012. (Cited on pages 2, 6, 7, 74, 108, 171, and 172).

[vdVW96]  A. W. van der Vaart and J. A. Wellner. *Weak Convergence and Empirical Process: With Applications to Statistics.* Springer Series in Statistics. Springer, 1996. (Cited on page 183).

[Ver05]  F. Verhulst. *Methods and Applications of Singular Perturbations. Boundary Layers and Multiple Timescale Dynamics.* Springer, 2005. (Cited on page 11).

[Vil03]  C. Villani. *Topics in optimal transportation.* Grad. Stud. Math. Amer. Math. Soc., Providence (R.I.), 2003. (Cited on pages 5, 74, and 171).

[Wer11]  K. Wertheim. Embryology and morphology of friction ridge skin. In *Fingerprint Sourcebook*, chapter 3. National Institute of Justice (NIJ), USA, 2011. (Cited on pages 3 and 71).

[WK91]  A. Witkin and M. Kass. Reaction-diffusion textures. In *Proceedings of the 18th Annual Conference on Computer Graphics and Interactive Techniques*, SIGGRAPH '91, pages 299–308, New York, NY, USA, 1991. ACM. (Cited on page 71).

[WS15]  L. Wu and D. Slepčev. Nonlocal interaction equations in environments with heterogeneities and boundaries. *Comm. Partial Differential Equations*, 40(7):1241–1281, 2015. (Cited on page 7).

[YDG+00]  G. D. Yancopoulos, S. Davis, N. W. Gale, J. S. Rudge, S. J. Wiegand, and J. Holash. Vascular-specific growth factors and blood vessel formation. *Nature*, 407:242–248, 2000. (Cited on pages 18 and 206).

[YJ15]  S. Yoon and A. K. Jain. Longitudinal study of fingerprint recognition. *Proc. Natl. Acad. Sci. USA*, 112(28):8555–8560, 2015. (Cited on page 72).